Multichannel Analysis of Surface Waves for Soil Site Characterization

Elín Ásta Ólafsdóttir

Faculty of Civil and Environmental Engineering
University of Iceland
2019

MULTICHANNEL ANALYSIS OF SURFACE WAVES FOR SOIL SITE CHARACTERIZATION

Elín Ásta Ólafsdóttir

Dissertation submitted in partial fulfillment of a
Philosophiae Doctor Degree in Civil Engineering

Ph.D. Committee
Dr. Bjarni Bessason
Dr. Sigurður Erlingsson
Dr. Amir M. Kaynia

Opponents
Dr. Steinar Nordal
Dr. Sebastiano Foti

Faculty of Civil and Environmental Engineering
School of Engineering and Natural Sciences
University of Iceland
Reykjavik, November 2019

Multichannel Analysis of Surface Waves for Soil Site Characterization
MASW for Soil Site Characterization
Dissertation submitted in partial fulfillment of a *Philosophiae Doctor* degree in Civil Engineering

Faculty of Civil and Environmental Engineering
School of Engineering and Natural Sciences
University of Iceland
Hjarðarhagi 2-6
107 Reykjavik
Iceland

Telephone: 525 4000

Bibliographic information:
Elín Ásta Ólafsdóttir, 2019, *Multichannel Analysis of Surface Waves for Soil Site Characterization*, Ph.D. dissertation, Faculty of Civil and Environmental Engineering, University of Iceland, 308 pp.

ISBN: 978-9935-9473-9-0
Author ORCID: 0000-0002-9166-8406

Printing: Háskólaprent, Fálkagata 2, 107 Reykjavík
Reykjavik, Iceland, November 2019

Abstract

Shear wave velocity (V_S) is a fundamental parameter in soil dynamics and geotechnical earthquake engineering. The Multichannel Analysis of Surface Waves (MASW) method is a relatively new non-invasive technique to evaluate the near-surface shear wave velocity profile by utilizing the dispersive properties of surface waves in a heterogeneous medium. The method is both time and cost efficient and can be applied at a wide variety of soil sites, including locations where conventional invasive techniques are difficult to apply.

The main objectives of the project were (i) to develop an open software to acquire, process and analyse MASW field data, (ii) to validate and calibrate field observations by comparison with results obtained by other measurement techniques and alternative software packages, and (iii) to implement and adapt MASW for analysis of the stiffness properties of Icelandic soil sites and man-made fillings.

Alongside software development, an effort has been made to develop methods for combining dispersion curves from a number of records gathered at a given site, with the aim of increasing the range in investigated depths, get more reliable results, and assess experimental uncertainties. Furthermore, a simple but effective Monte Carlo-based technique has been developed for use in the MASW inversion analysis.

To date, MASW has been applied at over twenty natural locations in Iceland, ranging from sites characterized by peat and loosely compacted sand to cemented soil materials and soft rock. Where available, the results were compared to existing measurements. The method has also been successively applied for analysis of earth dams. In order to benchmark results obtained by the new software, field measurements were carried out at Norway's National GeoTest Sites. The shear wave velocity profiles obtained by the new software (MASWaves) agreed well with results of existing measurements, thus verifying the performance of the set of data acquisition and analysis tools.

Útdráttur

Þekking á jarðtæknilegum eiginleikum setlaga og jarðvegsfyllinga, svo sem þykkt og stífni einstakra laga, er mikilvæg í jarðtæknilegri hönnun og jarðtæknilegri jarðskjálftaverkfræði. Fjölnemagreining á yfirborðsbylgjum (MASW) er nýleg aðferð sem byggir á tvístrunareiginleikum yfirborðsbylgna og tengslum milli útbreiðsluhraða þeirra og fjaðureiginleika jarðvegs. Yfirborðsbylgjur eru framkallaðar með höggi á yfirborð jarðar og útbreiðsla þeirra er mæld. Mæligögnin eru, ásamt eðlisfræðilegu reiknilíkani, notuð til að ákvarða skúfbylgjuhraða sem fall af dýpi. MASW mælingar eru hagkvæmar og fljótlegar í framkvæmd og valda ekki raski. Þá hentar MASW vel í grófum jarðvegi þar sem erfitt eða ómögulegt er að þrýsta niður kónískum nemum.

Meginmarkmið þessa verkefnis voru að (i) þróa opinn hugbúnað fyrir feltmælingar og úrvinnslu mæligagna, (ii) sannreyna niðurstöður með samanburði við mælingar sem framkvæmdar hafa verið af óháðum rannsakendum og (iii) aðlaga og þróa MASW til mælinga á íslenskum jarðvegi.

Samhliða gerð hugbúnaðar hefur verið þróuð aðferðafræði til að flétta saman tvístrunarferla, sem ákvarðaðir hafa verið með endurteknum höggum á yfirborð jarðar, með það fyrir augum að auka könnunardýpi MASW aðferðarinnar, meta gæði mæligagna og áætla óvissu í afleiddum stærðum. Líkan til bakreikninga á skúfbylgjuhraða, sem byggt er á Monte Carlo hermun, hefur einnig verið þróað.

Til þessa hafa MASW mælingar verið framkvæmdar á rúmlega tuttugu náttúrlegum stöðum hérlendis, auk þess sem mælingar hafa verið gerðar á jarðstíflum með góðum árangri. Enn fremur voru MASW mælingar framkvæmdar á prófunarstöðum í Noregi þar sem erlendir rannsóknahópar hafa mælt skúfbylgjuhraða með fjölda annarra aðferða. Niðurstöðum mælinga ber mjög vel saman við fyrirliggjandi niðurstöður. Því má ályktа að aðferðafræðin og sá hugbúnaður sem hefur verið þróaður (MASWaves) skili áreiðanlegum niðurstöðum.

List of Publications

This dissertation is based on work presented in papers published in or submitted to International Scientific Indexing (ISI) journals and peer-reviewed proceedings of major international conferences within the fields of Geotechnical Engineering and Earthquake Engineering. The papers will be referenced in the text by their Roman numbers.

Paper I
Ólafsdóttir, E. Á., Erlingsson, S., & Bessason, B. (2018). Tool for analysis of multichannel analysis of surface waves (MASW) field data and evaluation of shear wave velocity profiles of soils. *Canadian Geotechnical Journal, 55*(2), 217–233. doi:10.1139/cgj-2016-0302. [Open access]

Paper II
Ólafsdóttir, E. Á., Bessason, B., & Erlingsson, S. (2018). Combination of dispersion curves from MASW measurements. *Soil Dynamics and Earthquake Engineering, 113*, 473–487. doi:10.1016/j.soildyn.2018.05.025. [Open access]

Paper III
Ólafsdóttir, E. Á., Erlingsson, S., & Bessason, B. (2019). Shear wave velocity profiles from MASW inversion analysis using a simple Monte Carlo search technique for geotechnical engineering applications. *Soil Dynamics and Earthquake Engineering.* (Resubmitted.)

Paper IV
Ólafsdóttir, E. Á., Bessason, B., Erlingsson, S., & Kaynia, A. M. (2019). Verification of an open-source MASW software at Norwegian geo-test sites. *Journal of Geotechnical and Geoenvironmental Engineering.* (Submitted.)

Paper V
Ólafsdóttir, E. Á., Erlingsson, S., & Bessason, B. (2018). Open software for analysis of MASW data. In *Proceedings of the 16th European Conference on Earthquake Engineering*, 18–21 June 2018, Thessaloniki, Greece. (Paper no. 11168).

Paper VI
Ólafsdóttir, E. Á., Bessason, B., & Erlingsson, S. (2019). Application of MASW in the South Iceland Seismic Zone. In R. Rupakhety, S. Ólafsson, & B. Bessason (Eds.), *Proceedings of the International Conference on Earthquake Engineering and Structural*

Dynamics. Geotechnical, Geological and Earthquake Engineering, Vol. 47 (pp. 53–66). Cham, Switzerland: Springer. doi:10.1007/978-3-319-78187-7_5.

Paper VII
Ólafsdóttir, E. Á., Erlingsson, S., & Bessason, B. (2019). Open source MASW software and results from Icelandic soil sites. In *Proceedings of the 17th European Conference on Soil Mechanics and Geotechnical Engineering*, 1–6 September 2019, Reykjavík, Iceland. doi:10.32075/17ECSMGE-2019-0771.

Paper VIII
Ólafsdóttir, E. Á., Bessason, B., & Erlingsson, S. (2019). Stiffness profiles of earth dams based on the MASW technique. In *Proceedings of the 17th European Conference on Soil Mechanics and Geotechnical Engineering*, 1–6 September 2019, Reykjavík, Iceland. doi:10.32075/17ECSMGE-2019-0788.

Peer-reviewed conference publications not included in this dissertation:

Ólafsdóttir, E. Á., Bessason, B., Erlingsson, S., L'Heureux, J.-S., & Bazin, S. (2019). Benchmarking of an open-source MASW software using data from three Norwegian GeoTest Sites. In *Proceedings of the 17th European Conference on Soil Mechanics and Geotechnical Engineering*, 1–6 September 2019, Reykjavík, Iceland. doi:10.32075/17ECSMGE-2019-0772.

Erlingsson, S., Ólafsdóttir E. Á., & Bessason, B. (2017). Stiffness of sandy sites using the Multichannel Analysis of Surface Waves method. In *Proceedings of the 19th International Conference on Soil Mechanics and Geotechnical Engineering*, 17–22 September 2017, Seoul, South Korea (pp. 593–598).

Ólafsdóttir, E. Á., Erlingsson, S., & Bessason, B. (2016). Effects of measurement profile configuration on estimation of stiffness profiles of loose post glacial sites using MASW. In *Proceedings of the 17th Nordic Geotechnical Meeting*, 25–28 May 2016, Reykjavík, Iceland (pp. 327–336).

Ólafsdóttir, E. Á., Bessason, B., & Erlingsson, S. (2015). MASW for assessing liquefaction of loose sites. In *Proceedings of the 16th European Conference on Soil Mechanics and Geotechnical Engineering*, 13–17 September 2015, Edinburgh, Scotland (Vol. 5, pp. 2431–2436). doi:10.1680/ecsmge.60678.vol5.373.

Contents

List of Figures

List of Tables

Notation and symbols

Roman letters

a	Model parameter [Eq. (3.29)].
a	Model parameter [Eq. (3.86)].
$\mathbf{a}_i$	Amplitude vector.
a_i, a_i'	Layer parameters.
a_{max}	Peak ground acceleration.
$\hat{a}$	Acceleration parameter (BCa confidence intervals).
A	Correlation parameter for empirical estimates of G_{max}.
$A(x, \omega)$	Amplitude spectrum of $\tilde{u}(x, \omega)$.
$\mathbf{A}(z)$	Coefficient matrix for Rayleigh wave propagation in a vertically heterogeneous elastic medium.
A_i	Compressional wave up amplitude.
A_i'	Compressional wave down amplitude.
$A_j(\omega)$	Amplitude spectrum of $\tilde{u}_j(\omega)$.
$A_s(\omega, V_R)$	Summed (slant-stacked) amplitude for angular frequency ω and Rayleigh wave phase velocity V_R.
$A_{s,norm}(\omega, V_R)$	Normalized summed (slant-stacked) amplitude for angular frequency ω and Rayleigh wave phase velocity V_R.
b	Search-control parameter.
b_h	Layer thickness search-control parameter.
b_i, b_i'	Layer parameters.
b_S	Shear wave velocity search-control parameter.
B	Number of bootstrap samples.
B_i	Vertical shear wave up amplitude.
B_i'	Vertical shear wave down amplitude.
c	Rayleigh wave phase velocity.
C	Cementation.
d	Depth.
dt	Sampling interval.
dx	Receiver spacing.
D_i	Parameter used for computation of the element stiffness matrix of the i-th layer $\mathbf{K}_{e,i}$ [Eq. (3.64)].

e	Void ratio.
$\hat{\mathbf{e}}_z$	Unit vector along the z-axis.
$\mathbf{E}_i(z)$	Rayleigh wave eigenfunction matrix for the i-th layer.
E_{max}	Small-strain modulus of elasticity.
f	Frequency.
$f(e)$	Function of void ratio.
$f(z)$, $g(z)$	Functions describing Rayleigh wave amplitude variation in a homogeneous medium.
f_s	Sampling rate.
F	Probability distribution.
$\mathbf{F}_i$	$\mathbf{Z}_i\mathbf{E}_i\mathbf{Z}_i^{-1}$.
F_r	Normalized friction ratio.
$F_R(\ )$	Dispersion function.
$\hat{F}$	Empirical probability distribution.
$G(z)$	Small-strain shear modulus of a vertically heterogeneous elastic medium.
G_i	Small-strain shear modulus of the i-th layer.
G_{max}	Small-strain shear modulus (G).
$\mathbf{h}$	Layer thickness vector.
h_i	Thickness of the i-th layer.
$\mathbf{h_{test}}$	Testing layer thickness vector.
$h_{test,i}$	Testing layer thickness of the i-th layer.
$\mathbf{H}_{11,i}$, $\mathbf{H}_{12,i}$	Sub-matrices of $\mathbf{H}_i$.
$\mathbf{H}_{21,i}$, $\mathbf{H}_{22,i}$	
$\mathbf{H}_i$	Inverse of the transfer matrix for the i-th layer.
i	$\sqrt{-1}$.
i, j, k, l, m, q, b	Index parameters.
k	Overconsolidation ratio exponent.
k	Wave number.
$k_{Mj}(\omega)$	Mode j wave number at angular frequency ω.
$\mathbf{K}$	System stiffness matrix.
$\mathbf{K}_{11,i}$, $\mathbf{K}_{12,i}$	Sub-matrices of the element stiffness matrix for the i-th layer.
$\mathbf{K}_{21,i}$, $\mathbf{K}_{22,i}$	
$K_{2,max}$	Dimensional empirical coefficient [Eq. (2.7)] (K).
$\mathbf{K}_{e,i}$	Element stiffness matrix for the i-th layer.
$\mathbf{K}_{e,n+1}$	Half-space element stiffness matrix.
L	Receiver spread length.
L_T	Measurement profile length.
m	Number of surface wave records acquired at a test site.

$\mathbf{M}_i$	Rigidity matrix for the i-th layer.
n	Number of (finite thickness) layers.
n	Sample size.
n	Stress exponent.
n_j	Number of data points in the j-th experimental dispersion curve.
N	Number of receivers.
N_L	Number of loading cycles.
N_M	Number of Rayleigh wave modes.
N_{max}	Maximum number of iterations.
N_s	Number of sample points.
p	Percentage.
p	Slowness.
$\mathbf{p}$	System force vector.
p_1, p_2	Percentiles of the bootstrap distribution.
p_a	Atmospheric pressure.
$\mathbf{p}_{e,i}$	Element external load vector for the i-th layer.
$\mathbf{p}_i$	External load vector at the upper interface of the i-th layer.
$P(x,\omega)$	Phase spectrum of $\tilde{u}(x,\omega)$.
$\mathbf{P}_i$	Layer matrix for the i-th layer.
$P_j(\omega)$	Phase spectrum of $\tilde{u}_j(\omega)$.
Q	Number of data points.
Q	Number of wavelength intervals.
$\mathbf{Q}_i$	$\mathbf{M}_i\mathbf{P}_i$.
Q_{tn}	Normalized cone resistance.
r	Radial distance from seismic source.
$\mathbf{r}$	Displacement–stress eigenfunction vector.
r_1, r_2	Displacement eigenfunctions. Components of $\mathbf{r}$.
r_3, r_4	Stress eigenfunctions. Components of $\mathbf{r}$.
r_i	$\sqrt{1 - V_R^2/V_{P,i}^2}$ for $V_R < V_{P,i}$.
s	Sample standard deviation.
s_i	$\sqrt{1 - V_R^2/V_{S,i}^2}$ for $V_R < V_{S,i}$.
s_q	Standard deviation of phase velocity values within the q-th wavelength interval.
$\widehat{se}$	Standard error of $\hat{\theta}$.
$\mathbf{S}_i$	Transformation matrix.
$\tilde{S}(\omega, V_R)$	Slant-stack function (defined by an integral).
$\tilde{S}_s(\omega, V_R)$	Slant-stack function (defined by a sum).
t	Time.
t_g	Geologic age.

$t_{jk,i}$	Components of the transfer matrix for the i-th layer, $\mathbf{T}_i$.
t_m	Sample points.
$t_{n-1}^{(p)}$	$(1-p)100\%$ percentile of the t-distribution with $(n-1)$ degrees of freedom.
$\tilde{t}_{jk,i}$	Components of the transformed transfer matrix for the i-th layer, $\widetilde{\mathbf{T}}_i$.
T	Recording time, $T = T_{pre} + T_{post}$.
$\mathbf{T}$	System transfer matrix.
$\mathbf{T}_i$	Transfer matrix for the i-th layer, $\mathbf{T}_i = \mathbf{T}_i(h_i)$.
$\mathbf{T}_i(z)$	$\mathbf{Q}_i\mathbf{E}_i(z)\mathbf{Q}_i^{-1}$.
T_{pre}	Pre-trigger duration.
T_{post}	Post-trigger duration.
$\widetilde{\mathbf{T}}$	Transformed system transfer matrix.
$\widetilde{\mathbf{T}}_i$	Transformed transfer matrix for the i-th layer.
$\overline{\mathbf{T}}$	Order-2 delta matrix associated with $\widetilde{\mathbf{T}}$.
$\overline{\mathbf{T}}_i$	Order-2 delta matrix associated with $\widetilde{\mathbf{T}}_i$.
$\overline{T}_{jk,i}$	Components of the order-2 delta matrix transform of $\widetilde{\mathbf{T}}_i$, $\overline{\mathbf{T}}_i$.
$\mathbf{u}$	System displacement vector.
$\mathbf{u}$	Displacement field.
u, v, w	Displacement components.
$u(x,t)$	Multichannel surface wave record.
$\mathbf{u}_{e,i}$	Element displacement vector for the i-th layer.
$\mathbf{u}_i$	Displacement field of the i-th layer.
u_i, v_i, w_i	Displacement components of the i-th layer.
$\mathbf{u}_j$	Surface wave trace acquired by the j-th receiver (matrix).
$u_j(t)$	Surface wave trace acquired by the j-th receiver.
$\tilde{u}(x,\omega)$	Fourier transform of $u(x,t)$.
$\tilde{u}_j(\omega)$	Fourier transform of $u_j(t)$.
$\tilde{u}_{norm}(x,\omega)$	Normalized Fourier transform of $u(x,t)$.
$\tilde{u}_{j,norm}(\omega)$	Normalized Fourier transform of $u_j(t)$.
$\mathbf{U}$	Multichannel surface wave record (matrix).
$\mathbf{U}$	Boundary condition matrix.
$U_i(z)$, $W_i(z)$	Components of the state vector for the i-th layer, $\mathbf{y}_i$.
$X_i(z)$, $Z_i(z)$	
$\widetilde{\mathbf{U}}$	Transformed boundary condition matrix.
$\overline{\mathbf{U}}$	Order-2 delta matrix associated with $\widetilde{\mathbf{U}}$.
$\mathbf{V}$	Boundary condition matrix.
V_P	Compressional wave velocity.
$\mathbf{V_P}$	Compressional wave velocity vector.
$V_{P,i}$	Compressional wave velocity of the i-th layer.
V_R	Rayleigh wave phase velocity.
$\mathbf{V_{R,e}}$	Rayleigh wave phase velocity vector (experimental DC).
$V_{R,e}(\lambda)$	Experimental Rayleigh wave phase velocity at wavelength λ.

$V_{R,e,q}$	Rayleigh wave phase velocity of the q-th data point in an experimental DC.
$V_{R,e,q}$	Average phase velocity of Rayleigh wave components within the q-th wavelength interval.
$(V_{R,j,l}, \lambda_{j,l})$	The l-th point of an experimental DC obtained based on the j-th surface wave record.
$V_{R,Mj}(\omega)$	Mode j Rayleigh wave phase velocity at angular frequency ω.
$\mathbf{V_{R,t}}$	Rayleigh wave phase velocity vector (theoretical DC).
$V_{R,t,q}$	Rayleigh wave phase velocity of the q-th data point in a theoretical DC.
$V_{R,test}$	Testing Rayleigh wave phase velocity (c_T).
$V_{R,test,max}$	Maximum testing Rayleigh wave phase velocity ($c_{T,max}$).
$V_{R,test,min}$	Minimum testing Rayleigh wave phase velocity ($c_{T,min}$).
$V_{R,\lambda_{min}}, V_{R,\lambda_{max}}$	Asymptotic Rayleigh wave phase velocities.
V_S	Shear wave velocity.
$\mathbf{V_S}$	Shear wave velocity vector.
V_{S1}	Overburden stress corrected shear wave velocity.
V_{S30}	Average shear wave velocity of the uppermost 30 meters ($V_{S,30}$).
$V_{S,bias}$	Ratio between a CPT-based pseudo V_S-profile and a MASW V_S-profile.
$V_{S,i}$	Shear wave velocity of the i-th layer.
$\mathbf{V_{S,test}}$	Testing shear wave velocity vector.
$V_{S,test,i}$	Testing shear wave velocity of the i-th layer.
V_{SZ}	Average shear wave velocity of the uppermost z meters ($V_{S,z}$).
$\widetilde{\mathbf{V}}$	Transformed boundary condition matrix.
$\overline{\mathbf{V}}$	Order-2 delta matrix associated with $\widetilde{\mathbf{V}}$.
x, y, z	Cartesian coordinates.
x_1	Source offset.
$x_1, x_2, \ldots, x_6$	Elements of the fast delta matrix method recursion vector, $\overline{\mathbf{X}}_i$.
$\mathbf{x}_i$	Displacement vector at the upper interface of the i-th layer.
x_j	Distance from the impact load point to receiver j.
X_i	Random number, $X_i \sim \text{unif}\left(\frac{-b_S \cdot V_{S,i}}{100}, \frac{b_S \cdot V_{S,i}}{100}\right)$.
$\overline{\mathbf{X}}_i$	Fast delta matrix method recursion vector.
$\mathbf{y}$	Random sample, $\mathbf{y} = (y_1, y_2, \ldots, y_n)$.
$\mathbf{y}_{(j)}$	Jackknife sample no. j. $\mathbf{y}$ with its j-th sample point removed.
$\mathbf{y}_i$	State vector of the i-th layer.
y_j	Sample point.
$\mathbf{y}^*$	Bootstrap sample, $\mathbf{y}^* = (y_1^*, y_2^*, \ldots, y_n^*)$.
$\mathbf{y}^{*b}$	Bootstrap sample no. b.
y_j^*	Bootstrap sample point.
$\overline{y}$	Sample mean.
$\left(\overline{y}_{lo}, \overline{y}_{up}\right)$	Classical confidence interval.
Y_i	Random number, $Y_i \sim \text{unif}\left(\frac{-b_h \cdot h_i}{100}, \frac{b_h \cdot h_i}{100}\right)$.

$\mathbf{Y}_i$	Transformation matrix.
$z^{(p)}$	$\Phi^{-1}(1-p)$.
z_i	z coordinate at the top of the i-th layer.
$\mathbf{z}_i$	Stress vector at the upper interface of the i-th layer.
$z_{i,1}$, $z_{i,2}$	Depths within the i-th layer.
z_{max}	Maximum depth of investigation.
z_{min}	Minimum depth of investigation (h_1).
$\hat{z}_0$	Bias-correction factor (BCa confidence intervals).
$\overline{z}_i$	Average depth of the i-th layer.
$\mathbf{Z}_i$	$\mathbf{Y}_i\mathbf{P}_i$.

Greek letters

α	Compressional wave velocity.
$\boldsymbol{\alpha}$	Compressional wave velocity vector.
α_i	Compressional wave velocity of the i-th layer.
β	Shear wave velocity.
$\boldsymbol{\beta}$	Shear wave velocity vector.
β_i	Shear wave velocity of the i-th layer.
γ	Shear strain.
γ	Ratio of the maximum depth of a shear wave velocity profile to the longest retrieved wavelength.
$\dot{\gamma}$	Strain rate.
ϵ_{DC}	Dispersion misfit (ϵ).
ϵ_{max}	Maximum dispersion misfit.
ζ	Ratio of Rayleigh wave phase velocity to shear wave velocity.
ζ	Ratio of the minimum thickness of the top-most layer (in a V_S-profile) to the shortest retrieved wavelength.
η	Ratio of shear wave velocity to compressional wave velocity.
θ	Statistical parameter.
$\hat{\theta}$	Estimate of θ obtained from $\mathbf{y}$, $\hat{\theta} = d(\mathbf{y})$.
$\hat{\theta}_{(j)}$	j-th jackknife replication of $\hat{\theta}$, $\hat{\theta}_{(j)} = d(\mathbf{y}_{(j)})$.
$\hat{\theta}_{(\cdot)}$	Average of the jackknife replications of $\hat{\theta}$.
$(\hat{\theta}_{BCa,lo}, \hat{\theta}_{BCa,up})$	Bias-corrected and accelerated bootstrap confidence interval.
$(\hat{\theta}_{PB,lo}, \hat{\theta}_{PB,up})$	Percentile bootstrap confidence interval.
$(\hat{\theta}_{SB,lo}, \hat{\theta}_{SB,up})$	Standard normal bootstrap confidence interval.
$\hat{\theta}^*$	Bootstrap replication of $\hat{\theta}$ corresponding to $\mathbf{y}^*$, $\hat{\theta}^* = d(\mathbf{y}^*)$.

$\hat{\theta}^*(b)$	Bootstrap replication of $\hat{\theta}$ obtained from the b-th bootstrap sample, $\hat{\theta}^*(b) = d(\mathbf{y}^{*b})$.
$\hat{\theta}^*_s(b)$	b-th value in the ordered list of bootstrap replications, $\hat{\theta}$.
$\kappa_{jk,i}$	Components of the element stiffness matrix of the i-th layer, $\mathbf{K}_{e,i}$.
λ	Lamé parameter.
λ	Rayleigh wave wavelength.
$\boldsymbol{\lambda}$	Rayleigh wave wavelength vector.
$\lambda(z)$	Lamé parameter (of a vertically heterogeneous elastic medium).
$\lambda_{e,q}$	Wavelength of the q-th data point in an experimental DC.
$\lambda_{e,q}$	Reference point for the q-th wavelength interval.
$\lambda^L_{e,q}$, $\lambda^U_{e,q}$	Lower/upper bound of the q-th wavelength interval.
λ_i	Wavelength of the i-th point in an experimental DC.
λ_{max}	Maximum Rayleigh wave wavelength.
λ_{min}	Minimum Rayleigh wave wavelength.
$\lambda_{t,q}$	Wavelength of the q-th point in a theoretical DC.
μ	Population mean.
ν	Poisson's ratio.
$\boldsymbol{\nu}$	Poisson's ratio vector.
ν_i	Poisson's ratio of the i-th layer.
$\xi(z)$	Function of the Lamé parameters in a vertically heterogeneous elastic medium [Eq. (2.23)].
ρ	Mass density.
$\boldsymbol{\rho}$	Mass density vector.
$\rho(z)$	Mass density (of a vertically heterogeneous elastic medium).
ρ_i	Mass density of the i-th layer.
σ_i	$\sigma_{zz,i}$.
$\boldsymbol{\sigma}_i$	Vertical stress field for the i-th layer.
σ_x, σ_y, σ_z	Normal stress components.
$\sigma_{xz,i}$, $\sigma_{yz,i}$, $\sigma_{zz,i}$	Vertical stress components of the i-th layer.
σ'_m	Effective confining pressure (mean principle effective stress).
σ^2	Population variance.
τ	Shear stress.
τ_i	$\sigma_{xz,i}$.
τ_{xy}, τ_{xz}, τ_{yz}	Shear stress components.
ϕ	Angular wave number.
ϕ_{test}	Testing angular wave number.

Φ, Ψ	Displacement potentials.
$\Phi(\omega)$	Wave number spectrum.
Φ_i, Ψ_i	Displacement potentials for the i-th layer.
Φ^{-1}	Inverse of the standard normal cumulative distribution function.
ω	Angular frequency.
ω_l	Angular frequency of sample point l.
ω_s	Sampling rate expressed in terms of angular frequency.

Abbreviations

BCa	Bias-corrected and accelerated bootstrap confidence interval
BE	Bender element
BSSC	Building Seismic Safety Council
CDF	Cumulative distribution function
CEN	Comité Européen de Normalisation (European Standardisation Organisation)
CI	Confidence interval
COV, CV	Coefficient of variation
CPT	Cone Penetration Test
CRR	Cyclic Resistance Ratio
CSR	Cyclic Stress Ratio
CSW method	Continuous Surface Wave method
DAQ	Data acquisition
DC	Dispersion curve
DMT	Dilatometer Marchetti Test
EC8	Eurocode 8
FDSS	Frequency Decomposition and Slant Stacking
FFT	Fast Fourier Transform
GMPEs	Ground Motion Prediction Equations
GW	Well-graded gravel [USCS classification]
GWT	Groundwater table
HRLRT	High-Resolution Linear Radon Transformation
HVSR, H/V	Horizontal-to-Vertical Spectral Ratio
ICOLD	International Commission on Large Dams
Lab	Geotechnical laboratory testing

NCEER	National Center for Earthquake Engineering Research
NEHRP	National Earthquake Hazards Reduction Program
NGI	Norwegian Geotechnical Institute
NGTS	Norwegian GeoTest Sites
NSF	National Science Foundation
MASW	Multichannel Analysis of Surface Waves
MASWaves	Multichannel Analysis of Surface Waves for assessing shear wave velocity profiles of soils
MSOR	Multi-channel simulation with one receiver
OCR	Overconsolidation ratio
P-wave	Compressional wave (primary wave)
PB	Percentile bootstrap confidence interval
PFI	Programmable Function Interface
PI	Plasticity index
PVC	Polyvinyl chloride
Q-Q	Quantile-Quantile
RAM	Random-access memory
S-wave	Shear wave (secondary wave)
S_H-wave	Horizontal component of a shear wave
S_V-wave	Vertical component of a shear wave
SASW	Spectral Analysis of Surface Waves
SB	Standard normal bootstrap confidence interval
SBTn chart	Normalized Soil Behaviour Type chart
SCPT	Seismic Cone Penetration Test
SD, std	Standard deviation
SDMT	Seismic Dilatometer Marchetti Test
SISZ	South Iceland Seismic Zone
SM	Silty sand [USCS classification]
SP	Poorly graded sand [USCS classification]
SPT	Standard Penetration Test
SSRM	Steady State Rayleigh Method
SW	Well-graded sand [USCS classification]
TFZ	Tjörnes Fracture Zone
USCS	Unified Soil Classification System
$^{(B)}$	Bottom of layer
$^{(T)}$	Top of layer

Acknowledgements

First and foremost, I would like to thank my supervisors, Dr. Bjarni Bessason and Dr. Sigurður Erlingsson, for their guidance, collaboration, motivation and encouragement through each stage of this process. During the past years they have given me the chance to grow as a researcher and inspired me to continue along the academic pathway. Our first discussions back in the summer of 2013, which sparked my interest in surface wave testing, have truly snowballed into something far beyond what I could have imagined. I would also like to thank Dr. Amir M. Kaynia for being on my Ph.D. committee, and for his helpful feedback and suggestions.

There are of course others who have assisted me along the way. I would like to express my gratitude to the organizers of the NGTS project, in particular Dr. Jean-Sébastien L'Heureux and Dr. Sara Bazin, for their assistance prior to and during the measurements in Norway, as well as for providing access to results of geotechnical, geophysical and laboratory measurements conducted at the Norwegian sites. Furthermore, I would like to thank the organizers of the PARAGEO project, a collaboration between the University of Žilina, the Comenius University in Brateslava and the University of Iceland, for the opportunity of testing the methodology in Slovakia.

I am grateful for the financial support that the project has received from the University of Iceland Research Fund (Doktorsstyrkir Rannsóknasjóðs Háskóla Íslands), the Energy Research Fund of the National Power Company of Iceland (Orkurannsóknarsjóður Landsvirkjunar) and the Icelandic Road and Coastal Administration (Rannsóknasjóður Vegagerðarinnar). I also would like to thank the travel fund for Ph.D. students at the University of Iceland for the travel grant.

Last but not least, I would like to thank my family, friends and colleagues for their endless support and encouragement, now and always. Special thanks go to Stefán for his help and moral support at all hours during these last, extremely intense, two-three months of writing – and for finding the missing wires.

1 Introduction

Knowledge of the geotechnical properties of subsoil sites, such as the stiffness of the soil strata, is essential in various civil engineering projects. The characteristics of soil can either be assessed in-situ or in a laboratory. On the one hand, field testing has the advantage that the soil is analysed in its actual, undisturbed state. Moreover, many in-situ measurement techniques measure the response of a large volume of soil. In this way, the risk of the tested soil being unrepresentative for the site as a whole is reduced. On the other hand, laboratory tests provide the possibility of analysing the effects of different soil conditions on the parameter(s) being studied (Kramer, 1996).

Due to the unique geological setting of Iceland, the characteristics of Icelandic soil sites are in many aspects vastly different from sites in neighbouring countries. The soil deposits are primarily characterized by normally consolidated Holocene materials of basaltic origin (Erlingsson, 2019). Thick deposits have in many cases been rapidly formed due to catastrophic events, such as volcanic eruptions and glacial floods, and are therefore loosely packed. Icelandic soil deposits are generally characterized by coarse-grained aggregates (i.e., coarse silty particles and coarser grains), though thick peat deposits exist in some locations. Following the Unified Soil Classification System (USCS), Icelandic soils mainly classify as gravel, sand and silt, or mixtures of these fractions, as well as organic soils (peat). Hardly any clayey materials are found in Iceland (Erlingsson, 2019).

Iceland is a seismically active area, characterized by moderate to high seismic hazard, where earthquakes of magnitude up to seven can be expected in inhabited areas (Einarsson, 1991a, 2008; Halldórsson, 1992). The seismicity in Iceland is related to the Mid-Atlantic plate boundary that crosses the island. Within the country, the boundary is shifted towards the east through two complex fracture zones. One is in the South Iceland Lowlands, where it crosses the largest agricultural region in the country, while the other is mostly located off the northern coast (Fig. 1.1). The first is termed the South Iceland Seismic Zone (SISZ) and the second the Tjörnes Fracture Zone (TFZ). The largest earthquakes in Iceland have occurred within these zones, mostly associated with a strike-slip motion at shallow depth (5–10 km).

Shear wave velocity (V_S) is a fundamental parameter in soil dynamics and geotechnical earthquake engineering. In-situ measurements of V_S are commonly conducted with either in-hole seismic measurements or non-invasive surface wave analysis techniques (Kramer, 1996; Garofalo et al., 2016b, 2016a). The in-hole methods provide minimal decrease in resolution with depth, but the results are localized to the point where the

measurement is performed. Hence, multiple in-hole measurements would be required in order to characterize a larger area. Surface wave analysis provides a time- and cost-efficient alternative to the invasive techniques and has the advantage that the data acquisition is conducted on the surface. In addition, surface wave analysis techniques can be applied at a wide variety of soil sites, including very dense or coarse-grained/ gravelly sediments, or mixed soils including boulders or cobbles. In such soil conditions, the application of, for example, conventional penetration-based techniques is limited.

Multichannel Analysis of Surface Waves (MASW) is an active-source surface wave analysis method for evaluating near-surface shear wave velocity profiles by analysing Rayleigh wave propagation over a range of wavelengths (Gabriels et al., 1987; Park et al., 1999). Hence, MASW surveys can be divided into three main steps: (i) data acquisition, (ii) identification of experimental Rayleigh wave dispersion curves, and (iii) estimation of shear wave velocity profiles by inversion of the Rayleigh wave dispersion data. MASW has a wide range of possible applications within the fields of geotechnical and earthquake engineering. Furthermore, as compared to a two-receiver analysis (Nazarian et al., 1983; Nazarian & Stokoe, 1985, 1986), the use of MASW provides both more efficient data acquisition in-situ, and improved data processing procedures for distinguishing the fundamental mode of Rayleigh wave propagation from higher modes and incoherent and coherent noise sources.

1.1 Objectives and scope of the research

The overall aim of this work was to improve understanding of the characteristics of Icelandic soil sites. More precisely, to implement the MASW (Multichannel Analysis of Surface Waves) method for characterization of Icelandic soil deposits.

The application of multi-channel surface wave analysis techniques for characterization of Icelandic soil sites is a previously unexplored topic. Non-invasive measurements of shear wave velocity were first conducted by researchers at the University of Iceland in 1996 by application of the two-receiver SASW (Spectral Analysis of Surface Waves) method (Bessason et al., 1998; Bessason & Erlingsson, 2011). In addition, the SASW technique was applied in the 1980s by a group from the University of Texas at Austin, with measurements primarily aimed at hydropower electric stations in Iceland's south-central highlands (Silver et al., 1986).

In recent years, developments within the field of non-invasive soil site characterization have led to a proliferation in studies adopting a multi-channel survey configuration. The Engineering Research Institute, University of Iceland, bought in 2013 a set of twenty-four geophones, along with data acquisition hardware for active-source multi-channel field measurements, financed by grants from the Landsvirkjun Energy Research Fund and the Icelandic Road and Coastal Administration. Feasibility testing of the multi-channel surveying was conducted between 2013 and 2015 (Ólafsdóttir et al., 2014, 2015). The study presented in this dissertation is a direct continuation of that work.

The main objectives of the project were as follows:

(i) To develop an open-source software to acquire, process and analyse MASW field data.

(ii) To validate and calibrate the field observations by comparison with results that have been obtained using other measurement techniques and/or with alternative software packages.

(iii) To implement and adapt MASW for analysis of the stiffness properties of Icelandic soil sites and man-made fillings.

The primary incentives for developing the MASW software from scratch were to gain a thorough understanding of the methodology and, perhaps more importantly, to get confident, easy access and flexibility to modify and adapt the data acquisition and processing/analysis tools for further developments and engineering applications.

To date, MASW surveys have been conducted at over twenty locations in Iceland, ranging from sites characterized by peat and loosely compacted sand to cemented soil materials and soft rock. An overview of the test locations is provided in Fig. 1.1. For the purpose of benchmarking results obtained by the new software, measurements were also carried out at four well-characterized geotechnical research sites in central and south-eastern Norway.

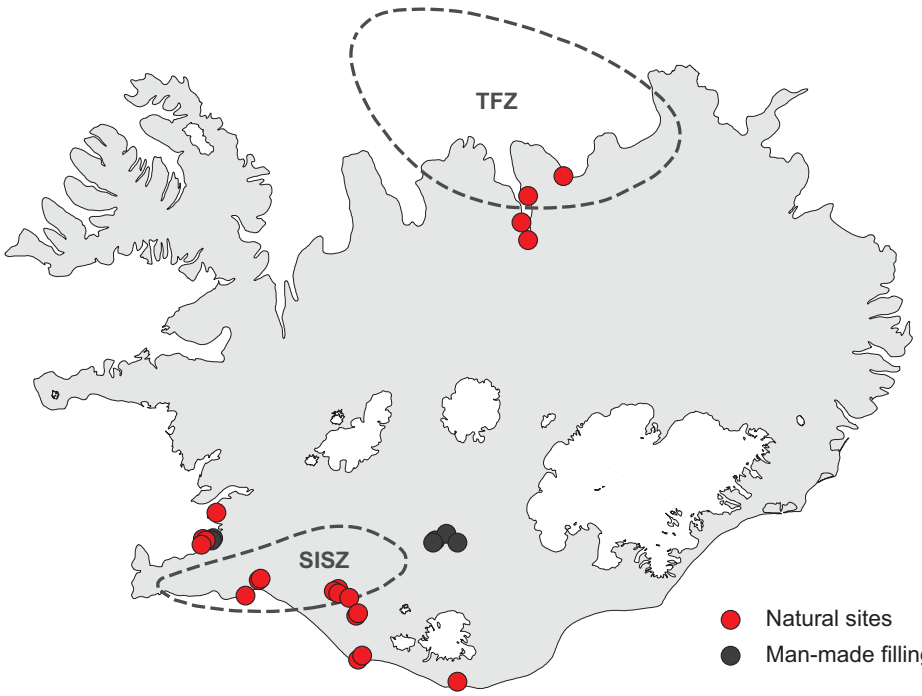

Figure 1.1: Overview of MASW test locations in Iceland.

1.2 Overview

This dissertation is divided into two main parts; an introduction and a summary of the appended papers [Part I], followed by the four journal papers and the four conference publications [Part II].

Part I consists of five chapters. Chapter 2 is devoted to the background of this work. Section 2.1 briefly addresses the mechanical properties of loose soils that are of main relevance to the project, followed by a general introduction to the propagation of seismic waves in elastic soils in Section 2.2. An overview of in-situ techniques for measurements of near-surface shear wave velocity profiles is provided in Section 2.3 and some engineering applications are summarized in Section 2.4. The three main steps of the MASW method are discussed in Chapter 3. A brief description of the software tools that have been developed is further provided. Main results in each of the eight appended papers are summarized in Chapter 4. Finally, conclusions, limitations of the study and reflections regarding future work are given in Chapter 5.

2 Background

2.1 Geotechnical parameters and seismic wave velocities

As outlined in Fig. 2.1, the behaviour of soil is highly dependent upon strain level (Ishihara, 1996). For deformations in the infinitesimal strain range ($< 10^{-5}$), the stress–strain characteristics of most soils are very close to being elastic and the shear modulus can be assumed constant at its maximum value (G_{max}). In the intermediate strain range (10^{-4}–10^{-2}), the behaviour of most soils is elasto-plastic, resulting in permanent deformations, and when large strains are imposed failure takes place. At increased deformations, the stiffness of soil diminishes as indicated by the decreasing slope of the stress–strain curve in Fig. 2.2.

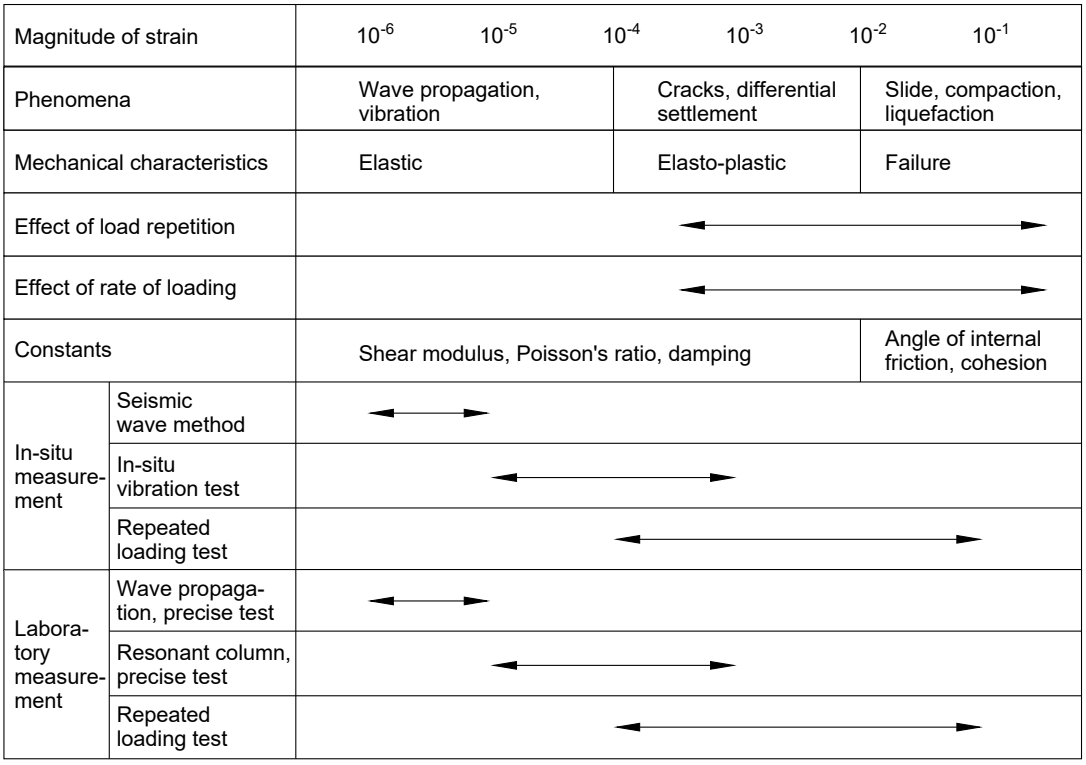

Figure 2.1: Variations in soil behaviour with shear strain. Approximate ranges of strain in which several conventional in-situ and laboratory-based testing methods are applicable to assess the dynamic properties of soil. After Ishihara (1996).

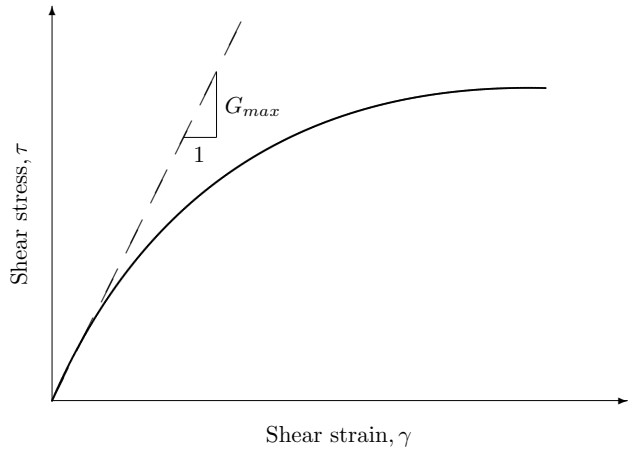

Figure 2.2: Typical stress–strain curve. The variation of the shear modulus with shear strain is indicated by the slope of the curve.

The body wave velocities of soil, shear wave velocity (V_S) and compressional wave velocity (V_P), are directly related to the elastic moduli of the wave medium. The relations between the elastic moduli and the body wave velocities allow evaluation of the spatially distributed geotechnical parameters of subsoil sites through analysis of the seismic wave propagation in the soil deposits. The shear wave velocity is especially a valuable indicator of the stress–strain behaviour of soil due to its relation to the shear modulus (Wair et al., 2012). The shear strains induced by most non-invasive surface wave analysis methods are small and well within the range where the behaviour of soil can reasonably be assumed elastic (see Fig. 2.1). This class of methods, therefore, estimates the small-strain shear modulus of the materials which the waves propagate through (Kramer, 1996)

$$G_{max} = \rho V_S^2 \tag{2.1}$$

where ρ is the mass density of the soil.

Based on the relations between the modulus of elasticity (E_{max}) and the shear modulus (G_{max}) of a homogeneous, isotropic, linear elastic material, the modulus of elasticity can further be estimated as (Everett, 2013)

$$E_{max} = 2G_{max}(1+\nu) = 2\rho V_S^2(1+\nu) \tag{2.2}$$

where ν is the Poisson's ratio.

By solving Eq. (2.2) for shear wave velocity, the following equation is obtained

$$V_S = \sqrt{\frac{G_{max}}{\rho}} = \sqrt{\frac{E_{max}}{2\rho(1+\nu)}} \tag{2.3}$$

A similar expression exists for compressional wave velocity (Everett, 2013)

$$V_P = \sqrt{\frac{(1-\nu)E_{max}}{(1+\nu)(1-2\nu)\rho}} \tag{2.4}$$

By taking the ratio of Eqs. (2.3) and (2.4), the following relation is obtained

$$\frac{V_P}{V_S} = \sqrt{\frac{2(1-\nu)}{1-2\nu}} \tag{2.5}$$

Thus, given estimated values of the shear wave velocity and the Poisson's ratio, the compressional wave velocity can be obtained with Eq. (2.5).

Theoretically, the values of the Poisson's ratio are $0 < \nu < 0.5$ (Megson, 2005), although a few innovative materials (i.e., auxetics) can display negative values (Lakes, 2017). Typical values of the Poisson's ratio for commonly encountered soil materials are summarized in Table 2.1.

Table 2.1: Representative values of Poisson's ratio. After Das (2010).

Soil type	**Poisson's ratio, ν [-]**
Loose sand	0.20–0.40
Medium sand	0.25–0.40
Dense sand	0.30–0.45
Silty sand	0.20–0.40
Soft clay	0.15–0.25
Medium clay	0.20–0.50

The velocity of compressional waves propagating through groundwater is approximately 1,500 m/s, slightly depending on water temperature and salinity (Kramer, 1996). Their propagation velocity through soft, saturated soils can reach those high values, i.e. the compressional waves propagate through the groundwater. Hence, the compressional wave velocity is not indicative of the stiffness of the saturated soil. In such cases, the soil's apparent Poisson's ratio will be substantially higher than in unsaturated materials (see Table 2.1), or close to 0.5 (Gazetas, 1991).

Expected values of the shear wave velocity of different types of soil and rock are summarized in Table 2.2.

Table 2.2: Representative values of shear wave velocity. Based on Foti et al. (2018).

Material	**Shear wave velocity, V_S [m/s]**
Peat	20–100
Soft clay	80–200
Stiff clay	200–600
Loose sand	80–250
Dense sand	200–500
Gravel	300–900
Weathered rock	600–1,000
Competent rock	1,200–2,500

2.1.1 Empirical correlations for the small-strain shear modulus

The small-strain shear modulus of soil (G_{max}) is affected by various environmental and load related factors, most importantly the effective confining pressure (σ'_m) and the void ratio (e) (Gazetas, 1991; Kramer, 1996). Experimental results have indicated that the small-strain shear modulus is directly proportional to $(\sigma'_m)^n$ where $n \approx 0.3$–0.6 for granular soils and $n \approx 0.5$–0.9 for silty and clayey soils (Gazetas, 1991). The small-strain shear modulus decreases with increasing void ratio (Kramer, 1996). A summary of various factors affecting the small-strain shear modulus of normally and moderately overconsolidated soils is provided in Table 2.3.

Table 2.3: Summary of environmental and load related factors affecting the small-strain shear modulus of normally and moderately overconsolidated soils. Modified from Kramer (1996).

Increasing factor	**Small-strain shear modulus, G_{max}**
Effective confining pressure (σ'_m)	Increases with σ'_m.
Void ratio (e)	Decreases with e.
Geologic age (t_g)	Increases with t_g.
Cementation (C)	Increases with C.
Overconsolidation ratio (OCR)	Increases with OCR.
Plasticity index (PI)	Increases with PI if OCR > 1. About constant if OCR $= 1$.
Strain rate ($\dot{\gamma}$)	Non-plastic soils: No effect. Plastic soils: Increases with $\dot{\gamma}$.
Number of loading cycles (N_L)	Clays: Decreases after N_L cycles of large cyclic strain but recovers later with time. Sands: Increases with N_L.

The use of experimentally measured values of shear wave velocity is generally considered the most reliable way of assessing the in-situ value of G_{max} (Kramer, 1996) and preferable to the application of empirical correlations. However, where site-specific measurements of shear wave velocity are not available, indirect estimations obtained from the application of empirical formulas relating G_{max} (or, equivalently, V_S) to other material properties, e.g. taking the form of Eq. (2.6), can be of value (Kramer, 1996; Hussien & Karray, 2016). The application of such empirical correlations also has some practical and economic benefits (Gazetas, 1991; Hussien & Karray, 2016), e.g., for feasibility studies and preliminary design parameter estimates and as screening tools to identify sites where in-situ measurements would be of most value. The empirical formulas may further be used to check the coherence between the results of geotechnical and geophysical measurements, as well as to provide an order of magnitude check against measured V_S values.

$$G_{max} \approx A f(e) (\mathrm{OCR})^k p_a^{1-n} (\sigma'_m)^n \tag{2.6}$$

where

σ'_m	Effective confining pressure.
p_a	Atmospheric pressure.
n	Stress exponent, commonly taken as $n = 0.5$.
OCR	Overconsolidation ratio.
k	Overconsolidation ratio exponent, between 0 (for non-plastic soils) and 0.5 (for very high plasticity clays).
$f(e)$	Function of the void ratio of the soil.
A	Correlation parameter.

Specific empirical correlations have been proposed for particular types of soil. For instance, the model of Seed and Idriss [Eq. (2.7)] is a well-known correlation for predicting the small-strain shear modulus of granular soils (Kramer, 1996; Gazetas, 1991)

$$G_{max} \approx 1000 K_{2,max} \sqrt{\sigma'_m} \tag{2.7}$$

where $K_{2,max}$ is an empirical coefficient which includes the effects of the void ratio. Suggested values of $K_{2,max}$ for several groups of granular soils are provided in Table 2.4. Preliminary evaluation of the applicability of the aforementioned model [Eq. (2.7)] for empirical assessments of the stiffness properties of typical Icelandic earth dams is a topic of *Paper VIII* in this dissertation.

Table 2.4: Suggested values of the empirical coefficient $K_{2,max}$ in Eq. (2.7) for granular materials. After Gazetas (1991).

Soil type	$\boldsymbol{K_{2,max}}$ **[(kPa)$^{0.5}$]**
Loose sand	8
Dense sand	12
Very dense sand	16
Very dense sand and gravel	25–40

Extensive research has been conducted to develop and evaluate empirical regression equations between G_{max} (or V_S) and data obtained with common geotechnical site investigation techniques, for example, the cone penetration test (CPT) and the standard penetration test (SPT). Summaries of empirical correlations, proposed for different soil types and conditions using CPT- and/or SPT-data as predictor variables are provided, e.g., by Wair et al. (2012) and Hussien and Karray (2016). In this work, selected CPT–V_S correlations have been used, in the absence of other relevant references for comparison, to evaluate measured V_S-profiles and to assess whether the results of the MASW surveys are consistent with exiting measurements at Icelandic sites (*Paper V*; Erlingsson et al., 2017; Erlingsson, 2019).

2.2 Seismic waves

Seismic waves are classified into two main categories, body waves and surface waves (Aki & Richards, 1980; Kramer, 1996). Body waves are transmitted through the body of the earth and are either compressional waves (P-waves, primary waves) or shear waves (S-waves, secondary waves). As implied by the terms 'primary' and 'secondary', the propagation velocity of P-waves is greater than that of S-waves (i.e., $V_P > V_S$). The particle motion associated with compressional waves is parallel to the wave propagation direction, causing dilatation and compression of elementary volume particles, as shown in Fig. 2.3. The particle motion of shear waves is perpendicular to the direction of wave propagation and has therefore both a vertical (S_V) and a horizontal (S_H) component. The transverse particle motion causes shear deformations of volume elements within the medium, as shown in Fig. 2.4. Compressional waves both propagate through solids and fluids, whereas shear waves cannot transmit through fluids (i.e., materials with no shear stiffness).

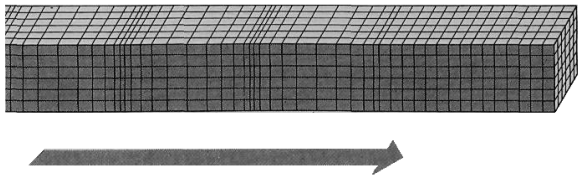

Figure 2.3: Particle motion associated with compressional waves (Bolt, 1976).

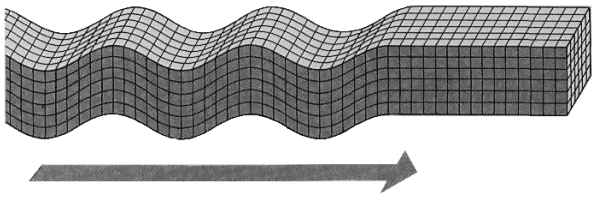

Figure 2.4: Particle motion associated with shear waves (Bolt, 1976).

Surface waves propagate along the interface between two different media. Rayleigh and Love waves form at air/solid interfaces, such as along the surface of the earth (Aki & Richards, 1980; Kramer, 1996). Rayleigh waves, which are the primary focus of this work, result from the interaction of P-waves and S_V-waves with the ground surface. The particle motion of Rayleigh waves has both a vertical and a horizontal component and is reminiscent of rolling ocean waves, as shown in Fig. 2.5. The wave motion is retrograde (anticlockwise) closest to the surface but becomes prograde (clockwise) at greater depths. Love waves result from the interaction of S_H-waves with a soft (low velocity) surficial layer. The particle motion of Love waves is horizontal and transverse to the direction of wave propagation (Fig. 2.6). Scholte and Stonely waves propagate along fluid/solid and solid/solid interfaces, respectively. Their use for geotechnical engineering applications (e.g., underwater surface wave analysis) is limited and outside the scope of this project.

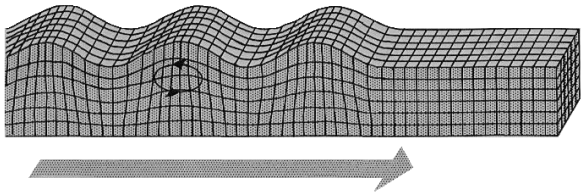

Figure 2.5: Particle motion associated with Rayleigh waves (Einarsson, 1991b).

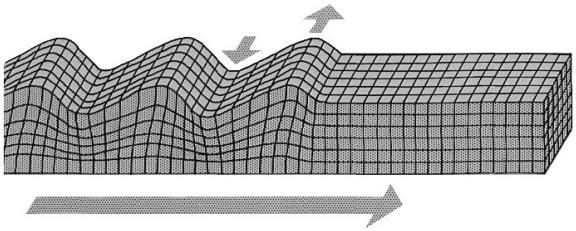

Figure 2.6: Particle motion associated with Love waves (Einarsson, 1991b).

2.2.1 Rayleigh waves

Rayleigh waves are nondispersive in a homogeneous, isotropic, linear elastic half-space. Their propagation velocity depends therefore on the elastic properties of the medium but is independent of frequency. A main characteristic of Rayleigh waves is that they are subjected to geometrical dispersion in a vertically heterogeneous medium. That is, wave components with different frequencies (and therefore different wavelengths) have different penetration depths and propagate at different velocities through the medium. The propagation velocity of individual frequency components is referred to as phase velocity (V_R) (Everett, 2013; Kramer, 1996). A plot of frequency versus phase velocity, known as a dispersion curve, visualizes these relations. The shape of the dispersion curve is referred to as the dispersion characteristic of the Rayleigh wave (Everett, 2013). The relation between Rayleigh wave phase velocity ($V_R(f)$), frequency (f) and wavelength ($\lambda(f)$) is described by

$$\lambda(f) = \frac{V_R(f)}{f} \tag{2.8}$$

The dispersive properties of Rayleigh waves in layered media form the basis of surface wave testing as illustrated in Fig. 2.7. The phase velocity of a Rayleigh wave component propagating in a layered medium is determined by a combination of the stiffness and density properties of the soil layers that it travels through (Everett, 2013). In Fig. 2.7 only the material properties of the top-most layer have an impact on the phase velocity of the wave component (1), whereas the phase velocities of wave components (2) and (3) also depend on the properties of the deeper layers. In a normally dispersive medium (i.e., a medium where the soil stiffness gradually increases with depth), Rayleigh wave velocities are in general observed to increase with wavelength. By inversion of an experimentally measured dispersion curve, the material properties of the medium (primarily the shear wave velocity profile) can be evaluated.

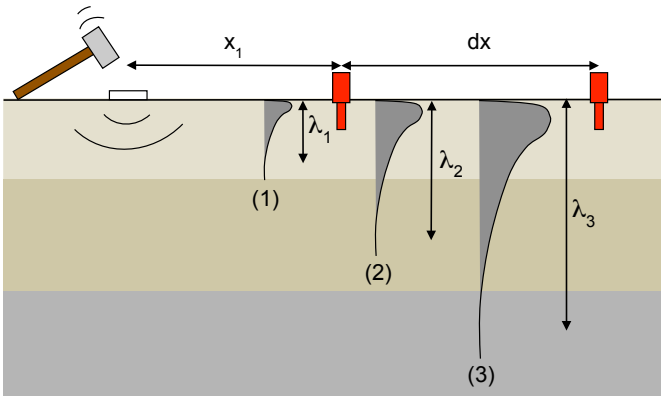

Figure 2.7: Rayleigh wave components of different wavelengths (frequencies) propagating through a layered medium. Wave components with different wavelengths reflect soil properties at different depths.

The propagation of Rayleigh waves is a multi-modal phenomenon. The mode with the lowest phase velocity at each frequency is referred to as the fundamental mode. Higher modes of vibration (overtones) are characterized by successively higher velocities and are only present above a certain cut-off frequency that depends on the mode (Aki & Richards, 1980; Everett, 2013). The fundamental mode of Rayleigh wave propagation typically dominates at sites where the stiffness increases gradually with depth (Gao et al., 2016; Foti et al., 2015; Gucunski & Woods, 1991; Tokimatsu et al., 1992), while higher modes may not be exited (Foti et al., 2018). A higher mode may further prevail in certain frequency ranges whilst being trivial in others. At sites characterized by irregularly varying stiffness profiles (e.g., with strong velocity contrasts at shallow depth or velocity reversals), higher modes can, in particular, play a significant role within certain frequency bands. Furthermore, at frequencies where successive modes have similar phase velocities (osculation points) apparent mode superposition can occur, making the individual modal dispersion curves indistinguishable in seismic testing and resulting in an effective (apparent) dispersion curve that does not correspond to any of the real modes (Gao et al., 2016; Zhang & Chan, 2003; Foti et al., 2015). The propagation of Rayleigh waves in a homogeneous medium and in a vertically heterogeneous medium is discussed further in the subsequent sections.

Rayleigh waves in homogeneous elastic half-space

A vertical seismic source applied on the surface of a homogeneous, isotropic, elastic half-space radiates a combination of compressional, shear and Rayleigh waves. Around 67% of the seismic energy is imparted into Rayleigh waves while about 26% is imparted into shear waves and 7% into compressional waves (Woods, 1968).

Rayleigh waves generated by a vertical point load propagate along cylindrical wave fronts away from the impact point (Richart et al., 1970). Body waves propagate radially outward from the source, both into the medium and along the surface, along a hemispherical wave front, as shown in Fig. 2.8. As the waves travel outward and encounter an increasingly larger volume of material, their amplitude decreases. This

is referred to as geometrical spreading (or geometrical damping) (Aki & Richards, 1980; Richart et al., 1970). In a homogeneous elastic half-space, the amplitude of Rayleigh waves diminishes as $r^{-0.5}$, where r is the distance from the impact point. For comparison, the amplitude of body waves decreases as r^{-2} along the surface and as r^{-1} into the medium. As two-thirds of the total seismic energy is imparted into Rayleigh waves and Rayleigh waves decay more slowly with distance than body waves, the wave field becomes dominated by Rayleigh wave motion at short distances from the seismic source (Richart et al., 1970).

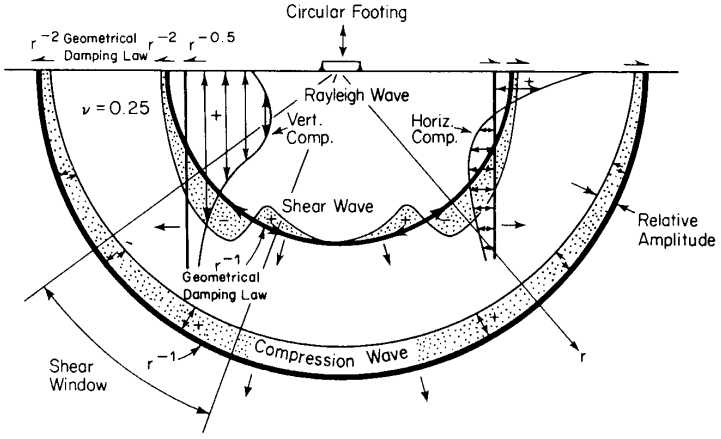

Figure 2.8: Distribution of compressional, shear and Rayleigh waves generated by a point load in a homogeneous, isotropic, elastic half-space (Woods, 1968).

The amplitude of Rayleigh waves decays exponentially with depth (Richart et al., 1970). Figure 2.9 shows the horizontal and vertical Rayleigh wave displacement amplitudes as a function of dimensionless depth for several values of the Poisson's ratio (ν).

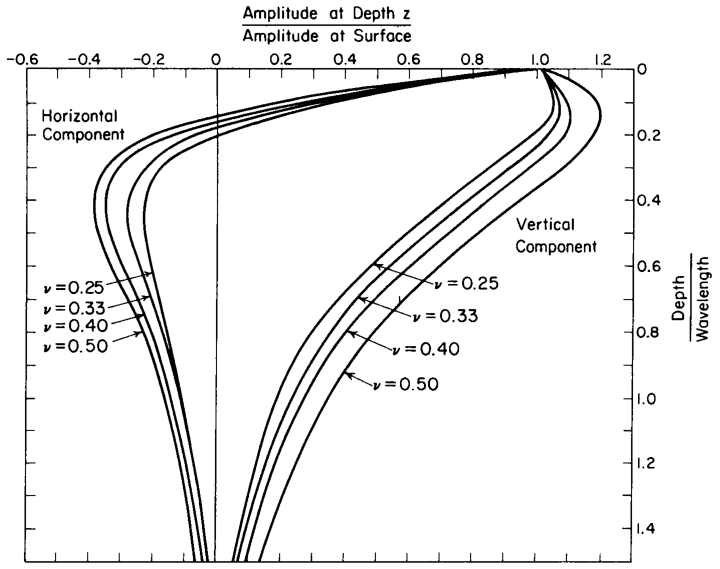

Figure 2.9: Displacement amplitude of Rayleigh waves versus dimensionless depth (Richart et al., 1970).

Equations describing the propagation of Rayleigh waves in a homogeneous, isotropic, elastic medium are obtained by solving the equations of motion with the appropriate boundary conditions (Aki & Richards, 1980; Ben-Menahem & Singh, 1981; Richart et al., 1970). The motion is confined to the x-z plane with the positive z-axis directed downwards ($z = 0$ at the free surface). In the absence of body forces, the equations of motion can be written as

$$G\nabla^2\mathbf{u} + (\lambda + G)\,\mathrm{grad}(\mathrm{div}\,\mathbf{u}) = \rho\frac{\partial^2\mathbf{u}}{\partial t^2} \tag{2.9}$$

where $\mathbf{u} = [u, v, w]^T$ is the displacement field, ρ is the medium density and λ and G are the Lamé parameters, with G more commonly referred to as the (small-strain) shear modulus. ∇^2 is the Laplacian operator.

Particle displacements of a plane wave propagating in the x-z plane are independent of the y direction. The displacements in the x and z directions can be expressed in terms of potential functions Φ and Ψ as (Richart et al., 1970)

$$\begin{aligned} u &= \frac{\partial\Phi}{\partial x} + \frac{\partial\Psi}{\partial z} \\ v &= 0 \\ w &= \frac{\partial\Phi}{\partial z} - \frac{\partial\Psi}{\partial x} \end{aligned} \tag{2.10}$$

Inserting Eq. (2.10) into Eq. (2.9) yields the two wave equations

$$\nabla^2\Phi = \frac{1}{V_P^2}\frac{\partial^2\Phi}{\partial t^2} \tag{2.11}$$

$$\nabla^2\Psi = \frac{1}{V_S^2}\frac{\partial^2\Psi}{\partial t^2} \tag{2.12}$$

where V_P and V_S are the propagation velocities of compressional and shear waves, respectively. V_P and V_S are related to the material parameters ρ, λ and G as follows

$$V_P = \left(\frac{\lambda + 2G}{\rho}\right)^{0.5} \qquad V_S = \left(\frac{G}{\rho}\right)^{0.5} \tag{2.13}$$

The plane Rayleigh wave is assumed to be harmonic with circular frequency ω and wave number k. The displacement potentials, Φ and Ψ, can therefore be assumed to have the form (Richart et al., 1970)

$$\Phi(x, z, t) = f(z)e^{i(kx-\omega t)} \tag{2.14}$$

$$\Psi(x, z, t) = g(z)e^{i(kx-\omega t)} \tag{2.15}$$

where $f(z)$ and $g(z)$ describe the variation of the wave's amplitude with depth and $i = \sqrt{-1}$.

By inserting Eqs. (2.14) and (2.15) into Eqs. (2.11) and (2.12), respectively, applying

the appropriate boundary conditions (zero stress at the free surface) and discarding solutions that allow the amplitude of the wave to become infinite with depth, the following characteristic equation is obtained

$$\zeta^6 - 8\zeta^4 + (24 - 16\eta^2)\zeta^2 + 16(\eta^2 - 1) = 0 \tag{2.16}$$

where

$$\zeta = \frac{V_R}{V_S} \qquad \text{and} \qquad \eta = \frac{V_S}{V_P} = \left(\frac{G}{\lambda + 2G}\right)^{0.5} = \left(\frac{1 - 2\nu}{2(1 - \nu)}\right)^{0.5}$$

Equation (2.16) is a cubic equation in ζ^2 and its solutions are functions of the Poisson's ratio of the medium. For each value of ν ($0 < \nu < 0.5$) only one real and acceptable solution to Eq. (2.16) exists. The Rayleigh wave propagation velocity is denoted by V_R. The solutions of Eq. (2.16) are independent of frequency, which indicates that Rayleigh waves do not disperse in a homogeneous medium.

An approximate solution to Eq. (2.16) was first obtained by Bergmann (1948), i.e.

$$V_R \approx \frac{0.87 + 1.12\nu}{1 + \nu} V_S \tag{2.17}$$

Figure 2.10 depicts the approximate solution of Eq. (2.16), as described by Eq. (2.17). The ratio of V_R to V_S for several different values of ν is further provided in Table 2.5.

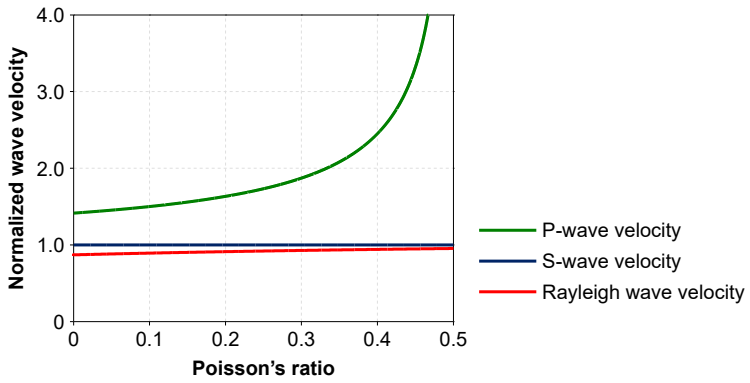

Figure 2.10: Variation of compressional, shear and Rayleigh wave propagation velocities in a homogeneous medium with Poisson's ratio. The seismic wave velocities are normalized with respect to V_S.

Table 2.5: Variation of the ratio of Rayleigh wave phase velocity to shear wave velocity ($\zeta = V_R/V_S$) in a homogeneous medium with Poisson's ratio.

Poisson's ratio, ν [-]	**Velocity ratio, $\zeta = V_R/V_S$ [-]**
0.20	0.912
0.25	0.920
0.30	0.928
0.35	0.935
0.40	0.941

Rayleigh waves in vertically heterogeneous elastic half-space

For a vertically heterogeneous elastic medium, i.e. where the medium density and the Lamé parameters vary with depth, the equations of motion in absence of body forces can be written as (Ben-Menahem & Singh, 1981)

$$G(z)\nabla^2\mathbf{u} + (\lambda(z)+G(z))\,\mathrm{grad}(\mathrm{div}\,\mathbf{u}) + \frac{dG(z)}{dz}\left(2\frac{\partial\mathbf{u}}{\partial z} + \hat{\mathbf{e}}_z \times \mathrm{curl}\,\mathbf{u}\right) + \hat{\mathbf{e}}_z\frac{d\lambda}{dz}\mathrm{div}\,\mathbf{u} = \rho(z)\frac{\partial^2\mathbf{u}}{\partial t^2} \tag{2.18}$$

where $\lambda(z)$ and $G(z)$ are the Lamé parameters and $\rho(z)$ is the medium density. $\hat{\mathbf{e}}_z$ is the unit vector along the z-axis and $\times$ denotes vector multiplication.

In order to solve Eq. (2.18), the following displacement field is assumed (Aki & Richards, 1980)

$$\mathbf{u} = \begin{bmatrix} u \\ v \\ w \end{bmatrix} = \begin{bmatrix} r_1(z,k,\omega)e^{i(kx-\omega t)} \\ 0 \\ ir_2(z,k,\omega)e^{i(kx-\omega t)} \end{bmatrix} \tag{2.19}$$

The stress components corresponding to the displacement field described by Eq. (2.19) are obtained as

$$\begin{aligned}
\sigma_x &= i\left(\lambda(z)\frac{dr_2}{dz} + k(\lambda(z)+2G(z))r_1\right)e^{i(kx-\omega t)} \\
\sigma_y &= i\left(\lambda(z)\frac{dr_2}{dz} + k\lambda(z)r_1\right)e^{i(kx-\omega t)} \\
\sigma_z &= i\left((\lambda(z)+2G(z))\frac{dr_2}{dz} + k\lambda(z)r_1\right)e^{i(kx-\omega t)} = r_4(z,k,\omega)e^{i(kx-\omega t)} \\
\tau_{xy} &= 0 \\
\tau_{xz} &= G(z)\left(\frac{dr_1}{dz} - kr_2\right)e^{i(kx-\omega t)} = r_3(z,k,\omega)e^{i(kx-\omega t)} \\
\tau_{yz} &= 0
\end{aligned} \tag{2.20}$$

Specifying the displacement–stress eigenfunction vector as $\mathbf{r}(z) = [r_1, r_2, r_3, r_4]^T$ and inserting Eq. (2.19) into Eq. (2.18) yields the following set of first order linear ordinary differential equations with variable coefficients (Aki & Richards, 1980)

$$\frac{d}{dz}\mathbf{r}(z) = \mathbf{A}(z)\mathbf{r}(z) \tag{2.21}$$

where

$$\mathbf{A}(z) = \begin{bmatrix} 0 & k & G^{-1}(z) & 0 \\ -k\lambda(z)[\lambda(z)+2G(z)]^{-1} & 0 & 0 & [\lambda(z)+2G(z)]^{-1} \\ k^2\xi(z)-\omega^2\rho(z) & 0 & 0 & k\lambda(z)[\lambda(z)+2G(z)]^{-1} \\ 0 & -\omega^2\rho(z) & -k & 0 \end{bmatrix} \tag{2.22}$$

and

$$\xi(z) = 4G(z)\frac{\lambda(z) + G(z)}{\lambda(z) + 2G(z)} \tag{2.23}$$

Equations (2.21) to (2.23) define a differential eigenvalue problem with the linear operator d/dz, displacement eigenfunctions r_1 and r_2 [see Eq. (2.19)] and stress eigenfunctions r_3 and r_4 [see Eq. (2.20)].

The boundary conditions for surface wave motion, vanishing traction at the free surface and no motion at infinite depth, require that (Aki & Richards, 1980)

$$\begin{aligned} &r_3(z,k,\omega) = r_4(z,k,\omega) = 0 && \text{at } z = 0 \\ &r_1(z,k,\omega) \to 0,\ r_2(z,k,\omega) \to 0 && \text{as } z \to \infty \end{aligned} \tag{2.24}$$

Moreover, for a multi-layered medium where the material parameters $\lambda(z)$, $G(z)$ and $\rho(z)$ have jump discontinuities, the displacement and stress fields must be continuous at all layer interfaces (Aki & Richards, 1980).

The resulting equation is generally known as the Rayleigh secular equation. It can be written in implicit form as

$$F_R(\lambda(z), G(z), \rho(z), k, \omega) = 0 \tag{2.25}$$

For a given frequency (ω) nontrivial solutions of the eigenvalue problem that fulfil the boundary conditions for surface wave motion only exist for certain wave numbers $k = k_{Mj}(\omega)$ (where $j = 0, \ldots, (N_M - 1)$ and N_M is the number of modes) (Aki & Richards, 1980). As the wave numbers that provide solutions of the Rayleigh secular equation at each frequency have been obtained, the Rayleigh wave phase velocity, i.e. the propagation velocity of individual frequency components $V_{R,Mj}(\omega)$, is obtained as

$$V_{R,Mj}(\omega) = \frac{\omega}{k_{Mj}(\omega)} \qquad j = 0, \ldots, (N_M - 1) \tag{2.26}$$

The Rayleigh secular equation cannot be solved analytically. However, there exist several numerical methods to solve the eigenvalue problem described by Eq. (2.25). Selected methods, that are of relevance to this work, are described in Section 3.6.1.

2.3 In-situ measurements of shear wave velocity

As discussed in preceding sections, the shear wave velocity is a fundamental parameter in soil dynamics and geotechnical earthquake engineering. In-situ measurements of V_S are typically conducted with either in-hole seismic techniques or non-invasive active- or passive-source surface wave analysis methods (Garofalo et al., 2016b, 2016a). The in-hole methods provide minimal decrease in resolution with depth, but the results are localized to the point where the measurement was performed. Hence, multiple in-hole measurements would be required to sufficiently characterize a large area. The non-invasive surface wave analysis methods provide a time- and cost-efficient alternative

to the in-hole techniques. They further have the advantage that the data acquisition is conducted on the surface, neither requiring heavy machinery nor leaving lasting marks at the site. In addition, surface wave methods can be applied at a wide variety of soil sites, including gravelly sites and sites characterized by partly cemented volcanic soil materials. Application of penetration-based methods is limited at such sites (see further in Section 2.3.1). The surface wave analysis methods survey larger areas than the in-hole techniques, but, as the measurement is conducted on the soil surface, their resolution decreases with depth. Furthermore, the inverse problem encountered as a part of the surface wave analysis (see further in Section 3.6) is non-linear and affected by solution non-uniqueness. Hence, if results of multiple measurements are available for a single site, the results obtained with the invasive methods are often considered as 'benchmark' values (Garofalo et al., 2016b).

2.3.1 Invasive methods

Well-known invasive seismic measurement techniques include the crosshole and downhole techniques, seismic cone and seismic dilatometer tests and P-S suspension logging.

The crosshole technique is based on measurements of the travel time of compressional and/or shear waves transmitted between a seismic source and three-component receivers located at the same depth in neighbouring boreholes (Kramer, 1996). An application of the crosshole technique, therefore, requires access to two or three cased boreholes. The source is activated and the energy from the shot is measured in the receiver hole(s). By progressively moving the source and the receiver(s) to greater depths, velocity profiles as a function of depth are obtained.

For downhole measurements, the seismic source is applied on the surface and the travel times of seismic waves are measured at different depths in a borehole by receiver(s) that are gradually advanced to greater depths (Kramer, 1996). A number of methods exist for interpretation of the recorded data that all have specific advantages and disadvantages relative to each other (Garofalo et al., 2016b). Downhole tests only require a single cased borehole, therefore, making them more economical than crosshole surveys. However, one drawback is that the investigation depth of the downhole test may be limited by the energy of the impulsive source. The seismic cone penetration test (SCPT) and the seismic dilatometer test (SDMT) are based on the same principles as the downhole method. In these tests, a seismic module is added to the CPT probe or the dilatometer, respectively, and the downhole measurement conducted during penetration of the cone or the dilatometer (Robertson et al., 1986; Martin & Mayne, 1997; Marchetti et al., 2008). Hence, as compared to the downhole method, the application of the penetration-based tests reduces costs as no borehole is required. However, the same limitations apply as to the application of traditional CPT and DMT surveys, making them best suited for surveying softer soil sites. Applications in very dense or coarse-grained/gravelly soils, or mixed soils including boulders or cobbles, are generally not possible as pushing the equipment through such materials might cause damage to the CPT cone or the membrane and blade of the DMT.

For P-S suspension logging (Ohya et al., 1984) a single probe, containing two (or more) geophones and a seismic source, is lowered into a fluid-filled borehole and measurements conducted at different depths to obtain the seismic (P- and S-wave) velocities of the local soils. Uncased boreholes are preferred, although the technique can also be applied within PVC-cased boreholes. As the seismic source is located at a constant distance from the receivers, the technique can provide high resolution measurements down to greater depths than are obtained by other invasive techniques where the seismic source is on the surface.

2.3.2 Non-invasive surface wave methods

Various non-invasive surface wave methods exist for evaluation of in-situ shear wave velocity profiles. Common surface wave analysis techniques can be divided into two main categories based on how the surface waves used for site characterization are generated. Active-source surface wave methods (e.g., SASW and MASW) require the generation of surface waves by application of impact or vibrating sources. Passive-source techniques are based on the analysis of microtremor or ambient noise generated by natural sources and human activity. The application of passive-source methods is outside the scope of this project. Hence, passive surveys will only be briefly mentioned in the current section.

Active-source techniques

The steady state vibration technique (or the steady state Rayleigh method, SSRM) (Jones, 1958, 1962) was the first method developed to utilize the dispersion properties of surface waves for near-surface engineering site characterization (Park & Ryden, 2007; Pelekis & Athanasopoulos, 2011; Foti et al., 2015). A small vibrator, operating at a fixed frequency, was used as a source and a single vibration sensor as a receiver. For data acquisition, the receiver was gradually moved away from the vibrator to record the vibration amplitude time histories at increasing distances from the source. The operating frequency was then changed, and the procedure repeated in order to construct an experimental dispersion curve over a range of frequencies. Finally, the experimental curve was inverted using a simple empirical procedure (Pelekis & Athanasopoulos, 2011). A comparable technique, with two (or more) receivers at fixed positions, became later known as the Continuous Surface Wave (CSW) method (Matthews et al., 1996).

In the early 1980s, researchers at the University of Texas at Austin proposed a two-receiver approach (Nazarian et al., 1983; Nazarian & Stokoe, 1985, 1986), known as Spectral Analysis of Surface Waves (SASW). Typically, data acquisition is conducted with between two and twelve geophones. The geophones are either lined up with equal spacing on the surface or, as is more common, with varying spacing in a symmetrical line-up. For a given site, multiple measurements are carried out using different types of seismic sources and/or by varying the source location in order to excite waves with different frequency contents. Furthermore, the data acquisition process is repeated from the other end of the geophone line-up. Based on prior experience, an estimate

of the shear wave velocity profile down to around 20 m depth can be obtained under optimal conditions, assuming that surface waves are generated with a reasonably heavy impact load, e.g. a sledgehammer (Bessason & Erlingsson, 2011).

Due to the necessity of repeated computations, the data processing associated with the application of SASW is time intensive. For evaluation of the experimental dispersion curve, data from each pair of receivers is analysed separately and the results examined in order to evaluate their quality. Moreover, as time series from only two receivers are used at a time, difficulties can arise in distinguishing the fundamental mode of Rayleigh wave propagation from higher modes (resulting in an apparent dispersion curve) or from incoherent and coherent noise (Park et al., 1999). Furthermore, as empirical criteria, manually adjusted to each test site, must be used to detect possible noise, the SASW method cannot be fully automated.

The use of multi-channel surface wave methods for characterization of subsoil sites for civil engineering purposes dates from the late 1980s. Gabriels et al. (1987) first reported a successful application of a multi-channel system. The use of multi-channel acquisition methods started to gain popularity within the civil engineering community in the early 2000s and has now become a common technique for estimating near-surface shear wave velocity profiles (Socco et al., 2010; Xia, 2014; Foti et al., 2018). The term MASW was first introduced by Park et al. (1999), both referring to analysis of surface waves generated by impulsive and vibrating sources. Since then, the abbreviation MASW has commonly been used for any type of multi-channel approach used for evaluation of V_S-profiles (Park & Ryden, 2007). In this work, the term MASW will only refer to active-source multi-channel surveys, though references to passive surveys using the abbreviation also exist (e.g., Pelekis & Athanasopoulos, 2011; Park et al., 2007). The main advantages of MASW, as compared to the SASW technique, include a more efficient data acquisition routine in the field, faster and less labour-consuming data processing procedures and improved identification and reduction of noise from recorded data (Park et al., 1999; Xia et al., 2002). Furthermore, the MASW method makes it possible to better identify higher mode dispersion curves (Xia et al., 2003). Finally, it may be possible to map deeper shear wave velocity profiles when using the same impact load.

Passive-source techniques and combined active/passive surveys

As previously mentioned, passive surface wave methods utilize passively generated surface waves, i.e. surface waves generated by natural phenomena or human activities (e.g., traffic). Passively generated surface waves are usually of relatively low frequencies and with wavelengths ranging from several tens of metres to a few kilometres. Hence, the investigation depth of passive surveys can reach several hundred metres. As the source and direction of the ambient vibrations is unknown, a two-dimensional receiver array (e.g., circular or triangular) is commonly used for data acquisition (Foti et al., 2018). Techniques using a linear receiver array, similar to the active-source MASW technique, also exist (Park & Miller, 2008; Louie, 2001). Results of active- and passive-source surveys may be combined, typically by merging of dispersion curves. The lower

frequency range of the composite curve is then obtained from passively generated surface waves, whilst the higher frequency range is obtained by an active survey. The advantages of such combined surveys, including, an increased range in investigation depths and improved identification of different modes of surface wave propagation, have been well documented in the literature (Park et al., 2007; Foti et al., 2018).

Another commonly used passive technique is the Horizontal to Vertical Spectral Ratio (HVSR or H/V) method (Nakamura, 1989; SESAME, 2004). The HVSR method is a widely adopted non-dispersion curve-based technique for estimating site effect parameters, even though some aspects of its physical and theoretical basis have been questioned (e.g., Lachetl & Bard, 1994; Mucciarelli & Gallipoli, 2001). HVSR data acquisition sessions entail a three-component single-station measurement of the ambient vibration ground motion. Hence, they are relatively inexpensive and can be conducted at confined sites. This is an advantage over many passive surface wave methods, where the use of a wide two-dimensional receiver array is required.

The primary parameter obtained by the HVSR method is the predominant frequency of the soil deposit. HVSR analysis can further be of value when assessing the 3D nature of a site and help to identify the presence of complex subsurface conditions. More advanced interpretation techniques involve inversion of the HVSR curve for identification of soil model parameters as in Rayleigh wave dispersion curve inversion (e.g., Fäh et al., 2001). Nonetheless, without additional constraints, the inversion of HVSR or Rayleigh wave ellipticity curves has been criticized for providing estimates of V_S with high uncertainties (Scherbaum et al., 2003; Hobiger et al., 2013; Gouveia et al., 2018). However, jointly inverting an active-source Rayleigh wave dispersion curve with information extracted from a single-station microtremor measurement provides an appealing possibility for future applications. A joint inversion of ellipticity and dispersion curves may provide better constrained estimates of V_S at depth (especially for deep interfaces), extend the investigation depth, and, hence, aid the selection of realistic V_S-profiles (e.g., Scherbaum et al., 2003; Arai & Tokimatsu, 2005; Parolai et al., 2005; Picozzi et al., 2005; Gouveia et al., 2016, 2018). The additional information provided by the single-station measurement also provides the possibility of evaluating the thickness of the overlying soft sedimentary layers, thus enabling identification or mapping of the depth to bedrock (Ibs-von Seht & Wohlenberg, 1999; Delgado et al., 2000; Bignardi, 2017), and may aid dispersion curve mode identification (Boaga et al., 2013; Hobiger et al., 2013). Several examples of the joint inversion of dispersion and HVSR or Rayleigh wave ellipticity curves (see above) exist in the literature. However, there is no general agreement on how to optimally implement the joint inversion process (Foti et al., 2018).

2.4 Engineering applications

This section provides a brief overview of some common engineering applications that are directly influenced by assessments of the near-surface shear wave velocity (small-stain shear stiffness) profile.

2.4.1 Seismic site amplifications and computation of ground response

It is well recognized that the local soil conditions have a predominant effect on the characteristics of the ground surface motion in the event of an earthquake and, hence, on the nature of the seismic induced damage. Ground response analysis aims at predicting ground surface motion given the characteristics of the soil deposit and the motion of the bedrock beneath it (Kramer, 1996). Hence, one of the primary applications of shear wave velocity measurements in earthquake engineering related studies, is the determination of subsoil models required for numerical 1D-modelling of site response (Foti et al., 2018). In this aspect, the application of low-cost active-source surface wave analysis techniques (e.g., MASW) is appealing, as equivalence problems that result from the inversion non-uniqueness have limited effects on the modelled 1D site response (Foti et al., 2009). That is, V_S-profiles whose theoretical dispersion curves fit the experimental data equally well have been shown to be likely equivalent also in terms of one-dimensional soil response.

2.4.2 Average shear wave velocity, site classification schemes and ground motion prediction equations

The average shear wave velocity (V_{SZ}) profile, corresponding to a given V_S-profile, is defined according to Eq. (2.27)

$$V_{SZ}(z) = \frac{z}{\sum_{i=1}^{n} \frac{h_i}{V_{S,i}}} \tag{2.27}$$

where $V_{S,i}$ and h_i denote the shear wave velocity and thickness of the i-th layer, respectively, for a total of n layers down to depth z. The V_{SZ}-profile is also commonly referred to as the harmonic-average or the time-average shear wave velocity profile.

In the absence of site-specific analysis, the European standard for design of structures in seismic zones, Eurocode 8 (EC8), allows that the site response is accounted for through a set of amplification factors defined on the basis of site classes (CEN, 2004). In Eurocode 8, the average shear wave velocity in the top 30 m (V_{S30}, Eq. (2.27) with $z = 30$ m) is used as a proxy for site classification, with construction sites classified into five categories, referred to as ground types A, B, C, D, and E. The ground type is further used to account for the effects of the local ground conditions on the seismic action and, hence, fundamental for determination of site-specific design spectrums. The definition of ground types A, B, C, D, and E, as presented in EC8, is summarized in Table 2.6. Comparable V_{S30}-based classification schemes are implemented in several other seismic building codes, such as the NEHRP provisions (BSSC, 2015). V_{S30} is further commonly used in ground motion prediction equations (GMPEs) as a site parameter for characterizing effects of sediment stiffness on ground motions (e.g., Power et al., 2008; Abrahamson et al., 2008; Bozorgnia et al., 2014).

Despite the extensive use of V_{S30}-based site classification schemes and GMPEs, they have been questioned by many. For instance, V_{S30} can be misleading at sites with velocity reversals, e.g., with reference to the local geology, at sites where lava overlies soft sediments (Bessason & Kaynia, 2002). The capability of a single parameter to sufficiently account for site effects has further been strongly debated (e.g., Castellaro et al., 2008; Lee & Trifunac, 2010; Zhao & Xu, 2013; Kamai et al., 2016). Hence, in recent years, numerous alternatives (e.g., Luzi et al., 2011; Héloïse et al., 2012; Pitilakis et al., 2018; Verdugo, 2019) have been proposed, supplementing or substituting V_{S30} by, e.g., the predominant (or fundamental) site frequency (period), the thickness of the soil deposit, or the average shear wave velocity for other depths than 30 m. Whilst the predominant site frequency is the primary parameter obtained by the HVSR method (refer to Section 2.3.2), the other aforementioned parameters may be determined from the V_S-profile provided a sufficient resolution at depth.

Table 2.6: Identification of EC8 ground types based on V_{S30}. After CEN (2004).

Ground type	**Description of stratigraphic profile**	$\boldsymbol{V_{S30}}$ **[m/s]**
A	Rock or other rock-like geological formation, including at most 5 m of weaker material at the surface.	$>$ 800
B	Deposits of very dense sand, gravel, or very stiff clay, at least several tens of metres in thickness, characterized by a gradual increase in mechanical properties with depth.	360–800
C	Deep deposits of dense or medium-dense sand, gravel or stiff clay with thickness from several tens to many hundreds of metres.	180–360
D	Deposits of loose-to-medium cohesionless soil (with or without some soft cohesive layers), or of predominantly soft-to-firm cohesive soil.	$<$180
E	A soil profile consisting of a surface alluvium layer with V_S values of type C or D and thickness varying between about 5 m and 20 m, underlain by stiffer material with $V_S > 800$ m/s.	

2.4.3 Liquefaction studies

The term liquefaction describes a number of related natural phenomena observed in loose saturated soils, where the soil loses strength due to earthquake shaking or other sudden changes in stress conditions. Liquefaction is attributed to the tendency of soils to compact during shaking. The resistance to shearing strains is further highly linked to the material shear modulus. Depending on the characteristics of the soil material and the site conditions, the liquefaction phenomena can lead to sudden or incremental lateral deformations, ground oscillations, vertical settlements, and development of sand boils (Kramer, 1996).

The liquefaction resistance of soil can be evaluated with laboratory tests or based on in-situ measurement results. Early developments highlighted the use of laboratory tests

(Kramer, 1996). However, as undisturbed samples are required to reliably characterize the liquefaction resistance, the use of in-situ geotechnical or geophysical measurements is an appealing choice (Kramer, 1996; Youd et al., 2001). Seed and Idriss (1971) initially developed the well-known 'simplified procedure' for evaluation of liquefaction hazard. It has later been modified and improved by a number of researchers (e.g., Seed, 1979; Seed et al., 1985; Andrus & Stokoe, 2000; Youd et al., 2001; Kayen et al., 2013). In the conclusions of the NCEER/NSF workshops (Youd et al., 2001) four in-situ techniques (or in-situ measured parameters) were recommended for evaluations based on the simplified procedure. That is the SPT, the CPT, the Becker hammer test, and measurements of shear wave velocity. As compared to the penetration techniques, surface wave measurements of shear wave velocity are less sensitive to subtle variations in stiffness with depth. Hence, it has been argued that non-invasive measurements of V_S may not be sufficient for evaluation of liquefaction potentials in all cases (Castellaro et al., 2015). However, measurements of V_S constitute the only abovementioned test that provides a metric that is a fundamental soil property. Furthermore, as discussed in preceding sections, the penetration-based methods have the disadvantage of only providing point information and being inapplicable to gravelly materials, where liquefaction has been reported in a few cases (Lin et al., 2004).

A single survey, utilizing results of surface wave analysis (i.e., MASW) measurements for liquefaction hazard analysis, has been carried out for Icelandic soil materials with promising results. Results are reported in *Paper VI* of this dissertation.

2.4.4 Analysis of man-made fillings and assessments of soil improvement

Various types of compacted soils are used in man-made fillings, such as foundation pads, embankments, dikes and earth dams. The application of different ground improvement techniques may further be required as a part of construction works in order to, e.g., increase the load-bearing capacity of soils, control deformations and/or increase the soils' resistance to liquefaction. In that sense, surface wave analysis techniques may be used as performance evaluation or monitoring tools, where repeated measurements are conducted over a period of time in order to assess the quality and depth of soil improvement or compaction (e.g., Karray et al., 2010; Bitri et al., 2013). Comparison of experimental dispersion curves (or spectral images), obtained at different stages, can provide a rapid indication of the changes in soil conditions, whereas the improvement may be quantified in terms of G_{max} (or V_S) through inversion of the experimental data.

The use of active-source surface wave analysis methods to study the dynamic properties of earthen dams and embankments has further been reported by several researchers (e.g., Karl et al., 2011; Cardarelli et al., 2014; Ha, 2017; Rahimi et al., 2018; Park & Kishida, 2018). However, as highlighted by Park and Kishida (2018), such applications are challenging, in particular, with regard to earth-core rock-filled dams. The dams' geometry and internal structure may significantly affect the observed spectral energy distribution and bias picked Rayleigh wave phase velocities (Zeng et al., 2012; Min

& Kim, 2006). For instance, surface wave data acquired on the crest of an earth-core rock-fill dam likely represents some mixture of the response of the different construction materials. The applicability of conventional inversion procedures that assume a semi-infinite plane-layered soil model has further been questioned and the application of three-dimensional inversion models proposed for more accurate interpretation of the experimental data (Min & Kim, 2006).

Paper VIII presents a case study where the MASW method was used to assess the stiffness properties of typical earth dams in Iceland. The tested structures both included a dam characterized by a relatively homogeneous unsaturated material and more complex structures with a central core. The aim of the work presented in *Paper VIII* was not to resolve the aforementioned technical challenges. Rather, the objectives were to gain practical experience in applying MASW to study earth- and rock-filled dams, evaluate the feasibility of such studies and create a base to be able to observe potential changes in the future. Furthermore, the experimentally evaluated stiffness profiles were compared to existing measurement results obtained based on the same simplifying assumptions.

2.4.5 Characterization of pavement systems

Surface wave analysis techniques are widely acknowledged as monitoring tools for maintenance inspections of pavement systems and as tools for quality control during construction. Early developments and applications of the SASW method were mainly related to the material characterization of pavement systems (Nazarian et al., 1983; Nazarian & Stokoe, 1985, 1986). More recent developments have further focused on multi-channel data acquisition techniques, both adopting true multi-channel (MASW) and multi-channel simulation with one receiver (MSOR) testing procedures (e.g., Ryden et al., 2004; Lin & Ashlock, 2015).

As compared to most conventional exploration surveys at natural sites, the intended investigation depth range for the analysis of pavement systems is minuscular. Hence, due to the high-frequency surface wave components required during data acquisition, accelerometers are usually used as receivers. The wave propagation in pavement systems is complex (Ryden et al., 2004). Furthermore, pavement systems are inherently inversely dispersive, that is the stiffness of the different structural layers decreases with depth. This significantly affects the inversion analysis, making commonly used fundamental mode-based schemes inapplicable. However, as the layer thicknesses are generally known beforehand, the number of unknown inversion parameters is reduced substantially, thus allowing the analysis to centre on assessing the stiffness properties of the different layers.

3 Methodology & software development

3.1 Overview

In general, an application of the MASW method is divided into three consecutive steps: (i) field measurements, (ii) dispersion analysis, and (iii) inversion analysis. An overview of the method, as it is applied in this work, is provided in Fig. 3.1. Each step of the analysis is described in successive sections of this chapter.

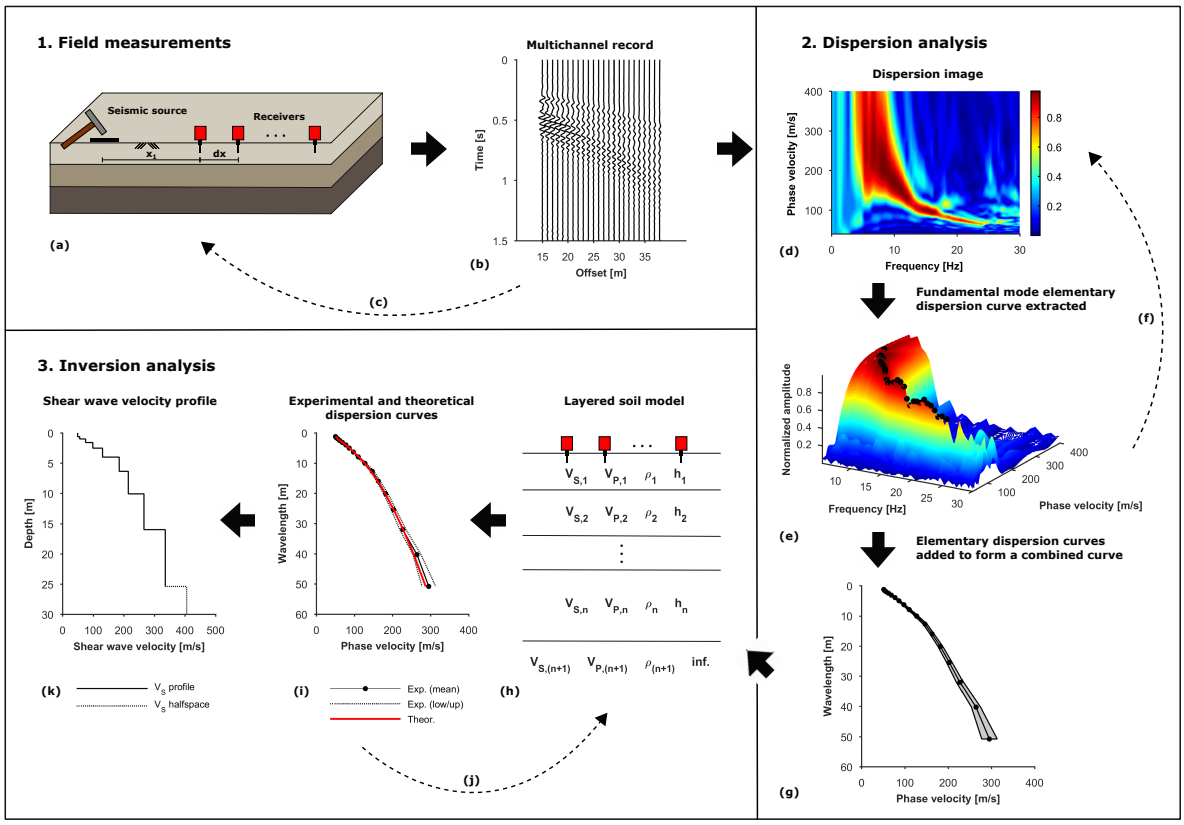

Figure 3.1: Application of the MASW method.

For data acquisition, twenty-four low-frequency geophones are lined up on the surface of the test site with equal receiver spacing dx (Fig. 3.1a). An impact load is applied at a distance x_1 from the end of the receiver spread and the wave propagation is recorded

(Fig. 3.1b). The data acquisition process is repeated by using different measurement profile configurations, i.e. profiles with different values of x_1 and/or dx, while keeping the midpoint of the receiver spread fixed (Fig. 3.1c).

The primary aim of the dispersion analysis is to identify the dispersion characteristics of the acquired surface waves. A dispersion image (phase velocity spectrum) (Fig. 3.1d) is obtained by transforming each multi-channel record into the frequency–phase velocity domain. The transformation visualizes the energy density of the recorded data, from which Rayleigh wave dispersion curve(s) are identified based on the spectral maxima observed at different frequencies (Fig. 3.1e). The different profile configurations provide information on different volumes of soil and may thus help identify whether significant lateral variations in soil properties are present beneath the receiver spread. The use of multiple source offsets further aids identification of near-field effects, which bias the experimental dispersion curve estimates. Furthermore, by obtaining a statistical sample of dispersion curves, through the repeated data acquisition, the variability in estimated phase velocity values can be quantified, providing an indicator of the reliability of the experimental measurements (Figs. 3.1f-g).

In the third step of the analysis, the shear wave velocity profile is obtained by inversion of the Rayleigh wave dispersion curve. The inversion is conducted based on the assumption that the underlying structure of the tested site can be adequately described by a semi-infinite stratified soil model, where each layer is assumed to be flat and have homogeneous and isotropic properties. In brief, the inversion is conducted by iteratively comparing theoretical dispersion curves, obtained from 'trial' subsurface models (Figs. 3.1h-k), to the experimental data in search of a model (or a set of models) that both fit the observed dispersion characteristics and incorporate any known features of the survey site (Fig. 3.1k).

3.2 MASWaves software

Development of specialized software tools to conduct the MASW data acquisition, dispersion analysis and inversion, was one of the main objectives of this project. The software that has been developed for acquiring, processing and inverting MASW field data is referred to as *MASWaves*. MASWaves is a free and open-source software, written in MATLAB, available online at masw.hi.is.

Development and benchmarking of the initial versions of the dispersion and inversion analysis tools is the topic of *Paper I* in this dissertation. *Paper II* and *Paper III* further describe aspects of the dispersion and inversion analysis, respectively, that have been implemented in updated versions of the software. The main objective of the work presented in *Paper IV* is to assess the reliability, accuracy and repeatability of results obtained by the new software for use in civil engineering work. A graphical overview of the workflow of MASWaves is provided in Fig. 3.2.

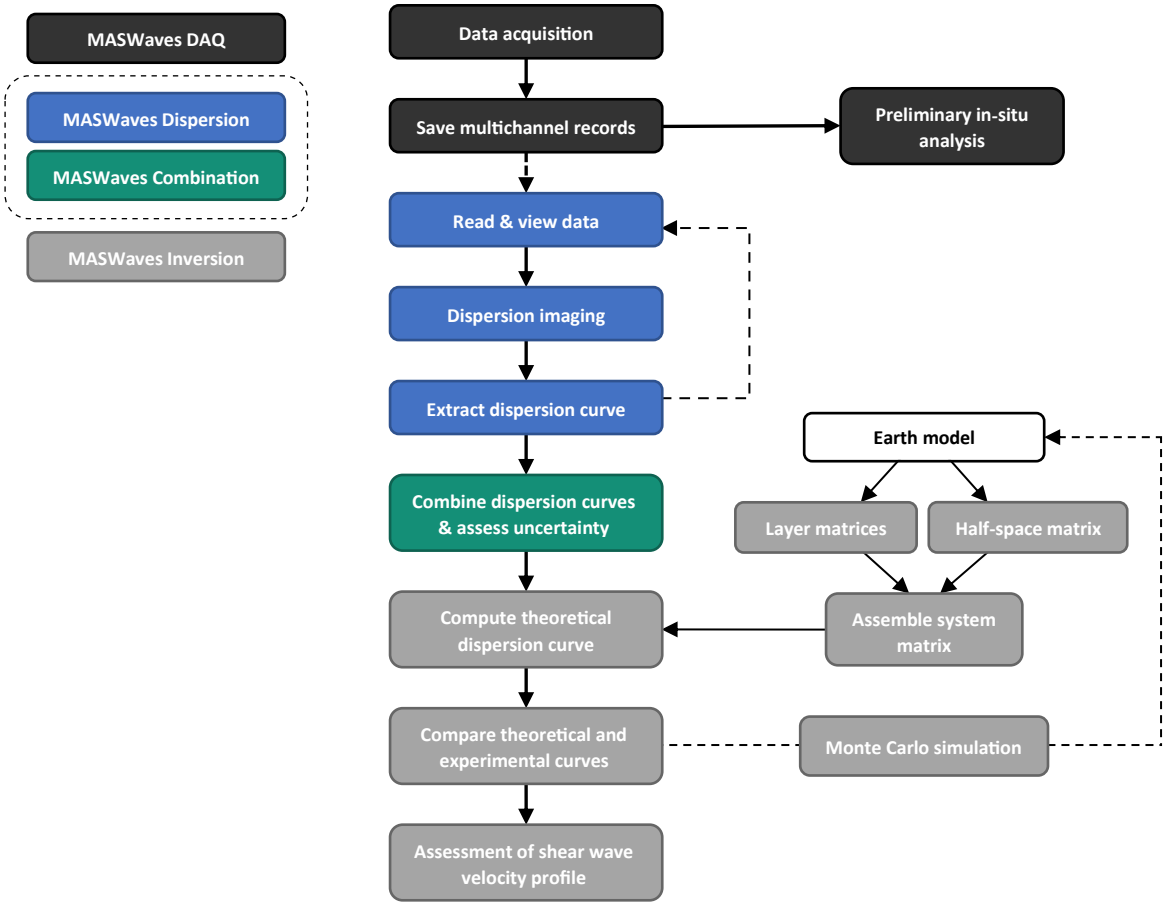

Figure 3.2: Diagram of MASWaves' workflow.

The processing part of MASWaves consists of three separate modules. First is a basic dispersion analysis tool (*MASWaves Dispersion*) to identify experimental dispersion curves from multi-channel surface wave records through adoption of the phase shift method (Park et al., 1998). An experimental curve obtained from a single multi-channel registration is referred to as an 'elementary dispersion curve' in the following discussion. Second is a tool to combine dispersion curves obtained from multiple surface wave registrations (*MASWaves Combination*). The composite curve is obtained by grouping the elementary dispersion curve data points together within logarithmically spaced wavelength intervals. Within each interval, the identified dispersion curve phase velocity values are added up and their arithmetic mean used as a point estimate of the phase velocity of the Rayleigh wave components belonging to the given wavelength range (refer to *Paper II*). The spread of the dispersion curve data points is represented by the standard deviation of the phase velocity values within each interval, whilst classical statistics and bootstrapping (Efron, 1979; Efron & Tibshirani, 1993) are applied to assess the uncertainty associated with the mean phase velocity estimates. Third is an inversion analysis tool (*MASWaves Inversion*) to evaluate the shear wave velocity profile of the tested site by inverting the composite fundamental mode dispersion curve. In the initial version of MASWaves (refer to *Paper I*) theoretical dispersion curves were computed by application of the stiffness matrix method (Kausel & Roësset, 1981) and

the optimization conducted manually. In later versions, the inversion is conducted through the application of a simple Monte Carlo-based global search algorithm (refer to *Paper III*) with the fast delta-matrix algorithm (Buchen & Ben-Hador, 1996) used for computation of theoretical dispersion curves. Inference is drawn from the set of simulated V_S-profiles based on the observed spread of elementary dispersion curve data points within each wavelength interval.

The data acquisition tool (*MASWaves DAQ*) provides a direct connection between the data acquisition hardware and the processing tools. That is, the data acquisition software provides the analyst the opportunity of carrying out preliminary real-time analysis of the recorded data, e.g., for quick assessments of data quality in-situ. Hence, if required, the configuration of the survey profile or values of different measurement control parameters (such as the recording time) can be adapted to better suit the characteristics of the tested site, as judged based on the results of the preliminary analysis.

3.3 Field measurements

For MASW field measurements, N low-frequency geophones are lined up with equal spacing in a straight line on the surface, with the use of at least twenty-four receivers recommended (Foti et al., 2018). Surface waves are generated at the end of the measurement profile, in-line with the receivers. The general profile set-up is illustrated in Fig. 3.3. The source offset, i.e. the distance from the impact load point to the first receiver in the geophone line-up, is denoted by x_1 and the receiver spacing is dx. The length of the receiver spread is therefore

$$L = (N-1)dx \tag{3.1}$$

Hence, the distance from the impact load point to receiver j is obtained as

$$x_j = x_1 + (j-1)dx \qquad j = 1, 2, \ldots, N \tag{3.2}$$

and the total length of the measurement profile (L_T) is

$$L_T = x_1 + L = x_1 + (N-1)dx = x_N \tag{3.3}$$

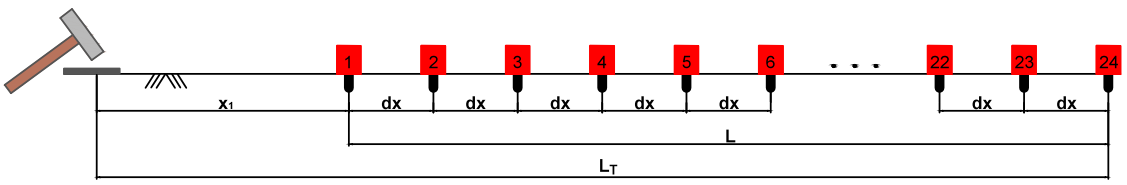

Figure 3.3: Line-up of N geophones with equal spacing dx. The source offset is x_1. The length of the receiver spread is L and the total length of the profile is L_T.

In subsequent sections the recorded time series are regarded as discrete functions of time (or offset and time) and written using function notation. The recorded wavefield is denoted by $u(x,t)$, where x is distance from the impact load point to a receiver and t is time. The record $u(x,t)$ consists of N traces. The trace acquired by geophone j is denoted by $u_j(t)$ $(j = 1, 2, \ldots, N)$. The number of sample points in each data sequence is denoted by $N_s = f_s(T_{pre} + T_{post})$, where f_s is the sampling frequency, T_{pre} is the pre-trigger duration and T_{post} is the post-trigger recording time. In terms of matrices, the recorded wavefield can be described by an $N \times N_s$ matrix

$$\mathbf{U} = [\mathbf{u}_1, \mathbf{u}_2, \ldots, \mathbf{u}_N] \tag{3.4}$$

where $\mathbf{u}_j$ $(j = 1, 2, \ldots, N)$ are column vectors of length N_s.

For interpretation of fundamental mode Rayleigh wave dispersion curves, the range in investigation depth is related to the range of Rayleigh wave wavelengths that are retrieved during data acquisition. Common practice (e.g., Cox & Teague, 2016; Foti et al., 2018; Garofalo et al., 2016a; Park et al., 1999) is to estimate the maximum investigated depth (z_{max}) as

$$z_{max} \approx \gamma \lambda_{max} \qquad \text{where} \qquad \frac{1}{3} \leq \gamma \leq \frac{1}{2} \tag{3.5}$$

where λ_{max} is the longest Rayleigh wave wavelength, and, similarly, to limit the thickness of the top-most soil layer (z_{min}) to

$$z_{min} \approx \zeta \lambda_{min} \qquad \text{where} \qquad \frac{1}{3} \leq \zeta \leq \frac{1}{2} \tag{3.6}$$

where λ_{min} is the shortest retrieved wavelength.

Hence, based on Eqs. (2.8), (3.5) and (3.6), the range in investigation depth is both affected by the velocity structure of the site and the frequency band over which Rayleigh waves are acquired. For instance, at soft (low velocity) sites (e.g., soft clay or peaty sites) generation and acquisition of lower frequencies will be required to achieve the same investigation depth as at stiff (high velocity) sites (e.g., compacted sand/gravel sites). The investigated depth is, therefore, further related to the type and location of the seismic source, the natural frequency of the geophones, and the configuration of the measurement profile, as shortly discussed below. For a more detailed discussion of this topic, the reader is referred to Foti et al. (2018).

For application of MASW, surface waves are most commonly generated by a reasonably heavy sledgehammer (e.g., 5–10 kg) that is either struck on an impact plate or directly on the ground surface. However, a source that can deliver more impact power into the ground (e.g., a heavy falling load or an accelerated weight drop) may create surface waves of lower frequencies (longer wavelengths) and therefore increase the investigation depth. Furthermore, combination of data obtained by use of different sources may be preferred in some cases (Foti et al., 2018). The use of electromechanical shakers or explosive sources is further possible but is limited and outside the scope of this project.

In order to sample the generated Rayleigh waves without distortion, the use of low-frequency geophones with a response curve suitable for the desired range of frequencies is required. In this aspect, the lower boundary of the response curve is generally more critical, that is, the geophones have a defined natural frequency below which their sensitivity tapers off. As the cut-off is gradual, it may be possible to sample frequencies below the geophones' natural frequency to some extent. However, such applications are limited in this work. To obtain an investigation depth of a few tens of meters, vertical geophones with a natural frequency of 4.5 Hz are commonly used (Xia et al., 2009). As the geophones only record vertical motion, it is important that they are placed vertically in the ground. Adequate coupling between the receivers and the ground is further essential, either through ground spikes or base plates.

3.3.1 Measurement profile configuration

It is commonly recognized that the configuration of the measurement profile can affect the quality of the dispersion data that is obtained (Dikmen et al., 2010; Ivanov et al., 2008; Park et al., 2001, 2002; Park & Carnevale, 2010; Wood & Cox, 2012; Xu et al., 2006; Zhang et al., 2004) and consequently the uncertainty associated with the dispersion curve identification and extraction. However, the 'optimal' values for the various data acquisition parameters are site-specific and depend on the objectives of the survey (e.g., the intended investigation depth) in each case. A summary of typical data acquisition parameters for MASW surveys is, e.g., provided by Park and Carnevale (2010) and Foti et al. (2018).

The length of the receiver spread is widely related to the longest wavelength that can be obtained during data acquisition (λ_{max}). A common rule-of-thumb is that the length of the receiver spread should at least be equal to the longest desired wavelength (Park & Carnevale, 2010; Foti et al., 2018), which based on Eq. (3.5) corresponds to an array length at least two times the desired maximum depth (z_{max}). However, relating both L and λ_{max} to z_{max} is not straightforward, as the maximum depth of profiling is also dependent on, e.g., the type/location of the source and the velocity structure of the site. The receiver spacing is further associated with the shortest wavelength that can be reliably sampled (λ_{min}). In general, the receiver spacing should not be greater than half the shortest wavelength in order to avoid spatial aliasing (Yilmaz, 1987), which can bias the dispersion curve identification in the higher frequency range.

Given that lateral changes in material properties are small, an increased length of the receiver spread provides improved spectral resolution as further discussed in *Paper II*. The high-amplitude peaks observed at each frequency appear sharper and better separation between different modes of surface wave propagation is observed (Ivanov et al., 2008; Ólafsdóttir et al., 2016), thus facilitating the dispersion curve picking. As previously mentioned, a longer receiver spread may also be preferred in order to acquire the lower frequency (longer wavelength) Rayleigh wave components that provide the deepest part of the shear wave velocity profile. However, an increased receiver spread length risks attenuation of higher frequency components and spatial aliasing if a fixed

number of geophones is used. In addition, long arrays are more susceptible to the influence of significant lateral variations in the subsoil. Overall, analysis of shots applied at both ends of the receiver spread (i.e., 'forward' and 'backward' shots) is of value in order to identify whether significant lateral variations are present and, hence, to assess the compliance of the 1D assumption adopted in the inversion analysis.

The analysis of the acquired data is based on the assumption that the wave front of the Rayleigh wave is plane. In general, the length of the source offset must be sufficient to assure plane wave propagation of surface wave components (Ivanov et al., 2008; Park & Carnevale, 2010; Yoon & Rix, 2009). The minimum source offset required to avoid near-field effects depends on the longest wavelength that is analysed. A very short source offset can result in an irregular and unreliable high-amplitude trend in the dispersion image at lower frequencies, usually displaying lower phase velocities than spectra free of this effect. An overly long source offset, however, risks excessive attenuation of fundamental mode components at higher frequencies (i.e., far-field effects).

3.3.2 Field procedures and measurement equipment

For the field measurements conducted as a part of this dissertation work, multi-channel surface wave records were acquired using a linear array of 24 equally spaced vertical geophones (see Fig. 3.4). The geophones used for data acquisition are of type GS-11D from Geospace Technologies and have a natural frequency of 4.5 Hz and a critical damping ratio of 0.5. The data from each geophone is recorded through a separate recording channel using a custom data acquisition system with two data acquisition cards of type NI USB-6218 from National Instruments in a custom enclosure (Fig. 3.6).

Figure 3.4: Geophone.

Figure 3.5: Cable.

Figure 3.6: Data acquisition cards connected to a laptop computer.

The field measurements are controlled with data acquisition software (MASWaves DAQ) written using the Data Acquisition Toolbox of MATLAB, which both displays the surface wave records in terms of recorded time-histories and spectral images. The two data acquisition cards are synchronized through external PFI lines to use a shared start trigger and a shared internal clock. The MASW measurement equipment is portable and can be contained in the two green boxes shown in Fig. 3.6.

A typical data acquisition set-up is shown in Fig. 3.7. The connection cable (Fig. 3.5) allows the geophones to be placed in the ground at up to 2 m intervals. Depending on the site conditions, as well as any logistical constraints, the test parameters (i.e., geophone spacing, source offset lengths and recording time) were adjusted to each test location. For the majority of the Icelandic test sites, survey profiles with receiver spacing of 0.5 m, 1.0 m and/or 2.0 m were used. The impact load was in most cases created by a 6–8 kg sledgehammer that was either struck vertically on a metallic base plate or directly on the surface at several different offsets from one or both ends of the receiver spread, with repeated shots recorded for each source location. As the triggering system did not provide sufficient accuracy for vertical stacking in the time domain during data acquisition, where required, stacking in the frequency–phase velocity domain was applied to improve the signal-to-noise ratio of the experimental data.

Figure 3.7: MASW measurement profile. Line-up of 24 geophones with equal spacing.

3.4 Dispersion analysis

In MASW testing, the dispersion analysis is usually achieved with spectral processing techniques (Socco et al., 2010) in which the multi-channel time series are transformed from the space–time domain into, e.g., the frequency–phase velocity domain or the frequency–wave number domain. Commonly used transform-based methods include the frequency–wave number (f–k) transform (e.g., Yilmaz, 1987), the slowness–frequency (p–ω) transform (McMechan & Yedlin, 1981), and the phase shift method (Park et al., 1998). Later variations include the selective-offset dispersion imaging scheme, proposed by Park (2011), and the slant f–k transform of Serdyukov et al. (2019). Dal Moro et al. (2003) compared the effectiveness of the phase shift method, the f–k transform and the p–ω transform to determine Rayleigh wave dispersion curves for near-surface applications in unconsolidated settlements. They concluded that the phase shift method is a robust and computationally efficient method that provides accurate fundamental mode phase velocities, even when data from as few as four geophones is available.

Alternative techniques for dispersion curve evaluation include the swept-frequency approach described by Park et al. (1999). Xia et al. (2007) further introduced a transform-based algorithm utilizing frequency-swept data along with linear move-out correlation and slant stacking, referred to as the frequency decomposition and slant stacking (FDSS) method. The accuracy of the FDSS algorithm was evaluated by comparison to the phase shift method. The results indicated that the fundamental mode phase velocities obtained with the two techniques were the same. Luo et al. (2008) further proposed the use of a high-resolution linear Radon transformation (HRLRT) (e.g., Sacchi & Ulrych, 1995) to improve the dispersion image resolution. However, as demonstrated by Shen et al. (2015), the f–k transform, p–ω transform, phase-shift method, and FDSS method all yield essentially equivalent results to the HRLRT, at least for noise-free data. By applying the power operation, the apparent dispersion image resolution can further be enhanced to be virtually the same as that obtained by the HRLRT (Shen et al., 2015).

The dispersion analysis software tool (MASWaves Dispersion) is based on application of the phase shift method. The phase shift method, as applied in this work, is described in Section 3.4.1.

3.4.1 Dispersion analysis process

An application of the phase shift method is divided into three main steps; Fourier transformation and amplitude normalization, dispersion imaging, and extraction of experimental dispersion curves. A comprehensive description of the computational procedure is provided in this section, whilst Fig. 3.8 provides a general overview of the dispersion analysis process.

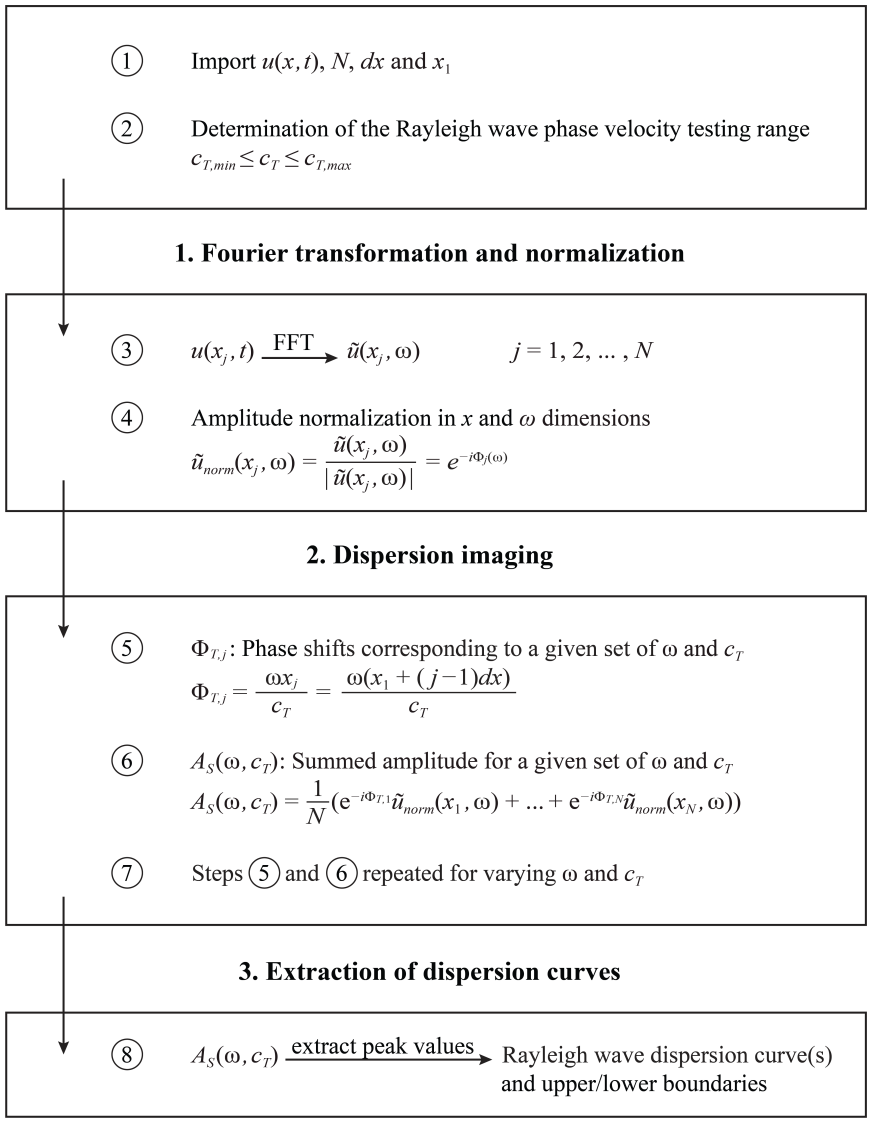

Figure 3.8: Overview of the dispersion analysis process (from Paper I).

The steps illustrated in Fig. 3.8 are the following:

1. Recorded data and information on survey layout is imported from the data acquisition software.
2. A phase velocity range for testing is established.
3. A Fast Fourier Transformation (FFT) is applied to each trace of the N-channel surface wave record ($u_j(t)$, $j = 1, 2, \ldots, N$) in order to decompose the record into individual frequency components ($\tilde{u}_j(\omega)$, $j = 1, 2, \ldots, N$).
4. The amplitude of the Fourier transformed record is normalized in both the offset and the frequency dimensions.
5. For a given testing phase velocity ($V_{R,test}$) and a given frequency (ω), the amount of phase shifts required to counterbalance the time delay corresponding to specific offsets is determined.

6. The phase shifts (determined in step 5 for a given testing phase velocity) are applied to distinct traces of the transformed record that are thereafter added to obtain the slant-stacked amplitude for each pair of ω and $V_{R,test}$.
7. Steps 5 and 6 are repeated for all the different frequency components of the transformed record in a scanning manner, changing $V_{R,test}$ in small increments within the previously specified range (step 2).
8. The phase velocity spectral image is obtained by plotting the summed amplitude in the frequency–phase velocity domain. The peak values (high-amplitude bands) display the dispersion characteristics of the recorded surface waves.

Fourier transformation and amplitude normalization

A Fourier transform is applied to the time axis of the recorded wavefield $u(x,t)$, resulting in its frequency-domain representation $\tilde{u}(x,\omega)$ where ω is angular frequency (Kreyszig, 2011; Park et al., 1998)

$$\tilde{u}(x,\omega) = \int_{-\infty}^{\infty} u(x,t)e^{-i\omega t}dt \tag{3.7}$$

As the recorded wavefield is discrete in both the offset and the time domain, Eq. (3.7) describes a one-dimensional discrete Fourier transform over time applied to each trace separately

$$\tilde{u}_j(\omega_l) = \sum_{m=0}^{N_s-1} u_j(t_m)e^{-i\omega_l t_m} \qquad j = 1,2,\ldots,N \tag{3.8}$$

where $\tilde{u}_j(\omega)$ is the Fourier transform of the j-th trace of the recorded wavefield ($u_j(t)$) and N_s is the number of sample points. The total recording time is $T = N_s dt$, where dt is the sampling interval, and the sample points are

$$t_m = mdt \qquad m = 0,1,\ldots,(N_s{-}1) \tag{3.9}$$

In $\tilde{u}(x,\omega)$, the frequency components of the original record have been separated into individual frequencies as indicated by Eq. (3.8). The frequency sample points are denoted by ω_l and given as (Schilling & Harris, 2012)

$$\omega_l = \frac{2\pi l}{T} = l\frac{\omega_s}{N_s} \qquad l = 0,1,\ldots,(N_s{-}1) \tag{3.10}$$

where ω_s is the sampling frequency (in radians).

The transformed wavefield $\tilde{u}(x,\omega)$ can be expressed in terms of amplitude $A(x,\omega)$ and phase $P(x,\omega)$ as

$$\tilde{u}(x,\omega) = A(x,\omega)P(x,\omega) \tag{3.11}$$

where information about the dispersion properties of the signal is preserved in $P(x,\omega)$ and $A(x,\omega)$ preserves information about other properties, such as the attenuation of the signal and its geometrical spreading (Everett, 2013; Park et al., 1998).

The transformed record can equivalently be expressed as

$$\tilde{u}(x,\omega) = A(x,\omega)e^{-i\Phi(\omega)x} \tag{3.12}$$

where

$$\Phi(\omega) = \frac{\omega}{V_R(\omega)} \tag{3.13}$$

and $V_R(\omega)$ is the phase velocity at angular frequency ω (Park et al., 1998).

Considering each discrete trace separately, Eq. (3.8) can be expressed as the product of amplitude $A_j(\omega_l)$ and phase $P_j(\omega_l)$ (Ryden et al., 2004)

$$\tilde{u}_j(\omega_l) = A_j(\omega_l)P_j(\omega_l) \tag{3.14}$$

for $j = 1, 2, \ldots, N$ and $l = 0, 1, \ldots, (N_s - 1)$.

The phase term in Eq. (3.14) is determined by the phase velocity of each frequency component

$$P_j(\omega_l) = e^{-i\Phi(\omega_l)x_j} \tag{3.15}$$

$$\Phi(\omega_l)x_j = \frac{\omega_l x_j}{V_R(\omega_l)} = \frac{\omega_l(x_1 + (j-1)dx)}{V_R(\omega_l)} \tag{3.16}$$

where x_1 is the source offset and dx is the receiver spacing.

As all information regarding the phase velocity of each frequency component is contained in $P_j(\omega_l)$, the amplitude can be normalized in both the offset and the frequency dimensions without loss of vital information (Ryden et al., 2004; Ryden & Park, 2006)

$$\tilde{u}_{j,norm}(\omega_l) = \frac{\tilde{u}_j(\omega_l)}{|\tilde{u}_j(\omega_l)|} = P_j(\omega_l) \tag{3.17}$$

where $\tilde{u}_{j,norm}(\omega_l)$ is the normalized representation of the j-th trace of the Fourier transformed wavefield at frequency ω_l.

The normalized wavefield has unit amplitude at different frequencies and offsets from the impact load point. In the subsequent discussion, it is also expressed as

$$\tilde{u}_{norm}(x,\omega) = \frac{\tilde{u}(x,\omega)}{|\tilde{u}(x,\omega)|} \tag{3.18}$$

Dispersion imaging and extraction of dispersion curves

The concept of the phase shift analysis is visualized in Fig. 3.9. Figure 3.9a shows an array of sinusoid curves with unit amplitudes. The curves can be thought of as multiple normalized traces from an N-channel impulsive surface wave record after a Fourier transform has been applied to the recorded wavefield. The frequency of the

sinusoid curves is assumed to be 20 Hz and they are assumed to propagate at a phase velocity of 140 m/s (Park, 2011).

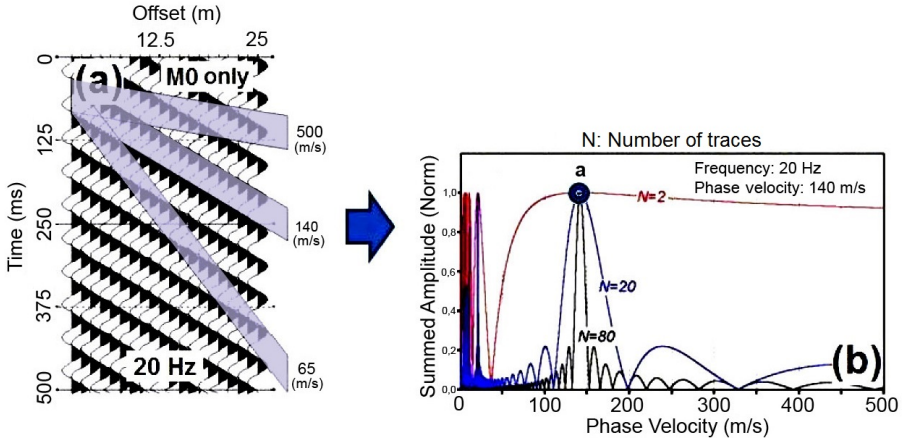

Figure 3.9: The concept of the phase shift method. (a) Normalized sinusoid curves with frequency of 20 Hz and phase velocity of 140 m/s. (b) Normalized summed amplitude as a function of phase velocity for different number of traces. After Park (2011).

The normalized sinusoid curves in Fig. 3.9a have the same phase along the slope corresponding to their actual phase velocity. However, the phase of the curves varies along slopes corresponding to other velocities. If the curves are added along the slope of 140 m/s, their sum will be another sinusoid curve with amplitude $A_s = N$ (normalized summed amplitude $A_{s,norm} = 1$) through a perfectly constructive superposition. If the curves are added together along any other slope, e.g., corresponding to a phase velocity of 65 m/s or 500 m/s (refer to Fig. 3.9a), the amplitude of the resulting summed curve will be less than N due to destructive superposition. This is illustrated in Fig. 3.9b. The point marked with an **a** corresponds to the summed amplitude along the slope of 140 m/s. This process of summing (or stacking) amplitudes in the offset domain along slanted paths is generally referred to as slant-stacking (Yilmaz, 1987). Figure 3.9b also indicates that the dispersion image resolution, implied by the sharpness of the peaks, can be enhanced by increasing the number of geophones used for data acquisition and keeping the receiver spacing unchanged.

Based on the previous description, the slant-stack function $\tilde{S}(\omega, V_{R,test})$ is defined as (Park et al., 1998; Ryden & Park, 2006)

$$\tilde{S}(\omega, V_{R,test}) = \int_{x_1}^{x_N} e^{-i\phi_{test}x} \frac{\tilde{u}(x,\omega)}{|\tilde{u}(x,\omega)|} dx = \int_{x_1}^{x_N} e^{-i\phi_{test}x} \tilde{u}_{norm}(x,\omega) dx \tag{3.19}$$

where ϕ_{test} is the angular wave number corresponding to testing phase velocity $V_{R,test}$ and angular frequency ω

$$\phi_{test} = \frac{\omega}{V_{R,test}} \tag{3.20}$$

The integral transformation in Eq. (3.19) includes summing over offsets of wavefields of a given frequency, after applying an offset-dependent phase shift determined for a given testing phase velocity. The normalization in Eq. (3.19) is applied in order to

assure equal weighting of traces from different offsets and gain control of effects of geometric damping and attenuation (Park et al., 1998).

For a given frequency ω, the maxima of $\tilde{S}(\omega, V_{R,test})$ will occur where

$$\phi_{test} = \Phi(\omega) \tag{3.21}$$

By utilizing Eqs. (3.13) and (3.20), Eq. (3.21) can be written as

$$\frac{\omega}{V_{R,test}} = \frac{\omega}{V_R(\omega)} \Leftrightarrow V_{R,test} = V_R(\omega) \tag{3.22}$$

Hence, in order to determine the dispersion characteristics of $u(x,t)$, the values of $\tilde{S}(\omega, V_{R,test})$ are examined. When the testing phase velocity is equal to the actual phase velocity corresponding to a given frequency, a maximum will be observed in $\tilde{S}(\omega, V_{R,test})$. Joining together the peak values of $\tilde{S}(\omega, V_{R,test})$ for different values of ω visualizes the dispersion characteristics of the acquired data. If higher modes get a substantial amount of energy, there will be two (or multiple) peak values for a given frequency, displaying the multi-modal characteristics of the recorded surface waves (Park et al., 1998; Ryden et al., 2004).

In practice the procedure is to vary $V_{R,test}$ for a given frequency ω, numerically evaluate the integral in Eq. (3.19) and study the maxima of $\tilde{S}(\omega, V_{R,test})$. The phase velocity is changed in small increments within a previously specified interval

$$V_{R,test,min} \leq V_{R,test} \leq V_{R,test,max} \tag{3.23}$$

By utilizing Eq. (3.17), Eq. (3.19) can be written in discrete form as

$$\tilde{S}_s(\omega_l, V_{R,test}) = \sum_{j=1}^{N} e^{-i\phi_{test}x_j} \tilde{u}_{j,norm}(\omega_l) = \sum_{j=1}^{N} e^{-i\phi_{test}x_j} P_j(\omega_l) \tag{3.24}$$

where

$$\phi_{test}x_j = \frac{\omega_l x_j}{V_{R,test}} = \frac{\omega_l(x_1 + (j-1)dx)}{V_{R,test}} \tag{3.25}$$

for $j = 1, 2, \ldots, N$ and $l = 0, 1, \ldots, (N_s - 1)$. The subscript s in Eq. (3.24) denotes summation.

The values of $\tilde{S}_s(\omega_l, V_{R,test})$, obtained by Eqs. (3.24) and (3.25), are complex numbers whose absolute value

$$A_s(\omega_l, V_{R,test}) = |\tilde{S}_s(\omega_l, V_{R,test})| \tag{3.26}$$

is the same as the summed (slant-stacked) amplitude for testing phase velocity $V_{R,test}$ and frequency ω_l. At each frequency ω_l, the value of $V_{R,test}$ that gives the maximum value of A_s is the value being sought (Park et al., 1998; Ryden et al., 2004). As the maximum value of A_s depends on the number of geophones used for data acquisition (N), A_s is normalized according to Eq. (3.27) so that the peak value is one in all cases.

$$A_{s,norm}(\omega_l, V_{R,test}) = \frac{A_s(\omega_l, V_{R,test})}{N} \tag{3.27}$$

The results obtained by Eqs. (3.24) to (3.27) for a given frequency ω_l and different values of $V_{R,test}$ may be represented by a plot of $V_{R,test}$ versus $A_{s,norm}$, as shown in Fig. 3.9b. However, the transformed surface wave records are customarily displayed by plotting the slant-stacked amplitude in the frequency–phase velocity domain, either in two or three dimensions (see Figs. 3.1df).

Overall, the fundamental mode dispersion curve is of most interest for the project presented in this dissertation. Hence the term 'dispersion curve' generally refers to the fundamental mode in the subsequent discussion.

3.5 Composite experimental dispersion curves

The dispersion analysis software includes a special module for combining dispersion curves that have been identified based on separate dispersion images, referred to as MASWaves Combination (see Fig. 3.2). The combined experimental dispersion curve is obtained by grouping the elementary dispersion curve data points together within $\log_a$ spaced wavelength intervals. Subsequently, the mean phase velocity within each interval is used as a point estimate of the velocity of Rayleigh wave components belonging to the given wavelength range. The aim is both to increase the range in wavelengths covered by the experimental dispersion curve, and to obtain error estimates of the experimental dispersion data prior to the inversion.

3.5.1 Uncertainties associated with surface wave measurements and dispersion curve identification

The uncertainty associated with the application of surface wave methods may be divided into aleatory and epistemic uncertainty (Foti et al., 2015). The term aleatoric uncertainty (i.e., stochastic variability) is associated with measurement uncertainties, whilst epistemic (i.e., model-based) uncertainty results from incomplete modelling (e.g., simplifications or assumptions incorporated in adopted models) and lack of scientific knowledge.

In the context of MASW measurements, uncertainty associated with the experimental data can arise from spatial variability in subsoil material properties, measurement and sampling errors (e.g. due to limitations of the measurement equipment or the data acquisition system, insufficient ground coupling of the geophones, or an imprecise measurement profile set-up) and coherent or incoherent noise in the recorded signal. Incoherent noise results from both natural phenomena and human activity such as traffic, vibrating machinery and construction activities. Electric and electronic noise, either in the measurement instruments (geophones, connection cables, DAQ cards) or from external sources (e.g., power lines), is further classified as incoherent noise.

Coherent noise comprises both non-surface wave events and non-compliant surface waves, that is surface wave energy that does not adhere to the assumed propagation model (e.g., near-field effects) (Foti et al., 2015). Non-surface wave events include the propagation of body waves, body wave refractions/reflections and air blasts.

Measures for the mitigation of the effects of incoherent noise include data acquisition during quite times (e.g., outside peak traffic hours or before/after work hours at construction sites) and averaging multiple measurements through stacking in the time- or frequency-domains. Furthermore, the measurement profile configuration affects the acquired data (refer to Section 3.3) and the use of different profile set-ups (including different shot locations) is important in order to, e.g., detect the presence of lateral variations and to assess the potential influence of near-field effects on the acquired records. Quantification of how the error associated with the recorded time series is propagated through the different data processing steps is, however, a challenging topic and outside the scope of this work. Direct estimates of the statistical distributions of the extracted phase velocity values (i.e., at each wavelength/frequency) may, however, provide some measure of the error associated with the Rayleigh wave dispersion data (see further in *Paper III*).

The processing of the recorded data and the dispersion curve identification/extraction can further introduce additional uncertainties to the experimental dispersion curves. This both includes imprecise picking of spectral maxima (e.g., due to limited spectral resolution at certain frequencies), misinterpretation of apparent dispersion curves and mode-number misidentification (i.e., incorrect enumeration of observed modal curves). Both mode misidentification and mode superposition may lead to severe errors if conventional modal inversion techniques are applied. A further source of uncertainty is potential inter-analyst variability associated with the manual or semi-manual dispersion curve picking. The human bias may be limited, however, by averaging dispersion curve picks obtained by several analysts. Previous studies have found that the low frequency (longer wavelength) part of the dispersion curve is generally characterized by higher uncertainty than the higher frequency (shorter wavelength) region (Lai et al., 2005). The results of field measurements conducted as a part of this work are consistent with those observations (see *Papers II–VI*).

3.5.2 Computational method

Assume that m multi-channel records have been obtained by repeated shots at the same survey site (eventually by using measurement profiles with different receiver spread lengths and/or different source offsets but the same midpoint). Each multi-channel record is processed separately (refer to Section 3.4.1) and an experimental dispersion curve (referred to as an elementary dispersion curve) consisting of n_j data points $(V_{R,j,l}, \lambda_{j,l})$ (where $l = 1, \ldots, n_j$ and $j = 1, \ldots, m$) is obtained based on the j-th record.

The composite experimental dispersion curve

$$(V_{R,e,q}, \lambda_{e,q}) \qquad q = 1, \ldots, Q \tag{3.28}$$

is obtained by grouping the data points of the m elementary dispersion curves together within $\log_a$ spaced (i.e. a^{-1}th octave) wavelength intervals $[\lambda^L_{e,q}, \lambda^U_{e,q})$. Q is the number of wavelength intervals, $\lambda_{e,q}$ is the reference point of the q-th interval and $\lambda^L_{e,q}$ and $\lambda^U_{e,q}$ are its upper and lower bounds, respectively. Hence, the wavelengths that characterize the q-th interval are obtained as

$$\begin{aligned} \lambda_{e,q} &= 2^{\frac{q-1}{a}} \\ \lambda^L_{e,q} &= \lambda_{e,q} \cdot 2^{\frac{-1}{2a}} \\ \lambda^U_{e,q} &= \lambda_{e,q} \cdot 2^{\frac{1}{2a}} \end{aligned} \tag{3.29}$$

Subsequently, all phase velocity values $V_{R,j,l}$ such that $\lambda_{j,l} \in [\lambda^L_{e,q}, \lambda^U_{e,q})$ are added up and their arithmetic mean (denoted by $V_{R,e,q}$) used as a point estimate of the phase velocity of Rayleigh wave components belonging to the given wavelength range.

The number and width of wavelength intervals used for computation of a composite dispersion curve are determined by the parameter a in Eq. (3.29). The width of each interval is inversely related to the value of a. As the interval length is logarithmically distributed, the effect of the different a-values on the interval length becomes more apparent with increasing wavelength. This is illustrated in Fig. 3.10. The reference wavelength value for each interval ($\lambda_{e,q}$) is indicated by a dot.

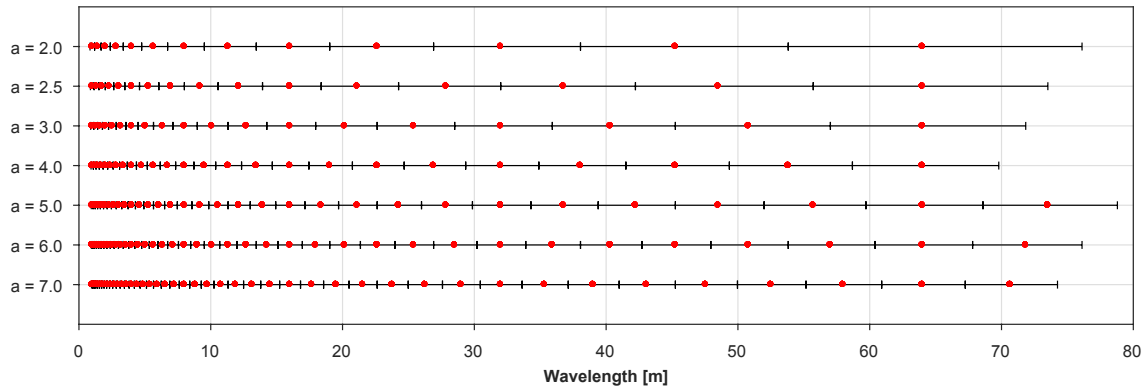

Figure 3.10: Effects of the parameter a in Eq. (3.29) on the length and range of the wavelength intervals used for computation of a composite dispersion curve.

Upper and lower bounds for the composite dispersion curve, Eq. (3.28), are obtained using the standard deviation of the phase velocity values within each wavelength interval (s_q). An upper bound dispersion curve corresponding to plus one standard deviation from the average curve is denoted by

$$(V_{R,e,q} + s_q, \lambda_{e,q}) \qquad q = 1, \ldots, Q \tag{3.30}$$

whilst a lower bound curve, corresponding to minus one standard deviation from the average curve, is

$$(V_{R,e,q} - s_q, \lambda_{e,q}) \qquad q = 1, \ldots, Q \tag{3.31}$$

3.5.3 Uncertainty assessments

The procedure described in Section 3.5.2 centres on estimating the mean Rayleigh wave phase velocity for each wavelength interval. Point estimates of sample statistics, such as the sample mean, are inevitably subject to error, especially when they are derived based on small sample sizes (in this context, a limited number of elementary dispersion curve data points within a given wavelength interval). Therefore, some variation from the true (population) mean is expected.

An interval estimate of an unknown parameter is a way to supplement the point estimate. The $(1-2p)100\%$ confidence interval (CI) of an unknown parameter is an interval such that it will enclose the true parameter value with a probability of $(1-2p)$. Using the classical statistical method, the $(1-2p)100\%$ confidence interval of the sample mean can be obtained by application of the central limit theorem (Ross, 2009). The bootstrap is an alternative, simulation based, method to estimate the confidence interval of a statistic without distributional assumptions (Efron, 1979; Efron & Tibshirani, 1993). Therefore, the use of the bootstrap is especially advantageous when the probability distribution of the statistic of interest is unknown or when the sample size is insufficient for application of classical statistical methods. For applications in geotechnical engineering, the bootstrap has been described as a valuable tool to estimate the variation of sample statistics that often, for example due to budget constraints, must be derived from small data sets (Li et al., 2015).

In *Paper II*, both classical statistics and the bootstrap were applied for evaluation of confidence intervals for composite dispersion curves obtained based on different elementary dispersion curve combinations.

Classical confidence intervals

Assume $\mathbf{y} = (y_1, y_2, \ldots, y_n)$ is a sample of size n drawn from a normal population with an unknown mean μ and an unknown variance σ^2. The $(1-2p)100\%$ confidence interval for the population mean is obtained as

$$\left(\overline{y}_{lo}, \overline{y}_{up}\right) = \left(\overline{y} - t_{n-1}^{(p)}\frac{s}{\sqrt{n}}, \overline{y} + t_{n-1}^{(p)}\frac{s}{\sqrt{n}}\right) \tag{3.32}$$

where $\overline{y}$ is the sample mean, s is the sample standard deviation and $t_{n-1}^{(p)}$ is the $(1-p)100\%$ percentile of the t-distribution with $(n-1)$ degrees of freedom (Snedecor & Cochran, 1989). Confidence intervals obtained by Eq. (3.32) are referred to as classical confidence intervals in this work.

If the sample size is sufficient, the central limit theorem states that the distribution of the sample mean will be approximately normal, regardless of the underlying probability distribution, given that $(y_1, y_2, \ldots, y_n)$ are independent, identically distributed variables. A general rule-of-thumb is that a sample size $n \geq 30$ is sufficient to use the normal distribution for $\overline{y}$, although in many cases the normal approximation is valid for substantially smaller sample sizes (Ross, 2009; Snedecor & Cochran, 1989).

The bootstrap and bootstrap confidence intervals

The bootstrap, introduced by Efron (1979), is a simulation-based method where Monte Carlo-style sampling is applied on the sample data. Subsequently, the value of the statistic of interest is computed for each resample and the relative frequency distribution of the replications used as an approximation of the sampling distribution of the given statistic. This section provides a brief overview of the nonparametric bootstrap and computation of bootstrap confidence intervals. A more detailed description is provided, e.g., by Efron and Tibshirani (1993).

Let $\mathbf{y} = (y_1, y_2, \ldots, y_n)$ be a sample of size n drawn from an unknown probability distribution F. It is further assumed that the sample is representative of the population from which it is drawn and that the observations are independently and identically distributed. The empirical distribution that puts equal probability on each value y_j $(j = 1, \ldots, n)$ is denoted by $\hat{F}$. Suppose that the objective is to estimate a parameter θ on the basis of $\mathbf{y}$ and to evaluate the accuracy of this estimate. The plug-in estimate of θ obtained from $\mathbf{y}$ is denoted by $\hat{\theta} = d(\mathbf{y})$. For instance, θ can denote the population mean (μ) and $\hat{\theta}$ the sample mean $(\overline{y})$. A bootstrap sample $\mathbf{y}^* = (y_1^*, y_2^*, \ldots, y_n^*)$ is a random sample of size n drawn from $\hat{F}$. The bootstrap replication of $\hat{\theta}$ corresponding to $\mathbf{y}^*$ is then $\hat{\theta}^* = d(\mathbf{y}^*)$.

B independent bootstrap samples $\mathbf{y}^{*1}, \mathbf{y}^{*2}, \ldots, \mathbf{y}^{*B}$ are drawn from $\hat{F}$ and the bootstrap replication corresponding to each sample $\hat{\theta}^*(b) = d(\mathbf{y}^{*b})$ $(b = 1, \ldots, B)$ is computed. The bootstrap samples contain the same number of data points as the original sample; however, each bootstrap sample can include some elements of $\mathbf{y}$ multiple times whilst not including other. Hence, the bootstrap replications will vary randomly. The subsequent empirical distribution of $\hat{\theta}^*(b)$ is referred to as the bootstrap distribution of the statistic and enables assessment of the uncertainty of $\hat{\theta}$.

Several types of confidence intervals can be obtained from the simulated bootstrap replications. These include the standard normal bootstrap confidence interval (SB), the percentile bootstrap confidence interval (PB) and the bias-corrected and accelerated (BCa) confidence interval. Standard normal confidence intervals are computed based on the assumption that the bootstrap replications are approximately normally distributed. The $(1 - 2p)100\%$ standard normal interval is obtained as

$$\left(\hat{\theta}_{SB,lo}, \hat{\theta}_{SB,up}\right) = \left(\hat{\theta} - z^{(p)}\widehat{se}, \hat{\theta} + z^{(p)}\widehat{se}\right) \tag{3.33}$$

where $\widehat{se}$ is the estimated standard error of $\hat{\theta}$ and $z^{(p)} = \Phi^{-1}(1-p)$ where Φ is the standard normal cumulative distribution function (CDF) and Φ^{-1} denotes its inverse.

If the bootstrap distribution is not approximately normal, the percentile confidence interval is preferable to the standard normal interval (Efron & Tibshirani, 1993). For computation of percentile intervals, the B bootstrap replications are ranked in order of increasing magnitude. The $(1-2p)100\%$ percentile interval is then obtained as

$$\left(\hat{\theta}_{PB,lo}, \hat{\theta}_{PB,up}\right) = \left(\hat{\theta}^*_s(Bp), \hat{\theta}^*_s(B\{1-p\})\right) \tag{3.34}$$

where $\hat{\theta}^*_s(b)$ is the b-th value in the ordered list of the bootstrap replications.

The percentile interval adjusts for bias in the bootstrap distribution. However, an advantage of the BCa method is that it incorporates both bias and skewness in the confidence interval computations (Efron & Tibshirani, 1993). The $(1-2p)100\%$ BCa interval endpoints are determined based on percentiles of the bootstrap distribution of $\hat{\theta}^*$ and two numerical parameters; the estimated bias correction ($\hat{z}_0$) and the acceleration ($\hat{a}$) which is a measure of how rapidly the standard error of $\hat{\theta}$ changes with respect to the true value θ. If $\hat{z}_0 = \hat{a} = 0$, the BCa confidence interval is identical to the percentile confidence interval.

$$\left(\hat{\theta}_{BCa,lo}, \hat{\theta}_{BCa,up}\right) = \left(\hat{\theta}^*_s(Bp_1), \hat{\theta}^*_s(Bp_2)\right) \tag{3.35}$$

where

$$p_1 = \Phi\left(\hat{z}_0 + \frac{\hat{z}_0 + z^{(1-p)}}{1-\hat{a}(\hat{z}_0 + z^{(1-p)})}\right),\ p_2 = \Phi\left(\hat{z}_0 + \frac{\hat{z}_0 + z^{(p)}}{1-\hat{a}(\hat{z}_0 + z^{(p)})}\right) \tag{3.36}$$

and $z^{(p)} = \Phi^{-1}(1-p)$.

The bias correction $\hat{z}_0$ is estimated as

$$\hat{z}_0 = \Phi^{-1}\left(\frac{\#\{\hat{\theta}^*(b) < \hat{\theta}\}}{B}\right) \tag{3.37}$$

where $\#\{\hat{\theta}^*(b) < \hat{\theta}\}$ denotes the number of bootstrap replications with values lower than that of the plug-in estimate of θ. The acceleration $\hat{a}$ is computed in terms of the jackknife values of $\hat{\theta}$ as

$$\hat{a} = \frac{\sum_{j=1}^{n}\left(\hat{\theta}_{(\cdot)} - \hat{\theta}_{(j)}\right)^3}{6\left\{\sum_{j=1}^{n}\left(\hat{\theta}_{(\cdot)} - \hat{\theta}_{(j)}\right)^2\right\}^{3/2}} \tag{3.38}$$

where $\mathbf{y}_{(j)}$ denotes the original sample $\mathbf{y}$ with its j-th point deleted, $\hat{\theta}_{(j)} = d(\mathbf{y}_{(j)})$ and $\hat{\theta}_{(\cdot)} = \sum_{j=1}^{n}\left(\hat{\theta}_{(j)}/n\right)$.

3.6 Inversion analysis

The objective of the inversion analysis is to obtain a shear wave velocity model that realistically represents the characteristics of the tested site. The inverse problem faced in this stage of the analysis is by nature ill-posed, non-linear, mix-determined, and non-unique. That is, the forward response of multiple significantly different shear wave velocity profiles can fit the experimental data similarly well in terms of dispersion misfit values (Foti et al., 2015). Hence, if available, a-priori information about the test area is of value to constrain the inversion and aid the selection of realistic V_S-profiles. Visual inspection of the experimental data can also assist in selection of V_S-models. For instance, to assess whether velocity reversals are likely to be encountered and help estimate the minimum thickness of the top-most soil layer and the maximum investigated depth (see further in Section 3.3.1).

In modern applications of MASW, the inversion analysis is generally formulated as an optimization problem where the objective is to minimize the value of a misfit function representing the distance between the experimental and theoretical dispersion curves. Different sets of soil model parameters (Fig. 3.11) are inserted into a previously established forward model (refer to Section 3.6.1) in an iterative way in search of a model that both fits the observed dispersion characteristics and incorporates the known features of the survey site. The uncertainty associated with the shear wave velocity profile assessment is both related to the experimental uncertainties and the challenges faced in the inversion analysis (e.g., solution non-uniqueness and discrete model parameterization).

3.6.1 Model parameterization and forward modelling

The modelling of Rayleigh wave dispersion curves for assumed soil models forms the basis of most conventional inversion analysis techniques. For computation of theoretical dispersion curves, the survey site is modelled as a linear elastic semi-infinite layered medium, consisting of a predefined number of finite-thickness layers (n) (Fig. 3.11). The forward modelling is further approximated as a plane-strain problem in the x-z plane where each layer is assumed to be flat and have homogeneous and isotropic properties. The parameters required to define the properties of the i-th layer are layer thickness (h_i), shear wave velocity ($V_{S,i}$), compressional wave velocity ($V_{P,i}$) (or Poisson's ratio (ν_i)) and mass density (ρ_i).

For the adopted model, the propagation of Rayleigh waves is described by the Rayleigh secular equation [Eq. (3.39)], written in implicit form as (Xia et al., 1999)

$$F_R(f, V_R, \mathbf{V_S}, \mathbf{V_P}, \boldsymbol{\rho}, \mathbf{h}) = 0 \tag{3.39}$$

where V_R is the phase velocity at frequency f. The soil model is described by the shear wave velocity vector $\mathbf{V_S} = [V_{S,1}, V_{S,2}, \ldots, V_{S,n}, V_{S,n+1}]$, the compressional wave velocity vector $\mathbf{V_P} = [V_{P,1}, V_{P,2}, \ldots, V_{P,n}, V_{P,n+1}]$, the density vector $\boldsymbol{\rho} = [\rho_1, \rho_2, \ldots, \rho_n, \rho_{n+1}]$

and the layer thickness vector $\mathbf{h} = [h_1, h_2, \ldots, h_n]$. Alternatively, using the relation described by Eq. (2.5), the values of the Poisson's ratio $\boldsymbol{\nu} = [\nu_1, \nu_2, \ldots, \nu_n, \nu_{n+1}]$ can be specified instead of the compressional wave velocity.

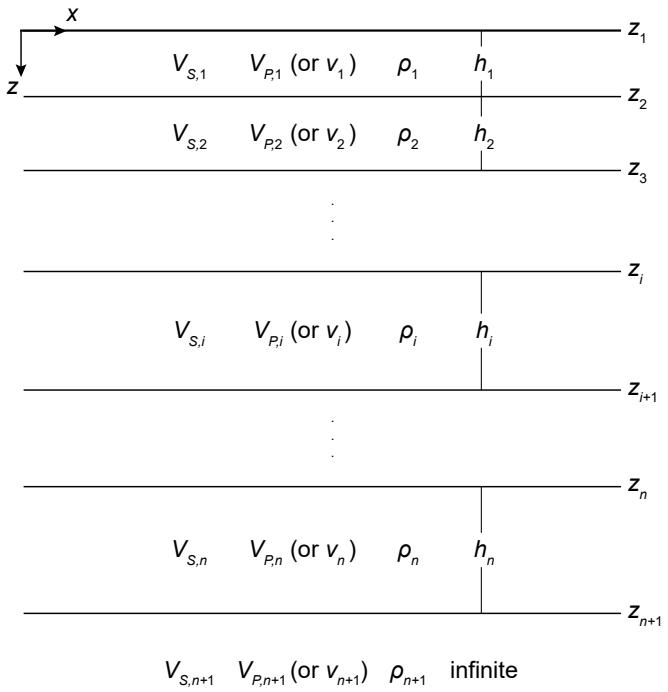

Figure 3.11: Semi-infinite layered soil model assumed for the inversion analysis.

The shear wave velocity has a dominant effect on the fundamental mode dispersion curve at frequencies higher than 5 Hz, followed by layer thicknesses (Xia et al., 1999), while variations in V_P (or ν) and ρ have much smaller influence. Hence, V_P (or ν) and ρ are commonly assigned fixed values based on a-priori information (including the estimated location of the groundwater table) or by using standard values for specific soil types. It should be noted, however, that an unreasonable assessment of the groundwater level can lead to significant errors in the inverted shear wave velocity profile. The initially specified layering parameterization (i.e., the number of layers) is further an important factor in the inversion process (Cox & Teague, 2016; Di Giulio et al., 2012; Foti et al., 2018) and the number of layers to include in the stratified soil model may be regarded as an additional inversion parameter. Implementing too few layers in the discrete soil model can inhibit the inversion scheme to correctly reproduce the variation in stiffness with depth, whilst over-parameterization may lead to an unreliable shear wave velocity model due to lack of data to constrain the inversion. However, no general rules exist for how to optimally specify the number of soil layers, but repeated analysis using different values of n has been recommended (Cox & Teague, 2016; Foti et al., 2018) so that the effects of the layering parameterization on the estimated V_S-profiles can be assessed. The results presented in this dissertation support those recommendations. Further discussion on this topic is provided in *Paper III*.

For modelling of theoretical dispersion curves, the values of V_R providing solutions to Eq. (3.39) for a given set of model parameters ($\mathbf{V_S}$, $\mathbf{V_P}$, $\boldsymbol{\rho}$, $\mathbf{h}$) over a particular range of frequencies are required. The Rayleigh secular equation can be established and solved using a variety of matrix-based methods that originated in the work of Thomson (1950) and Haskell (1953). Many of these methods were devised to resolve numerical overflow and loss-of-precision problems that may occur when the original Thomson-Haskell formulation is applied (Schwab, 1970). In general, a layer matrix is obtained for each of the $n+1$ layers in the assumed model, including the half-space. The layer matrices are then assembled in order to build the system (global) matrix that governs the problem. Different methods vary based on how the layer matrices are formulated and how they are assembled to form the system matrix. Commonly used algorithms include the Schwab-Knopoff method (Knopoff, 1964; Schwab, 1970; Schwab & Knopoff, 1970), the delta-matrix method (Dunkin, 1965; Thrower, 1965), the reduced delta-matrix method (Watson, 1970), the reflection-transmission method (Kennett, 1974; Kennett & Kerry, 1979), Abo-Zena's method (Abo-Zena, 1979; Menke, 1979), the stiffness matrix method (Kausel & Roësset, 1981), and the fast delta-matrix algorithm (Buchen & Ben-Hador, 1996). In the first version of the MASWaves software (*Paper I*), the stiffness matrix method was used for computation of theoretical dispersion curves. In revised versions (*Paper III* and *Paper IV*), the fast delta-matrix algorithm was implemented for enhanced computational efficiently.

Thomson–Haskell method (Transfer matrix method)

Thomson (1950) and Haskell (1953) formulated and presented the forward problem of surface wave propagation and dispersion in a vertically layered medium. The Thomson–Haskell method of determining surface wave dispersion curves is based on the use of transfer matrices in the frequency–wave number (ω–k) domain (Haskell, 1953) and thus also commonly referred to as the transfer matrix method. The main steps of the Thomson–Haskell method are summarized by Buchen and Ben-Hador (1996). Here, the main aspects of the notation of Buchen and Ben-Hador will be followed.

For layer i, the displacement field $\mathbf{u}_i = [u_i, v_i, w_i]^T$ can be obtained as

$$\begin{aligned} u_i &= u_i(x,z,t) = \frac{\partial \Phi_i}{\partial x} + \frac{\partial \Psi_i}{\partial z} \\ v_i &= v_i(x,z,t) = 0 \\ w_i &= w_i(x,z,t) = \frac{\partial \Phi_i}{\partial z} - \frac{\partial \Psi_i}{\partial x} \end{aligned} \tag{3.40}$$

where the potentials $\Phi_i = \Phi_i(x,z,t)$ and $\Psi_i = \Psi_i(x,z,t)$ are the solutions of the two-dimensional wave equations for the i-th layer

$$\nabla^2 \Phi_i = \frac{1}{V_{P,i}^2} \frac{\partial^2 \Phi_i}{\partial t^2} \qquad \nabla^2 \Psi_i = \frac{1}{V_{S,i}^2} \frac{\partial^2 \Psi_i}{\partial t^2} \tag{3.41}$$

The corresponding vertical stress field $\boldsymbol{\sigma}_i = [\sigma_{xz,i}, \sigma_{yz,i}, \sigma_{zz,i}]^T$ is subsequently obtained as

$$\begin{aligned}
\sigma_{xz,i}(x,z,t) &= \tau_i = G_i \left(2\frac{\partial^2 \Phi_i}{\partial x \partial z} + \frac{\partial^2 \Psi_i}{\partial^2 z} - \frac{\partial^2 \Psi_i}{\partial^2 x} \right) \\
\sigma_{yz,i}(x,z,t) &= 0 \\
\sigma_{zz,i}(x,z,t) &= \sigma_i = G_i \left(\frac{V_{P,i}^2}{V_{S,i}^2} \frac{\partial^2 \Phi_i}{\partial^2 z} + \left(\frac{V_{P,i}^2}{V_{S,i}^2} - 2 \right) \frac{\partial^2 \Phi_i}{\partial^2 x} - 2\frac{\partial^2 \Psi_i}{\partial x \partial z} \right)
\end{aligned} \tag{3.42}$$

The potentials Φ_i and Ψ_i for the i-th layer can be written as (Buchen & Ben-Hador, 1996)

$$\Phi_i(x,z,t) = (A_i e^{-kr_i z} + A_i' e^{kr_i z}) \cos(kx - \omega t) \tag{3.43}$$

$$\Psi_i(x,z,t) = (B_i e^{-ks_i z} + B_i' e^{ks_i z}) \sin(kx - \omega t) \tag{3.44}$$

where A_i and A_i' are P-wave up and down amplitudes, B_i and B_i' are S_V-wave up and down amplitudes, k is the wave number, ω is the angular frequency, $V_R = \omega/k$ is the Rayleigh wave phase velocity and

$$r_i = \sqrt{1 - \frac{V_R^2}{V_{P,i}^2}} \qquad s_i = \sqrt{1 - \frac{V_R^2}{V_{S,i}^2}} \qquad \text{for } V_R < V_{P,i} \text{ and } V_R < V_{S,i} \tag{3.45}$$

By inserting Eqs. (3.43) and (3.44) into Eqs. (3.40) and (3.42), the following matrix expression for the non-zero displacement–stress components of the i-th layer is obtained

$$\begin{bmatrix} u_i \\ w_i \\ \tau_i \\ \sigma_i \end{bmatrix} = \begin{bmatrix} -k\sin(kx-\omega t) & 0 & 0 & 0 \\ 0 & -k\cos(kx-\omega t) & 0 & 0 \\ 0 & 0 & k^2\sin(kx-\omega t) & 0 \\ 0 & 0 & 0 & k^2\cos(kx-\omega t) \end{bmatrix} \begin{bmatrix} U_i(z) \\ W_i(z) \\ X_i(z) \\ Z_i(z) \end{bmatrix}$$

where $\mathbf{y}_i(z) = [U_i(z),\ W_i(z),\ X_i(z),\ Z_i(z)]^T = \mathbf{M}_i \mathbf{P}_i \mathbf{E}_i(-z)\mathbf{a}_i = \mathbf{Q}_i \mathbf{E}_i(-z)\mathbf{a}_i$ is the state vector of the i-th layer. $\mathbf{M}_i$, $\mathbf{P}_i$ and $\mathbf{E}_i(z)$ are 4×4 matrices and $\mathbf{a}_i$ is a 4×1 amplitude vector, defined as follows, and $\mathbf{Q}_i = \mathbf{M}_i \mathbf{P}_i$.

$$\mathbf{M}_i = \begin{bmatrix} 1 & 0 & 0 & 0 \\ 0 & 1 & 0 & 0 \\ 0 & 0 & G_i & 0 \\ 0 & 0 & 0 & G_i \end{bmatrix} \qquad \mathbf{P}_i = \begin{bmatrix} 1 & 1 & s_i & -s_i \\ r_i & -r_i & 1 & 1 \\ 2r_i & -2r_i & \left(2 - \frac{V_R^2}{V_{S,i}^2}\right) & \left(2 - \frac{V_R^2}{V_{S,i}^2}\right) \\ \left(2 - \frac{V_R^2}{V_{S,i}^2}\right) & \left(2 - \frac{V_R^2}{V_{S,i}^2}\right) & 2s_i & -2s_i \end{bmatrix}$$

$$\mathbf{E}_i(z) = \begin{bmatrix} e^{kr_i z} & 0 & 0 & 0 \\ 0 & e^{-kr_i z} & 0 & 0 \\ 0 & 0 & e^{ks_i z} & 0 \\ 0 & 0 & 0 & e^{-ks_i z} \end{bmatrix} \qquad \mathbf{a}_i = \begin{bmatrix} A_i \\ A_i' \\ B_i \\ B_i' \end{bmatrix} \tag{3.46}$$

For a multi-layered medium, the displacement and stress fields must be continuous at all layer interfaces, i.e. for layer $i = 1, \ldots, n$ it is required that

$$\mathbf{y}_{i+1}^{(T)} = \mathbf{y}_i^{(B)} \tag{3.47}$$

where the superscripts (T) and (B) denote the top and bottom of the i-th layer, respectively.

The state vectors (i.e., the displacements and stresses) at any two depths $z_{i,1}$ and $z_{i,2}$ within the i-th layer can be related through a 4×4 matrix $\mathbf{T}_i(z) = \mathbf{Q}_i \mathbf{E}_i(z) \mathbf{Q}_i^{-1}$. Particularly, the state vectors at the top and bottom of the i-th layer can be related through the matrix $\mathbf{T}_i = \mathbf{T}_i(h_i)$. The matrix $\mathbf{T}_i$ is generally referred to as the transfer matrix of the i-th layer

$$\mathbf{y}_i^{(T)} = \mathbf{T}_i \mathbf{y}_i^{(B)} \tag{3.48}$$

The components of $\mathbf{T}_i$, written in terms of hyperbolic functions, are

$$\begin{aligned}
t_{11,i} &= 2\frac{V_{S,i}^2}{V_R^2}\cosh(kr_i h_i) - \left(2\frac{V_{S,i}^2}{V_R^2} - 1\right)\cosh(ks_i h_i) \\
t_{12,i} &= -\left(2\frac{V_{S,i}^2}{V_R^2} - 1\right) r_i^{-1}\sinh(kr_i h_i) + 2\frac{V_{S,i}^2}{V_R^2} s_i \sinh(ks_i h_i) \\
t_{13,i} &= (V_R^2\rho_i)^{-1}\left(r_i^{-1}\sinh(kr_i h_i) - s_i \sinh(ks_i h_i)\right) \\
t_{14,i} &= -(V_R^2\rho_i)^{-1}\left(\cosh(kr_i h_i) - \cosh(ks_i h_i)\right) \\
t_{21,i} &= 2\frac{V_{S,i}^2}{V_R^2} r_i \sinh(kr_i h_i) - \left(2\frac{V_{S,i}^2}{V_R^2} - 1\right) s_i^{-1}\sinh(ks_i h_i) \\
t_{22,i} &= -\left(2\frac{V_{S,i}^2}{V_R^2} - 1\right)\cosh(kr_i h_i) + 2\frac{V_{S,i}^2}{V_R^2}\cosh(ks_i h_i) \\
t_{23,i} &= -t_{14,i} \\
t_{24,i} &= (V_R^2\rho_i)^{-1}\left(-r_i \sinh(kr_i h_i) + s_i^{-1}\sinh(ks_i h_i)\right) \\
t_{31,i} &= V_R^2\rho_i\left(\left(2\frac{V_{S,i}^2}{V_R^2}\right)^2 r_i \sinh(kr_i h_i) - \left(2\frac{V_{S,i}^2}{V_R^2} - 1\right)^2 s_i^{-1}\sinh(ks_i h_i)\right) \\
t_{32,i} &= -2V_{S,i}^2\rho_i\left(2\frac{V_{S,i}^2}{V_R^2} - 1\right)\left(\cosh(kr_i h_i) - \cosh(ks_i h_i)\right) \\
t_{33,i} &= t_{11,i} \\
t_{34,i} &= -t_{21,i} \\
t_{41,i} &= -t_{32,i} \\
t_{42,i} &= V_R^2\rho_i\left(-\left(2\frac{V_{S,i}^2}{V_R^2} - 1\right)^2 r_i^{-1}\sinh(kr_i h_i) + \left(2\frac{V_{S,i}^2}{V_R^2}\right)^2 s_i \sinh(ks_i h_i)\right) \\
t_{43,i} &= -t_{12,i} \\
t_{44,i} &= t_{22,i}
\end{aligned} \tag{3.49}$$

Inserting Eq. (3.47) into Eq. (3.48) leads to the Thomson–Haskell recursion

$$\mathbf{y}_i^{(T)} = \mathbf{T}_i \mathbf{y}_{i+1}^{(T)} \qquad i = 1, \ldots, n \tag{3.50}$$

Applying Eq. (3.50) to all the layers of the assumed model relates the displacements and stresses at the surface to the displacements and stresses at the top of the half-space through the matrix product of all the layer transfer matrices $\mathbf{T} = \mathbf{T}_1 \mathbf{T}_2 \ldots \mathbf{T}_{n-1} \mathbf{T}_n$

$$\mathbf{y}_1^{(T)} = (\mathbf{T}_1 \mathbf{T}_2 \ldots \mathbf{T}_{n-1} \mathbf{T}_n) \mathbf{y}_{n+1}^{(T)} = \mathbf{T} \mathbf{y}_{n+1}^{(T)} \tag{3.51}$$

The boundary conditions for Rayleigh wave motion, zero stresses at the free surface and vanishing of the wavefield as $z \to \infty$, lead to the following form of the dispersion equation (Buchen & Ben-Hador, 1996)

$$F_R(V_R, k) = \det(\mathbf{UTV}) = 0 \tag{3.52}$$

where $\mathbf{U}$ and $\mathbf{V}$ are boundary condition matrices defined as

$$\mathbf{U} = \begin{bmatrix} 0 & 0 & 1 & 0 \\ 0 & 0 & 0 & 1 \end{bmatrix} \tag{3.53}$$

and

$$\mathbf{V} = \begin{bmatrix} 1 & s_{n+1} \\ r_{n+1} & 1 \\ 2G_{n+1} r_{n+1} & G_{n+1}\left(2 - \frac{V_R^2}{V_{S,n+1}^2}\right) \\ G_{n+1}\left(2 - \frac{V_R^2}{V_{S,n+1}^2}\right) & 2G_{n+1} s_{n+1} \end{bmatrix} \tag{3.54}$$

Stiffness matrix method

Kausel and Roësset (1981) presented an alternate formulation of the transfer matrix method utilizing stiffness matrices, similar to those frequently used in conventional structural analysis (the finite element method). An element stiffness matrix is obtained for each layer. The element stiffness matrix of a distinct layer relates the stresses at the upper and lower interfaces of the layer to the corresponding displacements. For a multi-layered model, the system stiffness matrix is assembled utilizing common layer interfaces (degrees of freedom). The system stiffness matrix can then be used, along with the prescribed external stresses at the layer interfaces, to solve for the displacements with techniques analogous to those used in the finite element method.

The Thomson–Haskell recursive formula, Eq. (3.50), relates the state vector at a given layer interface $\mathbf{y}_{i+1}^{(T)}$ to the state vector at the previous interface $\mathbf{y}_i^{(T)}$ through a transfer matrix $\mathbf{T}_i = \mathbf{T}_i(h_i)$ that is a function of the material properties of the i-th layer [see Eq. (3.49)].

The inverse of the transfer matrix for the i-th layer, here denoted by $\mathbf{H}_i$, is obtained as (Buchen & Ben-Hador, 1996)

$$\mathbf{H}_i = (\mathbf{T}_i(h_i))^{-1} = \mathbf{T}_i(-h_i) \tag{3.55}$$

Hence, the Thomson–Haskell recursive formula [Eq. (3.50)] can be rewritten as

$$\mathbf{y}_{i+1}^{(T)} = \mathbf{H}_i \mathbf{y}_i^{(T)} \qquad i = 1, \ldots, n \tag{3.56}$$

Kausel and Roësset (1981) partitioned the matrix $\mathbf{H}_i$ into four equally sized submatrices, here denoted by $\mathbf{H}_{11,i}$, $\mathbf{H}_{12,i}$, $\mathbf{H}_{21,i}$, and $\mathbf{H}_{22,i}$

$$\mathbf{H}_i = \begin{bmatrix} \mathbf{H}_{11,i} & \mathbf{H}_{12,i} \\ \mathbf{H}_{21,i} & \mathbf{H}_{22,i} \end{bmatrix} \tag{3.57}$$

The state vector at the upper interface of the i-th layer is further partitioned as

$$\mathbf{y}_i^{(T)} = \begin{bmatrix} \mathbf{x}_i \\ \mathbf{z}_i \end{bmatrix} \tag{3.58}$$

where $\mathbf{x}_i$ and $\mathbf{z}_i$ denote the displacement and stress vectors at the upper interface of the i-th layer, respectively. For simplification in notation, the superscripts (T) and (B) are omitted from the vectors $\mathbf{x}_i$ and $\mathbf{z}_i$. The vectors $\mathbf{x}_{i+1}$ and $\mathbf{z}_{i+1}$ are to be understood as the displacement and stress vectors at the upper interface of layer $i+1$ and the displacement and stress vectors at the lower interface of the i-th layer in accordance to Eq. (3.47). The recursive formula [Eq. (3.56)] thus becomes

$$\begin{bmatrix} \mathbf{x}_{i+1} \\ \mathbf{z}_{i+1} \end{bmatrix} = \begin{bmatrix} \mathbf{H}_{11,i} & \mathbf{H}_{12,i} \\ \mathbf{H}_{21,i} & \mathbf{H}_{22,i} \end{bmatrix} \begin{bmatrix} \mathbf{x}_i \\ \mathbf{z}_i \end{bmatrix} \tag{3.59}$$

The external loads applied at the upper and lower boundaries of the i-th layer are represented by an element external load vector, here denoted by $\mathbf{p}_{e,i} = [\mathbf{p}_i, \mathbf{p}_{i+1}]^T$. Equilibrium conditions for the i-th layer require that

$$\begin{bmatrix} \mathbf{p}_i \\ \mathbf{p}_{i+1} \end{bmatrix} = \begin{bmatrix} \mathbf{z}_i \\ -\mathbf{z}_{i+1} \end{bmatrix} \tag{3.60}$$

Inserting Eq. (3.60) into Eq. (3.59) and solving for the element external load vector results in

$$\begin{bmatrix} \mathbf{p}_i \\ \mathbf{p}_{i+1} \end{bmatrix} = \begin{bmatrix} -\mathbf{H}_{12,i}^{-1}\mathbf{H}_{11,i} & \mathbf{H}_{12,i}^{-1} \\ \mathbf{H}_{22,i}\mathbf{H}_{12,i}^{-1}\mathbf{H}_{11,i} - \mathbf{H}_{21,i} & -\mathbf{H}_{22,i}\mathbf{H}_{12,i}^{-1} \end{bmatrix} \begin{bmatrix} \mathbf{x}_i \\ \mathbf{x}_{i+1} \end{bmatrix} \tag{3.61}$$

or

$$\mathbf{p}_{e,i} = \mathbf{K}_{e,i}\mathbf{u}_{e,i} \tag{3.62}$$

where the matrix $\mathbf{K}_{e,i}$ is referred to as the element stiffness matrix of the i-th layer and $\mathbf{u}_{e,i} = [\mathbf{x}_i, \mathbf{x}_{i+1}]^T$ is the element displacement vector of the i-th layer. Equation (3.62) is referred to as the element matrix equation of the i-th layer.

The components of the element stiffness matrix $\mathbf{K}_{e,i}$ for layers $i = 1, \ldots, n$ can be written in terms of hyperbolic functions as

$$
\begin{aligned}
\kappa_{11,i} &= \frac{k\rho_i V_R^2}{D_i}\left(s_i^{-1}\cosh\left(kr_ih_i\right)\sinh\left(ks_ih_i\right) - r_i\sinh\left(kr_ih_i\right)\cosh\left(ks_ih_i\right)\right)\\
\kappa_{12,i} &= \frac{k\rho_i V_R^2}{D_i}\left(\cosh\left(kr_ih_i\right)\cosh\left(ks_ih_i\right) - r_is_i\sinh\left(kr_ih_i\right)\sinh\left(ks_ih_i\right) - 1\right)\\
&\quad - k\rho_i V_{S,i}^2(1+s_i^2)\\
\kappa_{13,i} &= \frac{k\rho_i V_R^2}{D_i}\left(r_i\sinh\left(kr_ih_i\right) - s_i^{-1}\sinh\left(ks_ih_i\right)\right)\\
\kappa_{14,i} &= \frac{k\rho_i V_R^2}{D_i}\left(-\cosh\left(kr_ih_i\right) + \cosh\left(ks_ih_i\right)\right)\\
\kappa_{21,i} &= \kappa_{12,i}\\
\kappa_{22,i} &= \frac{k\rho_i V_R^2}{D_i}\left(r_i^{-1}\sinh\left(kr_ih_i\right)\cosh\left(ks_ih_i\right) - s_i\cosh\left(kr_ih_i\right)\sinh\left(ks_ih_i\right)\right)\\
\kappa_{23,i} &= -\kappa_{14,i}\\
\kappa_{24,i} &= \frac{k\rho_i V_R^2}{D_i}\left(-r_i^{-1}\sinh\left(kr_ih_i\right) + s_i\sinh\left(ks_ih_i\right)\right)\\
\kappa_{31,i} &= \kappa_{13,i}\\
\kappa_{32,i} &= -\kappa_{14,i}\\
\kappa_{33,i} &= \kappa_{11,i}\\
\kappa_{34,i} &= -\kappa_{12,i}\\
\kappa_{41,i} &= \kappa_{14,i}\\
\kappa_{42,i} &= \kappa_{24,i}\\
\kappa_{43,i} &= -\kappa_{12,i}\\
\kappa_{44,i} &= \kappa_{22,i}
\end{aligned}
\tag{3.63}
$$

where r_i and s_i are given by Eq. (3.45) and

$$
D_i = 2\left(1-\cosh\left(kr_ih_i\right)\cosh\left(ks_ih_i\right)\right) + \left(\frac{1}{r_is_i} + r_is_i\right)\sinh\left(kr_ih_i\right)\sinh\left(ks_ih_i\right) \tag{3.64}
$$

The components of the half-space element stiffness matrix $\mathbf{K}_{e,n+1}$ are

$$
\begin{aligned}
\kappa_{11,n+1} &= k\rho_{n+1}V_{S,n+1}^2\frac{r_{n+1}(1-s_{n+1}^2)}{1-r_{n+1}s_{n+1}}\\
\kappa_{12,n+1} &= k\rho_{n+1}V_{S,n+1}^2\frac{1-s_{n+1}^2}{1-r_{n+1}s_{n+1}} - 2k\rho_{n+1}V_{S,n+1}^2\\
\kappa_{21,n+1} &= \kappa_{12,n+1}\\
\kappa_{22,n+1} &= k\rho_{n+1}V_{S,n+1}^2\frac{s_{n+1}(1-s_{n+1}^2)}{1-r_{n+1}s_{n+1}}
\end{aligned}
\tag{3.65}
$$

The element matrix equations [Eq. (3.62)] obtained for each layer are subsequently assembled at the common layer interfaces to form the system equation. The matrix $\mathbf{K}$ is referred to as the system stiffness matrix of the layered model. The vectors $\mathbf{p}$ and $\mathbf{u}$ are the system force vector and the system displacement vector, respectively

$$\mathbf{p} = \mathbf{K}\mathbf{u} \tag{3.66}$$

The natural modes of Rayleigh wave propagation are obtained by considering a system with no external loading, i.e. where $\mathbf{p} = \mathbf{0}$. Equation (3.66) thus becomes

$$\mathbf{K}\mathbf{u} = \mathbf{0} \tag{3.67}$$

For nontrivial solutions of Eq. (3.67), the determinant of the system stiffness matrix $\mathbf{K}$ must vanish. Hence, wave numbers that represent the modal solutions at various frequencies are obtained as the solutions of

$$F_R(V_R, k) = \det(\mathbf{K}) = 0 \tag{3.68}$$

where

$$\mathbf{K} = \begin{bmatrix} \mathbf{K}_{11,1} & \mathbf{K}_{12,1} & & & & & \\ \mathbf{K}_{21,1} & \mathbf{K}_{22,1}+\mathbf{K}_{11,2} & \mathbf{K}_{12,2} & & & & \\ & \mathbf{K}_{21,2} & \mathbf{K}_{22,2}+\mathbf{K}_{11,3} & \mathbf{K}_{12,3} & & & \\ & & \ddots & \ddots & \ddots & & \\ & & & \mathbf{K}_{21,n-1} & \mathbf{K}_{22,n-1}+\mathbf{K}_{11,n} & \mathbf{K}_{12,n} & \\ & & & & \mathbf{K}_{21,n} & \mathbf{K}_{22,n}+\mathbf{K}_{e,n+1} & \end{bmatrix} \tag{3.69}$$

$\mathbf{K}_{11,i}$, $\mathbf{K}_{12,i}$, $\mathbf{K}_{21,i}$ and $\mathbf{K}_{22,i}$ are the 2×2 sub-matrices of the element stiffness matrix for the i-th layer [see Eqs. (3.63) and (3.70)]

$$\mathbf{K}_{e,i} = \begin{bmatrix} \mathbf{K}_{11,i} & \mathbf{K}_{12,i} \\ \mathbf{K}_{21,i} & \mathbf{K}_{22,i} \end{bmatrix} = \left[\begin{array}{cc:cc} \kappa_{11,i} & \kappa_{12,i} & \kappa_{13,i} & \kappa_{14,i} \\ \kappa_{21,i} & \kappa_{22,i} & \kappa_{23,i} & \kappa_{24,i} \\ \hdashline \kappa_{31,i} & \kappa_{32,i} & \kappa_{33,i} & \kappa_{34,i} \\ \kappa_{41,i} & \kappa_{42,i} & \kappa_{43,i} & \kappa_{44,i} \end{array}\right] \qquad i = 1, \ldots, n \tag{3.70}$$

and $\mathbf{K}_{e,n+1}$ is the 2×2 half-space element stiffness matrix [see Eqs. (3.65) and (3.71)]

$$\mathbf{K}_{e,n+1} = \begin{bmatrix} \kappa_{11,n+1} & \kappa_{12,n+1} \\ \kappa_{21,n+1} & \kappa_{22,n+1} \end{bmatrix} \tag{3.71}$$

Fast delta matrix algorithm

The fast delta matrix formulation (Buchen & Ben-Hador, 1996) has origins in the transformation scheme of Schwab (1970) and the delta matrix representation initially adopted for surface wave dispersion computations by Thrower (1965) and Dunkin (1965). Buchen and Ben-Hador (1996) obtain the explicit matrix transformation

that reduces the Thomson–Haskell transfer matrix $\mathbf{T}_i$ [Eq. (3.49)] to the simpler and computationally more efficient algebraic form first presented by Schwab (1970). Subsequently, in order to handle the instability problem associated with the original Thomson–Haskell formulation, the dispersion equation [Eq. (3.52)] is expressed in terms of delta matrices, which also provides additional computational efficiency.

Starting from Eq. (3.46), the transformation $\mathbf{Z}_i = \mathbf{Y}_i\mathbf{P}_i$ (Buchen & Ben-Hador, 1996) where

$$\mathbf{Y}_i = \frac{V_{S,i}^2}{V_R^2}\begin{bmatrix} 2 & 0 & 0 & -1 \\ 0 & \left(2 - \frac{V_R^2}{V_{S,i}^2}\right) & -1 & 0 \\ 0 & 2 & -1 & 0 \\ -\left(2 - \frac{V_R^2}{V_{S,i}^2}\right) & 0 & 0 & 1 \end{bmatrix} \tag{3.72}$$

both transforms the layer matrix $\mathbf{P}_i$ to block diagonal form and separates matrix elements that are determined by the compressional wave velocity and the shear wave velocity of each layer, respectively.

$$\mathbf{Z}_i = \mathbf{Y}_i\mathbf{P}_i = \begin{bmatrix} 1 & 1 & 0 & 0 \\ -r_i & r_i & 0 & 0 \\ 0 & 0 & 1 & 1 \\ 0 & 0 & s_i & -s_i \end{bmatrix} \tag{3.73}$$

Subsequently, by utilizing Eq. (3.73) and, therefore, $\mathbf{P}_i = \mathbf{Y}_i^{-1}\mathbf{Z}_i$ and $\mathbf{P}_i^{-1} = \mathbf{Z}_i^{-1}\mathbf{Y}_i$, the transfer matrix [Eq. (3.49)] is reformulated as

$$\mathbf{T}_i = \mathbf{Q}_i\mathbf{E}_i\mathbf{Q}_i^{-1} = \mathbf{M}_i\mathbf{Y}_i^{-1}\mathbf{F}_i\mathbf{Y}_i\mathbf{M}_i^{-1} \tag{3.74}$$

where the block diagonal matrix $\mathbf{F}_i$ is defined as

$$\begin{aligned} \mathbf{F}_i &= \mathbf{Z}_i\mathbf{E}_i\mathbf{Z}_i^{-1} \\ &= \begin{bmatrix} \cosh(kr_ih_i) & -r_i^{-1}\sinh(kr_ih_i) & 0 & 0 \\ -r_i\sinh(kr_ih_i) & \cosh(kr_ih_i) & 0 & 0 \\ 0 & 0 & \cosh(ks_ih_i) & s_i^{-1}\sinh(ks_ih_i) \\ 0 & 0 & s_i\sinh(ks_ih_i) & \cosh(ks_ih_i) \end{bmatrix} \end{aligned} \tag{3.75}$$

By defining $\mathbf{z}_i^{(T)} = \mathbf{S}_i\mathbf{y}_i^{(T)}$ (Buchen & Ben-Hador, 1996), the Thomson–Haskell recursion equation [Eq. (3.50)] and the associated boundary conditions, i.e., $\mathbf{U}\mathbf{y}_1^{(T)} = \mathbf{0}$ (at the surface) and $\mathbf{y}_{n+1}^{(T)} = \mathbf{V}\left[A_{n+1}B_{n+1}\right]^T$ (for the half-space) may be transformed as follows

$$\begin{aligned} &\mathbf{z}_i^{(T)} = \widetilde{\mathbf{T}}_i\mathbf{z}_{i+1}^{(T)} \qquad i = 1, \ldots, n \\ &\widetilde{\mathbf{U}}\mathbf{z}_1^{(T)} = 0 \\ &\mathbf{z}_{n+1}^{(T)} = \widetilde{\mathbf{V}}\left[A_{n+1}B_{n+1}\right]^T \end{aligned} \tag{3.76}$$

where

$$\widetilde{\mathbf{T}}_i = \mathbf{S}_i \mathbf{T}_i \mathbf{S}_{i+1}^{-1} \qquad \widetilde{\mathbf{U}} = \mathbf{U}\mathbf{S}_1^{-1} \qquad \widetilde{\mathbf{V}} = \mathbf{S}_{n+1}\mathbf{V} \tag{3.77}$$

whilst the dispersion equation [Eq. (3.52)] remains invariant as $\widetilde{\mathbf{U}}\widetilde{\mathbf{T}}\widetilde{\mathbf{V}} = \mathbf{U}\mathbf{T}\mathbf{V}$ where $\widetilde{\mathbf{T}} = \widetilde{\mathbf{T}}_1\widetilde{\mathbf{T}}_2 \ldots \widetilde{\mathbf{T}}_{n-1}\widetilde{\mathbf{T}}_n$.

Hence, by specifying $\mathbf{S}_i = \mathbf{Y}_i\mathbf{M}_i^{-1}$ [refer to Eq. (3.74)] the elements of the transformed matrix $\widetilde{\mathbf{T}}_i$ (for layers $i = 1, \ldots, n$) can be written in terms of hyperbolic functions as

$$\begin{aligned}
\tilde{t}_{11,i} &= a_i \cosh(kr_i h_i) \\
\tilde{t}_{12,i} &= -b_i r_i^{-1} \sinh(kr_i h_i) \\
\tilde{t}_{13,i} &= -a_i' r_i^{-1} \sinh(kr_i h_i) \\
\tilde{t}_{14,i} &= -b_i' \cosh(kr_i h_i) \\
\tilde{t}_{21,i} &= -a_i r_i \sinh(kr_i h_i) \\
\tilde{t}_{22,i} &= b_i \cosh(kr_i h_i) \\
\tilde{t}_{23,i} &= a_i' \cosh(kr_i h_i) \\
\tilde{t}_{24,i} &= b_i' r_i \sinh(kr_i h_i) \\
\tilde{t}_{31,i} &= -a_i' s_i^{-1} \sinh(ks_i h_i) \\
\tilde{t}_{32,i} &= b_i' \cosh(ks_i h_i) \\
\tilde{t}_{33,i} &= a_i \cosh(ks_i h_i) \\
\tilde{t}_{34,i} &= b_i s_i^{-1} \sinh(ks_i h_i) \\
\tilde{t}_{41,i} &= -a_i' \cosh(ks_i h_i) \\
\tilde{t}_{42,i} &= b_i' s_i \sinh(ks_i h_i) \\
\tilde{t}_{43,i} &= a_i s_i \sinh(ks_i h_i) \\
\tilde{t}_{44,i} &= b_i \cosh(ks_i h_i)
\end{aligned} \tag{3.78}$$

where a_i, a_i', b_i, and b_i' are layer parameters, defined by Buchen and Ben-Hador (1996), that depend on the mass density and shear wave velocity of the i-th and $(i+1)$-th layers and the Rayleigh wave phase velocity, i.e.

$$a_i = \frac{\rho_{i+1}}{\rho_i} + 2\left(\frac{V_{S,i}^2}{V_R^2} - \frac{\rho_{i+1}}{\rho_i} \cdot \frac{V_{S,i+1}^2}{V_R^2}\right) \qquad a_i' = a_i - 1 \tag{3.79}$$

$$b_i = 1 - 2\left(\frac{V_{S,i}^2}{V_R^2} - \frac{\rho_{i+1}}{\rho_i} \cdot \frac{V_{S,i+1}^2}{V_R^2}\right) \qquad b_i' = b_i - 1 \tag{3.80}$$

The transformed boundary condition matrices $\widetilde{\mathbf{U}}$ and $\widetilde{\mathbf{V}}$ are further obtained as

$$\widetilde{\mathbf{U}} = G_1 \begin{bmatrix} 0 & -2 & \left(2 - \frac{V_R^2}{V_{S,1}^2}\right) & 0 \\ \left(2 - \frac{V_R^2}{V_{S,1}^2}\right) & 0 & 0 & 2 \end{bmatrix} \qquad \widetilde{\mathbf{V}} = \begin{bmatrix} 1 & 0 \\ -r_{n+1} & 0 \\ 0 & 1 \\ 0 & s_{n+1} \end{bmatrix} \tag{3.81}$$

resulting in the following form of the dispersion equation

$$F_R(V_R,k)=\det(\widetilde{\mathbf{U}}\widetilde{\mathbf{T}}\widetilde{\mathbf{V}})=0 \tag{3.82}$$

Expressing Eq. (3.82) in terms of delta matrices leads to the following representation for $F_R(V_R,k)$

$$F_R(V_R,k)=\overline{\mathbf{U}}\cdot\overline{\mathbf{T}}\cdot\overline{\mathbf{V}}=\overline{\mathbf{U}}(\overline{\mathbf{T}}_1\overline{\mathbf{T}}_2\ldots\overline{\mathbf{T}}_{n-1}\overline{\mathbf{T}}_n)\overline{\mathbf{V}}=0 \tag{3.83}$$

where $\overline{\mathbf{U}}$, $\overline{\mathbf{T}}_i$ $(i=1,2,\ldots,n)$ and $\overline{\mathbf{V}}$ denote the order-2 delta matrices corresponding to $\widetilde{\mathbf{U}}$, $\widetilde{\mathbf{T}}_i$, and $\widetilde{\mathbf{V}}$, respectively, i.e.

$$\overline{\mathbf{T}}_i=\begin{bmatrix}\overline{T}_{11,i} & \overline{T}_{12,i} & \overline{T}_{13,i} & \overline{T}_{14,i} & \overline{T}_{15,i} & \overline{T}_{16,i}\\ \overline{T}_{21,i} & \overline{T}_{22,i} & \overline{T}_{23,i} & \overline{T}_{24,i} & \overline{T}_{25,i} & \overline{T}_{26,i}\\ \overline{T}_{31,i} & \overline{T}_{32,i} & \overline{T}_{33,i} & \overline{T}_{34,i} & \overline{T}_{35,i} & \overline{T}_{36,i}\\ \overline{T}_{41,i} & \overline{T}_{42,i} & \overline{T}_{43,i} & \overline{T}_{44,i} & \overline{T}_{45,i} & \overline{T}_{46,i}\\ \overline{T}_{51,i} & \overline{T}_{52,i} & \overline{T}_{53,i} & \overline{T}_{54,i} & \overline{T}_{55,i} & \overline{T}_{56,i}\\ \overline{T}_{61,i} & \overline{T}_{62,i} & \overline{T}_{63,i} & \overline{T}_{64,i} & \overline{T}_{65,i} & \overline{T}_{66,i}\end{bmatrix} \tag{3.84}$$

where

$$\begin{aligned}
\overline{T}_{11,i}&=\tilde{t}_{11,i}\tilde{t}_{22,i}-\tilde{t}_{12,i}\tilde{t}_{21,i} & \overline{T}_{31,i}&=\tilde{t}_{11,i}\tilde{t}_{42,i}-\tilde{t}_{12,i}\tilde{t}_{41,i} & \overline{T}_{51,i}&=\tilde{t}_{21,i}\tilde{t}_{42,i}-\tilde{t}_{22,i}\tilde{t}_{41,i}\\
\overline{T}_{12,i}&=\tilde{t}_{11,i}\tilde{t}_{23,i}-\tilde{t}_{13,i}\tilde{t}_{21,i} & \overline{T}_{32,i}&=\tilde{t}_{11,i}\tilde{t}_{43,i}-\tilde{t}_{13,i}\tilde{t}_{41,i} & \overline{T}_{52,i}&=\tilde{t}_{21,i}\tilde{t}_{43,i}-\tilde{t}_{23,i}\tilde{t}_{41,i}\\
\overline{T}_{13,i}&=\tilde{t}_{11,i}\tilde{t}_{24,i}-\tilde{t}_{14,i}\tilde{t}_{21,i} & \overline{T}_{33,i}&=\tilde{t}_{11,i}\tilde{t}_{44,i}-\tilde{t}_{14,i}\tilde{t}_{41,i} & \overline{T}_{53,i}&=\tilde{t}_{21,i}\tilde{t}_{44,i}-\tilde{t}_{24,i}\tilde{t}_{41,i}\\
\overline{T}_{14,i}&=\tilde{t}_{12,i}\tilde{t}_{23,i}-\tilde{t}_{13,i}\tilde{t}_{22,i} & \overline{T}_{34,i}&=\tilde{t}_{12,i}\tilde{t}_{43,i}-\tilde{t}_{13,i}\tilde{t}_{42,i} & \overline{T}_{54,i}&=\tilde{t}_{22,i}\tilde{t}_{43,i}-\tilde{t}_{23,i}\tilde{t}_{42,i}\\
\overline{T}_{15,i}&=\tilde{t}_{12,i}\tilde{t}_{24,i}-\tilde{t}_{14,i}\tilde{t}_{22,i} & \overline{T}_{35,i}&=\tilde{t}_{12,i}\tilde{t}_{44,i}-\tilde{t}_{14,i}\tilde{t}_{42,i} & \overline{T}_{55,i}&=\tilde{t}_{22,i}\tilde{t}_{44,i}-\tilde{t}_{24,i}\tilde{t}_{42,i}\\
\overline{T}_{16,i}&=\tilde{t}_{13,i}\tilde{t}_{24,i}-\tilde{t}_{14,i}\tilde{t}_{23,i} & \overline{T}_{36,i}&=\tilde{t}_{13,i}\tilde{t}_{44,i}-\tilde{t}_{14,i}\tilde{t}_{43,i} & \overline{T}_{56,i}&=\tilde{t}_{23,i}\tilde{t}_{44,i}-\tilde{t}_{24,i}\tilde{t}_{43,i}\\
\overline{T}_{21,i}&=\tilde{t}_{11,i}\tilde{t}_{32,i}-\tilde{t}_{12,i}\tilde{t}_{31,i} & \overline{T}_{41,i}&=\tilde{t}_{21,i}\tilde{t}_{32,i}-\tilde{t}_{22,i}\tilde{t}_{31,i} & \overline{T}_{61,i}&=\tilde{t}_{31,i}\tilde{t}_{42,i}-\tilde{t}_{32,i}\tilde{t}_{41,i}\\
\overline{T}_{22,i}&=\tilde{t}_{11,i}\tilde{t}_{33,i}-\tilde{t}_{13,i}\tilde{t}_{31,i} & \overline{T}_{42,i}&=\tilde{t}_{21,i}\tilde{t}_{33,i}-\tilde{t}_{23,i}\tilde{t}_{31,i} & \overline{T}_{62,i}&=\tilde{t}_{31,i}\tilde{t}_{43,i}-\tilde{t}_{33,i}\tilde{t}_{41,i}\\
\overline{T}_{23,i}&=\tilde{t}_{11,i}\tilde{t}_{34,i}-\tilde{t}_{14,i}\tilde{t}_{31,i} & \overline{T}_{43,i}&=\tilde{t}_{21,i}\tilde{t}_{34,i}-\tilde{t}_{24,i}\tilde{t}_{31,i} & \overline{T}_{63,i}&=\tilde{t}_{31,i}\tilde{t}_{44,i}-\tilde{t}_{34,i}\tilde{t}_{41,i}\\
\overline{T}_{24,i}&=\tilde{t}_{12,i}\tilde{t}_{33,i}-\tilde{t}_{13,i}\tilde{t}_{32,i} & \overline{T}_{44,i}&=\tilde{t}_{22,i}\tilde{t}_{33,i}-\tilde{t}_{23,i}\tilde{t}_{32,i} & \overline{T}_{64,i}&=\tilde{t}_{32,i}\tilde{t}_{43,i}-\tilde{t}_{33,i}\tilde{t}_{42,i}\\
\overline{T}_{25,i}&=\tilde{t}_{12,i}\tilde{t}_{34,i}-\tilde{t}_{14,i}\tilde{t}_{32,i} & \overline{T}_{45,i}&=\tilde{t}_{22,i}\tilde{t}_{34,i}-\tilde{t}_{24,i}\tilde{t}_{32,i} & \overline{T}_{65,i}&=\tilde{t}_{32,i}\tilde{t}_{44,i}-\tilde{t}_{34,i}\tilde{t}_{42,i}\\
\overline{T}_{26,i}&=\tilde{t}_{13,i}\tilde{t}_{34,i}-\tilde{t}_{14,i}\tilde{t}_{33,i} & \overline{T}_{46,i}&=\tilde{t}_{23,i}\tilde{t}_{34,i}-\tilde{t}_{24,i}\tilde{t}_{33,i} & \overline{T}_{66,i}&=\tilde{t}_{33,i}\tilde{t}_{44,i}-\tilde{t}_{34,i}\tilde{t}_{43,i}
\end{aligned}$$

and

$$\overline{\mathbf{U}}=G_1^2\begin{bmatrix}2\left(2-\frac{V_R^2}{V_{S,1}^2}\right) & -\left(2-\frac{V_R^2}{V_{S,1}^2}\right)^2 & 0 & 0 & -4 & 2\left(2-\frac{V_R^2}{V_{S,1}^2}\right)\end{bmatrix} \qquad \overline{\mathbf{V}}=\begin{bmatrix}0\\1\\s_{n+1}\\-r_{n+1}\\-r_{n+1}s_{n+1}\\0\end{bmatrix}$$

The fast delta matrix algorithm is subsequently formulated by utilizing the following recursion. Hence, the algorithm is expressed in terms of a single 1×6 row vector $\overline{\mathbf{X}} = \begin{bmatrix} x_1 & x_2 & x_3 & x_4 & x_5 & x_6 \end{bmatrix}$. Furthermore, as $x_1 = x_6$ in each iteration, only five distinct components are required.

$$\begin{aligned} &\overline{\mathbf{X}}_1 = \overline{\mathbf{U}} \\ &\overline{\mathbf{X}}_{i+1} = \overline{\mathbf{X}}_i \overline{\mathbf{T}}_i \qquad i = 1, 2, \ldots, n \\ &F_R = \overline{\mathbf{X}}_{n+1} \overline{\mathbf{V}} \end{aligned} \tag{3.85}$$

Buchen and Ben-Hador (1996) describe the computational procedure and discuss its optimization for numerical computations.

3.6.2 Inversion methods

Various methods have been developed for inversion of experimental Rayleigh wave dispersion data, ranging from simplified empirical techniques to methods incorporating full waveform simulations. As this project is focused on the application of dispersion curve-based techniques, alternative inversion strategies will be only briefly mentioned in this section.

Simplified empirical estimations

In early applications of surface wave analysis techniques (e.g., Jones, 1958), a simple empirical procedure for mapping the experimental dispersion curve into approximate values of shear wave velocity as a function of depth was adopted. That is, for a given Rayleigh wave wavelength λ, the value of V_S at a depth of $\lambda/3$ to $\lambda/2$ was estimated as $V_S \approx 1.1 V_R$ based on the ratio between the propagation velocities of shear waves and Rayleigh waves in a homogeneous medium (refer to Table 2.5). For normally dispersive sites, characterized by a gradual increase in shear wave velocity with depth, such a simplified empirical method can provide reasonable estimates (Foti et al., 2015). However, for inversely dispersive sites it may not be adequate.

For current applications, the main advantage of this approach is that it can provide a rapid, preliminary estimate of the shear wave velocity profile, for instance during data acquisition at relatively simple sites. Such preliminary analysis has been implemented in MASWaves DAQ. Furthermore, the empirically estimated pseudo shear wave velocity profile can provide a reasonable starting model for an iterative inversion algorithm or a manual trial-and-error search procedure.

Recently, several alternatives to this empirical wavelength–depth approach have been proposed (Leong & Aung, 2012; Haney & Tsai, 2015; Socco et al., 2017; Passeri, 2019), such as directly transforming the wavelength of the experimental dispersion curve to the depth of a corresponding pseudo V_{SZ}-profile [see Eq. (2.27)].

Manual inversion/optimization

If the inversion process is conducted manually, the analyst adjusts the model parameters between iterations with the objective of minimizing the misfit between the experimental and theoretical dispersion curves. A manual inversion is to a high degree operator dependent and calls for a certain level of expertise in order to obtain an acceptable fit within a reasonable time frame. However, if carried out by an experienced practitioner, it can yield substantial information about the velocity structure of a site and may represent the only viable approach if automated search algorithms fail to converge.

For analysis of SASW data acquired at Icelandic sites, the inversion was conducted manually (Bessason & Erlingsson, 2011) with the WinSASW software (Version 1.2, UTAustin, 1992). Interactive inversion was also adopted for initial applications of the MASW method in this dissertation work (refer to *Paper I*).

Automated inversion: Global and local search techniques

The application of various automated search techniques has been proposed to aid the quest of soil models that reproduce the observed dispersion curve. In general, they can be divided into two main categories; local search and global search procedures (Sen & Stoffa, 2013), though the combined use of global and local search algorithms has also been proposed (e.g., Socco et al., 2009).

Local search algorithms are iterative schemes which, by starting from an initial estimate of the inversion parameters, generate a sequence of improved model assessments. Hence, the result is provided in the form of a single V_S-profile. Assessments of uncertainty may be obtained through the Jakobian matrix or by repeated analysis by use of different initial models and/or model parameterizations (Lai et al., 2005; Foti et al., 2018). Well-known local optimization methods include the Levenberg–Marquardt algorithm (also referred to as the damped least-squares method) (Levenberg, 1944; Marquardt, 1963) and Occam's algorithm (Constable et al., 1987).

In global search procedures, it is attempted to systematically search for the global stationary point of the dispersion misfit function by exploring the entire solution space. Subsequently, inference is drawn from the set of simulated V_S-profiles in order to identify those profiles that can be considered as acceptable solutions. With the aim of making the global search more efficient, the use of various advanced optimization methods has been suggested to guide the search towards the high-probability-density regions of the solution space (e.g., Beaty et al., 2002; Pezeshk & Zarrabi, 2005; Socco & Boiero, 2008; Song et al., 2008, 2012, 2014, 2015; Wathelet et al., 2004; Wathelet, 2008).

An inherent risk associated with local search methods is that the algorithm may converge to a local minimum of the dispersion misfit function (Sen & Stoffa, 2013). Hence, a reasonable initial estimate of the stratified soil model is essential. Furthermore, no simple procedures exist to determine whether a given stationary point, found by a local search technique, corresponds to a local or a global minimum of the misfit function

(Foti et al., 2015). Inaccurate values of the partial derivatives of the dispersion curve with respect to the model parameters can further severely affect the performance of a local search algorithm. Despite these drawbacks, local search methods may be preferred by engineers as they are both easier to handle and usually provide more computational speed than advanced global search schemes. Furthermore, local search methods are more common in commercial software (Song et al., 2014).

By application of global search techniques, all assumptions of linearity between the experimental data and the model parameters are avoided. As a result, this class of methods may be considered more robust in finding the global minimum of the dispersion misfit function. The definition of the model parameter space though requires the analyst to find a balance between not overly constraining the solution (i.e., providing sufficiently wide ranges for the model parameters) and enhancing the odds of the algorithm getting close to the global minimum. Global search methods are, in general, computationally more demanding as a high number of forward simulations is required to adequately sample the model parameter space (Socco et al., 2010), thereby imposing some practical limitations on the analysis. It should be noted, however, that the computational time is very dependent upon the complexity of the soil layer model and the experimental dispersion data (e.g., the number of data points and whether higher modes should be included in the analysis). Nevertheless, although global search methods are better suited for the non-uniqueness of the inverse problem encountered, the use of advanced optimization algorithms might be considered excessive for general geotechnical engineering applications. Hence, in this dissertation work, the use of a simple but effective Monte Carlo-based global search inversion procedure was tested. The inversion procedure is presented in Section 3.6.3 (see also *Paper III*).

Alternative inversion strategies

The manual, local search and global search techniques discussed in the preceding sections can, in principle, be conducted on fundamental and higher mode dispersion curves simultaneously. Simultaneous inversion of multiple modes can be of value to better constrain the inversion process if considerable energy is carried by the higher modes. Such measures are, however, crucially limited to instances where different modes are fully separated in the dispersion processing and the mode numbers can be confidently (correctly) identified (see also Section 3.5.1). An alternative approach is to define the misfit function based on the forward operator [Eq. (3.39)] whose zeros correspond to the modal dispersion curves (Maraschini et al., 2010), thus, eliminating the need of associating individual dispersion curve data points to specific modes. Furthermore, the inversion can be conducted using the apparent dispersion curve. Such procedures, though, require forward modelling of the apparent curve, taking both the source properties and the measurement profile configuration into account (Lai et al., 2014). Furthermore, for challenging soil profiles, several authors have proposed the use of wavefield inversion methods using dispersion spectra (e.g., Ryden & Park, 2006; Forbriger, 2003a, 2003b; Dou & Ajo-Franklin, 2014) or full waveform inversion techniques that attempt to compare synthetic signals to the experimental time-domain data (e.g., Tran & Hiltunen, 2012).

3.6.3 Inversion scheme

In this work, the focus is on inversion of fundamental mode Rayleigh wave dispersion curves for the elements of $\mathbf{V_S}$ and $\mathbf{h}$. The Poisson's ratio (or compressional wave velocity) and mass density are assessed beforehand, along with the location of the groundwater table. Hence, the number of unknown model parameters (given a fixed value of n) is reduced from $4n+3$ to $2n+1$. Initial estimates of n and $\mathbf{h}$ are required as a starting point of the inversion process. Other, user-defined, input parameters required for initiation of the inversion scheme are the search-control parameters b_S and b_h, and the maximum number of iterations N_{max}. During the inversion process, the parameters b_S and b_h specify the range of shear wave velocity and layer thickness values, respectively, that the algorithm can sample in each iteration. The effects of specifying different values for the 'b-parameters' are studied in *Paper III* and briefly summarized in Section 4.3. A schematic overview of the inversion strategy is provided in Fig. 3.12.

The initial value of the shear wave velocity for each layer ($V_{S,i}$) is obtained by mapping the experimental dispersion curve into approximate values of V_S. Subsequently, the resulting pseudo shear wave velocity profile is discretized to match the previously assumed layer structure, following a method comparable to the schemes adopted by Xia et al. (1999) and de Lucena and Taioli (2014), i.e.

$$\begin{aligned} V_{S,1} &= a \cdot V_{R,\lambda_{min}} && \text{for the top-most soil layer} \\ V_{S,i} &= a \cdot V_{R,e}(\lambda_i) && \text{for layers } i = 2,3,\ldots,n \\ V_{S,n+1} &= a \cdot V_{R,\lambda_{max}} && \text{for the half-space} \end{aligned} \tag{3.86}$$

where the wavelength λ_i is estimated as $2\overline{z}_i$ to $3\overline{z}_i$. $\overline{z}_i$ is the average depth of the i-th layer, i.e., $\overline{z}_i = 0.5(z_i + z_{i+1})$. In the synthetic and real-world examples presented in *Paper III*, a value of $2.5\overline{z}_i$ was used and the multiplication factor a in Eq. (3.86) was specified as 1.09 based on the ratio between the propagation velocities of shear waves and Rayleigh waves in a homogeneous medium. The value of a can also be estimated for specific soil materials according to Eq. (2.17).

At sites where the experimental dispersion curve has vertical asymptotes, these can be used to improve the estimate of the initial shear wave velocity values (e.g., Xia et al., 1999). Hence, the use of the asymptotic velocities $V_{R,\lambda_{min}}$ and $V_{R,\lambda_{max}}$ is implemented in Eq. (3.86) for initial assessments of $V_{S,1}$ and $V_{S,n+1}$, respectively. Here, $V_R = V_{R,\lambda_{min}}$ denotes a vertical asymptote to the experimental dispersion curve at short wavelengths and $V_R = V_{R,\lambda_{max}}$ denotes a vertical asymptote at the longest retrieved wavelengths. If the experimental dispersion curve does not show such vertical asymptotes, $V_{R,\lambda_{min}}$ and $V_{R,\lambda_{max}}$ can be estimated as $V_R(\lambda_{min})$ and $V_R(\lambda_{max})$, respectively.

The theoretical fundamental mode Rayleigh wave phase velocities $V_{R,t}$ that correspond to each element of $\boldsymbol{\lambda}$ are obtained based on the initial set of model parameters (i.e., $\mathbf{h}$, $\mathbf{V_S}$, $\mathbf{V_P}$ (or $\boldsymbol{\nu}$) and $\boldsymbol{\rho}$) (refer to Section 3.6.1). The misfit ϵ_{DC} between the theoretical

and experimental dispersion curves is defined as

$$\epsilon_{DC} = \frac{1}{Q}\sum_{q=1}^{Q}\frac{\sqrt{(V_{R,t,q} - V_{R,e,q})^2}}{V_{R,e,q}} \cdot 100\% \tag{3.87}$$

where $\mathbf{V_{R,e}} = [V_{R,e,1}, V_{R,e,2}, \ldots, V_{R,e,Q}]$ and $\mathbf{V_{R,t}} = [V_{R,t,1}, V_{R,t,2}, \ldots, V_{R,t,Q}]$ are the Q-dimensional experimental and theoretical phase velocity vectors, respectively.

For updating the shear wave velocity vector between iterations, a set of $n+1$ numbers X_i $(i = 1, 2, \ldots, n, n+1)$ is sampled from the uniform distribution and added to the elements of $\mathbf{V_S}$. The resulting vector $\mathbf{V_{S,test}} = [V_{S,test,1}, V_{S,test,2}, \ldots, V_{S,test,n}, V_{S,test,n+1}]$ is referred to as the 'testing shear wave velocity vector'

$$V_{S,test,i} = V_{S,i} + X_i \quad \text{with} \quad X_i \sim \text{unif}\left(\frac{-b_S \cdot V_{S,i}}{100}, \frac{b_S \cdot V_{S,i}}{100}\right) \tag{3.88}$$

for $i = 1, 2, \ldots, n+1$.

The layer thickness vector is updated in an analogous way, with a random number Y_i $(i = 1, 2, \ldots, n)$ sampled for each of the finite-thickness layers and added to h_i, resulting in the 'testing layer thickness vector' $\mathbf{h_{test}} = [h_{test,1}, h_{test,2}, \ldots, h_{test,n}]$, i.e.,

$$h_{test,i} = h_i + Y_i \quad \text{with} \quad Y_i \sim \text{unif}\left(\frac{-b_h \cdot h_i}{100}, \frac{b_h \cdot h_i}{100}\right) \tag{3.89}$$

for $i = 1, 2, \ldots, n$.

Hence, the elements of $\mathbf{V_{S,test}}$ and $\mathbf{h_{test}}$ will vary randomly but will at most differ by $b_S\%$ and $b_h\%$ from the corresponding elements of $\mathbf{V_S}$ and $\mathbf{h}$, respectively, in each iteration.

Based on prior knowledge of the geological conditions of the tested site, or as implied by the shape of the experimental dispersion curve, implementing additional constraints may be useful to further focus the search on the high-probability-density regions of the solution space. These include a normally dispersive inversion parameterization or predefined ranges for the elements of $\mathbf{V_S}$ or $\mathbf{h}$ within certain depths. In cases where such constraints have been implemented, they have either been introduced by further restricting the Monte Carlo sampling to fulfil the additional conditions or by conducting the sampling as described by Eqs. (3.88) and (3.89) and subsequently reject those sets of simulated parameters that do not conform to the added restrictions.

The elements of $\mathbf{V_S}$ and $\mathbf{h}$ are updated in each successful Monte Carlo simulation iteration (Fig. 3.12). The theoretical dispersion curve $(\mathbf{V_{R,t}}, \boldsymbol{\lambda})$ is re-evaluated based on the testing profile defined by $\mathbf{V_{S,test}}$, $\mathbf{h_{test}}$, $\mathbf{V_P}$ (or $\boldsymbol{\nu}$) and $\boldsymbol{\rho}$. If the testing profile provides a better fit to the observed data (i.e., a lower value of the dispersion misfit function) than any previously tested profile, the shear wave velocity and layer thickness vectors are updated as $\mathbf{V_S} = \mathbf{V_{S,test}}$ and $\mathbf{h} = \mathbf{h_{test}}$. Otherwise, the model parameters

are not changed. Hence, the search is centred around the 'best-fitting' shear wave velocity profile that has been obtained at each point during the inversion.

3.7 Software verification and validation

Verification and validation of the set of software modules is an important part of this dissertation work. In general terms, software verification and validation are aimed at ensuring that the software both fulfils its intended purpose (i.e., that it executes the correct tasks) and, vitally, that it is executing the tasks correctly (Pham, 2000).

In initial stages of the software development, special attention was devoted to verifying and validating the dispersion analysis process and the algorithms used for forward modelling of modal Rayleigh wave dispersion curves. The process is described in general terms in both *Paper I* and *Paper V* with some examples provided. Validation of the dispersion analysis procedure implemented in MASWaves was conducted by comparison to the Linear F-K for active experiments toolbox of the Geopsy software package (www.geopsy.org). The forward modelling tool was both validated against theoretical dispersion curves in the literature, and by comparison to modelling results obtained with the forward modelling scheme used in prior works at the University of Iceland (Bessason et al., 1998; Bessason & Erlingsson, 2011). Validation and calibration of the global search inversion algorithm (refer to Section 3.6.3) was conducted through inversion of synthetic data, including dispersion curves that had been perturbed by introduction of Gaussian noise. Examples are provided in *Paper III*.

Furthermore, inverted V_S-profiles were compared to available independent assessments of V_S, and other existing measurement results, to simultaneously evaluate the data acquisition hardware and the set of software modules. For the Norwegian geotechnical research sites (refer to *Paper IV*) this included measurements of shear wave velocity obtained with invasive techniques, results of laboratory tests and surface wave analysis measurements conducted with different hardware and processed independently through different software packages. However, for the Icelandic test sites, only limited data was available for comparison purposes (*Papers V–VIII*). As a result, for Icelandic soil materials, the comparison was limited to results of SASW surveys, empirically assessed pseudo V_S-profiles (e.g., obtained from CPT measurement results) and prior knowledge of the geology of the tested areas.

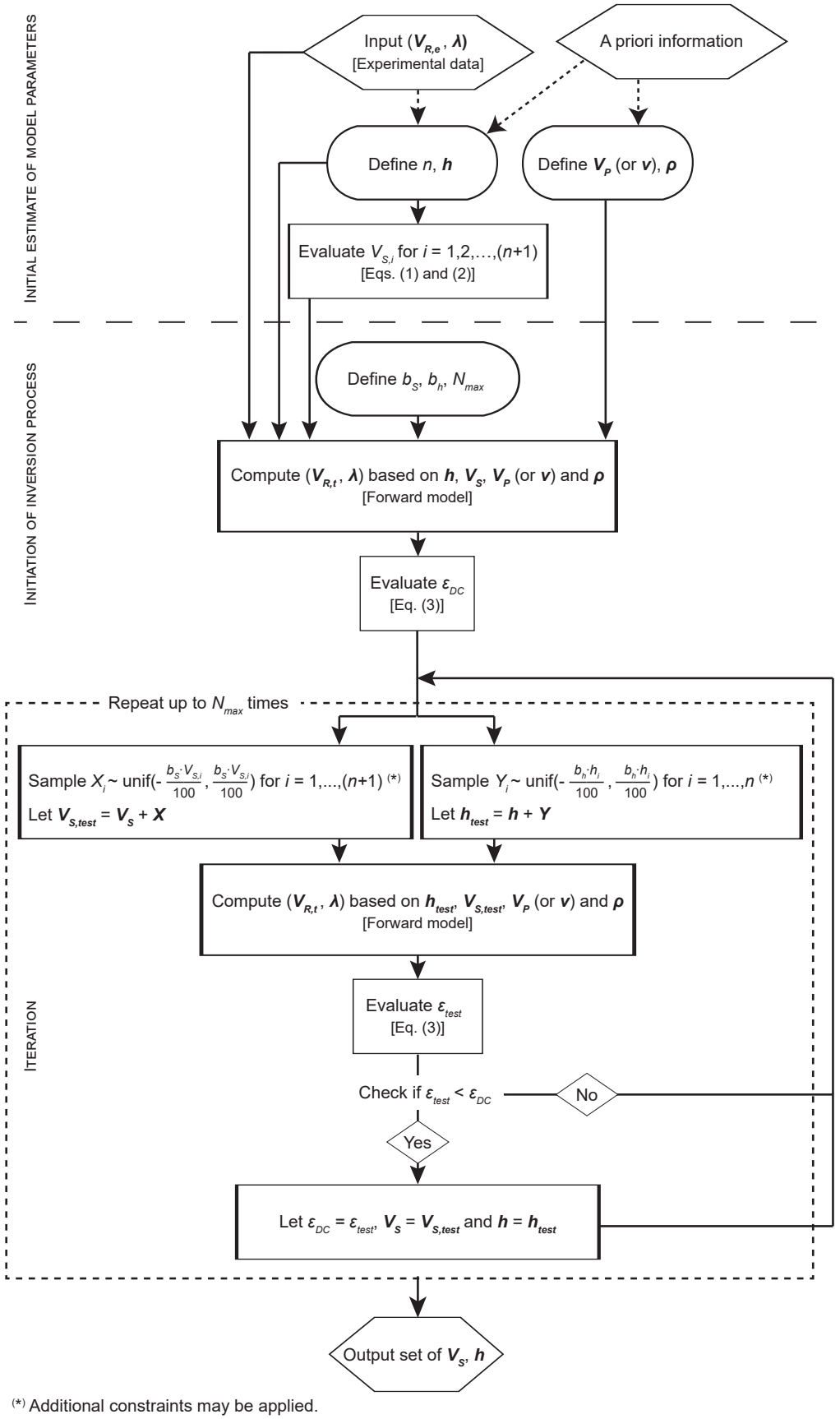

Figure 3.12: Overview of the inversion analysis process presented in Paper III.

4 Summary of appended papers

4.1 Paper I

Paper I introduces the first version of the MASWaves software. This initial version consists of two modules for dispersion analysis (MASWaves Dispersion) and inversion (MASWaves Inversion), respectively. The dispersion analysis is conducted using the phase shift method (Park et al., 1998). The inversion analysis module includes a tool for computation of theoretical dispersion curves based on the stiffness matrix method of Kausel and Roësset (1981) and an algorithm to evaluate the misfit between the experimental and theoretical dispersion curves and allow the user to manually update the set of model parameters.

For verification of the dispersion analysis procedure implemented in MASWaves, results obtained with MASWaves Dispersion were compared to results obtained with the Linear F-K for active experiments toolbox of the Geopsy software package. Figures 4.1 and 4.2 present processed multi-channel surface wave records, along with the associated experimental dispersion curves, acquired at two test sites in North Iceland. The test sites are characterized by silty sand and loosely compacted sand/gravel, respectively. Comparable results have been obtained based on records acquired at other sites, thus, further confirming the precision of the software and its ability to identify and extract experimental dispersion curves (see also *Paper V*).

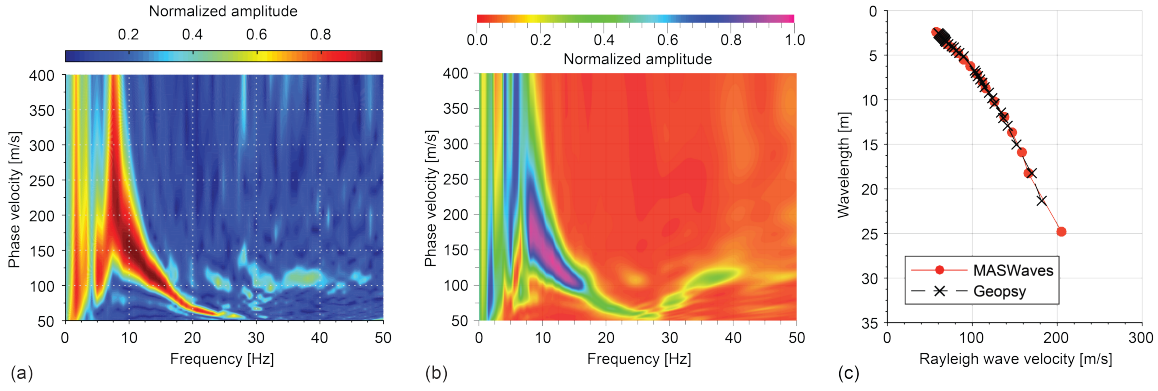

Figure 4.1: Results from a silty sand test site in North Iceland (Akureyri airport). Dispersion images obtained by (a) MASWaves and (b) Geopsy. (c) Comparison of experimental dispersion curves extracted from the spectra in (a, b).

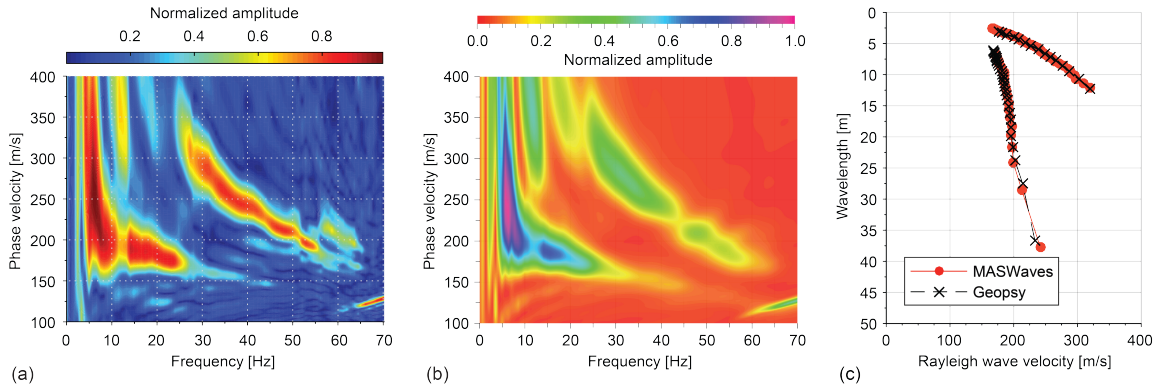

Figure 4.2: Results from a sandy/gravelly test site in North Iceland (Sjálfandafljót river delta). Dispersion images obtained by (a) MASWaves and (b) Geopsy. (c) Comparison of fundamental- and higher-mode dispersion curves extracted from the spectra in (a, b).

The forward modelling algorithm was tested on soil layer models previously used by Tokimatsu et al. (1992) and Tokimatsu (1997). In profile 1, the shear wave velocity gradually increases with increasing depth. The stiffness of the soil layers varies more irregularly in profiles 2 and 3. A stiff surficial layer is present in profile 2, whereas a stiffer layer is located between two softer layers in profile 3. Hence, for profiles 2 and 3, the higher modes play a more significant role in the Rayleigh wave propagation. Using MASWaves Inversion, the theoretical fundamental and first mode dispersion curves were computed for frequencies in the range of 3–70 Hz. The comparison of the dispersion curves obtained with MASWaves and those presented in the literature is depicted in Fig. 4.3. The theoretical dispersion curve computations were further verified by comparison to results obtained with the software WinSASW (version 1.2; UTAustin, 1992).

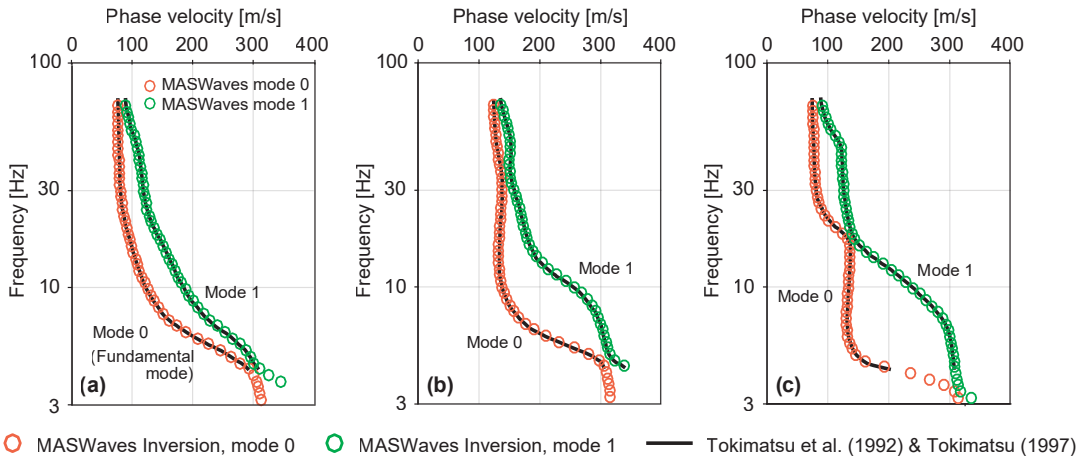

Figure 4.3: Comparison of theoretical fundamental and first mode dispersion curves obtained with MASWaves and presented by Tokimatsu et al. (1992) and Tokimatsu (1997). (a) Profile 1. (b) Profile 2. (c) Profile 3. Four-layer models characterized by a gradual increase in shear wave velocity with depth (Profile 1), a stiff surficial layer (Profile 2), and a stiffer layer sandwiched between two softer layers (Profile 3).

Paper I further presents results of MASW field tests conducted at three sites in South Iceland for the purpose of demonstrating the performance and robustness of the new software. The soil deposits at the three sites range from loose sand to cemented silty sand. The repeatability of the analysis was assessed with repeated measurements at one of the sites (Fig. 4.4). In addition, at one test location, results of previously conducted SASW measurements (Bessason & Erlingsson, 2011) were compared to the results obtained with MASWaves (Fig. 4.5).

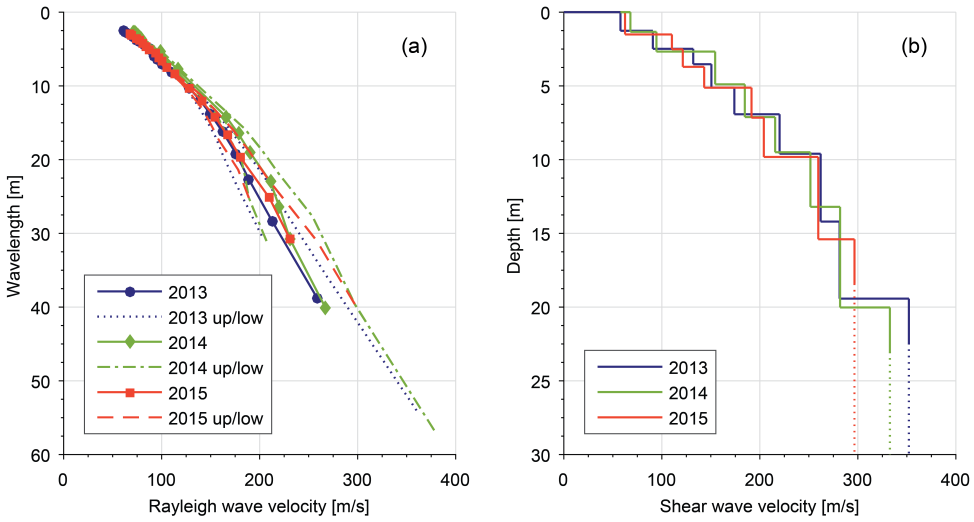

Figure 4.4: (a) Comparison of experimental dispersion curves for the Arnarbæli test site acquired in three separate field tests in September 2013, August 2014 and July 2015. (b) Comparison of shear wave velocity profiles for the Arnarbæli test site evaluated based on data acquired in 2013, 2014 and 2015.

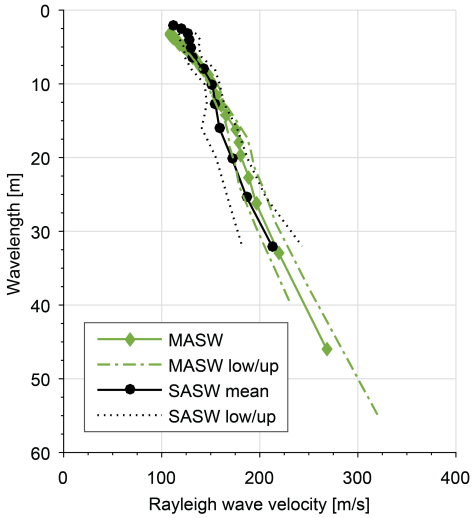

Figure 4.5: Comparison of experimental dispersion curves obtained at the Bakkafjara test site by application of SASW and MASW.

Main findings in Paper I

- The first version of MASWaves, an open-source software for processing surface wave data using the MASW method, was presented.

- The performance of the dispersion analysis tool was validated by comparison with results obtained by the Geopsy software package. The agreement of the estimated dispersion curves was in all cases excellent, confirming the precision of the new software.

- Theoretical dispersion curves obtained with MASWaves were both consistent with results obtained with the software WinSASW (version 1.2) and theoretical dispersion curves presented in the literature.

- Analysis of data collected in three separate field testing campaigns confirmed the repeatability of the analysis.

- Results of MASW measurements processed with the new software were in good agreement with results of existing SASW measurements.

4.2 Paper II

Paper II presents the methodology used for combining dispersion curves obtained from separate spectral images (see Section 3.5.2). The dispersion curves were added up within $\log_a$ spaced wavelength intervals and the uncertainty associated with the mean phase velocity estimates quantified using both classical statistics and bootstrapping (Section 3.5.3). Recommendations for optimal measurement profile parameter and dispersion curve combinations in the context of ranges of wavelengths and phase velocities were presented. Moreover, combined dispersion curves were compared to curves extracted from stacked dispersion images.

A set of multi-channel records acquired at a silty sand site in South Iceland (referred to as the Arnarbæli site) was used to illustrate the effects of the measurement profile configuration on the acquired dispersion data (see Figs. 4.6 and 4.7) and present the combination method. The high number of records gathered using multiple receiver spacings and source offset lengths made this dataset an appropriate choice for testing the methodology. Although the conclusions presented in *Paper II* were only supported by data from this single site, the same trends and results have been found in data gathered at a number of other Icelandic sites (additional examples are provided in *Paper V*).

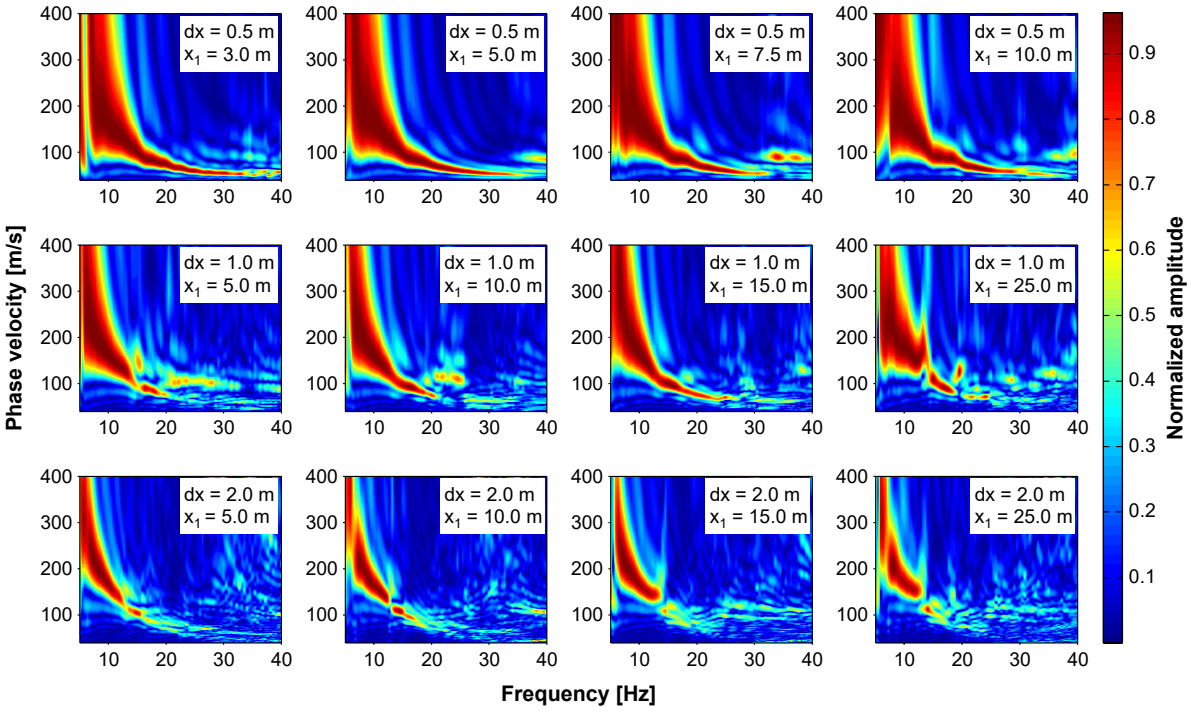

Figure 4.6: Dispersion images of multi-channel surface wave records acquired with receiver spreads of different lengths and with different source offsets at the Arnarbæli site.

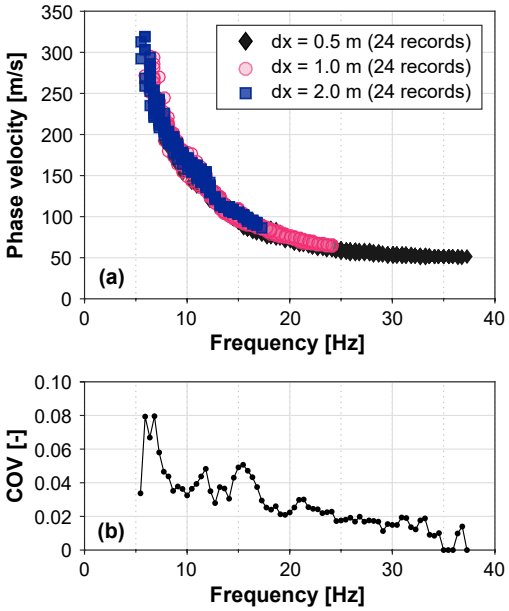

Figure 4.7: (a) Fundamental mode dispersion curve estimates obtained with receiver spreads of different lengths at the Arnarbæli site. (b) Variation of extracted Rayleigh wave phase velocity values. The variability is quantified in terms of the coefficient of variation (COV) among the estimated phase velocity values at each frequency.

Figures 4.8 and 4.9 present composite dispersion curves for the Arnarbæli test site, obtained by using several different values of the a-parameter [refer to Eq. (3.29)]. The identified (elementary) dispersion curve phase velocity values were added up within each wavelength interval, and their arithmetic mean used as a point estimate of the phase velocity of the Rayleigh wave components belonging to the given range. Overall, the optimum value of a varies with dataset and should be chosen after initial inspection of the available data.

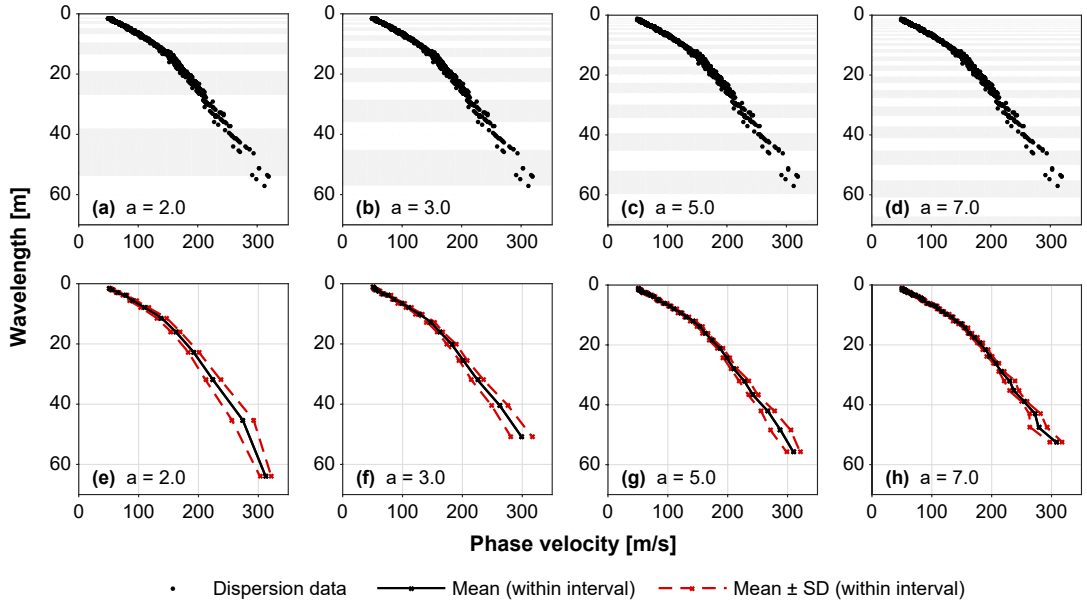

Figure 4.8: Composite dispersion curves [lower row] obtained by adding the elementary dispersion data [upper row] within (a, e) $\log_2$, (b, f) $\log_3$, (c, g) $\log_5$, and (d, h) $\log_7$ spaced wavelength intervals. The dashed lines in (e–h) correspond to plus-minus one standard deviation of the mean curve.

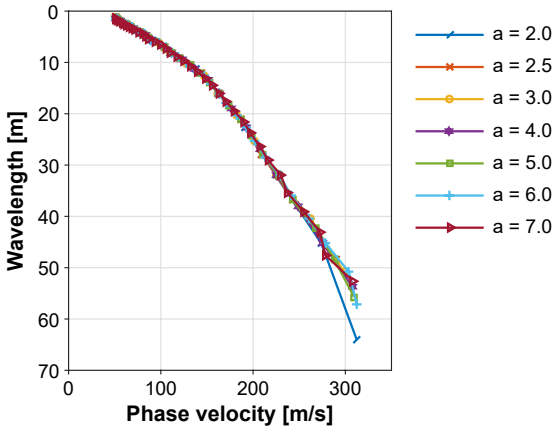

Figure 4.9: Comparison of combined mean dispersion curves obtained by using different values of the parameter a in Eq. (3.29).

The point estimate of each wavelength interval's mean phase velocity is supplemented by the 95% confidence interval for the sample mean. Computations were conducted both based on the t-distribution and by applying the bootstrap. Figures 4.10 and 4.11 illustrate this for three representative wavelength intervals.

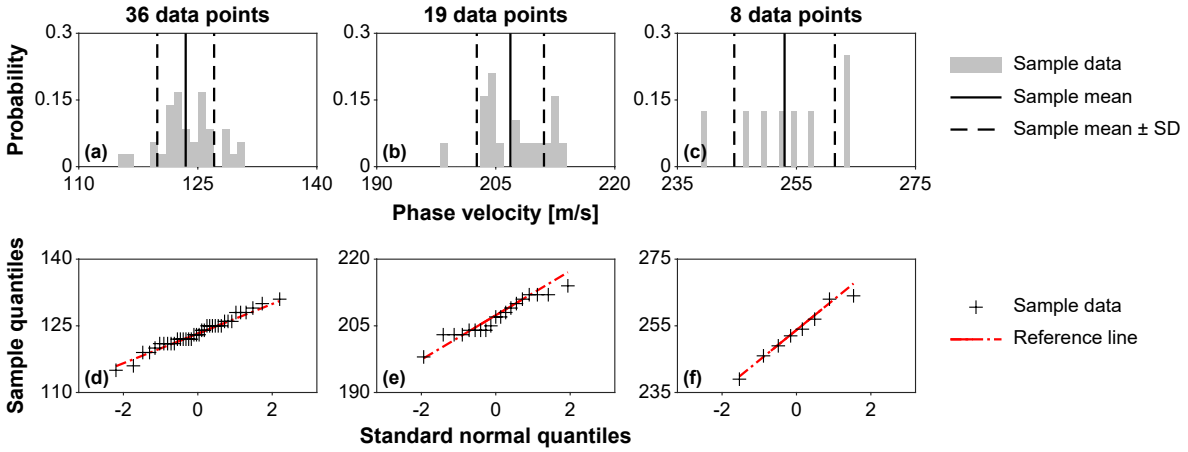

Figure 4.10: Probability distributions and normal Q-Q plots of Rayleigh wave phase velocity values within three wavelength intervals.

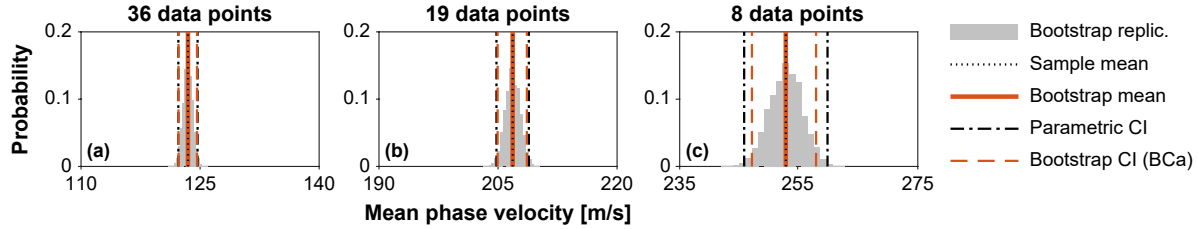

Figure 4.11: Bootstrap replications of the sample mean for the wavelength intervals in Fig. 4.10 along with 95% confidence intervals for the sample mean obtained based on parametric statistics and the bootstrap.

For assessing the effects of adding up elementary dispersion data acquired by receiver spreads of different lengths, as well as the effects of the uncertainty associated with the mean phase velocity estimates, Fig. 4.12 depicts V_S-profiles obtained by inverting composite (i.e., mean, upper and lower boundary) experimental curves corresponding to different elementary curve combinations. To aid comparison of the resulting V_S-profiles, the experimental data was only inverted for the elements of $\mathbf{V_S}$. The elements of $\mathbf{h}$ were fixed a-priori, though with a reduced investigation depth for the $dx = 0.5$ m profile (Fig. 4.12a) and an increased first-layer thickness for the $dx = 2.0$ m profile (Fig. 4.12b) in accordance with the wavelengths covered by the experimental curves [refer to Eqs. (3.5) and (3.6)]. In brief, the shear wave velocity estimates obtained by inverting the mean, upper boundary and lower boundary experimental curves were very consistent at shallow depth (COV of 0.1%–2.5% at depths less than about 5 m). For deeper layers, the wider confidence intervals lead to more differences among the shear wave velocity estimates (COV of 5.9%–11.8%).

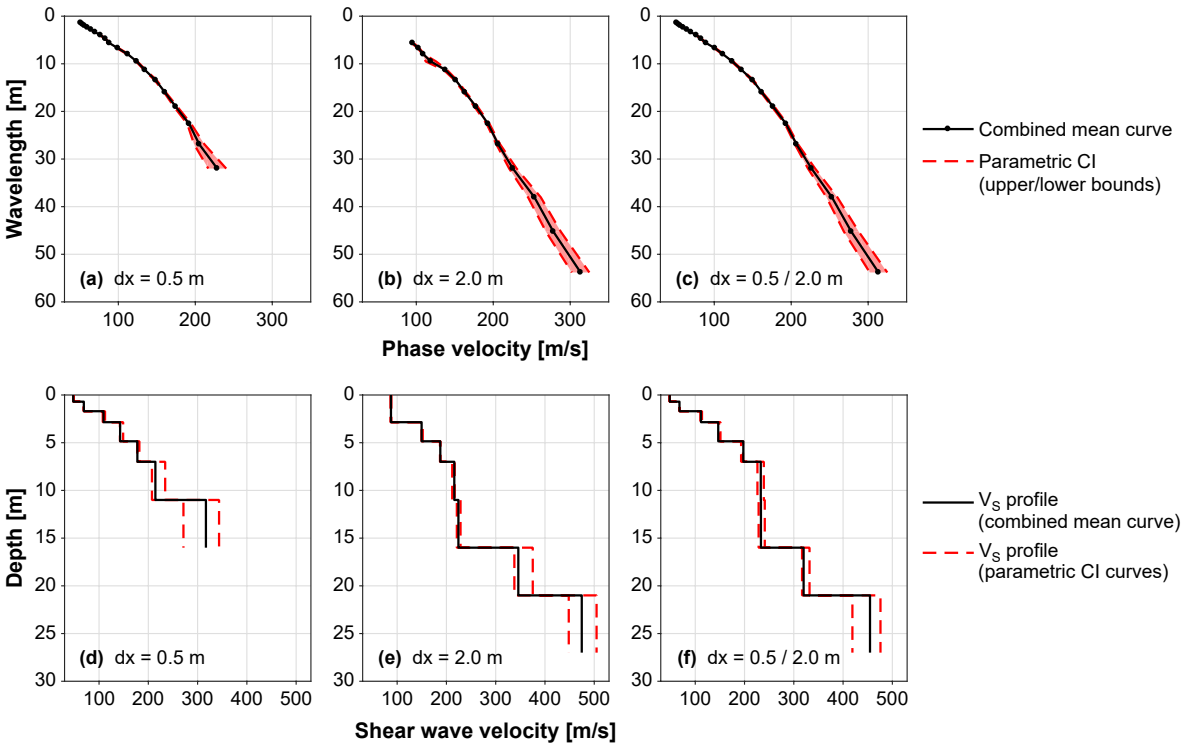

Figure 4.12: Combined mean dispersion curves ($a = 4$) with 95% parametric confidence intervals [shaded areas] for the (a) $dx = 0.5$ m profile, (b) $dx = 2.0$ m profile and (c) $dx = 0.5$ m & $dx = 2.0$ m profiles. Shear wave velocity profiles obtained by inverting the combined mean, upper and lower boundary dispersion curves, respectively, for the (d) $dx = 0.5$ m profile, (e) $dx = 2.0$ m profile and (f) $dx = 0.5$ m & $dx = 2.0$ m profiles.

Main findings in Paper II

- The measurement profile set-up has a significant effect on the resolution of the resulting dispersion images. Combined or repeated analysis of data acquired with different profile configurations can help in correctly identifying the fundamental mode dispersion curve.

- Stacked spectral images can allow more confident dispersion curve identification and, in some cases, extraction of the fundamental mode over a wider range of frequencies. However, in other cases, the spectral stacking might not be beneficial as parts of the high-amplitude bands can cancel out.

- Given that lateral variations in soil properties are small, a combination of multiple dispersion curves (obtained using receiver spreads of different lengths) can both increase the investigation depth of the survey and improve its resolution at shallow depths.

- The use of a short receiver spread ($dx = 0.5$ m) and a long receiver spread

($dx = 2.0$ m) was sufficient for the Arnarbæli site and the intended investigation depth (i.e., 20–30 m). The effects of adding an intermediate length spread were minor.

- The number and distribution of the elementary dispersion curve data points in the longest wavelength range is the primary factor affecting the optimum number of wavelength intervals. Present experience indicates that $\log_{5/2}$ to $\log_5$ spaced intervals are appropriate for most sites. The $\log_3$ or $\log_4$ spaced intervals will be sufficient in many cases.

- By averaging the dispersion data post dispersion curve extraction, the composite curve can be represented by a series of confidence intervals, and the effects of the uncertainty associated with the computation of the mean phase velocity values on the inverted V_S-profiles can be studied.

- The confidence intervals for the mean phase velocity could, in most cases, be reasonably estimated based on the standard error of the elementary dispersion curve data points by assuming the normal distribution for the sample data. The normal assumption was valid in many cases where the number of dispersion curve data points was substantially lower than 30.

- The parametric confidence intervals should be interpreted with caution in cases where the sample size is small and graphical and/or statistical tests carried out for evaluation of the near-normality assumption prior to computations. The bootstrap is a useful method for computation of confidence intervals in those cases where the normal assumption might not be valid.

4.3 Paper III

The focus of *Paper III* was on the inverse problem faced in the third step of the MASW analysis (Fig. 3.1). A simple global search procedure (refer to Section 3.6.3) was implemented in the MASWaves Inversion module and its applicability and performance assessed through analysis of three synthetic datasets and field data acquired at a geotechnical research site in Norway, referred to as Halden.

A statistical sample of dispersion curves was obtained and the variability in estimated phase velocity values quantified. After conducting the Monte Carlo-based search, using different layering parameterizations, inference was drawn from the set of simulated V_S-profiles. In the paper, 'accepted V_S-profiles' are defined as the set of profiles whose associated theoretical dispersion curves fall within one standard deviation of the experimental composite curve. For comparable interpretation of inversion results for the unperturbed synthetic data, the 'experimental standard deviation' was, for simplification purposes, assumed to be 5% of the true phase velocity at each wavelength.

The synthetic soil models were selected with the aim of mimicking loose to medium-dense sand sites and soft clay sites commonly encountered in geotechnical engineering practice. Model A depicts a simple two-layer structure. Model B is characterized by a gradual increase in stiffness with depth, whilst a stiffer layer is sandwiched between two softer layers in model C. For simulation of real-world scenarios, where picked dispersion curve phase velocity values are inevitably subjected to noise, the synthetic dispersion curves were perturbed by introduction of Gaussian noise (refer to Fig. 4.13) and the inversion procedure also tested on the perturbed data. In each of the three synthetic models, the groundwater table is assumed to be located at a great depth.

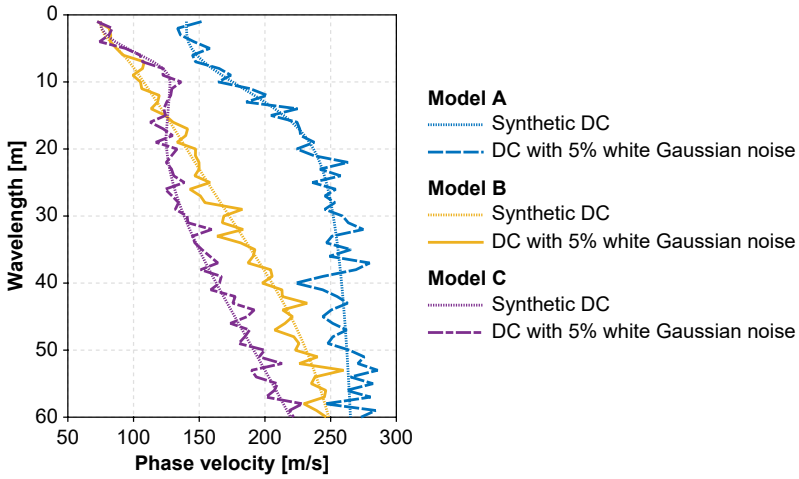

Figure 4.13: Fundamental mode dispersion curves, with and without 5% white Gaussian noise, for model A (two-layer model), model B (four-layer model with a gradual increase in stiffness with depth) and model C (four-layer model with a stiffer layer between two softer layers).

Figure 4.14 depicts inversion of the unperturbed synthetic data from the two-layer model A. The number of iterations in each run of the inversion algorithm (refer to Fig. 3.12) was $N_{max} = 1{,}000$. As the search is based on a Monte Carlo process, the inversion scheme was initiated ten times to reduce the effects of the randomization, and inference drawn from the resulting dataset consisting of $10 \times 1{,}000$ V_S-profiles. For application of the search algorithm, upper and lower bounds for the search area are not specified. However, the size of the sampled model parameter space is affected by two user-defined search-control parameters, denoted by b_S and b_h in Eqs. (3.88) and (3.89). In each iteration, the shear wave velocity and layer thickness testing values may deviate up to $b_S\%$ and $b_h\%$, respectively, from the corresponding parameters in the lowest dispersion misfit model obtained at that point in the inversion (see further in Section 3.6.3). The effects of specifying several different values for the b-parameters (with $b_S = b_h = b$) are illustrated in Figs. 4.14 and 4.15.

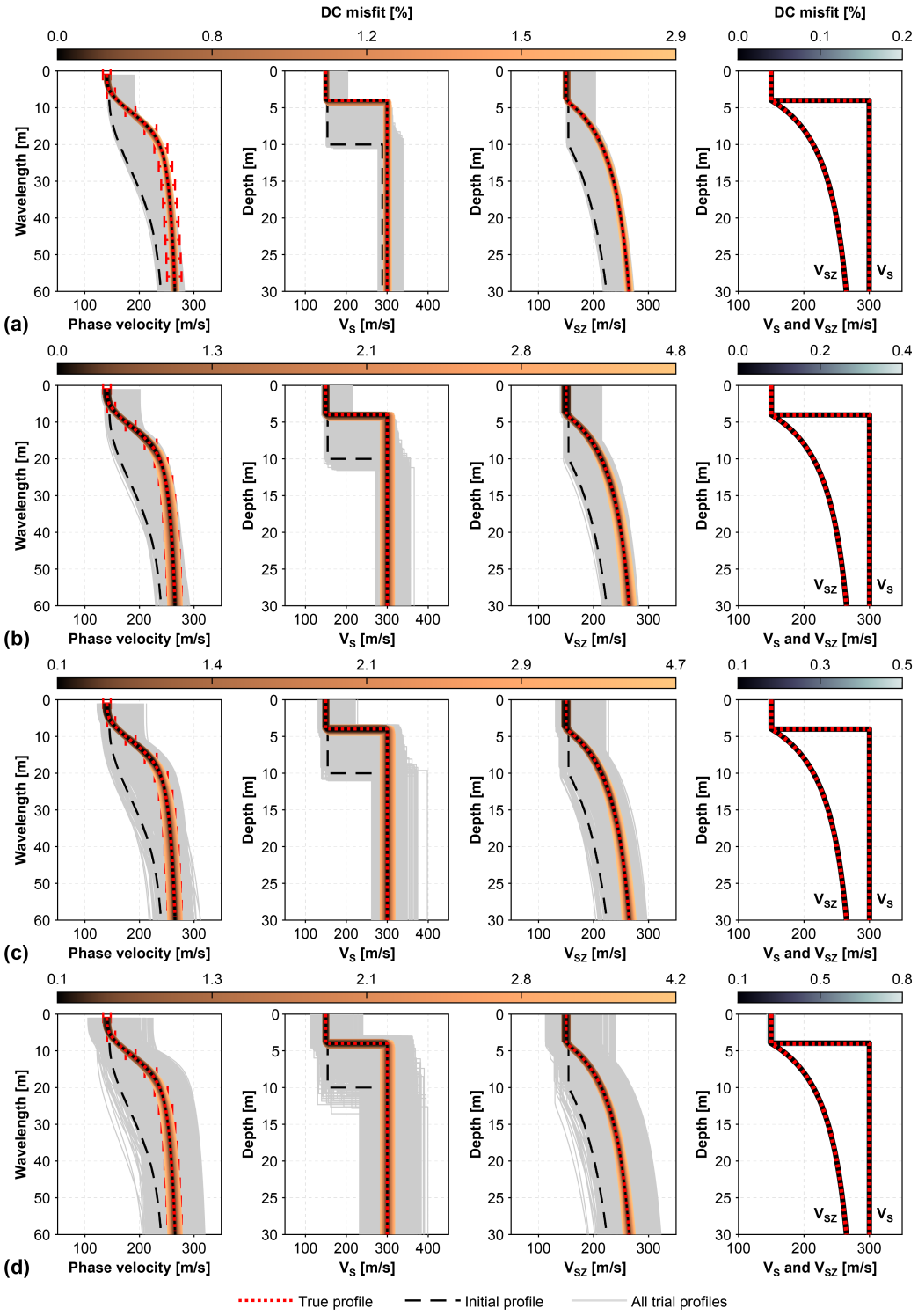

Figure 4.14: Inversion of the unperturbed synthetic dispersion curve from model A. A two-layer geologic structure is assumed with the layer interface initially at 10 m depth (true depth 4 m). The search-control parameters (with $b_S = b_h = b$) are specified as (a) $b = 2.5$, (b) $b = 5$, (c) $b = 10$, and (d) $b = 20$. Grey areas display all sampled models and profiles whose dispersion curves deviate less than 5% from the synthetic curve at all wavelengths are shown by a colour scale. The lowest DC misfit profiles within each independent set of 1,000 iterations are shown in the rightmost column.

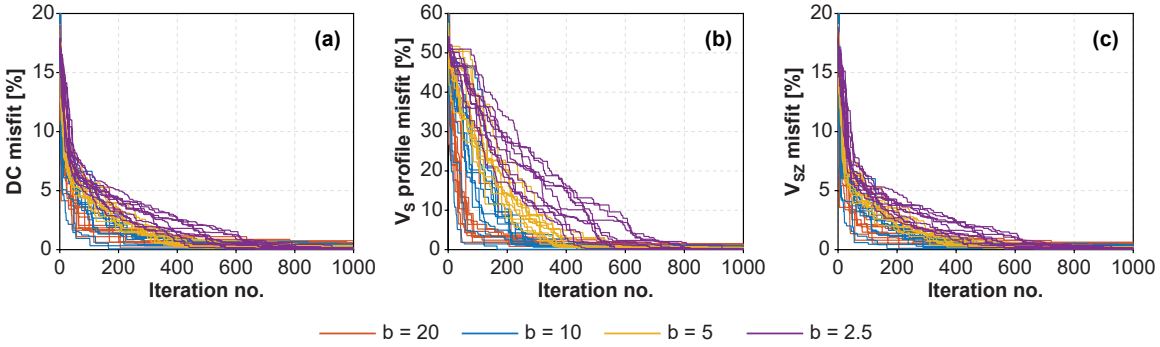

Figure 4.15: Inversion of the unperturbed synthetic dispersion curve from model A. (a) Data fitting progression. Model fitting progression in terms of (b) V_S-profile misfit and (c) V_{SZ}-profile misfit. Ten curves are shown for each value of b as the Monte Carlo simulation is based on 10 × 1,000 iterations.

For evaluating the behaviour of the inversion scheme when subjected to an inversely dispersive target model, the algorithm was tested on the synthetic data from model C. Results are reported in Figs. 4.16 and 4.17 using the same format as in Fig. 4.14. Overall, the inverted V_S-profiles in Fig. 4.16 (obtained by assuming a four-layer parameterization) correctly retrieve the existence and approximate location of the velocity inversion. By including more than four layers in the trial V_S-profiles (Fig. 4.17), the search algorithm was further able to adequately identify the location and characteristic velocity of the stiffer layer, and provide estimates of V_{SZ} consistent with their true values. However, by incorporating an excessive number of layers in the trial models, the inversion tended to smooth out prominent changes in V_S. The findings for the normally dispersive model B were comparable. Inversion results for the perturbed synthetic dispersion curves are depicted in Fig. 4.18.

The inversion of the experimental data acquired at the Halden site (see also Section 4.4) was conducted without using the already established layer structure of the site to guide the layering parameterization. This was done to mimic the common situation encountered in geotechnical investigations where information about the layering of the tested area is limited or non-existent. Hence, the number of layers was considered as an additional inversion parameter and the inversion conducted repeatedly starting with a two-layer model. Subsequently, the number of layers was increased until the dispersion misfit had reached a stable value. The mass density profile and the depth to groundwater were specified based on results of independent soil investigations (Blaker et al., 2016, 2019) and velocity reversals were permitted within the uppermost 10 m. Overall, the same considerations hold regarding selection of b-parameter values as for inversion of the synthetic data. Particularly, an increased value of b_S and/or b_h prompts more variability within the set of tested shear wave velocity and layer thickness values, respectively. For inversion of the experimental data, the values of the b-parameters were specified as $b_S = 5$ and $b_h = 10$. The initial pseudo-V_S estimates obtained by Eq. (3.86) were overall adequately close to their inverted values, prompting the use of a lower b_S. However, as the initially specified layer thicknesses were manually defined, a larger value of b_h was deemed more appropriate to allow for more variation within the set of sampled layer thicknesses.

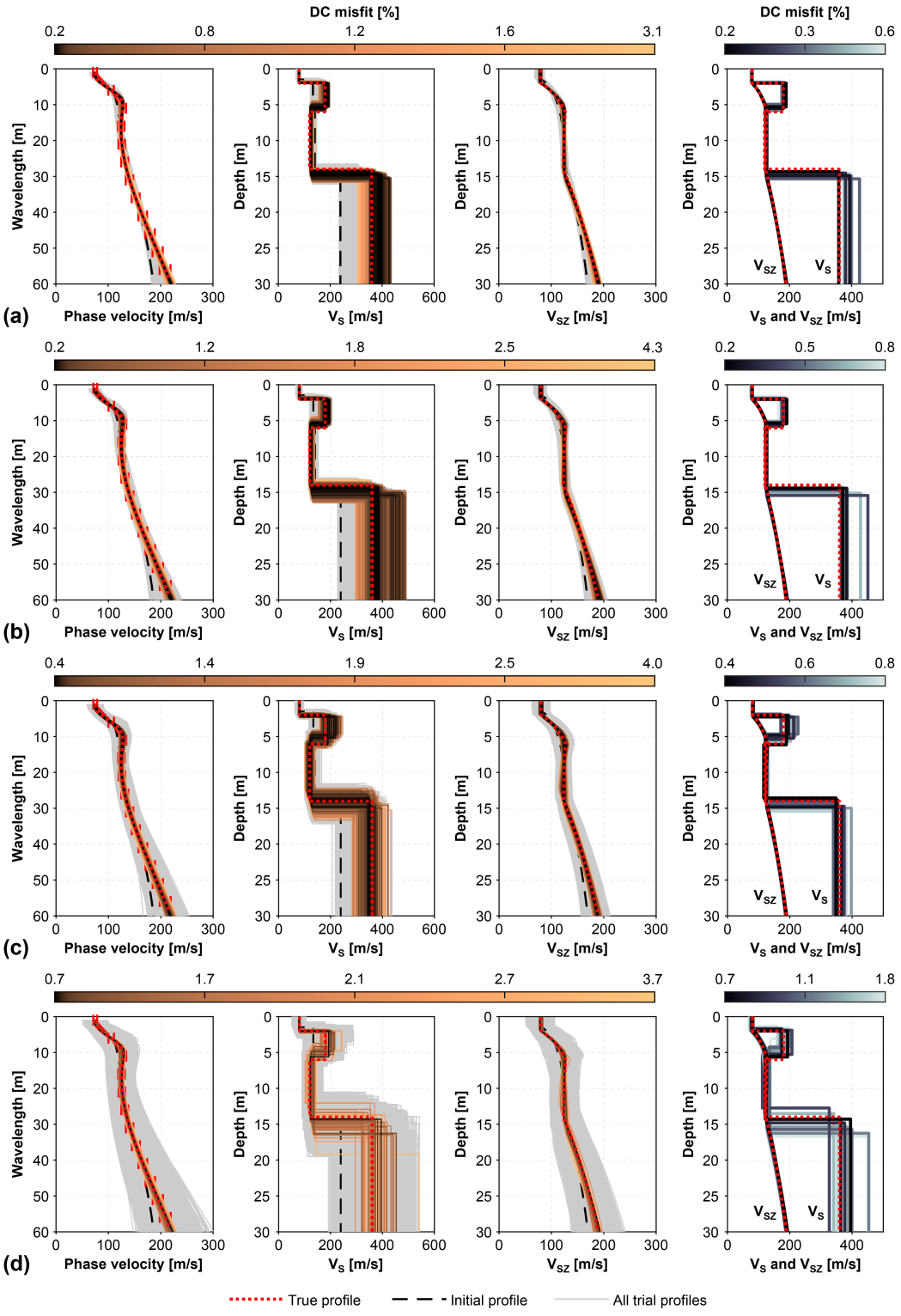

Figure 4.16: Inversion of the unperturbed synthetic dispersion curve from model C. A four-layer geologic structure is assumed for the testing V_S-models. The values of the search-control parameters (with $b_S = b_h = b$) are specified as (a) $b = 2.5$, (b) $b = 5$, (c) $b = 10$, and (d) $b = 20$. Grey areas display all sampled models and profiles whose dispersion curves deviate less than 5% from the synthetic curve at all wavelengths are shown using a colour scale. The lowest DC misfit V_S- and V_{SZ}-profiles obtained within each independent set of 1,000 iterations are shown in the rightmost column.

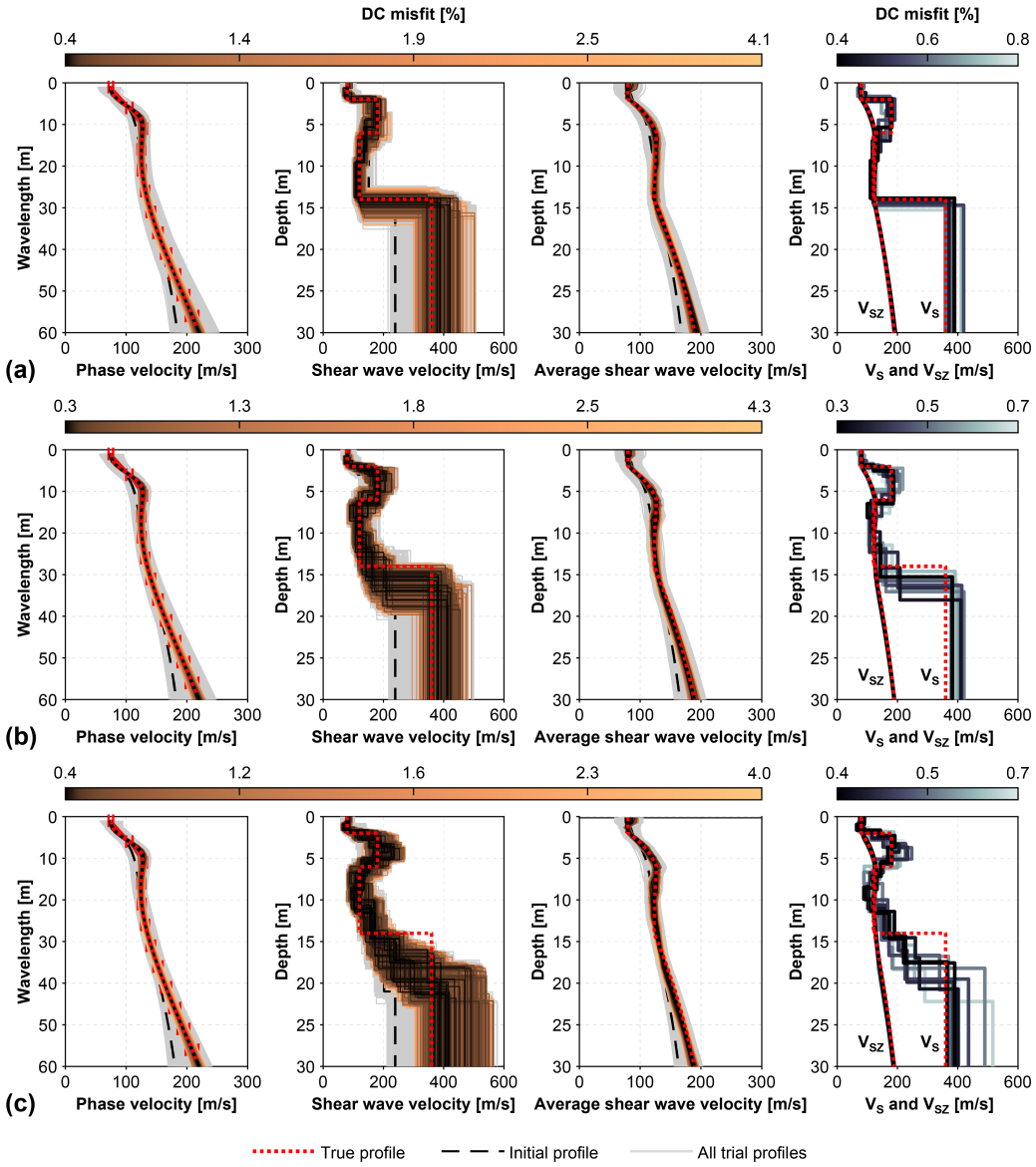

Figure 4.17: Inversion of the unperturbed synthetic dispersion curve from model C. A geologic structure consisting of (a) six, (b) eight, and (c) twelve layers (including the half-space) is assumed for the testing V_S-models. The values of the search-control parameters are specified as $b_S = b_h = 10$.

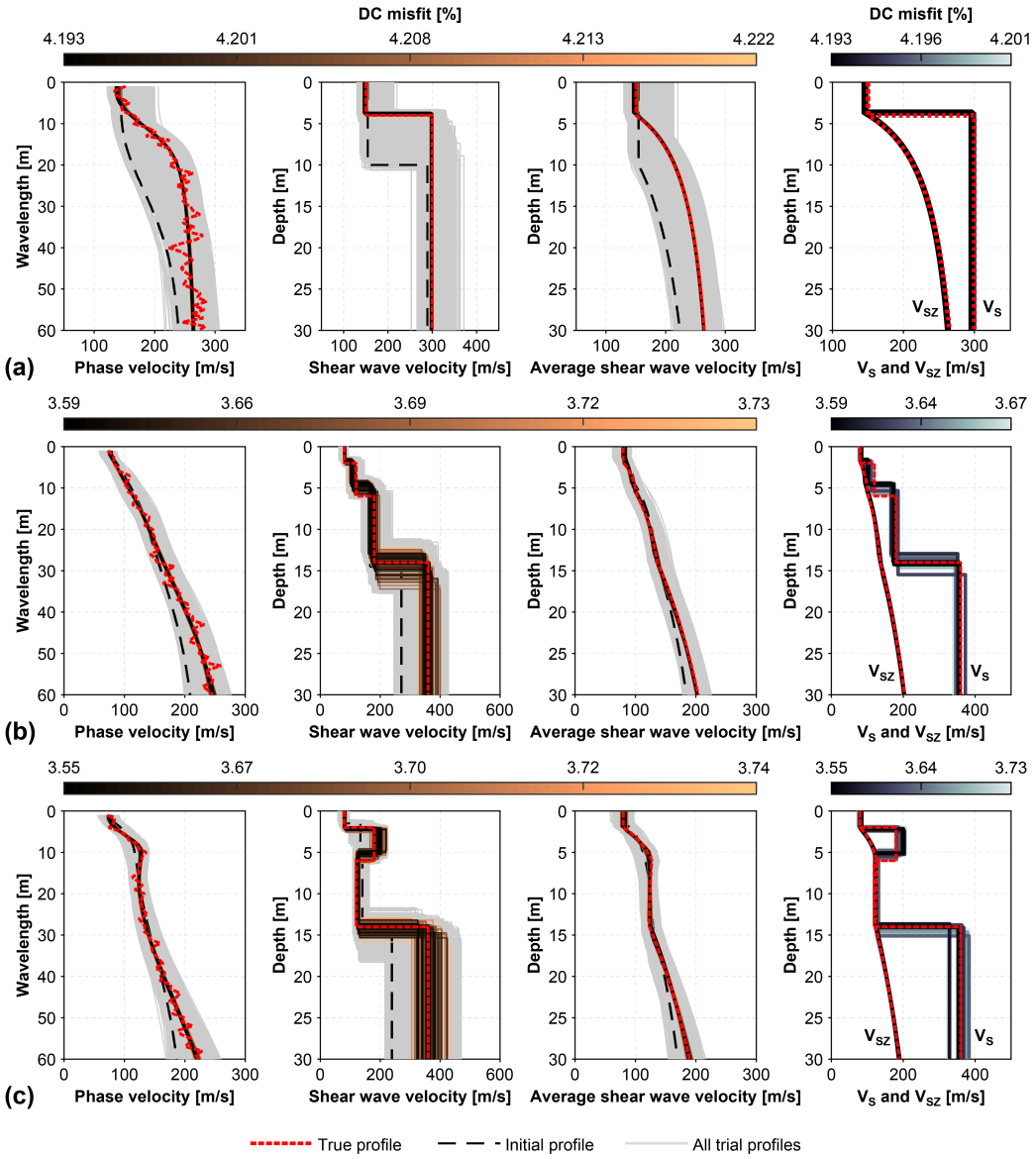

Figure 4.18: Inversion of synthetic dispersion curves for (a) model A, (b) model B and (c) model C. The target curves have been perturbed by introduction of a 5% white Gaussian noise. A two-layer geologic structure is assumed for inversion of the perturbed data from model A. A geologic structure consisting of four layers is assumed for models B and C. The 100 (i.e., 1%) lowest DC misfit V_S- and V_{SZ}-profiles obtained in each case are shown using a colour scale based on dispersion misfit values. The values of the search-control parameters are specified as $b_S = b_h = 10$.

Inversion results obtained by parameterizing the Halden site as three, four, six, and eight layers, respectively, are presented in Fig. 4.19. Figure 4.20b compares the lowest DC misfit V_S-profiles resulting from each tested layering parameterization, whilst the associated dispersion curves are compared to the experimental data in Fig. 4.20a. Corresponding V_{SZ}-profiles are shown in Fig. 4.20c. Figure 4.20b further compares the set of inverted V_S-profiles to results of invasive and laboratory measurements of V_S previously conducted at the Halden site.

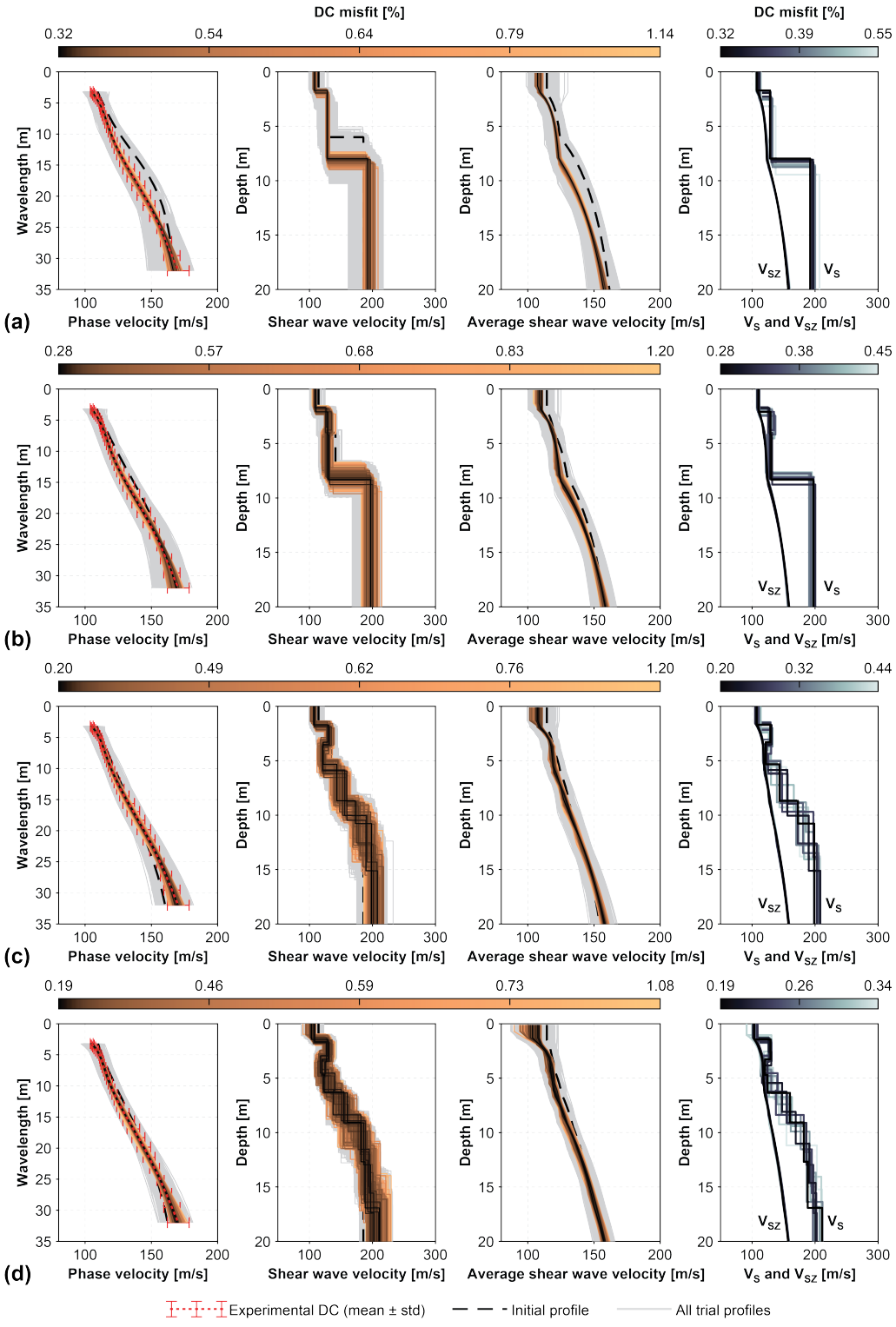

Figure 4.19: Inversion of the composite experimental dispersion curve for the Halden site. A geologic structure consisting of (a) three, (b) four, (c) six, and (d) eight layers (including the half-space) is assumed for the testing V_S-profiles. Profiles whose dispersion curves fall within one standard deviation of the composite curve at all wavelengths are presented using a colour scale based on dispersion misfit values. The lowest DC misfit V_S- and V_{SZ}-profiles within each independent set of 1,000 iterations are shown in the rightmost column.

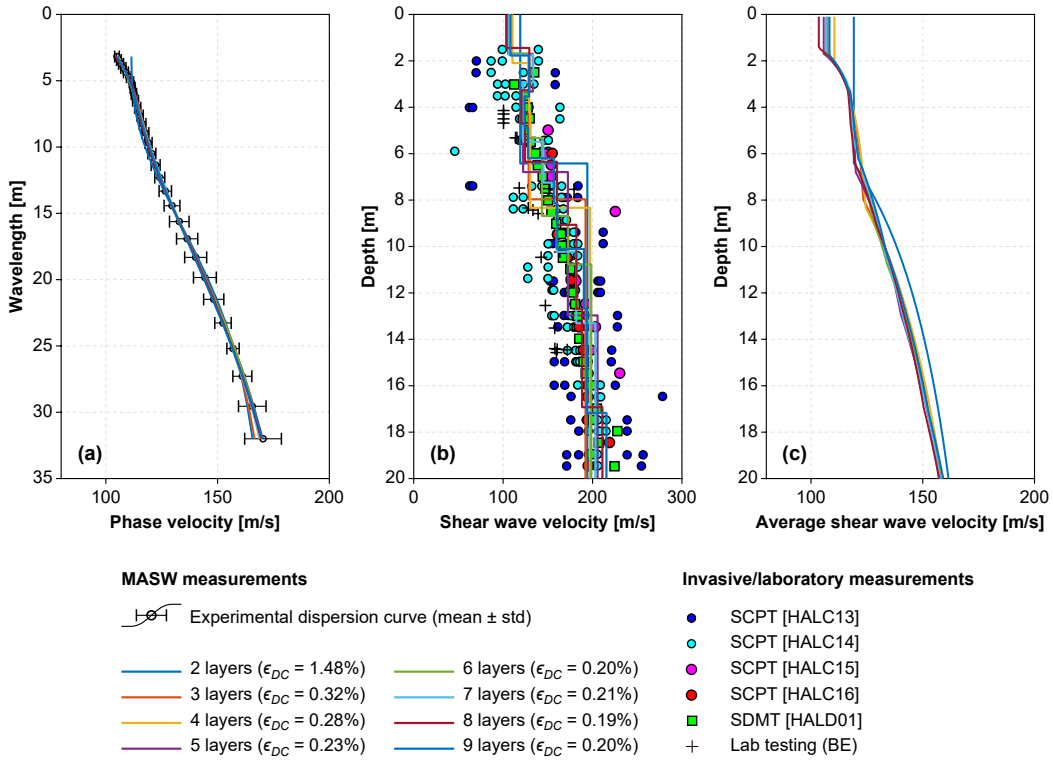

Figure 4.20: MASW measurement results for the Halden site. Comparison with results of SCPT, SDMT and laboratory measurements conducted in close proximity to the MASW profile.

Main findings in Paper III

– A simple but effective Monte Carlo-based scheme for solving the inverse problem of identifying V_S-profiles from actively generated fundamental mode Rayleigh wave dispersion curves is presented.

– Analysis of synthetic datasets, both with and without added white Gaussian noise, and experimental data acquired at a national geotechnical test site in Norway verified the performance of the inversion scheme. For the experimental case, the obtained shear wave velocity estimates matched those obtained by invasive techniques and were consistent with results of laboratory measurements.

– Definition of the model parameter space requires a balance between not overly constraining the solution and enhancing the odds of the algorithm getting close to the global minimum. In general, larger values of the b-parameters (b_S and b_h) increase the size of the explored solution space. However, given a fixed number of iterations, an increased value of b also leads to more variation within the set of trial V_S-profiles and, hence, sparser sampling.

– The use of b-parameters in the range of 5 to 10 was sufficient for all the studied models. Therefore $b_S, b_h \in [5, 10]$ may be a suitable range. This applies, in

particular, to near-surface applications at sites similar to those modelled in the paper.

- The inverse problem faced in MASW is inherently non-unique and multiple significantly different V_S-profiles can provide comparable values of the dispersion misfit function. The results of this study support recommendations presented in the literature on repeating the inversion using different layering parameterizations (i.e., number of layers). However, the number of parameterizations that may need to be tested seems highly site-specific. Therefore, no specific guidelines applicable to all sites can be given based on the results of this study.

- For applications where the sole objective is to assess the average parameters of a site (e.g., V_{S30}), the results indicate that the layering parameterization plays a minor role, provided that the inversion converges to a model that is consistent with the experimental data. This is in line with previous findings demonstrating the robustness of surface wave analysis for assessment of V_{SZ}.

- Values of the dispersion misfit function may not be comparable between different sites. Making the search algorithm complete a specific number of iterations and subsequently draw inference from the set of simulated profiles based on the observed spread in the experimental data is therefore recommended. Using $N_{max} = 1{,}000$ and ten initiations gave fair results for engineering purposes in all the cases in this study. In our experience, such computations (i.e., ten initiations) routinely take approximately 5 minutes when performed on a standard office PC desktop computer (with an Intel i7-8700 processor and 16 GB of RAM).

4.4 Paper IV

The objective of *Paper IV* was to assess the reliability, accuracy and repeatability of results obtained with the data acquisition equipment of the University of Iceland and the new MASWaves software, thus linking together the work presented in *Paper I*, *Paper II* and *Paper III*.

In-situ measurements were conducted at four geotechnical research sites in Norway (see Fig. 4.21) following the procedures outlined in Section 3.3.2. The sites are characterized by silt, soft clay, sand and quick clay deposits, respectively, and are referred to as Halden (silt site), Onsøy (soft clay site), Øysand (sand site), and Tiller-Flotten (quick clay site). The Halden, Øysand and Tiller-Flotten sites were developed through the Norwegian GeoTest Site (NGTS) project (L'Heureux et al., 2017), whilst the tested site at Onsøy was established in the late 1960s by the Norwegian Geotechnical Institute (NGI) (Lunne et al., 2003). Independent assessments of shear wave velocity, obtained with invasive, non-invasive and laboratory-based techniques, exist for the Norwegian sites and were used for comparison and verification purposes in this study. Table 4.1 summarizes the main characteristics of the four test locations and the existing measurements that are available for each site.

Figure 4.21: Test sites in south-eastern and central Norway. [The map is based on data from the Norwegian Mapping Authority. ©Kartverket]

Table 4.1: Overview of site characteristics and previous work at the Halden, Onsøy, Øysand and Tiller-Flotten sites.

	Halden	**Onsøy**	**Øysand**	**Tiller-Flotten**
Soil type	Silt	Soft clay	Silty sand	Quick clay
Unit weight	19–20.5 kN/m^3	∼16 kN/m^3	18–19 kN/m^3	17–19 kN/m^3
Water content	21%–32%	50%–70%	∼20%–30%	30%–50%
Depth to bedrock	∼21 m [southern part of the site]	∼40 m	>80 m	>50 m
Detected groundwater table	About 2–2.5 m depth	Below the surficial crust	∼2 m depth	Below the surficial crust (1–2 m depth)
Comparison data	SCPT, SDMT, Lab (BE)	SCPT, MASW, Lab	SCPT, SDMT, MASW, Lab (BE)	SCPT, SDMT
References	Blaker et al. (2016, 2019)	Lunne et al. (2003)	Gundersen et al. (2018); Quinteros et al. (2019)	L'Heureux et al. (2019)

At each of the four test locations, emphasis was on placing the survey profile as close as possible to relevant previous work. Typical dispersion images for each of the four sites are shown in Fig. 4.22. Repeated shots were recorded for each source location in order to obtain a statistical sample of dispersion curves and, hence, allow for quantification

of the variability in the estimated phase velocity values. The experimentally evaluated dispersion curve estimates were added up within logarithmically spaced wavelength intervals following the procedure described in *Paper II* (see also Section 3.5.2). The inversion of the composite dispersion curves was then conducted following the global search procedure outlined in *Paper III* (see also Section 3.6.3).

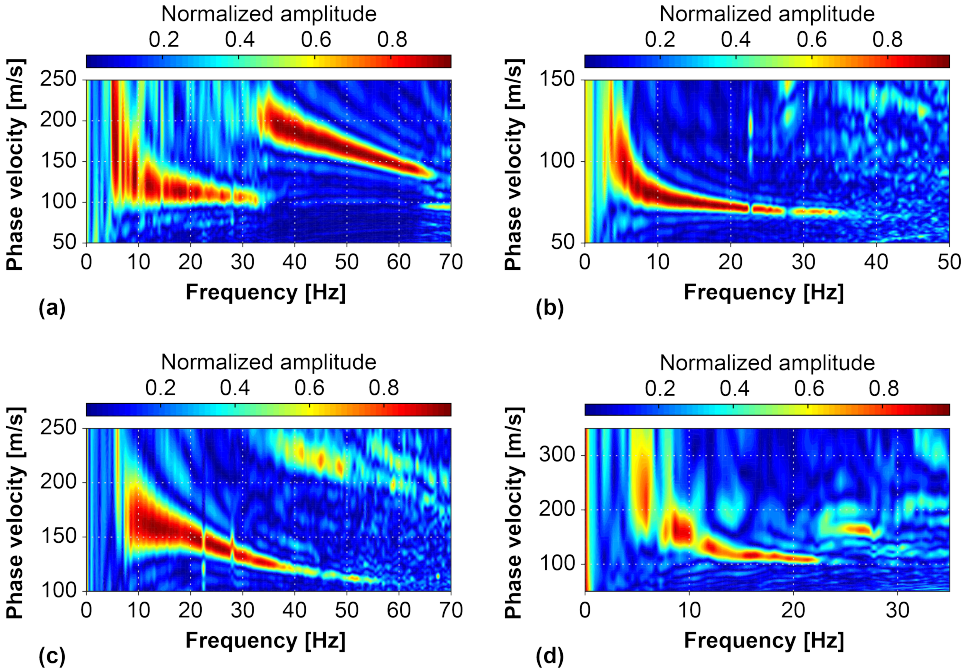

Figure 4.22: Dispersion images of multi-channel surface wave records acquired at the (a) Halden, (b) Onsøy, (c) Øysand, and (d) Tiller-Flotten test sites.

Figure 4.23 presents the results of the MASW measurements together with the results of invasive, non-invasive and/or laboratory-based measurements conducted at each of the sites by independent teams of researchers. In Fig. 4.23, the MASW measurement results are summarized in terms of the mean and median of the tested V_S models whose associated theoretical dispersion curves fall within one standard deviation of the experimental data. The lowest dispersion misfit V_S-profiles are further shown.

For assessment of the repeatability of the analysis, repeated field measurements were conducted between 2013 and 2019 at a volcanic sand site on the bank of the Ölfus River in South Iceland. Data from six field measurements exist, i.e. from 2013, 2014, 2015, 2017, 2018, and 2019. The midpoints of the MASW survey profiles were in all cases positioned at approximately the same location (i.e., within a 2 m radius). The orientation of all six profiles was the same. Figure 4.24a presents a comparison of the six experimental dispersion curves. The upper and lower boundary curves, depicted in Fig. 4.24a using dashed lines, correspond to plus-minus one standard deviation of the composite mean curve. The variability of the mean experimental curves is evaluated in terms of COV as a function of wavelength in Fig. 4.24b. Shear wave velocity profiles, obtained by inversion of each experimental curve, are shown in Fig. 4.24c and the variability of the inverted V_S values is quantified using the COV statistic in Fig. 4.24d.

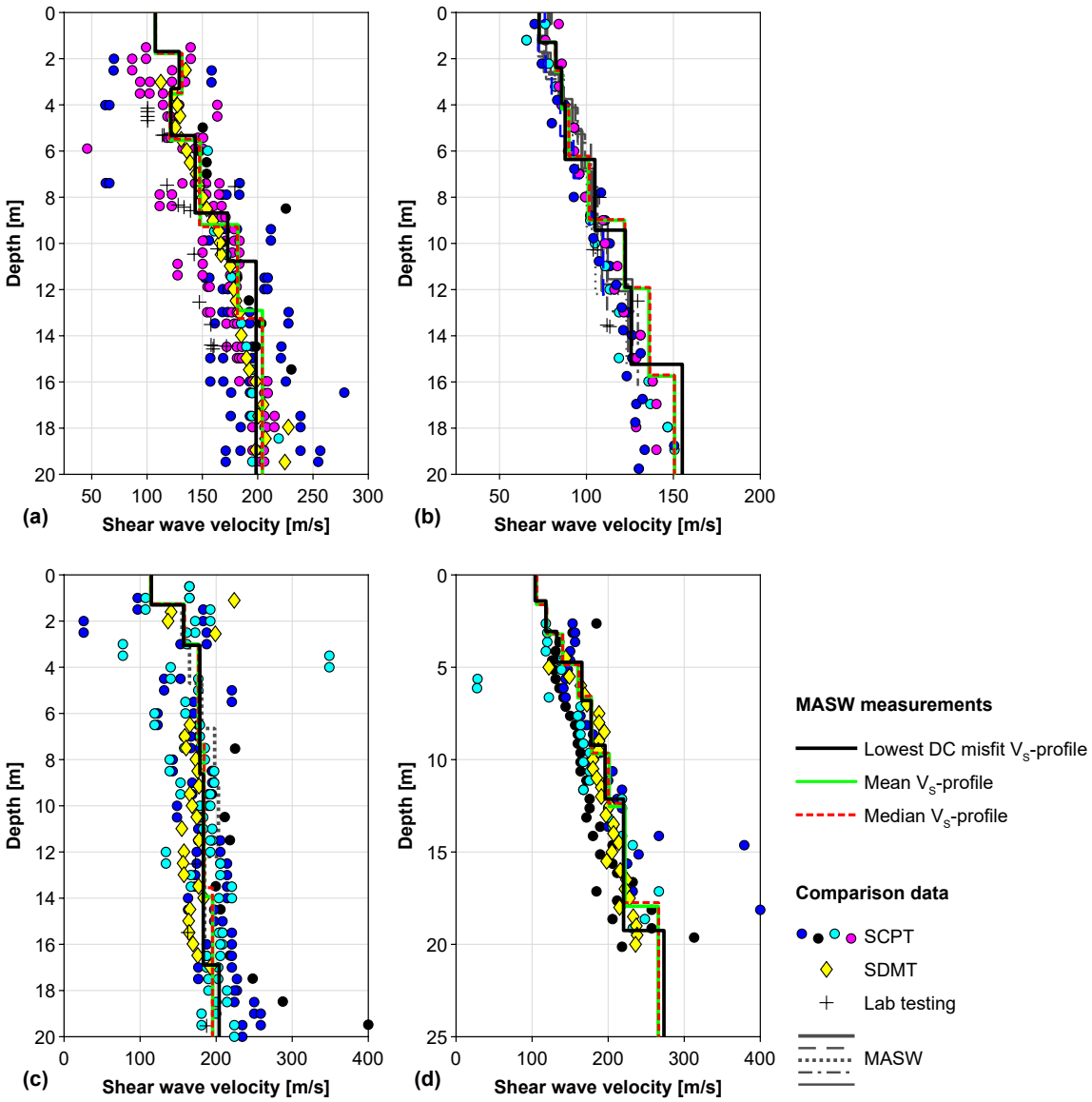

Figure 4.23: Comparison of MASW V_S-profiles and results of invasive, non-invasive and laboratory measurements previously conducted at the four research sites; (a) Halden, (b) Onsøy, (c) Øysand and (d) Tiller-Flotten.

Main findings in Paper IV

– A revised version of the MASWaves software package was introduced. It includes: (i) A specialized data acquisition module that allows for preliminary analysis in-situ. (ii) A tool to add up dispersion curves from multiple multi-channel registrations using the procedure presented in *Paper II*. (iii) An improved inversion analysis tool, based on the simple global search algorithm described in *Paper III*, to replace or supplement the interactive scheme of *Paper I*.

– MASW surveys were conducted at geotechnical research sites in Norway in order to verify results obtained with the MASWaves software.

– Results obtained with MASWaves were comparable to results obtained with invasive methods and laboratory techniques, as well as being in good agreement with results of MASW surveys conducted using different hardware and processed through different software packages.

– The repeatability of the analysis was confirmed with repeated measurements at a volcanic sand site in South Iceland over a seven-year period.

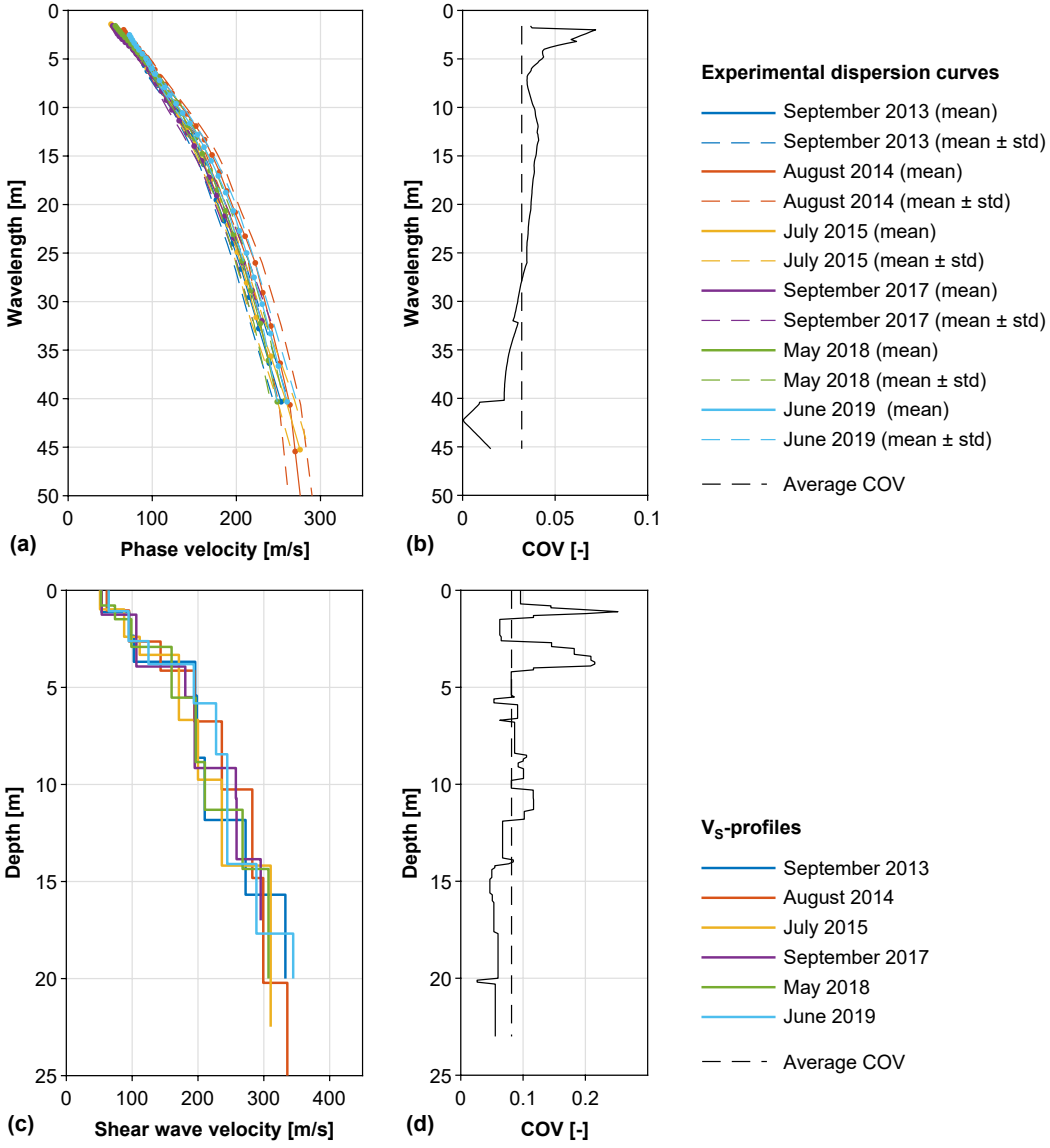

Figure 4.24: (a, b) Comparison of experimental dispersion curves acquired based on six separate field tests between 2013 and 2019. (c, d) Comparison of shear wave velocity profiles assessed based on the repeated measurements.

4.5 Papers V, VI & VII

Paper V, *Paper VI* and *Paper VII* all discuss the application of the MASW method for characterization of Icelandic soil sites. MASW measurement results from a number of locations were summarized (Fig. 4.25), with the main emphasis on densely populated areas in the Southern Rangárvellir county and important infrastructure in the South Iceland region. The sites were selected such that they represented several commonly encountered local soil materials.

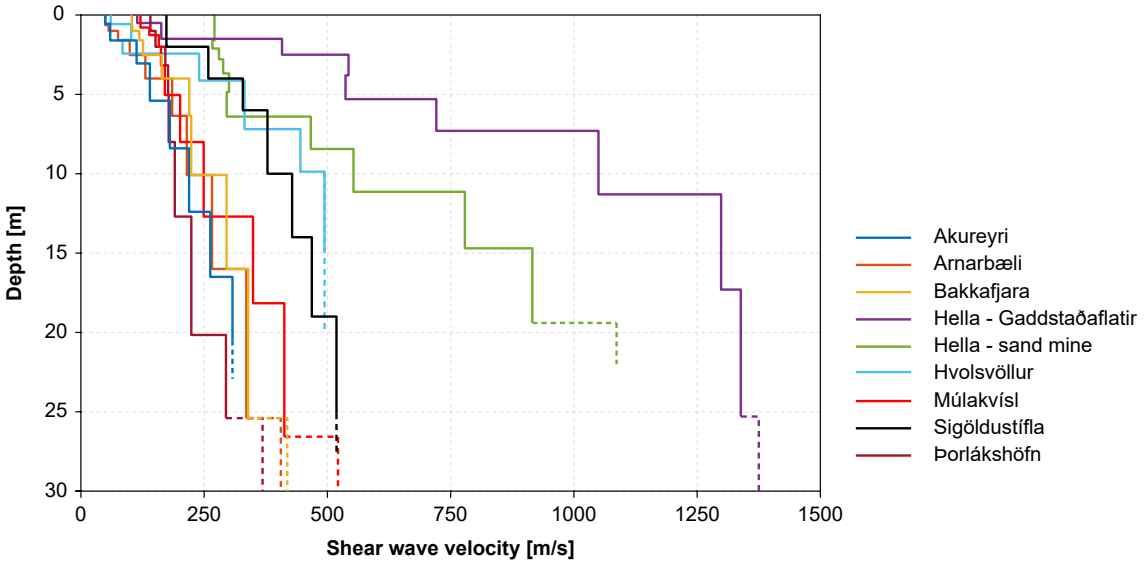

Figure 4.25: Comparison of shear wave velocity profiles obtained for eight natural sites and one earth dam site in Iceland (refer to Table 4.2).

Table 4.2: Overview of site characteristics of several MASW test sites in Iceland.

Site	**Type**	**Soil**	**USCS group**
Akureyri airport	Natural site	Holocene fluvial sand	SM
Arnarbæli on the bank of the River Ölfusá	Natural site	Holocene glaciofluvial sand/silty sand	SW-SM
Bakkafjara by Landeyjahöfn harbour	Natural site	Modern littoral sand	SW
Gaddstaðaflatir in the village *Hella*	Natural site	Late-glacial cemented Aeolian silty sand	-
Sand mine close to the village *Hella*	Natural site	Late-glacial (slightly) cemented Aeolian silty sand	-
Hvolsvöllur (village)	Natural site	[Unknown]	[Unknown]
Bridge over River *Múlakvísl*	Natural site	Modern littoral sand	SW
Sigalda dam (*Sigöldustífla*)	Earth dam	Well graded gravel	GW
Miðalda east of the village *Þorlákshöfn*	Natural site	Alluvial sand	SP

In addition, *Paper VII* describes initial efforts to build an online database of MASW measurement results, hosted by the University of Iceland. The database will provide the user with an interface where results from different sites can be viewed simultaneously and compared. Whilst not replacing site specific measurements, such database can be of value for engineers and researchers to access data and interpreted results for design and future studies.

Paper V contributes to the calibration of the analysis procedure for Icelandic soil conditions by comparing MASW measurement results to results of other available in-situ measurements. In particular, results of an MASW survey conducted in the Landeyjar area were compared to results of Cone Penetration Tests (CPT) carried out in conjunction with construction of the Landeyjahöfn harbour (a major ferry portal in South Iceland) in 2009. Although the soil deposits in the area are very thick, the deepest CPT probing (see Fig. 4.26) was terminated at a depth of around 7 m due to high resistance and consequent risk of damage to the CPT cone. This was likely because the cone hit larger boulders which frequently occur in the local soils. Comparable occurrences have been observed at other MASW tests sites where results of CPT measurements have been available (Erlingsson et al., 2017; Erlingsson, 2019).

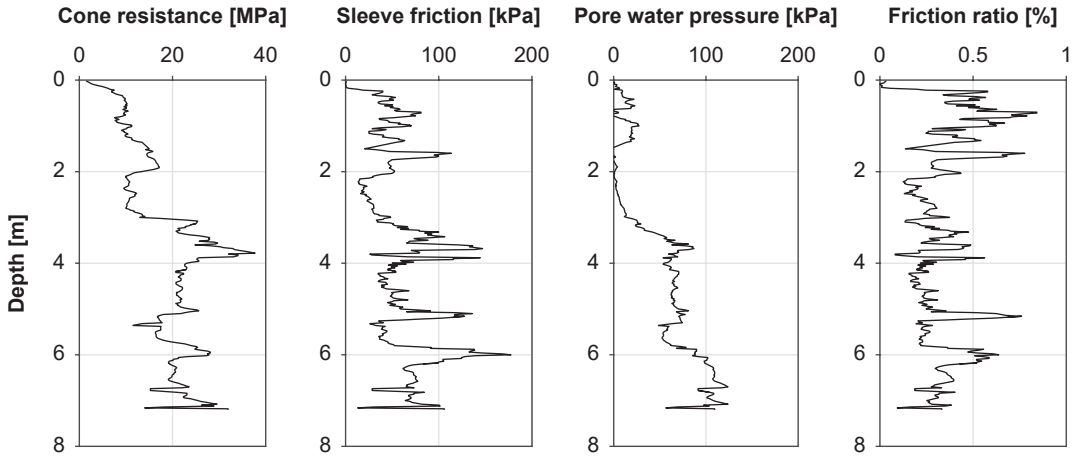

Figure 4.26: Results of a CPT measurement by the Landeyjahöfn harbour [CPT-5375].

The area surrounding Landeyjahöfn harbour is a long sandy beach, characterized by uniform sandy materials with a low fines content. Hence, the material properties of the soil beneath the MASW receiver spread are expected to be approximately the same as the properties of the soil where the CPT probings were conducted. Based on the normalized soil behaviour type (SBTn) chart (Robertson, 1990, 2009) (Fig. 4.27), the soil materials are classified as 'sands – clean sand to silty sand' [soil behaviour type 6] and 'gravelly sand to dense sand' [type 7].

As briefly discussed in Section 2.1.1, various correlation equations exist between shear wave velocity and different CPT-related parameters. A few examples of CPT-V_S correlations, either intended for sands or for all soil types, are summarized in *Paper V*. Figure 4.28 compares V_S-profiles predicted based on selected CPT-V_S correlations to a profile that was obtained with MASW.

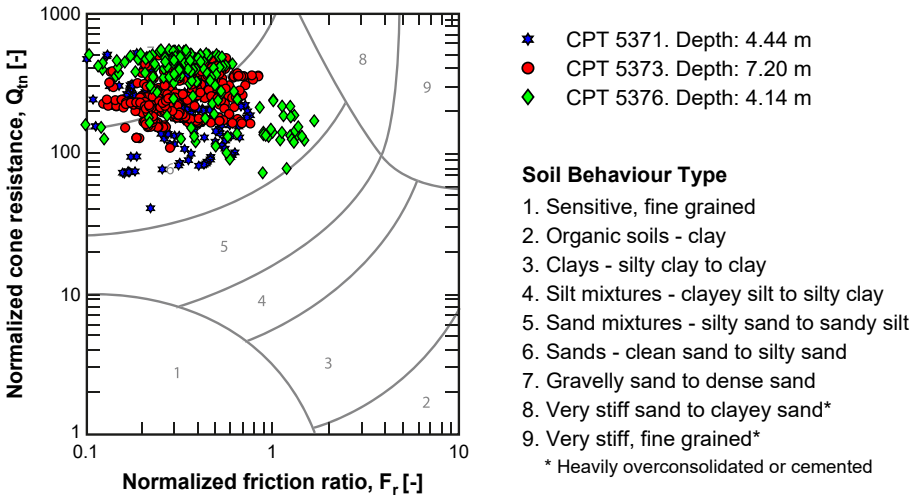

Figure 4.27: Normalized soil behaviour type (SBTn) chart with results of CPT measurements by the Landeyjahöfn harbour.

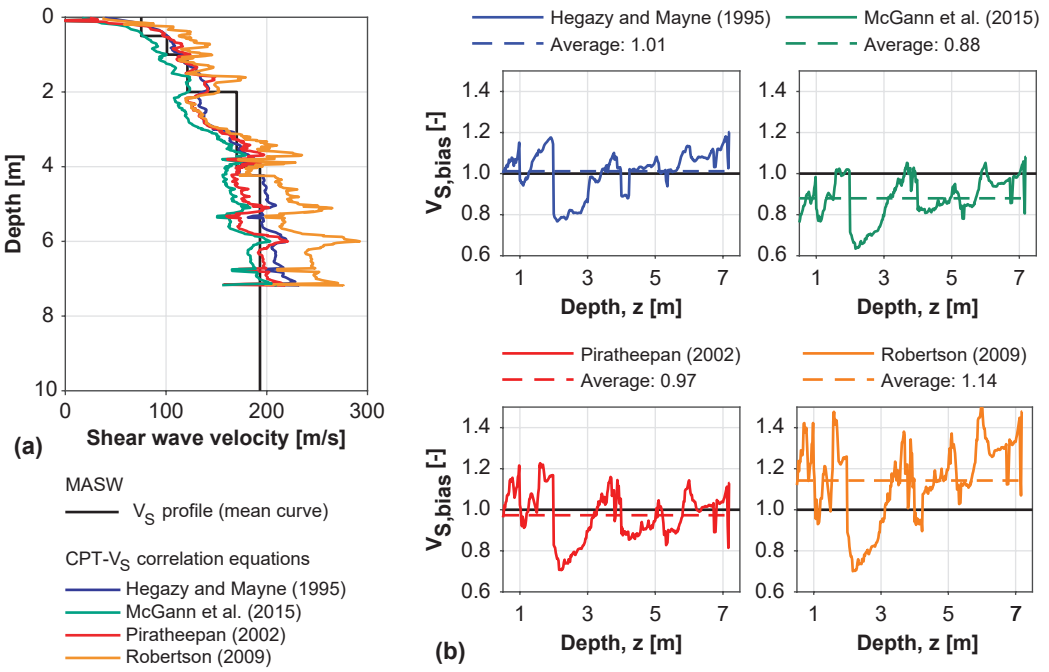

Figure 4.28: (a) Near-surface V_S-profiles for the Landeyjahöfn harbour site predicted based on selected CPT-V_S correlations and obtained with MASW. (b) Comparison of V_S-profiles obtained based on CPT and MASW measurements. The pseudo V_S-profiles were obtained with empirical correlations proposed by Hegazy and Mayne (1995), McGann et al. (2015), Piratheepan (2002) and Robertson (2009). $V_{S,bias}$ is defined as the ratio between the CPT-based pseudo V_S-profiles and the MASW V_S-profile.

The focus of *Paper VI* was on seismic hazard applications in the South Iceland region, in or close to the South Iceland Seismic Zone. The paper further reports the first attempt to utilize MASW measurement results for liquefaction hazard evaluation of Icelandic soil materials. Field measurements were conducted at a loosely compacted volcanic sand site on the bank of the River Ölfusá, where liquefaction was observed following the South Iceland M_w6.3 Ölfus earthquake in 2008 (Fig. 4.29(left)). The simplified procedure of assessing cyclic stress ratio to normalized shear wave velocity (Andrus & Stokoe, 2000) was used to evaluate the liquefaction hazard at the site (Fig. 4.29(right)). The results indicated liquefaction occurrence down to a depth of 3–4 m, which is consistent with reported observations on site.

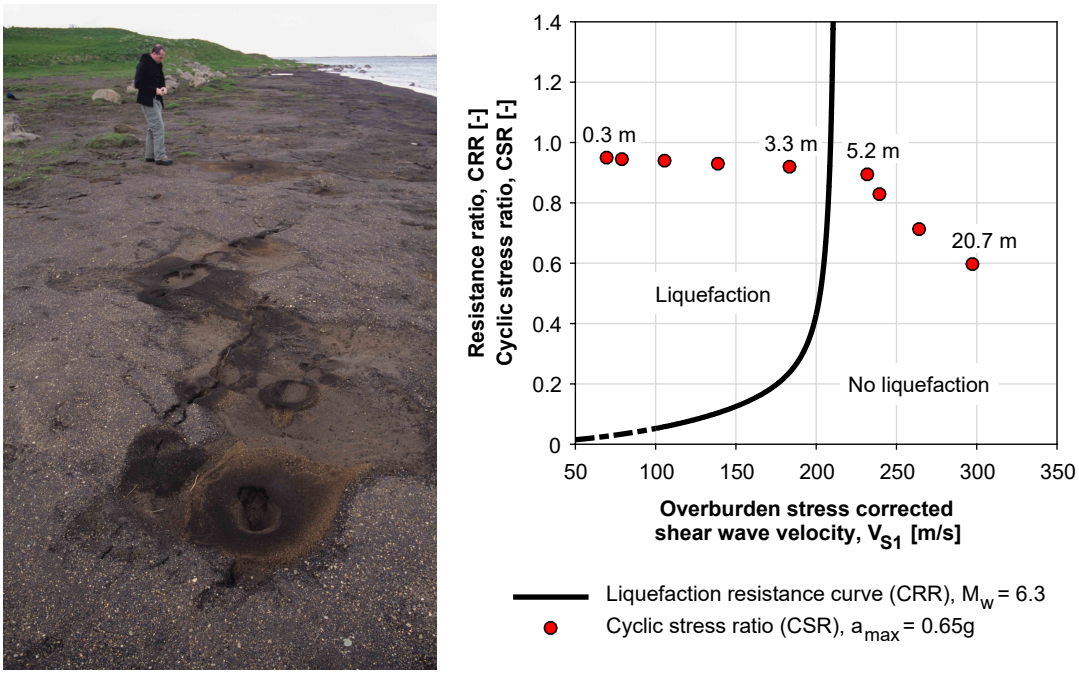

Figure 4.29: (Left) Sand boils on the bank of the River Ölfusá close to the epicentre of the 29 May 2008 M_w6.3 earthquake. (Photo: Oddur Sigurðsson). (Right) Liquefaction evaluation chart. The soil stratum at the site is uniform down to a great depth with the groundwater table close to the surface. Its grain size distribution lies well within the boundaries for potentially liquefiable soils, and partially within the boundaries identified as 'most liquefiable soils' (Green et al., 2012; Tsuchida, 1970). The estimated peak ground acceleration for the site (a_{max}) is 0.65g.

Main findings in Papers V, VI & VII

– MASW measurements have been successfully conducted at a number of Icelandic sites. The method seems well suited for shear wave velocity/shear stiffness profiling of many commonly encountered local soil materials, including gravelly sites and sites characterized by thick deposits of cemented silty sand. The nature

of the tested sites is, however, in all cases relatively simple. Further testing at more challenging sites is required.

- Due to the unique characteristics of Icelandic soils, local measurements and dissemination of test results are valuable for the Icelandic engineering community.

- For Icelandic test sites, verification of MASW V_S-profiles against results obtained with other measurement techniques is limited by the lack of comparison data.

- Results of existing CPT measurements at the Landeyjahöfn harbour site are consistent with results of an MASW survey conducted in the area. In particular, the proposed CPT-V_S correlation equations of Hegazy and Mayne (1995) and Piratheepan (2002) fit the data relatively well. However, it is necessary to note that this is a relatively shallow profile. Hence, further validation is needed.

- Although very limited in scope, a preliminary study aimed at the prediction of liquefaction of Icelandic soils based on results of MASW measurements showed promising results.

4.6 Paper VIII

Hydropower accounts for over 70% of all electricity production in Iceland (Orkustofnun, 2018; Bjarnason et al., 2019). Most of the larger hydroelectric power stations in the country are on glacial rivers, characterized by a seasonally varied flow rate. Hence, in order to regulate flow, water reservoirs with associated dams are an indispensable part of the Icelandic hydropower system.

As of 2019, 29 dams in Iceland meet the criteria set by the International Commission on Large Dams (ICOLD). A large majority (i.e., 23 dams) are earth-rockfill dams with a central impervious moraine core, abutted by gravel filters, supporting fills and riprap for erosion and wave protection. Many of these structures are in the Þjórsá-Tungnaá-Kaldakvísl area in the outskirts of the South Iceland Seismic Zone (SISZ). Hence, seismic aspects must be considered in the design process.

Paper VIII presents a study aimed at extending the application of MASW to the analysis of Icelandic earth dam structures. The purpose was to estimate their structural health and to create a base in order to be able to observe potential changes in the future. Measurements were conducted on the crests of three dams in the catchment area of the Rivers Þjórsá and Tungnaá in Iceland's south-central highlands; Sigalda dam, Sporðalda dam and Sultartangi dam (see Fig. 4.30). Their main characteristics are summarized in Table 4.3.

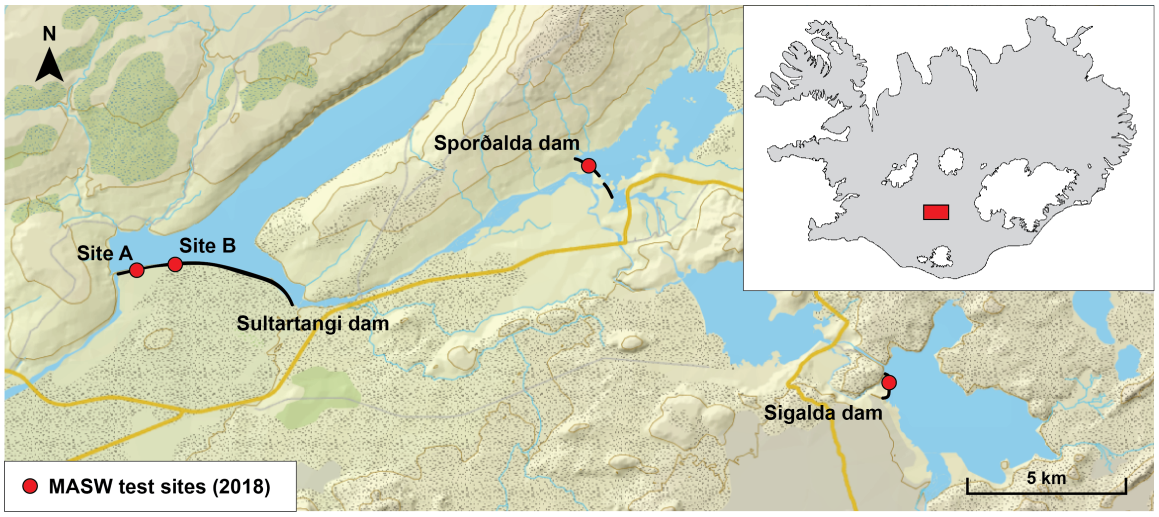

Figure 4.30: Location of MASW test sites at Sigalda dam, Sporðalda dam and Sultartangi dam. [The map is based on data from the National Land Survey of Iceland.]

Table 4.3: Main characteristics of the Sigalda, Sporðalda and Sultartangi dams.

	Sigalda dam	**Sporðalda dam**	**Sultartangi dam**
Type of dam	Rock-fill dam with an asphalt cladding	Earth-/rock-fill dam with a central core of moraine	Earth-/rock-fill dam with a central core of moraine and loess
Year completed	1977	2013	1984/1999
Length	0.9 km	1.1 km (N-W part) 0.3 km (S-E part)	6.1 km
Height (maximum)	40 m	28 m	23 m
	Fill	*Core*	*Core*
Material description	Reworked moberg, breccia, tuff and sand	Moraine	Loess [within the tested section]
USCS classification	GW	-	SM

Results from the two MASW surveys at the Sultartangi dam site are illustrated in Fig. 4.31. The experimentally evaluated shear wave velocity and average shear wave velocity profiles were compared to available in-situ measurements conducted with the SASW technique (Silver et al., 1986).

Paper VIII further compares the experimentally evaluated small-strain shear stiffness (G_{max}) profiles to profiles obtained with empirical methods, with the aim of identifying appropriate formulas and parameter sets for empirical assessments of the stiffness properties of typical Icelandic earth dams. Results obtained using the model proposed by Seed and Idriss [Eq. (2.7)] are presented in Fig. 4.32.

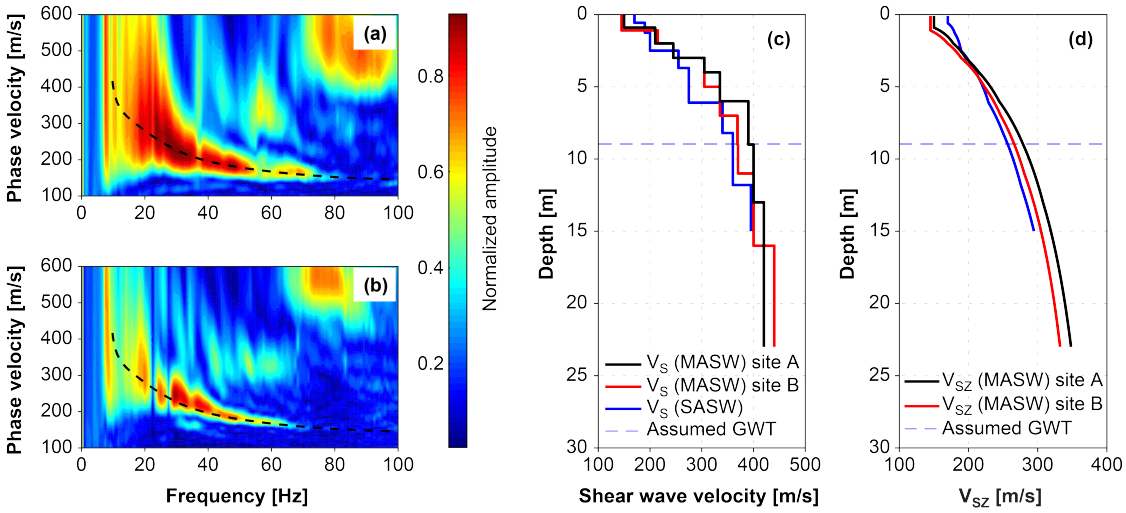

Figure 4.31: Results of MASW measurements conducted at two locations on the crest of the Sultartangi dam. Dispersion images obtained at Sultartangi site A with survey profiles of length (a) 11.5 m and (b) 23 m. Estimated (c) shear wave velocity (V_S) and (d) average shear wave velocity (V_{SZ}) profiles. The theoretical dispersion curve associated with the estimated V_S-profile for site A is shown with a black dashed line in (a, b). The assumed location of the groundwater table (GWT) within the central core of the dam is shown using a blue dashed line in (c, d).

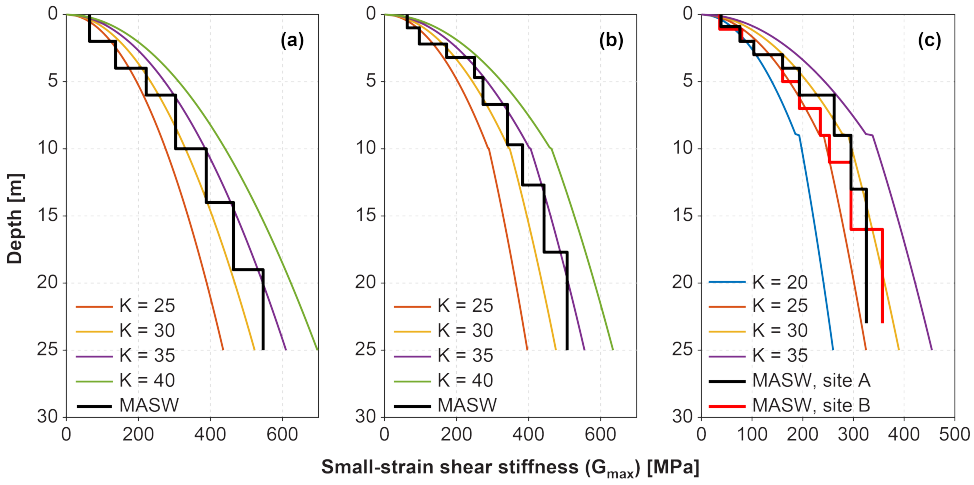

Figure 4.32: Comparison of empirical and experimental G_{max}-profiles for the (a) Sigalda dam site, (b) Sporðalda dam site and (c) Sultartangi dam sites. The empirical profiles were obtained using the model of Seed and Idriss $G_{max} \approx 1000 K_{2,max} \sqrt{\sigma'_m}$. A value of $K_{2,max}$ in the range of 25–40 is classified as very dense sand and gravel (Gazetas, 1991) (see also Table 2.4).

Main findings in Paper VIII

– MASW is a promising technique to assess the shear stiffness of typical Icelandic earth dam structures.

– Results of MASW measurements were consistent with available experimental results.

– The correlation of Seed and Idriss [Eq. (2.7)] with a value of $K_{2,max}$ in the range of 25–35, depending on the type of soil material used for construction of the dam, appeared to provide a good fit between the experimental and empirical profiles. However, comparison of experimentally and empirically estimated G_{max}-profiles from other Icelandic dam sites is considered necessary for further verifying its applicability, and for making specific recommendations regarding appropriate parametric values.

– The depth to groundwater varies greatly within an earth dam structure and is further highly correlated to, e.g., the water level in the associated reservoir. Hence, considering a survey carried out on a dam's crest, obtaining a clear-cut estimate of the location of the groundwater table is impossible. Results of parametric studies indicated that the uncertainty associated with the assumed groundwater level is in the order of 5%–10% for the surficial layers.

– Due to the geometry of earth-rockfill dams with a central core, the acquired surface wave data likely contains a combination of the response of the core and shell materials. Hence, the results of an MASW survey, may, to some extent, represent a composite shear stiffness profile for the two materials. Further work will need to be devoted to the analysis and modelling of such structures.

5 Conclusions & future perspectives

5.1 Summary

The characteristics of Icelandic soil sites are in many respects vastly different from those commonly encountered in other countries. Surface wave analysis methods have wide practical application possibilities within the field of civil engineering. The past two decades have seen a rapid development of surface wave methods, along with a considerable increase in studies where the dispersive properties of surface waves are utilised for soil site characterization purposes. However, active-source surface wave analysis techniques have only seen limited use for the characterization of Icelandic soil deposits. In addition, all prior studies have focused on the application of two-receiver techniques.

The aim of this project was to develop and implement the MASW (Multichannel Analysis of Surface Waves) technique for analysis of Icelandic soil conditions and thus contribute to the improved understanding of the engineering characteristics of basaltic soil sites in Iceland. This work has been divided into three main, though somewhat intersecting, objectives. (i) To develop software for acquiring, processing and inverting active-source multi-channel surface wave registrations. The primary motivation for developing the MASW software from scratch was to gain a thorough understanding of the methodology and to get a confident, easy access and flexibility to modify and advance the data acquisition, processing and analysis tools for further developments and future applications. (ii) To verify and validate the set of software modules and the overall applicability of the adopted/developed methodologies. (iii) To implement and adapt MASW for characterization of the stiffness properties of Icelandic soil sites, both including natural soil deposits and man-made fillings.

The software developed in this project (referred to as *MASWaves*) consists of four separate modules. *DAQ* for data acquisition, visualization of measurement data in terms of recorded time histories and spectral images, and preliminary in-situ analysis. *Dispersion* for identifying and extracting experimental dispersion curves from acquired multi-channel surface wave records. *Combination* to add up experimental dispersion data from repeated shots. *Inversion* to assess the shear wave velocity structure of the tested site through inversion of the experimental dispersion data. Furthermore, methods for combining dispersion curves from a number of records gathered at a given site have been developed, aiming to increase the range in investigated depths, get more

reliable results, and assess the uncertainty associated with the experimental dispersion curve for use in the inversion. Moreover, a simple but effective Monte Carlo-based technique has been developed for use in the MASW inversion analysis.

During the initial stages of the software development, verification and validation of the dispersion and inversion (i.e., forward modelling) modules was primarily conducted by comparison with other software packages. Comparative studies were conducted for composite evaluation of the custom-made multi-channel data acquisition hardware and the set of software modules. Results of MASW surveys at four of Norway's national geo-test sites were in good agreement with invasive, non-invasive and laboratory-based measurements of shear wave velocity conducted at the sites by independent researchers. At Icelandic test locations, results of MASW measurements were overall consistent with a-priori information and available measurement results. The repeatability of the analysis was confirmed through repeated measurements at a volcanic silty sand site in South Iceland over a seven-year period, starting from the initial test measurements conducted using the hardware of the University of Iceland.

Turning to the project's third objective, the MASW method has been successfully applied at over twenty locations in Iceland, with emphasis on loose soil sites in or close to the South Iceland Seismic Zone and the Tjörnes Fracture Zone, which are the two seismically most active areas in the country. Therefore, the results of this study indicate that the MASW technique is well suited for shear wave velocity/stiffness profiling of many of the commonly encountered local soil materials. Hence, this work will serve as a basis for future studies on the application of active-source multi-channel surface wave analysis techniques at Icelandic soil sites. Initial attempts to utilize the MASW technique to assess the shear stiffness of typical earth dam structures and predict the liquefaction occurrence of Icelandic soils indicated promising results, although further work will need to be devoted to these topics. Finally, the initial version of an open online database of MASW measurement results was introduced as a part of this project. Whilst not substituting site-specific measurements, such a database is believed to be of value for the Icelandic engineering community for design and future studies.

5.2 Assumptions and limitations

Many of the assumptions and restrictions associated with this work are related to the well-documented limitations of surface wave analysis. This, in particular, relates to the one-dimensional model assumed for computation of theoretical dispersion curves, the decreased survey resolution with depth, and the non-uniqueness associated with the inversion analysis.

For forward modelling of dispersion curves, the tested site was approximated as a semi-infinite stack of homogeneous, linear elastic layers, thus neglecting any variations in soil material properties below the receiver spread. Hence, if tested soil deposits do not reasonably comply to this assumption, the final shear wave velocity models will be biased to some extent. The natural test sites reported in this work are believed

to be relatively uniform and without sharp two- or three-dimensional variations, at least from a geotechnical engineering perspective. However, for the earth dam sites, horizontal variations in material properties (i.e., perpendicular to the measurement profile) are of concern. Due to the geometry of earth-rockfill dams with a central core, the acquired data likely contains a combination of the response of the different construction materials. The resulting shear wave velocity/shear stiffness profiles, thus, presumably represent some combination of these.

The inversion of Rayleigh wave dispersion curves is non-linear, mix-determined and non-unique, resulting in the so-called equivalence problem. Therefore, interpretation ambiguities arise in the inversion analysis and the final estimate of the shear wave velocity model entails a certain degree of uncertainty. Deterministic estimates of the shear wave velocity profile, as obtained for many of the Icelandic test sites in early stages of this work, do not reflect this uncertainty. Hence, more rigorous analysis may be required, both taking into consideration experimental uncertainties (that can be quantified based on existing datasets) and the effects of the layering parameterization. Furthermore, the analysis is affected by uncertainties related to assessments of material density and Poisson's ratio. In addition, the location of the groundwater table was, in general, only assessed based on general environmental factors, as direct measurements were not available for any of the Icelandic sites. Finally, this study focused mainly on the utilization of fundamental mode dispersion curves and, therefore, acquired information on higher-mode propagation was generally not incorporated.

Also resulting from the limited availability of in-situ measurement results for Icelandic soil sites, verification against results obtained by other measurement techniques (or by independent researchers) was restricted by the lack of data for comparison. For instance, invasive measurements of shear wave velocity have not been conducted at any of the Icelandic sites. Therefore, in this work, comparison studies for verification and validation purposes were mainly conducted at Norwegian sites that are, in general, softer than the most commonly encountered natural soil sites in Iceland.

5.3 Recommendations for future work

Despite its exploratory nature, this study has offered insight into the stiffness properties of commonly encountered Icelandic soil materials and, to a lesser extent, man-made fillings. However, the measurement sites are still rather sparse, restricted to 1D surveying and, in many cases, deeper shear wave velocity profiling would be beneficial. Hence, future work may both be aimed at obtaining deeper and better constrained estimates of shear wave velocity, e.g., through a joint analysis of data acquired with active-source measurements and passive three-component single-station measurements, and to extend the use of the MASW method to include pseudo-spatial surveys.

The extension of the analysis to produce pseudo-2D (or 3D) sections of V_S for Icelandic sites could be achieved by using a land-streamer (i.e., an array of geophones that is designed to be towed along the surface) in conjunction with the current hardware. For

efficient assessments of pseudo-2D V_S sections, new features specifically designed for the analysis of active-source measurements conducted in a roll-along format may be added to the existing set of software modules. These might, for instance, include tools for spatial interpolation of dispersion curves and V_S-profiles, and inversion procedures making use of the geological constraints associated with neighbouring 1D profiles.

The University of Iceland owns hardware for conducting single-station microtremor measurements, making the joint inversion of dispersion and ellipticity curves another logical extension of the work presented in this dissertation. The additional information provided by the single-station measurement may also provide the possibility to assess the thickness of the overlying sedimentary layers and, thus, help identify the location of the soil/bedrock interface. The approximate depth to bedrock is generally not known for Icelandic soil sites and, hence, such assessments would be of high value.

In this work, emphasis has been on utilization of fundamental mode Rayleigh wave dispersion curves. However, for future applications, development and implementation of techniques accounting for higher mode propagation (or mode superposition) can improve the reliability of the analysis and allow for surveying at more geologically complex sites. In addition, further studies on the experimental uncertainties associated with the application of MASW at Icelandic sites, and their impact on the inverted shear wave velocity models, are of great importance, together with further validation and calibration of the results.

A potential engineering application of the MASW surveying that is of interest for future studies is the utilization of Rayleigh wave dispersion curves and/or inverted V_S-profiles for soil type classification of the local soils. Widely used schemes for soil type classification, e.g., charts based on CPT measurement results, tend to lump most Icelandic soils together. In addition, at Icelandic soil sites the application of conventional penetration-based methods is commonly restricted to relatively shallow depths (e.g., $<$4–7 m) due to high gravel content or the presence of larger boulders. Hence, development of alternative methods for soil classification would be of value for the local engineering community.

The current findings indicate that MASW is a promising technique to assess the shear stiffness of typical man-made fillings, earth dams and other embankments. However, further work must be undertaken to better adapt the set of software tools to the analysis of dam structures, especially regarding earth-core rock-fill dams. This may include the implementation of more advanced processing and inversion strategies that take the geometry of the dam structures into account. Future development of the MASW technique for assessment and/or quantification of the compaction of engineered fills made of volcanic soils, as commonly used in engineering practice in Iceland, is further of interest, along with an exploration of the method's sensitivity to changes in compaction within the upper-most 1–5 m at such sites.

The knowledge of the local soil structure in terms of shear wave velocity is essential for the assessment of seismic site amplifications through numerical analysis. To date,

limited use has been made of numerical methods for analysis of site response at Icelandic sites, notably for sites underlain by late-glacial or postglacial sediments. In a special geological environment like Iceland, site effects should be characterized in more detail. The impact of the seismic hazard on earth dams and uncompacted embankments also requires further study. Hence, a natural progression of this work is to perform numerical analysis of site response, using scenario ground motion time histories, to derive a set of site response curves for engineering design of above ground and geotechnical structures. Results of such numerical analysis would also be of value for comparison with current and proposed soil classification schemes, given the ongoing revision of EC8, as well as for potential future seismic microzonation studies in South Iceland.

References

Abo-Zena, A. (1979). Dispersion function computations for unlimited frequency values. *Geophysical Journal International*, *58*(1), 91–105. doi: 10.1111/j.1365-246X.1979.tb01011.x

Abrahamson, N., Atkinson, G., Boore, D., Bozorgnia, Y., Campbell, K., Chiou, B., ... Youngs, R. (2008). Comparisons of the NGA Ground-Motion Relations. *Earthquake Spectra*, *24*(1), 45–66. doi: 10.1193/1.2924363

Aki, K., & Richards, P. G. (1980). *Quantitative Seismology: Theory and Methods* (Vol. 1). San Francisco, CA: W. H. Freeman and Co.

Andrus, R. D., & Stokoe, K. H. (2000). Liquefaction Resistance of Soils from Shear-Wave Velocity. *Journal of Geotechnical and Geoenvironmental Engineering*, *126*(11), 1015–1025. doi: 10.1061/(ASCE)1090-0241(2000)126:11(1015)

Arai, H., & Tokimatsu, K. (2005). S-Wave Velocity Profiling by Joint Inversion of Microtremor Dispersion Curve and Horizontal-to-Vertical (H/V) Spectrum. *Bulletin of the Seismological Society of America*, *95*(5), 1766–1778. doi: 10.1785/0120040243

Beaty, K. S., Schmitt, D. R., & Sacchi, M. (2002). Simulated annealing inversion of multimode Rayleigh wave dispersion curves for geological structure. *Geophysical Journal International*, *151*(2), 622–631. doi: 10.1046/j.1365-246X.2002.01809.x

Ben-Menahem, A., & Singh, S. J. (1981). *Seismic waves and sources*. New York, NY: Springer-Verlag.

Bergmann, L. (1948). *Ultrasonics and their Scientific and Technical Applications*. New York, NY: John Wiley & Sons.

Bessason, B., Baldvinsson, G. I., & Þórarinsson, Ó. (1998). SASW for evaluation of site-specific earthquake excitation. In *Proceedings of the 11th European Conference on Earthquake Engineering*, 6–11 September 1998, Paris, France. CD-ROM.

Bessason, B., & Erlingsson, S. (2011). Shear wave velocity in surface sediments. *Jökull*, *61*, 51–64.

Bessason, B., & Kaynia, A. M. (2002). Site amplification in lava rock on soft sediments. *Soil Dynamics and Earthquake Engineering*, *22*(7), 525–540. doi: 10.1016/S0267-7261(02)00035-0

Bignardi, S. (2017). The uncertainty of estimating the thickness of soft sediments with the HVSR method: A computational point of view on weak lateral variations. *Journal of Applied Geophysics*, *145*, 28–38. doi: 10.1016/j.jappgeo.2017.07.017

Bitri, A., Samyn, K., Brûlé, S., & Javelaud, E. H. (2013). Assessment of ground compaction using multi-channel analysis of surface wave data and cone penetration tests. *Near Surface Geophysics*, *11*(6), 683–690. doi: 10.3997/1873-0604.2013037

Bjarnason, H., Pálmason, P. R., Arnalds, S. S., & Aðalsteinsson, H. (2019). *Hydropower and Large Dams in Iceland.* Reykjavík, Iceland: Icelandic Committee on Large Dams.

Blaker, Ø., Carroll, R., L'Heureux, J.-S., & Klug, M. (2016). Characterisation of Halden silt. In *Proceedings of the 5th International Conference on Geotechnical and Geophysical Site Characterisation*, 5–9 September 2016, Queensland, Australia (Vol. 2, pp. 975–980).

Blaker, Ø., Carroll, R., Paniagua, P., DeGroot, D. J., & L'Heureux, J.-S. (2019). Halden research site: geotechnical characterization of a post glacial silt. *AIMS Geosciences*, *5*(2), 184–234. doi: 10.3934/geosci.2019.2.184

Boaga, J., Cassiani, G., Strobbia, C. L., & Vignoli, G. (2013). Mode misidentification in Rayleigh waves: Ellipticity as a cause and a cure. *Geophysics*, *78*(4), EN17–EN28. doi: 10.1190/geo2012-0194.1

Bolt, B. A. (1976). *Nuclear Explosions and Earthquakes: The Parted Vail.* San Francisco, CA: W. H. Freeman and Co.

Bozorgnia, Y., Abrahamson, N. A., Al Atik, L., Ancheta, T. D., Atkinson, G. M., Baker, J. W., ... Youngs, R. (2014). NGA-West2 Research Project. *Earthquake Spectra*, *30*(3), 973–987. doi: 10.1193/072113EQS209M

BSSC. (2015). *NEHRP (National Earthquake Hazards Reduction Program) recommended seismic provisions for new buildings and other structures (FEMA P-1050-1) 2015 edition. Vol. 1. Part 1: Provisions. Part 2: Commentary.* Washington DC: Federal Emergency Management Agency.

Buchen, P. W., & Ben-Hador, R. (1996). Free-mode surface-wave computations. *Geophysical Journal International*, *124*(3), 869–887. doi: 10.1111/j.1365-246X.1996.tb05642.x

Cardarelli, E., Cercato, M., & De Donno, G. (2014). Characterization of an earth-filled dam through the combined use of electrical resistivity tomography,

P-and SH-wave seismic tomography and surface wave data. *Journal of Applied Geophysics*, *106*, 87–95. doi: 10.1016/j.jappgeo.2014.04.007

Castellaro, S., Mulargia, F., & Rossi, P. L. (2008). Vs30: Proxy for Seismic Amplification? *Seismological Research Letters*, *79*(4), 540–543. doi: 10.1785/gssrl.79.4.540

Castellaro, S., Panzeri, R., Mesiti, F., & Bertello, L. (2015). A surface seismic approach to liquefaction. *Soil Dynamics and Earthquake Engineering*, *77*, 35–46. doi: 10.1016/j.soildyn.2015.04.023

CEN. (2004). *EN1998-1:2004, Eurocode 8: Design of structures for earthquake resistance. Part 1: General rules, seismic actions and rules for buildings.* Brussels, Belgium: European Committee for Standardization (CEN).

Constable, S. C., Parker, R. L., & Constable, C. G. (1987). Occam's inversion: A practical algorithm for generating smooth models from electromagnetic sounding data. *Geophysics*, *52*(3), 289–300. doi: 10.1190/1.1442303

Cox, B. R., & Teague, D. P. (2016). Layering ratios: a systematic approach to the inversion of surface wave data in the absence of a priori information. *Geophysical Journal International*, *207*(1), 422–438. doi: 10.1093/gji/ggw282

Dal Moro, G., Pipan, M., Forte, E., & Finetti, I. (2003). Determination of Rayleigh wave dispersion curves for near surface applications in unconsolidated sediments. In *SEG Technical Program Expanded Abstracts 2003*, 24–31 October 2003, Dallas, Texas (pp. 1247–1250). doi: 10.1190/1.1817508

Das, B. M. (2010). *Principles of Geotechnical Engineering* (7th ed.). Stamford, CT: Cengage Learning.

Delgado, J., López Casado, C., Giner, J., Estévez, A., Cuenca, A., & Molina, S. (2000). Microtremors as a Geophysical Exploration Tool: Applications and Limitations. *Pure and Applied Geophysics*, *157*(9), 1445–1462. doi: 10.1007/PL00001128

de Lucena, R. F., & Taioli, F. (2014). Rayleigh wave modeling: A study of dispersion curve sensitivity and methodology for calculating an initial model to be included in an inversion algorithm. *Journal of Applied Geophysics*, *108*, 140–151. doi: 10.1016/j.jappgeo.2014.07.007

Di Giulio, G., Savvaidis, A., Ohrnberger, M., Wathelet, M., Cornou, C., Knapmeyer-Endrun, B., ... Bard, P.-Y. (2012). Exploring the model space and ranking a best class of models in surface-wave dispersion inversion: Application at European strong-motion sites. *Geophysics*, *77*(3), B147–B166. doi: 10.1190/geo2011-0116.1

Dikmen, Ü., Arısoy, M. Ö., & Akkaya, İ. (2010). Offset and linear spread geometry in the MASW method. *Journal of Geophysics and Engineering*, *7*(2), 211–222.

doi: 10.1088/1742-2132/7/2/S07

Dou, S., & Ajo-Franklin, J. B. (2014). Full-wavefield inversion of surface waves for mapping embedded low-velocity zones in permafrost. *Geophysics*, *79*(6), EN107–EN124. doi: 10.1190/geo2013-0427.1

Dunkin, J. W. (1965). Computation of modal solutions in layered, elastic media at high frequencies. *Bulletin of the Seismological Society of America*, *55*(2), 335–358.

Efron, B. (1979). Bootstrap Methods: Another Look at the Jackknife. *The Annals of Statistics*, *7*(1), 1–26.

Efron, B., & Tibshirani, R. J. (1993). *An Introduction to the Bootstrap*. New York, NY: Chapman & Hall.

Einarsson, P. (1991a). Earthquakes and present-day tectonism in Iceland. *Tectonophysics*, *189*(1–4), 261–279. doi: 10.1016/0040-1951(91)90501-I

Einarsson, P. (1991b). Jarðskjálftabylgjur. *Náttúrufræðingurinn*, *61*(1), 57–69. [In Icelandic].

Einarsson, P. (2008). Plate boundaries, rifts and transforms in Iceland. *Jökull*, *58*, 35–58.

Erlingsson, S. (2019). Geotechnical Challenges in Iceland. In *Proceedings of the 17th European Conference on Soil Mechanics and Geotechnical Engineering*, 1–6 September 2019, Reykjavík, Iceland (pp. 34–51). doi: 10.32075/17ECSMGE-2019-1109

Erlingsson, S., Ólafsdóttir, E. Á., & Bessason, B. (2017). Stiffness of sandy sites using the Multichannel Analysis of Surface Waves method. In *Proceedings of the 19th International Conference on Soil Mechanics and Geotechnical Engineering*, 17–22 September 2017, Seoul, South Korea (pp. 593–597).

Everett, M. E. (2013). *Near-Surface Applied Geophysics*. Cambridge: Cambridge University Press.

Fäh, D., Kind, F., & Giardini, D. (2001). A theoretical investigation of average H/V ratios. *Geophysical Journal International*, *145*(2), 535–549. doi: 10.1046/j.0956-540x.2001.01406.x

Forbriger, T. (2003a). Inversion of shallow-seismic wavefields: I. Wavefield transformation. *Geophysical Journal International*, *153*(3), 719–734. doi: 10.1046/j.1365-246X.2003.01929.x

Forbriger, T. (2003b). Inversion of shallow-seismic wavefields: II. Inferring subsurface properties from wavefield transforms. *Geophysical Journal International*, *153*(3), 735–752. doi: 10.1046/j.1365-246X.2003.01985.x

Foti, S., Comina, C., Boiero, D., & Socco, L. V. (2009). Non-uniqueness in surface-wave inversion and consequences on seismic site response analyses. *Soil Dynamics and Earthquake Engineering*, *29*(6), 982–993. doi: 10.1016/j.soildyn.2008.11.004

Foti, S., Hollender, F., Garofalo, F., Albarello, D., Asten, M., Bard, P.-Y., ... Socco, V. (2018). Guidelines for the good practice of surface wave analysis: a product of the InterPACIFIC project. *Bulletin of Earthquake Engineering*, *16*(6), 2367–2420. doi: 10.1007/s10518-017-0206-7

Foti, S., Lai, C. G., Rix, G. J., & Strobbia, C. (2015). *Surface Wave Methods for Near-Surface Site Characterization*. Boca Raton, FL: CRC Press, Taylor & Francis Group.

Gabriels, P., Snieder, R., & Nolet, G. (1987). In situ measurements of shear-wave velocity in sediments with higher-mode Rayleigh waves. *Geophysical Prospecting*, *35*(2), 187–196. doi: 10.1111/j.1365-2478.1987.tb00812.x

Gao, L., Xia, J., Pan, Y., & Xu, Y. (2016). Reason and Condition for Mode Kissing in MASW Method. *Pure and Applied Geophysics*, *173*(5), 1627–1638. doi: 10.1007/s00024-015-1208-5

Garofalo, F., Foti, S., Hollender, F., Bard, P.-Y., Cornou, C., Cox, B. R., ... Yamanaka, H. (2016a). InterPACIFIC project: Comparison of invasive and non-invasive methods for seismic site characterization. Part I: Intra-comparison of surface wave methods. *Soil Dynamics and Earthquake Engineering*, *82*, 222–240. doi: 10.1016/j.soildyn.2015.12.010

Garofalo, F., Foti, S., Hollender, F., Bard, P.-Y., Cornou, C., Cox, B. R., ... Vergniault, C. (2016b). InterPACIFIC project: Comparison of invasive and non-invasive methods for seismic site characterization. Part II: Inter-comparison between surface-wave and borehole methods. *Soil Dynamics and Earthquake Engineering*, *82*, 241–254. doi: 10.1016/j.soildyn.2015.12.009

Gazetas, G. (1991). Foundation Vibrations. In H.-Y. Fang (Ed.), *Foundation Engineering Handbook* (2nd ed., pp. 553–593). New York, NY: Van Nostrand Reinhold.

Gouveia, F., da Fonseca, A. V., Gomes, R. C., & Teves-Costa, P. (2018). Deeper V_S profile constraining the dispersion curve with the ellipticity curve: A case study in Lower Tagus Valley, Portugal. *Soil Dynamics and Earthquake Engineering*, *109*, 188–198. doi: 10.1016/j.soildyn.2018.03.010

Gouveia, F., Lopes, I., & Gomes, R. C. (2016). Deeper V_S profile from joint analysis of Rayleigh wave data. *Engineering Geology*, *202*, 85–98. doi: 10.1016/j.enggeo.2016.01.006

Green, R. A., Halldórsson, B., Kurtulus, A., Steinarsson, H., & Erlendsson, Ö. (2012). A Unique Liquefaction Case Study from the 29 May 2008, M_w6.3 Olfus

Earthquake, Southwest Iceland. In *Proceedings of the 15th World Conference on Earthquake Engineering*, 24–28 September 2012, Lisbon, Portugal.

Gucunski, N., & Woods, R. D. (1991). Use of Rayleigh Modes in Interpretation of SASW Test. In *Proceedings of the 2nd International Conference on Recent Advances in Geotechnical Earthquake Engineering and Soil Dynamics*, 11–15 March 1991, St. Louis, MO (pp. 1399–1408).

Gundersen, A. S., Quinteros, S., L'Heureux, J.-S., & Lunne, T. (2018). Soil classification of NGTS sand site (Øysand, Norway) based on CPTU, DMT and laboratory results. In *Proceedings of the 4th International Symposium on Cone Penetration Testing*, 21–22 June 2018, Delft, The Netherlands (pp. 323–328).

Ha, I.-S. (2017). Comparison of shear wave velocities evaluated in the core zone of an existing fill dam by field and laboratory tests. *Soil Dynamics and Earthquake Engineering*, *100*, 276–285. doi: 10.1016/j.soildyn.2017.06.013

Halldórsson, P. (1992). Seismic Hazard Assessment Based on Historical Data and Seismic Measurements. In *Proceedings of the International Conference on Preparedness and Mitigation for Natural Disasters '92*, 28–29 May 1992, Reykjavík, Iceland (pp. 53–63).

Haney, M. M., & Tsai, V. C. (2015). Nonperturbational surface-wave inversion: A Dix-type relation for surface waves. *Geophysics*, *80*(6), EN167–EN177. doi: 10.1190/geo2014-0612.1

Haskell, N. A. (1953). The dispersion of surface waves on multilayered media. *Bulletin of the Seismological Society of America*, *43*(1), 17–34.

Hegazy, Y. A., & Mayne, P. W. (1995). Statistical correlations between V_S and cone penetration data for different soil types. In *Proceedings of the International Symposium on Cone Penetration Testing*, 4–5 October 1995, Linköping, Sweden (Vol. 2, pp. 173–178).

Héloïse, C., Bard, P.-Y., Duval, A.-M., & Bertrand, E. (2012). Site effect assessment using KiK-net data: part 2—site amplification prediction equation based on f_0 and V_{SZ}. *Bulletin of Earthquake Engineering*, *10*(2), 451–489. doi: 10.1007/s10518-011-9298-7

Hobiger, M., Cornou, C., Wathelet, M., Di Giulio, G., Knapmeyer-Endrun, B., Renalier, F., ... Theodoulidis, N. (2013). Ground structure imaging by inversions of Rayleigh wave ellipticity: sensitivity analysis and application to European strong-motion sites. *Geophysical Journal International*, *192*(1), 207–229. doi: 10.1093/gji/ggs005

Hussien, M. N., & Karray, M. (2016). Shear wave velocity as a geotechnical parameter: an overview. *Canadian Geotechnical Journal*, *53*(2), 252–272. doi: 10.1139/cgj-2014-0524

Ibs-von Seht, M., & Wohlenberg, J. (1999). Microtremor measurements used to map thickness of soft sediments. *Bulletin of the Seismological Society of America*, *89*(1), 250–259.

Ishihara, K. (1996). *Soil Behaviour in Earthquake Geotechnics*. Oxford, UK: Oxford University Press.

Ivanov, J., Miller, R. D., & Tsoflias, G. (2008). Some Practical Aspects of MASW Analysis and Processing. In *Proceedings of the 21st Symposium on the Application of Geophysics to Engineering and Environmental Problems 2008*, 6–10 April 2008, Philadelphia, PA (pp. 1186–1198). doi: 10.4133/1.2963228

Jones, R. (1958). In-Situ Measurement of the Dynamic Properties of Soil by Vibration Methods. *Geotechnique*, *8*(1), 1–21. doi: 10.1680/geot.1958.8.1.1

Jones, R. (1962). Surface wave technique for measuring the elastic properties and thickness of roads: Theoretical development. *British Journal of Applied Physics*, *13*(1), 21–29. doi: 10.1088/0508-3443/13/1/306

Kamai, R., Abrahamson, N. A., & Silva, W. J. (2016). V_{S30} in the NGA GMPEs: Regional Differences and Suggested Practice. *Earthquake Spectra*, *32*(4), 2083–2108. doi: 10.1193/072615EQS121M

Karl, L., Fechner, T., Schevenels, M., François, S., & Degrande, G. (2011). Geotechnical characterization of a river dyke by surface waves. *Near Surface Geophysics*, *9*(6), 515–527. doi: 10.3997/1873-0604.2011030

Karray, M., Lefebvre, G., Ethier, Y., & Bigras, A. (2010). Assessment of deep compaction of the Péribonka dam foundation using "modal analysis of surface waves" (MASW). *Canadian Geotechnical Journal*, *47*(3), 312–326. doi: 10.1139/T09-108

Kausel, E., & Roësset, J. M. (1981). Stiffness matrices for layered soils. *Bulletin of the Seismological Society of America*, *71*(6), 1743–1761.

Kayen, R., Moss, R. E. S., Thompson, E. M., Seed, R. B., Cetin, K. O., Der Kiureghian, A., ... Tokimatsu, K. (2013). Shear-Wave Velocity–Based Probabilistic and Deterministic Assessment of Seismic Soil Liquefaction Potential. *Journal of Geotechnical and Geoenvironmental Engineering*, *139*(3), 407–419. doi: 10.1061/(ASCE)GT.1943-5606.0000743

Kennett, B. L. N. (1974). Reflections, rays, and reverberations. *Bulletin of the Seismological Society of America*, *64*(6), 1685–1696.

Kennett, B. L. N., & Kerry, N. J. (1979). Seismic waves in a stratified half space. *Geophysical Journal International*, *57*(3), 557–583. doi: 10.1111/j.1365-246X.1979.tb06779.x

Knopoff, L. (1964). A matrix method for elastic wave problems. *Bulletin of the Seismological Society of America*, *54*(1), 431–438.

Kramer, S. L. (1996). *Geotechnical Earthquake Engineering*. Upper Saddle River, NJ: Prentice-Hall.

Kreyszig, E. (2011). *Advanced Engineering Mathematics* (10th ed.). Hoboken, NJ: John Wiley & Sons.

Lachetl, C., & Bard, P.-Y. (1994). Numerical and Theoretical Investigations on the Possibilities and Limitations of Nakamura's Technique. *Journal of Physics of the Earth*, *42*(5), 377–397. doi: 10.4294/jpe1952.42.377

Lai, C. G., Foti, S., & Rix, G. J. (2005). Propagation of Data Uncertainty in Surface Wave Inversion. *Journal of Environmental and Engineering Geophysics*, *10*(2), 219–228. doi: 10.2113/JEEG10.2.219

Lai, C. G., Mangriotis, M.-D., & Rix, G. J. (2014). An explicit relation for the apparent phase velocity of Rayleigh waves in a vertically heterogeneous elastic half-space. *Geophysical Journal International*, *199*(2), 673–687. doi: 10.1093/gji/ggu283

Lakes, R. S. (2017). Negative-Poisson's-Ratio Materials: Auxetic Solids. *Annual Review of Materials Research*, *47*, 63–81. doi: 10.1146/annurev-matsci-070616-124118

Lee, V. W., & Trifunac, M. D. (2010). Should average shear-wave velocity in the top 30 m of soil be used to describe seismic amplification? *Soil Dynamics and Earthquake Engineering*, *30*(11), 1250–1258. doi: 10.1016/j.soildyn.2010.05.007

Leong, E. C., & Aung, A. M. W. (2012). Weighted average velocity forward modelling of Rayleigh surface waves. *Soil Dynamics and Earthquake Engineering*, *43*, 218–228. doi: 10.1016/j.soildyn.2012.07.030

Levenberg, K. (1944). A method for the solution of certain non-linear problems in least squares. *Quarterly of Applied Mathematics*, *2*(2), 164–168.

L'Heureux, J.-S., Lindgård, A., & Emdal, A. (2019). The Tiller-Flotten research site: Geotechnical characterization of a very sensitive clay deposit. *AIMS Geosciences*, *5*(4), 831–867. doi: 10.3934/geosci.2019.4.831

L'Heureux, J.-S., Lunne, T., Lacasse, S., Carroll, R., Strandvik, S. O., Ozkul, Z., ... Nordal, S. (2017). Norway's National GeoTest Site Research Infrastructure (NGTS). In *Proceedings of the 19th International Conference on Soil Mechanics and Geotechnical Engineering*, 17–22 September 2017, Seoul, South Korea (pp. 611–614).

Li, D.-Q., Tang, X.-S., Zhou, C.-B., & Phoon, K.-K. (2015). Characterization of uncertainty in probabilistic model using bootstrap method and its application

to reliability of piles. *Applied Mathematical Modelling*, *39*(17), 5310–5326. doi: 10.1016/j.apm.2015.03.027

Lin, P.-S., Chang, C.-W., & Chang, W.-J. (2004). Characterization of liquefaction resistance in gravelly soil: large hammer penetration test and shear wave velocity approach. *Soil Dynamics and Earthquake Engineering*, *24*(9–10), 675–687. doi: 10.1016/j.soildyn.2004.06.010

Lin, S., & Ashlock, J. C. (2015). Comparison of MASW and MSOR for Surface Wave Testing of Pavements. *Journal of Environmental and Engineering Geophysics*, *20*(4), 277–285. doi: 10.2113/JEEG20.4.277

Louie, J. N. (2001). Faster, Better: Shear-Wave Velocity to 100 Meters Depth from Refraction Microtremor Arrays. *Bulletin of the Seismological Society of America*, *91*(2), 347–364. doi: 10.1785/0120000098

Lunne, T., Long, M., & Forsberg, C. F. (2003). Characterisation and engineering properties of Onsøy clay. In *Characterisation and Engineering Properties of Natural Soils: Proceedings of the International Workshop*, 2–4 December 2002, Singapore (Vol. 1, pp. 395–428).

Luo, Y., Xia, J., Miller, R. D., Xu, Y., Liu, J., & Liu, Q. (2008). Rayleigh-Wave Dispersive Energy Imaging Using a High-Resolution Linear Radon Transform. *Pure and Applied Geophysics*, *165*(5), 903–922. doi: 10.1007/s00024-008-0338-4

Luzi, L., Puglia, R., Pacor, F., Gallipoli, M. R., Bindi, D., & Mucciarelli, M. (2011). Proposal for a soil classification based on parameters alternative or complementary to $V_{S,30}$. *Bulletin of Earthquake Engineering*, *9*(6), 1877–1898. doi: 10.1007/s10518-011-9274-2

Maraschini, M., Ernst, F., Foti, S., & Socco, L. V. (2010). A new misfit function for multimodal inversion of surface waves. *Geophysics*, *75*(4), G31–G43. doi: 10.1190/1.3436539

Marchetti, S., Monaco, P., Totani, G., & Marchetti, D. (2008). In Situ Tests by Seismic Dilatometer (SDMT). In J. E. Laier, D. K. Crapps, & M. H. Hussein (Eds.), *From Research to Practice in Geotechnical Engineering* (pp. 292–311). Reston, VA: American Society of Civil Engineers.

Marquardt, D. W. (1963). An Algorithm for Least-Squares Estimation of Nonlinear Parameters. *Journal of the Society for Industrial and Applied Mathematics*, *11*(2), 431–441. doi: 10.1137/0111030

Martin, G. K., & Mayne, P. W. (1997). Seismic Flat Dilatometer Tests in Connecticut Valley Varved Clay. *Geotechnical Testing Journal*, *20*(3), 357–361. doi: 10.1520/GTJ19970011

Matthews, M. C., Hope, V. S., & Clayton, C. R. I. (1996). The use of surface waves

in the determination of ground stiffness profiles. *Proceedings of the Institution of Civil Engineers - Geotechnical Engineering*, *119*(2), 84–95. doi: 10.1680/igeng.1996.28168

McGann, C. R., Bradley, B. A., Taylor, M. L., Wotherspoon, L. M., & Cubrinovski, M. (2015). Development of an empirical correlation for predicting shear wave velocity of Christchurch soils from cone penetration test data. *Soil Dynamics and Earthquake Engineering*, *75*, 66–75. doi: 10.1016/j.soildyn.2015.03.023

McMechan, G. A., & Yedlin, M. J. (1981). Analysis of dispersive waves by wave field transformation. *Geophysics*, *46*(6), 869–874. doi: 10.1190/1.1441225

Megson, T. H. G. (2005). *Structural and Stress Analysis* (2nd ed.). Oxford, UK: Elsevier, Butterworth-Heinemann.

Menke, W. (1979). Comment on 'Dispersion function computations for unlimited frequency values' by Anas Abo-Zena. *Geophysical Journal International*, *59*(2), 315–323. doi: 10.1111/j.1365-246X.1979.tb06769.x

Min, D.-J., & Kim, H.-S. (2006). Feasibility of the surface-wave method for the assessment of physical properties of a dam using numerical analysis. *Journal of Applied Geophysics*, *59*(3), 236–243. doi: 10.1016/j.jappgeo.2005.09.004

Mucciarelli, M., & Gallipoli, M. R. (2001). A critical review of 10 years of microtremor HVSR technique. *Bollettino di Geofisica Teorica ed Applicata*, *42*(3–4), 255–266.

Nakamura, Y. (1989). A method for dynamic characteristics estimation of subsurface using microtremor on the ground surface. *Railway Technical Research Institute, Quarterly Reports*, *30*(1), 25–33.

Nazarian, S., & Stokoe, K. H. (1985). *In situ determination of elastic moduli of pavement systems by spectral-analysis-of-surface-waves method (practical aspects)*. Report no. FHWA/TX-86/13+368-1F. Austin, TX: Center for Transportation Research, University of Texas at Austin.

Nazarian, S., & Stokoe, K. H. (1986). *In situ determination of elastic moduli of pavement systems by spectral-analysis-of-surface-waves method (theoretical aspects)*. Report no. FHWA/TX-87/46+437-2. Austin, TX: Center for Transportation Research, University of Texas at Austin.

Nazarian, S., Stokoe, K. H., & Hudson, W. R. (1983). Use of Spectral Analysis of Surface Waves Method for Determination of Moduli and Thicknesses of Pavement Systems. *Transportation Research Record*, *930*, 38–45.

Ohya, S., Ogura, K., & Imai, T. (1984). The Suspension PS Velocity Logging System. In *Proceedings of the 16th Annual Offshore Technology Conference*, 7–9 May, Houston, TX. doi: 10.4043/4680-MS

Ólafsdóttir, E. Á., Bessason, B., & Erlingsson, S. (2014). Multichannel Analysis of Surface Waves for Estimation of Soils Stiffness Profiles. In *Proceedings of the 23rd European Young Geotechnical Engineers Conference,* 2–5 September 2014, Barcelona, Spain (pp. 45–48).

Ólafsdóttir, E. Á., Bessason, B., & Erlingsson, S. (2015). MASW for assessing liquefaction of loose sites. In *Proceedings of the 16th European Conference on Soil Mechancis and Geotechnical Engineering,* 13–17 September 2015, Edinburgh, Scotland (Vol. 5, pp. 2431–2436). doi: 10.1680/ecsmge.60678.vol5.373

Ólafsdóttir, E. Á., Bessason, B., & Erlingsson, S. (2018). Combination of dispersion curves from MASW measurements. *Soil Dynamics and Earthquake Engineering*, *113*, 473–487. doi: 10.1016/j.soildyn.2018.05.025

Ólafsdóttir, E. Á., Bessason, B., & Erlingsson, S. (2019a). Application of MASW in the South Iceland Seismic Zone. In R. Rupakhety, S. Ólafsson, & B. Bessason (Eds.), *Proceedings of the International Conference on Earthquake Engineering and Structural Dynamics. Geotechnical, Geological and Earthquake Engineering, Vol. 47* (pp. 53–66). Cham, Switzerland: Springer International Publishing. doi: 10.1007/978-3-319-78187-7_5

Ólafsdóttir, E. Á., Bessason, B., & Erlingsson, S. (2019b). Stiffness profiles of earth dams based on the MASW technique. In *Proceedings of the 17th European Conference on Soil Mechanics and Geotechnical Engineering,* 1–6 September 2019, Reykjavík, Iceland. doi: 10.32075/17ECSMGE-2019-0788

Ólafsdóttir, E. Á., Bessason, B., Erlingsson, S., & Kaynia, A. M. (2019). Verification of an open-source MASW software at Norwegian geo-test sites. *Journal of Geotechnical and Geoenvironmental Engineering*. (Submitted.)

Ólafsdóttir, E. Á., Bessason, B., Erlingsson, S., L'Heureux, J.-S., & Bazin, S. (2019). Benchmarking of an open-source MASW software using data from three Norwegian GeoTest Sites. In *Proceedings of the 17th European Conference on Soil Mechanics and Geotechnical Engineering,* 1–6 September 2019, Reykjavík, Iceland. doi: 10.32075/17ECSMGE-2019-0772

Ólafsdóttir, E. Á., Erlingsson, S., & Bessason, B. (2016). Effects of measurement profile configuration on estimation of stiffness profiles of loose post glacial sites using MASW. In *Proceedings of the 17th Nordic Geotechnical Meeting,* 25–28 May 2016, Reykjavík, Iceland (pp. 327–336).

Ólafsdóttir, E. Á., Erlingsson, S., & Bessason, B. (2018a). Open software for analysis of MASW data. In *Proceedings of the 16th European Conference on Earthquake Engineering,* 18–21 June 2018, Thessaloniki, Greece. (Paper no. 11168).

Ólafsdóttir, E. Á., Erlingsson, S., & Bessason, B. (2018b). Tool for analysis of multichannel analysis of surface waves (MASW) field data and evaluation of shear wave velocity profiles of soils. *Canadian Geotechnical Journal*, *55*(2), 217–233.

doi: 10.1139/cgj-2016-0302

Ólafsdóttir, E. Á., Erlingsson, S., & Bessason, B. (2019a). Open source MASW software and results from Icelandic soil sites. In *Proceedings of the 17th European Conference on Soil Mechanics and Geotechnical Engineering,* 1–6 September 2019, Reykjavík, Iceland. doi: 10.32075/17ECSMGE-2019-0771

Ólafsdóttir, E. Á., Erlingsson, S., & Bessason, B. (2019b). Shear wave velocity profiles from MASW inversion analysis using a simple Monte Carlo search technique for geotechnical engineering applications. *Soil Dynamics and Earthquake Engineering*. (Resubmitted.)

Orkustofnun. (2018). *OS-2018-T006-01: Installed capacity and electricity production in Icelandic power stations in 2017.* Retrieved from: https://orkustofnun.is/gogn/Talnaefni/OS-2018-T006-01.pdf.

Park, C. B. (2011). Imaging Dispersion of MASW Data—Full vs. Selective Offset Scheme. *Journal of Environmental and Engineering Geophysics*, *16*(1), 13–23. doi: 10.2113/JEEG16.1.13

Park, C. B., & Carnevale, M. (2010). Optimum MASW Survey—Revisit after a Decade of Use. In *Proceedings of GeoFlorida 2010: Advances in Analysis, Modeling & Design*, 20–24 February 2010, Orlando, FL (pp. 1303–1312). doi: 10.1061/41095(365)130

Park, C. B., & Miller, R. D. (2008). Roadside Passive Multichannel Analysis of Surface Waves (MASW). *Journal of Environmental and Engineering Geophysics*, *13*(1), 1–11. doi: 10.2113/JEEG13.1.1

Park, C. B., Miller, R. D., & Miura, H. (2002). Optimum Field Parameters of an MASW Survey [Expanded Abstract]. In *Proceedings of the 6th SEGJ International Symposium,* 22–23 May 2002, Tokyo, Japan.

Park, C. B., Miller, R. D., & Xia, J. (1998). Imaging dispersion curves of surface waves on multi-channel record. In *SEG Technical Program Expanded Abstracts of the Society of Exploration Geophysicists International Exposition and 68th Annual Meeting*, 13–18 September 1998, New Orleans, LA (pp. 1377–1380). doi: 10.1190/1.1820161

Park, C. B., Miller, R. D., & Xia, J. (1999). Multichannel analysis of surface waves. *Geophysics*, *64*(3), 800–808. doi: 10.1190/1.1444590

Park, C. B., Miller, R. D., & Xia, J. (2001). Offset and Resolution of Dispersion Curve in Multichannel Analysis of Surface Waves (MASW). In *Proceedings of the Symposium on the Application of Geophysics to Engineering and Environmental Problems 2001*, 4–7 March 2001, Denver, CO (p. SSM4). doi: 10.4133/1.2922953

Park, C. B., Miller, R. D., Xia, J., & Ivanov, J. (2007). Multichannel analysis of surface

waves (MASW)—active and passive methods. *The Leading Edge*, *26*(1), 60–64. doi: 10.1190/1.2431832

Park, C. B., & Ryden, N. (2007). Historical Overview of the Surface Wave Method. In *Proceedings of the Symposium on the Application of Geophysics to Engineering and Environmental Problems 2007*, 1–5 April 2007, Denver, CO (pp. 897–909). doi: 10.4133/1.2924752

Park, D., & Kishida, T. (2018). Shear wave velocity profiles of fill dams. *Soil Dynamics and Earthquake Engineering*, *104*, 250–258. doi: 10.1016/j.soildyn.2017.10.013

Parolai, S., Picozzi, M., Richwalski, S. M., & Milkereit, C. (2005). Joint inversion of phase velocity dispersion and H/V ratio curves from seismic noise recordings using a genetic algorithm, considering higher modes. *Geophysical Research Letters*, *32*(1), L01303. doi: 10.1029/2004GL021115

Passeri, F. (2019). *Development of an advanced geostatistical model for shear wave velocity profiles to manage uncertainties and variabilities in Ground Response Analyses.* [Ph.D. Thesis] Politecnico di Torino, Torino, Italy.

Pelekis, P. C., & Athanasopoulos, G. A. (2011). An overview of surface wave methods and a reliability study of a simplified inversion technique. *Soil Dynamics and Earthquake Engineering*, *31*(12), 1654–1668. doi: 10.1016/j.soildyn.2011.06.012

Pezeshk, S., & Zarrabi, M. (2005). A New Inversion Procedure for Spectral Analysis of Surface Waves Using a Genetic Algorithm. *Bulletin of the Seismological Society of America*, *95*(5), 1801–1808. doi: 10.1785/0120040144

Pham, H. (2000). *Software Reliability.* Singapore: Springer-Verlag.

Picozzi, M., Parolai, S., & Richwalski, S. M. (2005). Joint inversion of H/V ratios and dispersion curves from seismic noise: Estimating the S-wave velocity of bedrock. *Geophysical Research Letters*, *32*(11), L11308. doi: 10.1029/2005GL022878

Piratheepan, P. (2002). *Estimating Shear-Wave Velocity from SPT and CPT Data.* [M.Sc. Thesis] Clemson University, Clemson SC.

Pitilakis, K., Riga, E., Anastasiadis, A., Fotopoulou, S., & Karafagka, S. (2018). Towards the revision of EC8: Proposal for an alternative site classification scheme and associated intensity dependent spectral amplification factors. *Soil Dynamics and Earthquake Engineering*. (In Press) doi: 10.1016/j.soildyn.2018.03.030

Power, M., Chiou, B., Abrahamson, N., Bozorgnia, Y., Shantz, T., & Roblee, C. (2008). An Overview of the NGA Project. *Earthquake Spectra*, *24*(1), 3–21. doi: 10.1193/1.2894833

Quinteros, S., Gundersen, A., L'Heureux, J.-S., Carraro, J. A. H., & Jardine, R. (2019). Øysand research site: Geotechnical characterisation of deltaic sandy-silty soils.

AIMS Geosciences, *5*(4), 750–783. doi: 10.3934/geosci.2019.4.750

Rahimi, S., Wood, C. M., Coker, F., Moody, T., Bernhardt-Barry, M., & Kouchaki, B. M. (2018). The combined use of MASW and resistivity surveys for levee assessment: A case study of the Melvin Price Reach of the Wood River Levee. *Engineering Geology*, *241*, 11–24. doi: 10.1016/j.enggeo.2018.05.009

Richart, F. E., Hall, J. R., & Woods, R. D. (1970). *Vibrations of Soils and Foundations*. Englewood Cliffs, NJ: Prentice-Hall.

Robertson, P. K. (1990). Soil classification using the cone penetration test. *Canadian Geotechnical Journal*, *27*(1), 151–158. doi: 10.1139/t90-014

Robertson, P. K. (2009). Interpretation of cone penetration tests—a unified approach. *Canadian Geotechnical Journal*, *46*(11), 1337–1355. doi: 10.1139/T09-065

Robertson, P. K., Campanella, R. G., Gillespie, D., & Rice, A. (1986). Seismic CPT to Measure In Situ Shear Wave Velocity. *Journal of Geotechnical Engineering*, *112*(8), 791–803. doi: 10.1061/(ASCE)0733-9410(1986)112:8(791)

Ross, S. M. (2009). *Introduction to Probability and Statistics for Engineers and Scientists* (4th ed.). Burlington, MA: Elsevier Academic Press.

Ryden, N., & Park, C. B. (2006). Fast simulated annealing inversion of surface waves on pavement using phase-velocity spectra. *Geophysics*, *71*(4), R49–R58. doi: 10.1190/1.2204964

Ryden, N., Park, C. B., Ulriksen, P., & Miller, R. D. (2004). Multimodal Approach to Seismic Pavement Testing. *Journal of Geotechnical and Geoenvironmental Engineering*, *130*(6), 636–645. doi: 10.1061/(ASCE)1090-0241(2004)130:6(636)

Sacchi, M. D., & Ulrych, T. J. (1995). High-resolution velocity gathers and offset space reconstruction. *Geophysics*, *60*(4), 1169–1177. doi: 10.1190/1.1443845

Scherbaum, F., Hinzen, K.-G., & Ohrnberger, M. (2003). Determination of shallow shear wave velocity profiles in the Cologne, Germany area using ambient vibrations. *Geophysical Journal International*, *152*(3), 597–612. doi: 10.1046/j.1365-246X.2003.01856.x

Schilling, R. J., & Harris, S. L. (2012). *Introduction to Digital Signal Processing using MATLAB* (2nd ed.). Stamford, CT: Cengage Learning.

Schwab, F. (1970). Surface-wave dispersion computations: Knopoff's method. *Bulletin of the Seismological Society of America*, *60*(5), 1491–1520.

Schwab, F., & Knopoff, L. (1970). Surface-wave dispersion computations. *Bulletin of the Seismological Society of America*, *60*(2), 321–344.

Seed, H. B. (1979). Soil Liquefaction and Cyclic Mobility Evaluation for Level Ground

during Earthquakes. *Journal of the Geotechnical Engineering Division*, *105*(2), 201–255.

Seed, H. B., & Idriss, I. M. (1971). Simplified Procedure for Evaluating Soil Liquefaction Potential. *Journal of the Soil Mechanics and Foundations Division*, *97*(9), 1249–1274.

Seed, H. B., Tokimatsu, K., Harder, L. F., & Chung, R. M. (1985). Influence of SPT Procedures in Soil Liquefaction Resistance Evaluations. *Journal of Geotechnical Engineering*, *111*(12), 1425–1445. doi: 10.1061/(ASCE)0733-9410(1985)111:12(1425)

Sen, M. K., & Stoffa, P. L. (2013). *Global Optimization Methods in Geophysical Inversion* (2nd ed.). Cambridge, UK: Cambridge University Press.

Serdyukov, A. S., Yablokov, A. V., Duchkov, A. A., Azarov, A. A., & Baranov, V. D. (2019). Slant *f*-*k* transform of multichannel seismic surface wave data. *Geophysics*, *84*(1), A19–A24. doi: 10.1190/geo2018-0430.1

SESAME. (2004). *Guidelines for the implementation of the H/V spectral ratio technique on ambient vibrations: Measurements, processing and interpretation.* SESAME European research project. WP12 – Deliverable D23.12.

Shen, C., Wang, A., Wang, L., Xu, Z., & Cheng, F. (2015). Resolution equivalence of dispersion-imaging methods for noise-free high-frequency surface-wave data. *Journal of Applied Geophysics*, *122*, 167–171. doi: 10.1016/j.jappgeo.2015.09.019

Silver, M. L., Björnsson, B. J., Kiefer, T., Sharma, M., Kotsopoulou, E., & Thomas, P. (1986). *Evaluation of the seismic safety of embankment structures of the Thjorsa and Tungnaa river basin development in Iceland, final report, Vol. 1-3.* Chicago, IL: Marshall Silver and Associates Ltd.

Snedecor, G. W., & Cochran, W. G. (1989). *Statistical Methods* (8th ed.). Ames, IA: Iowa State University Press.

Socco, L. V., & Boiero, D. (2008). Improved Monte Carlo inversion of surface wave data. *Geophysical Prospecting*, *56*(3), 357–371. doi: 10.1111/j.1365-2478.2007.00678.x

Socco, L. V., Boiero, D., Foti, S., & Wisén, R. (2009). Laterally constrained inversion of ground roll from seismic reflection records. *Geophysics*, *74*(6), G35–G45. doi: 10.1190/1.3223636

Socco, L. V., Comina, C., & Khosro Anjom, F. (2017). Time-average velocity estimation through surface-wave analysis: Part 1 – S-wave velocity. *Geophysics*, *82*(3), U49–U59. doi: 10.1190/geo2016-0367.1

Socco, L. V., Foti, S., & Boiero, D. (2010). Surface-wave analysis for building

near-surface velocity models — Established approaches and new perspectives. *Geophysics*, *75*(5), 75A83–75A102. doi: 10.1190/1.3479491

Song, X., Gu, H., Zhang, X., & Liu, J. (2008). Pattern search algorithms for nonlinear inversion of high-frequency Rayleigh-wave dispersion curves. *Computers & Geosciences*, *34*(6), 611–624. doi: 10.1016/j.cageo.2007.05.019

Song, X., Li, L., Zhang, X., Huang, J., Shi, X., Jin, S., & Bai, Y. (2014). Differential evolution algorithm for nonlinear inversion of high-frequency Rayleigh wave dispersion curves. *Journal of Applied Geophysics*, *109*, 47–61. doi: 10.1016/j.jappgeo.2014.07.014

Song, X., Tang, L., Lv, X., Fang, H., & Gu, H. (2012). Application of particle swarm optimization to interpret Rayleigh wave dispersion curves. *Journal of Applied Geophysics*, *84*, 1–13. doi: 10.1016/j.jappgeo.2012.05.011

Song, X., Zhang, X., Zhao, S., & Li, L. (2015). Backtracking search algorithm for effective and efficient surface wave analysis. *Journal of Applied Geophysics*, *114*, 19–31. doi: 10.1016/j.jappgeo.2015.01.002

Thomson, W. T. (1950). Transmission of Elastic Waves through a Stratified Solid Medium. *Journal of Applied Physics*, *21*(2), 89–93. doi: 10.1063/1.1699629

Thrower, E. N. (1965). The computation of the dispersion of elastic waves in layered media. *Journal of Sound and Vibration*, *2*(3), 210–226. doi: 10.1016/0022-460X(65)90109-4

Tokimatsu, K. (1997). Geotechnical site characterization using surface waves. In *Proceedings of IS-Tokyo, the First International Conference on Earthquake Geotechnical Engineering*, 14–16 November 1995, Tokyo, Japan (Vol. 3, pp. 1333–1368).

Tokimatsu, K., Tamura, S., & Kojima, H. (1992). Effects of Multiple Modes on Rayleigh Wave Dispersion Characteristics. *Journal of Geotechnical Engineering*, *118*(10), 1529–1543. doi: 10.1061/(ASCE)0733-9410(1992)118:10(1529)

Tran, K. T., & Hiltunen, D. R. (2012). One-Dimensional Inversion of Full Waveforms using a Genetic Algorithm. *Journal of Environmental and Engineering Geophysics*, *17*(4), 197–213.

Tsuchida, H. (1970). Prediction and countermeasure against the liquefaction in sand deposits. *Abstract of the Seminar in the Port and Harbour Research Institute, Yokohama, Japan*, 3.1–3.33.

UTAustin. (1992). *WinSASW. Data reduction program for Spectral-Analysis-of-Surface-Wave (SASW) tests. Version 1.2. User's guide.* Austin, TX: The University of Texas at Austin.

Verdugo, R. (2019). Seismic site classification. *Soil Dynamics and Earthquake Engineering*, *124*, 317–329. doi: 10.1016/j.soildyn.2018.04.045

Wair, B. R., DeJong, J. T., & Shantz, T. (2012). *Guidelines for Estimation of Shear Wave Velocity Profiles. PEER Report 2012/08.* Davis, CA: Pacific Earthquake Engineering Research Center.

Wathelet, M. (2008). An improved neighborhood algorithm: Parameter conditions and dynamic scaling. *Geophysical Research Letters*, *35*(9), L09301. doi: 10.1029/2008GL033256

Wathelet, M., Jongmans, D., & Ohrnberger, M. (2004). Surface-wave inversion using a direct search algorithm and its application to ambient vibration measurements. *Near Surface Geophysics*, *2*(4), 211–221. doi: 10.3997/1873-0604.2004018

Watson, T. H. (1970). A note on fast computation of Rayleigh wave dispersion in the multilayered elastic half-space. *Bulletin of the Seismological Society of America*, *60*(1), 161–166.

Wood, C. M., & Cox, B. R. (2012). A Comparison of MASW Dispersion Uncertainty and Bias for Impact and Harmonic Sources. In *GeoCongress 2012: State of the Art and Practice in Geotechnical Engineering*, 25–29 March 2012, Oakland, CA (pp. 2756–2765). doi: 10.1061/9780784412121.282

Woods, R. D. (1968). Screening of Surface Wave in Soils. *Journal of the Soil Mechanics and Foundations Division*, *94*(4), 951–980.

Xia, J. (2014). Estimation of near-surface shear-wave velocities and quality factors using multichannel analysis of surface-wave methods. *Journal of Applied Geophysics*, *103*, 140–151. doi: 10.1016/j.jappgeo.2014.01.016

Xia, J., Miller, R. D., & Park, C. B. (1999). Estimation of near-surface shear-wave velocity by inversion of Rayleigh waves. *Geophysics*, *64*(3), 691–700. doi: 10.1190/1.1444578

Xia, J., Miller, R. D., Park, C. B., Hunter, J. A., Harris, J. B., & Ivanov, J. (2002). Comparing shear-wave velocity profiles inverted from multichannel surface wave with borehole measurements. *Soil Dynamics and Earthquake Engineering*, *22*(3), 181–190. doi: 10.1016/S0267-7261(02)00008-8

Xia, J., Miller, R. D., Park, C. B., & Tian, G. (2003). Inversion of high frequency surface waves with fundamental and higher modes. *Journal of Applied Geophysics*, *52*(1), 45–57. doi: 10.1016/S0926-9851(02)00239-2

Xia, J., Miller, R. D., Xu, Y., Luo, Y., Chen, C., Liu, J., ... Zeng, C. (2009). High-Frequency Rayleigh-Wave Method. *Journal of Earth Science*, *20*(3), 563–579. doi: 10.1007/s12583-009-0047-7

Xia, J., Xu, Y., & Miller, R. D. (2007). Generating an Image of Dispersive Energy by Frequency Decomposition and Slant Stacking. *Pure and Applied Geophysics*, *164*(5), 941–956. doi: 10.1007/s00024-007-0204-9

Xu, Y., Xia, J., & Miller, R. D. (2006). Quantitative estimation of minimum offset for multichannel surface-wave survey with actively exciting source. *Journal of Applied Geophysics*, *59*(2), 117–125. doi: 10.1016/j.jappgeo.2005.08.002

Yilmaz, Ö. (1987). *Seismic Data Processing.* Tulsa, OK: Society of Exploration Geophysicists.

Yoon, S., & Rix, G. J. (2009). Near-Field Effects on Array-Based Surface Wave Methods with Active Sources. *Journal of Geotechnical and Geoenvironmental Engineering*, *135*(3), 399–406. doi: 10.1061/(ASCE)1090-0241(2009)135:3(399)

Youd, T. L., Idriss, I. M., Andrus, R. D., Arango, I., Castro, G., Christian, J. T., ... Stokoe, K. H. (2001). Liquefaction Resistance of Soils: Summary Report from the 1996 NCEER and 1998 NCEER/NSF Workshops on Evaluation of Liquefaction Resistance of Soils. *Journal of Geotechnical and Geoenvironmental Engineering*, *127*(10), 817–833. doi: 10.1061/(ASCE)1090-0241(2001)127:10(817)

Zeng, C., Xia, J., Miller, R. D., Tsoflias, G. P., & Wang, Z. (2012). Numerical investigation of MASW applications in presence of surface topography. *Journal of Applied Geophysics*, *84*, 52–60. doi: 10.1016/j.jappgeo.2012.06.004

Zhang, S. X., & Chan, L. S. (2003). Possible effects of misidentified mode number on Rayleigh wave inversion. *Journal of Applied Geophysics*, *53*(1), 17–29. doi: 10.1016/S0926-9851(03)00014-4

Zhang, S. X., Chan, L. S., & Xia, J. (2004). The Selection of Field Acquisition Parameters for Dispersion Images from Multichannel Surface Wave Data. *Pure and Applied Geophysics*, *161*(1), 185–201. doi: 10.1007/s00024-003-2428-7

Zhao, J. X., & Xu, H. (2013). A Comparison of V_{S30} and Site Period as Site-Effect Parameters in Response Spectral Ground-Motion Prediction Equations. *Bulletin of the Seismological Society of America*, *103*(1), 1–18. doi: 10.1785/0120110251

Paper I

Tool for analysis of multichannel analysis of surface waves (MASW) field data and evaluation of shear wave velocity profiles of soils

Elín Ásta Ólafsdóttir, Sigurður Erlingsson & Bjarni Bessason

Ólafsdóttir, E.Á., Erlingsson, S. & Bessason, B. (2018). Tool for analysis of multichannel analysis of surface waves (MASW) field data and evaluation of shear wave velocity profiles of soils. *Canadian Geotechnical Journal, 55*(2), 217–233. doi:10.1139/cgj-2016-0302.

NRC Research Press

ARTICLE

Tool for analysis of multichannel analysis of surface waves (MASW) field data and evaluation of shear wave velocity profiles of soils

Elin Asta Olafsdottir, Sigurdur Erlingsson, and Bjarni Bessason

Abstract: Multichannel analysis of surface waves (MASW) is a fast, low-cost, and environmentally friendly technique to estimate shear wave velocity profiles of soil sites. This paper introduces a new open-source software, MASWaves, for processing and analysing multichannel surface wave records using the MASW method. The software consists of two main parts: a dispersion analysis tool (MASWaves Dispersion) and an inversion analysis tool (MASWaves Inversion). The performance of the dispersion analysis tool is validated by comparison with results obtained by the Geopsy software package. Verification of the inversion analysis tool is carried out by comparison with results obtained by the software WinSASW and theoretical dispersion curves presented in the literature. Results of MASW field tests conducted at three sites in south Iceland are presented to demonstrate the performance and robustness of the new software. The soils at the three test sites ranged from loose sand to cemented silty sand. In addition, at one site, the results of existing spectral analysis of surface waves (SASW) measurements were compared with the results obtained by MASWaves.

Key words: multichannel analysis of surface waves (MASW), dispersion analysis, inversion analysis, open-source software, shear wave velocity.

Résumé : L'analyse multicanal des ondes de surface (« MASW ») est un moyen technique rapide, peu coûteux et respectueux de l'environnement pour estimer les profils de vitesse des ondes de cisaillement de sites de sols. L'article présente un nouveau logiciel à source ouverte, MASWaves, pour le traitement et l'analyse d'enregistrements des ondes de surface multicanal à l'aide de la méthode MASW. Le logiciel se compose de deux parties principales; un outil d'analyse de la dispersion (la dispersion MASWaves) et un outil d'analyse d'inversion (l'inversion MASWaves). La performance de l'outil d'analyse de la dispersion est validée par la comparaison aux résultats obtenus par le logiciel Geopsy. La vérification de l'outil d'analyse d'inversion est effectuée par rapport aux résultats obtenus par le logiciel WinSASW et les courbes de dispersion théoriques présentés dans la littérature. Les résultats des essais sur le terrain de MASW effectués dans trois sites dans le sud de l'Islande sont présentés afin de démontrer les performances et la robustesse de ce nouveau logiciel. Les sols à l'essai aux trois sites allant de sable lâche au sable limoneux cimenté. De plus, sur un site, les résultats de mesures de l'analyse spectrale des ondes de surface (« SASW ») ont été comparés aux résultats obtenus par MASWaves. [Traduit par la Rédaction]

Mots-clés : analyse multicanal des ondes de surface (MASW), analyse de la dispersion, analyse de l'inversion, logiciels à source ouverte, vitesse des ondes de cisaillement.

Introduction

Knowledge of the geotechnical properties of subsoil sites is essential in various civil engineering projects. The shear wave velocity of the top-most soil layers is a key parameter in this sense. The small-strain shear modulus of individual soil layers (G_{max}) is directly proportional to the square of their characteristic shear wave velocity. Furthermore, the shear wave velocity is vital in assessments of both liquefaction potential and soil amplification and for seismic site classification (Kramer 1996). For instance, the time-average shear wave velocity of the uppermost 30 m ($V_{S,30}$) is used to account for the effects of the local ground conditions on the seismic action when site-specific design spectra are defined according to Eurocode 8 (CEN 2004).

Several in situ methods can be applied to estimate the shear wave velocity profile of near-surface materials (Gazetas 1991; Kramer 1996). Among these are methods that require access to a drilled borehole such as down-hole and cross-hole seismic surveys, methods where the resistance of soil to penetration is measured as in the standard penetration test and the cone penetration test and surface wave analysis methods. Surface wave analysis methods are based on the dispersive properties of surface waves propagating through a heterogeneous medium (Aki and Richards 1980). In published studies, the main focus has been on the analysis of Rayleigh waves as they are both easy to generate and to detect on the ground surface using low-frequency receivers (Socco et al. 2010). Compared to other available methods, surface wave analysis methods are low-cost, as well as being noninvasive and environmentally friendly because they neither require heavy machinery nor leave lasting marks on the surface of the test site. This makes the application of surface wave analysis methods for estimating the shear wave velocity profile of subsoil sites very appealing.

Received 2 June 2016. Accepted 23 May 2017.

E.A. Olafsdottir, S. Erlingsson, and B. Bessason. Faculty of Civil and Environmental Engineering, University of Iceland, Hjardarhagi 2-6, IS-107 Reykjavik, Iceland.

Corresponding author: Elin Asta Olafsdottir (email: eao4@hi.is).

The basis of most surface wave analysis methods is accurate determination of the frequency-dependent phase velocity of fundamental-mode Rayleigh waves (Park et al. 1999), i.e., the experimental fundamental-mode dispersion curve. Apart from being a function of frequency, the Rayleigh wave phase velocity is related to several groups of soil properties, most importantly the shear wave velocity (Xia et al. 1999). Hence, by inversion of the experimental dispersion curve, the shear wave velocity profile for the test site can be determined.

Several types of surface wave analysis methods can be applied to estimate the shear wave velocity profile of the top-most soil layers. Among them are spectral analysis of surface waves (SASW) and multichannel analysis of surface waves (MASW). The SASW method has been used since the early 1980s and is based on analysis of surface wave records acquired by multiple pairs of receivers (Nazarian et al. 1983). The MASW method is a newer and more advanced technique, developed to overcome some of the weaknesses of the SASW method (Park et al. 1999). In recent years, the MASW method has attracted increasingly more attention and has become one of the key surface wave analysis methods to determine near-surface shear wave velocity profiles for applications in civil engineering (Xia 2014). The main advantages of MASW, as compared to the SASW method, include a more efficient data-acquisition routine in the field, faster and less labour-consuming data processing procedures, and improved identification and elimination of noise from recorded data (Park et al. 1999; Xia et al. 2002). Reduction of noise leads to a more accurate experimental dispersion curve and ultimately a more precise shear wave velocity profile. Furthermore, the MASW method makes it possible to observe and extract higher-mode dispersion curves based on the recorded surface wave data (Xia et al. 2003). Finally, it is possible to map deeper shear wave velocity profiles when using the same impact load. The observed difference between results obtained by MASW and direct borehole measurements has been estimated as approximately 15% or less and random (Xia et al. 2002).

The maximum depth of investigation in a MASW survey varies with site, the configuration of the measurement profile, the natural frequency of the receivers, and the type of seismic source that is used (Park and Carnevale 2010; Park et al. 2002, 2007). The investigation depth is determined by the longest Rayleigh wave wavelength that is retrieved. A commonly adopted empirical criterion (Park and Carnevale 2010) is that

$$z_{max} \approx 0.5\lambda_{max} \quad (1)$$

where z_{max} is the maximum investigation depth and λ_{max} is the longest wavelength.

The investigation depth that can be achieved by a MASW survey is usually a few tens of metres, assuming that the surface waves are generated by a reasonably heavy impulsive (active) source, e.g., a sledgehammer (Park et al. 2005, 2007). Surface waves that are generated by natural sources and (or) man-made activities have lower frequencies (longer wavelengths) than waves generated by impact loads. Multiple techniques have been applied for analysis of ambient noise (passive-source) vibrations acquired by a linear receiver array (e.g., Louie 2001; Park and Miller 2008), a two-dimensional array (e.g., Asten 2006; Di Giulio et al. 2006; Garofalo et al. 2016; Wathelet et al. 2008) or a single station (e.g., Gouveia et al. 2016; Hobiger et al. 2009, 2013). By combining results of active-source and passive-source surveys, an increased range in investigation depth can be obtained.

This paper introduces the first version of a new open-source software, MASWaves (*M*ultichannel *A*nalysis of *S*urface *W*aves for *a*ssessing shear wave *ve*locity profiles of *s*oils), for application of the MASW method, developed at the Faculty of Civil and Environmental Engineering, University of Iceland (Olafsdottir 2016). MASWaves contains two fundamental parts: a tool for processing of MASW field data and evaluation of experimental dispersion curves (MASWaves Dispersion) and a tool for computation of theoretical dispersion curves and evaluation of shear wave velocity profiles by inversion of the experimental data (MASWaves Inversion). Verification of MASWaves Dispersion is carried out by comparison with results obtained by using the open-source software Geopsy. Theoretical dispersion curves computed by MASWaves Inversion were compared with theoretical fundamental-mode curves obtained by using the software WinSASW (version 1.2; UTAustin 1992) as well as fundamental- and first higher-mode dispersion curves presented by Tokimatsu et al. (1992) and Tokimatsu (1997).

Results of MASW field tests conducted at three test sites in south Iceland are presented to demonstrate the performance and robustness of the new software. Moreover, at one test site, the results of the MASW analysis were compared with results of SASW measurements carried out previously at the site.

The software MASWaves, which is written in Matlab, can be downloaded free of charge at masw.hi.is, along with a user guide and sample data.

Multichannel analysis of surface waves

The MASW method is divided into three main steps: field measurements, dispersion analysis, and inversion analysis (Park et al. 1999). The software MASWaves is designed to perform the dispersion analysis and the inversion analysis. A single multichannel surface wave record is sufficient to carry out the analysis. The main data acquisition and computational steps are illustrated in Fig. 1.

For data acquisition, low-frequency receivers (geophones) are lined up on the surface of the test site (Fig. 1*a*). A wave is generated by an impulsive source that is applied at one end of the measurement profile and the geophones record the resulting wave propagation as a function of time (Fig. 1*b*). The number of receivers is denoted by N. An illustration of a typical MASW measurement profile is provided in Fig. 2. The distance from the impact load point to the first receiver in the geophone line is referred to as the source offset and denoted by x_1 and the receiver spacing is dx. Hence, the length of the receiver spread is $L = (N - 1)\text{dx}$ and the total length of the measurement profile is $L_T = x_1 + (N - 1)\text{dx}$.

In the dispersion analysis, dispersion curves are extracted from the acquired surface wave data. Several different methods can be used. Transform-based methods, in which the acquired time series are transformed from the space–time domain into a different domain, are most commonly used for active-source surveys (Socco et al. 2010), i.e., the frequency–wave number (f–k) transform (Yilmaz 1987), the slowness–frequency (p–ω) transform (McMechan and Yedlin 1981), and the phase shift method (Park et al. 1998). Each transform provides an image of the dispersive properties of the recorded surface waves (Fig. 1*c*) from which the Rayleigh wave dispersion curve(s) are identified and extracted based on the spectral maxima (Fig. 1*d*). Dal Moro et al. (2003) compared the effectiveness of the phase shift method, the f–k transform, and the p–ω transform to determine Rayleigh wave dispersion curves for near-surface applications in unconsolidated settlements. They concluded that the phase shift method, which was used in this work, is a robust and computationally efficient method that provides accurate fundamental-mode phase velocities even when data from as little as four geophones are available.

The inversion analysis involves obtaining a shear wave velocity profile by backcalculation of the experimental dispersion curve. A theoretical dispersion curve is computed based on an assumed set of model parameters, including an assumed shear wave velocity profile for the test site. Different sets of parameters are inserted into the theoretical model in an iterative way in search of the theoretical dispersion curve that is the most consistent with the measured curve (Fig. 1*e*). The shear wave velocity profile that results in a theoretical dispersion curve that fits the experimental

Fig. 1. Overview of the MASW method: (*a*, *b*) field measurements; (*c*, *d*) dispersion analysis; (*e*, *f*) inversion analysis. [Colour online.]

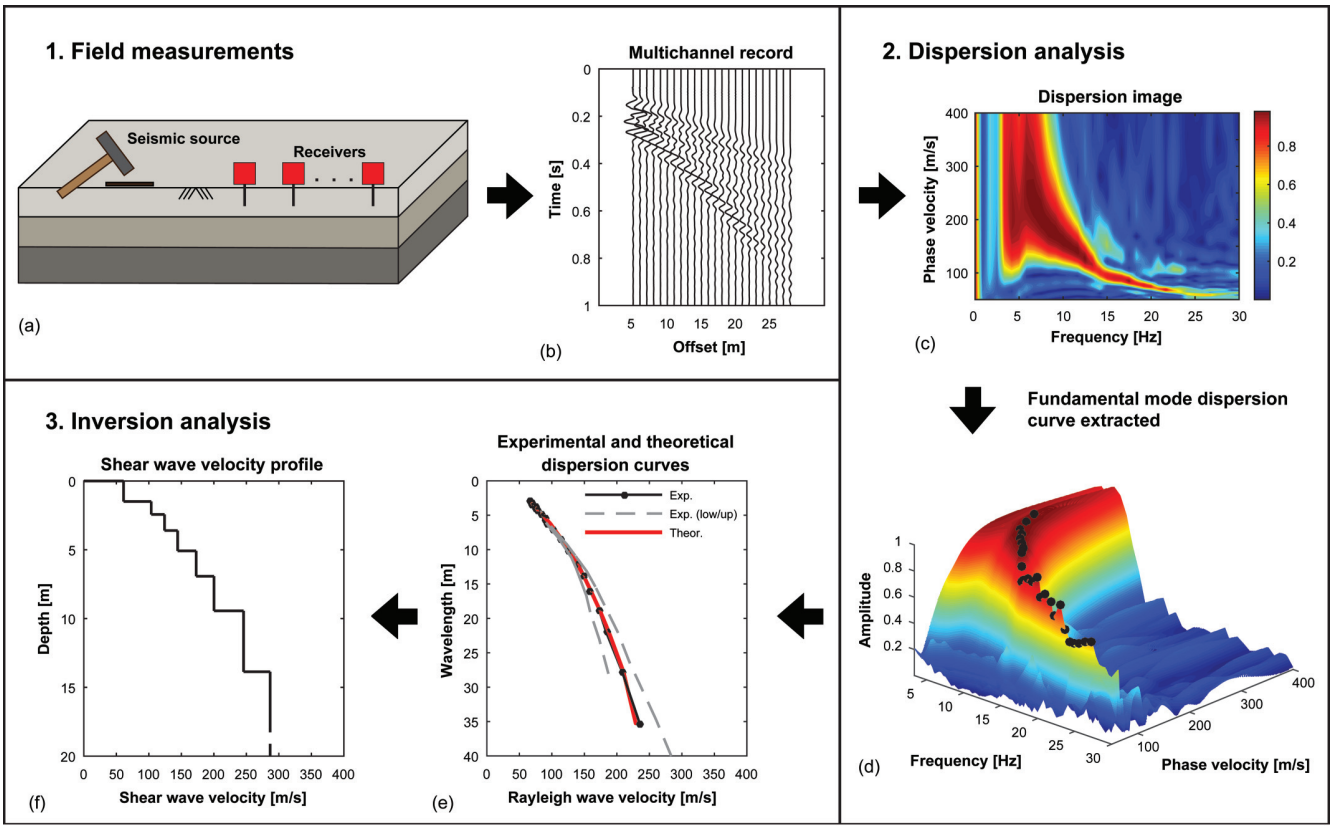

Fig. 2. Typical MASW measurement profile with 24 receivers. [Colour online.]

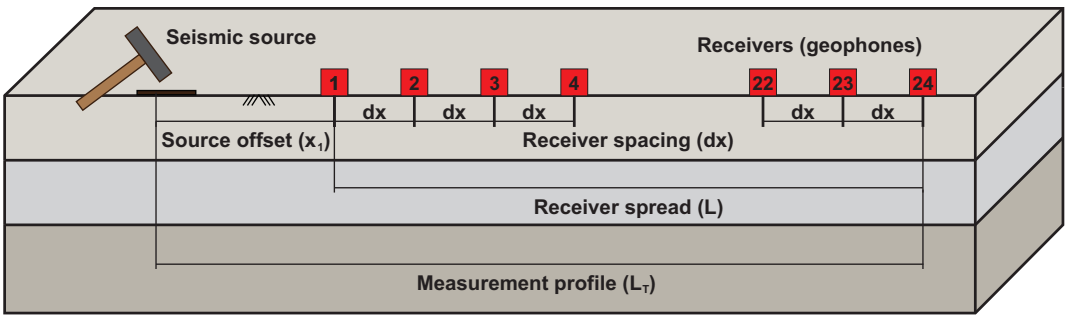

curve up to an acceptable level is taken as the result of the survey (Fig. 1*f*).

Theoretical dispersion curves are in most cases determined by matrix methods that originate in the work of Thomson (1950) and Haskell (1953), assuming a layered earth model. Various methods have been developed based on the Thomson–Haskell formulation to study surface wave propagation in a layered medium. Many of these were formulated to resolve numerical overflow and loss-of-precision problems that can occur at high frequencies when the original Thomson–Haskell method is applied (Schwab 1970). Available methods include the propagator-matrix approach described by Knopoff (1964) and Schwab (1970) with later improvements of, e.g., Abo-Zena (1979), Menke (1979), and Buchen and Ben-Hador (1996); the stiffness matrix formulation of Kausel and Roësset (1981); and the reflection–transmission matrix method developed by Kennett (1974) and Kennett and Kerry (1979). In this work, the stiffness matrix method was used for computations of theoretical dispersion curves.

The inversion problem encountered in MASW can be regarded as a nonunique and nonlinear optimization problem where the objective is to minimize the misfit between the theoretical and the experimental dispersion curves (Foti et al. 2015). The inversion can either be performed as a fundamental-mode inversion, i.e., by considering only the fundamental mode of Rayleigh wave propagation, or by including higher modes as well. Fundamental-mode inversion is easier to implement and in general more computationally efficient. However, consideration of higher modes can in some cases be of importance to better constrain the inversion process, especially at sites where the shear wave velocity does not gradually increase with depth (Socco et al. 2010). In this work, the experimental and the theoretical dispersion curves were compared in terms of their fundamental modes.

Dispersion analysis

A flowchart of the dispersion analysis process is shown in Fig. 3 and a brief description of each step is provided below. A more

Fig. 3. Overview of the dispersion analysis.

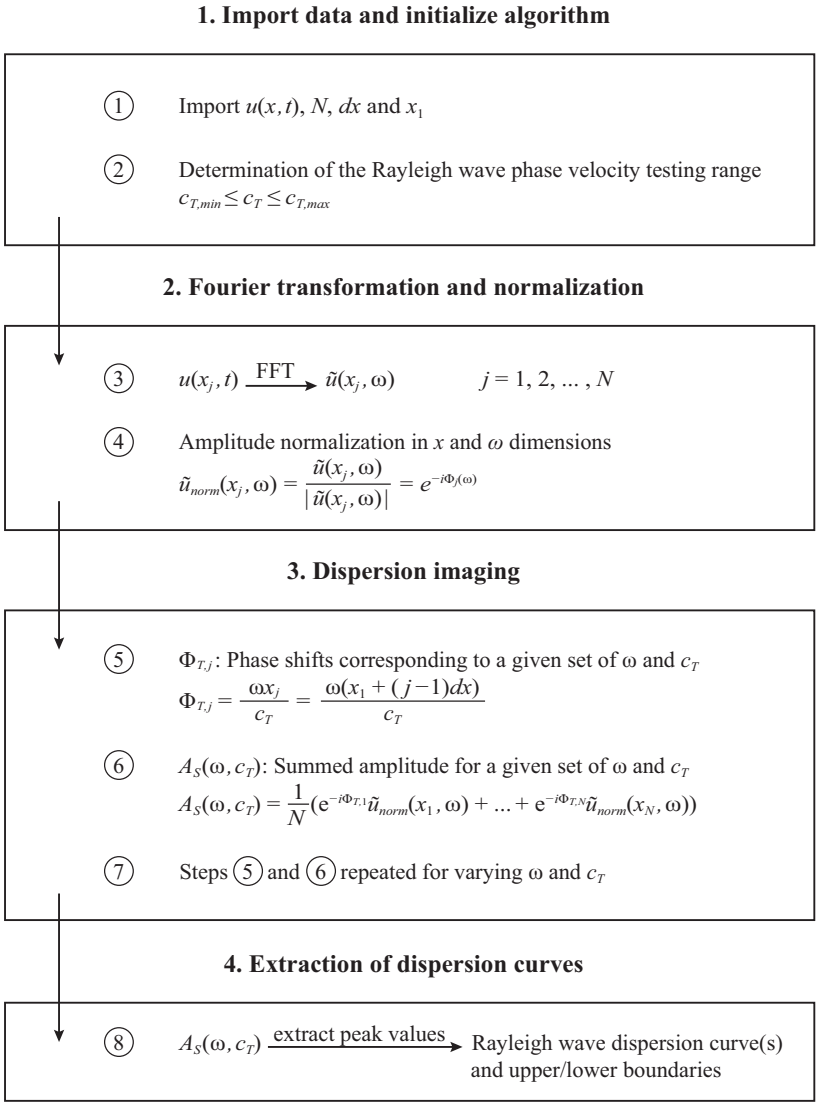

detailed description of the computational procedure is provided by Olafsdottir (2016).

The multichannel surface wave record is denoted by $u(x_j, t)$, where $x_j = x_1 + (j - 1)dx$ is the distance from the impact load point to the jth receiver ($j = 1, \ldots, N$) and t is time. A Fourier transform is applied to each trace of the multichannel record providing its frequency-domain representation $\tilde{u}(x_j, \omega)$ (Park et al. 1998; Park 2011)

$$(2) \qquad \tilde{u}(x_j, \omega) = FFT[u(x_j, t)]$$

where $\omega = 2\pi f$ is angular frequency.

The transformed record can be expressed in terms of amplitude $A_j(\omega)$ and phase $\Phi_j(\omega)$. The phase term is determined by the characteristic phase velocity of each frequency component $c(\omega)$ and the offset x_j. The amplitude term preserves information regarding other properties such as the attenuation of the signal and its geometrical spreading (Park et al. 1998; Park 2011)

$$(3) \qquad \tilde{u}(x_j, \omega) = A_j(\omega)e^{-i\Phi_j(\omega)}$$

where

$$(4) \qquad \Phi_j(\omega) = \frac{\omega x_j}{c(\omega)} = \frac{\omega[x_1 + (j - 1)\mathrm{dx}]}{c(\omega)}$$

and $i^2 = -1$.

The amplitude of the transformed record is subsequently normalized in both the offset and the frequency dimensions to remove the effects of geometrical spreading and attenuation (Park et al. 1998; Park 2011). Hence, the analysis is focused on the dispersive properties of the signal.

$$(5) \qquad \tilde{u}_{\mathrm{norm}}(x_j, \omega) = \frac{\tilde{u}(x_j, \omega)}{\left|\tilde{u}(x_j, \omega)\right|} = e^{-i\Phi_j(\omega)}$$

The time domain representation of each frequency component of $\tilde{u}_{\mathrm{norm}}(x_j, \omega)$ is an array of normalized sinusoidal curves that have the same phase along the slope determined by their actual phase velocity $c(\omega)$. The phase of the curves varies along slopes corre-

Fig. 4. Dispersion images obtained by receiver spreads of length (*a*) L = 11.5 m (dx = 0.5 m and N = 24) and (*b*) L = 23.0 m (dx = 1.0 m and N = 24). The midpoint of both receiver spreads was the same. [Colour online.]

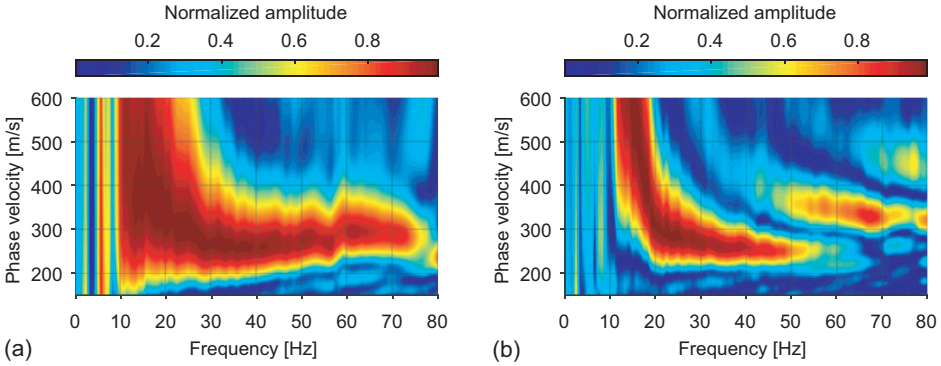

sponding to other phase velocities. If the normalized sinusoidal curves are added up along the slope corresponding to $c(\omega)$, their sum will be another sinusoidal curve with amplitude N through a perfectly constructive superposition. However, if the normalized curves are added up along any other slope, the amplitude of the resulting summed curve will be less than N due to destructive superposition (Ryden et al. 2004; Park 2011). The process of summing amplitudes in the offset domain along slanted paths is generally referred to as slant-stacking (Yilmaz 1987).

For a given testing phase velocity, c_T, and a given frequency, ω, the amount of phase shifts required to counterbalance the time delay corresponding to specific offsets x_j are determined. The phase shifts are applied to distinct traces of the normalized, transformed record $\tilde{u}_{norm}(x_j, \omega)$ that are thereafter added to obtain the slant-stacked amplitude $A_s(\omega, c_T)$ corresponding to each pair of ω and c_T (Park et al. 1998; Park 2011). The slant-stacked amplitude is generally normalized with respect to N so that the peak value will not depend on the number of receivers

$$(6) \qquad A_s(\omega, c_T) = \frac{1}{N}\sum_{j=1}^{N} e^{-i\Phi_{T,j}}\tilde{u}_{norm}(x_j, \omega)$$

where

$$(7) \qquad \Phi_{T,j} = \frac{\omega x_j}{c_T}$$

The summation operation defined by eqs. (6) and (7) is repeated for all the different frequency components of the transformed record in a scanning manner, changing the testing phase velocity in small increments within a previously specified testing range ($c_{T,min} \le c_T \le c_{T,max}$). The dispersion image is thereafter obtained by plotting the slant-stacked amplitude in the frequency–phase velocity domain, in either two or three dimensions (see Figs. 1*c* and 1*d*). The high-amplitude bands visualize the dispersion properties of all types of waves contained in the recorded data and are used to construct the fundamental-mode (and higher-mode) dispersion curve(s) for the site (Park et al. 1998; Park 2011). Upper and lower boundaries for the modal dispersion curves ($(p_A/100)A_{s,max} \le A_s \le A_{s,max}$) can be obtained by identifying the testing phase velocity values that provide p_A% of the corresponding spectral peak value ($A_{s,max}$) at each frequency.

The experimental fundamental-mode dispersion curve is denoted by ($c_{e,q}$, $\lambda_{e,q}$) (q = 1, …, Q) where Q is the number of data points, $c_{e,q}$ is the Rayleigh wave phase velocity of the qth data point, and $\lambda_{e,q}$ is the corresponding wavelength. For application of the software MASWaves, the fundamental-mode dispersion curve is of main interest and also referred to as the dispersion curve in the subsequent discussion.

Challenges associated with the dispersion analysis and effects of the measurement profile configuration

Determination of the experimental Rayleigh wave dispersion curve is a critical stage in the application of MASW. An inaccurate or erroneous experimental dispersion curve can cause substantial errors in the inverted shear wave velocity profile (Gao et al. 2016; Park et al. 1999; Zhang and Chan 2003).

Ideally, the dispersion analysis should provide identification and extraction of the dispersion curve for each mode. However, in reality, surface wave registrations are incomplete to some extent, imposing various challenges when dispersion curves are identified based on a dispersion image. The fundamental mode of Rayleigh wave propagation typically prevails at sites where the stiffness (shear wave velocity) increases gradually with increasing depth (Foti et al. 2015; Gao et al. 2016; Gucunski and Woods 1991; Tokimatsu et al. 1992). However, at sites characterized by a more irregularly varying stiffness profile, e.g., the presence of a stiff surface layer, a stiff layer sandwiched between two softer layers or a sudden increase in stiffness with depth, higher modes can play a significant role in certain frequency ranges. In such cases, misidentification of mode numbers or superposition of dispersion data from two (or more) modes can occur (Foti et al. 2015; Gao et al. 2016; Zhang and Chan 2003). Mode misidentification can, for example, involve a higher mode being incorrectly identified as the fundamental mode, whereas mode superposition results in an apparent dispersion curve that does not correspond to any of the real modes. Such overestimation of the fundamental-mode phase velocity will, in the inversion analysis, lead to both overestimation of the shear wave velocity and erroneous depth.

The length of the receiver spread (L) affects the spectral resolution of the dispersion image, i.e., the width of the high-amplitude band, and hence, the ability to separate different modes of Rayleigh wave propagation as well as the accuracy of the identified spectral maximum at each frequency (Foti et al. 2015). This is illustrated in Fig. 4. The dispersion image in Fig. 4*a* was obtained based on a multichannel record acquired by a receiver spread of length 11.5 m, whereas the data used for computation of Fig. 4*b* were obtained at the same test site using a 23.0 m receiver spread. The receiver spread length of 11.5 m was not sufficient to separate the fundamental and higher modes. However, the longer receiver spread provided improved spectral resolution and allowed identification of a higher mode at frequencies above 40–50 Hz. The use of an even longer receiver spread was not possible due to the nature of the site.

Based on the previous discussion, a longer receiver spread is, in general, preferable to improve the resolution of the dispersion image. However, an increased receiver spread length risks significant lateral variations along the geophone array (thus violating the one-dimensional soil model assumption made in the inversion analysis), attenuation of higher frequency surface wave com-

Fig. 5. Test site 1: dispersion images obtained by (*a*) MASWaves and (*b*) Geopsy. [Colour online.]

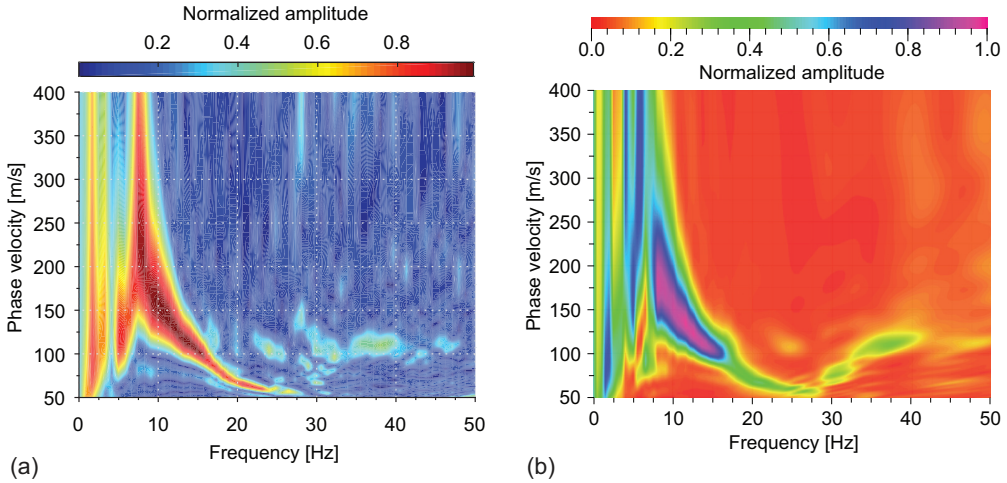

Fig. 6. Test site 2: dispersion images obtained by (*a*) MASWaves and (*b*) Geopsy. [Colour online.]

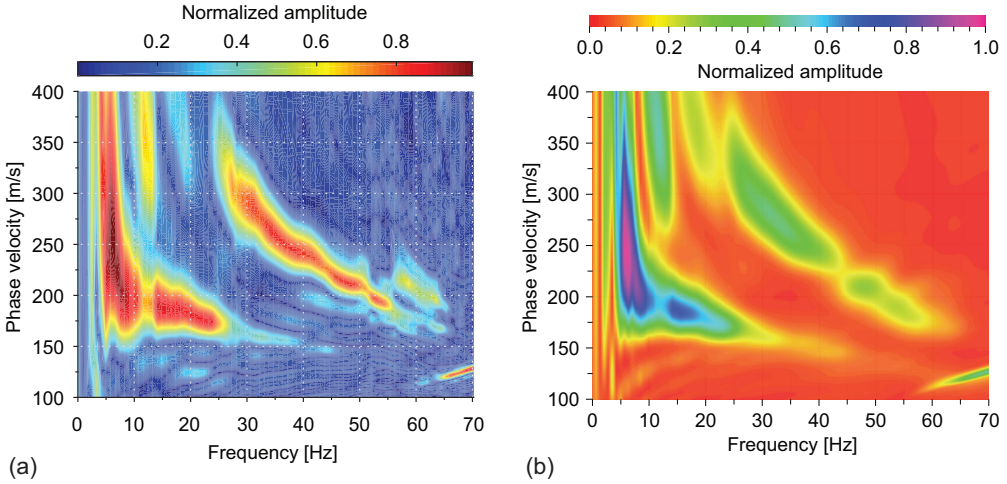

ponents (which reduces the minimum resolvable investigation depth of the survey), and spatial aliasing if a fixed number of receivers is used (Foti et al. 2015).

The analysis of the multichannel surface wave records is based on the assumption that the wave front of the Rayleigh wave is plane. Hence, propagation of nonplanar surface waves and interference of body waves near the impact load point, referred to as near-field effects, can bias the experimental dispersion curve estimate (Ivanov et al. 2008; Park and Carnevale 2010; Yoon and Rix 2009). In general, the length of the source offset (x_1) has to be sufficient to assure plane wave propagation of surface wave components. The minimum source offset required to avoid near-field effects depends on the longest wavelength that is analysed. A very short source offset can result in an irregular and unreliable high-amplitude trend in the dispersion image at lower frequencies, usually displaying lower phase velocities than images free of near-field effects. An overly long source offset, however, risks excessive attenuation of fundamental-mode components at higher frequencies. A simple, widely accepted rule-of-thumb indicates that the investigation depth of the survey is around the same as the receiver spread length (L) and that the minimum source offset is in the range of $0.25L$–L (Ivanov et al. 2008). However, it should be noted that such empirical rules-of-thumb might not be applicable at specific sites.

Validation of the dispersion analysis procedure

The dispersion analysis procedure implemented in MASWaves has been verified by comparison with the Linear F-K for active experiments toolbox of the Geopsy software package (geopsy.org). The comparison is provided in the form of dispersion images and extracted fundamental- and higher-mode dispersion curves. Multichannel surface wave records acquired at two test sites in north Iceland were used for comparison purposes. At test site 1, the fundamental mode dominated the surface wave signal (Fig. 5). At test site 2, however, a higher mode was dominant at frequencies higher than 25–30 Hz (Fig. 6). At both test sites, the two computational procedures provided fundamental-mode Rayleigh wave dispersion curve estimates within the approximately same frequency ranges, as well as higher-mode dispersion curve estimates within comparable frequency ranges at test site 2. The extracted fundamental- and higher-mode dispersion curves agreed very well in both cases (Fig. 7).

Inversion analysis

Figure 8 illustrates the stratified earth model used in the inversion analysis. For computation of a theoretical dispersion curve corresponding to the assumed layer structure, the problem is approximated as a plane strain problem in the x–z plane (Haskell

Fig. 7. (*a*) Test site 1: comparison of fundamental-mode dispersion curves extracted from the spectra in Figs. 5*a* and 5*b*. (*b*) Test site 2: comparison of fundamental- and higher-mode dispersion curves extracted from the spectra in Figs. 6*a* and 6*b*. [Colour online.]

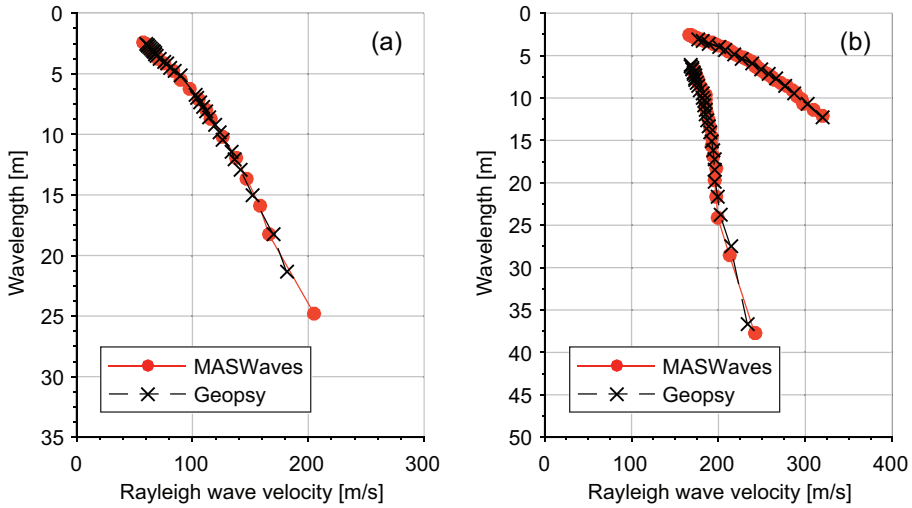

Fig. 8. A layered soil model for the inversion analysis. [Colour online.]

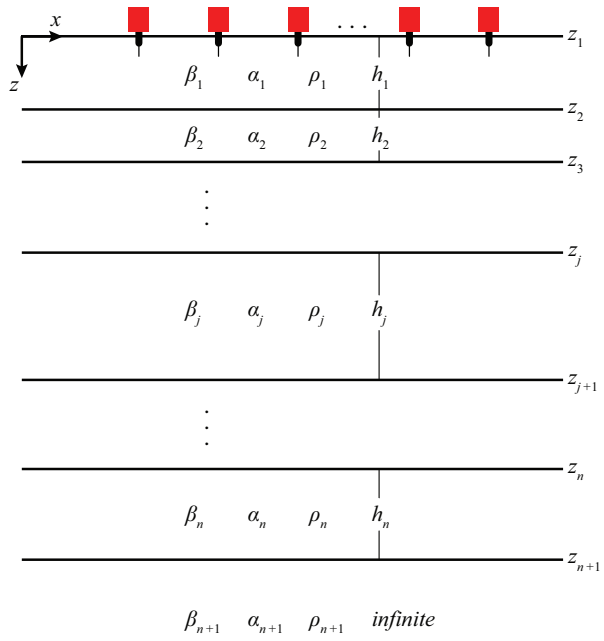

1953; Kausel and Roësset 1981). The *x*-axis is parallel to the layers, with a positive *x* in the direction of surface wave propagation, and the positive *z*-axis is directed downwards. Each layer is assumed to be flat and have homogeneous and isotropic properties. The top of the first layer corresponds to the surface of the earth. The number of finite thickness layers is denoted by *n*. The last layer, referred to as layer $n + 1$, is assumed to be a half-space. The parameters required to define the properties of each layer are layer thickness (h), shear wave velocity (β), Poisson's ratio (ν) or compressional wave velocity (α) and mass density (ρ).

An overview of the inversion analysis procedure is provided in Fig. 9. The first step is to obtain an initial estimate of the required model parameters. For a plane-layered earth model, the shear wave velocity has a dominant effect on the fundamental-mode dispersion curve at frequencies $f > 5$ Hz, followed by layer thicknesses (Xia et al. 1999). As the effect of change in Poisson's ratio (or compressional wave velocity) and mass density are less significant, these parameters are assumed known and assigned fixed values to simplify the inversion process.

The layer thicknesses and the initial shear wave velocity of each layer can be estimated based on the experimental dispersion curve ($c_{e,q}$, $\lambda_{e,q}$) ($q = 1, \ldots, Q$) utilizing a methodology described by Park et al. (1999) where the shear wave velocity, β, at depth z is estimated as 1.09 times the experimental Rayleigh wave phase velocity, c, at the frequency where the wavelength, λ, fulfils

$$z = a\lambda \tag{8}$$

The parameter a is a coefficient that does not change considerably with frequency (Park et al. 1999) and can be chosen close to 0.5 (see eq. (1)). The multiplication factor 1.09 originates from the ratio between the shear and Rayleigh wave propagation velocities in a homogeneous medium (Kramer 1996). Alternatively, the initial values of the layer thicknesses and the shear wave velocities can be assigned manually.

The Poisson's ratio (or the compressional wave velocity) and the mass density of each layer are either estimated based on independent soil investigations or experience of similar soil types from other sites. For estimation of these parameters, it is important to pay special attention to the presence and the expected position of the groundwater table. The velocity of compressional waves propagating through groundwater is close to 1500 m/s, depending slightly on water temperature and salinity (Kramer 1996). Their propagation velocity through soft, saturated soil can reach these high velocities. Hence, in such cases the compressional wave velocity is not indicative of the stiffness of the saturated soil and the soil's apparent Poisson's ratio will be close to 0.5 (Foti et al. 2015; Gazetas 1991). The saturated density should be used for the soil layers that are below the expected groundwater table. The stiffness of the soft soil can be significantly overestimated if the presence of the groundwater table is ignored (Kramer 1996).

Theoretical fundamental-mode dispersion curves are computed by the stiffness matrix method of Kausel and Roësset (1981) in an iterative way. In each iteration, the theoretical fundamental-mode dispersion curve ($c_{t,q}$, $\lambda_{t,q}$) ($q = 1, \ldots, Q$) is computed at the same wavelengths as are included in the experimental dispersion curve ($c_{e,q}$, $\lambda_{e,q}$) ($q = 1, \ldots, Q$), i.e.,

$$\lambda_{t,q} = \lambda_{e,q} \qquad q = 1, \ldots, Q \tag{9}$$

Fig. 9. Overview of the inversion analysis.

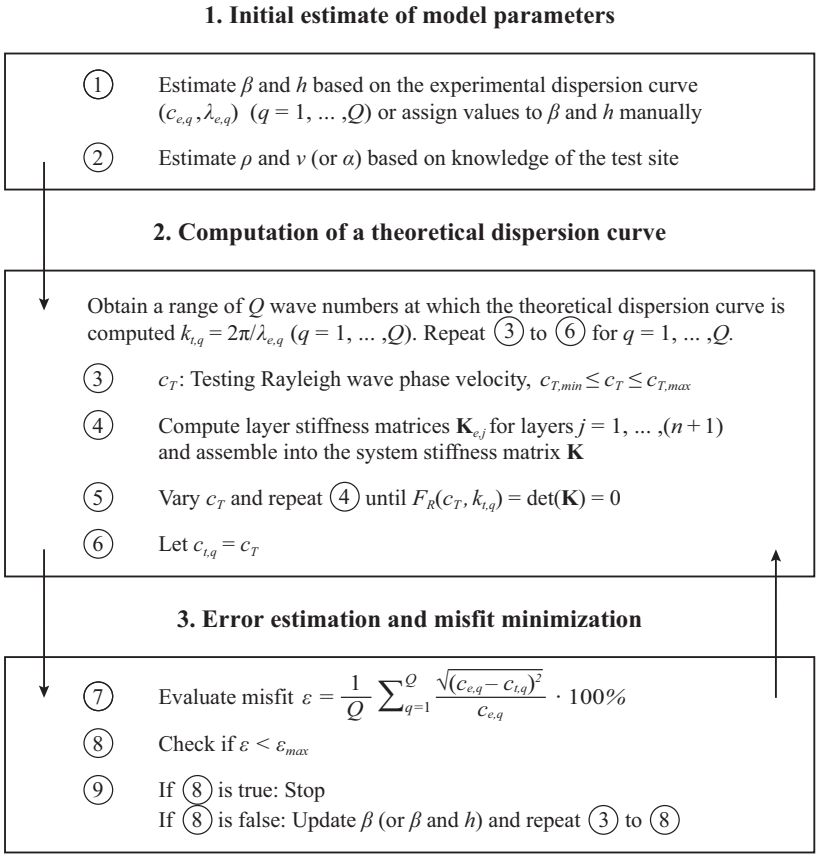

The corresponding wave numbers $k_{t,q}$ are

$$k_{t,q} = \frac{2\pi}{\lambda_{t,q}} \qquad q = 1, \ldots, Q \tag{10}$$

An element stiffness matrix $\mathbf{K}_{e,j}$ is obtained for each layer, including the half-space, for a given value of $k_{t,q}$ and an assumed testing phase velocity c_T. The element stiffness matrix of a given layer relates the stresses at the upper and lower interfaces of the layer to the corresponding displacements (Kausel and Roësset 1981)

$$\boldsymbol{p}_{e,j} = \mathbf{K}_{e,j}\boldsymbol{u}_{e,j} \qquad j = 1, \ldots, (n+1) \tag{11}$$

where $\boldsymbol{p}_{e,j}$ is the element external load vector of the jth layer and $\boldsymbol{u}_{e,j}$ is the element displacement vector of the jth layer. Equation (11) is referred to as the element matrix equation for the jth layer. The components of the element stiffness matrix $\mathbf{K}_{e,j}$ are provided in Appendix A.

The element matrix equations (eq. (11)) are subsequently assembled at the common layer interfaces (see Appendix A) to form the system equation

$$\boldsymbol{p} = \mathbf{K}\boldsymbol{u} \tag{12}$$

where the matrix $\mathbf{K}$ is referred to as the system stiffness matrix and the vectors $\boldsymbol{p}$ and $\boldsymbol{u}$ are the system external load vector and the system displacement vector, respectively. The natural modes of Rayleigh wave propagation are obtained by considering a system with no external loading, i.e., where

$$\mathbf{K}\boldsymbol{u} = 0 \tag{13}$$

For nontrivial solutions of eq. (13), the determinant of the system stiffness matrix $\mathbf{K}$ must vanish. Hence, wave numbers that represent the modal solutions at various frequencies are obtained as the solutions of

$$F_R(c, k) = \det(\mathbf{K}) = 0 \tag{14}$$

For a given value of $k_{t,q}$, the solution of the dispersion equation (eq. (14)) is determined by varying the testing phase velocity, c_T, in small increments (Δc_T), starting from an underestimated initial value, and recomputing the system stiffness matrix until its determinant has a sign change. The testing phase velocity increment (Δc_T) is an input parameter of MASWaves Inversion. Based on testing of the program, its recommended value is in the range of $\Delta c_T \in [0.1, 0.5]$ m/s, with $\Delta c_T = 0.1$ m/s recommended for soil layer models characterized by an irregularly varying shear wave velocity (stiffness) profile where a higher mode can be expected to play a significant role. For computations based on earth models where the shear wave velocity increases gradually with depth, a larger value of Δc_T (e.g., $\Delta c_T = 1$ m/s) is, however, in many cases sufficient. As a consequence of choosing a too large value of Δc_T, the algorithm may fail to correctly separate the fundamental- and higher-mode dispersion curves, especially at osculation points or "mode kissing" points where the fundamental- and first higher-mode dispersion curves are very close to each other.

As the value of c_T that provides the fundamental-mode solution of eq. (14) has been obtained with sufficient accuracy, the value of $c_{t,q}$ is taken as

Table 1. Test profile, case A (after Xia et al. 2007).

Layer number	Shear wave velocity (m/s)	Compressional wave velocity (m/s)	Mass density (kg/m³)	Layer thickness (m)
1	200	800	2000	10.0
2 (half-space)	400	1200	2000	Infinite

Table 2. Test profile, case B (after Xia et al. 1999).

Layer number	Shear wave velocity (m/s)	Compressional wave velocity (m/s)	Mass density (kg/m³)	Layer thickness (m)
1	194	650	1820	2.0
2	270	750	1860	2.3
3	367	1400	1910	2.5
4	485	1800	1960	2.8
5	603	2150	2020	3.2
6 (half-space)	740	2800	2090	Infinite

Fig. 10. Comparison of theoretical dispersion curves obtained by MASWaves and the software WinSASW: (*a*) case A and (*b*) case B. [Colour online.]

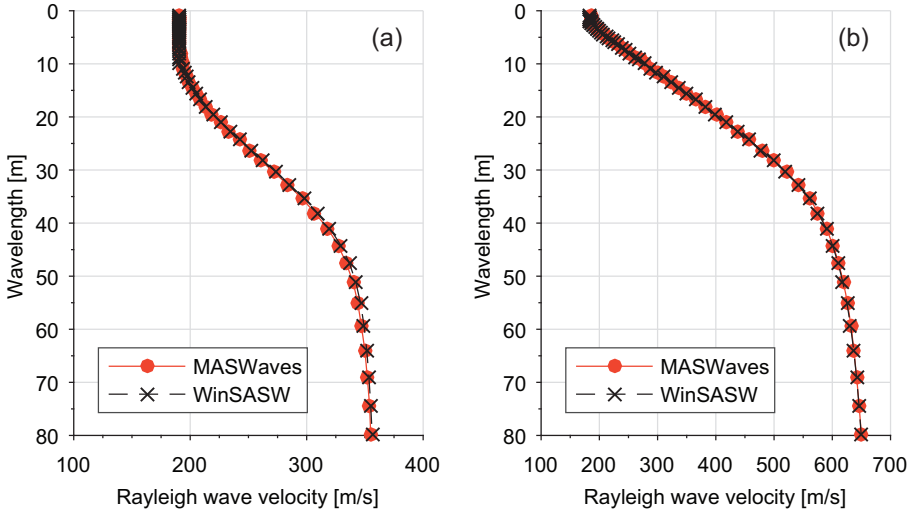

Table 3. Test profiles, cases 1, 2, and 3 (after Tokimatsu et al. 1992 and Tokimatsu 1997).

	Shear wave velocity (m/s)					
Layer number	Case 1	Case 2	Case 3	Compressional wave velocity (m/s)	Mass density (kg/m³)	Layer thickness (m)
1	80	180	80	360	1800	2.0
2	120	120	180	1000	1800	4.0
3	180	180	120	1400	1800	8.0
4 (half-space)	360	360	360	1400	1800	Infinite

(15) $$c_{t,q} = c_T$$

By repeating the computations for different wave numbers $k_{t,q}$ (different wavelengths $\lambda_{t,q}$), the theoretical fundamental-mode dispersion curve is constructed.

The misfit ϵ between the theoretical dispersion curve and the observed experimental curve is subsequently evaluated as

(16) $$\epsilon = \frac{1}{Q}\sum_{q=1}^{Q}\frac{\sqrt{(c_{e,q} - c_{t,q})^2}}{c_{e,q}} \times 100\%$$

If a given estimate of the model parameters does not provide a theoretical dispersion curve that is sufficiently close to the experimental curve, the shear wave velocity profile and (or) the layer structure needs to be updated manually by the user. The iteration procedure is terminated when ϵ has reached an acceptably small value, i.e., when $\epsilon < \epsilon_{max}$, where ϵ_{max} is the maximum allowed misfit. A maximum misfit of 2.0%–5.0% is commonly used by the authors. In the field tests presented later in the paper, the maximum misfit was specified as 2.0%. It should, however, be noted that the suggested range for the maximum misfit, as computed by eq. (16), is solely based on the authors' experience and may not be applicable in all cases.

The results of the inversion analysis are provided in the form of experimental and theoretical dispersion curves, estimated shear wave velocity as a function of depth, and the time-average shear wave velocity, $V_{S,d}$, computed for different depths d (CEN 2004)

Fig. 11. Comparison of theoretical fundamental- and first higher-mode dispersion curves obtained by MASWaves and presented by Tokimatsu et al. (1992) and Tokimatsu (1997): (*a*) case 1, (*b*) case 2, and (*c*) case 3. [Colour online.]

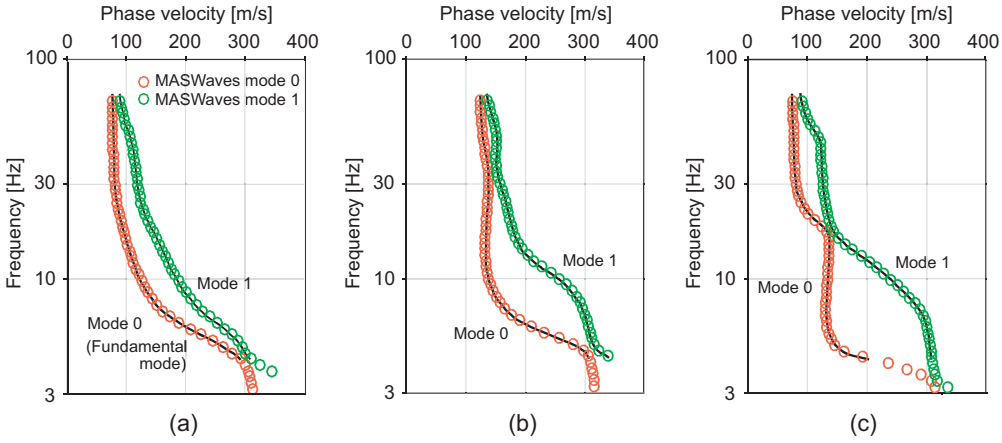

Fig. 12. Location of MASW test sites in south Iceland (map is based on data from the National Land Survey of Iceland). [Colour online.]

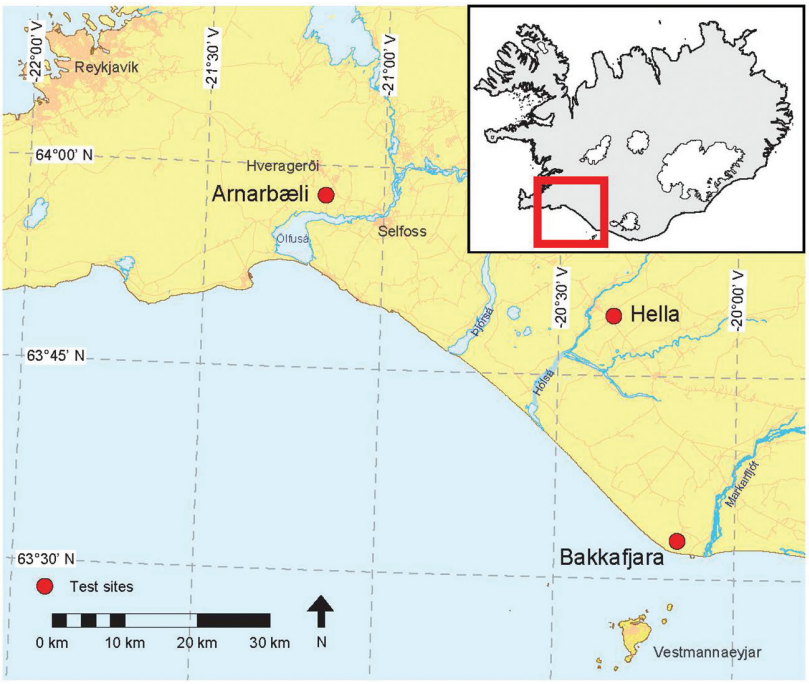

$$V_{S,d} = \frac{d}{\sum_{j=1}^{M} \frac{h_j}{\beta_j}} \quad (17)$$

where β_j and h_j denote the shear wave velocity and the thickness of the jth layer, respectively, for a total of M layers. If the estimated shear wave velocity profile goes down to a depth less than d, the profile is extrapolated using the half-space velocity (Fig. 8) down to depth d.

Challenges associated with the inversion analysis

For this paper, a manual (trial-and-error) inversion was used, i.e., the parameters of the initially estimated soil layer model were gradually adjusted to minimize the misfit between the experimental and theoretical dispersion curves. On one hand, a manual search is to a certain extent operator-dependent and requires a certain experience to achieve an acceptable fit within a reasonable amount of time. On the other hand, a manual search can represent the only viable approach if automatic local or global search algorithms fail to converge (Foti et al. 2015).

The goal of the inversion analysis is to obtain a shear wave velocity profile that realistically represents the characteristics of the test site. The inverse problem faced during this stage of the analysis is by nature ill-posed, nonlinear, mix-determined, and nonunique, i.e., multiple significantly different shear wave velocity profiles can provide theoretical dispersion curves that correspond similarly well (provide comparable misfits) to the measured data (Cox and Teague 2016; Foti et al. 2015). Hence, when available, a priori information about the test site should be used to constrain the inversion process to some extent and aid the selection of realistic shear wave velocity profiles. In cases where such data are not available, the operator must decide blindly the number of layers, credible ranges for the required inversion parameters (layer thicknesses and shear wave velocity values for each layer),

Table 4. Overview of site characteristics, test configuration, and analysis results at the Arnarbæli, Bakkafjara, and Hella test sites in south Iceland.

	Arnarbæli	Bakkafjara	Hella
Site characteristics			
Soil type	Holocene glaciofluvial sand	Modern littoral sand	Late-glacial (slightly) cemented aeolian silty sand
USCS classification	SW-SM*	SW†	—
Location of groundwater table	At surface‡	At 4 m depth§	—
Mass density, ρ (kg/m^3)	—	1850	2200
Saturated mass density, ρ_{sat} (kg/m^3)	1850*	2000	—
Poisson's ratio, ν	—	0.35	0.35
Field measurements			
Month/year of MASW field test	09/2013, 08/2014, 07/2015	08/2014	07/2015
Number of geophones, N	24	24	24
Receiver spacing, dx (m)	1.0	2.0	1.0
Source offset, x_1 (m)	10.0	15.0	10.0
Sampling rate, f_s (Hz)	1000	1000	1000
Recording time, T (s)	1.2	1.2	1.2
Dispersion analysis			
Frequency range for fundamental-mode dispersion curve (Hz)	7.5–22.5	5.8–33.3	15.7–60.3
Inversion analysis			
Misfit between theoretical and experimental curves, ϵ (%)	1.8	1.8	1.5
Maximum misfit, ϵ_{max} (%)	2.0	2.0	2.0
Time-average shear wave velocity of the uppermost 30 m, $V_{S,30}$ (m/s)	204	218	558
Soil classification (EC8)‖	C	C	B

Note: USCS, Unified Soil Classification System.
*Green et al. (2012).
†Bessason and Erlingsson (2011).
‡Olafsdottir et al. (2015).
§Olafsdottir et al. (2016).
‖CEN (2004).

and the location of the groundwater table. The layering parameterization plays a critical role in the inversion analysis and has been shown to critically affect its outcome (Di Giulio et al. 2012; Cox and Teague 2016). An inappropriate parameterization can result in either an overly simplistic or complicated shear wave velocity profile that, despite a low misfit value, does not correctly represent the characteristics of the test site. As a countermeasure it is recommended to try multiple parameterizations to increase the likelihood of obtaining a realistic shear wave velocity profile and to evaluate the uncertainty associated with those profiles (Cox and Teague 2016).

Validation of the theoretical dispersion curve computations

The ability of MASWaves Inversion to compute theoretical dispersion curves has been verified by comparison with the software WinSASW (version 1.2; UTAustin 1992) and results presented by Tokimatsu et al. (1992) and Tokimatsu (1997).

Two sets of earth model parameters, both used previously for generation of synthetic surface wave data in references (see Tables 1 and 2), are used here as examples of comparison of theoretical fundamental-mode dispersion curves obtained by MASWaves Inversion and WinSASW (version 1.2). Both soil layer models (i.e., cases A and B) are normally dispersive without strong velocity contrasts and thus represent sites where the fundamental mode of Rayleigh wave propagation is expected to prevail.

The theoretical fundamental-mode dispersion curves were computed for the same wavelengths in the range of 0–80 m. In WinSASW, the two-dimensional analysis option was used for computation of the curves. For application of MASWaves, the testing phase velocity increment (Δc_T) was specified as 1 m/s. In both cases, the agreement between the two computational methods was good (Fig. 10).

For further confirmation of the ability of MASWaves Inversion to separate fundamental- and higher-mode dispersion curves, as well as to comply with more complex layering, the program was tested on three additional soil layer modes, all used previously by Tokimatsu et al. (1992) and Tokimatsu (1997). The three four-layer models, referred to as cases 1, 2, and 3, are listed in Table 3. In case 1, the shear wave velocity (stiffness) increases with increasing depth. The stiffness of the soil layers varies more irregularly in cases 2 and 3, i.e., a stiff surface layer is present in case 2 and a stiff layer is located between two softer layers in case 3. Hence, in cases 2 and 3, the higher modes play a more significant role (Tokimatsu et al. 1992; Tokimatsu 1997).

Using MASWaves, the theoretical fundamental- and first higher-mode dispersion curves were computed for frequencies in the range of 3–70 Hz using a testing phase velocity increment (Δc_T) of 0.1 m/s. The comparison of the fundamental- and first higher-mode dispersion curves obtained by MASWaves and those presented by Tokimatsu et al. (1992) and Tokimatsu (1997) is illustrated in Fig. 11. In Fig. 11, the curves obtained by MASWaves are indicated by circles, whereas the dispersion curves of Tokimatsu et al. (1992) and Tokimatsu (1997) are shown with black lines. In all three cases, the agreement between the fundamental- and first higher-mode dispersion curves obtained by MASWaves and Tokimatsu et al. (1992) and Tokimatsu (1997) was good.

Field tests

MASW measurements were conducted at three locations in south Iceland — Arnarbæli, Bakkafjara, and Hella — between 2013 and 2015 (see Fig. 12 and Table 4). At the three test sites, surface wave records were collected using a linear array of 24 vertical geophones (GS-11D from Geospace Technologies, Houston, Texas) with a natural frequency of 4.5 Hz and a critical damp-

Fig. 13. 24-channel surface wave record acquired at (*a*) Arnarbæli test site with dx = 1 m and x_1 = 10 m (2015 measurement), (*d*) Bakkafjara test site with dx = 2 m and x_1 = 15 m, and (*g*) Hella test site with dx = 1 m and x_1 = 10 m. Dispersion image for (*b*) Arnarbæli site, (*e*) Bakkafjara site, and (*h*) Hella site. Fundamental-mode dispersion curve and upper- and lower-bound curves for (*c*) Arnarbæli site, (*f*) Bakkafjara site, and (*i*) Hella site. [Colour online.]

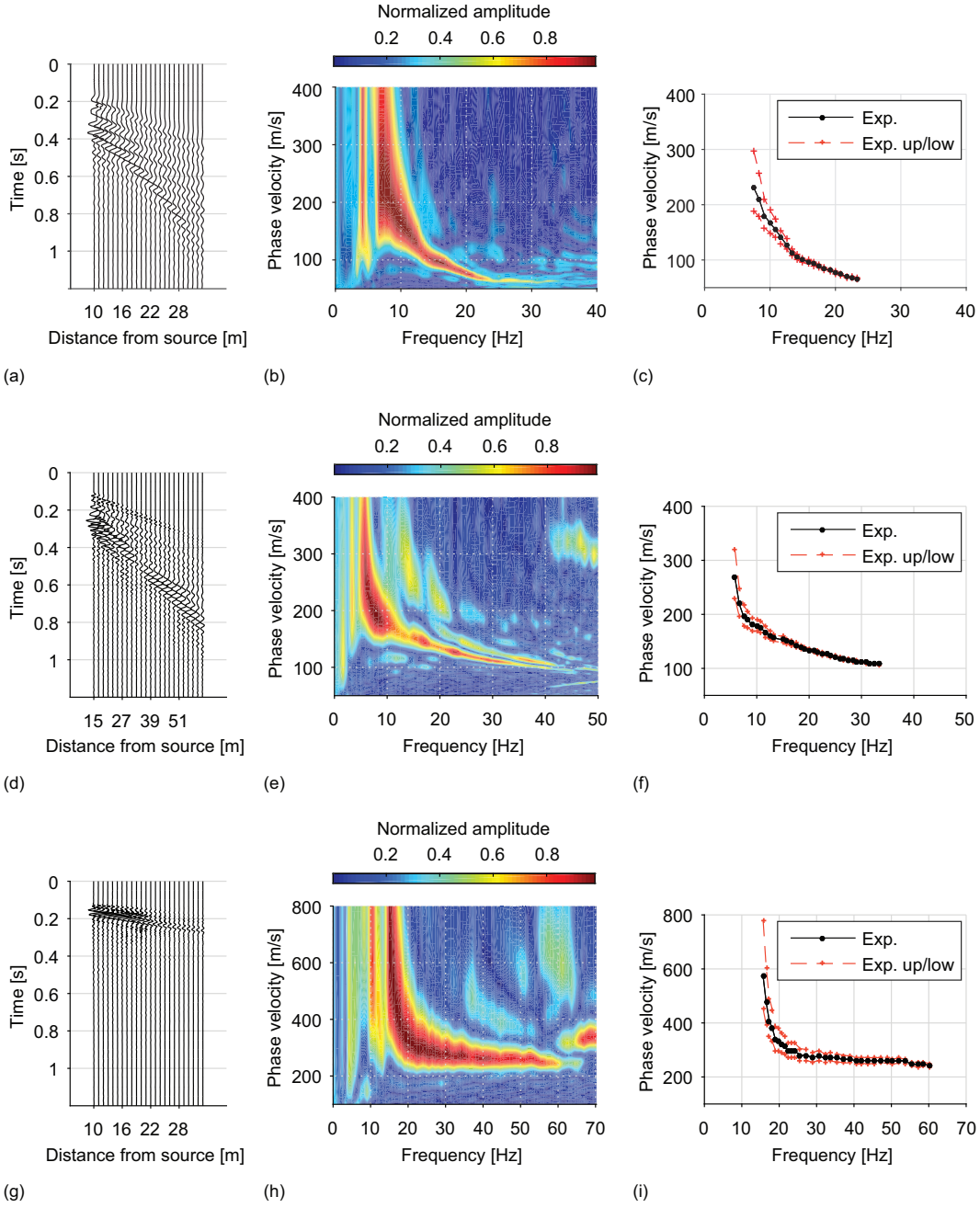

ing ratio of 0.5. The geophones were connected to two data acquisition cards (NI USB-6218 from National Instruments, Austin, Texas) and a computer equipped with a customized multichannel data-acquisition software. A 6.3 kg sledgehammer was used as an impact source in all cases. A summary of the main parameters related to the field measurements is provided in Table 4.

Figures 13*a*, 13*d*, and 13*g* show velocity time series acquired at the test sites at Arnarbæli, Bakkafjara, and Hella, respectively. The corresponding dispersion images are provided in Figs. 13*b*, 13*e*, and 13*h*. The fundamental-mode dispersion curves that were extracted from the spectra are shown in Figs. 13*c*, 13*f*, and 13*i*, respectively. The frequency ranges at which the fundamental mode could be identified in each case are provided in Table 4. The upper- and lower-bound curves shown in Figs. 13*c*, 13*f*, and 13*i* correspond to 95% of the identified fundamental-mode peak spectral amplitude value ($A_{s,max}$) at each frequency.

It must be underlined that identification of the fundamental-mode dispersion curve is not a straightforward task in all cases. Irregularities in the suspected fundamental-mode high-amplitude band, e.g., abrupt bends or jumps to higher or lower phase velocities at certain frequencies, might indicate that the peak energy is not following the fundamental-mode over the entire frequency

Fig. 14. (*a*) Comparison of experimental and theoretical dispersion curves for the Arnarbæli, Bakkafjara, and Hella test sites. (*b*) Estimated shear wave velocity profiles for the test sites. [Colour online.]

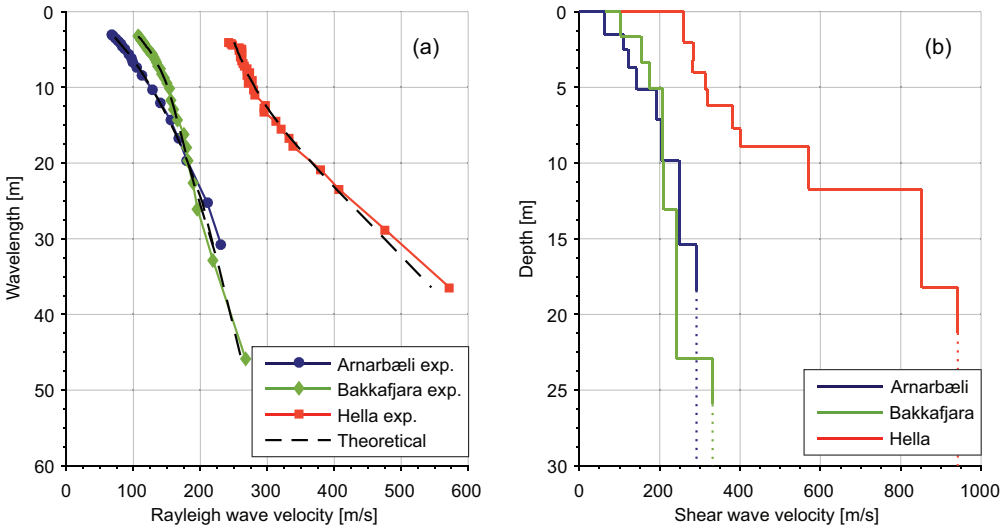

range (see also Fig. 4*a*). The dispersion images in Figs. 13*b*, 13*e*, and 13*h*, and the corresponding dispersion curves in Figs. 13*c*, 13*f*, and 13*i* are based on a single surface wave record in each case. Relying on a dispersion curve identified based on a single record is not always advisable. Furthermore, the configuration of the measurement profile can have a substantial effect on the energy distribution represented in the dispersion image and consequently the uncertainty associated with the dispersion curve identification and extraction. Hence, based on the authors' experience, combined or repeated analysis of data acquired by using several different measurement profile configurations should be carried out to help confident identification of the fundamental-mode dispersion curve.

Results of the inversion analysis of the data acquired at the Arnarbæli, Bakkafjara, and Hella test sites are illustrated in Fig. 14. The misfit between the experimental dispersion curves observed at each site and the optimum theoretical curves (Fig. 14*a*), evaluated according to eq. (16), is in all cases less than 2%. The time-average shear wave velocity of the uppermost 30 m at the three test sites and their corresponding soil classification group according to Eurocode 8 is provided in Table 4.

Repeatability of the MASW analysis

At the Arnarbæli test site, surface wave data were collected in three separate field tests in September 2013, August 2014, and July 2015. The test configuration, i.e., the number of receivers, the receiver spacing, and the source offset, was the same in all cases (see Table 4).

Figure 15*a* shows a comparison of experimental dispersion curves for the Arnarbæli test site, evaluated based on surface wave records acquired in 2013, 2014, and 2015. The upper- and lower-bound curves shown in Fig. 15*a* correspond to 95% of the identified fundamental-mode peak spectral amplitude value at each frequency. The shear wave velocity profiles obtained by inversion of each experimental curve are provided in Fig. 15*b*. The shear wave velocity profiles are compared in terms of the time-average shear wave velocities of the uppermost 5, 10, 20, and 30 m in Table 5. The results provided in Fig. 15 and Table 5 indicate that the agreement between the three measurements is good, illustrating the consistency of the methodology and the software that has been developed.

Comparison of MASW and SASW measurement results

SASW measurements were carried out in 2009 at Bakkafjara (Bessason and Erlingsson 2011) approximately 0.5 km east of the site where the MASW field data were acquired. Bakkafjara is a long sandy beach area that can be considered to be quite uniform.

Figure 16 shows comparison of the experimental dispersion curves estimated based on the 2009 SASW measurements and the 2014 MASW measurements. The SASW dispersion curve (SASW mean in Fig. 16) was obtained by adding up experimental dispersion curves computed for multiple receiver pairs within 1/3 octave wavelength intervals. The upper- and lower-bound SASW dispersion curves correspond to plus–minus one standard deviation of the mean curve. The upper- and lower-bound MASW curves correspond to 95% of the identified fundamental-mode peak spectral amplitude value at each frequency. The results presented in Fig. 16 indicate that the SASW dispersion curve agrees well with the MASW dispersion curve.

Conclusions

This paper presents the first version of a new open-source software, MASWaves, for processing and analysing multichannel surface wave records using the MASW method. The software consists of two main parts: a tool for dispersion analysis (MASWaves Dispersion) and a tool for inversion analysis (MASWaves Inversion). The software can be downloaded free of charge along with a user guide and sample data at masw.hi.is.

The aim of the dispersion analysis is to identify and extract experimental Rayleigh wave dispersion curves from the recorded multichannel surface wave data. Computations are carried out utilizing the phase shift method (Park et al. 1998). The phase shift method provides visualization of the dispersion properties of all types of waves contained in the acquired data in the form of a two- or three-dimensional dispersion image (phase velocity spectra), from which the Rayleigh wave dispersion curve(s) are identified based on the spectral maxima. Upper and lower boundaries for the extracted dispersion curve(s) can be obtained and visualized in either the frequency-phase velocity or the phase velocity-wavelength domain. Experimental fundamental- and higher-mode dispersion curves obtained by MASWaves Dispersion were compared with results acquired using the open-source software Geopsy. The agreement of the estimated dispersion curves was in all cases good, confirming the precision of the new software and its ability

Fig. 15. (*a*) Comparison of experimental dispersion curves for Arnarbæli test site acquired based on three separate field tests in September 2013, August 2014, and July 2015. (*b*) Comparison of shear wave velocity profiles for Arnarbæli test site evaluated based on data acquired in 2013, 2014, and 2015. [Colour online.]

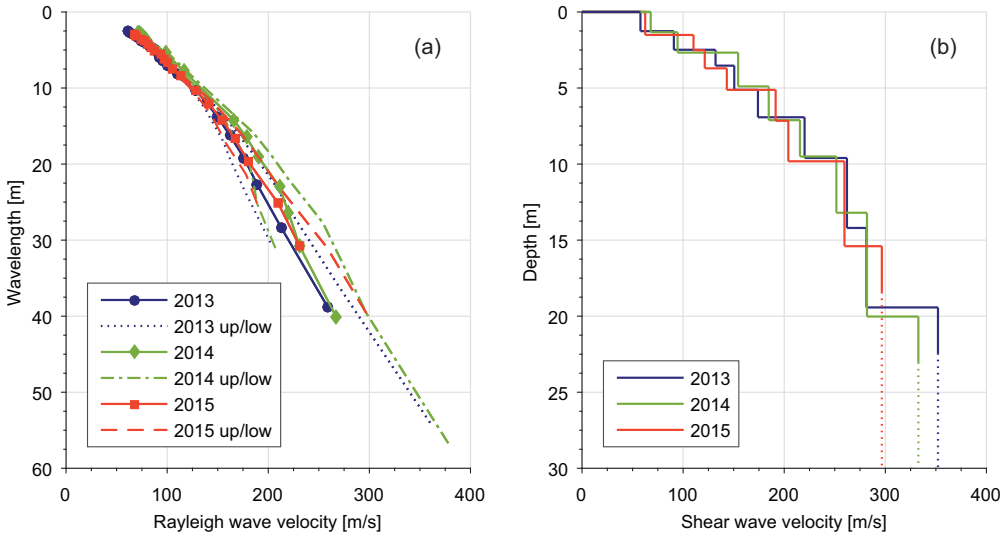

Table 5. Time-average shear wave velocity of the uppermost 5, 10, 20, and 30 m at the Arnarbæli test site evaluated based on data acquired in 2013, 2014, and 2015.

Year of data acquisition	$V_{S,5}$ (m/s)	$V_{S,10}$ (m/s)	$V_{S,20}$ (m/s)	$V_{S,30}$ (m/s)
2013	94	128	175	211
2014	103	137	182	214
2015	96	129	176	204

Fig. 16. Comparison of experimental dispersion curves obtained at Bakkafjara test site by the SASW and MASW methods. [Colour online.]

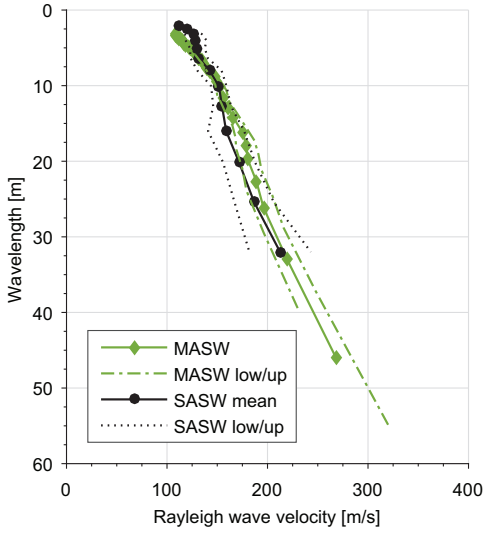

to separate fundamental- and higher-mode experimental dispersion curves.

Determination of the experimental Rayleigh wave dispersion curve is a critical stage in the application of MASW. The operator should be aware that the most obvious coherent high-amplitude band of the dispersion image cannot be assumed to provide the fundamental-mode dispersion curve in all cases. Due to the geology of the test site (e.g., the presence of a stiff surface layer, a stiff layer sandwiched between two softer layers or abrupt increase in stiffness with depth), higher modes can play a significant role over certain frequency ranges, thus violating the fundamental-mode assumption. In such cases, misidentification of mode numbers and (or) superposition of dispersion data from multiple modes is likely to occur. Mistaking a higher mode or an apparent dispersion curve as the fundamental-mode dispersion curve can cause severe errors in the subsequent inversion analysis.

The configuration of the measurement profile has been shown to affect the resolution and the viable frequency range of the dispersion image. A longer receiver spread is, in general, preferable to improve the spectral resolution, but risks significant lateral variations along the geophone array, attenuation of higher-frequency surface wave components, and spatial aliasing. Hence, based on the authors' experience, combined or repeated analysis of data acquired by using several different measurement profile configurations can help in correctly identifying the fundamental-mode dispersion curve without reducing the investigation depth range of the survey.

The inversion analysis involves obtaining a shear wave velocity profile by inversion of the experimental fundamental-mode dispersion curve, assuming a plane-layered elastic earth model. The inversion analysis tool, MASWaves Inversion, consists of two main components. First, a mathematical model to compute theoretical dispersion curves using the stiffness matrix method of Kausel and Roësset (1981) and, second, an algorithm to evaluate the misfit between the experimental and theoretical curves and to allow the user to update the set of model parameters. The theoretical dispersion curve computations of MASWaves Inversion were validated by comparison to results obtained by the software WinSASW (version 1.2) and results presented by Tokimatsu et al. (1992) and Tokimatsu (1997).

However, the inverse problem faced in the inversion analysis is inherently nonunique, i.e., multiple drastically different shear wave velocity profiles can provide theoretical dispersion curves that correspond similarly well to the experimental curve. An unsuitable layering parameterization can result in an "optimal" shear wave velocity profile that does not realistically represent the subsurface conditions. To minimize the potentially adverse effect of the layering parameterization and, hence, increase the potential of obtaining a realistic shear wave velocity profile, in-

vestigating multiple different parameterizations during the inversion analysis is recommended (Cox and Teague 2016).

The new software has been used to obtain site-specific shear wave velocity profiles based on MASW field data acquired at three sites with different stiffness characteristics in south Iceland: Arnarbæli, Bakkafjara, and Hella. At the Arnarbæli test site, data were collected in three separate field test campaigns to confirm the repeatability of the analysis and the consistency of the new software. The agreement between the three measurements was good. Moreover, the results of the MASW analysis at Bakkafjara were compared with results of SASW measurements previously carried out at the site. Good agreement between the SASW and the MASW dispersion curves was observed, further validating the performance of the dispersion analysis tool.

Acknowledgements

The project has been supported financially by grants from the University of Iceland Research Fund, the Icelandic Road and Coastal Administration, and the Energy Research Fund of the National Power Company of Iceland.

References

Abo-Zena, A. 1979. Dispersion function computations for unlimited frequency values. Geophysical Journal of the Royal Astronomical Society, **58**(1): 91–105. doi:10.1111/j.1365-246X.1979.tb01011.x.

Aki, K., and Richards, P.G. 1980. Quantitative seismology: theory and methods. Vol. 1. W.H. Freeman and Co., San Francisco, Calif.

Asten, M.W. 2006. On bias and noise in passive seismic data from finite circular array data processed using SPAC methods. Geophysics, **71**(6): V153–V162. doi:10.1190/1.2345054.

Bessason, B., and Erlingsson, S. 2011. Shear wave velocity in surface sediments. Jökull, **61**: 51–64.

Buchen, P.W., and Ben-Hador, R. 1996. Free-mode surface-wave computations. Geophysical Journal International, **124**(3): 869–887. doi:10.1111/j.1365-246X.1996.tb05642.x.

CEN. 2004. Eurocode 8: Design of structures for earthquake resistance – Part 1: General rules, seismic actions and rules for buildings. European Committee for Standardization (CEN), Brussels, Belgium.

Cox, B.R., and Teague, D.P. 2016. Layering ratios: a systematic approach to the inversion of surface wave data in the absence of a priori information. Geophysical Journal International, **207**: 422–438. doi:10.1093/gji/ggw282.

Dal Moro, G., Pipan, M., Forte, E., and Finetti, I. 2003. Determination of Rayleigh wave dispersion curves for near surface applications in unconsolidated sediments. *In* SEG Technical Program Expanded Abstracts of the Society of Exploration Geophysicists (SEG) International Exposition and 73rd Annual Meeting, Dallas, Tex., 26–31 October 2003. Society of Exploration Geophysicists, Tulsa, Okla. pp. 1247–1250. doi:10.1190/1.1817508.

Di Giulio, G., Cornou, C., Ohrnberger, M., Wathelet, M., and Rovelli, A. 2006. Deriving wavefield characteristics and shear-velocity profiles from two-dimensional small-aperture arrays analysis of ambient vibrations in a small-size alluvial basin, Colfiorito, Italy. Bulletin of the Seismological Society of America, **96**(5): 1915–1933. doi:10.1785/0120060119.

Di Giulio, G., Savvaidis, A., Ohrnberger, M., Wathelet, M., Cornou, C., Knapmeyer-Endrun, B., Renalier, F., Theodoulidis, N., and Bard, P.Y. 2012. Exploring the model space and ranking a best class of models in surface-wave dispersion inversion: Application at European strong-motion sites. Geophysics, **77**: B147–B166. doi:10.1190/geo2011-0116.1.

Foti, S., Lai, C.G., Rix, G.J., and Strobbia, C. 2015. Surface wave methods for near-surface site characterization. CRC Press, Taylor & Francis Group, Boca Raton, Fla.

Gao, L., Xia, J., Pan, Y., and Xu, Y. 2016. Reason and Condition for Mode Kissing in MASW Method. Pure and Applied Geophysics, **173**(5): 1627–1638. doi:10.1007/s00024-015-1208-5.

Garofalo, F., Foti, S., Hollender, F., Bard, P.-Y., Cornou, C., Cox, B.R., Ohrnberger, M., Sicilia, D., Asten, M., et al. 2016. InterPACIFIC project: comparison of invasive and non-invasive methods for seismic site characterization. Part I: Intra-comparison of surface wave methods. Soil Dynamics and Earthquake Engineering, **82**: 222–240. doi:10.1016/j.soildyn.2015.12.010.

Gazetas, G. 1991. Foundation vibrations. *In* Foundation engineering handbook. *Edited by* H.-Y. Fang. Van Nostrand Reinhold, New York. pp. 553–593.

Gouveia, F., Lopes, I., and Gomes, R.C. 2016. Deeper V_S profile from joint analysis of Rayleigh wave data. Engineering Geology, **202**: 85–98. doi:10.1016/j.enggeo.2016.01.006.

Green, R.A., Halldorsson, B., Kurtulus, A., Steinarsson, H., and Erlendsson, O. 2012. A unique liquefaction case study from the 29 May 2008, M_w6.3 Olfus earthquake, southwest Iceland. *In* Proceedings of the 15th World Conference on Earthquake Engineering, Lisbon, Portugal, 24–28 September 2012. The Portuguese Earthquake Engineering Community, Lisbon, Portugal.

Gucunski, N., and Woods, R.D. 1991. Use of Rayleigh Modes in interpretation of SASW test. *In* Proceedings of the Second International Conference on Recent Advances in Geotechnical Earthquake Engineering and Soil Dynamics, St. Louis, Mo., 11–15 March 1991. Paper No. 10.10.

Haskell, N.A. 1953. The dispersion of surface waves on multilayered media. Bulletin of the Seismological Society of America, **43**(1): 17–34.

Hobiger, M., Bard, P.-Y., Cornou, C., and Le Bihan, N. 2009. Single station determination of Rayleigh wave ellipticity by using the random decrement technique (RayDec). Geophysical Research Letters, **36**: L14303. doi:10.1029/2009GL038863.

Hobiger, M., Cornou, C., Wathelet, M., Di Giulio, G., Knapmeyer-Endrun, B., Renalier, F., Bard, P.-Y., Savvaidis, A., Hailemikael, S., et al. 2013. Ground structure imaging by inversions of Rayleigh wave ellipticity: sensitivity analysis and application to European strong-motion sites. Geophysical Journal International, **192**(1): 207–229. doi:10.1093/gji/ggs005.

Ivanov, J., Miller, R.D., and Tsoflias, G. 2008. Some practical aspects of MASW analysis and processing. *In* Proceedings of the 21st EEGC Symposium on the Application of Geophysics to Engineering and Environmental Problems, Philadelphia, Pa., 6–10 April 2008. pp. 1186–1198.

Kausel, E., and Roësset, J.M. 1981. Stiffness matrices for layered soils. Bulletin of the Seismological Society of America, **71**(6): 1743–1761.

Kennett, B.L.N. 1974. Reflections, rays, and reverberations. Bulletin of the Seismological Society of America, **64**(6): 1685–1696.

Kennett, B.L.N., and Kerry, N.J. 1979. Seismic waves in a stratified half space. Geophysical Journal International, **57**(3): 557–583. doi:10.1111/j.1365-246X.1979.tb06779.x.

Knopoff, L. 1964. A matrix method for elastic wave problems. Bulletin of the Seismological Society of America, **54**(1): 431–438.

Kramer, S.L. 1996. Geotechnical Earthquake Engineering. Prentice-Hall, Inc., Upper Saddle River, N.J.

Louie, J.N. 2001. Faster, better: shear-wave velocity to 100 meters depth from refraction microtremor arrays. Bulletin of the Seismological Society of America, **91**(2): 347–364. doi:10.1785/0120000098.

McMechan, G.A., and Yedlin, M.J. 1981. Analysis of dispersive waves by wave field transformation. Geophysics, **46**(6): 869–874. doi:10.1190/1.1441225.

Menke, W. 1979. Comment on 'Dispersion function computations for unlimited frequency values' by Anas Abo-Zena. Geophysical Journal of the Royal Astronomical Society, **59**(2): 315–323. doi:10.1111/j.1365-246X.1979.tb06769.x.

Nazarian, S., Stokoe, K.H., II, and Hudson, W.R. 1983. Use of spectral analysis of surface waves method for determination of moduli and thicknesses of pavement systems. Transportation Research Record, **930**: 38–45.

Olafsdottir, E.A. 2016. Multichannel analysis of surface waves for assessing soil stiffness. M.Sc. thesis, Faculty of Civil and Environmental Engineering, University of Iceland, Reykjavík, Iceland. Available from http://hdl.handle.net/1946/23646.

Olafsdottir, E.A., Bessason, B., and Erlingsson, S. 2015. MASW for assessing liquefaction of loose sites. *In* Proceedings of the 16th European Conference on Soil Mechanics and Geotechnical Engineering, Edinburgh, UK, 13–17 September 2015. ICE Publishing, London, UK. pp. 2431–2436.

Olafsdottir, E.A., Erlingsson, S., and Bessason, B. 2016. Effects of measurement profile configuration on estimation of stiffness profiles of loose post glacial sites using MASW. *In* Proceedings of the 17th Nordic Geotechnical Meeting, Reykjavik, Iceland, 25–28 May 2016. The Icelandic Geotechnical Society, Reykjavik, Iceland. pp. 327–336.

Park, C.B. 2011. Imaging dispersion of MASW data – full vs. selective offset scheme. Journal of Environmental and Engineering Geophysics, **16**(1): 13–23. doi:10.2113/JEEG16.1.13.

Park, C.B., and Carnevale, M. 2010. Optimum MASW survey–revisit after a decade of use. *In* Proceedings of GeoFlorida 2010: Advances in Analysis, Modeling & Design, Geo-Institute Annual Meeting Conference Proceedings, West Palm Beach, Fla., 20–24 February 2010. American Society of Civil Engineers, Reston, Va. pp. 1303–1312. doi:10.1061/41095(365)130.

Park, C.B., and Miller, R.D. 2008. Roadside passive multichannel analysis of surface waves (MASW). Journal of Environmental & Engineering Geophysics, **13**(1): 1–11. doi:10.2113/JEEG13.1.1.

Park, C.B., Miller, R.D., and Xia, J. 1998. Imaging dispersion curves of surface waves on multi-channel record. *In* SEG Technical Program Expanded Abstracts of the Society of Exploration Geophysicists (SEG) International Exposition and 68th Annual Meeting, New Orleans, La., 13–18 September 1998. Society of Exploration Geophysicists, Tulsa, Okla., pp. 1377–1380. doi:10.1190/1.1820161.

Park, C.B., Miller, R.D., and Xia, J. 1999. Multichannel analysis of surface waves. Geophysics, **64**(3): 800–808. doi:10.1190/1.1444590.

Park, C.B., Miller, R.D., and Miura, H. 2002. Optimum field parameters of an MASW survey. [Expanded abstract.] *In* Proceedings of the 6th SEG-J International Symposium, Tokyo, Japan, 22–23 May 2002.

Park, C.B., Miller, R.D., Rydén, N., Xia, J., and Ivanov, J. 2005. Combined use of active and passive surface waves. Journal of Environmental and Engineering Geophysics, **10**(3): 323–334. doi:10.2113/JEEG10.3.323.

Park, C.B., Miller, R.D., Xia, J., and Ivanov, J. 2007. Multichannel analysis of surface waves (MASW)–active and passive methods. The Leading Edge, **26**(1): 60–64. doi:10.1190/1.2431832.

Ryden, N., Park, C.B., Ulriksen, P., and Miller, R.D. 2004. Multimodal approach to

seismic pavement testing. Journal of Geotechnical and Geoenvironmental Engineering, **130**(6): 636–645. doi:10.1061/(ASCE)1090-0241(2004)130:6(636).
Schwab, F. 1970. Surface-wave dispersion computations: Knopoff's method. Bulletin of the Seismological Society of America, **60**(5): 1491–1520.
Socco, L.V., Foti, S., and Boiero, D. 2010. Surface-wave analysis for building near-surface velocity models – established approaches and new perspectives. Geophysics, **75**(5): 75A83–75A102. doi:10.1190/1.3479491.
Thomson, W.T. 1950. Transmission of elastic waves through a stratified solid medium. Journal of Applied Physics, **21**(2): 89–93. doi:10.1063/1.1699629.
Tokimatsu, K. 1997. Geotechnical site characterization using surface waves. *In* Proceedings of IS-Tokyo, the First International Conference on Earthquake Geotechnical Engineering, Tokyo, Japan, 14–16 November 1995. Balkema, Rotterdam, the Netherlands. Vol. 3, pp. 1333–1368.
Tokimatsu, K., Tamura, S., and Kojima, H. 1992. Effects of multiple modes on Rayleigh wave dispersion characteristics. Journal of Geotechnical Engineering, **118**(10): 1529–1543. doi:10.1061/(ASCE)0733-9410(1992)118:10(1529).
UTAustin. 1992. WinSASW. Data reduction program for Spectral-Analysis-of-Surface-Wave (SASW) tests. Ver. 1.2. User's guide. The University of Texas at Austin (UTAustin), Austin, Tex.
Wathelet, M., Jongmans, D., Ohrnberger, M., and Bonnefoy-Claudet, S. 2008. Array performances for ambient vibrations on a shallow structure and consequences over V_S inversion. Journal of Seismology, **12**(1): 1–19. doi:10.1007/s10950-007-9067-x.
Xia, J. 2014. Estimation of near-surface shear-wave velocities and quality factors using multichannel analysis of surface-wave methods. Journal of Applied Geophysics, **10**: 140–151. doi:10.1016/j.jappgeo.2014.01.016.
Xia, J., Miller, R.D., and Park, C.B. 1999. Estimation of near-surface shear-wave velocity by inversion of Rayleigh waves. Geophysics, **64**(3): 691–700. doi:10.1190/1.1444578.
Xia, J., Miller, R.D., Park, C.B., Hunter, J.A., Harris, J.B., and Ivanov, J. 2002. Comparing shear-wave velocity profiles inverted from multichannel surface wave with borehole measurements. Soil Dynamics and Earthquake Engineering, **22**(3): 181–190. doi:10.1016/S0267-7261(02)00008-8.
Xia, J., Miller, R.D., Park, C.B., and Tian, G. 2003. Inversion of high frequency surface waves with fundamental and higher modes. Journal of Applied Geophysics, **52**(1): 45–57. doi:10.1016/S0926-9851(02)00239-2.
Xia, J., Xu, Y., and Miller, R.D. 2007. Generating an image of dispersive energy by frequency decomposition and slant stacking. Pure and Applied Geophysics, **164**(5): 941–956. doi:10.1007/s00024-007-0204-9.
Yilmaz, Ö. 1987. Seismic data processing. Society of Exploration Geophysicists, Tulsa, Okla.
Yoon, S., and Rix, G.J. 2009. Near-field effects on array-based surface wave methods with active sources. Journal of Geotechnical and Geoenvironmental Engineering, **135**(3): 399–406. doi:10.1061/(ASCE)1090-0241(2009)135:3(399).
Zhang, S.X., and Chan, L.S. 2003. Possible effects of misidentified mode number on Rayleigh wave inversion. Journal of Applied Geophysics, **53**(1): 17–29. doi:10.1016/S0926-9851(03)00014-4.

List of symbols

$A_j(\omega)$	amplitude spectrum of $\tilde{u}(x_j, \omega)$
A_s	summed (slant-stacked) amplitude
$A_{s,max}$	maximum summed (slant-stacked) amplitude
a	user-defined coefficient
c	Rayleigh wave phase velocity
$c_{e,q}$	experimental Rayleigh wave phase velocity
c_T	testing Rayleigh wave phase velocity
$c_{T,min}$, $c_{T,max}$	minimum and maximum Rayleigh wave testing phase velocities
$c_{t,q}$	theoretical Rayleigh wave phase velocity
$c(\omega)$	Rayleigh wave phase velocity at frequency ω
d	depth
dx	receiver spacing
F_R	dispersion function
f	frequency
f_s	sampling rate
G_{max}	small-strain shear modulus
h	layer thickness
h_j	thickness of jth layer
i	$i^2 = -1$
j, q	indices
$\mathbf{K}$	system stiffness matrix
$\mathbf{K}_{e,j}$	element stiffness matrix of jth layer
k	wave number
$k_{t,q}$	theoretical Rayleigh wave wave number
L	length of receiver spread
L_T	length of measurement profile
M	number of layers from the surface to depth d
N	number of receivers
n	number of finite thickness layers
p	slowness
$\boldsymbol{p}$	system external load vector
p_A	percentage
$\boldsymbol{p}_{e,j}$	element external load vector of jth layer
Q	number of data points in an experimental dispersion curve
T	recording time
t	time
$\boldsymbol{u}$	system displacement vector
$\boldsymbol{u}_{e,j}$	element displacement vector of jth layer
$u(x_j, t)$	multichannel surface wave record
$\tilde{u}(x_j, \omega)$	Fourier transformed multichannel surface wave record
$\tilde{u}_{norm}(x_j, \omega)$	Fourier transformed multichannel surface wave record normalized in the offset and frequency dimensions
$V_{S,d}$	time-average shear wave velocity of the uppermost d metres
x	horizontal coordinate
x_1	source offset
x_j	distance from the impact load point to receiver j
z	vertical coordinate
z_j	z-coordinate at the top of jth layer
z_{j+1}	z-coordinate at the bottom of jth layer
z_{max}	maximum investigation depth
α	compressional wave velocity
α_j	compressional wave velocity of jth layer
β	shear wave velocity
β_j	shear wave velocity of jth layer
Δc_T	testing phase velocity increment
ϵ	misfit
ϵ_{max}	maximum misfit
λ	wavelength
$\lambda_{e,q}$	experimental Rayleigh wave wavelength
λ_{max}	maximum wavelength
$\lambda_{t,q}$	theoretical Rayleigh wave wavelength
ν	Poisson's ratio
ν_j	Poisson's ratio of jth layer
ρ	mass density
ρ_j	mass density of jth layer
ρ_{sat}	saturated mass density
$\Phi_j(\omega)$	phase spectrum of $\tilde{u}(x_j, \omega)$
$\Phi_{T,j}$	testing angular wave number
ω	angular frequency

Appendix A. Stiffness matrix method

The components of the element stiffness matrix $\mathbf{K}_{e,j}$ for layers $j = 1, \ldots, n$ are

$$
\begin{aligned}
\kappa_{11,j} &= \frac{k\rho_j c^2}{D_j}\left[s_j^{-1}\cosh(kr_jh_j)\sinh(ks_jh_j) - r_j\sinh(kr_jh_j)\cosh(ks_jh_j)\right]\\
\kappa_{12,j} &= \frac{k\rho_j c^2}{D_j}[\cosh(kr_jh_j)\cosh(ks_jh_j) - r_js_j\sinh(kr_jh_j)\sinh(ks_jh_j) - 1]\\
&\qquad - k\rho_j\beta_j^2(1+s_j^2)\\
\kappa_{13,j} &= \frac{k\rho_j c^2}{D_j}\left[r_j\sinh(kr_jh_j) - s_j^{-1}\sinh(ks_jh_j)\right]\\
\kappa_{14,j} &= \frac{k\rho_j c^2}{D_j}[-\cosh(kr_jh_j) + \cosh(ks_jh_j)]\\
\kappa_{21,j} &= \kappa_{12,j}\\
\kappa_{22,j} &= \frac{k\rho_j c^2}{D_j}\left[r_j^{-1}\sinh(kr_jh_j)\cosh(ks_jh_j) - s_j\cosh(kr_jh_j)\sinh(ks_jh_j)\right]\\
\kappa_{23,j} &= -\kappa_{14,j}\\
\kappa_{24,j} &= \frac{k\rho_j c^2}{D_j}\left[-r_j^{-1}\sinh(kr_jh_j) + s_j\sinh(ks_jh_j)\right]\\
\kappa_{31,j} &= \kappa_{13,j}\\
\kappa_{32,j} &= \kappa_{23,j} = -\kappa_{14,j}\\
\kappa_{33,j} &= \kappa_{11,j}\\
\kappa_{34,j} &= -\kappa_{12,j}\\
\kappa_{41,j} &= \kappa_{14,j}\\
\kappa_{42,j} &= \kappa_{24,j}\\
\kappa_{43,j} &= -\kappa_{21,j} = -\kappa_{12,j}\\
\kappa_{44,j} &= \kappa_{22,j}
\end{aligned}
\tag{A1}
$$

where r_j and s_j are obtained as

$$r_j = \sqrt{1 - \frac{c^2}{\alpha_j^2}} \text{ and } s_j = \sqrt{1 - \frac{c^2}{\beta_j^2}} \tag{A2}$$

and

$$D_j = 2[1 - \cosh(kr_jh_j)\cosh(ks_jh_j)] + \left(\frac{1}{r_js_j} + r_js_j\right)\sinh(kr_jh_j)\sinh(ks_jh_j) \tag{A3}$$

The components of the half-space element stiffness matrix $\mathbf{K}_{e,n+1}$ are

$$\begin{aligned}
\kappa_{11,n+1} &= k\rho_{n+1}\beta_{n+1}^2\frac{r_{n+1}(1 - s_{n+1}^2)}{1 - r_{n+1}s_{n+1}} \\
\kappa_{12,n+1} &= k\rho_{n+1}\beta_{n+1}^2\frac{1 - s_{n+1}^2}{1 - r_{n+1}s_{n+1}} - 2k\rho_{n+1}\beta_{n+1}^2 \\
\kappa_{21,n+1} &= \kappa_{12,n+1} \\
\kappa_{22,n+1} &= k\rho_{n+1}\beta_{n+1}^2\frac{s_{n+1}(1 - s_{n+1}^2)}{1 - r_{n+1}s_{n+1}}
\end{aligned} \tag{A4}$$

The system stiffness matrix $\mathbf{K}$ is assembled from the element stiffness matrices at the common layer interfaces, i.e.,

$$\mathbf{K} = \begin{bmatrix}
\mathbf{K}_{11,1} & \mathbf{K}_{12,1} & & & & & \\
\mathbf{K}_{21,1} & \mathbf{K}_{22,1} + \mathbf{K}_{11,2} & \mathbf{K}_{12,2} & & & & \\
 & \mathbf{K}_{21,2} & \mathbf{K}_{22,2} + \mathbf{K}_{11,3} & \mathbf{K}_{12,3} & & & \\
 & & \ddots & \ddots & \ddots & & \\
 & & & \mathbf{K}_{21,n-1} & \mathbf{K}_{22,n-1} + \mathbf{K}_{11,n} & \mathbf{K}_{12,n} & \\
 & & & & \mathbf{K}_{21,n} & \mathbf{K}_{22,n} + \mathbf{K}_{e,n+1}
\end{bmatrix} \tag{A5}$$

where $\mathbf{K}_{11,j}$, $\mathbf{K}_{12,j}$, $\mathbf{K}_{21,j}$, and $\mathbf{K}_{22,j}$ are the 2 × 2 submatrices of the element stiffness matrix for the jth layer

$$\mathbf{K}_{e,j} = \begin{bmatrix} \mathbf{K}_{11,j} & \mathbf{K}_{12,j} \\ \mathbf{K}_{21,j} & \mathbf{K}_{22,j} \end{bmatrix} = \begin{bmatrix} \kappa_{11,j} & \kappa_{12,j} & \kappa_{13,j} & \kappa_{14,j} \\ \kappa_{21,j} & \kappa_{22,j} & \kappa_{23,j} & \kappa_{24,j} \\ \kappa_{31,j} & \kappa_{32,j} & \kappa_{33,j} & \kappa_{34,j} \\ \kappa_{41,j} & \kappa_{42,j} & \kappa_{43,j} & \kappa_{44,j} \end{bmatrix} \quad j = 1, \ldots, n \tag{A6}$$

and $\mathbf{K}_{e,n+1}$ is the 2 × 2 half-space element stiffness matrix

$$\mathbf{K}_{e,n+1} = \begin{bmatrix} \kappa_{11,n+1} & \kappa_{12,n+1} \\ \kappa_{21,n+1} & \kappa_{22,n+1} \end{bmatrix} \tag{A7}$$

List of symbols

c	Rayleigh wave phase velocity
D_j	parameter used for computation of the element stiffness matrix of jth layer
h_j	thickness of jth layer
j	index
$\mathbf{K}$	system stiffness matrix
$\mathbf{K}_{e,j}$	element stiffness matrix of jth layer
$\mathbf{K}_{11,j}$ $\mathbf{K}_{12,j}$ $\mathbf{K}_{21,j}$ $\mathbf{K}_{22,j}$	submatrices of the element stiffness matrix of jth layer
k	wave number
n	number of finite thickness layers
r_j	$\sqrt{1 - c^2/\alpha_j^2}$
s_j	$\sqrt{1 - c^2/\beta_j^2}$
α_j	compressional wave velocity of jth layer
β_j	shear wave velocity of jth layer
$\kappa_{lm,j}$	components of the element stiffness matrix of jth layer
ρ_j	mass density of jth layer

Paper II

Combination of dispersion curves from MASW measurements

Elín Ásta Ólafsdóttir, Bjarni Bessason & Sigurður Erlingsson

Ólafsdóttir, E.Á., Bessason, B. & Erlingsson, S. (2018). Combination of dispersion curves from MASW measurements. *Soil Dynamics and Earthquake Engineering, 113*, 473-487. doi:10.1016/j.soildyn.2018.05.025.

Soil Dynamics and Earthquake Engineering 113 (2018) 473–487

Contents lists available at ScienceDirect

Soil Dynamics and Earthquake Engineering

journal homepage: www.elsevier.com/locate/soildyn

Combination of dispersion curves from MASW measurements

Elin Asta Olafsdottir[a,*], Bjarni Bessason[a], Sigurdur Erlingsson[a,b]

[a] Faculty of Civil and Environmental Engineering, University of Iceland, Hjardarhagi 2-6, IS-107 Reykjavik, Iceland
[b] Pavement Technology, Swedish National Road and Transport Research Institute, SE-581 95 Linköping, Sweden

ARTICLE INFO

Keywords:
Multichannel analysis of surface waves
MASW
Dispersion curves
Measurement profile configuration
Combination
Stacking
Uncertainty analysis
Confidence intervals
Bootstrap

ABSTRACT

Multichannel analysis of surface waves (MASW) is a seismic exploration method for determination of near-surface shear wave velocity profiles based on analysis of horizontally travelling Rayleigh waves. This paper aims to propose a methodology and recommendations for combining dispersion data from several multichannel records. The dispersion curves are added up within logarithmically spaced wavelength intervals and the uncertainty of the mean phase velocity estimates is evaluated by using classical statistics and the bootstrap. The results indicate that combining multiple dispersion curves, which have been gathered by receiver spreads of different lengths (but with the same midpoint), can increase the investigation depth of the survey, improve its resolution at shallow depth and overall improve the reliability of the results as compared to the use of a single record. Moreover, the uncertainty of the combined mean dispersion curve can be determined and further used to present the shear wave velocity profile with upper and lower boundaries.

1. Introduction

The shear wave velocity (V_S) of near-surface materials is an important parameter in various geotechnical and earthquake engineering projects. The small-strain shear modulus of individual soil layers (G_0) is directly proportional to the square of their characteristic shear wave velocity. Furthermore, the shear wave velocity is fundamental in assessing soil amplification and for seismic site classification [1–3].

Several in-situ methods exist for evaluation of near-surface shear wave velocity profiles [1,4]. These include methods that require access to a drilled borehole, such as down-hole and cross-hole seismic surveys, methods where the resistance of soil to penetration is measured like the standard penetration test (SPT) and the cone penetration test (CPT), and surface wave analysis methods, such as the multichannel analysis of surface waves (MASW) method. Surface wave analysis methods utilize the dispersive properties of surface waves, commonly Rayleigh waves, propagating through a heterogeneous medium [5,6]. The shear wave velocity profile is subsequently obtained by backcalculation of the dispersion data by assuming a layered soil model. Compared to other available methods, surface wave analysis methods are low cost, as well as being non-invasive and environmentally friendly since they neither require heavy machinery nor leave lasting marks on the surface of the test site. Moreover, surface wave methods are applicable at a wide variety of sites, ranging from very fine grained silty soil sites to coarse grained gravelly sites, and even soft rock, hence, including locations where for example penetration tests are difficult to apply. MASW is a relatively new surface wave analysis technique [7,8] that has attracted an increased attention in recent years [9]. The main advantages of the MASW method, as compared to a two-receiver analysis [10], include a more efficient data acquisition in the field and improved data processing procedures where data from multiple receivers is analysed simultaneously [8]. Furthermore, the MASW method makes it possible to identify higher mode dispersion curves based on the recorded surface wave data [11].

Determination of experimental Rayleigh wave dispersion curves is a critical stage in the application of MASW. An inaccurate or erroneous experimental dispersion curve can cause severe errors in the back-calculated shear wave velocity profile [8,12,13]. At locations where the fundamental mode of the Rayleigh wave prevails, the retrieved fundamental mode wavelength range constrains the investigation depth range of the survey [14]. In short, the longer the maximum retrieved wavelength, the greater the prospective maximum investigated depth, and the shorter the minimum recorded wavelength, the better the resolution of the survey at shallow depth. The configuration of the measurement profile, including the length of the receiver spread (L) and the distance from the impact load point to the first receiver (x_1), is known to affect the acquired dispersion data [15–23]. The observed effects suggest that a wider range of dispersion curve wavelengths can be obtained by combination of data acquired using measurement profiles with different L and/or x_1 [16,17,24,25]. Furthermore, the acquired surface wave records are affected by correlated and uncorrelated noise sources. The manual aspect of the analysis, particularly the visual identification of dispersion curves based on images of

* Corresponding author.
E-mail addresses: eao4@hi.is (E.A. Olafsdottir), bb@hi.is (B. Bessason), sigger@hi.is (S. Erlingsson).

https://doi.org/10.1016/j.soildyn.2018.05.025
Received 5 May 2017; Received in revised form 25 February 2018; Accepted 23 May 2018

processed data, also adds to the uncertainty associated with the dispersion curve estimates. Hence, when repeated measurements are carried out, some variability among the resulting dispersion curve estimates will be observed. Multiple records thus result in multiple curves, which combined may improve the estimation of the actual dispersion curve. As the individual dispersion curves may cover different wavelength ranges, the combined curve can include a wider range of wavelengths than any single experimental curve, and, hence, lead to an increased investigation depth range. Combination of dispersion data from several multichannel records can also be achieved by adding (stacking) multiple dispersion images before extracting a single dispersion curve. Stacking of multiple dispersion images can reduce noise and help identification of the fundamental mode dispersion curve [24,26–28]. By averaging the dispersion data post dispersion curve extraction, the uncertainty of the mean dispersion curve estimate can be evaluated, for instance, in terms of parametric or non-parametric confidence intervals for the mean dispersion curve. The uncertainty analysis can provide the analyst a more rational evaluation of the quality of the dispersion data and the combined dispersion curve. The uncertainty of the combined mean dispersion curve can further be utilized to present the shear wave velocity profile with upper and lower boundaries.

Few authors have obtained composite experimental dispersion curves with phase velocity uncertainties as a part of an active-source MASW survey. The combined curves have been constructed based on dispersion curves obtained by repeated shots [29,30], dispersion data gathered using different shot positions [21,31,32] or measurement profiles of different lengths [25]. Furthermore, in a few studies where the experimental dispersion curve has been identified from a stacked dispersion image, the experimental uncertainty has been assessed using the dispersion curves extracted from the single shot images [27,28]. However, in all above-mentioned studies, the main objective has not been computation of composite experimental dispersion curves, hence, the dispersion curve combination and uncertainty evaluation procedure is not well described and no general recommendations are given.

This paper aims to propose a methodology for combining dispersion curves from several multichannel records for the purpose of producing a reliable combined mean dispersion curve over a wide range of wavelengths. In this work, only the fundamental mode of Rayleigh wave propagation is considered. However, the methodology can be extended to higher modes as well. A number of records acquired by different measurement profile configurations at a silty sand test site are used to demonstrate the methodology. Recommendations for optimal measurement profile parameter/dispersion curve combinations in the context of ranges of wavelengths and phase velocities are presented. The uncertainty of the combined mean dispersion curve estimates was quantified, using both classical statistics and bootstrapping. The inverted shear wave velocity profiles are presented to further assess the effects of the different dispersion curve combinations. Similar results have been observed at other sandy test sites where the proposed methodology has been applied.

2. Multichannel analysis of surface waves

An application of MASW includes three steps; field measurements, dispersion analysis and inversion analysis [8]. An overview of the MASW method, as it is applied in this paper, is provided in Fig. 1. Surface waves are generated by an active seismic source and the wave propagation is recorded by multiple geophones that are evenly spaced along the survey line (Fig. 1a–c). Each multichannel surface wave record is transformed into a dispersion image and the corresponding (elementary) fundamental mode dispersion curve is identified (Fig. 1d–f). The elementary dispersion curves are subsequently combined into a single experimental curve and the uncertainty associated with the combined mean curve evaluated (Fig. 1g). Finally, the shear wave velocity profile is obtained by inversion of the combined mean dispersion curve by assuming a plane-layered elastic earth model (Fig. 1h–k). Under a mild lateral shear wave velocity variation, the backcalculated shear wave velocity profile can reasonably be assigned to the centre of the receiver spread [33].

In general, the resolution of surface wave analysis techniques, such as MASW, diminishes with increasing depth [34]. That is, while the analysis can resolve relatively thin layers and modest shear wave velocity variations close to the surface, only major variations in shear wave velocity/layering can be detected at greater depths. Furthermore, the fundamental mode Rayleigh wave dispersion curve is poorly sensitive to variations in material properties at depths greater than one third to half the maximum resolved wavelength (λ_{max}) [14,34,35]. Hence, a commonly used rule of thumb for interpretation of fundamental mode dispersion curves is to limit the maximum depth of the shear wave velocity profile (z_{max}) by the longest retrieved wavelength (e.g. [8,14,34,36]) as

$$z_{max} \leq \gamma \lambda_{max}, \quad \frac{1}{3} \leq \gamma \leq \frac{1}{2} \tag{1}$$

where γ is the ratio of the maximum depth of the shear wave velocity profile to the longest wavelength. Similarly, limiting the thickness of the top-most layer (h_1) by the shortest retrieved Rayleigh wave wavelength (λ_{min}) has been recommended (e.g. [8,14,36]), i.e.

$$h_1 \geq \zeta \lambda_{min}, \quad \frac{1}{3} \leq \zeta \leq \frac{1}{2} \tag{2}$$

where ζ is the ratio of the minimum thickness of the top-most layer to the shortest wavelength, as the fundamental mode dispersion data does not provide sufficient information to constrain the solution at shallower depths. When MASW surveys are carried out, the focus is commonly on achieving a particular investigation depth, and, therefore, on obtaining a certain maximum Rayleigh wave wavelength. However, as the shallowest soil layers have an influence on the entire experimental dispersion curve, information about the short wavelength wave components is also of importance [34]. Thus, even in cases where a detailed analysis of the shallowest soil layers is not a main objective, an experimental dispersion curve covering a wide range of wavelengths can be of value in order to constrain the inversion and increase the accuracy of the inverted shear wave velocity profile.

Ideally, the dispersion analysis should provide identification and extraction of the (elementary) dispersion curve for each mode. However, in-situ surface wave registrations are incomplete to some extent, imposing various challenges when dispersion curves are identified based on a dispersion image. Uncertainty associated with the experimental dispersion data can arise from an improper application of the middle-of-receiver spread assumption, measurement and sampling errors (e.g. due to limitations of the measurement equipment or an imprecise measurement profile set-up), and coherent or uncorrelated noise in the recorded signal [30,34,37]. Quantification of how the error associated with the recorded surface waves is propagated through the different data processing steps has however been reported as problematic [30]. Direct estimates of the statistical distributions of the extracted phase velocity values (i.e. at each wavelength/frequency) can nevertheless provide a measure of the error associated with the Rayleigh wave dispersion data. The processing of the recorded data and the dispersion curve identification/extraction can further introduce uncertainty in the experimental dispersion curves [30,34,37]. The fundamental mode of Rayleigh wave propagation typically prevails at sites where the shear wave velocity increases gradually with increasing depth [12,34,38,39]. At sites characterized by a more irregularly varying stiffness profile, higher modes can play a significant role in certain frequency ranges, thus making the identification of the fundamental mode dispersion curve difficult. In such cases, misidentification of mode numbers or superposition of dispersion data from two (or more) modes can occur, resulting in an apparent dispersion curve that does not correspond to any of the real modes [12,13,34]. A further source of uncertainty is potential inter-analyst variability associated

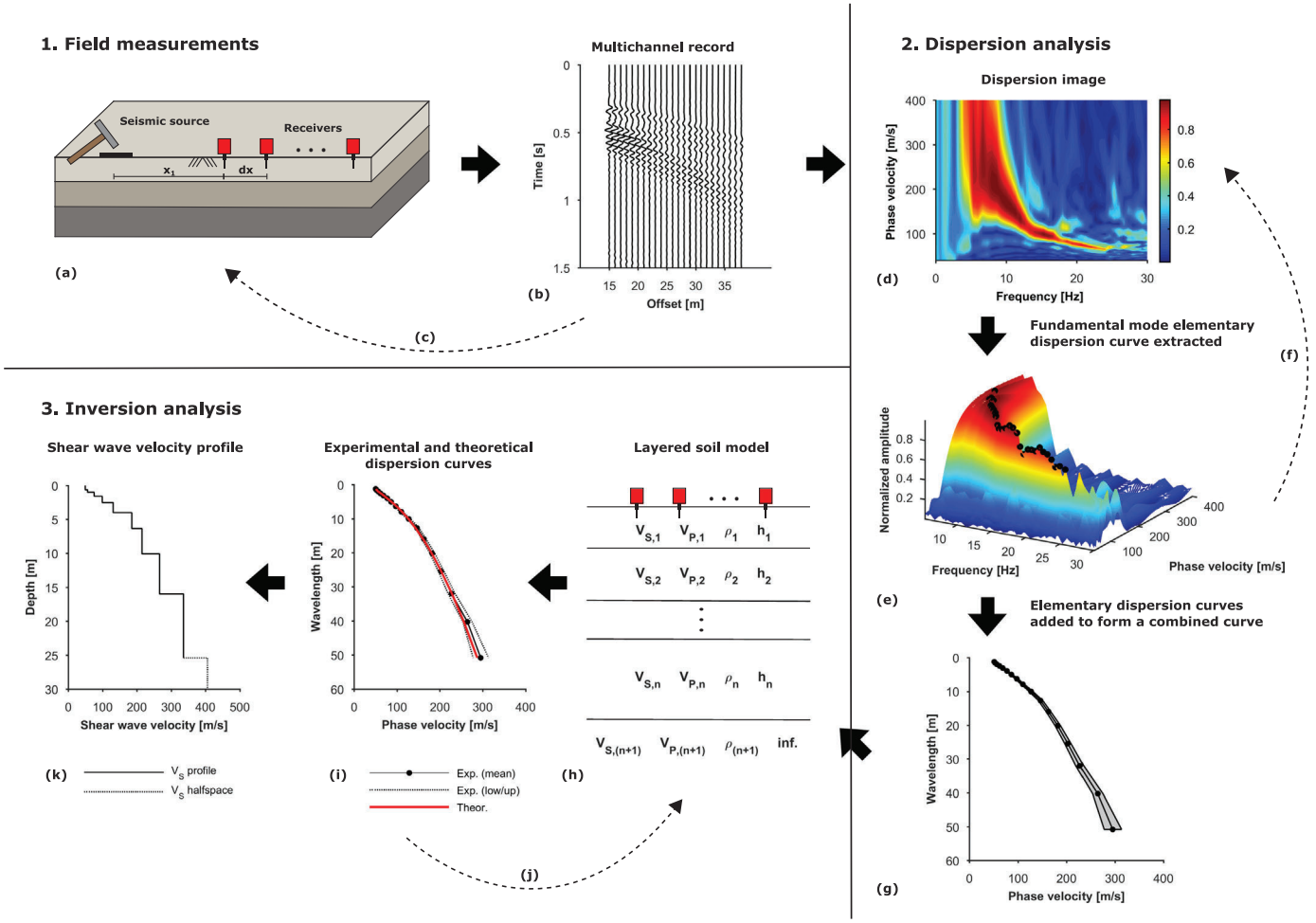

Fig. 1. Application of the MASW method. (a) Geophones are lined up on the surface of the test site with equal receiver spacing dx. A wave is generated using an impulsive source that is applied at a distance x_1 from one end of the receiver spread. (b) The wave propagation is recorded. (c) Steps (a) and (b) are repeated several times using different values of dx and/or x_1, while keeping the midpoint of the receiver spread fixed. (d) A dispersion image is obtained based on each multichannel surface wave record. (e) The high-amplitude bands display the dispersion characteristics and are used to identify the elementary fundamental mode Rayleigh wave dispersion curve. (f) Steps (d) and (e) are carried out for each acquired surface wave record. (g) The extracted elementary dispersion curves are added up to obtain a combined mean experimental curve along with upper/lower boundary curves. (h) An initial estimate of a layered soil model for the test site is obtained. The parameters required to describe the properties of each layer are shear wave velocity (V_S), compressional wave velocity (V_P), mass density (ρ) and layer thickness (h). The last layer is assumed to be a half-space. (i) A theoretical dispersion curve is computed based on the assumed soil model and compared to the combined mean experimental dispersion curve. (j) The layered soil model is updated and the theoretical dispersion curve is recomputed until the misfit between the theoretical and experimental curves has reached an acceptably small value. (k) The shear wave velocity profile and the layer structure that result in an acceptable fit, and can realistically represent the characteristics of the test site, are taken as the results of the survey.

with the manual or semi-manual dispersion curve picking. The human bias may, however, be limited by averaging dispersion curve picks obtained by several analysts [37]. In general, the low frequency (longer wavelength) part of the dispersion curve is characterized by higher uncertainty than the higher frequency (shorter wavelength) region [30].

It is further commonly recognised that the configuration of the measurement profile can affect the quality of the dispersion image that is obtained [15–23] and consequently the uncertainty associated with the dispersion curve identification and extraction. In general, given that the lateral changes in shear wave velocity are small, an increased length of the receiver spread provides improved spectral resolution. The high-amplitude peaks observed at each frequency appear sharper and better separation between different modes of surface wave propagation is observed [16,17], thus facilitating the dispersion curve picking. A longer receiver spread is also preferred in order to acquire the lower frequency (longer wavelength) Rayleigh wave components that provide the deepest part of the shear wave velocity profile. However, an increased receiver spread length risks attenuation of higher frequency (shorter wavelength) fundamental mode components (which reduces the minimum resolvable investigation depth) and spatial aliasing if a fixed number of geophones is used [34,40]. Furthermore, an increased length of the receiver spread risks significant lateral variations in material properties along the geophone array [16]. The analysis is based on the assumption that the wave front of the Rayleigh wave is plane. In general, the length of the source offset has to be sufficient to assure plane wave propagation of surface wave components [16,20,41]. The minimum source offset required to avoid near-field effects depends on the longest wavelength that is analysed. A very short source offset can result in an irregular and unreliable high-amplitude trend in the dispersion image at lower frequencies, usually displaying lower phase velocities than images free of this effect. An overly long source offset, however, risks excessive attenuation of fundamental mode components at higher frequencies.

3. Dispersion analysis

The objective of the dispersion analysis is to identify experimental

dispersion curves based on the acquired multichannel surface wave records. Transform-based methods, in which the multichannel time series are transformed from the space-time domain into a different domain, are most commonly used for active-source surveys [6], i.e. the frequency–wave number (f–k) transform [42], the slowness–frequency (p–ω) transform [43] and the phase shift method [44]. A comparison of the effectiveness of the three methods has revealed that the phase shift method is a robust and computationally effective method that provides accurate fundamental mode phase velocities, even when data from only a limited number of geophones are available [45]. Hence, in this work, the acquired surface wave records were analysed by the phase shift method. Identification and extraction of elementary dispersion curves was carried out by using the open source Matlab software MASWaves [46] (see also masw.hi.is). The original dispersion analysis tool of MASWaves was modified in order to include the proposed methodology for combining dispersion curves from several records.

An application of the phase shift method can be divided into three main steps; (i) Fourier transformation and amplitude normalization, (ii) dispersion imaging, and (iii) identification/extraction of dispersion curves [44,47]. The multichannel surface wave record is denoted by $u(x_j, t)$ where x_j is the distance from the impact load point to the j-th receiver and is time. The number of geophones is denoted by N. First, each trace of the multichannel record is transformed into the frequency domain by a Fourier transform. The j-th trace of the transformed record $\tilde{u}(x_j,\omega)$ can be expressed in terms of its amplitude $A_j(\omega)$ and phase $\Phi_j(\omega)$ as

$$\tilde{u}(x_j, \omega) = A_j(\omega)\exp(-i\Phi_j(\omega)) = A_j(\omega)\exp\left(-i\frac{\omega x_j}{c(\omega)}\right) \tag{3}$$

where $c(\omega)$ is the characteristic phase velocity of the frequency component ω, $\Phi_j(\omega)= \frac{\omega x_j}{c(\omega)}$ and $i^2 = -1$. The amplitude of the transformed record does not include any information on phase velocity. Hence, $\tilde{u}(x_j,\omega)$ is normalized in order to remove the effects of geometrical spreading and attenuation on the acquired data. The analysis is thus concentrated on the phase velocity effect only.

$$\tilde{u}_{norm}(x_j, \omega) = \frac{\tilde{u}(x_j, \omega)}{|\tilde{u}(x_j, \omega)|} = \exp\left(-i\frac{\omega x_j}{c(\omega)}\right) \tag{4}$$

For a given testing phase velocity (c_T) and a given frequency (ω), the amount of phase shifts required to counterbalance the time delay corresponding to specific offsets (x_j) is determined. The phase shifts are applied to distinct traces of $\tilde{u}_{norm}(x_j,\omega)$ that are thereafter added to obtain the slant-stacked amplitude $S(\omega,c_T)$ corresponding to the ordered couple (ω,c_T)

$$S(\omega, c_T) = \frac{1}{N}\sum_{j=1}^{N}\exp\left(-i\frac{\omega x_j}{c_T}\right)\tilde{u}_{norm}(x_j, \omega) \tag{5}$$

The summation operation described by Eq. (5) is repeated for all the different frequency components of the transformed record in a scanning manner using varying testing phase velocity values. When the testing phase velocity becomes equal to the true phase velocity $c(\omega)$ a maximum is observed in $S(\omega,c_T)$. The values of $S(\omega,c_T)$ are visualized as a two (or three) dimensional dispersion image (phase velocity spectrum). The spectral high-amplitude bands display the dispersion characteristics of all types of waves contained in the recorded data (Fig. 1d) and are used to identify and extract the elementary Rayleigh wave dispersion curve(s) (Fig. 1e).

For determination of a combined mean dispersion curve (Fig. 1 g), assume that m multichannel surface wave records have been obtained at the same location (i.e. by using measurement profiles with the same midpoint and possibly different receiver spread lengths and/or different source offsets). Each surface wave record is processed separately (e.g. by use of the phase shift method) resulting in m experimental elementary dispersion curves. Each elementary curve consists of n_j data points $(c_{j,l}, \lambda_{j,l})$ (where $l = 1,..., n_j$ and $j = 1, ...,m$).

The combined mean experimental dispersion curve, denoted by $(c_{e,q}, \lambda_{e,q})$ (where $q = 1, ...,Q$) is obtained by grouping the data points included in the m elementary dispersion curves together within $\log_a$ spaced (i.e. a^{-1}th octave) wavelength intervals $[\lambda_{e,q}^L, \lambda_{e,q}^U)$. Q is the number of wavelength intervals, $\lambda_{e,q}$ is the reference point of the q-th interval and $\lambda_{e,q}^L$ and $\lambda_{e,q}^U$ are its upper and lower bounds, respectively. Hence, the wavelengths that characterize the q-th interval are obtained as

$$\begin{aligned}\lambda_{e,q} &= 2^{\frac{q-1}{a}}\\ \lambda_{e,q}^L &= \lambda_{e,q}\cdot 2^{-\frac{1}{2a}}\\ \lambda_{e,q}^U &= \lambda_{e,q}\cdot 2^{\frac{1}{2a}}\end{aligned} \tag{6}$$

Subsequently, all phase velocity values $c_{j,l}$ such that $\lambda_{j,l}\in[\lambda_{e,q}^L, \lambda_{e,q}^U)$ are added up and their arithmetic mean (denoted by $c_{e,q}$) used as a point estimate of the phase velocity of Rayleigh wave components belonging to the given wavelength range.

4. MASW dispersion data

4.1. Field measurements

Multichannel surface wave records were acquired in 2015 at Arnarbæli in Ölfus, South Iceland. The soil at the Arnarbæli site consists of a relatively homogeneous glaciofluvial volcanic sand deposited on the western bank of the estuary of the Ölfus River [48,49]. The surface wave records were collected using a linear array of 24 vertical geophones with a natural frequency of 4.5 Hz. Three measurement profiles with the same midpoint but varying receiver spacing (dx) were tested, i.e. $dx = 0.5$ m, $dx = 1.0$ m and $dx = 2.0$ m. For each receiver spacing, four different source offsets (x_1) were used. For each combination of dx and x_1, six surface wave records (where each record consisted of 24 time series) were acquired, resulting in a total of 72 records. The impact load was in all cases created by a 6.3 kg sledgehammer. The high number of records gathered using multiple measurement profile configurations makes this dataset an appropriate choice for testing the proposed methodology. A summary of the main parameters related to the field measurements is provided in Table 1.

4.2. Dispersion curves

Each multichannel record was processed separately by using the

Table 1
Overview of site characteristics and MASW test configuration at the Arnarbæli test site.

Site characteristics			
Soil type			Holocene glaciofluvial sand
USCS classification			SW-SM
Location of groundwater table			At surface
Saturated mass density	ρ_{sat}	[kg/m^3]	1850
Field measurements			
No. geophones	N		24
No. profiles			3
Receiver spacing (source offsets)	dx (x_1)	[m]	0.5 (3.0/5.0/7.5/10.0) 1.0 (5.0/10.0/15.0/25.0) 2.0 (5.0/10.0/15.0/25.0)
No. measurements per combination of dx and x_1			6
Sampling rate	f_s	[Hz]	1000
Recording time	T	[s]	2.4

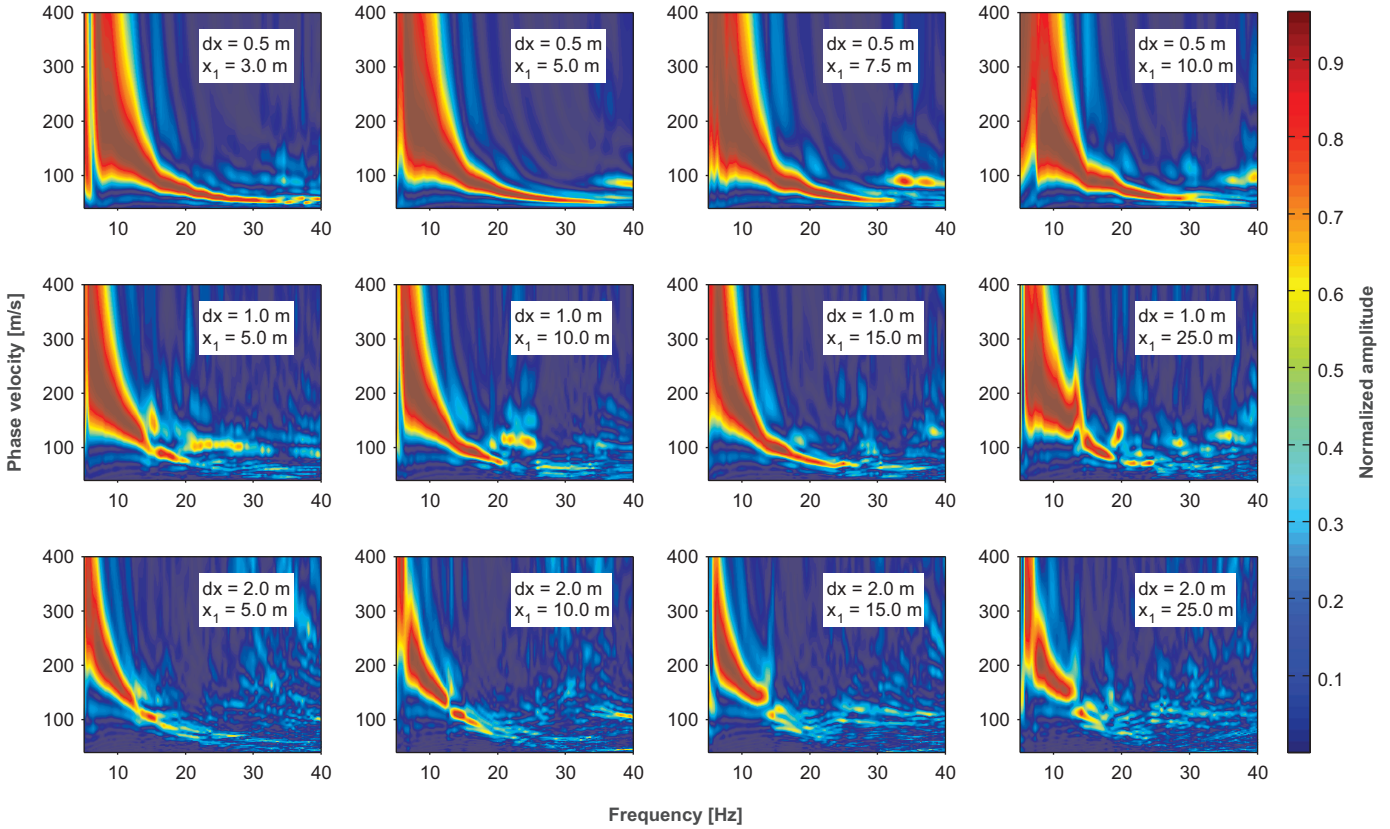

Fig. 2. Dispersion images of multichannel surface wave records acquired with receiver spreads of different lengths and with different source offsets.

phase shift method. The variability among the extracted elementary dispersion curves was subsequently evaluated in terms of the coefficient of variation (C_V) among the estimated phase velocity values at each frequency

$$C_V = \frac{s_c}{\bar{c}} \tag{7}$$

where $\bar{c}$ is the average of the estimated phase velocity values at frequency f and s_c is the corresponding standard deviation (SD).

Typical dispersion images of records acquired with each measurement profile configuration are shown in Fig. 2. The fundamental mode dispersion curves that were identified based on the data are presented in Fig. 3a. The dispersion curve estimates obtained by using diverse measurement profile configurations agreed well, being characterized by a C_V between 1% and 8% at each frequency (Fig. 3b). As expected, the lowest frequency components displayed more variability than components in the higher frequency range.

As shown in Fig. 2, the configuration of the measurement profile, i.e. the length of the receiver spread and the source offset, had a considerable effect on the dispersion images that were obtained, and subsequently on the retrievable dispersion curve frequency range in each case. Time series recorded by the shortest receiver spread provided in general the most information about the dispersion properties of the short wavelength (higher frequency) wave components that propagated through the top-most soil layers (Fig. 3a). However, with increasing receiver spread length, the observed spectral resolution increased (Fig. 2) which facilitated the identification of the fundamental mode at lower frequencies (Fig. 3a). Hence, time series recorded by the longer receiver spreads tended to provide the greatest investigation depth. The observations were in accordance with existing recommendations where

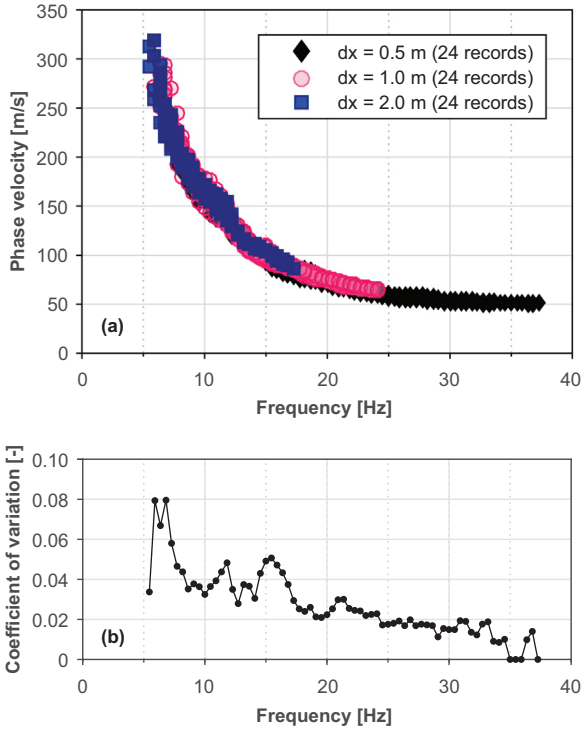

Fig. 3. (a) Fundamental mode dispersion curve estimates obtained by using receiver spreads of different lengths. (b) Variation of extracted Rayleigh wave phase velocity values at each frequency.

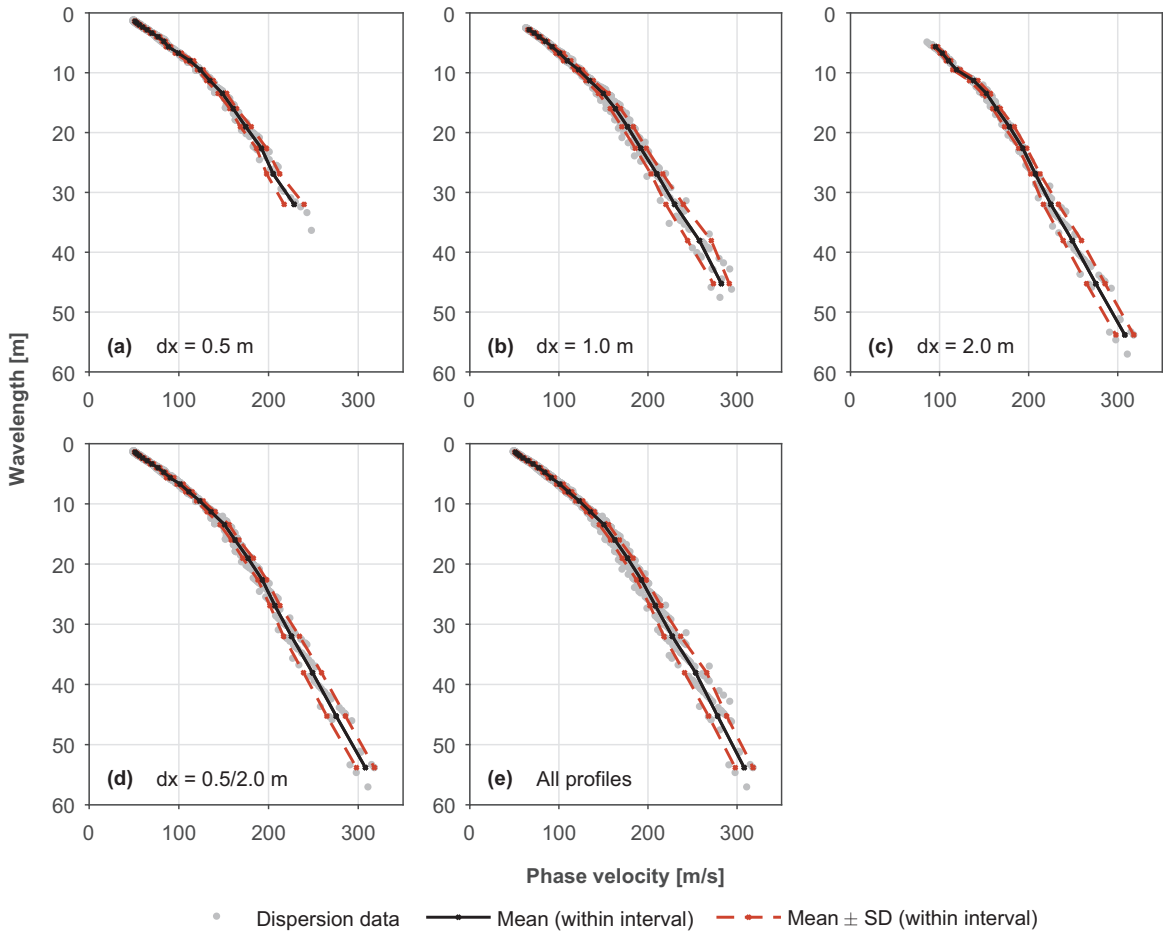

Fig. 4. Elementary dispersion curve data points and combined mean dispersion curves with upper and lower bound curves (mean ± one standard deviation) for the three profiles and the two profile combinations (with $a = 4.0$ in Eq. (6)).

the obtainable investigation depth is suggested as directly related to the length of the receiver spread [20].

5. Combining dispersion curves

Fig. 4 illustrates the computation of composite dispersion curves for the three profiles (same midpoint) and the two profile combinations tested at the Arnarbæli site. The combined mean curves in Fig. 4a–c were obtained by grouping data points from each set of 24 elementary curves (i.e. 24 curves for the $dx = 0.5$ m profile, the $dx = 1.0$ m profile and the $dx = 2.0$ m profile, respectively) together within $\log_4$ spaced wavelength intervals, i.e. with $a = 4.0$ in Eq. (6). The optimal width and number of wavelength intervals was determined after initial inspection of the data (see further in Section 5.1). The mean phase velocity within each interval was used as an estimate of the phase velocity of the Rayleigh wave components belonging to the given wavelength range. The upper and lower bound curves shown in Fig. 4 correspond to plus/minus one standard deviation from the combined mean curve; hence, the upper and lower bound curves provide a measure of the spread of the elementary dispersion curve data points within each wavelength interval. In general, the spread of the data points increased with increased wavelength. Furthermore, the number of points associated with each wavelength interval decreased with increasing wavelength.

As indicated by the dispersion data shown in Fig. 3a, there was a considerable difference in the dispersion curve wavelength range that could be achieved by using each of the three profiles. The shortest ($dx = 0.5$ m) profile provided combined dispersion curve wavelengths in the range of 1.4–32.0 m (Fig. 4a), the intermediate length ($dx = 1.0$ m) profile provided wavelengths in the range of 2.8–45.3 m (Fig. 4b), and the longest ($dx = 2.0$ m) profile provided wavelengths in the range of 5.7–53.8 m (Fig. 4c).

The dispersion curves obtained by combining (i) the 48 dispersion curves acquired by the $dx = 0.5$ m and $dx = 2.0$ m profiles and (ii) the 72 dispersion curves acquired by all three profiles within $\log_4$ spaced wavelength intervals are shown in Fig. 4d and Fig. 4e, respectively. In both cases, the minimum combined curve wavelength was 1.4 m and the maximum wavelength was 53.8 m.

5.1. Number and width of wavelength intervals for combined dispersion curves

The number and width of wavelength intervals used for computation of a combined dispersion curve is controlled by the parameter a in Eq. (6). The width of each interval is inversely related to the value of a. Simultaneously, the number of intervals within a given wavelength range increases with increasing value of a. This is illustrated in Fig. 5. The reference wavelength value for each interval ($\lambda_{e,q}$) is specially indicated by a dot. As the interval length is logarithmically distributed, the effect of the different a-values on the interval length becomes more apparent with increasing wavelength.

The optimum value of a varies with dataset and should be chosen after initial inspection of the available data. Fig. 6 shows the effects of using selected values of the parameter a, i.e. $a = 2.0$, $a = 3.0$, $a = 5.0$ and $a = 7.0$, for computation of a composite dispersion curve based on the dispersion data acquired by the $dx = 0.5$ m and $dx = 2.0$ m profiles at the Arnarbæli site. The elementary dispersion curve data points that

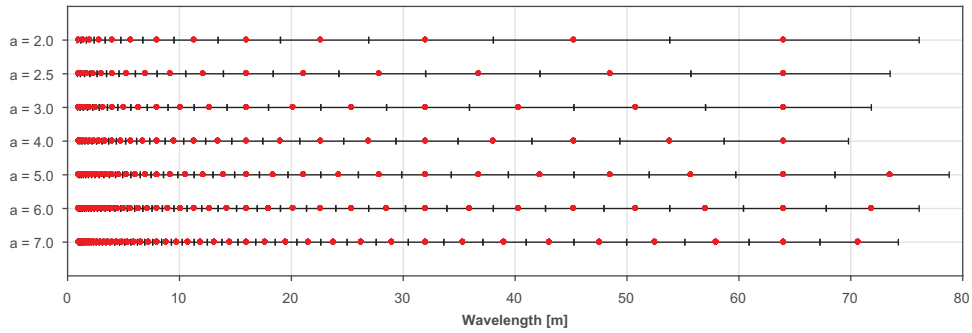

Fig. 5. Effects of the parameter a in Eq. (6) on the length and range of the wavelength intervals used for computation of a combined dispersion curve (here shown for assumed elementary dispersion curve wavelengths in the range of 1 m to approximately 70–80 m). The reference point for each wavelength interval ($\lambda_{e,q}$) is indicated by a dot.

fall within each wavelength interval (indicated by the alternating grey and white bands) are shown in Fig. 6a–d. The resulting combined mean dispersion curves are shown in Fig. 6e–h. The upper and lower bound curves also shown correspond to plus/minus one standard deviation from the combined mean curve in each case. The combined mean, upper and lower bound dispersion curves that were obtained for the same dataset by using $a = 4.0$ are shown in Fig. 4d. A comparison of the combined mean dispersion curves obtained by using the a values illustrated in Fig. 5 is provided in Fig. 7.

The results presented in Figs. 6 and 7 indicate that the selection of a did not have a substantial effect on the combined mean dispersion curve at wavelengths shorter than approximately 40 m. However, for longer wavelengths, where the wavelength intervals were wider and fewer data points were available, the effects of the different values of a become more visible.

The ideal value of a depends on the number and distribution of the available elementary dispersion curve data points. Based on present experience with applying the methodology, the following factors are of main importance for selection of a: (i) the elementary dispersion curve

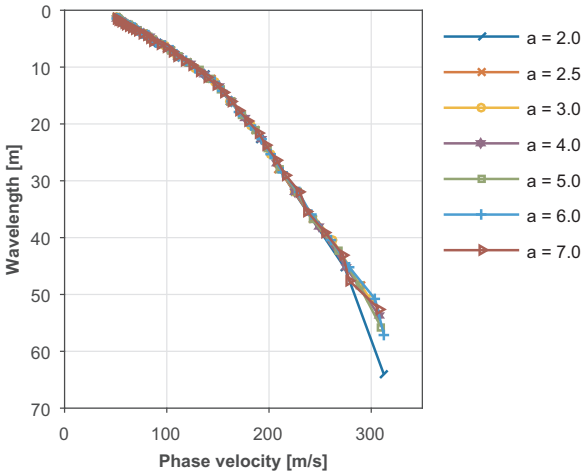

Fig. 7. Comparison of combined mean dispersion curves obtained by using different values of the parameter a in Eq. (6).

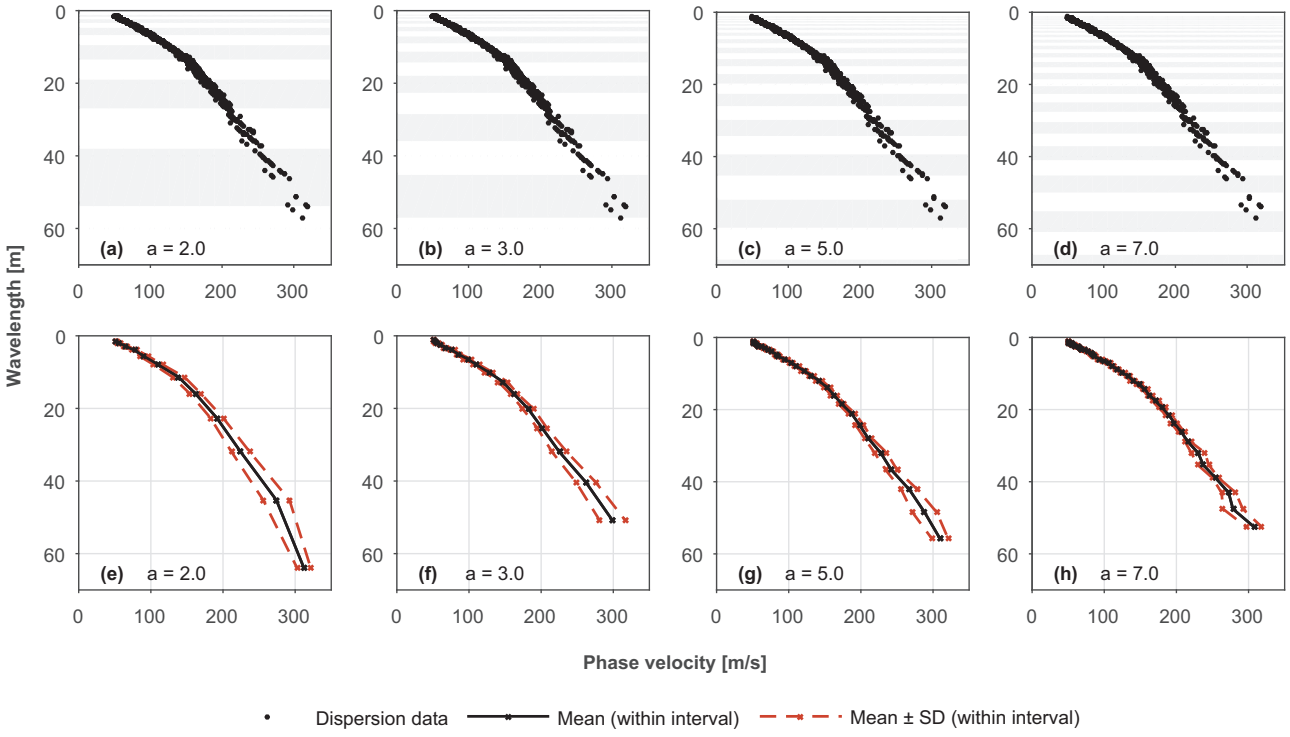

Fig. 6. Effects of using different values of the parameter a in Eq. (6) for determination of a combined mean dispersion curve. The combined curves are obtained based on the dispersion data acquired by the $dx = 0.5$ m and $dx = 2.0$ m profiles.

data points should be approximately evenly distributed within each wavelength interval, (ii) a sufficient number of data points should fall within each interval, and (iii) a higher value of a is in general preferable to a lower value.

An uneven distribution of the elementary dispersion curve data points or an insufficient number of data points falling within certain wavelength intervals can either result in an underestimated or overestimated combined curve phase velocity value ($c_{e,q}$) for the given wavelength range $[\lambda_{e,q}^{L}, \lambda_{e,q}^{U})$ (see e.g. the last wavelength interval, $\lambda \in [53.8, 76.1)$ m, in Fig. 6a, e). "Zigzagging" of the combined mean curve can be observed if either occurs for multiple adjacent wavelength intervals (see Fig. 6d, h). Moreover, an uneven distribution of the elementary dispersion curve data points can manifest itself by an increased standard deviation of the phase velocity values for the given interval (see e.g. the second last wavelength interval, $\lambda \in [45.3, 52.0)$ m, in Fig. 6c, g). In cases where the dispersion curve data points cluster together, there is also a risk that the standard deviation is not representative of the actual variability of the phase velocity values of the wave components that belong to the given wavelength range.

In general, the highest value of a that does not cause any of the previously described complications should be used. Increasing the number of wavelength intervals both provides more data points in the combined mean dispersion curve and, in general, decreases the uncertainty associated with its computation. Present experience with applying the methodology indicates that the optimum value of a for most test sites is in the range from $a = 2.5$ to $a = 5.0$. A default or initial value of $a = 3.0$ or $a = 4.0$ will in many cases be sufficient.

5.2. Number of elementary dispersion curves

The effects of using different number of elementary dispersion curves for computation of a combined mean curve for the Arnarbæli site are reported in Figs. 8–10. For each measurement profile/profile combination, the use of one, two, four and six multichannel surface wave records for each source offset was studied. Moreover, the effects of stacking two and four dispersion images, respectively, prior to identification of elementary dispersion curves, are shown and compared to the use of elementary curves identified based on single records. Hence, the use of a total of 30 elementary dispersion curve combinations was studied. An overview of the dispersion curve combinations and the number of elementary dispersion curves included in each combination is provided in Table 2.

Fig. 8 illustrates the grouping of the elementary dispersion curve data points into $\log_4$ spaced wavelength intervals (with $a = 4.0$ in Eq. (6)) for selected study cases, i.e. the $dx = 0.5$ m profile and the $dx = 0.5$ m/$dx = 2.0$ m combination. Also shown is the combined mean dispersion curve obtained for each case. The data acquired by the $dx = 1.0$ m profile, the $dx = 2.0$ m profile and the $dx = 0.5$ m/$dx = 1.0$ m/$dx = 2.0$ m combination, respectively, showed essentially the same characteristics as the data that is presented in Fig. 8.

The number of data points that fell within each wavelength interval for each of the 30 elementary dispersion curve combinations is reported in Fig. 9. By combining elementary dispersion curves obtained by profiles of different lengths (i.e. $dx = 0.5$ m/$dx = 2.0$ m or $dx = 0.5$ m/$dx = 1.0$ m/$dx = 2.0$ m) a more even distribution of the dispersion curve data points was obtained, as well as a substantially increased wavelength range, as previously described.

The combined mean dispersion curves that were obtained for each elementary curve combination are compared in Fig. 10. The agreement between the curves reported was in all cases good with a coefficient of variation (Eq. (7)) less than 2.5% for each reference wavelength. At wavelengths shorter than approximately 30 m, the combined mean curves were nearly identical. However, at longer wavelengths a minor difference between the curves was observed.

In general, the results indicate that in order to obtain the longest possible combined curve wavelength, it is preferable to use several (e.g. four or six) elementary dispersion curves for each profile length/source offset, rather than using a single record for each configuration. When a small number of records is used for computation of a combined curve (i.e. one or two records for each combination of dx and x_1) there is the risk of an inadequate number of elementary dispersion curve data points falling within each wavelength interval. In general, the fundamental mode dispersion curve trend of the longer wavelength (lower frequency) wave components is the most difficult to identify and to confidently extract from a dispersion image. Moreover, the mapping of the dispersion curve data points from the frequency-phase velocity domain into the phase velocity-wavelength domain spreads the lower

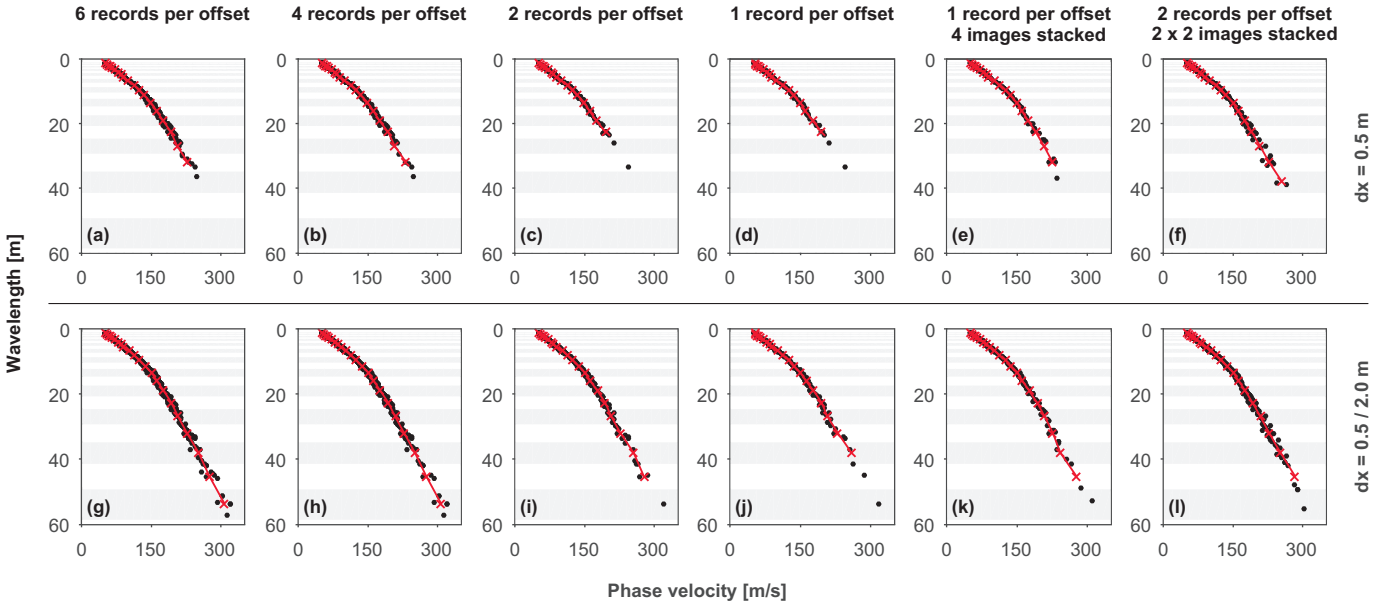

Fig. 8. Grouping of elementary dispersion curve data points into $\log_4$ spaced wavelength intervals (with $a = 4.0$ in Eq. (6)) for selected study cases from Table 2. The combined mean dispersion curve obtained for each case is shown with an unbroken line.

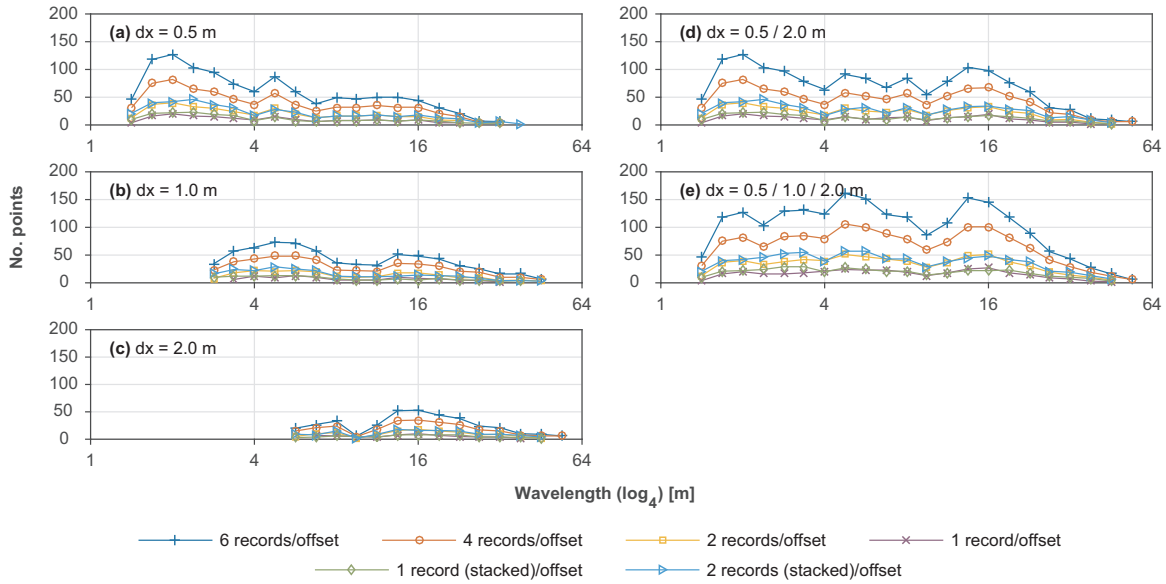

Fig. 9. Number of dispersion curve data points that fell into each $\log_4$ spaced wavelength interval (with $a = 4.0$ in Eq. (6)) for the study cases in Table 2.

frequency data points further apart than data points corresponding to higher frequencies. Hence, the risk of an insufficient number of data points falling within a given wavelength interval is the greatest at the longest wavelengths.

By stacking two or more dispersion images obtained by using the same measurement profile configuration (the same receiver spacing and the same source offset), prior to the dispersion curve extraction, a better defined (i.e. sharper and more continuous) high-amplitude band can in some cases be obtained. Therefore, for computation of a composite curve, it can be advantageous (in order to obtain an increased investigation depth range without having to identify and extract multiple elementary dispersion curves for each source offset) to stack several sets of dispersion images and use the dispersion curves extracted from the stacked images in the subsequent analysis. This can be noticed by inspection of the data presented in Fig. 8. For the $dx = 0.5$ m profile, a maximum combined curve wavelength of 32 m was obtained by using a single stacked dispersion image for each source offset (Fig. 8e), which was the same maximum wavelength as was obtained by using four and six (unstacked) records, respectively, for each source offset (Fig. 8a, b). For comparison, the maximum combined curve wavelength obtained by using one (unstacked) record per source offset (Fig. 8d) was approximately 23 m. Similar observations were made for the other two measurement profile lengths.

5.3. Comparison of combining several dispersion curves and the use of stacking

Fig. 11 shows stacked dispersion images for the Arnarbæli site obtained from data acquired by each of the three measurement profiles, i.e. with $dx = 0.5$ m, $dx = 1.0$ m and $dx = 2.0$ m, respectively, and the two profile combinations ($dx = 0.5$ m/$dx = 2.0$ m and $dx = 0.5$ m/$dx = 1.0$ m/$dx = 2.0$ m). In each case, 16 dispersion images were stacked per receiver spread length (i.e. four records for each receiver spacing/source offset). The stacked dispersion images provide in all cases a relatively well-defined fundamental mode high-amplitude trend; however, a notable break in the high-amplitude band is present in Fig. 11c, and to a slightly lesser extent in Fig. 11d, e.

The dispersion curves that were identified based on the stacked dispersion images in Fig. 11a, c, d (hereafter referred to as "stacked-image-based" curves) are shown in Fig. 12. Furthermore, Fig. 12 provides comparison of the "stacked-image-based" curves and the combined mean dispersion curves obtained on the basis of the same data, either by extracting a single dispersion curve based on each record, or by stacking each set of four dispersion images prior to the dispersion curve identification. Though not shown here, the same characteristics were observed by analysis of the data acquired by the $dx = 1.0$ m profile and by the $dx = 0.5$ m/$dx = 1.0$ m/$dx = 2.0$ m profile combination.

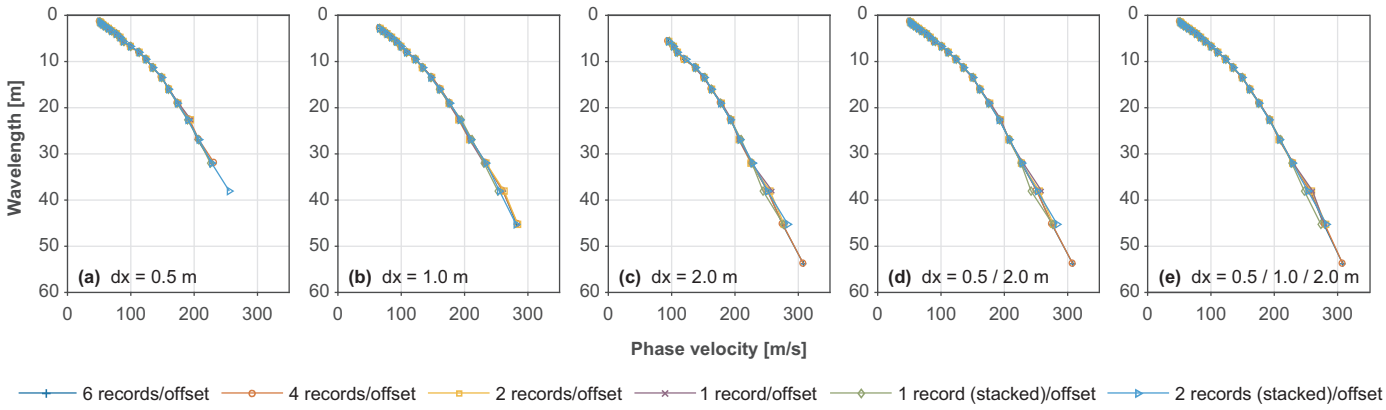

Fig. 10. Combined mean dispersion curves (with $a = 4.0$ in Eq. (6)) obtained for the study cases in Table 2.

Table 2
Overview of studied elementary dispersion curve combinations.

Number of records for each source offset	Profile/combination of profiles				
	dx = 0.5 m	dx = 1.0 m	dx = 2.0 m	dx = 0.5 m/dx = 2.0 m	dx = 0.5 m/dx = 1.0 m/dx = 2.0 m
	Number of elementary dispersion curves				
1[a]	4	4	4	8	12
2[b]	8	8	8	16	24
4[c]	16	16	16	32	48
6	24	24	24	48	72
1 (4 images stacked)[d]	4	4	4	8	12
2 (2 images stacked)[e]	8	8	8	16	24

[a] Record no. 4 for each combination of dx and x_1 (see Table 1 for x_1 values for different dx).
[b] Records no. 4 and 5 for each combination of dx and x_1.
[c] Records no. 2–5 for each combination of dx and x_1.
[d] Dispersion images computed based on records no. 2–5 stacked prior to the dispersion curve identification.
[e] Dispersion images computed based on records no. 2 and 3 and records no. 4 and 5, respectively, stacked prior to the dispersion curve identification.

The results presented in Fig. 12 indicate that similar dispersion curves were obtained by using the three ways of combining/averaging the multichannel surface wave data. However, in some cases (see Fig. 12a, c), the maximum wavelength values of the combined mean dispersion curves were slightly higher than those included in the "stacked-image-based" curves. In general, the low frequency part of the fundamental mode dispersion curve is the most difficult to attain in field measurements carried out using an active seismic source. When multiple dispersion images are stacked (averaged), those containing a less clear low frequency high-amplitude band can cancel out parts of the better defined high-amplitude bands that are present in other images, making the low frequency fundamental mode dispersion trend difficult to identify on the stacked image. Moreover, some breaks were observed in the "stacked-image-based" dispersion curves (see Fig. 12b, c), which correspond to the previously addressed breaks in the high-amplitude bands of the stacked dispersion images (Fig. 11c, d). Hence, the results indicate that, in these cases, a combination of several dispersion curves is more advantageous than the use of a single "stacked-image-based" curve. Furthermore, by averaging the dispersion data after the dispersion curve extraction, it becomes possible to estimate the accuracy of the estimated mean phase velocity values in terms of confidence intervals, as discussed in the following section.

6. Uncertainty associated with the combined mean dispersion curve

The procedure discussed in Section 5 centres on estimating the mean Rayleigh wave phase velocity for each wavelength interval. Point estimates of sample statistics, such as the sample mean, are inevitably subject to error, especially when they are derived based on small sample sizes (here a limited number of elementary dispersion curve data points within a given wavelength interval). Therefore, some variation from the true (population) mean is expected. An interval estimation of the mean phase velocity is a way to supplement the point

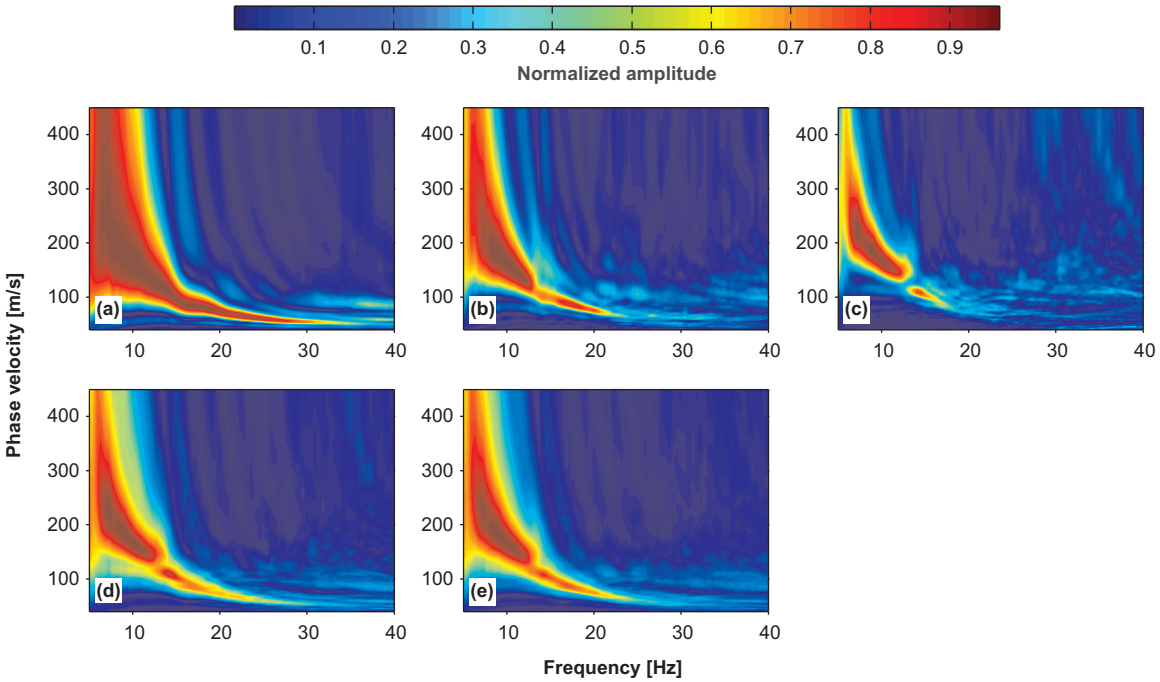

Fig. 11. Dispersion images obtained by stacking (a) 16 dispersion images obtained by the dx = 0.5 m profile (four images for each source offset), (b) 16 dispersion images obtained by the dx = 1.0 m profile (four images for each source offset), (c) 16 dispersion images obtained by the dx = 2.0 m profile (four images for each source offset), (d) 32 dispersion images obtained by the dx = 0.5 m and dx = 2.0 m profiles and (e) 48 dispersion images obtained by the three measurement profiles.

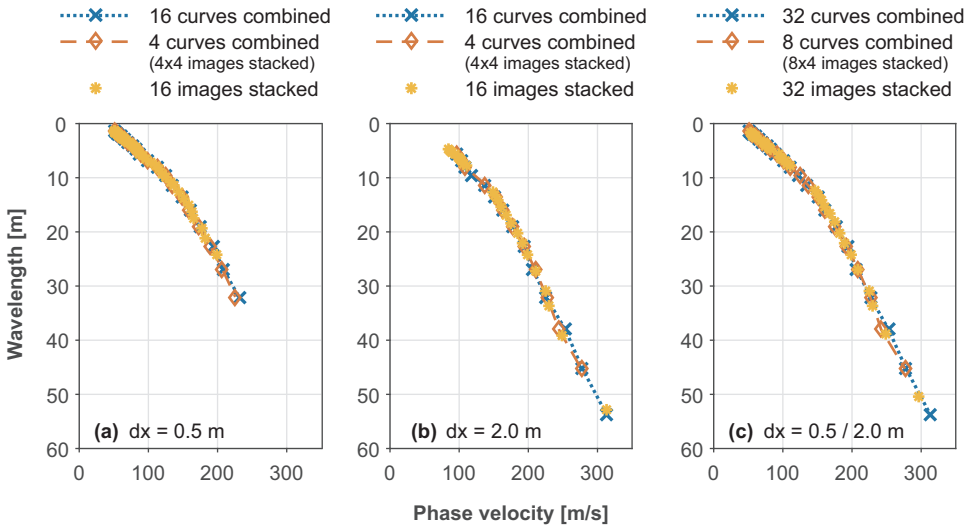

Fig. 12. Comparison of results obtained by combining multiple elementary dispersion curves to form a mean curve (a = 4. 0 in Eq. (6)) and by extracting a single dispersion curve from a stacked dispersion image.

estimate. Using parametric statistical methods, the p% confidence interval (CI) of the mean phase velocity can be obtained by application of the central limit theorem, or based on the t-distribution by assuming a normal distribution of the sample data [50]. The bootstrap is an alternative method for estimation of confidence intervals without distributional assumptions [51,52], and, hence advantageous when the probability distribution of the statistic of interest is unknown or when the sample size is insufficient for application of the central limit theorem (e.g. smaller than 30 data points [50]).

For application of the bootstrap, a Monte Carlo-style sampling is applied on the phase velocity values within each wavelength interval. That is, a large number of resamples, each having the same number of elements as the original sample, is randomly drawn from the original sample with replacement. Hence, the resamples will randomly vary from the original sample. Subsequently, the mean phase velocity value is computed for each resample and the relative frequency distribution of the bootstrap replications used as an approximation of the sampling distribution of the mean phase velocity for the given wavelength interval. Several different types of confidence intervals can be computed based on the simulated replications, e.g. the standard normal bootstrap confidence interval (SB), the percentile bootstrap confidence interval (PB) and the bias-corrected and accelerated (BC_a) confidence interval [52]. SB intervals are computed based on the assumption that the bootstrap replications are approximately normally distributed. The PB interval adjusts for potential bias in the bootstrap distribution, whereas the BC_a method incorporates the effects of both bias and skewness in the confidence interval computations. The three aforementioned methods were used for evaluation of confidence intervals for mean dispersion curves that were obtained by using different elementary dispersion curve combinations. In general, the difference between the three bootstrap confidence intervals (SB, PB and BC_a) was minor and, in many cases, negligible. Hence, in this section, only bootstrap confidence intervals obtained by the BC_a method are presented.

Fig. 13a–c illustrate the distribution of the phase velocity values of the elementary dispersion curve data points acquired by the dx = 0.5 m/dx = 2.0 m profiles at the Arnarbæli station (four records for each receiver spacing/source offset) within three selected wavelength intervals; (a) $\lambda \in$ [8.7,10.4) m, (b) $\lambda \in$ [24.7,29.3) m and (c) $\lambda \in$ [34.9,41.5) m. The wavelength intervals were selected so that they contained different numbers of dispersion curve data points, i.e. 36, 19 and 8 points, respectively. The solid line indicates the point estimate of the mean phase velocity in each case. The dashed lines correspond to plus/minus one standard deviation from the sample mean. However, due to the small sample sizes, it is difficult to draw a conclusion regarding the distribution type of the sample data based on the histograms. Fig. 13d–f show the normal Q-Q plots of the phase velocity

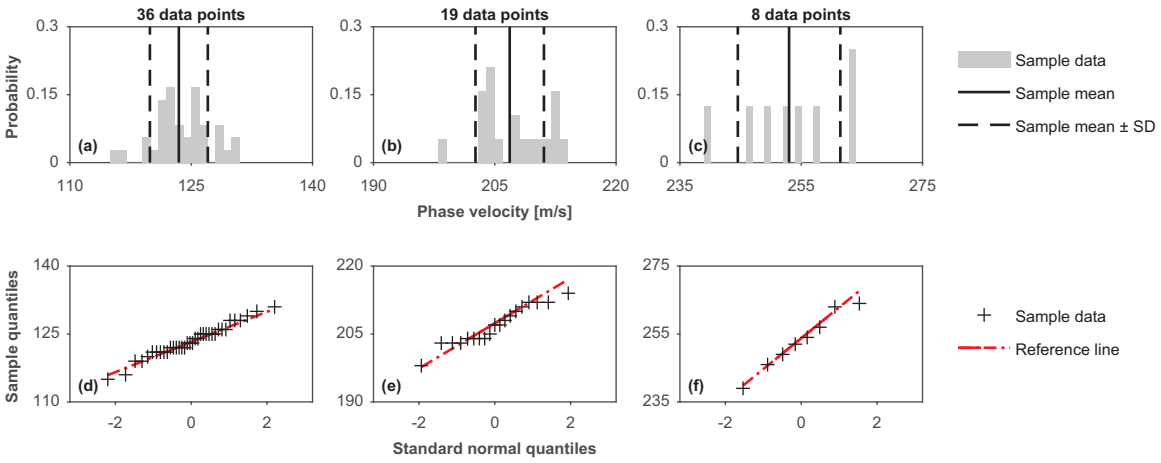

Fig. 13. Probability distributions and normal Q-Q plots of Rayleigh wave phase velocity values within three wavelength intervals (a, d) $\lambda \in$ [8.7, 10.4) m, (b, e) $\lambda \in$ [24.7, 29.3) m and (c, f) $\lambda \in$ [34.9, 41.5) m.

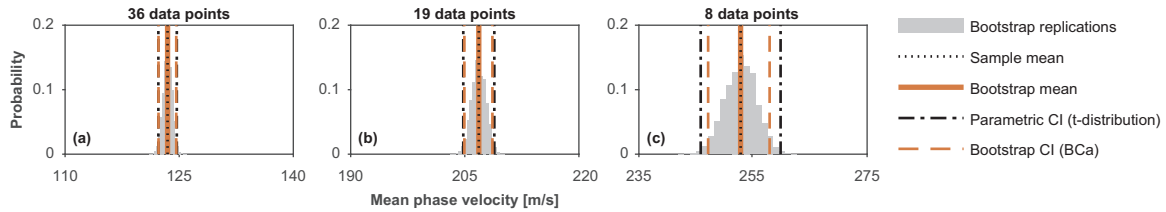

Fig. 14. Bootstrap replications of the sample mean for the wavelength intervals in Fig. 13 along with 95% confidence intervals for the sample mean obtained by using parametric statistics and the bootstrap.

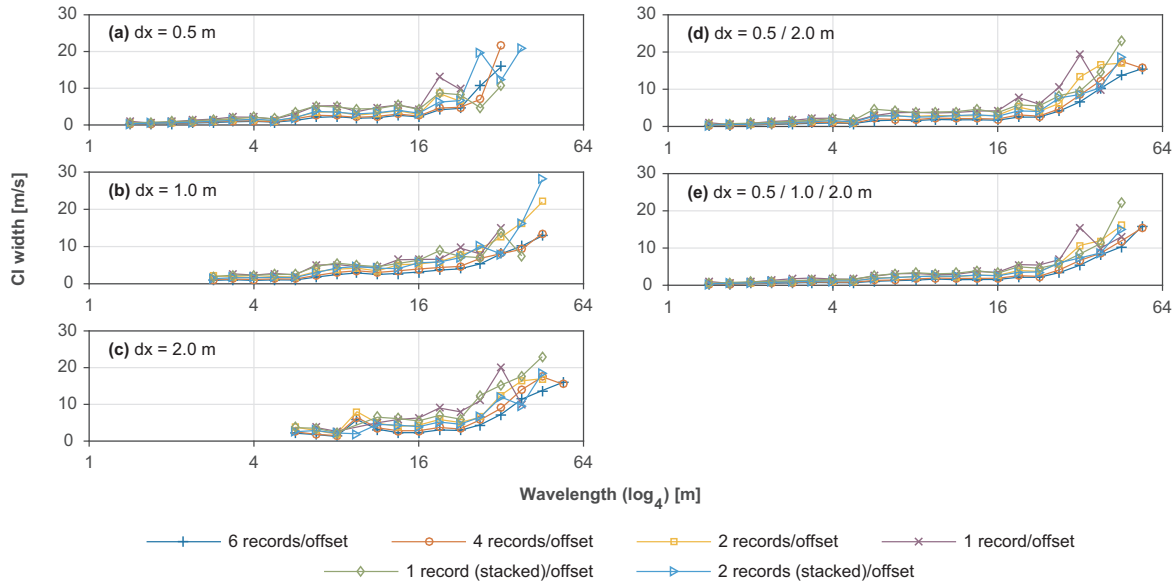

Fig. 15. Width of the 95% BC_a confidence intervals of the combined mean dispersion curves presented in Fig. 10.

values within each of the three wavelength intervals. Overall, the Q-Q plots indicate a fairly linear behaviour of the data, and, hence, that it appears to be justifiable to assume the normal distribution for the phase velocity values in each case. The Shapiro-Wilk test [53] also did not indicate a significant departure from normality at a 5% significance level.

The accuracy of the point estimate of each wavelength interval's mean phase velocity value was evaluated in terms of the 95% confidence interval for the sample mean. Fig. 14 shows the 10,000 bootstrap replications of the sample mean that were obtained for each of the three wavelength intervals in Fig. 13. The bootstrapped mean phase velocity value is shown to match the sample mean for all three intervals. A good match between the bootstrapped and sample mean values was also observed for the other wavelength intervals/elementary dispersion curve combinations that were studied. The dashed lines in Fig. 14 indicate the width of the 95% BC_a confidence intervals for the sample mean. For comparison with the results obtained by the bootstrapping analysis, 95% confidence intervals for the sample mean were also obtained by using the t-distribution. The parametric confidence intervals were, in general, in very good agreement with the bootstrap confidence intervals, even in cases where the number of data points was as little as 10–12. In cases where the number of data points was considerably lower, the parametric confidence intervals were, in general, wider than those obtained by the bootstrap (Fig. 14c). The parametric confidence intervals should, however, be interpreted with caution in cases where the sample size is small and graphical and/or statistical tests carried out for evaluation of the near-normality assumption prior to computations.

Fig. 15 compares the widths of the 95% BC_a confidence intervals for the mean dispersion curves obtained for the study cases reported in Table 2 (Fig. 10). In general, the confidence interval width decreased with decreased wavelength and increased number of observations (i.e. available dispersion curve data points). Hence, by increasing the number of elementary dispersion curves used for computation of the combined mean curve, the width of the confidence intervals generally decreases. However, the observed difference between using four and six records (for each receiver spacing/source offset combination) was in most cases minor, even at longer wavelengths. In cases where only a small number of dispersion curve data points fell into a given wavelength interval, "zigzagging" of the confidence interval width was observed in many cases. Stacking multiple dispersion images and using the dispersion curves extracted from the stacked images in the subsequent analysis provided, in general, similar or slightly narrower confidence intervals than were obtained by using the same number of unstacked records.

7. Effects on shear wave velocity profile estimates

For further assessing the effects of combining elementary dispersion data acquired by receiver spreads of different lengths, as well as the effects of the uncertainty associated with the point estimate of the mean phase velocity for each wavelength interval, Fig. 16 illustrates the inversion of the combined dispersion curves for the (i) $dx = 0.5$ m profile, (ii) $dx = 2.0$ m profile and (iii) $dx = 0.5$ m/$dx = 2.0$ m profiles (six records for each receiver spacing/source offset). Based on the ranges of wavelengths covered by the curves, the approximate maximum investigation depth was estimated according to Eq. (1) (with $\gamma = 1/2$) as 16 m for the $dx = 0.5$ m profile, and 27 m for the $dx = 2.0$ m and $dx = 0.5$ m/$dx = 2.0$ m profiles. The minimum investigation depth, as estimated by Eq. (2) (with $\zeta = 1/2$), was 0.7 m for the $dx = 0.5$ m and $dx = 0.5$ m/$dx = 2.0$ m profiles, and 2.9 m for the $dx = 2.0$ m profile.

Inversion problems involving the dispersion of Rayleigh waves in a

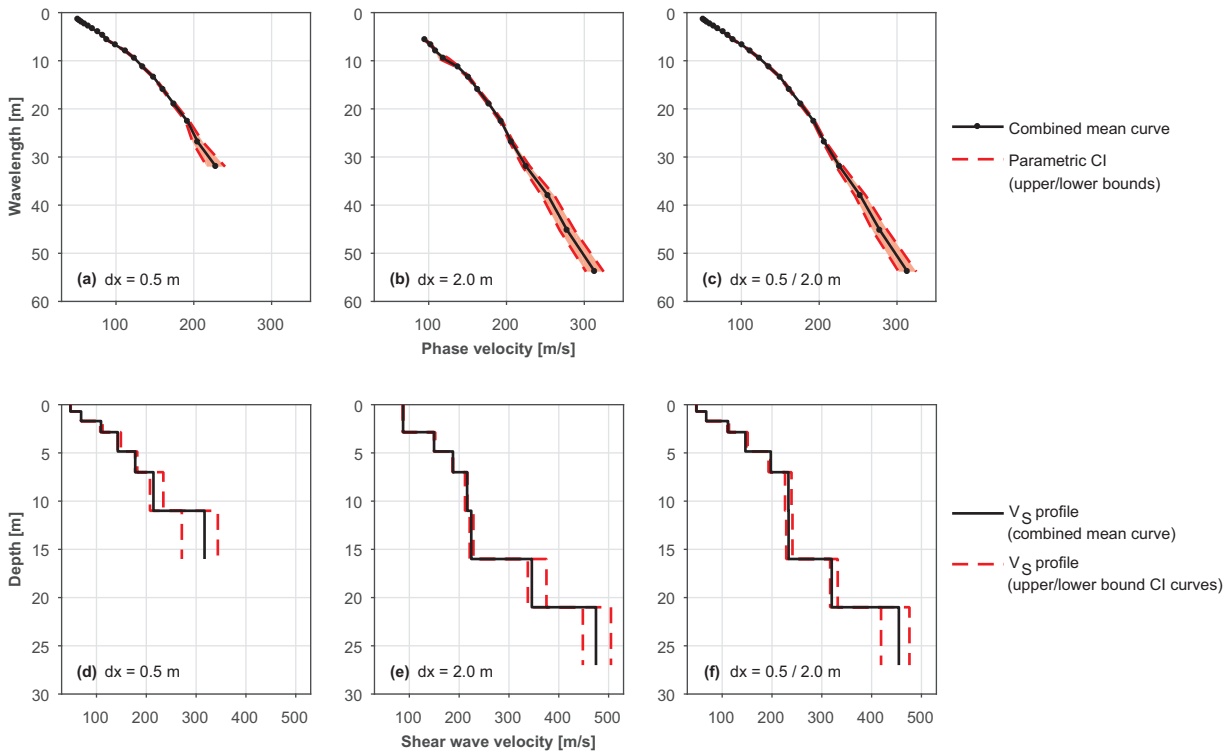

Fig. 16. Combined mean dispersion curves (a = 4. 0 in Eq. (6)) with 95% parametric confidence intervals for the (a) dx = 0.5 m profile, (b) dx = 2.0 m profile and (c) dx = 0.5 m/dx = 2.0 m profiles. Shear wave velocity profiles obtained from the combined mean, upper bound and lower bound dispersion curves, respectively, for the (d) dx = 0.5 m profile, (e) dx = 2.0 m profile and (f) dx = 0.5 m/dx = 2.0 m profiles.

layered elastic medium are by nature both non-linear and non-unique [34]. In short, the inversion is carried out by iteratively comparing theoretical dispersion curves obtained from 'trial' semi-infinite soil layer models to the experimental data (see also Fig. 1). Here, the stiffness matrix method [54] was used for computations of theoretical dispersion curves and a semi-automated trial-and-error procedure [55] used in order to fit the experimental observations with theoretical predictions from assumed soil models. The shear wave velocity of each layer was updated during the inversion process, while the other model parameters were kept unchanged. The misfit (ϵ) between the theoretical dispersion curve and the experimental curve was evaluated as

$$\epsilon = \frac{1}{Q}\sum_{i=1}^{Q}\frac{\sqrt{(c_{e,i}-c_{t,i})^2}}{c_{e,i}}\cdot 100\% \quad (8)$$

where Q is the number of data points included in the experimental/theoretical dispersion curves, $c_{t,i}$ is the phase velocity value of the i-th data point in the theoretical dispersion curve and $c_{e,i}$ is the phase velocity value of the i-th data point in the experimental curve. A convergence of the search procedure was defined as achieving a misfit of 1.0% or less.

For inversion of each of the three combined mean dispersion curves (Fig. 16a–c), a layered soil model was suggested where the thickness of the top-most soil layer and the depth of the half-space top coincided with the approximate investigation depth ranges obtained with Eqs. (1) and (2). To aid the comparison of the shear wave velocity profiles obtained by using the different experimental curves, the same layering was used in the three inversions, though with a reduced investigation depth for the dx = 0.5 m profile and an increased first-layer thickness for the dx = 2.0 m profile. The initial value of the shear wave velocity for each layer was obtained by mapping the points of the combined mean dispersion curves into approximate values of shear wave velocity [8] and subsequently discretising the resulting pseudo-shear wave velocity profiles to match the previously assumed layer structure. The half-space shear wave velocity was set equal to the shear wave velocity of the bottom-most finite thickness layer throughout the inversion. The compressional wave velocity and the mass density of each layer were estimated based on independent soil investigations [48,49], as well as based on prior knowledge of the Arnarbæli test site. Furthermore, as the Arnarbæli test site is considered normally dispersive, velocity reversals were not permitted during the inversion process.

The resulting shear wave velocity profiles are shown in Fig. 16d–f (solid lines). In general, similar shear wave velocity estimates were obtained by using the three combined mean dispersion curves, though characterized by the different investigation depth ranges. The lack of short wavelength wave components (i.e. λ < 5–6 m) obtained by the dx = 2.0 m measurement profile is reflected by the relatively thick surficial layer in the corresponding shear wave velocity profile (Fig. 16e). At depths greater than 2.9 m, the dx = 2.0 m profile provided very similar shear wave velocity estimates as the dx = 0.5 m/dx = 2.0 m profile. The dx = 0.5 m and dx = 0.5 m/dx = 2.0 m profiles provided nearly the same shear wave velocity values for the uppermost 11 m. However, at depths ranging from 11 m to 16 m, the shear wave velocity estimate obtained with the dx = 0.5 m profile was higher than those obtained by the other profiles.

The shaded areas in Fig. 16a–c illustrate the 95% parametric (t-distribution) confidence intervals for the mean phase velocity within each wavelength interval. The upper and lower bound combined dispersion curves (indicated by the dashed lines in Fig. 16a–c) correspond to the upper/lower bound phase velocity CI values for each wavelength interval. For inversion of the upper and lower bound curves, the shear wave velocity profile obtained from the corresponding mean curve was used as a starting profile for the trial-and-error search procedure. The shear wave velocity profiles obtained by inverting the upper and lower bound combined curves, respectively, are shown using dashed lines in Fig. 16d–f. At wavelengths shorter than 20–25 m, the confidence intervals for the combined mean dispersion curves are very narrow (Fig. 16a–c). Hence, the shear wave velocity estimates obtained from the combined mean curves and the corresponding upper/lower bound

curves were very consistent at shallow depth (Fig. 16d–f). For deeper layers, the wider confidence intervals lead to more differences among the shear wave velocity estimates. This is reflected by the coefficient of variation (Eq. (7)) of the shear wave velocity values for each of the layers, which ranged from 0.1–2.5% for the shallowest layers (i.e. layers at depths less than approximately 5 m) to 5.9–11.8% for the deepest finite-thickness layer included in each profile.

8. Summary and conclusions

This paper presents a methodology for combining dispersion curves that have been extracted from separate MASW dispersion images. The combined experimental dispersion curve is obtained by grouping the elementary dispersion curve data points together within $\log_a$ spaced wavelength intervals. Subsequently, the mean phase velocity within each interval is used as a point estimate of the phase velocity of Rayleigh wave components belonging to the given wavelength range.

Results of MASW field tests conducted at a silty sand test site were used in order to demonstrate the performance and the robustness of the methodology and for evaluation of the number of records and/or different measurement profile configurations needed to obtain a reliable combined mean curve. In the study 24 geophones were used in all cases. The uncertainty of the combined mean curves was evaluated, both by using parametric statistics, assuming the normal distribution for the dispersion curve data points within each wavelength interval, and by the bootstrap. Moreover, the combined dispersion curves were compared to curves extracted from stacked dispersion images. Finally, shear wave velocity profiles obtained by inversion of the combined curves were presented to further assess the effects of the different dispersion curve combinations.

The results of the study indicate that combining multiple dispersion curves that have been gathered by receiver spreads of different lengths at the same site can both increase the maximum depth of the resulting shear wave velocity profile and improve its resolution at shallow depth. Moreover, combination of dispersion data from multiple measurements can help compensate for segments of missing (or limited) data at certain frequencies in individual dispersion images/dispersion curves. Use of a short receiver spread (i.e. $dx = 0.5$ m) and a long receiver spread (i.e. $dx = 2.0$ m) was sufficient for the silty sand site in this study and the intended investigation depth (i.e. 20–30 m). Visual comparison of several dispersion images, acquired by using different measurement profile parameters, can furthermore be essential in order to correctly identify and separate the fundamental mode dispersion curve from overtones or noise, which in some cases may be difficult to do based on a single image. Hence, the use of several source offsets (i.e. three to four) for each receiver spread length can help identification of the fundamental mode trend. For each source offset, around four multichannel surface wave records should be sufficient.

The number of extracted elementary dispersion curves, used for evaluation of the combined mean curve, has to be sufficient to provide a number of, approximately evenly spaced, dispersion curve data points within each wavelength interval. Present experience indicates that the preferred number of data points within each interval is at least five to six, though highly dependent on the interval length and the distribution of the points within the interval. In general, an increased number of dispersion curve data points (within each interval) results in a more precise point estimate of the mean phase velocity. The number and distribution of the elementary dispersion curve data points in the longest wavelength (lowest frequency) range is the main factor affecting the optimum number of wavelength intervals used for computation of the combined curve. The optimum value of the parameter a, which defines the wavelength intervals, should be chosen after initial inspection of the available data. Present experience with applying the methodology indicates that $\log_{5/2}$ to $\log_5$ spaced wavelength intervals are appropriate for most test sites (i.e. $a = 2.5$ to $a = 5.0$ in Eq. (6)). The $\log_3$ or $\log_4$ spaced wavelength intervals (i.e. $a = 3.0$ or $a = 4.0$) will be sufficient in many cases.

Identification and extraction of dispersion curves can be a time-consuming and labour-intensive part of the MASW data processing. As the number of dispersion curve data points, in general, decreases with increasing wavelength, it can be of value to use a higher number of elementary dispersion curves acquired by a longer measurement profile (which should provide the longer wavelength wave components) than by a shorter profile. Moreover, the number of dispersion curves that have to be extracted can be somewhat reduced by stacking several dispersion images, obtained by using the same (or very similar) measurement profile configuration, prior to the (elementary) dispersion curve extraction and the computation of the combined curve. The stacked images can allow more confident dispersion curve extraction and, in some cases, identification of the fundamental mode at higher and/or lower frequencies than can be extracted from a single (unstacked) image. However, in other cases, the dispersion image stacking might not be beneficial as parts of the high-amplitude bands can be cancelled out.

By averaging the dispersion data post dispersion curve extraction, the uncertainty of the combined mean curve estimate can be evaluated and presented by a series of confidence intervals. This enables the analyst to more rationally evaluate the quality of the dispersion data and the combined mean dispersion curve. Furthermore, by inverting the boundary dispersion curves resulting from the confidence interval computations (and/or other combinations of the upper/lower bound phase velocity CI values), the effects of the uncertainty associated with the computation of the mean phase velocity values on the shear wave velocity profile can be studied.

The confidence intervals for the mean phase velocity can, in most cases, be estimated based on the standard error of the elementary dispersion curve data points (within each wavelength interval) by assuming the normal distribution for the sample data. The bootstrap is a useful method for computation of confidence intervals for those wavelength intervals that contain a small number of data points, or in cases where the normal assumption might not be valid. Comparison of series of confidence intervals obtained for different combined mean dispersion curves revealed that the parametric confidence intervals for the mean phase velocity were, in general, in good agreement with the bootstrap confidence intervals. In cases where the number of data points was considerably lower than 10–12, the parametric confidence intervals were, however, somewhat wider than those obtained by the bootstrap.

Although the conclusions presented in this paper are only supported by data from a single test site, the same trend and results can be found in data gathered at a number of other sites. However, relatively similar sand materials characterize the majority of these test sites. Therefore, further measurements will be required in order to conclude about sites characterized by other kinds of soil materials, e.g. fine-grained and/or organic soils.

Acknowledgements

This work was supported by the University of Iceland Research Fund [Grant no. 73077]; the Icelandic Road and Coastal Administration [Grant no. 1800-373]; and the Energy Research Fund of the National Power Company of Iceland [Grant no. NYR-18-2017].

References

[1] Kramer SL. Geotechnical earthquake engineering. Upper Saddle River, NJ: Prentice-Hall; 1996.
[2] CEN. EN1998-1:2004. Eurocode 8: design of structures for earthquake resistance. Part 1: general rules, seismic actions and rules for buildings. Brussels: European Committee for Standardization; 2004.
[3] BSSC. NEHRP (National Earthquake Hazards Reduction Program) recommended seismic provisions for new buildings and other structures (FEMA P-1050-1) 2015 edition. Vol. 1. Part 1: provisions. Part 2: commentary. Washington DC: Federal Emergency Management Agency; 2015.
[4] Gazetas G. Foundation vibrations. In: Fang H-Y, editor. Foundation engineering

handbook. New York, NY: Van Nostrand Reinhold; 1991. p. 553–93.
[5] Aki K, Richards PG. Quantitative seismology: theory and methods 1. San Francisco, CA: W.H. Freeman and Co.; 1980.
[6] Socco LV, Foti S, Boiero D. Surface-wave analysis for building near-surface velocity models – established approaches and new perspectives. Geophysics 2010;75(5):75A83–102A83. http://dx.doi.org/10.1190/1.3479491.
[7] Gabriels P, Snieder R, Nolet G. In situ measurements of shear-wave velocity in sediments with higher-mode Rayleigh waves. Geophys Prospect 1987;35(2):187–96. http://dx.doi.org/10.1111/j.1365-2478.1987.tb00812.x.
[8] Park CB, Miller RD, Xia J. Multichannel analysis of surface waves. Geophysics 1999;64(3):800–8. http://dx.doi.org/10.1190/1.1444590.
[9] Xia J. Estimation of near-surface shear-wave velocities and quality factors using multichannel analysis of surface-wave methods. J Appl Geophys 2014;103:140–51. http://dx.doi.org/10.1016/j.jappgeo.2014.01.016.
[10] Nazarian S, Stokoe II KH, Hudson WR. Use of spectral analysis of surface waves method for determination of moduli and thicknesses of pavement systems. Transp Res Rec 1983;930:38–45.
[11] Xia J, Miller RD, Park CB, Tian G. Inversion of high frequency surface waves with fundamental and higher modes. J Appl Geophys 2003;52(1):45–57. http://dx.doi.org/10.1016/S0926-9851(02)00239-2.
[12] Gao L, Xia J, Pan Y, Xu Y. Reason and condition for mode kissing in MASW method. Pure Appl Geophys 2016;173(5):1627–38. http://dx.doi.org/10.1007/s00024-015-1208-5.
[13] Zhang SX, Chan LS. Possible effects of misidentified mode number on Rayleigh wave inversion. J Appl Geophys 2003;53(1):17–29. http://dx.doi.org/10.1016/S0926-9851(03)00014-4.
[14] Garofalo F, Foti S, Hollender F, Bard PY, Cornou C, Cox BR, et al. InterPACIFIC project: comparison of invasive and non-invasive methods for seismic site characterization. Part I: intra-comparison of surface wave methods. Soil Dyn Earthq Eng 2016;82:222–40. http://dx.doi.org/10.1016/j.soildyn.2015.12.010.
[15] Dikmen Ü, Arısoy MÖ, Akkaya İ. Offset and linear spread geometry in the MASW method. J Geophys Eng 2010;7(2):211–22. http://dx.doi.org/10.1088/1742-2132/7/2/S07.
[16] Ivanov J, Miller RD, Tsoflias G. Some practical aspects of MASW analysis and processing. In: Proceedings of the symposium on the application of geophysics to engineering and environmental problems 2008. Philadelphia, PA; 2008, p. 1186–98. ⟨http://dx.doi.org/10.4133/1.2963228⟩.
[17] Olafsdottir EA, Erlingsson S, Bessason B. Effects of measurement profile configuration on estimation of stiffness profiles of loose post glacial sites using MASW. In: Proceedings of the 17th Nordic geotechnical meeting. Reykjavik, Iceland; 2016, p. 327–36.
[18] Park CB, Miller RD, Xia J. Offset and resolution of dispersion curve in multichannel analysis of surface waves (MASW). In: Proceedings of the symposium on the application of geophysics to engineering and environmental problems 2001. Denver, CO; 2001, p. SSM4. ⟨http://dx.doi.org/10.4133/1.2922953⟩.
[19] Park CB, Miller RD, Miura H. Optimum field parameters of an MASW survey [Exp. Abs.]. In: Proceedings of the 6th SEG-J international symposium. Tokyo, Japan; 2002.
[20] Park CB, Carnevale M. Optimum MASW survey–revisit after a decade of use. In: Proceedings of GeoFlorida 2010: advances in analysis, modeling & design. West Palm Beach, FL; 2010, p. 1303–12. ⟨http://dx.doi.org/10.1061/41095(365)130⟩.
[21] Wood CM, Cox BR. A comparison of MASW dispersion uncertainty and bias for impact and harmonic sources. In: Proceedings of GeoCongress 2012. Oakland, CA; 2012, p. 2756–65. ⟨http://dx.doi.org/10.1061/9780784412121.282⟩.
[22] Xu Y, Xia J, Miller RD. Quantitative estimation of minimum offset for multichannel surface-wave survey with actively exciting source. J Appl Geophys 2006;59(2):117–25. http://dx.doi.org/10.1016/j.jappgeo.2005.08.002.
[23] Zhang SX, Chan LS, Xia J. The selection of field acquisition parameters for dispersion images from multichannel surface wave data. Pure Appl Geophys 2004;161(1):185–201. http://dx.doi.org/10.1007/s00024-003-2428-7.
[24] Yaede JR, McBride JH, Nelson ST, Park CB, Flores JA, Turnbull SJ, et al. A geophysical strategy for measuring the thickness of the critical zone developed over basalt lavas. Geosphere 2015;11(2):514–32. http://dx.doi.org/10.1130/GES01142.1.
[25] Shakir AM, Foti S, Garofalo F, Hijab BR, Laftah AA. Laterally constrained inversion of surface wave data at Najaf city (Iraq). Soil Dyn Earthq Eng 2013;45:89–95. http://dx.doi.org/10.1016/j.soildyn.2012.11.003.
[26] Neducza B. Stacking of surface waves. Geophysics 2007;72(2):V51–8. http://dx.doi.org/10.1190/1.2431635.
[27] Socco LV, Boiero D, Foti S, Wisén R. Laterally constrained inversion of ground roll from seismic reflection records. Geophysics 2009;74(6):G35–45. http://dx.doi.org/10.1190/1.3223636.
[28] Piatti C, Foti S, Socco LV, Boiero D. Building 3D shear-wave velocity models using surface waves testing: the Tarcento basin case history. Bull Seismol Soc Am 2013;103(2A):1038–47. http://dx.doi.org/10.1785/0120120089.
[29] Song X, Gu H. Utilization of multimode surface wave dispersion for characterizing roadbed structure. J Appl Geophys 2007;63(2):59–67. http://dx.doi.org/10.1016/j.jappgeo.2007.04.001.
[30] Lai CG, Foti S, Rix GJ. Propagation of data uncertainty in surface wave inversion. J Environ Eng Geophys 2005;10(2):219–28. http://dx.doi.org/10.2113/JEEG10.2.219.
[31] Cox BR, Bachhuber J, Rathje E, Wood CM, Dulberg R, Kottke A, et al. Shear wave velocity- and geology-based seismic microzonation of Port-au-Prince, Haiti. Earthq Spectra 2011;27(S1):S67–92. http://dx.doi.org/10.1193/1.3630226.
[32] Cardarelli E, Cercato M, De Donno G. Characterization of an earth-filled dam through the combined use of electrical resistivity tomography, P- and SH-wave seismic tomography and surface wave data. J Appl Geophys 2014;106:87–95. http://dx.doi.org/10.1016/j.jappgeo.2014.04.007.
[33] Luo Y, Xia J, Liu J, Xu Y, Liu Q. Research on the middle-of-receiver-spread assumption of the MASW method. Soil Dyn Earthq Eng 2009;29(1):71–9. http://dx.doi.org/10.1016/j.soildyn.2008.01.009.
[34] Foti S, Lai CG, Rix GJ, Strobbia C. Surface wave methods for near-surface site characterization. Boca Raton, FL: CRC Press, Taylor & Francis Group; 2015.
[35] Richart FE, Hall JR, Woods RD. Vibrations of soils and foundations. Englewood Cliffs, NJ: Prentice-Hall; 1970.
[36] Cox BR, Teague DP. Layering ratios: a systematic approach to the inversion of surface wave data in the absence of a priori information. Geophys J Int 2016;207(1):422–38. http://dx.doi.org/10.1093/gji/ggw282.
[37] Pei D. Modeling and inversion of dispersion curves of surface waves in shallow site investigations [Ph.D. Thesis]. Reno, NV: University of Nevada; 2007.
[38] Gucunski N, Woods RD. Use of Rayleigh modes in interpretation of SASW test. In: Proceedings of the 2nd international conference on recent advances in geotechnical earthquake engineering and soil dynamics. St. Louis, MO; 1991, p. 1399–408.
[39] Tokimatsu K, Tamura S, Kojima H. Effects of multiple modes on Rayleigh wave dispersion characteristics. J Geotech Eng 1992;118(10):1529–43. http://dx.doi.org/10.1061/(ASCE)0733-9410(1992)118:10(1529).
[40] Xia J, Miller RD, Xu Y, Luo Y, Chen C, Liu J, et al. High-frequency Rayleigh-wave method. J Earth Sci 2009;20(3):563–79. http://dx.doi.org/10.1007/s12583-009-0047-7.
[41] Yoon S, Rix GJ. Near-field effects on array-based surface wave methods with active sources. J Geotech Geoenviron Eng 2009;135(3):399–406. http://dx.doi.org/10.1061/(ASCE)1090-0241(2009)135:3(399).
[42] Yilmaz Ö. Seismic data processing. Tulsa, OK: Society of Exploration Geophysicists; 1987.
[43] McMechan GA, Yedlin MJ. Analysis of dispersive waves by wave field transformation. Geophysics 1981;46(6):869–74. http://dx.doi.org/10.1190/1.1441225.
[44] Park CB, Miller RD, Xia J. Imaging dispersion curves of surface waves on multichannel record. In: SEG technical program expanded abstracts 1998. New Orleans, LA; 1998, p. 1377–80. ⟨http://dx.doi.org/10.1190/1.1820161⟩.
[45] Dal Moro G, Pipan M, Forte E, Finetti I. Determination of Rayleigh wave dispersion curves for near surface applications in unconsolidated sediments. In: SEG technical program expanded abstracts 2003. Dallas, TX; 2003, p. 1247–50. ⟨http://dx.doi.org/10.1190/1.1817508⟩.
[46] Olafsdottir EA, Erlingsson S, Bessason B. Tool for analysis of multichannel analysis of surface waves (MASW) field data and evaluation of shear wave velocity profiles of soils. Can Geotech J 2018;55(2):217–33. http://dx.doi.org/10.1139/cgj-2016-0302.
[47] Park CB. Imaging dispersion of MASW data – full vs. selective offset scheme. J Environ Eng Geophys 2011;16(1):13–23. http://dx.doi.org/10.2113/JEEG16.1.13.
[48] Green RA, Halldorsson B, Kurtulus A, Steinarsson H, Erlendsson O. A unique liquefaction case study from the 29 May 2008, M_w 6.3 Olfus earthquake, Southwest Iceland. In: Proceedings of the 15th world conference on earthquake engineering. Lisbon, Portugal; 2012.
[49] Olafsdottir EA, Bessason B, Erlingsson S. MASW for assessing liquefaction of loose sites. In: Proceedings of the 16th European conference on soil mechanics and geotechnical engineering. Edinburgh, UK; 2015, p. 2431–6.
[50] Ross SM. Introduction to probability and statistics for engineers and scientists. 4th ed. Burlington, MA: Elsevier Academic Press; 2009.
[51] Efron B. Bootstrap methods: another look at the jackknife. Ann Stat 1979;7(1):1–26. http://dx.doi.org/10.1214/aos/1176344552.
[52] Efron B, Tibshirani RJ. An introduction to the bootstrap. New York, NY: Chapman & Hall; 1993.
[53] Shapiro SS, Wilk MB. An analysis of variance test for normality (complete samples). Biometrika 1965;52(3–4):591–611. http://dx.doi.org/10.2307/2333709.
[54] Kausel E, Roësset JM. Stiffness matrices for layered soils. Bull Seismol Soc Am 1981;71(6):1743–61.
[55] Olafsdottir EA. Multichannel analysis of surface waves for assessing soil stiffness [M.Sc. Thesis]. Reykjavik, Iceland: Faculty of Civil and Environmental Engineering, University of Iceland; 2016⟨http://hdl.handle.net/1946/23646⟩.

Paper III

Shear wave velocity profiles from MASW inversion analysis using a simple Monte Carlo search technique for geotechnical engineering applications

Elín Ásta Ólafsdóttir, Sigurður Erlingsson & Bjarni Bessason

Ólafsdóttir, E.Á., Erlingsson, S. & Bessason, B. (2019). Shear wave velocity profiles from MASW inversion analysis using a simple Monte Carlo search technique for geotechnical engineering applications. *Soil Dynamics and Earthquake Engineering* (resubmitted).

Shear wave velocity profiles from MASW inversion analysis using a simple Monte Carlo search technique for geotechnical engineering applications

Elín Ásta Ólafsdóttir[1)], Sigurður Erlingsson[1,2)], & Bjarni Bessason[1)]

[1)] Faculty of Civil and Environmental Engineering, University of Iceland, Reykjavik, Iceland
[2)] Pavement Technology, The National Road and Transport Research Institute, Linköping, Sweden

Abstract

The shear wave velocity profile is of primary interest for geotechnical characterization of soil sites. Multichannel Analysis of Surface Waves (MASW) is a seismic exploration method for determination of near-surface shear wave velocity profiles by analyzing Rayleigh wave propagation over a wide range of wavelengths. The inverse problem faced during the application of MASW involves finding one or more layered soil models whose theoretical dispersion curves match the observed dispersion characteristics. In this paper, the use of a simple but effective Monte Carlo-based search technique is proposed for use in the MASW inversion analysis. The performance and applicability of the inversion scheme is demonstrated with synthetic datasets, as well as field data acquired at a well-characterized geotechnical research site.

Keywords

Multichannel Analysis of Surface Waves; MASW; non-invasive testing; shear wave velocity; soil characterization; Rayleigh wave dispersion curves; inversion; Monte Carlo simulation; search algorithm

1. Introduction

The shear wave velocity (V_S) profile is a fundamental parameter in geotechnical engineering due to its relations to the small-strain shear stiffness (G_{max}). Information on the shear wave velocity distribution is further essential for assessing the dynamic behavior of soil, e.g., for the purpose of seismic site response analysis (Kramer, 1996) and soil-structure interaction analysis (Wolf, 1985). Current building codes use the average shear wave velocity in the top-most 30 m (V_{S30}) as a proxy to classify soil sites and define seismic design loads (BSSC, 2015; CEN, 2004). V_{S30} is also commonly implemented in ground motion prediction equations to consider expected soil amplifications (Abrahamson et al., 2008; Douglas and Aochi, 2008; Douglas and Edwards, 2016). Moreover, recently proposed classification schemes have suggested the use of the average shear wave velocity (V_{SZ}), alongside other geotechnical parameters, for seismic zonation purposes (e.g., Héloïse et al., 2012; Luzi et al., 2011; Pitilakis et al., 2013; 2018).

The dispersive nature of Rayleigh waves in a heterogeneous medium provides key information for geotechnical characterization of near-surface materials (Kramer, 1996). At a given site, the shear wave velocity profile has a dominant effect on the Rayleigh wave dispersion. Multichannel Analysis of Surface Waves (MASW) (Park et al., 1999) is a non-invasive surface wave analysis method that has become a common technique for estimating near-surface V_S-profiles for civil engineering applications (Socco et al., 2010; Xia, 2014; Foti et al., 2018). MASW is a time- and cost-effective technique. The method can further be applied at a wide variety of soil sites, including locations where invasive techniques, e.g., penetration tests, are difficult to apply (Bessason and Erlingsson, 2011; Olafsdottir et al., 2019). An application of MASW is, in general, divided into three consecutive steps: (i) field measurements, (ii) identification of experimental dispersion curves, and (iii) estimation of shear wave velocity by inversion of the Rayleigh wave dispersion data.

Overall, the resolution of surface wave analysis methods diminishes with increasing depth (Foti et al., 2015). While the analysis can resolve modest variations in shear wave velocity close to the surface, only major variations can be detected at greater depths. A common practice for interpretation of fundamental mode dispersion curves (e.g., Cox and Teague, 2016; Foti et al., 2018; Garofalo et al., 2016a; Park et al., 1999) is to estimate the investigated depth as one-third to half the maximum Rayleigh wave wavelength, and, similarly, to limit the thickness of the top-most soil layer to a minimum of one-third to half the shortest retrieved wavelength. Recently, alternatives to this empirical wavelength-depth approach have been proposed (Leong and Aung, 2012; Haney and Tsai, 2015; Socco et al., 2017; Passeri, 2019), such as directly transforming the wavelength of the experimental dispersion curve to the depth of a corresponding pseudo V_{SZ}-profile.

The present paper addresses the inverse problem faced in the third step of MASW analysis. Forward modelling of Rayleigh wave dispersion curves is the basis of the inversion analysis. The survey site is typically modeled as a linear elastic semi-infinite layered medium, consisting of a predefined number (n) of homogeneous and isotropic layers over a half-space. The parameters required to define the properties of each layer are shear wave velocity (V_S), layer

thickness (h), Poisson's ratio (ν) (or compressional wave velocity (V_P)) and mass density (ρ). The shear wave velocity has a dominant effect on the fundamental mode dispersion curve at frequencies higher than 5 Hz, followed by layer thicknesses (Xia et al., 1999), while variations in ν (or V_P) and ρ have much less effect. Hence, ν (or V_P) and ρ are commonly assigned fixed values based on a-priori information or by using standard values for specific soil types (de Lucena and Taioli, 2014; Foti et al., 2015). The initially specified layering parameterization is further an important factor in the inversion process (Cox and Teague, 2016; Di Giulio et al., 2012) and the number of layers to include in the stratified soil model should be regarded as an additional inversion parameter. No general recommendations exist for how to optimally specify the number of soil layers but repeated analysis using different values of n has been recommended (Cox and Teague, 2016; Foti et al., 2018) so the effects of the layering parameterization on the estimated V_S-profiles can be assessed.

Conventionally, the inversion of Rayleigh wave dispersion curves is formulated as an optimization problem where the objective is to minimize the value of a misfit function representing the distance between the experimental and theoretical curves. Hence, in its most general form, the inversion is conducted by iteratively comparing theoretical dispersion curves, obtained from 'trial' subsurface models, to the experimental data in search of a model that both fits the observed dispersion characteristics and incorporates the known features of the survey site. The use of various automated search techniques has been suggested to aid the quest of soil models that reproduce the observed dispersion curve. In general, they can be divided into two main categories; local and global search procedures (Sen and Stoffa, 2013; Socco et al., 2010). On the one hand, local search methods are iterative schemes which, by starting from an initial estimate of the inversion parameters, generate a sequence of improved model assessments. Global search methods, on the other hand, attempt to search for the global stationary point by exploring the entire solution space. The use of various advanced optimization methods has been suggested to guide the search towards the high-probability-density regions of the solution space (e.g., Beaty et al., 2002; Pezeshk and Zarrabi, 2005; Socco and Boiero, 2008; Song et al., 2008; 2012; 2014; 2015; Wathelet et al., 2004; Wathelet, 2008). An inherent risk associated with local search methods is that the algorithm may converge to a local minimum of the misfit function. Inaccurate values of the partial derivatives of the dispersion curve with respect to the model parameters can further severely affect the performance of the search algorithm. Despite these drawbacks, local search methods may be preferred by engineers as they are easier to handle than advanced global search procedures. They further provide the result in the form of a single V_S-profile, which is desirable for many engineering applications (Socco et al., 2010). Local search methods are also more common in commercial software (Song et al., 2014). By application of global search procedures, all assumptions of linearity between the experimental data and the model parameters are avoided. However, global search methods are computationally more demanding as a high number of forward simulations is required to adequately sample the model parameter space (Socco et al., 2010), thereby imposing some practical limitations on the analysis. Although global search methods are better suited for the non-uniqueness of the inverse problem encountered, the use of advanced optimization algorithms might be considered excessive for general geotechnical engineering applications.

In this paper, the use of a simple but effective Monte Carlo-based, global search inversion procedure, aimed at geotechnical engineering applications of the MASW method, is proposed. Hence, the emphasis of this work is on demonstrating that a simple global search technique, i.e., not incorporating any advanced optimization, can deliver sufficient results for applications in practice. The applicability and performance of the search algorithm is initially studied by analysis of synthetic dispersion curves, representing loose to medium-dense sand and soft clay sites commonly encountered in geotechnical engineering practice. For simulation of real-world scenarios, the inversion scheme is further tested on synthetic dispersion curves that have been perturbed by introduction of Gaussian noise. Finally, a dataset acquired at a well-characterized geotechnical research site is analyzed to verify the robustness of the proposed strategy. A statistical sample of dispersion curves is obtained through repeated data acquisition and the variability in estimated phase velocity values quantified. After conducting the Monte Carlo-based search, using different layering parameterizations, inference is drawn from the set of simulated V_S-profiles based on the observed spread in the experimental data. The inversion results are compared to results of invasive and laboratory-based measurements of shear wave velocity previously conducted at the site.

2. Method

A schematic overview of the inversion strategy is provided in Fig. 1. The properties of the layered medium are described by the shear wave velocity vector $\boldsymbol{V_S} = [V_{S,1}, V_{S,2}, \dots, V_{S,n}, V_{S,n+1}]$, the layer thickness vector $\boldsymbol{h} = [h_1, h_2, \dots, h_n]$, the mass density vector $\boldsymbol{\rho} = [\rho_1, \rho_2, \dots, \rho_n, \rho_{n+1}]$ and the Poisson's ratio vector $\boldsymbol{\nu} = [\nu_1, \nu_2, \dots, \nu_n, \nu_{n+1}]$. Alternatively, the elements of the compressional wave velocity vector $\boldsymbol{V_P} = [V_{P,1}, V_{P,2}, \dots, V_{P,n}, V_{P,n+1}]$ can be specified instead of the Poisson's ratio. The observed (experimental) Rayleigh wave dispersion curve is denoted by $(\boldsymbol{V_{R,e}}, \boldsymbol{\lambda})$.

In this work, the focus is on inversion of fundamental mode Rayleigh wave dispersion curves for the elements of $\boldsymbol{V_S}$ and $\boldsymbol{h}$. The Poisson's ratio (or compressional wave velocity) and mass density are assessed beforehand, with the location of the groundwater table taken into consideration. Hence, the number of unknown model parameters (given a fixed value of n) is reduced from $4n + 3$ to $2n + 1$. Initial estimates of n and $\boldsymbol{h}$ are required as a starting point of the inversion process. Other, user-defined, input parameters required for initiation of the inversion process are the search-control parameters b_S and b_h, and the maximum number of iterations N_{max}. During the inversion process, the parameters b_S and b_h specify the range of shear wave velocity and layer thickness values, respectively, that the algorithm can sample in each iteration. The effects of specifying different values for the 'b-parameters' are studied in subsequent sections.

In this study, the initial shear wave velocity value for each layer is obtained by mapping the experimental dispersion curve into approximate values of V_S. Subsequently, the resulting pseudo-shear wave velocity profile is discretized to match the previously assumed layer

structure following a method comparable to the schemes adopted by Xia et al. (1999) and de Lucena and Taioli (2014), i.e.

$$
\begin{aligned}
V_{S,1} &= a \cdot V_{R,\lambda min} && \text{for the top-most soil layer } (j = 1) \\
V_{S,j} &= a \cdot V_{R,e}(\lambda_j) && \text{for layers } j = 2,3,\dots,n \\
V_{S,n+1} &= a \cdot V_{R,\lambda max} && \text{for the half-space } (j = n+1)
\end{aligned}
\tag{1}
$$

where the wavelength λ_j is estimated as $2\bar{z}_j$ to $3\bar{z}_j$ where $\bar{z}_j$ is the average depth of the j-th layer, i.e., $\bar{z}_j = 0.5(z_j + z_{j+1})$. In the synthetic and real-world examples presented in Sections 3 and 4, a value of $2.5\bar{z}_j$ is used and the multiplication factor a in Eq. (1) is specified as 1.09 based on the ratio between the propagation velocities of shear waves and Rayleigh waves in a homogenous medium. The value of a can also be estimated for specific soil materials as (Bergmann, 1948)

$$
a = \frac{1+\nu}{0.87+1.12\nu}\ ,\quad \nu \in [0.0\ ,0.5] \tag{2}
$$

where ν is the medium's characteristic Poisson's ratio.

At test sites where the observed fundamental mode dispersion curve ($\boldsymbol{V_{R,e}, \lambda}$) has vertical asymptotes (see e.g. model A in Fig. 2), those can be used to improve the estimate of the initial shear wave velocity values (e.g., Xia et al., 1999). Hence, the use of the asymptotic velocities $V_{R,\lambda min}$ and $V_{R,\lambda max}$ is implemented in Eq. (1) for assessment of $V_{S,1}$ and $V_{S,n+1}$. Here, $V_R = V_{R,\lambda min}$ denotes a vertical asymptote to the experimental dispersion curve at short wavelengths and $V_R = V_{R,\lambda max}$ denotes a vertical asymptote at the longest retrieved wavelengths. If the experimental dispersion curve does not show such vertical asymptotes, $V_{R,\lambda min}$ and $V_{R,\lambda max}$ can be estimated as $V_R(\lambda_{min})$ and $V_R(\lambda_{max})$, respectively.

The theoretical fundamental mode Rayleigh wave phase velocities $\boldsymbol{V_{R,t}}$ that correspond to each element of $\boldsymbol{\lambda}$ are obtained based on the initial set of model parameters (i.e., $\boldsymbol{h}$, $\boldsymbol{V_S}$, $\boldsymbol{V_P}$ (or $\boldsymbol{\nu}$) and $\boldsymbol{\rho}$). The fast delta-matrix algorithm (Buchen and Ben-Hador, 1996), implemented in a modified version of the MASWaves software (Olafsdottir et al., 2018a), is used for computation of theoretical dispersion curves in the subsequent sections. The misfit ϵ_{DC} between the theoretical and experimental dispersion curves is defined as

$$
\epsilon_{DC} = \frac{1}{Q}\sum_{q=1}^{Q} \frac{\sqrt{\left(V_{R,t,q} - V_{R,e,q}\right)^2}}{V_{R,e,q}} \cdot 100\% \tag{3}
$$

where $\boldsymbol{V_{R,e}} = [V_{R,e,1}\ , V_{R,e,2}\ , \dots , V_{R,e,Q}]$ and $\boldsymbol{V_{R,t}} = [V_{R,t,1}\ , V_{R,t,2}\ , \dots , V_{R,t,Q}]$ are the Q-dimensional experimental and theoretical phase velocity vectors, respectively. The dispersion misfit is abbreviated as DC misfit in the following discussion.

For updating the shear wave velocity vector between iterations, a set of $n+1$ numbers X_j ($j = 1,2,\dots,n,n+1$) is sampled from the uniform distribution and added to the elements of $\boldsymbol{V_S}$, i.e.,

$$V_{S,test,j} = V_{S,j} + X_j \quad \text{with} \quad X_j \sim unif\left(\frac{-b_S \cdot V_{S,j}}{100}, \frac{b_S \cdot V_{S,j}}{100}\right) \quad \text{for} \quad j = 1,2,\dots,n+1 \tag{4}$$

where the resulting vector $\boldsymbol{V_{S,test}} = [V_{S,test,1}, V_{S,test,2}, \dots, V_{S,test,n}, V_{S,test,n+1}]$ is referred to as the 'testing shear wave velocity vector'. The layer thickness vector is updated in an analogous way, with a random number Y_j ($j = 1,2,\dots,n$) sampled for each of the finite-thickness layers and added to h_j, resulting in the 'testing layer thickness vector' $\boldsymbol{h_{test}} = [h_{test,1}, h_{test,2}, \dots, h_{test,n}]$, i.e.,

$$h_{test,j} = h_j + Y_j \quad \text{with} \quad Y_j \sim unif\left(\frac{-b_h \cdot h_j}{100}, \frac{b_h \cdot h_j}{100}\right) \quad \text{for} \quad j = 1,2,\dots,n \tag{5}$$

Hence, the elements of $\boldsymbol{V_{S,test}}$ and $\boldsymbol{h_{test}}$ will vary randomly but will at most differ by b_S% and b_h% from the corresponding elements of $\boldsymbol{V_S}$ and $\boldsymbol{h}$, respectively, in each iteration.

Based on prior knowledge of the geological conditions of the test site, or as suggested by the shape of the experimental dispersion curve, implementation of additional constraints may be useful to further focus the search on the high-probability-density regions of the solution space. These include a normally dispersive inversion parameterization (i.e., an increase in shear wave velocity with increased depth) or predefined ranges for the elements of $\boldsymbol{V_S}$ or $\boldsymbol{h}$ within certain depths. In cases where such constraints are to be implemented, these can either be introduced by further restricting the Monte Carlo sampling to fulfill the additional conditions or by conducting the sampling as described by Eqs. (4) and (5) and subsequently reject those sets of simulated parameters that do not conform to the added restrictions.

The elements of $\boldsymbol{V_S}$ and $\boldsymbol{h}$ are updated in each successful Monte Carlo simulation iteration (Fig. 1). The theoretical dispersion curve ($\boldsymbol{V_{R,t}}, \boldsymbol{\lambda}$) is reevaluated based on the testing profile defined by $\boldsymbol{V_{S,test}}$, $\boldsymbol{h_{test}}$, $\boldsymbol{V_P}$ (or $\boldsymbol{\nu}$) and $\boldsymbol{\rho}$. If the testing profile provides a better fit to the observed data (i.e., a lower value of the dispersion misfit function) than any previously tested profile, the shear wave velocity and layer thickness vectors are updated as $\boldsymbol{V_S} = \boldsymbol{V_{S,test}}$ and $\boldsymbol{h} = \boldsymbol{h_{test}}$. Otherwise, the model parameters are not changed. Hence, the search is centred around the 'best-fitting' shear wave velocity profile that has been obtained at each point during the inversion.

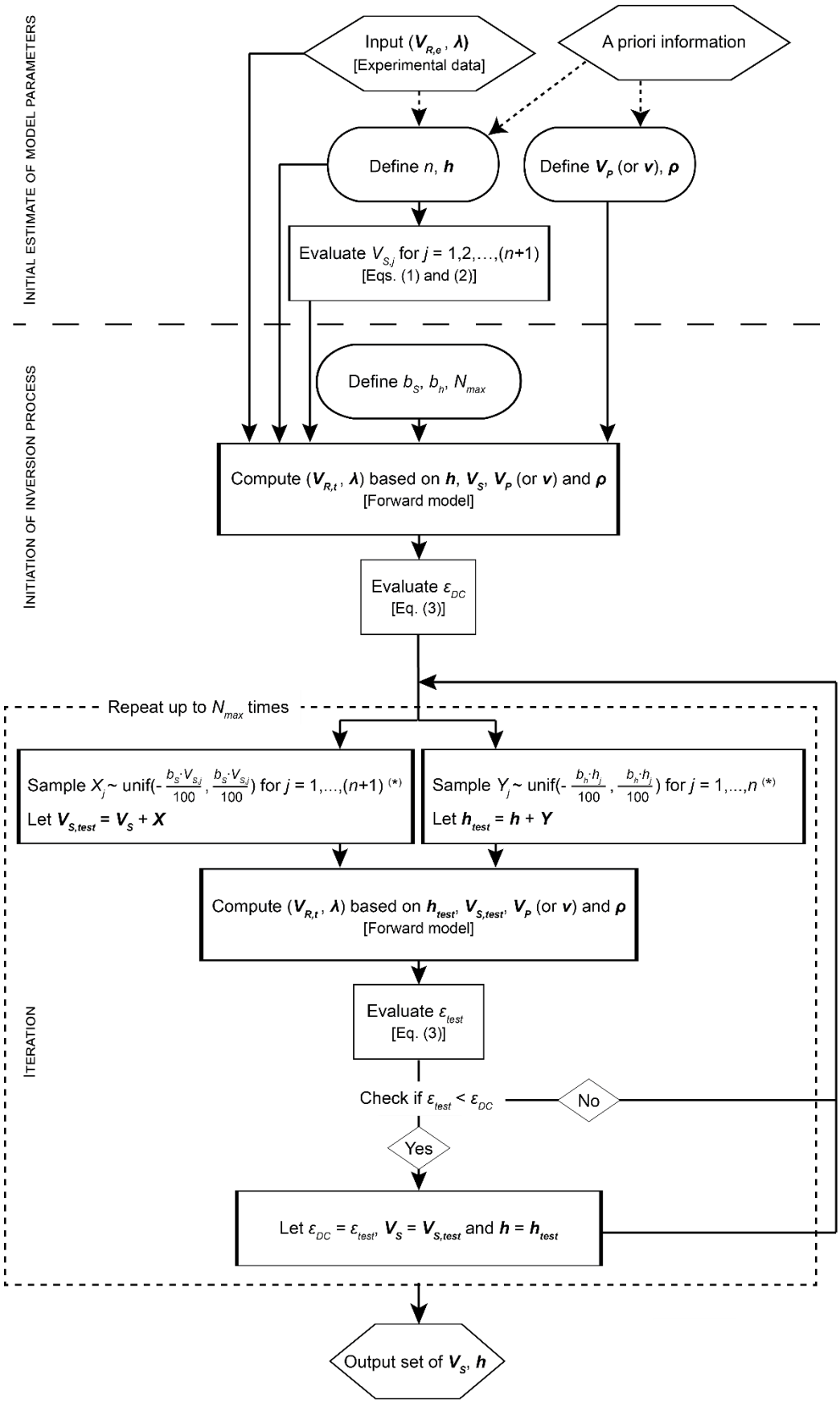

***Figure 1**: A schematic overview of the proposed inversion strategy.*

3. Synthetic data inversion

Three synthetic soil models are used to demonstrate the performance of the inversion scheme (Fig. 1). The models represent different situations that may be encountered in geotechnical site investigations, including both normally dispersive soil profiles and a profile with velocity reversals. Model A (Table 1) depicts a simple two-layer structure, consisting of one homogeneous layer over a half-space. Models B and C (Table 2) represent different multi-layered structures and are based on models used by Tokimatsu et al. (1992) to study the dispersion properties of fundamental and higher mode Rayleigh waves in a layered medium. Model B is characterized by a gradual increase in shear wave velocity (stiffness) with depth, whilst in model C, a stiffer layer is sandwiched between two softer layers. The shear wave velocity structure of the synthetic models was selected so that the profiles could represent loose to medium-dense sand sites and soft clay sites (Foti et al., 2018; Long and Donohue, 2007; NGI, 2015). In each of the three synthetic models, the groundwater table is assumed to be located at a great depth.

Table 1*: Model A. Two-layer model characterized by an increase in shear wave velocity (stiffness) with depth.*

Layer number	Shear wave velocity V_S [m/s]	Poisson's ratio ν [-]	Mass density ρ [kg/m^3]	Layer thickness h [m]
1	150	0.35	1800	4
(Half-space)	300	0.35	1800	-

Table 2*: Models B and C. Four-layer models characterized by a gradual increase in shear wave velocity (stiffness) with depth [model B] and a stiffer layer sandwiched between two softer layers [model C].*

Layer number	Shear wave velocity V_S [m/s]		Poisson's ratio ν [-]	Mass density ρ [kg/m^3]	Layer thickness h [m]
	Model B	Model C			
1	80	80	0.35	1800	2
2	120	180	0.35	1800	4
3	180	120	0.35	1800	8
(Half-space)	360	360	0.35	1800	-

Figure 2 depicts the fundamental mode dispersion curves corresponding to the three synthetic models. For inversion of the synthetic data, the dispersion curves were sampled at 60 equally spaced points within a wavelength interval of 1–60 m. This range is consistent with what might be expected when conducting (active-source) MASW measurements at comparable loose to medium-dense sand and soft clay sites.

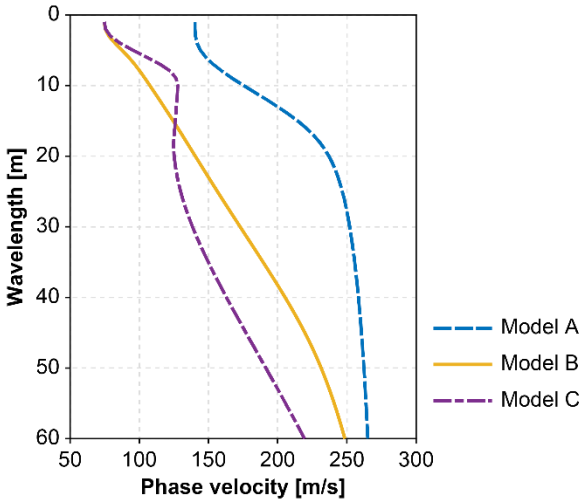

***Figure 2**: Fundamental mode dispersion curves for model A (two-layer model), model B (four-layer model characterized by a gradual increase in stiffness with depth) and model C (four-layer model with a stiffer layer between two softer layers).*

For inversion of the synthetic dispersion curves, the search-control parameters (hereafter also referred to as 'b-parameters') were specified as $b = b_S = b_h$, where $b \in \{2.5, 5, 10, 20\}$. Hence, in each iteration, both the shear wave velocity and layer thickness testing values could deviate up to b% from the corresponding parameters of the 'best-fitting' (i.e., lowest dispersion misfit) model obtained at that point in the inversion process. The mass density and Poisson's ratio were fixed at their original values. In each iteration, the elements of $\boldsymbol{V_P}$ were recomputed based on the Poisson's ratio and the elements of the testing shear wave velocity vector. For inversion of the dispersion data from models A and B, a normally dispersive parameterization was specified, whereas velocity reversals were permitted within the top 15 m for inversion of the data from model C. The number of iterations in each run of the algorithm (Fig. 1) was N_{max} = 1,000. As a Monte Carlo-based process is utilized in the search of the optimum V_S-profile, the inversion scheme was initiated ten times (using identical starting models) in order to reduce the effects of the randomization. Inference was subsequently drawn from the resulting dataset consisting of 10 × 1,000 V_S-profiles.

Quantification of how the error associated with multichannel surface wave registrations is propagated through the different data processing steps of a MASW analysis is not straightforward (Lai et al., 2005). Estimates of the statistical distributions of the extracted phase velocity values at each wavelength (or frequency) can nevertheless provide a measure of the error associated with the experimental data. In general, the longer wavelength (lower frequency) part of the dispersion curve is characterized by higher uncertainty than its shorter wavelength (higher frequency) range (Lai et al., 2005; Olafsdottir et al., 2018b). In this work, 'accepted V_S-profiles' are defined as the set of profiles whose associated dispersion curves fall within one standard deviation of the experimental curve. For interpretation of inversion results for the unperturbed synthetic data, the 'experimental standard deviation' is approximated as a ratio of the true phase velocity at each wavelength, i.e.

$$\boldsymbol{V_{R,e,low}} = (1 - p) \cdot \left[V_{R,e,1}\,, V_{R,e,2}\,, \ldots, V_{R,e,Q}\right] \tag{6}$$

$$\boldsymbol{V_{R,e,up}} = (1 + p) \cdot [V_{R,e,1}\,, V_{R,e,2}\,, \ldots, V_{R,e,Q}]$$

For simplification purposes, the value of p is estimated as p = 0.05 independent of wavelength. It is, however, noted that in real-world scenarios p may be positively correlated with wavelength.

In addition to presenting the inversion results in terms of interval velocity profiles, they are evaluated in terms of how accurately they recover the true values of V_S as averaged over the top-most z meters,

(7) $$V_{SZ} = \frac{z}{\sum_{i=1}^{N}\left(\frac{h_i}{V_{S,i}}\right)}$$

where V_{SZ} is the average shear wave velocity of the upper-most z m, and $V_{S,i}$ and h_i denote the shear wave velocity and thickness of the i-th layer, respectively, for a total of N layers down to depth z (CEN, 2004).

3.1. Two-layer unperturbed synthetic model

The inversion of the unperturbed synthetic data from model A was first conducted by assuming a two-layer geologic structure (i.e., one finite-thickness layer over a half-space) for the trial shear wave velocity profiles and with b = 10. For further evaluating the abilities of the inversion scheme to recover the true V_S-profile, the inversion was carried out using two initial models with the layer interface located at depths of 2 m and 10 m, respectively (true depth 4 m). The initial shear wave velocity values of the finite-thickness layer and the half-space were determined as described by Eq. (1). Figures 3 and 4c illustrate the inversion results. The true shear wave velocity and layer thickness values from Table 1, along with the corresponding true dispersion curve and V_{SZ}-profile, are shown using red dotted lines. Dashed lines indicate the initial models and the associated dispersion curves. The V_S- and V_{SZ}-profiles whose dispersion curves deviate less than 5% from the synthetic curve at all wavelengths are sorted based on dispersion misfit values (Eq. (3)), with the darkest colors visualizing profiles whose dispersion curves best fit the synthetic data. The lowest dispersion misfit V_S-profiles (V_{SZ}-profiles) resulting from each run of the algorithm (i.e. the lowest DC misfit profile within each set of N_{max} = 1,000 iterations) are further shown. Note that these profiles are not necessarily the ten profiles whose dispersion curves best fit the target curve within the combined set of 10,000 iterations. In the case of the two-layer trial models, the lowest DC misfit profiles from each of the ten runs are visually indistinguishable and almost identical to the true profile.

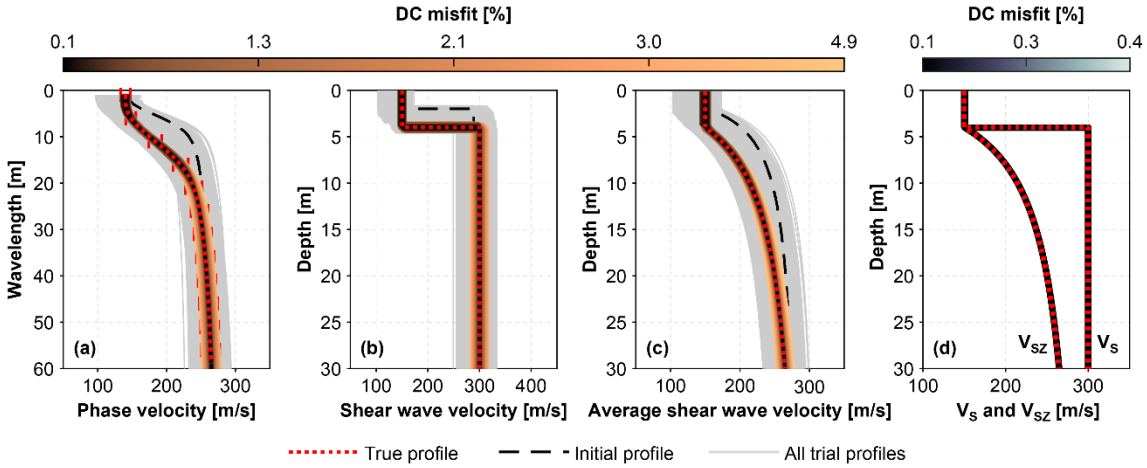

***Figure 3**: Inversion of the unperturbed synthetic dispersion curve from model A. A two-layer geologic structure is assumed for the trial shear wave velocity profiles with the initial position of the layer interface at a depth of 2 m. The values of the search-control parameters are specified as b = 10. **(a-c)** Profiles whose dispersion curves deviate less than 5% from the synthetic curve at all wavelengths [color scale based on dispersion curve (DC) misfit values]. Gray areas display all sampled models. **(d)** Lowest DC misfit V_S- and V_{SZ}-profiles obtained within each independent set of 1,000 iterations.*

Figure 4 further illustrates the effects of specifying the search-control parameters as b = 2.5 (Fig. 4a), b = 5 (Fig. 4b) and b = 20 (Fig. 4d). The results depicted were obtained by initially placing the layer interface at a depth of 10 m. The simple algorithm managed in all cases to deliver V_S-profiles that match the synthetic profile, even though the initial estimate of the theoretical dispersion curve corresponded very poorly to the synthetic curve. For application of the search algorithm, upper and lower bounds for the search area are not specified. However, the light gray areas in Fig. 4, which display all the simulated trial profiles, provide a visual indication of the part of the model parameter space that has been sampled. Overall, increasing the value of b increases the size of the explored solution space. However, given a fixed number of iterations, an increased value of b inevitably leads to more variation within the set of trial V_S-profiles (i.e., more sparse sampling of the parameter space). Figure 5 shows the effects of the different b-values on the data and model fitting progression for each of the cases in Fig. 4. The model fitting is defined in terms of V_S- and V_{SZ}-profile misfit values (Eqs. (8) and (9)), defined analogously to the DC misfit, i.e.

$$\epsilon_{V_S} = \frac{1}{(2n+1)}\left(\sum_{i=1}^{n+1}\frac{\sqrt{(V_{S,t,i}-V_{S,i})^2}}{V_{S,i}} + \sum_{i=1}^{n}\frac{\sqrt{(h_{t,i}-h_i)^2}}{h_i}\right)\cdot 100\% \tag{8}$$

$$\epsilon_{V_{SZ}} = \frac{1}{M}\sum_{i=1}^{M}\frac{\sqrt{(V_{SZ,t,i}-V_{SZ,i})^2}}{V_{SZ,i}}\cdot 100\% \tag{9}$$

where $V_{S,i}$ and h_i are the true shear wave velocity and layer thickness values of the i-th layer and $V_{S,t,i}$ and $h_{t,i}$ are the corresponding trial values. The true and trial V_{SZ}-profiles, both sampled at M distinctive depths, are denoted by $\boldsymbol{V_{SZ}} = [V_{SZ,1}, V_{SZ,2}, \ldots, V_{SZ,M}]$ and $\boldsymbol{V_{SZ,t}} = [V_{SZ,t,1}, V_{SZ,t,2}, \ldots, V_{SZ,t,M}]$, respectively.

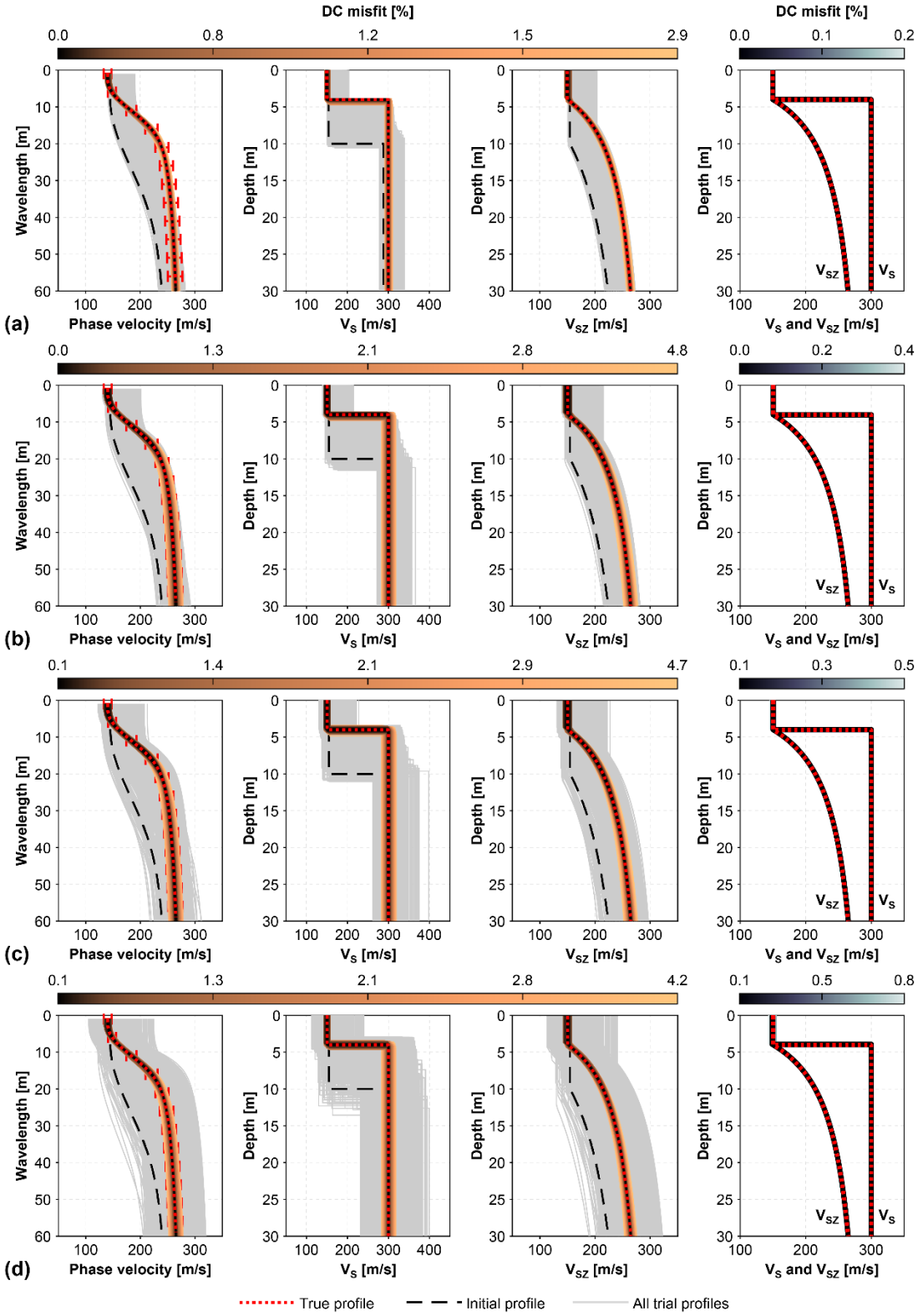

***Figure 4**: Inversion of the unperturbed synthetic dispersion curve from model A. A two-layer geologic structure is assumed with the layer interface initially located at a depth of 10 m. The search-control parameters are specified as **(a)** b = 2.5, **(b)** b = 5, **(c)** b = 10, and **(d)** b = 20. Gray areas display all sampled models and profiles whose dispersion curves deviate less than 5% from the synthetic curve at all wavelengths are shown using a color scale. The lowest DC misfit V_S- and V_{SZ}-profiles obtained within each independent set of 1,000 iterations are shown in the column furthest to the right.*

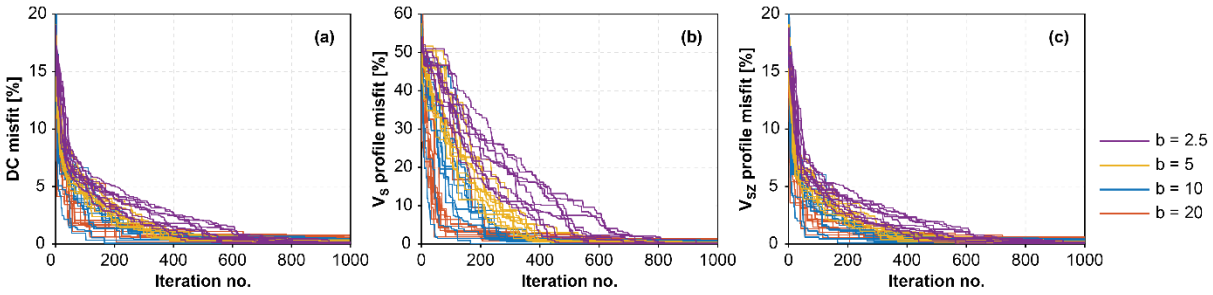

Figure 5*: Inversion of the unperturbed synthetic dispersion curve from model A. A two-layer geologic structure is assumed with the initial position of the layer interface at a depth of 10 m.* ***(a)*** *Data fitting progression. Model fitting progression defined in terms of* ***(b)*** *V_S-profile (shear wave velocity and layer thickness) misfit and* ***(c)*** *V_{SZ}-profile misfit. Ten curves are shown for each b-value as the Monte Carlo simulation is based on 10 × 1,000 iterations.*

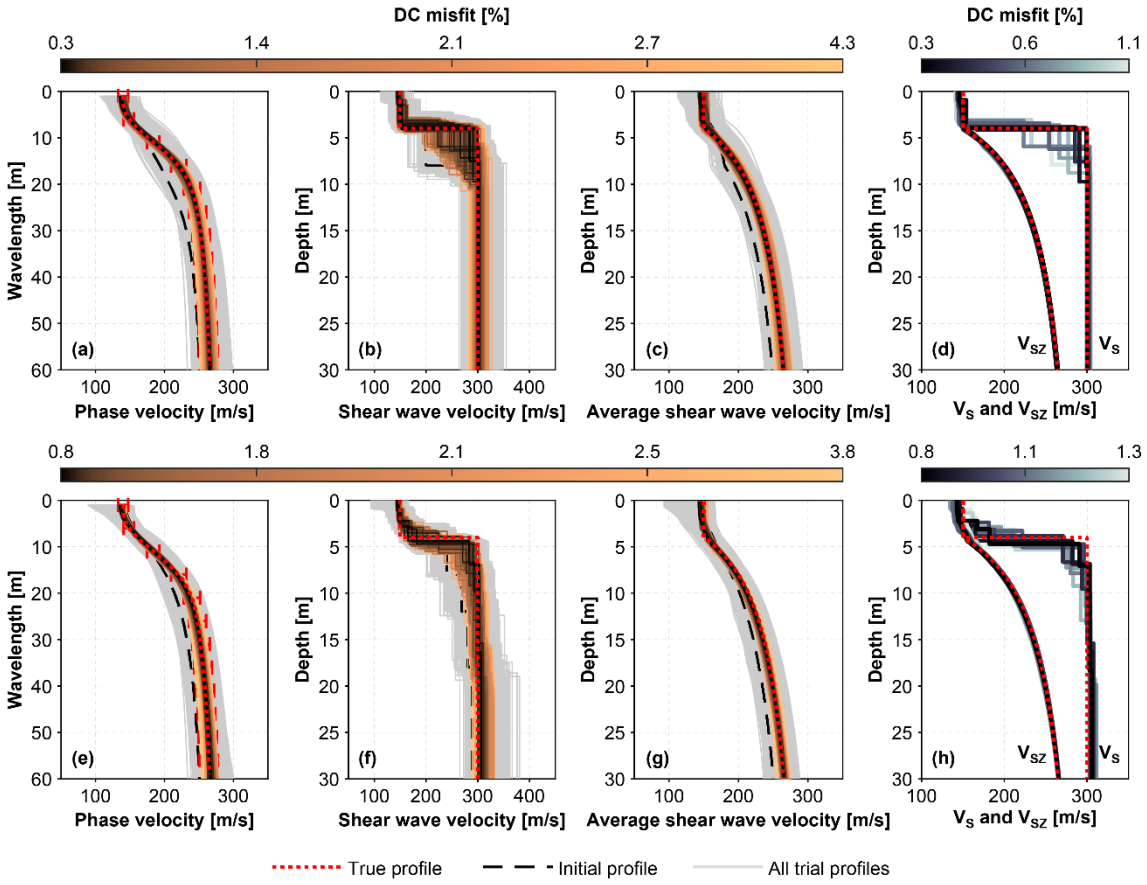

Figure 6: *Inversion of the unperturbed synthetic dispersion curve from model A. A geologic structure consisting of* ***(a-d)*** *four and* ***(e-h)*** *eight layers is assumed for the trial shear wave velocity profiles. Gray areas display all sampled models and profiles whose dispersion curves deviate less than 5% from the synthetic curve at all wavelengths are shown using a color scale based on dispersion curve misfit values. The lowest DC misfit V_S- and V_{SZ}-profiles obtained within each independent set of 1,000 iterations are shown in (d) and (h).*

To evaluate the effects of over-parameterizing the inversion of the synthetic data from model A, the analysis was repeated by assuming trial V_S-profiles with four ($n = 3$) and eight ($n = 7$) layers (including the half-space) and a value of b = 10. The initial sets of model parameters were specified such that the layer thicknesses were constant or increased with depth. That is, $\boldsymbol{h}$ = [1, 2, 5] m for the $n = 3$ model and $\boldsymbol{h}$ = [1, 1, 1, 2, 3, 4, 6] m for the $n = 7$ model, where

$\boldsymbol{h}$ denotes the initially specified layer thickness vector. The initial shear wave velocity values for each layer were obtained as described by Eq. (4) by using the mid-point of each finite-thickness layer as a reference for evaluation of λ_j. The inversion results are illustrated in Fig. 6. In both cases, within the 10 × 1,000 iterations, the inversion algorithm converged to theoretical dispersion curves that fit the synthetic data well, as indicated by dispersion misfit values of 0.3% and 0.8%, respectively. The corresponding reconstructed shear wave velocity profiles are further in reasonably good agreement with the true V_S-profile and do correctly indicate the existence and the location of the sharp layer interface that characterizes the true model. However, as a result of the over-parameterization, there is substantially more variation within the set of 'accepted' V_S-profiles as compared to the results obtained by assuming the two-layer trial profiles (see Figs. 3 and 4). The same applies to the variability within the set of lowest DC misfit V_S- and V_{SZ}-profiles obtained with the ten independent initializations.

3.2. Four-layer unperturbed synthetic models

Model B depicts a normally dispersive soil profile consisting of three finite-thickness layers over a half-space. First, the inversion of the unperturbed synthetic data from model B was carried out by assuming a four-layer geologic structure ($n = 3$) for the testing V_S-profiles, where the initially specified layer thicknesses increased with depth (Fig. 7). The target dispersion curve for model B (Fig. 2) does not display predominant vertical asymptotes. Hence, the initial V_S values for the surficial layer and the half-space were obtained using the Rayleigh wave velocity values corresponding to the wavelengths λ_{min} = 1 m and λ_{max} = 60 m, respectively.

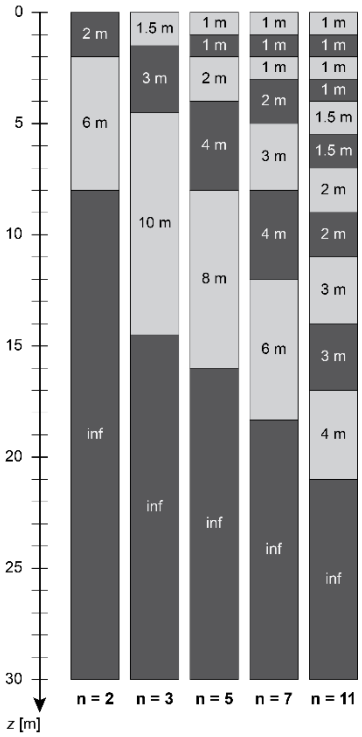

Figure 7: *Initial layer thicknesses assumed for inversion of the synthetic dispersion curves from models B and C.*

Figure 8 illustrates the inversion results of the unperturbed synthetic data from model B, as obtained by specifying the values of the search-control parameters as (a) b = 2.5, (b) $b = 5$, (c) b = 10, and (d) b = 20. The V_S- and V_{SZ}-profiles whose dispersion curves deviate less than 5% from the synthetic curve at each wavelength are plotted over the 10 × 1,000 randomly generated trial profiles, with the profiles characterized by the lowest dispersion misfit values indicated by the darkest colors. The lowest DC misfit V_S-profiles resulting from each run of the algorithm are further compared in the rightmost column of Fig. 8. These ten models all provide dispersion curves that adequately match the synthetic data. However, due to the non-uniqueness of the task encountered, there is some variation within the set of profiles, especially for the b = 20 case (Fig. 8d) and, to lesser extent, the b = 10 case (Fig. 8c). The corresponding estimates of V_{SZ} for different depths are further compared to the true values in the column furthest to the right in Fig. 8.

Analysis of inversely dispersive soil profiles presents a challenge for the application of MASW, both regarding the dispersion analysis and the inversion. For evaluating the behavior of the simple inversion strategy when subjected to an inversely dispersive target model, the algorithm was tested on the synthetic dispersion curve from model C (Fig. 2), where a stiffer layer is trapped between two softer layers. The inversion was conducted using the same initial layering parameterization and the same b-parameter values as for inversion of the data from model B. The results are reported in Fig. 9 using the same format as in Fig. 8. Overall, the inverted V_S-profiles in Figs. 9a-c (obtained with b = 2.5, b = 5 and b = 10) are consistent with the true profile and retrieve the existence and approximate location of the velocity inversion. However, substantially more variation is observed within the set of 'accepted' V_S-profiles in the b = 20 case.

Figures 10 and 11 illustrate the effects of the different b-values on the data and model fitting progression for each of the cases presented in Fig. 8 for model B and Fig. 9 for model C, respectively. The data fitting is quantified in terms of the dispersion curve misfit values, whilst the V_S- and V_{SZ}-profile misfits, defined according to Eqs. (8) and (9), are used as measures of the model fitting. The unbroken lines in Figs. 10 and 11 indicate the average fitness behavior of the ten independent initializations shown for each b-value in Figs. 8 and 9. The shaded areas correspond to plus-minus one standard deviation of the average behavior.

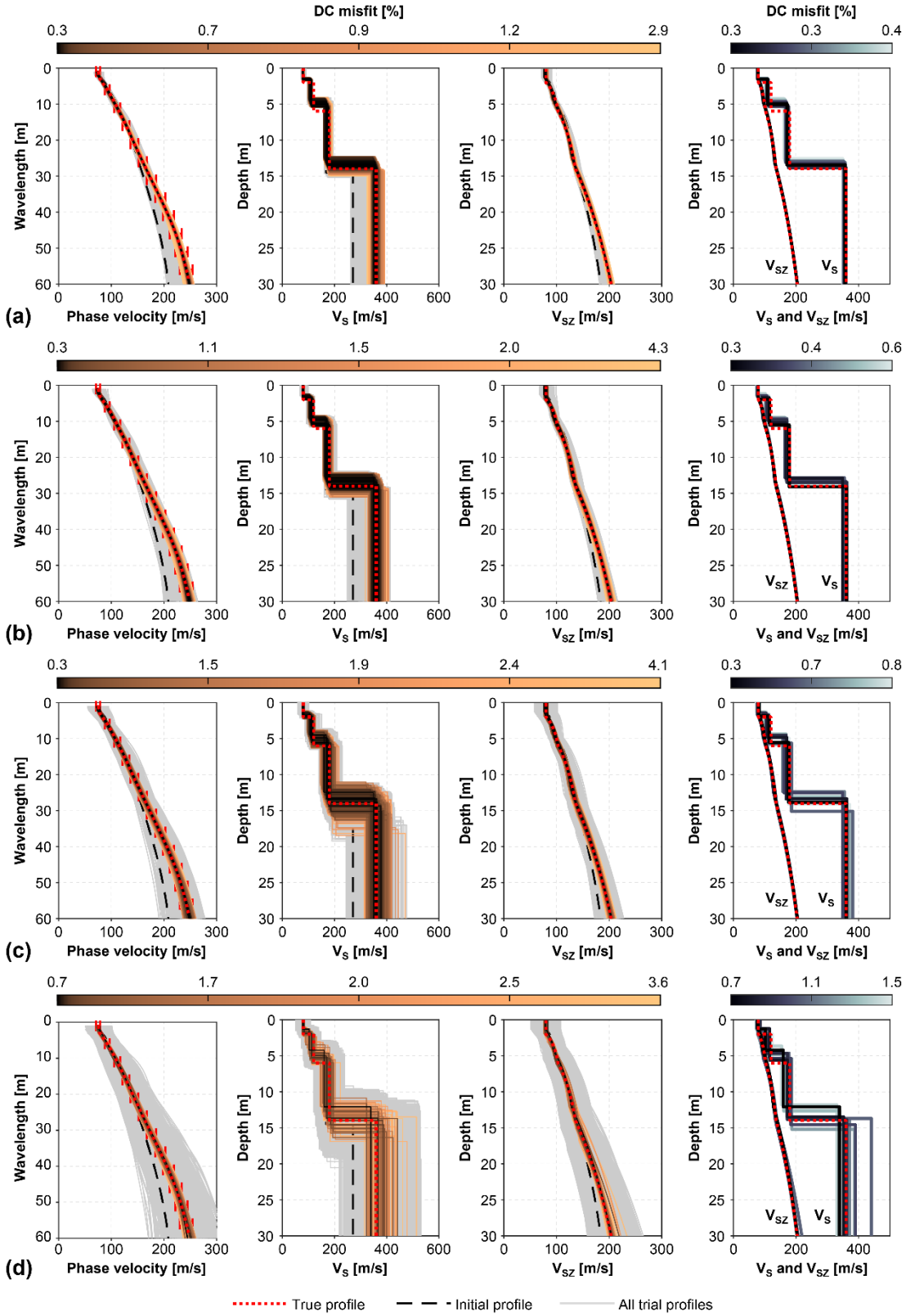

***Figure 8**: Inversion of the unperturbed synthetic dispersion curve from the normally dispersive model B. A four-layer geologic structure is assumed for the trial models. The values of the search-control parameters are specified as **(a)** b = 2.5, **(b)** b = 5, **(c)** b = 10 and **(d)** b = 20. Gray areas display all sampled models and profiles whose dispersion curves deviate less than 5% of the synthetic curve at all wavelengths are shown using a color scale based on dispersion curve misfit values. The lowest DC misfit V_S- and V_{SZ}-profiles obtained within each independent set of 1,000 iterations are shown in the column furthest to the right.*

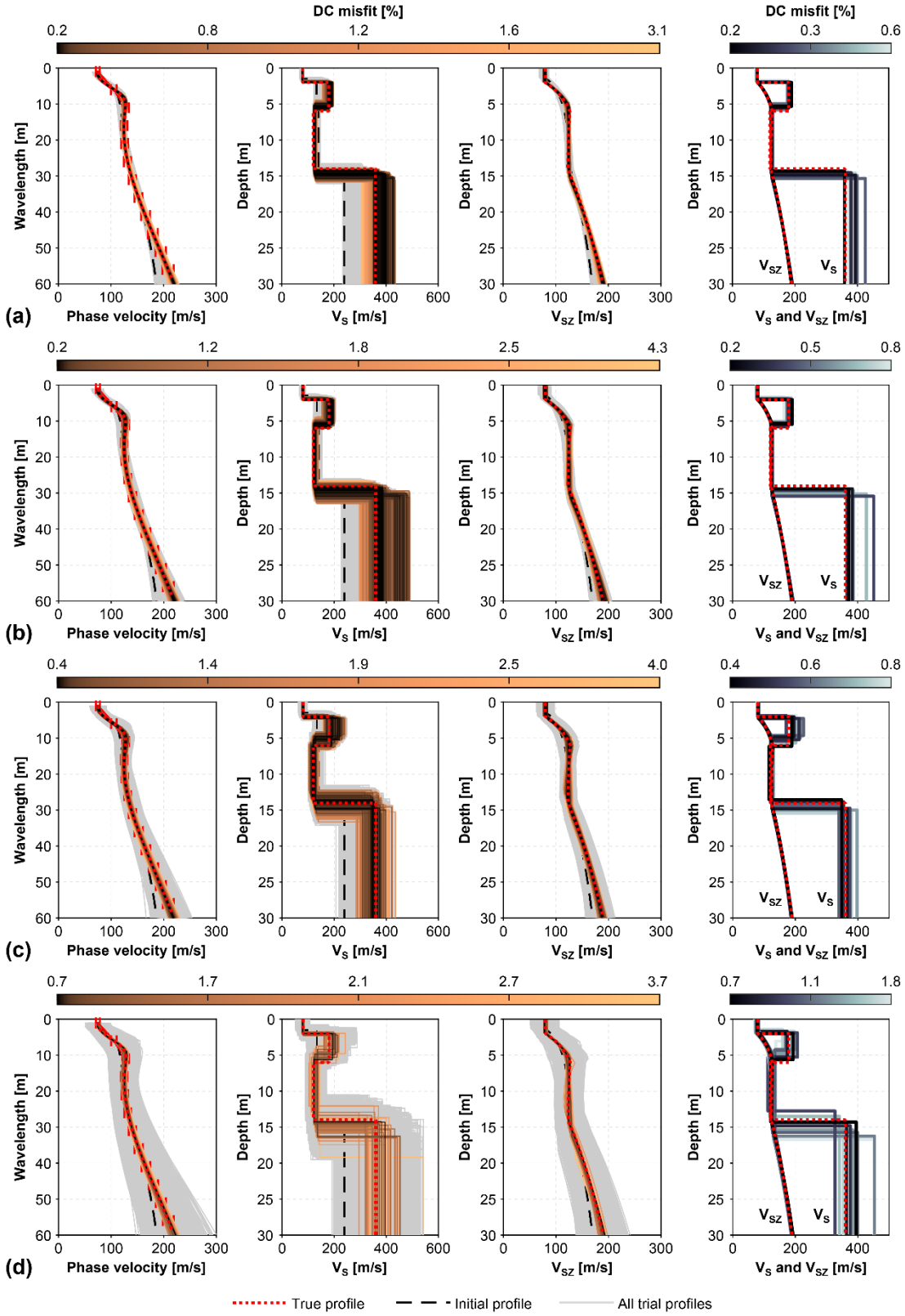

***Figure 9**: Inversion of the unperturbed synthetic dispersion curve from the inversely dispersive model C. A four-layer geologic structure is assumed for the trial models. The values of the search-control parameters are specified as **(a)** b = 2.5, **(b)** b = 5, **(c)** b = 10 and **(d)** b = 20. Gray areas display all sampled models and profiles whose dispersion curves deviate less than 5% of the synthetic curve at all wavelengths are shown using a color scale based on dispersion curve misfit values. The lowest DC misfit V_S- and V_{SZ}-profiles obtained within each independent set of 1,000 iterations are shown in the column furthest to the right.*

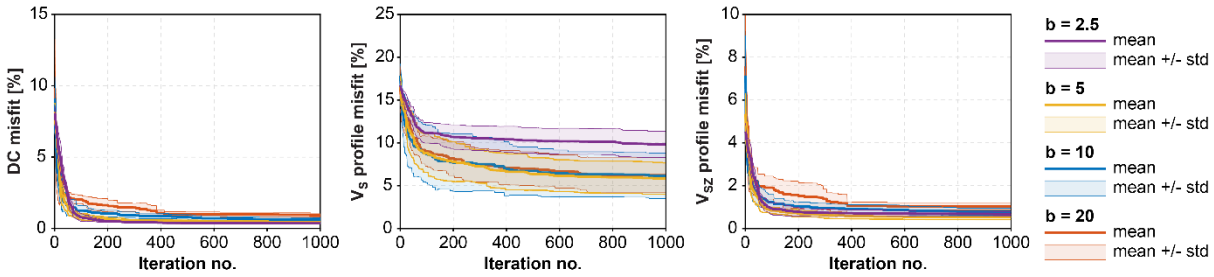

Figure 10: *Model B. Data and model fitting progression (mean behavior plus-minus one standard deviation) for the inversion results presented in Fig. 8.*

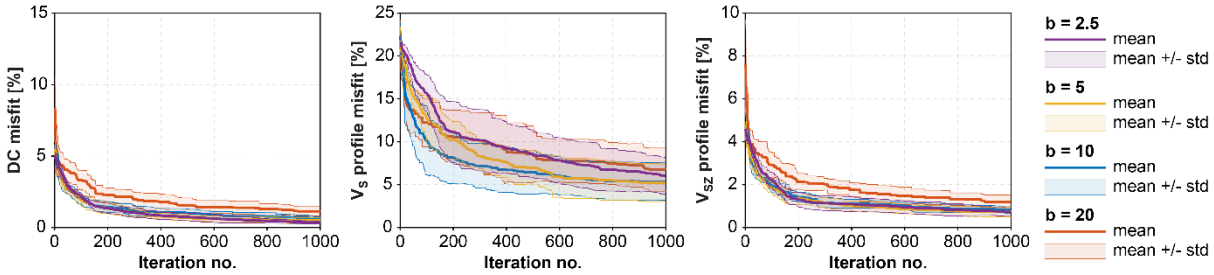

Figure 11: *Model C. Data and model fitting progression (mean behavior plus-minus one standard deviation) for the inversion results presented in Fig. 9.*

To study the effects of under- or over-parameterizing the soil model, the inversion of the unperturbed dispersion curves of models B and C was repeated by assuming trial V_S-profiles with three, six, eight and twelve layers (Fig. 7). The inversion results are presented in Fig. 12 (for model B) and Fig. 13 (for model C), using the same format as in Figs. 8 and 9. Overall, the results indicate that an improper parameterization, that is, an assumption of too few or excessively many layers, can result in either an overly simplistic or complicated V_S-profile that, despite a low dispersion misfit value, does not correctly represent prominent features of the true model. For instance, the inversion results for model B obtained by assumption of a twelve-layer trial profile, indicate a gradual increase in shear wave velocity with depth, but fail to detect the prominent increase in V_S at a depth of 14 m. Nevertheless, the average shear wave velocity values (V_{SZ}), obtained based on the under- and over-parameterized inversion results are, overall, very consistent with their true values (Fig. 12).

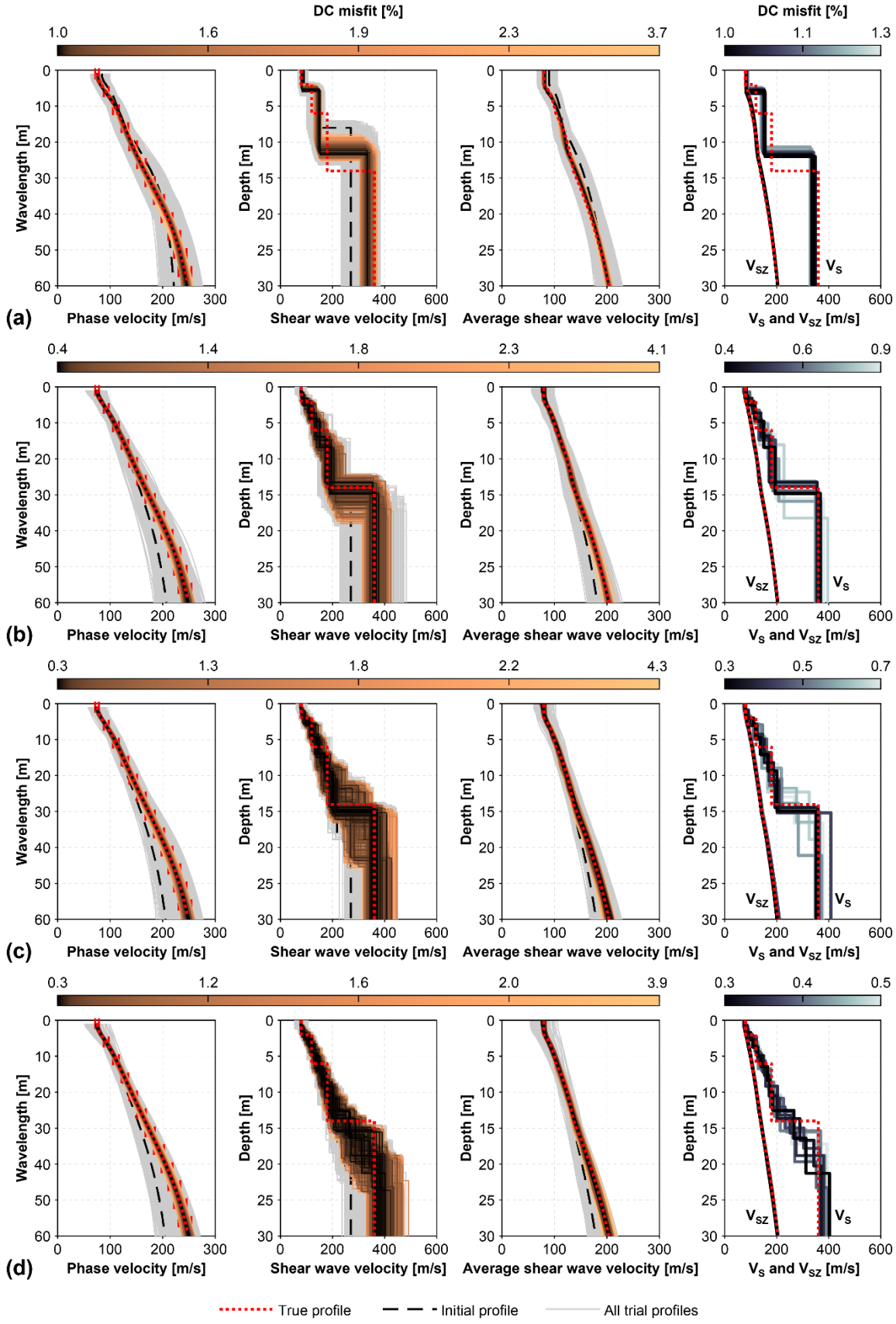

***Figure 12**: Inversion of the unperturbed synthetic dispersion curve from model B. A geologic structure consisting of **(a)** three, **(b)** six, **(c)** eight, and **(d)** twelve layers (including the half-space) is assumed for the trial shear wave velocity profiles.*

By including more than four layers in the trial V_S-profiles for model C, the search algorithm was further able to identify the approximate location and characteristic velocity of the stiffer layer, and provide estimates of V_{SZ} consistent with their true values (see Fig 13). However, by severely over-parameterizing the trial model (e.g., Fig. 13c), the inversion scheme tended to smooth out prominent changes in V_S in the same way as was observed for model B. Under-parameterizing the assumed model provides insufficient resolution for detection of the higher-velocity layer, leading to insufficient inversion results with the best fitting dispersion curve (within the combined set of 10,000 iterations) deviating more than 5% from the true curve at multiple wavelengths.

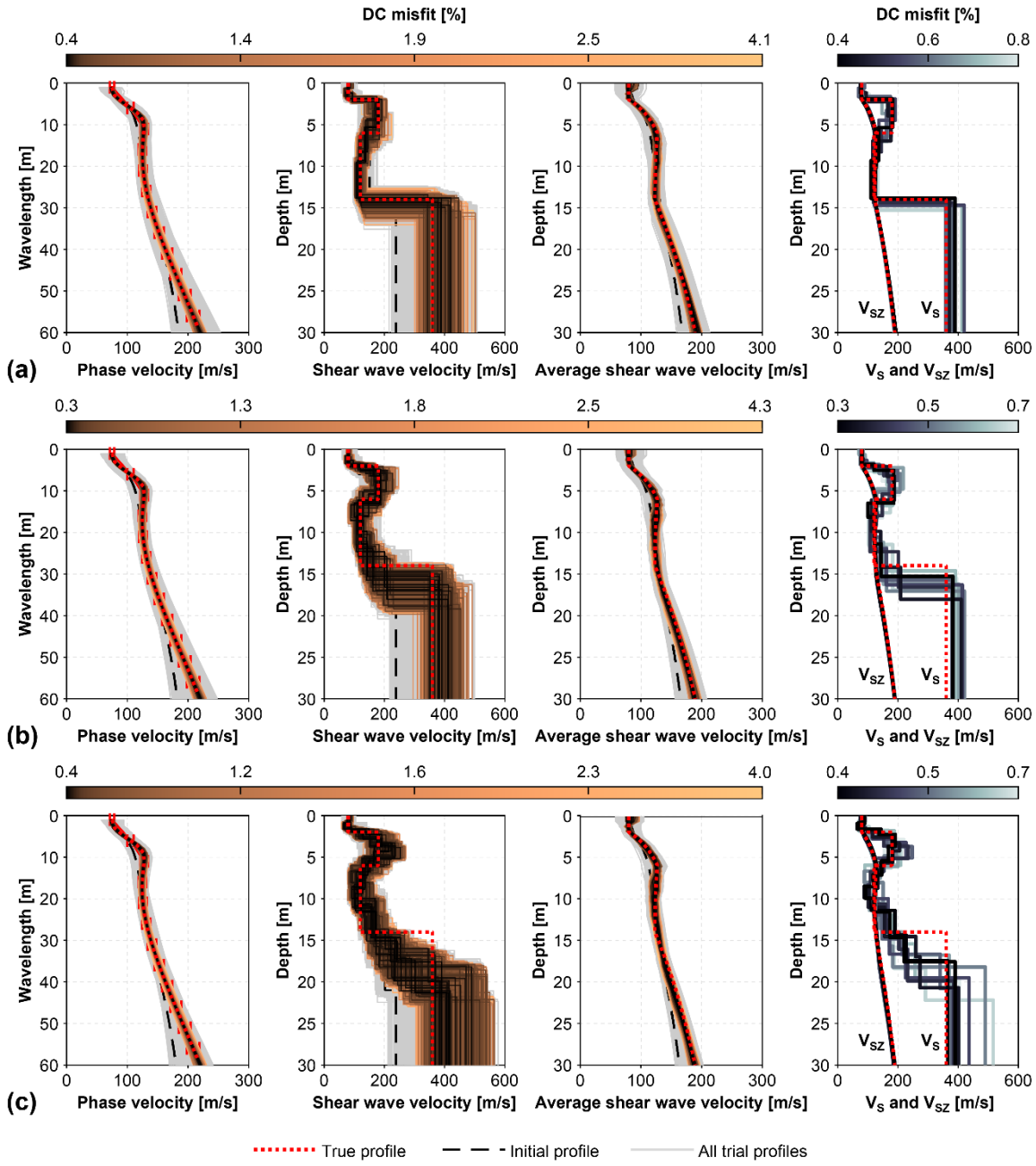

Figure 13: *Inversion of the synthetic dispersion curve from model C. A geologic structure consisting of* ***(a)*** *six,* ***(b)*** *eight, and* ***(c)*** *twelve layers (including the half-space) is assumed for the trial shear wave velocity profiles.*

3.3. Inversion of perturbed synthetic dispersion curves

In real-world situations, acquired surface wave records are affected by measurement and sampling errors (e.g., due to limitations of the measurement equipment or an imprecise measurement profile set-up) and coherent or uncorrelated noise in the recorded signal (Lai et al., 2005; Pei, 2007). The manual aspect of the analysis, particularly the visual identification of dispersion curves based on images of processed data, also adds to the uncertainty associated with the experimental dispersion curve estimates. Hence, the picked dispersion curve phase velocity values are inevitably subjected to noise, which can alter the misfit function topography and complicate the inversion process (Fernández Martínez et al., 2012; Song et al., 2015). In order to assess the performance of the inversion scheme when subjected to noisy data, the synthetic dispersion curves of models A, B and C, respectively, were perturbed by introduction of a 5% white Gaussian noise (see Fig. 14) and the inverse procedure applied on the perturbed data.

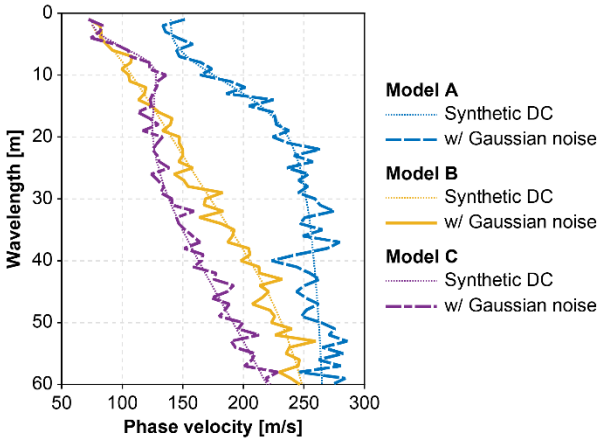

***Figure 14**: Fundamental mode dispersion curves for model A (two-layer model), model B (four-layer model characterized by a gradual increase in stiffness with depth) and model C (four-layer model with a stiffer layer between two softer layers). The synthetic dispersion curves are perturbed by introduction of a 5% white Gaussian noise.*

The inversion was conducted using identical layering parameterizations as in Figs. 4, 8 and 9, for the three models respectively. That is, a two-layer structure with the initial location of the layer interface at a depth of 10 m for model A, and the four-layer structure depicted in Fig. 7 for models B and C. Figure 15 illustrates the inversion of the perturbed synthetic dispersion curves for the three models. The values of the search-control parameters ('b-parameters', refer to Fig. 1) were specified as b_S = b_h = 10. The 100 (i.e., 1%) lowest DC misfit V_S- and V_{SZ}-profiles within each simulated dataset are plotted on top of the 10 × 1,000 randomly generated trial profiles in Figs. 15bc (for model A), Figs. 15fg (for model B) and Figs. 15jk (for model C). The profiles whose dispersion curves best fit the corresponding target curve are indicated by the darkest colors. The dispersion curves corresponding to each trial model are compared to the perturbed dispersion curves using the same color scale in Figs. 15aei. The lowest DC misfit V_S- and V_{SZ}-profiles resulting from each run of the algorithm (i.e. the lowest DC misfit profile within each set of 1,000 iterations) are further shown in Figs. 15dhl, for models A, B and C, respectively. As shown in Fig. 15, the inversion scheme provided in all three cases acceptable

V_S- and V_{SZ}-profiles that are consistent with the underlying true profiles. Therefore, the results demonstrate the robustness of the simple Monte Carlo based inversion scheme in the presence of Gaussian noise.

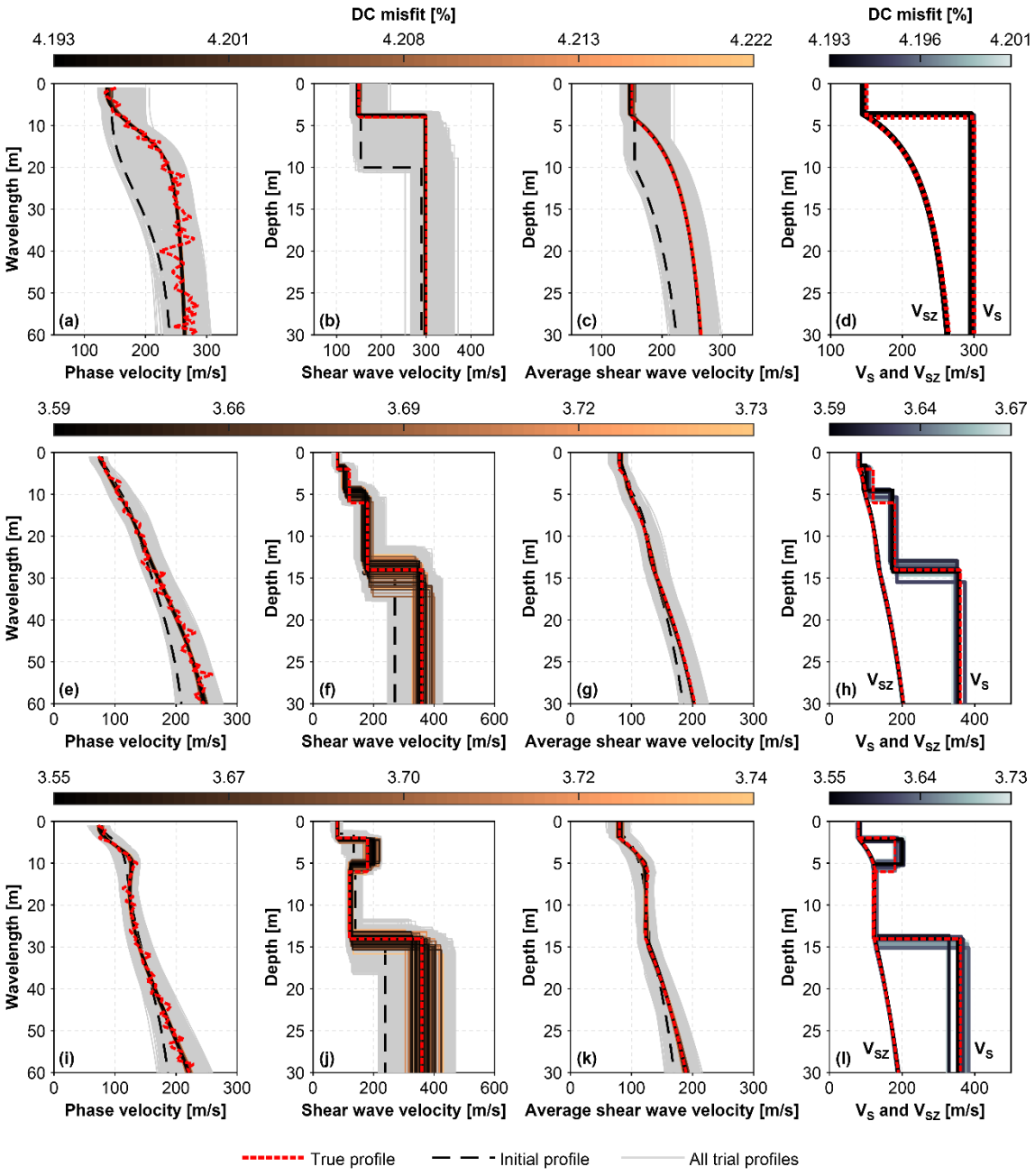

***Figure 15**: Inversion of synthetic dispersion curves for **(a-d)** model A, **(e-h)** model B and **(i-l)** model C. The target dispersion curves have been perturbed by introduction of a 5% white Gaussian noise. A two-layer geologic structure (including the half-space) is assumed for inversion of the perturbed data from model A. A geologic structure consisting of four layers (including the half-space) is assumed for models B and C.*

4. Field data inversion

For further evaluation of the proposed inversion scheme, the methodology was tested on MASW field data acquired at a Norway's National GeoTest Site (www.geotestsite.no) in the town of Halden in South Norway (L'Heureux et al., 2017). The soil profile at the site consists of a ca. 4.5 m thick layer of loose to medium-dense silty sand on top of a layer of normally consolidated, low plasticity silt with a thickness in the order of 10 m. A clay unit is found at the bottom of the silt deposit (Blaker et al., 2016; 2019). The depth to bedrock within the area varies (NGI, 2018). The groundwater table at the site is located at a depth of about 2 m, as measured from an in-situ stand pipe (Blaker et al., 2019).

Several techniques have previously been used to evaluate the shear wave velocity of the soil deposits at the Halden site. Seismic Cone Penetration Tests (SCPT) and Seismic Dilatometer Marchetti Tests (SDMT) were conducted as part of the NGTS project (Blaker et al., 2016; L'Heureux et al., 2017; NGI, 2018) and are used for comparison purposes in this work. In addition, the shear wave velocity of the Halden silt has been assessed by bender element (BE) tests performed on triaxial and direct simple shear specimens (Blaker et al., 2019; NGI, 2018).

The MASW measurements presented in this section were conducted by using 24 vertical geophones, with a natural frequency of 4.5 Hz and a critical damping ratio of 0.5, as receivers. The geophones were arranged in a linear array with an equal receiver spacing of 1 m. The survey profile was positioned in the part of the testing area where the depth to bedrock is the most and, due to the non-uniformity of the area, as close as possible to relevant previous work at the site. The impact load was created by a sledgehammer that was struck on a 15 cm-diameter metallic base plate at a 3 m and 5 m distance, respectively, from each end of the receiver spread. Repeated shots were recorded for each source location in order to obtain a statistical sample of dispersion curves and to allow for quantification of the variability in the estimated phase velocity values. Due to logistic constraints, as well as the varying depth to bedrock within the testing area, the use of a longer receiver spread than 23 m was not attempted.

The dispersion analysis tool of the open-source software MASWaves (Olafsdottir et al., 2018a) was used for processing the acquired multichannel surface wave records. The experimental dispersion curves obtained by using different source offset lengths were in good agreement, as indicated by a coefficient of variation (i.e., the ratio of the standard deviation of the extracted phase velocity values at specified frequencies to the corresponding mean) below 5% at each frequency. In line with previous findings (Lai et al., 2005; Olafsdottir et al., 2018b), the lowest frequency components displayed more variability than components in the higher frequency range. Analysis of shots applied at both ends of the receiver spread, further indicated essentially the same dispersion characteristics, therefore, not implying the presence of significant lateral variations in material properties below the receiver spread. The experimental dispersion curve estimates were subsequently added up within logarithmically (i.e., $\log_3$) spaced wavelength intervals following the procedure described by Olafsdottir et al. (2018b), resulting in a composite experimental dispersion curve over the wavelength range of 2–32 m.

The inversion of the dispersion data acquired at the Halden site was conducted without using the already established layer structure of the site to guide the layering parameterization. This was done in order to mimic the common situation encountered in geotechnical investigations, where limited information about the layering of the tested area is available. Hence, the number of finite-thickness layers (n) was considered as an unknown parameter and the inversion conducted using eight different parameterizations consisting of two to nine layers (including the half-space). Velocity reversals were permitted within the testing shear wave velocity profiles down to a depth of 10 m. The mass density profile was specified based on results of independent soil investigations previously conducted at the site (Blaker et al., 2016; 2019). The compressional wave velocity was fixed at V_P = 1,440 m/s below the groundwater level. The Poisson's ratio of the unsaturated soil layer(s) was estimated at 0.35 (Das, 2010) and the corresponding V_P-values recomputed in each iteration based on the elements of testing shear wave velocity vector. As for analysis of the synthetic data, the inversion algorithm was run ten times (using identical starting profiles) in order to compensate for the effects of the randomization associated with the Monte Carlo-based sampling. The number of iterations in each run of the algorithm was specified as N_{max} = 1,000. In our experience, computations (i.e., ten initiations) routinely take approximately 5 minutes when performed on a standard office PC desktop computer (with i7-8700 processor and 16 GB RAM).

Overall, the same considerations hold regarding selection of b-parameter values as for inversion of the synthetic data discussed in Sections 3.2 and 3.3 (refer to Figs. 4, 8 and 9). Particularly, an increased b-parameter (i.e., b_S and/or b_h) value prompts more variability within the set of tested shear wave velocity and layer thickness values, respectively. Hence, the somewhat sparser sampling (given a fixed number of iterations) risks inferior fit (i.e., higher DC misfit values) between the experimental and theoretical dispersion data, although the lowest DC misfit profiles associated with the different b-parameter values may be visually comparable.

Based on the inversion results presented in preceding sections, as well as preliminary inversion of the dispersion data from the Halden site, the values of the b-parameters were specified as b_S = 5 and b_h = 10. The initial pseudo-shear wave velocity estimates obtained by Eq. (1) (indicated by dashed lines in Fig. 16) were overall adequately close to their inverted values, prompting the use of a lower b_S. However, as the initially specified layer thicknesses are manually defined, a larger value of b_h is deemed more appropriate to allow for more variation within the set of sampled layer thicknesses. Figure 16 presents results obtained by parameterizing the soil profile as (a) three layers (n = 2), (b) four layers ($n = 3$), (c) six layers ($n = 5$), and (d) eight layers ($n = 7$). The theoretical dispersion curves that best fit the observed dispersion characteristics (i.e., fall within one standard deviation of the composite experimental curve at all wavelengths) are illustrated using a color scale. The corresponding V_S- and V_{SZ}-profiles are indicated by the same colors. Also shown are the lowest DC misfit profiles resulting from each of the ten independent initiations. Figure 17b compares the lowest DC misfit V_S-profiles obtained from each tested layering parameterization, whilst the associated theoretical dispersion curves are compared to the experimental data in Fig. 17a. The corresponding V_{SZ}-profiles are shown in Fig. 17c. Figure 17b further compares the set of inverted V_S-profiles to

results of SDMT and SCPT measurements carried out in close proximity to the MASW profile, as well as results of laboratory measurements conducted on samples collected at the site.

Overall, the results presented in Fig. 17 indicate a very good agreement between the MASW and SDMT measurements. The SCPT data are slightly scattered, however, the MASW results are very comparable with the general V_S trend demonstrated by the SCPT. The results of the BE measurements tended to indicate slightly lower shear wave velocities than were measured by the in-situ techniques (i.e., MASW, SCPT and SDMT). Except for the two-layer parametrization, all the theoretical dispersion curves shown in Fig. 17a visually match the experimental data and provide dispersion misfit values well below 0.5%. Hence, given a deterministic analysis assuming a fixed layering parameterization, each one of them might be considered an adequate solution. The V_{SZ}-profiles associated with the different layering parameterizations (except for the two-layer parameterization) are further nearly identical. However, by increasing the number of layers (see Fig. 16cd), even lower dispersion misfit values and smoother velocity interval profiles, that visually seem to agree better with the invasive measurement results, can be obtained. Hence, a six- or eight-layer parametrization may be considered more appropriate for the site.

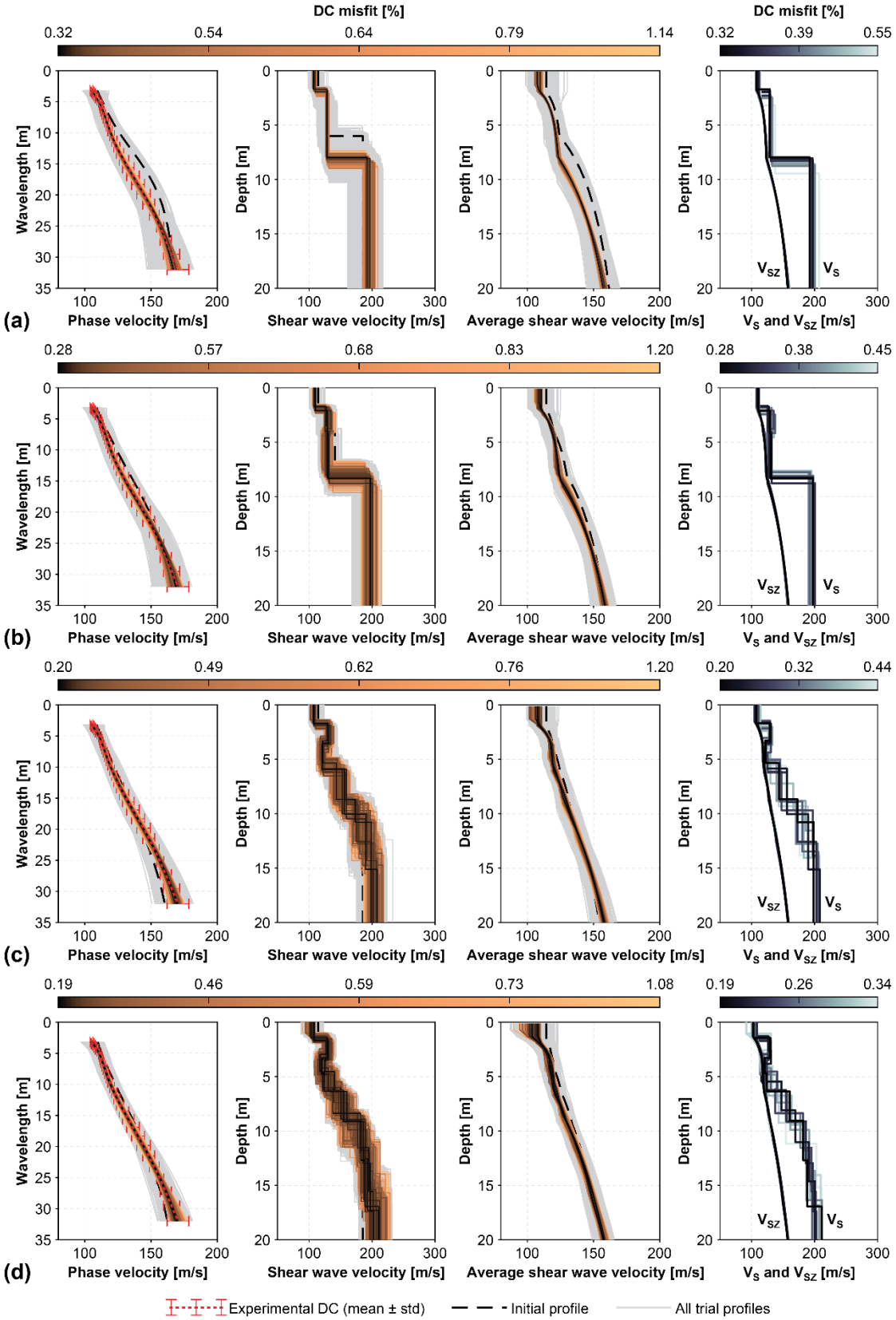

***Figure 16**: Inversion of the composite dispersion curve for the Halden site. A geologic structure consisting of **(a)** three, **(b)** four, **(c)** six, and **(d)** eight layers (including the half-space) is assumed for the trial V_S-profiles. Profiles whose corresponding dispersion curves fall within one standard deviation of the composite curve at all wavelengths are presented using a color scale based on dispersion misfit values. The lowest DC misfit V_S- and V_{SZ}-profiles obtained within each independent set of 1,000 iterations are shown in column furthest to the right.*

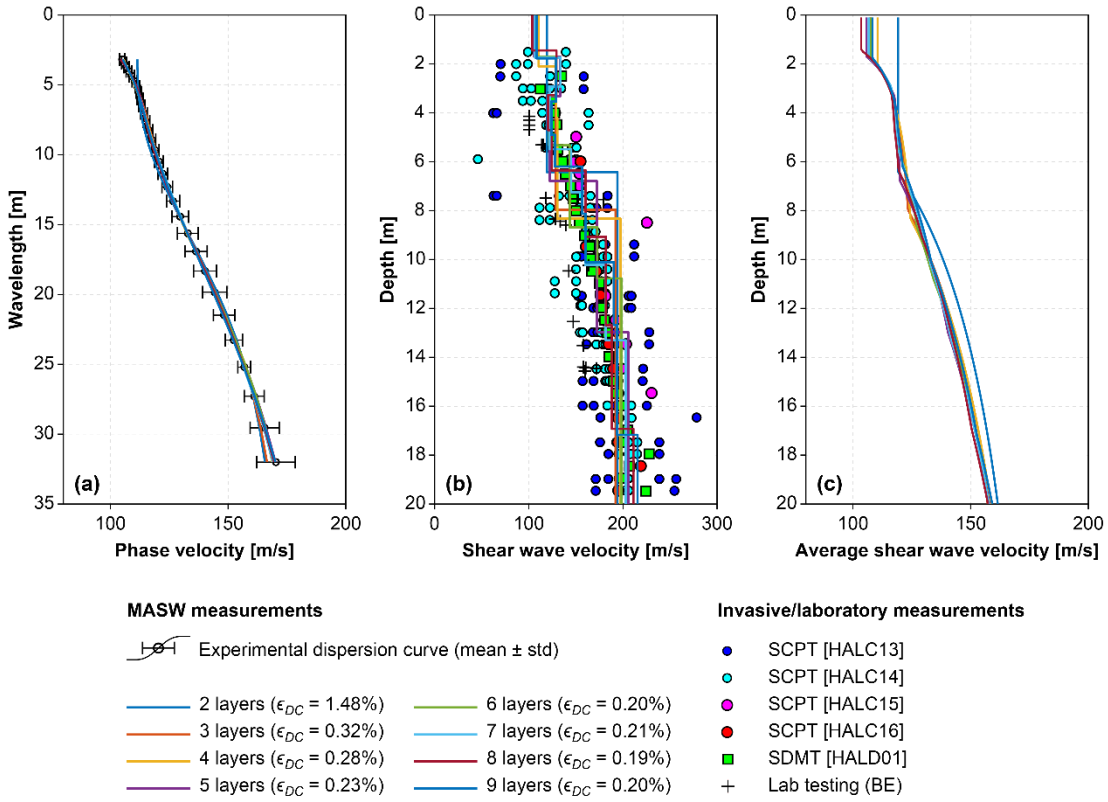

***Figure 17**: Results of MASW measurements carried out at the Halden site. Comparison with results of SCPT, SDMT and laboratory measurements conducted in close proximity to the MASW profile.*

5. Discussion

The objective of the inversion analysis is to obtain a V_S-model that realistically represents the characteristics of the test site. The inverse problem faced in the third step of a MASW survey is by nature ill-posed, non-linear, mix-determined, and non-unique. That is, multiple significantly different V_S-profiles can provide theoretical dispersion curves that match the experimental data similarly well in terms of dispersion misfit values (Cox and Teague, 2016; Foti et al., 2015). Hence, available information about the test area should be used to constrain the inversion and aid the selection of realistic V_S-profiles. Visual inspection of the experimental data, prior to initiation of the inversion analysis, can also assist in selection of realistic V_S-models, for instance, to assess whether velocity reversals are likely to be encountered.

Discrete parameterization of the survey site in terms of n linear elastic layers underlain by a half-space is a crucial starting point of the inversion process. In the absence of relevant a-priori information, the analyst must assess blindly the number of layers to be included in the trial models. As previously discussed, an inappropriate layering parameterization can result in an overly simplistic or overly complicated V_S-profile that, despite providing a low dispersion misfit value, does not correctly represent the characteristics of the test site. Conducting the inversion by using several different parameterizations has been strongly encouraged in previous studies (e.g., Cox and Teague, 2016; Foti et al., 2018). The findings of this work

further support the necessity of implementing the number of finite-thickness layers (n) as an additional inversion parameter and conduct repeated analysis to assess the effects of the model parameterization.

The strategy adopted here was to start the analysis of the experimental data with a small number of layers (i.e., $n = 1$). Subsequently, the number of layers included in the trial models was increased and the inversion process repeated. Due to the mix-determined nature of the inverse problem, the layer thicknesses were specified such that they were constant or increased with depth. The thickness of the top-most soil layer and the depth to the half-space top were further specified such that they fulfilled the general recommendations associated with the empirical wavelength-depth approach. Based on our experience, the number of different parameterizations that may need to be investigated is highly site-specific. Therefore, no specific guidelines applicable to all sites can be given. If two different parameterizations result in similar dispersion misfit values and provide V_S-profiles whose dispersion curves visually fit the experimental data equally well over the entire frequency/wavelength range, the model consisting of fewer layers is generally chosen by the authors. This approach is consistent with the recommendations provided by Foti et al. (2018). It is worth mentioning, however, that for applications of MASW where the sole objective is to assess the average parameters of the site (e.g., V_{S30}), the results presented here suggest that the layering parameterization plays a minor role, provided that the inversion converges to a model whose theoretical dispersion curve is consistent with the experimental data. This is consistent with previous findings (e.g., Brown et al. 2000; Comina et al. 2011; Aung and Leong 2015; Garofalo et al. 2016b) demonstrating the robustness of surface wave analysis for assessment of V_{SZ}.

For applications of the simple Monte Carlo-based inversion scheme presented in this paper, the maximum number of iterations (in each run of the algorithm) was specified as $N_{max} = 1{,}000$. The values of the search-control parameters b_S and b_h were specified in the range of 2.5 to 20 (i.e., 2.5% to 20%). The results of this study demonstrated that the use of b-parameters in the range of 5 to 10 was sufficient in all the cases. The findings indicate, therefore, that this may be a suitable range, in particular for near-surface applications at loose to medium-dense clay, sand or silt sites with velocity ranges comparable to those presented here. Due to the experimental uncertainties associated with both the data acquisition and the dispersion analysis, values of the dispersion misfit function may not be comparable between different sites. In other words, a value of the misfit function that is considered adequately low for one dataset, may not correspond to a sufficiently good match between the experimental and theoretical dispersion curves for another site. Making the search algorithm complete a specific number of iterations and subsequently draw inference from the set of simulated profiles based on the observed spread within the experimental data is therefore recommended. The choice of N_{max} = 1,000 is, however, somewhat arbitrary. Allowing the algorithm to continue for more than 1,000 iterations (in each run) might, in some cases, have provided even lower dispersion misfit values and could have resulted in the final inverted parameter values being even closer to their true values for inversion of the synthetic dispersion data. However, for real datasets, where the observed dispersion curves are, to some extent, affected by coherent and uncorrelated noise, extremely low dispersion misfit values may not be realistic (Ryden and Park, 2006). Using

N_{max} = 1,000 and ten initiations (10 × 1,000) gave fair results for engineering purposes in all the cases in this study.

6. Conclusions

The dispersive properties of Rayleigh waves propagating through a heterogeneous medium provide key information about the elastic properties of the sub-surface materials. This paper presents a simple but effective Monte Carlo-based scheme for solving the inverse problem of identifying realistic V_S-profiles from actively generated Rayleigh wave dispersion curves.

The performance and applicability of the inversion algorithm is demonstrated using both synthetic datasets, representing loose to medium-dense sand and soft clay sites commonly encountered in geotechnical engineering practice, and field data acquired at a well-characterized geotechnical research site in Norway. Overall, the inversion results for the synthetic datasets indicate that the algorithm can be successfully used for inversion of fundamental mode Rayleigh wave dispersion curves for geotechnical engineering applications. The analysis of the real-world data further verifies the performance of the inversion scheme. The obtained shear wave velocity estimates match those obtained by invasive techniques. The inverted V_S-profiles are further consistent with results of laboratory measurements conducted on samples gathered at the site. Hence, these findings indicate that a simple global search technique, i.e., not incorporating any advanced optimization, can deliver sufficient results for engineering applications in practice.

The inverse problem faced in the third step of a MASW survey is inherently non-unique, that is, multiple substantially different V_S-profiles can provide comparable values of the misfit function representing the difference between the theoretical and experimental dispersion curves. Hence, interpretation of surface wave data requires subjective judgment and fully automatic search processes are difficult to implement. For instance, an unsuitable parameterization of the survey site can result in an 'optimal' shear wave velocity model that does not realistically represent the subsurface conditions. The results of this study therefore support the recommendation of conducting a preliminary analysis using multiple different parameterizations. Taking into consideration any a-priori information about the test site and the shape and wavelength range covered by the observed dispersion curve is further essential to aid the selection of realistic models. In addition, presenting the inversion results as a set of layered earth models those theoretical dispersion curves fit the observed data (e.g., fall within one standard deviation of the experimental curve) provides an indication of the uncertainty associated with the V_S assessments for subsequent applications.

The conclusions presented in this paper are only supported by field data acquired at a single site. However, the inversion scheme has been successfully used at other sites where either direct measurements of V_S are available or prior assessments of V_S have been made by use of non-invasive techniques conducted in independent field testing campaigns.

Acknowledgements

This work was supported by the University of Iceland Research Fund [Grant no. 73077]; the Icelandic Road and Coastal Administration [Grant no. 1800-373]; and the Energy Research Fund of the National Power Company of Iceland [Grant no. NYR-18-2017].

The authors would like to thank the organizers of the NGTS project (www.geotestsite.no) for assistance prior to and during the in-situ measurements at the Halden research site, as well as for providing access to results of geotechnical and geophysical measurements conducted at the site.

References

Abrahamson, N., Atkinson, G., Boore, D., Bozorgnia, Y., Campbell, K., Chiou, B., Idriss, I.M., Silva, W. and Youngs, R. (2008). Comparisons of the NGA ground-motion relations. *Earthquake Spectra*, *24*(1), 45–66. doi:10.1193/1.2924363.

Aung, A.M.W. and Leong, E.C. (2015). Application of weighted average velocity (WAVe) method to determine $V_{S,30}$. *Soils and Foundations, 55*(3), 548–558. doi:10.1016/j.sandf.2015.04.007.

Beaty, K.S., Schmitt, D.R. and Sacchi, M. (2002). Simulated annealing inversion of multimode Rayleigh wave dispersion curves for geological structure. *Geophysical Journal International*, *151*(2), 622–631. doi:10.1046/j.1365-246X.2002.01809.x.

Bergmann, L. (1948). *Ultrasonics and their scientific and technical applications*. John Wiley & Sons, New York, NY.

Bessason, B. and Erlingsson, S. (2011). Shear wave velocity in surface sediments. *Jökull, 61*, 51–64.

Blaker, Ø., Carroll, R., L'Heureux, J.-S. and Klug, M. (2016). Characterisation of Halden silt. In *Proceedings of the Fifth International Conference on Geotechnical and Geophysical Site Characterisation*, Queensland, Australia (pp. 975–980).

Blaker, Ø., Carroll, R., Paniagua, P., DeGroot, D.J. and L'Heureux, J.S. (2019). Halden research site: geotechnical characterization of a post glacial silt, *AIMS Geosciences, 5*(2), 184–234. doi:10.3934/geosci.2019.2.184.

Brown, L.T., Diehl, J.G. and Nigbor, R.L. (2000). A simplified procedure to measure average shear-wave velocity to a depth of 30 meters (VS30). In *Proceedings of the 12th World Conference on Earthquake Engineering*, Auckland, New Zealand.

BSSC. (2015). *NEHRP (National Earthquake Hazards Reduction Program) recommended seismic provisions for new buildings and other structures (FEMA P-1050-1) 2015 edition. Vol. 1. Part 1: Provisions. Part 2: Commentary*. Federal Emergency Management Agency, Washington DC.

Buchen, P.W. and Ben-Hador, R. (1996). Free-mode surface-wave computations. *Geophysical Journal International*, *124*(3), 869–887. doi:10.1111/j.1365-246X.1996.tb05642.x.

CEN. (2004). *EN1998-1:2004. Eurocode 8: Design of structures for earthquake resistance. Part 1: General rules, seismic actions and rules for building*s. European Committee for Standardization (CEN), Brussels, Belgium.

Comina, C., Foti, S., Boiero, D. and Socco, L.V. (2011). Reliability of $V_{S,30}$ evaluation from surface-wave tests. *Journal of Geotechnical and Geoenvironmental Engineering, 137*(6), 579–586. doi:10.1061/(ASCE)GT.1943-5606.0000452.

Cox, B.R. and Teague, D.P. (2016). Layering ratios: a systematic approach to the inversion of surface wave data in the absence of a priori information. *Geophysical Journal International*, *207*(1), 422–438. doi:10.1093/gji/ggw282.

Das, B.M. (2010). *Principles of Geotechnical Engineering* (7th ed.). Cengage Learning, Stamford, CT.

Di Giulio, G., Savvaidis, A., Ohrnberger, M., Wathelet, M., Cornou, C., Knapmeyer-Endrun, B., Renalier, F., Theodoulidis, N. and Bard, P.-Y. (2012). Exploring the model space and ranking a best class of models in surface-wave dispersion inversion: Application at European strong-motion sites. *Geophysics*, *77*(3), B147–B166. doi:10.1190/geo2011-0116.1.

de Lucena, R.F. and Taioli, F. (2014). Rayleigh wave modeling: A study of dispersion curve sensitivity and methodology for calculating an initial model to be included in an inversion algorithm. *Journal of Applied Geophysics*, *108*, 140–151. doi:10.1016/j.jappgeo.2014.07.007.

Douglas, J. and Aochi, H. (2008). A survey of techniques for predicting earthquake ground motions for engineering purposes. *Surveys in Geophysics*, *29*, 187–220. doi:10.1007/s10712-008-9046-y.

Douglas, J. and Edwards, B. (2016). Recent and future developments in earthquake ground motion estimation. *Earth-Science Reviews*, *160*, 203–219. doi:10.1016/j.earscirev.2016.07.005.

Fernández Martínez, J.L., Fernández Muñiz, M.Z. and Tompkins, M.J. (2012). On the topography of the cost functional in linear and nonlinear inverse problems. *Geophysics*, *77*(1), W1–W15. doi:10.1190/GEO2011-0341.1.

Foti, S., Lai, C.G., Rix, G.J. and Strobbia, C. (2015). *Surface wave methods for near-surface site characterization*. CRC Press, Taylor & Francis Group, Boca Raton, FL.

Foti, S., Hollender, F., Garofalo, F., Albarello, D., Asten, M., Bard, P.-Y., Comina, C., Cornou, C., Cox, B., Di Giulio, G., Forbriger, T., Hayashi, K., Lunedei, E., Martin, A., Mercerat, D., Ohrnberger, M., Poggi, V., Renalier, F., Sicilia, D. and Socco, V. (2018). Guidelines for the good practice of surface wave analysis: a product of the InterPACIFIC project. *Bulletin of Earthquake Engineering*, *16*(6), 2367–2420. doi:10.1007/s10518-017-0206-7.

Garofalo, F., Foti, S., Hollender, F., Bard, P.-Y., Cornou, C., Cox, B.R., Ohrnberger, M., Sicilia, D., Asten, M., Di Giulio, G., Forbriger, T., Guillier, B., Hayashi, K., Martin, A., Matsushima, S., Mercerat, D., Poggi, V. and Yamanaka, H. (2016a). InterPACIFIC project: Comparison of invasive and non-invasive methods for seismic site characterization. Part I: Intra-comparison of surface wave methods. *Soil Dynamics and Earthquake Engineering*, *82*, 222–240. doi:10.1016/j.soildyn.2015.12.010.

Garofalo, F., Foti, S., Hollender, F., Bard, P.-Y., Cornou, C., Cox, B.R., Dechamp, A., Ohrnberger, M., Perron, V., Sicilia, D., Teague, D. and Vergniault, C. (2016b). InterPACIFIC project: Comparison of invasive and non-invasive methods for seismic site characterization. Part II: Inter-comparison between surface-wave and borehole methods. *Soil Dynamics and Earthquake Engineering, 82*, 241–254. doi:10.1016/j.soildyn.2015.12.009.

Haney, M.M. and Tsai, V.C. (2015). Nonperturbational surface-wave inversion: A Dix-type relation for surface waves. *Geophysics*, *80*(6), EN167–EN177. doi:10.1190/GEO2014-0612.1.

Héloïse, C., Bard, P.-Y., Duval, A.-M. and Bertrand, E. (2012). Site effect assessment using KiK-net data: part 2—site amplification prediction equation based on f_0 and V_{SZ}. *Bulletin of Earthquake Engineering, 10*(2), 451–489. doi:10.1007/s10518-011-9298-7.

Kramer, S.L. (1996). *Geotechnical earthquake engineering*. Prentice-Hall, Inc., Upper Saddle River, NJ.

Lai, C.G., Foti, S. and Rix, G.J. (2005). Propagation of data uncertainty in surface wave inversion. *Journal of Environmental & Engineering Geophysics*, *10*(2), 219–228. doi:10.2113/JEEG10.2.219.

Leong, E.C. and Aung, A.M.W. (2012). Weighted average velocity forward modelling of Rayleigh surface waves. *Soil Dynamics and Earthquake Engineering*, *43*, 218–228. doi:10.1016/j.soildyn.2012.07.030.

L'Heureux, J.-S., Lunne, T., Lacasse, S., Carroll, R., Strandvik, S.O., Ozkul, Z., Instanes, A., Sinitsyn, A., Degago, S. and Nordal, S. (2017). Norway's National GeoTest Site Research Infrastructure (NGTS). In *Proceedings of the 19th International Conference on Soil Mechanics and Geotechnical Engineering*, Seoul, Korea (pp. 611–614).

Long, M. and Donohue, S. (2007). In situ shear wave velocity from multichannel analysis of surface waves (MASW) tests at eight Norwegian research sites. *Canadian Geotechnical Journal*, *44*(5), 533–544. doi:10.1139/t07-013.

Luzi, L., Puglia, R., Pacor, F., Gallipoli, M.R., Bindi, D. and Mucciarelli, M. (2011). Proposal for a soil classification based on parameters alternative or complementary to $V_{S,30}$. *Bulletin of Earthquake Engineering*, *9*(6), 1877–1898. doi:10.1007/s10518-011-9274-2.

NGI. (2015). *SP8-GEODIP. Correlations between shear wave velocity and geotechnical parameters in Norwegian clays. Report 20150030-04-R*. Norwegian Geotechnical Institute, Oslo.

NGI. (2018). *Field and laboratory test results Halden. Norwegian GeoTest Sites (NGTS). Factual report 20160154-04-R.* Norwegian Geotechnical Institute, Oslo.

Olafsdottir, E.A., Bessason, B. and Erlingsson, S. (2019). Application of MASW in the South Iceland Seismic Zone. In *Proceedings of the International Conference on Earthquake Engineering and Structural Dynamics. Geotechnical, Geological and Earthquake Engineering, Vol. 47*, Reykjavík, Iceland (pp. 53–66). doi:10.1007/978-3-319-78187-7_5.

Olafsdottir, E.A., Erlingsson, S. and Bessason, B. (2018a). Tool for analysis of multichannel analysis of surface waves (MASW) field data and evaluation of shear wave velocity profiles of soils. *Canadian Geotechnical Journal*, *55*(2), 217–233. doi:10.1139/cgj-2016-0302.

Olafsdottir, E.A., Bessason, B. and Erlingsson, S. (2018b). Combination of dispersion curves from MASW measurements. *Soil Dynamics and Earthquake Engineering*, *113*, 473–487. doi:10.1016/j.soildyn.2018.05.025.

Park, C.B., Miller, R.D. and Xia, J. (1999). Multichannel analysis of surface waves. *Geophysics*, *64*(3), 800–808. doi:10.1190/1.1444590.

Passeri, F. (2019). *Development of an advanced geostatistical model for shear wave velocity profiles to manage uncertainties and variabilities in Ground Response Analyses* [Ph.D. Thesis]. Politecnico di Torino, Torino, Italy.

Pei, D. (2007). *Modeling and inversion of dispersion curves of surface waves in shallow site investigations* [Ph.D. Thesis]. University of Nevada, Reno, NV.

Pezeshk, S. and Zarrabi, M. (2005). A new inversion procedure for spectral analysis of surface waves using a genetic algorithm. *Bulletin of the Seismological Society of America*, *95*(5), 1801–1808. doi:10.1785/0120040144.

Pitilakis, K., Riga, E. and Anastasiadis, A. (2013). New code site classification, amplification factors and normalized response spectra based on a worldwide ground-motion database. *Bulletin of Earthquake Engineering*, *11*(4), 925–966. doi:10.1007/s10518-013-9429-4.

Pitilakis, K., Riga, E., Anastasiadis, A., Fotopoulou, S. and Karafagka, S. (2018). Towards the revision of EC8: Proposal for an alternative site classification scheme and associated intensity dependent spectral amplification factors. *Soil Dynamics and Earthquake Engineering*. doi:10.1016/j.soildyn.2018.03.030. [In press]

Ryden, N. and Park, C.B. (2006). Fast simulated annealing inversion of surface waves on pavement using phase-velocity spectra. *Geophysics*, *71*(4), R49–R58. doi:10.1190/1.2204964.

Sen, M.K. and Stoffa, P.L. (2013). *Global Optimization Methods in Geophysical Inversion* (2nd ed.). Cambridge University Press, New York, NY.

Socco, L.V. and Boiero, D. (2008). Improved Monte Carlo inversion of surface wave data. *Geophysical Prospecting*, *56*(3), 357–371. doi:10.1111/j.1365-2478.2007.00678.x.

Socco, L.V., Comina, C. and Khosro Anjom, F. (2017). Time-average velocity estimation through surface-wave analysis: Part 1 – S-wave velocity. *Geophysics*, *82*(3), U49–U59. doi:10.1190/GEO2016-0367.1.

Socco, L.V., Foti, S. and Boiero, D. (2010). Surface-wave analysis for building near-surface velocity models – Established approaches and new perspectives. *Geophysic*s, *75*(5), 75A83–75A102. doi:10.1190/1.3479491.

Song, X., Gu, H., Zhang, X. and Liu, J. (2008). Pattern search algorithms for nonlinear inversion of high-frequency Rayleigh-wave dispersion curves. *Computers & Geosciences*, *34*(6), 611–624. doi:10.1016/j.cageo.2007.05.019.

Song, X., Tang, L., Lv, X., Fang, H. and Gu, H. (2012). Application of particle swarm optimization to interpret Rayleigh wave dispersion curves. *Journal of Applied Geophysics*, *84*, 1–13. doi:10.1016/j.jappgeo.2012.05.011.

Song, X., Li, L., Zhang, X., Huang, J., Shi, X., Jin, S. and Bai, Y. (2014). Differential evolution algorithm for nonlinear inversion of high-frequency Rayleigh wave dispersion curves. *Journal of Applied Geophysics*, *109*, 47–61. doi:10.1016/j.jappgeo.2014.07.014.

Song, X., Zhang, X., Zhao, S. and Li, L. (2015). Backtracking search algorithm for effective and efficient surface wave analysis. *Journal of Applied Geophysics*, *114*, 19–31. doi: 10.1016/j.jappgeo.2015.01.002.

Tokimatsu, K., Tamura, S. and Kojima, H. (1992). Effects of multiple modes on Rayleigh wave dispersion characteristics. *Journal of Geotechnical Engineering*, *118*(10), 1529–1543. doi:10.1061/(ASCE)0733-9410(1992)118:10(1529).

Wathelet, M. (2008). An improved neighborhood algorithm: Parameter conditions and dynamic scaling. *Geophysical Research Letters*, *35*, L09301. doi:10.1029/2008GL033256.

Wathelet, M., Jongmans, D. and Ohrnberger, M. (2004). Surface-wave inversion using a direct search algorithm and its application to ambient vibration measurements. *Near Surface Geophysics*, *2*(4), 211–221. doi:10.3997/1873-0604.2004018.

Wolf, J.P. (1985). *Dynamic soil-structure interaction*. Prentice-Hall, Inc., Englewood Cliffs, NJ.

Xia, J. (2014). Estimation of near-surface shear-wave velocities and quality factors using multichannel analysis of surface-wave methods. *Journal of Applied Geophysics*, *103*, 140–151. doi:10.1016/j.jappgeo.2014.01.016.

Xia, J., Miller, R.D. and Park, C.B. (1999). Estimation of near-surface shear-wave velocity by inversion of Rayleigh waves. *Geophysics*, *64*(3), 691–700. doi:10.1190/1.1444578.

Paper IV

Verification of an open-source MASW software at Norwegian geo-test sites

Elín Ásta Ólafsdóttir, Bjarni Bessason, Sigurður Erlingsson & Amir M. Kaynia

Ólafsdóttir, E.Á., Bessason, B., Erlingsson, S. & Kaynia, A.M. (2019). Verification of an open-source MASW software at Norwegian geo-test sites. *Journal of Geotechnical and Geoenvironmental Engineering* (submitted).

Verification of an open-source MASW software at Norwegian geo-test sites

Elín Ásta Ólafsdóttir[1)], Bjarni Bessason[1)], Sigurður Erlingsson[1,2)], & Amir M. Kaynia[3)]

[1)] Faculty of Civil and Environmental Engineering, University of Iceland, Reykjavik, Iceland
[2)] Pavement Technology, The National Road and Transport Research Institute, Linköping, Sweden
[3)] Norwegian Geotechnical Institute, Oslo, Norway

Abstract

Multichannel analysis of surface waves (MASW) is a non-invasive technique for assessment of near-surface shear wave velocity (V_S) profiles. An open-source tool for acquiring, processing and analysing MASW field data, MASWaves, has been under development in recent years. In order to verify results obtained with the new tool, field measurements were conducted at four geotechnical research sites in south-eastern and central Norway. The sites are characterized as silt, soft clay, silty sand and quick clay, respectively, and have all been thoroughly studied in other field-testing campaigns. The results obtained with MASWaves were compared with results of seismic cone penetration tests, seismic dilatometer tests and laboratory measurements, as well as results of other MASW measurements. The results show that the V_S-profiles obtained with MASWaves are quite comparable to those obtained with the other techniques, thus verifying the performance of the new software. The repeatability of the analysis was confirmed with repeated measurements at a volcanic sand site in South Iceland over a seven-year period.

Keywords

Multichannel Analysis of Surface Waves; MASW; shear wave velocity; open-source software; benchmarking

1. Introduction

Shear wave velocity (V_S) is a fundamental parameter in soil dynamics and geotechnical earthquake engineering. In-situ measurements of V_S are typically conducted by use of either in-hole seismic measurements or non-invasive surface wave analysis techniques (Kramer 2014; Garofalo et al. 2016a, 2016b). The in-hole methods provide minimal decrease in resolution with depth, but the results are localized to the point where the measurement was performed. Hence, multiple in-hole measurements would be required to characterize a larger area. Surface wave analysis techniques provide a time- and cost-efficient alternative to the invasive surveys. They further have the advantage that the data acquisition is conducted on the surface, neither requiring heavy machinery nor leaving lasting marks at the site. In addition, surface wave analysis techniques can be applied at a wide variety of soil sites, including very dense or coarse-grained/gravelly sediments, or mixed soils including boulders or cobbles. Application of penetration-based methods is limited at such sites. Surface wave analysis methods survey larger areas than the in-hole techniques, thus, averaging the soil stiffness parameters over the tested area. This is important from a design perspective, as opposed to the inherent variability associated with pointwise data. However, as the measurement is conducted along a single boundary of the wave medium, their resolution decreases with depth. Furthermore, the inverse problem encountered as a part of the analysis is non-linear and affected by solution non-uniqueness. Hence, if results obtained by both invasive and non-invasive techniques are available for a single site, the results of the invasive measurements are often considered as 'benchmark' values (Garofalo et al. 2016b).

Multichannel Analysis of Surface Waves (MASW) is an active-source surface wave analysis method for evaluating near-surface V_S-profiles by analyzing Rayleigh wave propagation over a wide range of wavelengths (Gabriels et al. 1987; Park et al. 1999). In recent years, MASW has become a common technique for estimating V_S-profiles of soil sites for civil engineering applications (Socco et al. 2010; Xia 2014; Foti et al. 2018). As compared to a two-receiver analysis (Nazarian et al. 1983; Nazarian & Stokoe 1985, 1986), the use of MASW provides both a more efficient data acquisition in-situ, and improved data processing procedures for distinguishing the fundamental mode of Rayleigh wave propagation from higher modes and incoherent and coherent noise sources.

Through several years of research, the authors have developed an open-source MATLAB-based software, MASWaves, for acquiring, processing and inverting MASW field data (Olafsdottir et al. 2018a, see also masw.hi.is). The primary incentives for developing the MASW software from scratch were to gain easy access and flexibility to modify and adapt the data acquisition and processing/analysis tools for further developments and engineering applications. The objective of this work is to assess the reliability, accuracy and repeatability of results obtained by the new MASWaves software for use in civil engineering studies. In-situ measurements were conducted at four well-characterized geotechnical research sites in Norway (Lunne et al. 2003; L'Heureux et al. 2017; Olafsdottir et al. 2019b), dominated by silt, sand, soft clay and quick clay, respectively, and at a volcanic sand site in South Iceland. Independent assessments of shear wave velocity, obtained by use of invasive, non-invasive and laboratory-based

techniques, exist for the four Norwegian sites and were used for comparison and verification purposes in this study. At the site in South Iceland (Green et al. 2012; Olafsdottir et al. 2015, 2019a), repeated MASW measurements have been conducted over a seven-year period from 2013 to 2019. These were used to verify the repeatability of the analysis.

2. Method

An overview of the MASW method, as it is applied in this work, is provided in Fig. 1. The application is divided into three consecutive steps: field measurements, dispersion analysis, and inversion analysis.

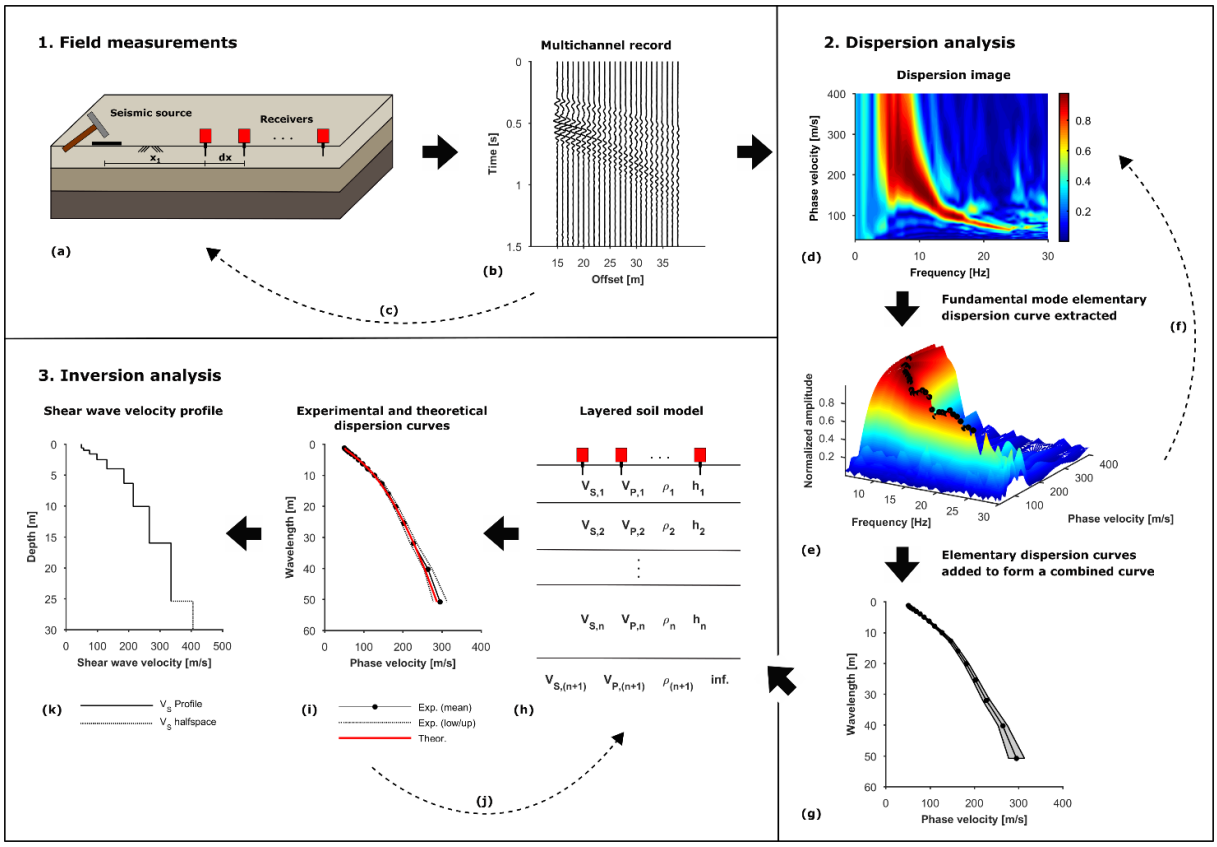

***Figure 1**: Application of the MASW method.*

For data acquisition in-situ, low-frequency geophones are lined up on the surface with equal receiver spacing dx (Fig. 1a). The geophones used in this work have a natural frequency of 4.5 Hz and a critical damping ratio of 0.5. An impact load (i.e., a sledgehammer blow) is applied at a distance x_1 from one end of the receiver spread and the wave propagation is recorded (Fig. 1b). The data acquisition process is repeated by using different measurement profile configurations, i.e. profiles with different values of x_1 and/or dx, while keeping the midpoint of the receiver spread fixed (Fig. 1c).

The primary aim of the dispersion analysis is to identify the dispersion characteristics of the acquired Rayleigh waves. A dispersion image (Fig. 1d) is obtained by transforming each multi-channel record into the frequency-phase velocity domain. The transformation visualizes the energy density of the recorded data, from which Rayleigh wave dispersion curve(s) are identified based on the spectral maxima observed at different frequencies (Fig. 1e). The different profile configurations provide information on different volumes of soil and may thus help identifying whether significant lateral variations in soil properties are present beneath the receiver spread. The use of multiple source offsets further aids identification of potential near-field effects, which bias the experimental dispersion curve estimates. Furthermore, by obtaining a statistical sample of dispersion curves through the repeated data acquisition, the variability in estimated phase velocity values can be quantified, hence, providing an indicator of the reliability of the experimental data (Figs. 1f-g).

In the third step of the analysis, the shear wave velocity profile is obtained by inversion of the experimental Rayleigh wave dispersion curve. The inversion is conducted based on the assumption that the tested site can be adequately approximated by a semi-infinite stratified soil model, where each layer is assumed to be flat and have homogeneous and isotropic properties. The parameters used to describe the properties of each layer are shear wave velocity, compressional wave velocity (V_P) (or Poisson's ratio (ν)), mass density (ρ), and layer thickness (h) (Fig. 1h). Conventionally, the inversion is formulated as an optimization problem where the objective is to minimize the value of a misfit function representing the distance between the experimental and theoretical dispersion curves. Hence, in its most general form, the inversion is carried out by iteratively comparing theoretical dispersion curves, obtained from 'trial' subsurface models (Figs. 1h-k), to the experimental data in search of a model (or a set of models) that both fit the observed dispersion characteristics and incorporate any known features of the survey site (Fig. 1k). The shear wave velocity has a dominant effect on the fundamental mode dispersion curve at frequencies higher than 5 Hz, followed by layer thicknesses (Xia et al. 1999), while variations in V_P (or ν) and ρ have much less effect. Hence, V_P (or ν) and ρ are commonly assigned fixed values based on a-priori information or by using standard values for specific soil types (e.g., de Lucena & Taioli 2014; Foti et al. 2015).

In this work, the focus is on inversion of fundamental mode Rayleigh wave dispersion curves for the shear wave velocity and layer thickness values. The Poisson's ratio (or compressional wave velocity) and mass density are assessed based on prior in-situ and/or laboratory measurements, with the detected groundwater level taken into consideration, thus reducing the number of unknown parameters. The initially specified layering parameterization (i.e., the number of layers) is also an important factor in the inversion process (Di Giulio et al. 2012; Cox & Teague 2016; Foti et al. 2018) and can affect its outcome substantially. Hence, the number of layers to include in the stratified soil model is regarded as an additional unknown model parameter.

2.1. MASWaves approach

MASWaves has been under development at the University of Iceland for the past few years. The development and benchmarking of the initial versions of its dispersion and inversion analysis tools is described by Olafsdottir et al. (2018a) (see also masw.hi.is). Olafsdottir et al. (2018b, 2019c) further describe aspects of the dispersion and inversion analysis, respectively, that have been implemented in the current version of the software. The software consists of two parts, i.e., a data acquisition part in one module (MASWaves DAQ) and a processing part containing three separate modules (MASWaves Dispersion, Combination and Inversion). A graphical overview of the workflow of MASWaves is provided in Fig. 2.

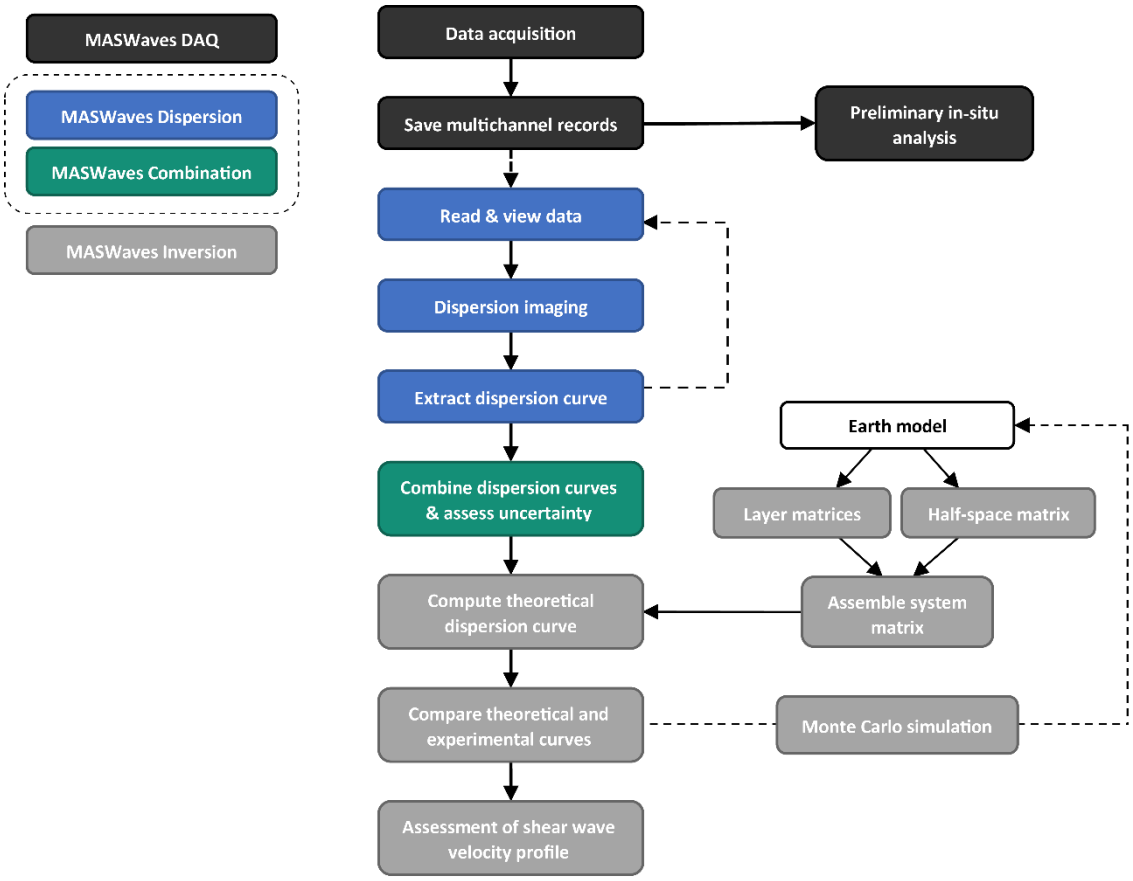

***Figure 2**: Diagram of MASWaves' workflow.*

For current applications, the data acquisition hardware consists of a pair of NI USB-6218 multifunction I/O devices from National Instruments and a set of GS-11D geophones from Geospace Technologies. The specialized data acquisition tool (MASWaves DAQ) links the data acquisition hardware to the processing tools. It further allows for preliminary in-situ analysis of the recorded data, e.g., for assessment of data quality in the field. Hence, if required, the survey configuration, including the measurement profile layout and the values of different measurement control parameters such as the recording time, can be adapted to better suit the characteristics of the tested site as judged based on results of a preliminary analysis. The DAQ

module can be replaced by any other similar product delivering recorded multi-channel time series that can be read by the processing tools.

The function of the basic dispersion analysis tool (MASWaves Dispersion) is to identify experimental dispersion curves (DC) from multi-channel surface wave records through adoption of the phase shift method (Park et al. 1998). An experimental curve obtained from a single multi-channel registration is referred to as an 'elementary dispersion curve' in the following discussion. The purpose of the second processing tool (MASWaves Combination) is to combine dispersion curves obtained from multiple surface wave registrations. The composite curve is obtained by grouping the elementary dispersion curve data points together within logarithmically spaced wavelength intervals. The arithmetic mean of the dispersion curve phase velocity values within each interval is used as a point estimate of the phase velocity of the Rayleigh wave components in the given wavelength range (Olafsdottir et al. 2018b). The standard deviation of the phase velocity values within each interval represents the spread of the dispersion curve data points, whilst classical statistics or bootstrapping (Efron 1979; Efron & Tibshirani 1993) can be applied to assess the uncertainty associated with the mean phase velocity estimates. The inversion tool (MASWaves Inversion) is used to evaluate the shear wave velocity profile of the tested site by inverting the composite fundamental mode dispersion curve. The inversion is conducted by application of a simple Monte Carlo-based global search algorithm (Olafsdottir et al. 2019c) with the fast delta-matrix algorithm (Buchen & Ben-Hador 1996) used for computation of theoretical dispersion curves. Inference is drawn from the set of simulated V_S-profiles based on the observed spread of elementary dispersion curve data points within each wavelength interval.

3. MASW measurements at Norwegian research sites

For verification of the data acquisition and analysis tools of MASWaves, in-situ measurements were conducted at four well-characterized geotechnical research sites in south-eastern and central Norway in June 2018. The sites are referred to as Halden (silt site), Onsøy (soft clay site), Øysand (sand site), and Tiller-Flotten (quick clay site). The Halden, Øysand and Tiller-Flotten sites were developed through the Norwegian GeoTest Site (NGTS) project (L'Heureux et al. 2017), whilst the tested site at Onsøy was established in the late 1960s by the Norwegian Geotechnical Institute (NGI) (Lunne et al. 2003). A brief description of each site is provided in the following section. The main characteristics of the research sites are summarized in Table 1, along with relevant references, and their locations are shown in Fig. 3. An overview of relevant field and laboratory tests, conducted at each site by independent researchers, is further provided in Table 1.

***Figure 3**: Test sites in south-eastern and central Norway. [The map is based on data from the Norwegian Mapping Authority. ©Kartverket]*

***Table 1**: Overview of site characteristics and previous work used for comparison at the Halden, Onsøy, Øysand and Tiller-Flotten sites.*

	Halden	**Onsøy**	**Øysand**	**Tiller-Flotten**
Characteristic soil type	Silt	Soft clay	Silty sand	Quick clay
Unit weight	19–20.5 kN/m^3	~16 kN/m^3	18–19 kN/m^3	17–19 kN/m^3
Water content	21%–32%	50%–70%	~20%–30%	30%–50%
Depth to bedrock	~21 m in the southern part of the site	~40 m	>80 m	>50 m
Detected groundwater table	About 2–2.5 m below ground level	Below the surficial crust	~2 m below ground level	Below the surficial crust (~1–2 m depth)
Previous work used for comparison	SCPT, SDMT, Lab (BE)	SCPT, MASW, Lab	SCPT, SDMT, MASW, Lab (BE)	SCPT, SDMT
References	Blaker et al. (2016, 2019)	Lunne et al. (2003)	Gundersen et al. (2018) Quinteros et al. (2019)	L'Heureux et al. (2019a, 2019b)

3.1. Research sites

The first site is located in a small public park in the town of Halden in south-eastern Norway (Fig. 3). The site is almost flat, however, the depth to bedrock within the research area (approximately 6,000 m^2) varies considerably. In the southern part of the site, where the MASW measurements were conducted, bedrock is typically identified at around 21 m depth (NGI 2018; Blaker et al. 2019). Blaker et al. (2019) provide a thorough description of the geology of the area and the geotechnical engineering properties of the Halden silt. The top-most soil unit at the site consists of loose- to medium-dense silty sand and extends down to around 4.5–5 m depth. It rests on a layer of normally consolidated, low plasticity silt with a thickness in the order of 10 m. A clay unit, consisting of low to medium strength clay, is found at the bottom of the silt deposit (Blaker et al. 2016, 2019). The groundwater table is detected at a depth of around 2–2.5 m, as measured from an in-situ stand pipe (Blaker et al. 2019).

The Onsøy site is in the northern part of the town Gressvik, approximately 100 km southeast of Oslo (Fig. 3). The testing area is characterized by deposits of uniform, dark-gray silty clay with a thickness in the order of 40 m (Lunne et al. 2003; Long & Donohue 2007). Below a thin surficial crust, the soil is expected to be fully saturated. Extensive work, commencing in the late 1960s, has been carried out to study the properties of the Onsøy clay. In brief, it has been classified as normally to lightly overconsolidated, of high to very high plasticity and of medium sensitivity. Its characteristics and engineering properties are summarized by Lunne et al. (2003).

The Øysand research area is located in central Norway, around 15 km south-west of the city of Trondheim (Fig. 3). The testing area is currently used for agricultural purposes and its topography is relatively flat. Quinteros et al. (2019) and Gundersen et al. (2018) summarize existing studies on the geotechnical properties of the soil materials at Øysand. Overall, the site is characterized by thick deposits of fluvial and deltaic materials. Results of in-situ soundings, borehole logs and geophysical measurements indicate the presence of two main soil units within the upper-most 20 m at the site, although significant lateral variability was also identified. The upper unit consists of fine to coarse sand with presence of gravel and has a thickness of up to 10 m, whilst the lower unit is characterized by medium silty sand and sandy silt with traces of organic material (Quinteros et al. 2019; Gundersen et al. 2018). The depth to bedrock at the Øysand site has not been established, however, based on geotechnical investigations conducted in the area in the 1940s, it is expected to exceed 80 m (Quinteros et al. 2019). The groundwater level at the site was detected at a depth of around 2 m.

The fourth site is referred to as Tiller-Flotten and located in an agricultural area approximately 10 km south of Trondheim (Fig. 3). The site is underlain by deposits of uniform marine clay and results of in-situ soundings have indicated that the total sediment thickness is more than 50 m (L'Heureux et al. 2019a, 2019b). The Tiller-Flotten clay is slightly overconsolidated and of low to medium plasticity. The soil profile at the site has been divided into two main stratigraphic units (L'Heureux et al. 2019b). The upper unit mostly consists of desiccated and weathered clay and extends down to a depth of approximately 2 m. The lower unit is divided into two parts based on soil sensitivity. Down to around 7.5 m below ground level, the Tiller-Flotten clay shows low to medium sensitivity. Below this, the clay is highly sensitive and quick (i.e.,

remoulded undrained shear strength below 0.5 kPa) down to a depth of at least 20 m. The groundwater table has been identified below the surficial crust at a depth of 1–2 m, but the groundwater pressures are far below hydrostatic conditions due to drainage to the Nidelva River (L'Heureux et al. 2019a, 2019b).

3.2. In-situ measurements and dispersion processing

At each of the four sites, MASW field measurements were conducted using an equally spaced linear array of twenty-four vertical geophones. Emphasis was on placing the survey profile as close as possible to relevant previous work at each site (refer to Table 1). Depending on the site conditions, as well as any logistical constraints, the testing parameters (i.e., geophone spacing, source offset lengths and recording time) were adjusted to each location. The impact load was in all cases created by a sledgehammer that was struck vertically on a 15 cm-diameter metallic base plate at several different offsets from one or both ends of the receiver spread. Repeated shots (usually four to six) were recorded for each source offset in order to obtain a statistical sample of dispersion curves and, hence, to allow for quantification of the variability in the estimated phase velocity values. Furthermore, where possible, dispersion curves obtained from shots applied at both ends of the receiver spread were compared, in order to identify whether significant lateral variations were present along the survey line. The test configurations are summarized in Table 2.

For analysis of the experimental data, each acquired multi-channel record was processed separately as outlined in Section 2. The variability among the extracted elementary dispersion curves was subsequently evaluated in terms of the coefficient of variation (COV)

$$COV = \frac{s}{\bar{x}} \tag{1}$$

where, in the current section, $\bar{x}$ denotes the average of the estimated phase velocity values at frequency f, and s is the corresponding standard deviation (std).

Figure 4 shows typical dispersion images of multi-channel records acquired at each of the four sites. All elementary dispersion curves, which were identified from the repeated shots at each site and used in the subsequent analysis, are illustrated in Fig. 5a. Figure 5b presents comparison of the extracted dispersion curves represented by the coefficient of variation of the estimated phase velocity values at each frequency. Table 2 further summarizes the variation of the interpreted experimental Rayleigh wave phase velocity values for each of the four test locations.

***Table 2**: Overview of MASW test parameters at the Halden, Onsøy, Øysand and Tiller-Flotten sites.*

		Halden	Onsøy	Øysand	Tiller-Flotten
Data acquisition					
Number of geophones	[-]	24	24	24	24
Geophone spacing (source offsets)	[m]	1 (3–5)[1)]	1 (3–15)[2)] 2 (3–20)[3)]	2 (3–30)[4)]	2 (3–30)[4)]
Sampling rate	[Hz]	1000	1000	1000	1000
Recording time	[s]	2.0	2.2	2.0	2.0
Dispersion analysis					
DC frequency	[Hz]	5.5–35.8	3.6–45.0	5.5–56.8	4.1–27.6
Coefficient of variation	[%]				
- Range		0.1–4.8	0.1–5.8	0.2–4.0	0.2–10.8
- Below 10 Hz (max.)		4.8	5.8	4.0	10.8
- Above 10 Hz (max.)		1.3	2.1	2.6	3.2
- Average (all freq.)		1.0	1.0	1.0	2.5

[1)] Source offsets $x_1 \in \{3, 4, 5\}$ m

[2)] Source offsets $x_1 \in \{3, 5, 7.5, 10, 15\}$ m

[3)] Source offsets $x_1 \in \{3, 5, 7.5, 10, 15, 20\}$ m

[4)] Source offsets $x_1 \in \{3, 5, 7.5, 10, 15, 20, 30\}$ m

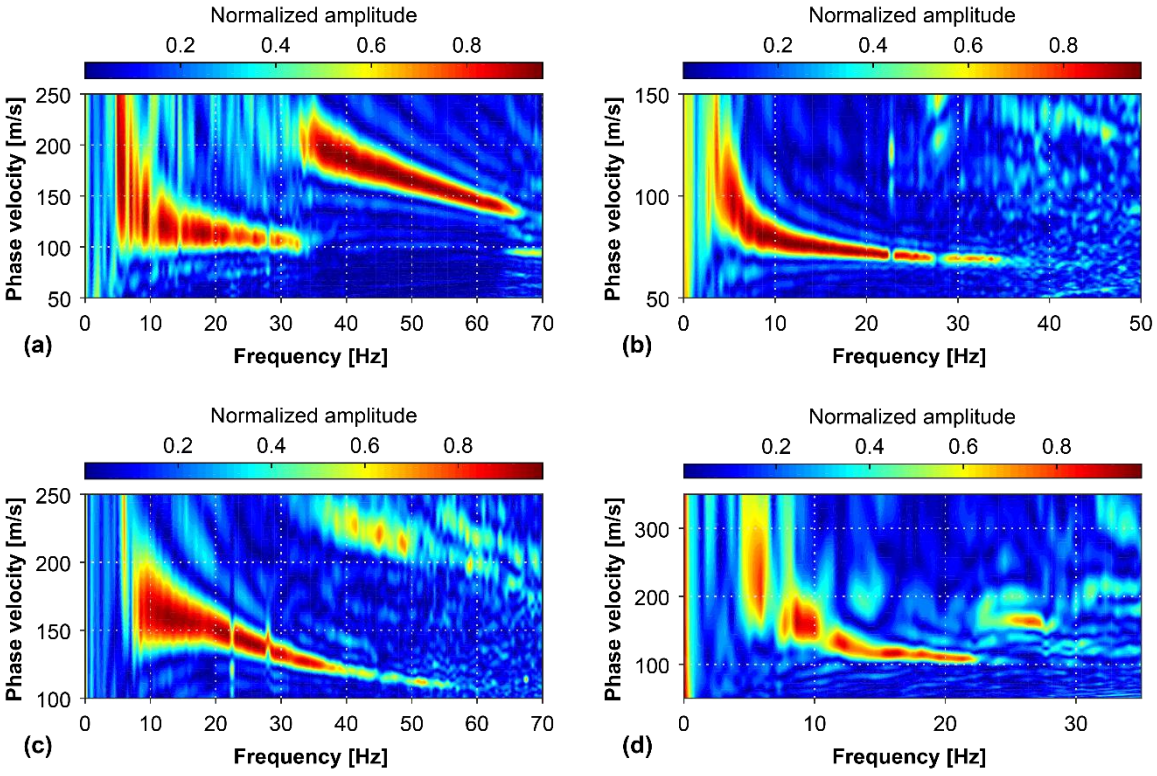

***Figure 4**: Dispersion images of multi-channel surface wave records acquired at the **(a)** Halden, **(b)** Onsøy, **(c)** Øysand, and **(d)** Tiller-Flotten test sites.*

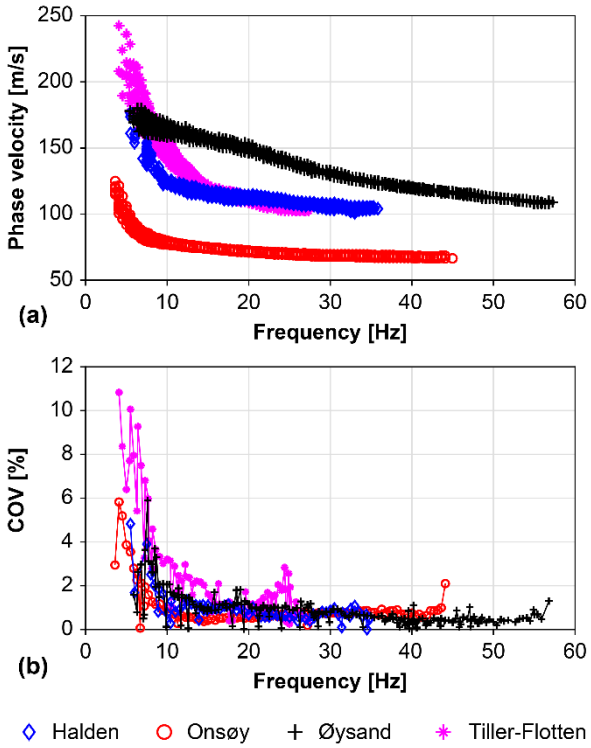

***Figure 5**: **(a)** Fundamental mode (elementary) dispersion curve estimates obtained for the Halden, Onsøy, Øysand, and Tiller-Flotten sites (data from all shots). **(b)** Variation of extracted Rayleigh wave phase velocity values at each frequency.*

The observed dispersion properties of the Halden silt are illustrated in Fig. 4a. Due to the varying depth to bedrock within the testing area, the use of a longer receiver spread than 23 m was not attempted at this site. The dispersion image further displays a clear higher (or apparent) mode above 35 Hz, which is believed to result from the fact that the site is far from a 1D structure. However, only the fundamental mode data was used in the subsequent analysis. Analysis of shots applied at both ends of the receiver spread indicated essentially the same dispersion characteristics. Overall, by combination of data from repeated shots and different shot locations, fundamental mode Rayleigh wave dispersion curve estimates were obtained over a frequency range of 5.5–35.8 Hz (Fig. 5a). The dispersion curve estimates agreed well, as indicated by a coefficient of variation less than 5% at all frequencies (Fig. 5b). In line with previous findings (Lai et al. 2005; Olafsdottir et al. 2018b), the lowest frequency components displayed more variability than components in the higher frequency range (see also Table 2).

For the uniform soft-clay site at Onsøy, a coherent dispersion trend, characterized by a continuous decrease in phase velocity with increasing frequency (Fig. 4b), was observed. The data acquisition was conducted using two survey profiles with the same midpoint and direction but different lengths, i.e., 23 m and 46 m, respectively. Overall, the experimental dispersion curve was identified within a frequency band of 3.6–45.0 Hz (Fig. 5a). The shorter profile contributed to the higher frequency range, whilst the longer profile allowed for improved dispersion curve identification at lower frequencies. Based on combination of curves from repeated shots, the COV values were in the range of 0.1–5.8%, indicating little spread in the experimental data (Fig. 5b).

Figure 4c displays the observed dispersion properties at Øysand. The dispersion images for the site displayed prominent spectral high-amplitude bands, providing elementary dispersion curve estimates over a frequency range spanning 5.5–56.8 Hz (Fig. 5a). The dispersion curve estimates obtained by repeated shots and different source offset lengths/shot locations were in good agreement, as indicated by a coefficient of variation at or below 4% at each frequency (Fig. 5b).

A typical dispersion image for the Tiller-Flotten site is shown in Fig. 4d. By combination of data acquired by using several different source offsets, elementary dispersion curve estimates were obtained over a frequency band of 4.1–27.6 Hz (Fig. 5a). As indicated by the COV values summarized in Table 2 and visualized in Fig. 5b, the dispersion data for the Tiller-Flotten site was substantially more scattered than the data acquired at Halden, Onsøy, and Øysand, especially below a frequency of 10 Hz. At higher frequencies, however, the scatter within the experimental data decreased, displaying the same trend as observed at the other three sites.

The experimental dispersion curve estimates for each of the four sites were subsequently added up within logarithmically spaced wavelength intervals following the procedure described by Olafsdottir et al. (2018b). The resulting composite dispersion curves are illustrated in Fig. 6. Also shown are upper and lower boundary curves, corresponding to plus-minus one standard deviation of the mean curve.

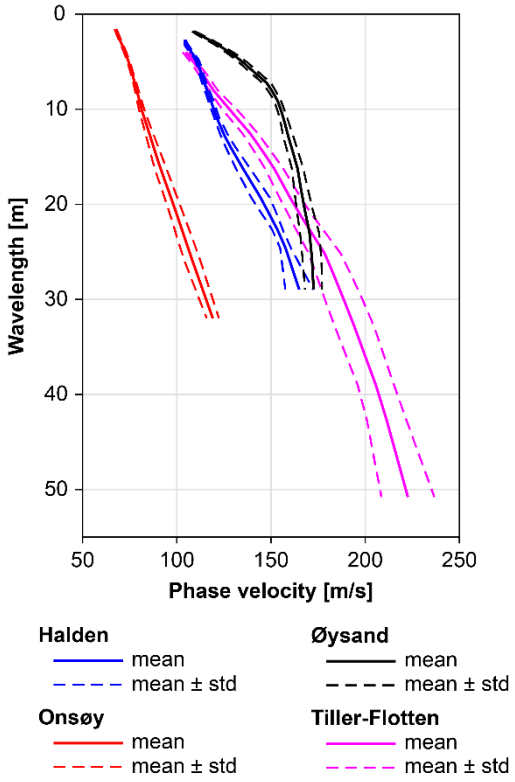

***Figure 6**: Composite experimental dispersion curves with upper and lower boundaries for the Halden, Onsøy, Øysand and Tiller-Flotten sites.*

3.3. Inversion

The inversion of the composite dispersion curves in Fig. 6 was conducted following the global search procedure outlined by Olafsdottir et al. (2019c) with the dispersion misfit (ϵ) defined as

$$\epsilon = \frac{1}{Q}\sum_{q=1}^{Q}\frac{\sqrt{\left(V_{R,t,q}-V_{R,e,q}\right)^2}}{V_{R,e,q}}\cdot 100\% \quad (2)$$

where $\boldsymbol{V_{R,e}} = (V_{R,e,1}, V_{R,e,2}, \ldots, V_{R,e,Q})$ and $\boldsymbol{V_{R,t}} = (V_{R,t,1}, V_{R,t,2}, \ldots, V_{R,t,Q})$ denote the experimental and theoretical dispersion curve phase velocity values, respectively. The inversion algorithm was run ten times (using identical starting profiles) in order to compensate for the effects of the randomization associated with the Monte Carlo-based search process. The number of iterations in each run of the algorithm was specified as 1,000, resulting in a total of 10 × 1,000 simulated V_S-profiles for each site.

The inversion was in all four cases conducted without using results of available invasive measurements to guide the layering parameterization and, thus, constrain the inversion process. This was done in order to mimic the common situation encountered in geotechnical investigations, where limited information about the layering of the tested area is available. Hence, in order to assess the effects of the layering parameterization on the estimated V_S-profiles, the number of finite thickness layers (n) was considered an unknown parameter and preliminary analysis conducted by assuming different parameterizations, with velocity reversals permitted within the uppermost layers. The strategy adopted was to start the preliminary analysis of the experimental data with two layers (i.e., one finite-thickness layer over a half-space). Subsequently, the number of layers included in the trial models was increased and the inversion process repeated until the dispersion misfit had reached a stable value. If two different parameterizations resulted in comparable dispersion misfit values and provided V_S-profiles whose dispersion curves visually fitted the experimental data equally well over the entire wavelength range, the simpler model containing fewer layers was chosen for further analysis. The mass density profile of each site was specified based on results of independent geotechnical investigations (Blaker et al. 2019; Lunne et al. 2003; Gundersen et al. 2018; Quinteros et al. 2019; L'Heureux et al. 2019a, 2019b). The compressional wave velocity was fixed at 1,440 m/s below the detected groundwater level at each site (Table 2). For the unsaturated surficial layer(s), the values of the compressional wave velocity were, in each iteration, linked to the trial shear wave velocity profile through the Poisson's ratio. In lack of site-specific values, the Poisson's ratio for each of the four sites was assessed based on standard values for the different soil types, as summarized by Das (2010).

The inversion results for each of the four sites are presented in Fig. 7 through Fig. 10. Sampled V_S-profiles whose theoretical dispersion curves fall within one standard deviation of the composite experimental curve at all wavelengths are sorted based on dispersion misfit values [Eq. (2)] in Figs. 7b–10b, with the darkest colours illustrating profiles characterized by the lowest misfit values. This set of profiles is also referred to as 'accepted profiles' in the subsequent discussion. The corresponding theoretical dispersion curves are compared to the experimental data using the same colour scheme in Figs. 7a–10a. As a measure of the variation

within each set of 'accepted' interval velocity profiles, Figs. 7c–10c present the coefficient of variation [Eq. (1)] of the profiles in Figs. 7b–10b, respectively, as a function of depth. For a given depth z, $\bar{x}$ [in Eq. (1)] denotes the average of the shear wave velocity values at depth z and s is the corresponding standard deviation. The average COV value for each of the four sites is further shown. Overall, the results depicted in Figs. 7c, 8c and 10c indicate a comparable degree of variation within the set of 'accepted' profiles for the Halden, Onsøy and Tiller-Flotten sites, with COV values on average around 5%. At the Øysand site, smaller variation was observed, with COV values typically around 2.5%.

The mean and median V_S-profiles, along with the corresponding theoretical dispersion curves, are further presented for each of the four sites. For a given test location, the mean profile is comprised of the mean of the $V_{S,1}$ values, the mean of the h_1 values, etc., as included in the 'accepted' interval velocity profiles. The median profiles are obtained analogously using the median values of each of the inverted parameters. The dispersion curves computed on the basis of the mean and median profiles match the target experimental curves (Figs. 7a–10a). It is further noted that the mean and median V_S-profiles are in all cases fairly close together, indicating a relatively symmetrical distribution for each of the inversion parameters illustrated in Figs. 7b–10b.

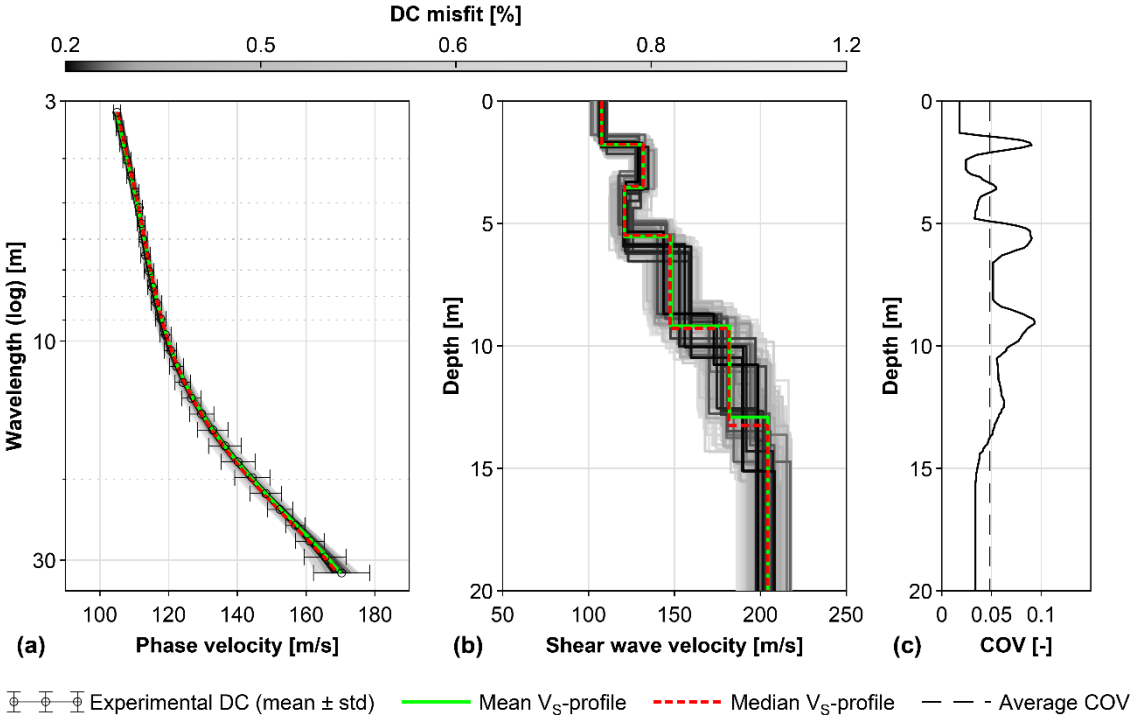

***Figure 7**: Results of MASW measurements at the Halden site. The proposed methodology resulted in trial shear wave velocity profiles consisting of six layers. **(a)** Dispersion curves. **(b)** Shear wave velocity profiles. **(c)** Variation of shear wave velocity values with depth.*

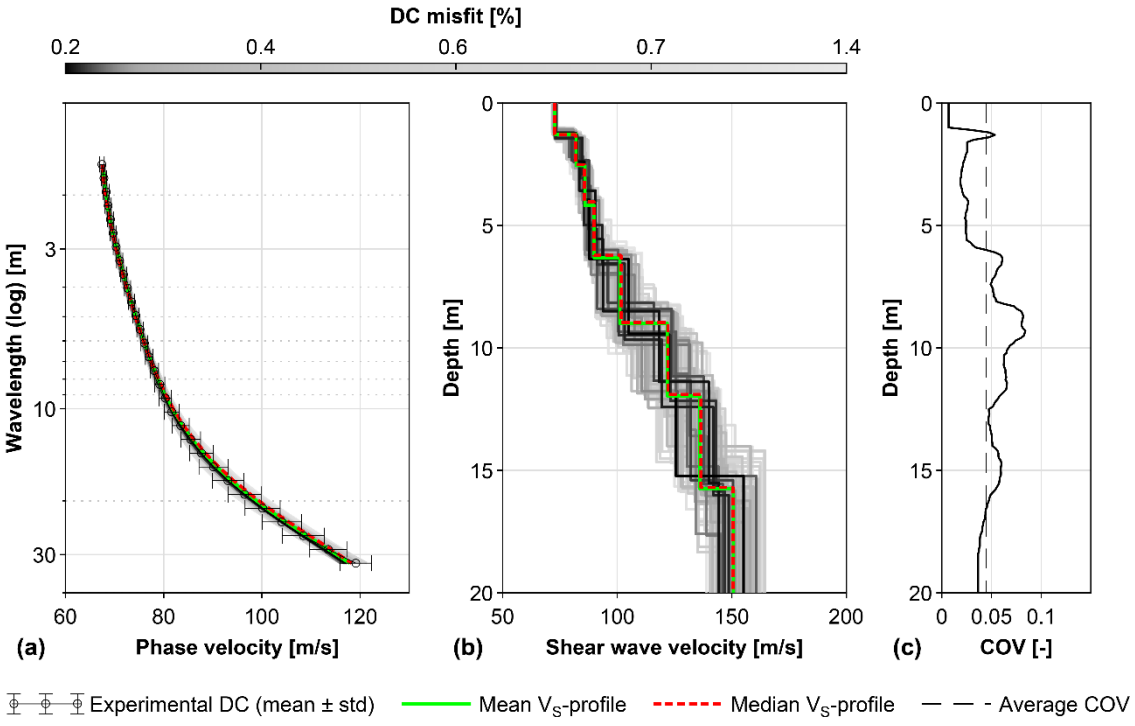

***Figure 8**: Results of MASW measurements at the Onsøy site. The proposed methodology resulted in trial shear wave velocity profiles consisting of eight layers. **(a)** Dispersion curves. **(b)** Shear wave velocity profiles. **(c)** Variation of shear wave velocity values with depth.*

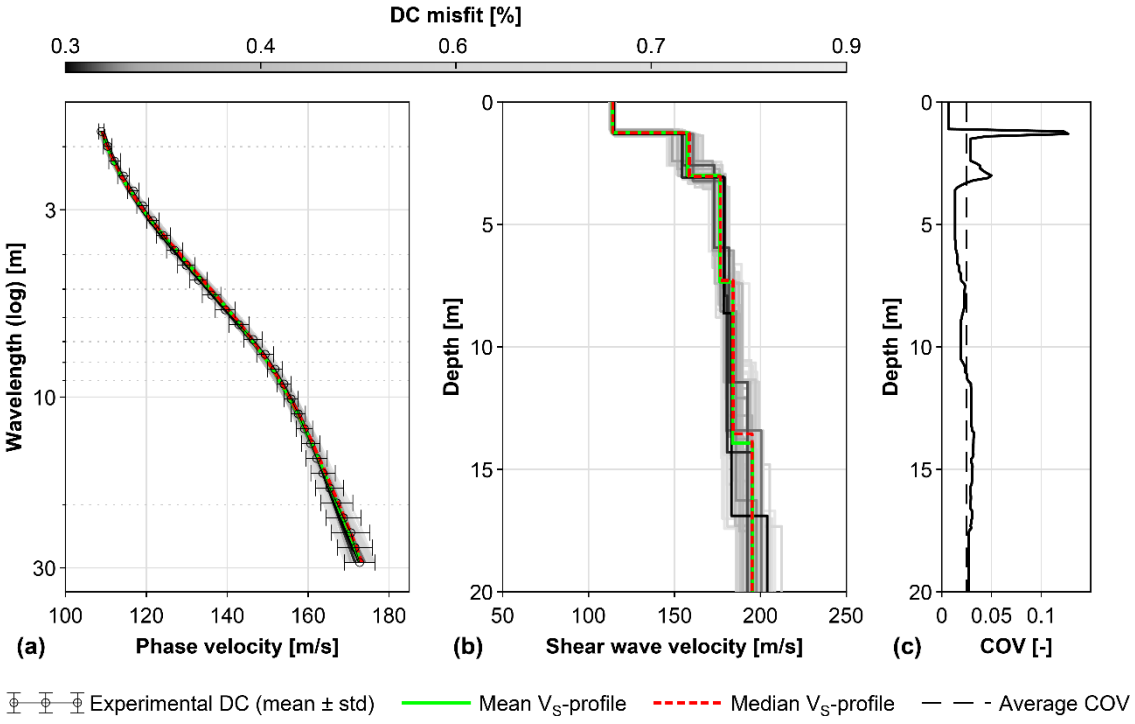

***Figure 9**: Results of MASW measurements at the Øysand site. The proposed methodology resulted in trial shear wave velocity profiles consisting of five layers. **(a)** Dispersion curves. **(b)** Shear wave velocity profiles. **(c)** Variation of shear wave velocity values with depth.*

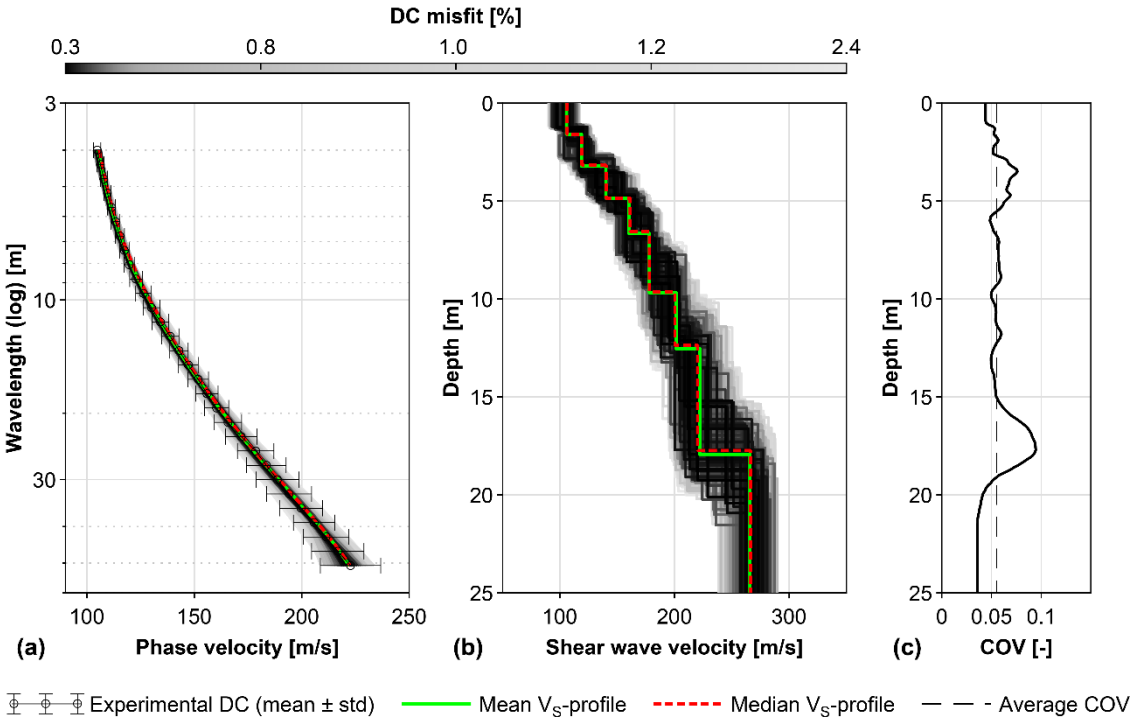

***Figure 10**: Results of MASW measurements at the Tiller-Flotten site. The proposed methodology resulted in trial shear wave velocity profiles consisting of eight layers. **(a)** Dispersion curves. **(b)** Shear wave velocity profiles. **(c)** Variation of shear wave velocity values with depth.*

4. Comparison with existing measurements of V_S

In order to verify the performance of the data acquisition and analysis tools of MASWaves, the results of the measurements presented in Sections 3.2 and 3.3 were compared with independent assessments of V_S. Figure 11 presents the results obtained by using MASWaves together with results of invasive, non-invasive and/or laboratory-based measurements conducted at each of the sites. In Fig. 11, the MASW measurement results (refer to Figs. 7–10) are summarized in terms of the mean and median of the tested V_S models whose theoretical dispersion curves fall within one standard deviation of the experimental data. The lowest dispersion misfit profiles are further shown.

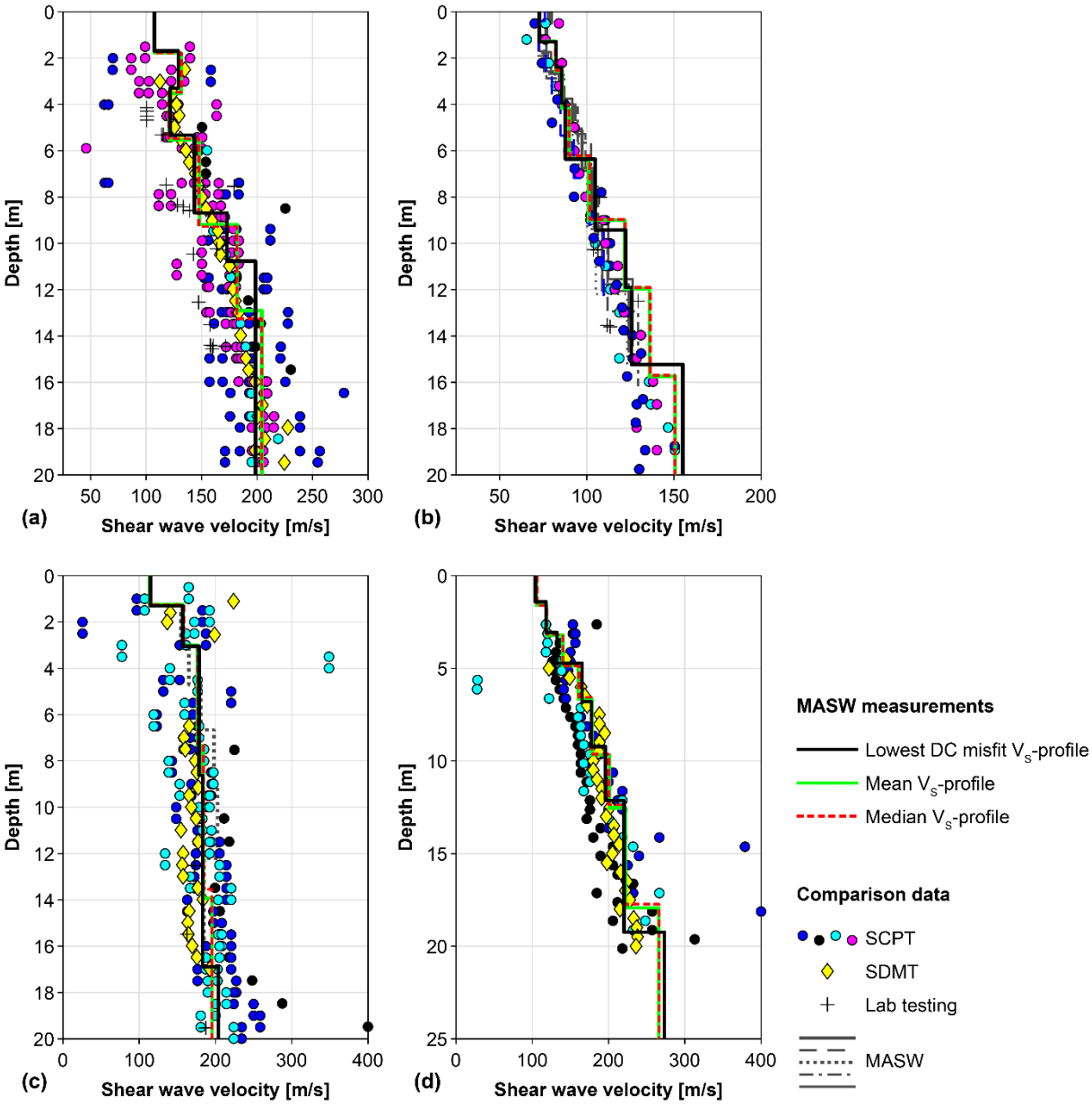

***Figure 11**: Comparison of MASWaves V_S-profiles and results of invasive, non-invasive and laboratory measurements previously conducted at the four research sites; **(a)** Halden, **(b)** Onsøy, **(c)** Øysand and **(d)** Tiller-Flotten.*

Since 2015, several techniques have been applied to evaluate the shear wave velocity of the soil deposits at the Halden site. A number of Seismic Cone Penetration Tests (SCPT) and Seismic Dilatometer Marchetti Tests (SDMT) were conducted at the site as a part of the NGTS project (Blaker et al. 2016, 2019; L'Heureux et al. 2017; NGI 2018). In these tests, the CPT/DMT rod is equipped with a seismic module and down-hole measurements of V_S collected during the penetration of the cone or the DMT blade, with the impulse source located at ground level (Robertson et al. 1986; Martin & Mayne 1997; Marchetti et al. 2008). The shear wave velocity of the Halden silt has also been assessed by bender element (BE) tests performed on triaxial and direct simple shear specimens (Blaker et al. 2019; NGI 2018). The results presented in Fig. 11a indicate a very good agreement between the results of the MASW and SDMT

measurements. The SCPT results are slightly scattered. However, the MASW results are very comparable with the general V_S trend demonstrated by the SCPT, i.e. V_S values increasing from 100–120 m/s at approximately 2 m depth to about 200 m/s at a depth of 16–19 m. The BE measurements tended to indicate slightly lower shear wave velocities than were measured by the in-situ techniques.

For interpretation of fundamental mode Rayleigh wave dispersion curves, common practice (e.g., Cox & Teague 2016; Foti et al. 2018; Garofalo et al. 2016a; Park et al. 1999) is to limit the maximum investigated depth to one-third to half the maximum retrieved wavelength (i.e., $\lambda_{max}/3$ to $\lambda_{max}/2$). Hence, based on the wavelengths covered by the composite dispersion curve for the Halden site (refer to Fig. 6), the investigation depth of the MASW survey may be estimated as 10–15 m. However, the MASW V_S-profile is very comparable to the direct measurements below this level, indicating that the results might be fully reliable down to a greater depth than the commonly used rule-of-thumb value of $\lambda_{max}/3$ to $\lambda_{max}/2$ at the Halden site.

The shear wave velocity of the Onsøy clay has been assessed using a variety of techniques over a time period spanning more than three decades (Bazin et al. 2016). Measurements of V_S were conducted with a number of SCPTs in the Onsøy research area in 1984 by the University of British Columbia (Eidsmoen et al. 1985; Lunne et al. 2003) and in 2004 by the University of Massachusetts (Landon 2007; Bazin et al. 2016). MASW measurements were conducted in the area in 2005 (Long & Donohue 2007). Seismic data were recorded along several profiles and the analysis conducted by use of the SurfSeis software. Results of laboratory measurements of V_S, carried out on block samples of the Onsøy clay, are also available (Bazin et al. 2016). Overall, the results of the current MASW measurements are consistent with the previously evaluated V_S-profiles (Fig. 11b). Below a depth of around 10 m, the 2018 MASW V_S-profile though tends to indicate slightly higher shear wave velocity values than the previous measurements. The investigation depth of the 2018 survey and the previous MASW surveys at the site, as assessed on the basis of the $\lambda_{max}/2$ criterion, is comparable, or generally in the range of 15–16 m. However, SCPT data was, on both occasions, collected down to a depth of around 20 m.

Figure 11c compares the MASW measurement results for the Øysand site with previous assessments of V_S. Since 2016, a number of geotechnical, geophysical and laboratory tests have been used for characterization of the gravelly-sandy-silty sediments at Øysand (Quinteros et al. 2019). In particular, down-hole measurements of V_S, resulting from SCPT and SDMT surveys conducted in close vicinity to the midpoint of the MASW profile, are used for comparison. Furthermore, laboratory values, obtained with BE tests on samples collected at approximately the same location, are available. There is substantial scatter in the SCPT and SDMT data within the upper-most 5 m. However, the MASW measurement results are consistent with the general trend indicated by the SDMT and SCPT measurements for that depth range. Between depths of approximately 5–15 m, the results of the MASW survey further correspond well with the fairly constant V_S values of about 200 m/s that are implied by the penetration tests. At greater depths, however, the scatter in the SCPT/SDMT data increases again due to site heterogeneities. Hence, it is difficult to draw conclusions regarding the reliability of the MASW profile at depths greater

than approximately 15–16 m based on comparison with the SCPT and SDMT data. Furthermore, results of an independent MASW survey carried out at Øysand in 2016 (NGTS data) are in good agreement with the 2018 MASW V_S-profile. The midpoints of the MASW survey profiles were positioned at the approximately same location and the orientation of the profiles was the same. The measurement profiles used in the 2016 survey were, however, significantly longer than the profile used in this work, or 69 m and 92 m as compared to 46 m. Despite this difference, the estimated investigation depth of the 2018 survey was comparable with that of the 2016 survey.

Results of independent measurements of V_S at the Tiller-Flotten site, obtained by means of SCPT and SDMT, are compared to the results of the current MASW survey in Fig. 11d. Overall, the results obtained by the different in-situ measurement techniques are consistent, indicating an increase in measured shear wave velocity values from around 120 m/s at a depth of 2 m to approximately 200–225 m/s at a depth of 15–18 m. However, the inverted MASW V_S-profiles tend to indicate slightly higher shear wave velocity values than the invasive measurements. The in-situ values of V_S obtained for the Tiller-Flotten site are further consistent with characteristics values for Norwegian soft clays, and comparable to those obtained at comparable sites in the Trondheim region (Long & Donohue 2007; L'Heureux & Long 2017; L'Heureux et al. 2019b).

5. Repeatability of the MASW analysis

For assessment of the repeatability of the analysis, repeated field tests were conducted between 2013 and 2019 at a site on the western bank of the Ölfus River in South Iceland. Data from six field measurements exist, i.e. from 2013, 2014, 2015, 2017, 2018, and 2019. The midpoints of the MASW survey profiles were in all cases positioned at approximately the same location (i.e., within a radius of 2 m). The orientation of all six survey profiles was the same. The soil at the site consists of a relatively homogeneous glaciofluvial volcanic sand and the groundwater level is close to ground surface (Green et al. 2012; Olafsdottir et al. 2015). The test configuration, including the number and type of receivers and the impact load source, was the same in all cases. During each field measurement, a statistical sample of dispersion curves was gathered, both by applying repeated shots for a fixed profile configuration, and by exploring different profile lengths and/or different source locations. The data processing and analysis was conducted in the same way as described in the preceding sections. Based on a-priori information on the characteristics of the tested site, a normally dispersive parameterization was specified. To aid comparison of the V_S-profiles obtained by inverting the different experimental curves, the same initial layering parameterization (i.e., number of layers) was assumed in all cases. The mass density profile was determined based on values reported by Green et al. (2012).

Figure 12a presents a comparison of the six composite experimental dispersion curves. The upper and lower boundary curves, illustrated in Fig. 12a, correspond to plus-minus one standard deviation of the mean curve. The variability of the mean experimental curves is evaluated in terms of COV as a function of wavelength in Fig. 12b. Overall, the experimental dispersion curves are quite comparable, characterized by an average COV value of 3.2% over the

wavelength range of 1.6–45 m, although larger COV values are observed at the shortest wavelengths. It should, however, be noted that the sample size used to compute the COV statistic is very small (i.e., between two and six curves/profiles depending on wavelength/depth). Shear wave velocity profiles, obtained by inversion of each experimental dataset, are shown in Fig. 12c and the variability of the inverted V_S values is quantified using the COV statistic in Fig. 12d. The results provided in Figs. 12cd indicate that the agreement between the six measurements is, in general, adequate, illustrating the consistency of the methodology and the software that has been developed. The larger COV values at shallow depth (Fig. 12d) are attributed to the increased variability in interpreted experimental Rayleigh wave velocity values at short wavelengths, and may further relate to, e.g., changes in groundwater level positions and surficial soil compaction between measurements.

6. Conclusions

MASWaves is a new open-source software for acquiring, processing and analysing MASW data. The primary objective of this work was to assess the reliability, accuracy and repeatability of results obtained with the MASWaves software for the purpose of civil engineering site characterization. Results obtained with the new software were compared with results of in-situ and laboratory measurements conducted at four benchmark test sites in Norway, characterized by silt, soft clay, sand and quick clay, respectively. The repeatability of the analysis was confirmed with repeated measurements at a volcanic sand site in South Iceland over a seven-year period.

The results of the study indicate that the V_S-profiles obtained by using MASWaves are for all practical purposes very comparable to profiles obtained by application of invasive techniques (i.e., SCPT and SDMT), thus verifying the performance of the data acquisition, dispersion and inversion analysis modules. The MASWaves V_S-profiles further compare well with results of MASW measurements conducted in independent field-testing campaigns by use of different data acquisition and analysis tools, as well as results of laboratory tests carried out on samples gathered at the Norwegian research sites.

At each site, emphasis was on placing the MASW measurement profile as close as possible to relevant previous work, in particular at the Halden (silt) and Øysand (sand) sites where significant lateral variabilities in soil properties and/or soil stratigraphy had been identified in previous studies. However, some differences may be observed as the invasive tests are point measurements, whilst the MASW shear wave velocity profiles average the soil properties over a larger area. Furthermore, some variability is observed in the inverted MASW V_S-profiles, both relating to the data processing/dispersion analysis, and interpretation ambiguities that arise during the inversion analysis, for instance, due to the non-uniqueness of the Rayleigh wave dispersion curve inversion and the choice of layering parameterization. Environmental factors, such as changes in groundwater level positions and surficial soil compaction between repeated measurements, may further contribute to the observed difference.

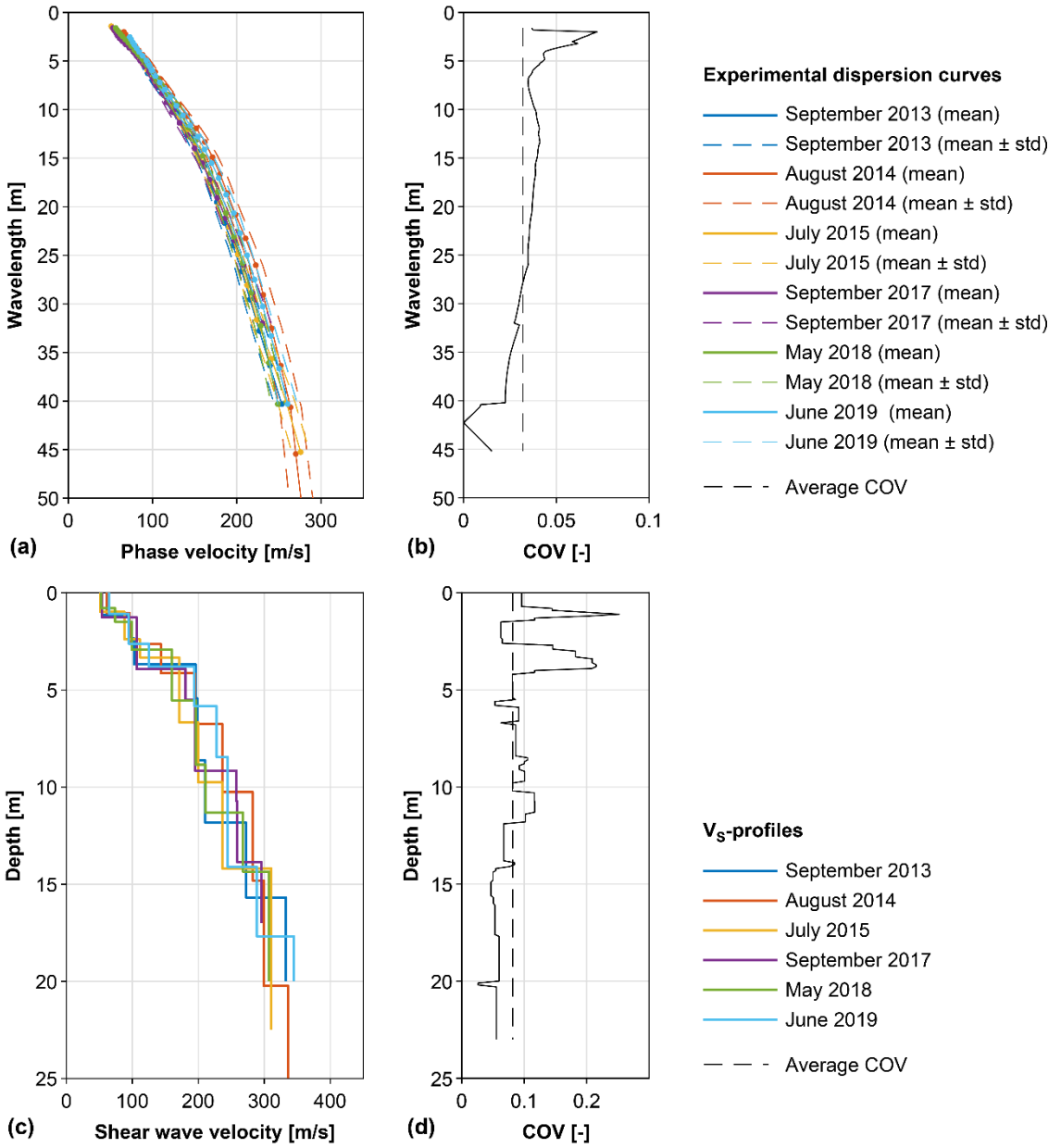

***Figure 12**: Comparison of experimental dispersion curves acquired in six separate field tests between 2013 and 2019. **(a)** Experimental dispersion curves. **(b)** Variability expressed in terms of COV. Comparison of shear wave velocity profiles from repeated tests. The trial shear wave velocity profiles consisted of eight layers. **(c)** Shear wave velocity profiles. **(d)** Variability expressed in terms of COV.*

Acknowledgements

The project is supported by grants from the University of Iceland Research Fund, the Icelandic Road and Coastal Administration and the Energy Research Fund of the National Power Company of Iceland.

The authors would like to thank the organizers of the NGTS project (www.geotestsite.no) for assistance prior to and during the in-situ measurements at the Norwegian research sites, as well as for providing access to results of geotechnical, geophysical and laboratory measurements conducted at the sites.

References

Bazin, S., Anschütz, H., Sauvin, G., Helle, T. E., Gribben, S., Donohue, S. & Long, M. (2016). Geophysical characterisation of marine and quick clay sites: field and laboratory tests. *Proceedings of the 5th International Conference on Geotechnical and Geophysical Site Characterisation*, Queensland, Australia, Vol. 2, pp. 831–836.

Blaker, Ø., Carroll, R., L'Heureux, J.-S. & Klug, M. (2016). Characterisation of Halden silt. *Proceedings of the 5th International Conference on Geotechnical and Geophysical Site Characterisation*, Queensland, Australia, Vol. 2, pp. 975–980.

Blaker, Ø., Carroll, R., Paniagua, P., DeGroot, D. J. & L'Heureux, J.-S. (2019). Halden research site: geotechnical characterization of a post glacial silt. *AIMS Geosciences* **5**, No. 2, 184–234. http://dx.doi.org/10.3934/geosci.2019.2.184.

Buchen, P. W. & Ben-Hador, R. (1996). Free-mode surface-wave computations. *Geophysical Journal International* **124**, No. 3, 869–887. http://dx.doi.org/10.1111/j.1365-246X.1996.tb05642.x.

Cox, B. R. & Teague, D. P. (2016). Layering ratios: a systematic approach to the inversion of surface wave data in the absence of a priori information. *Geophysical Journal International* **207**, No. 1, 422–438. http://dx.doi.org/10.1093/gji/ggw282.

Di Giulio, G., Savvaidis, A., Ohrnberger, M., Wathelet, M., Cornou, C., Knapmeyer-Endrun, B., Renalier, F., Theodoulidis, N. & Bard, P.-Y. (2012). Exploring the model space and ranking a best class of models in surface-wave dispersion inversion: Application at European strong-motion sites. *Geophysics* **77**, No. 3, B147–B166. http://dx.doi.org/10.1190/geo2011-0116.1.

de Lucena, R. F. & Taioli, F. (2014). Rayleigh wave modeling: A study of dispersion curve sensitivity and methodology for calculating an initial model to be included in an inversion algorithm. *Journal of Applied Geophysics* **108**, 140–151. http://dx.doi.org/10.1016/j.jappgeo.2014.07.007.

Efron, B. (1979). Bootstrap methods: another look at the jackknife. *The Annals of Statistics* **7**, No. 1, 1–26. http://dx.doi.org/10.1214/aos/1176344552.

Efron, B. & Tibshirani, R. J. (1993). *An introduction to the bootstrap*. New York, NY: Chapman & Hall.

Eidsmoen, T., Gillespie, J., Lunne, T. & Campanella, R. G. (1985). *Tests with the UBC seismic cone at three Norwegian sites. NGI report No. 59040-1*. Oslo: Norwegian Geotechnical Institute.

Foti, S., Lai, C. G., Rix, G. J. & Strobbia, C. (2015). *Surface wave methods for near-surface site characterization*. Boca Raton, FL: CRC Press, Taylor & Francis Group.

Foti, S., Hollender, F., Garofalo, F., Albarello, D., Asten, M., Bard, P.-Y., Comina, C., Cornou, C., Cox, B., Di Giulio, G., Forbriger, T., Hayashi, K., Lunedei, E., Martin, A., Mercerat, D., Ohrnberger, M., Poggi, V., Renalier, F., Sicilia, D. & Socco, V. (2018). Guidelines for the good practice of surface wave analysis: a product of the InterPACIFIC project. *Bulletin of*

Earthquake Engineering **16**, No. 6, 2367–2420. http://dx.doi.org/10.1007/s10518-017-0206-7.

Gabriels, P., Snieder, R. & Nolet, G. (1987). In situ measurements of shear-wave velocity in sediments with higher-mode Rayleigh waves. *Geophysical Prospecting* **35**, No. 2, 187–196. http://dx.doi.org/10.1111/j.1365-2478.1987.tb00812.x.

Garofalo, F., Foti, S., Hollender, F., Bard, P.-Y., Cornou, C., Cox, B. R., Ohrnberger, M., Sicilia, D., Asten, M., Di Giulio, G., Forbriger, T., Guillier, B., Hayashi, K., Martin, A., Matsushima, S., Mercerat, D., Poggi, V. & Yamanaka, H. (2016a). InterPACIFIC project: Comparison of invasive and non-invasive methods for seismic site characterization. Part I: Intra-comparison of surface wave methods. *Soil Dynamics and Earthquake Engineering* **82**, 222–240. http://dx.doi.org/10.1016/j.soildyn.2015.12.010.

Garofalo, F., Foti, S., Hollender, F., Bard, P.-Y., Cornou, C., Cox, B. R., Dechamp, A., Ohrnberger, M., Perron, V., Sicilia, D., Teague, D. & Vergniault, C. (2016b). InterPACIFIC project: Comparison of invasive and non-invasive methods for seismic site characterization. Part II: Inter-comparison between surface-wave and borehole methods. *Soil Dynamics and Earthquake Engineering* **82**, 241–254. http://dx.doi.org/10.1016/j.soildyn.2015.12.009.

Green, R. A., Halldorsson, B., Kurtulus, A., Steinarsson, H. & Erlendsson O. (2012). A unique liquefaction case study from the 29 May 2008, M_w6.3 Olfus earthquake, Southwest Iceland. *Proceedings of the 15th World Conference on Earthquake Engineering*, Lisbon.

Gundersen, A. S., Quinteros, S., L'Heureux, J.-S. & Lunne, T. (2018). Soil classification of NGTS sand site (Øysand, Norway) based on CPTU, DMT and laboratory results. *Proceedings of the 4th International Symposium on Cone Penetration Testing*, Delft, pp. 323–328.

Kramer, S. L. (2014). *Geotechnical earthquake engineering*. Harlow: Pearson Education Limited.

Lai, C. G., Foti, S. & Rix, G. J. (2005). Propagation of data uncertainty in surface wave inversion. *Journal of Environmental & Engineering Geophysics* **10**, No. 2, 219–228. http://dx.doi.org/10.2113/JEEG10.2.219.

Landon, M. M. (2007). *Development of a non-destructive sample quality assessment method for soft clays*. PhD Thesis, University of Massachusetts Amherst, Amherst, MA.

L'Heureux, J.-S., Emdal, A. & Lindgård, A. (2019a). Geotechnical characterization of the Tiller-Flotten quick clay site in Norway. *Proceedings of the 17th European Conference on Soil Mechanics and Geotechnical Engineering, Reykjavik*. http://dx.doi.org/10.32075/17ECSMGE-2019-0314.

L'Heureux, J.-S., Lindgård, A. & Emdal, A. (2019b). The Tiller-Flotten research site: Geotechnical characterization of a very sensitive clay deposit. *AIMS Geosciences* **5**, No. 4, 831–867. http://dx.doi.org/10.3934/geosci.2019.4.831.

L'Heureux, J.-S. & Long, M. (2017). Relationship between shear-wave velocity and geotechnical parameters for Norwegian clays. *Journal of Geotechnical and*

Geoenvironmental Engineering **143**, No. 6, 04017013. https://doi.org/10.1061/(ASCE)GT.1943-5606.0001645.

L'Heureux, J.-S., Lunne, T., Lacasse, S., Carroll, R., Strandvik, S. O., Ozkul, Z., Instanes, A., Sinitsyn, A., Degago, S. & Nordal, S. (2017). Norway's National GeoTest Site Research Infrastructure (NGTS). *Proceedings of the 19th International Conference on Soil Mechanics and Geotechnical Engineering*, Seoul, pp. 611–614.

Long, M. & Donohue, S. (2007). In situ shear wave velocity from multichannel analysis of surface waves (MASW) tests at eight Norwegian research sites. *Canadian Geotechnical Journal* **44**, No. 5, 533–544. http://dx.doi.org/10.1139/t07-013.

Lunne, T., Long, M. & Forsberg, C. F. (2003). Characterisation and engineering properties of Onsøy clay. *Characterisation and Engineering Properties of Natural Soils: Proceedings of the International Workshop*, Singapore, Vol. 1, 395–428.

Nazarian, S., Stokoe II, K. H. & Hudson, W. R. (1983). Use of spectral analysis of surface waves method for determination of moduli and thicknesses of pavement systems. *Transportation Research Record* **930**, 38–45.

Nazarian S. & Stokoe II, K. H. (1985). *In situ determination of elastic moduli of pavement systems by spectral-analysis-of-surface-waves method: practical aspects*. FHWA, Report No. FHWA/TX-86/13+368-1F.

Nazarian S. & Stokoe II, K. H. (1986). *In situ determination of elastic moduli of pavement systems by spectral-analysis-of-surface-waves method (theoretical aspects)*. FHWA, Report No. FHWA/TX-87/46+437-2.

NGI. (2018). *Field and laboratory test results Halden. Norwegian GeoTest Sites (NGTS). Factual report 20160154-04-R*. Oslo: Norwegian Geotechnical Institute.

Marchetti, S., Monaco, P., Totani, G. & Marchetti, D. (2008). In situ tests by seismic dilatometer (SDMT). In *From Research to Practice in Geotechnical Engineering* (eds. J. E. Laier, D. K. Crapps and M. H. Hussein), pp. 292–311. Reston, VA: American Society of Civil Engineers. http://dx.doi.org/10.1061/40962(325)7.

Martin, G. K. & Mayne, P. W. (1997). Seismic flat dilatometer tests in Connecticut valley varved clay. *Geotechnical Testing Journal* **20**, No. 3, 357–361. http://dx.doi.org/10.1520/GTJ19970011.

Olafsdottir, E. A., Erlingsson, S. & Bessason, B. (2018a). Tool for analysis of multichannel analysis of surface waves (MASW) field data and evaluation of shear wave velocity profiles of soils. *Canadian Geotechnical Journal* **55**, No. 2, 217–233. http://dx.doi.org/10.1139/cgj-2016-0302.

Olafsdottir, E. A., Bessason, B. & Erlingsson, S. (2015). MASW for assessing liquefaction of loose sites. *Proceedings of the 16th European Conference on Soil Mechanics and Geotechnical Engineering*, Edinburgh, Vol. 5, pp. 2431–2436. http://dx.doi.org/10.1680/ecsmge.60678.

Olafsdottir, E. A., Bessason, B. & Erlingsson, S. (2019a). Application of MASW in the South Iceland Seismic Zone. *Proceedings of the International Conference on Earthquake Engineering and Structural Dynamics, Geotechnical, Geological and Earthquake Engineering, Vol. 47*, Reykjavik, Iceland, pp. 53–66. http://dx.doi.org/10.1007/978-3-319-78187-7_5.

Olafsdottir, E. A., Bessason, B. & Erlingsson, S. (2018b). Combination of dispersion curves from MASW measurements. *Soil Dynamics and Earthquake Engineering* **113**, 473–487. http://dx.doi.org/10.1016/j.soildyn.2018.05.025.

Olafsdottir, E. A., Bessason, B., Erlingsson, S., L'Heureux, J.-S. & Bazin, S. (2019b). Benchmarking of an open-source MASW software using data from three Norwegian GeoTest Sites. *Proceedings of the 17th European Conference on Soil Mechanics and Geotechnical Engineering*, Reykjavik, Iceland. http://dx.doi.org/10.32075/17ECSMGE-2019-0772.

Olafsdottir, E. A., Erlingsson, S. & Bessason, B. (2019c – under review) Shear wave velocity profiles from MASW inversion analysis using a simple Monte Carlo search technique for geotechnical engineering applications. Manuscript resubmitted to *Soil Dynamics and Earthquake Engineering*.

Park, C. B., Miller, R. D. & Xia, J. (1998). Imaging dispersion curves of surface waves on multi-channel record. *SEG Technical Program Expanded Abstracts*, New Orleans, LA, pp. 1377–1380. http://dx.doi.org/10.1190/1.1820161.

Park, C. B., Miller, R. D. & Xia, J. (1999). Multichannel analysis of surface waves. *Geophysics* **64**, No. 3, 800–808. http://dx.doi.org/10.1190/1.1444590.

Quinteros, S., Gundersen A., L'Heureux J.-S., Carraro, J. A. H. & Jardine, R. (2019). Øysand research site: Geotechnical characterisation of deltaic sandy-silty soils. *AIMS Geosciences* **5**, No. 4, 750–783. http://dx.doi.org/10.3934/geosci.2019.4.750.

Robertson, P. K., Campanella, R. G., Gillespie, D. & Rice, A. (1986). Seismic CPT to measure in situ shear wave velocity. *Journal of Geotechnical Engineering* **112**, No. 8, 791–803. http://dx.doi.org/10.1061/(ASCE)0733-9410(1986)112:8(791).

Socco, L. V., Foti, S. & Boiero, D. (2010). Surface-wave analysis for building near-surface velocity models – Established approaches and new perspectives. *Geophysics* **75**, No. 5, 75A83–75A102. http://dx.doi.org/10.1190/1.3479491.

Xia, J. (2014). Estimation of near-surface shear-wave velocities and quality factors using multichannel analysis of surface-wave methods. *Journal of Applied Geophysics* **103**, 140–151. http://dx.doi.org/10.1016/j.jappgeo.2014.01.016.

Xia, J., Miller, R. D. & Park, C. B. (1999). Estimation of near-surface shear-wave velocity by inversion of Rayleigh waves. *Geophysics* **64**, No. 3, 691–700. http://dx.doi.org/10.1190/1.1444578.

Paper V

Open software for analysis of MASW data

Elín Ásta Ólafsdóttir, Sigurður Erlingsson & Bjarni Bessason

Ólafsdóttir, E.Á., Erlingsson, S. & Bessason, B. (2018). Open software for analysis of MASW data. In *Proceedings of the 16th European Conference on Earthquake Engineering*, 18–21 June 2018, Thessaloniki, Greece. (Paper no. 11168).

16TH EUROPEAN CONFERENCE ON EARTHQUAKE ENGINEERING THESSALONIKI 18 - 21 JUNE 2018

OPEN SOFTWARE FOR ANALYSIS OF MASW DATA

Elin Asta OLAFSDOTTIR[1], Sigurdur ERLINGSSON[2], Bjarni BESSASON[3]

ABSTRACT

Multichannel Analysis of Surface Waves (MASW) is a non-invasive, fast, and low-cost method for evaluation of near-surface shear wave velocity profiles. This paper presents a revised version of an open-source software, MASWaves, for analyzing multichannel surface wave records using the MASW method. The software consists of three parts: a tool for dispersion analysis (MASWaves Dispersion), a tool to add up dispersion curves obtained based on multiple surface wave registrations (MASWaves Combination), and an inversion analysis tool (MASWaves Inversion). The dispersion and inversion analysis tools are validated by comparison with results obtained by other software packages and results presented in the literature. Results of MASW field tests conducted at two locations in Iceland are presented in order to demonstrate the performance of the software. The field tests illustrate how the maximum investigation depth of the survey and its resolution at shallow depth can be enhanced by combining dispersion data gathered by receiver spreads of different lengths. Moreover, at one site, results of existing Spectral Analysis of Surface Waves (SASW) and Cone Penetration Test (CPT) measurements are compared with results obtained by MASWaves.

Keywords: Multichannel Analysis of Surface Waves (MASW); dispersion analysis; inversion analysis; open-source software; shear wave velocity

1. INTRODUCTION

The shear wave velocity (V_S) is an important parameter for site characterization of natural soil sites and man-made fillings. The small-strain shear modulus (G_0) is directly proportional to the square of the shear wave velocity. Furthermore, the shear wave velocity is vital for assessing soil amplifications, and for seismic site classification on the basis of widely used structural design standards (e.g., CEN 2004). Multichannel Analysis of Surface Waves (MASW) is seismic exploration method for evaluation of near-surface V_S profiles. The method is based on analysis of the dispersion properties of horizontally propagating Rayleigh waves acquired by a line of receivers. MASW is a non-invasive, fast method that involves low-cost and portable equipment. Furthermore, the method can be applied at a wide variety of sites, ranging from clay and silt sites to coarse-grained gravelly sites and soft rock, hence, including locations where, e.g., penetration tests are difficult to carry out.

This paper presents a revised version of MASWaves, an open-source Matlab-based tool for analyzing multichannel surface wave records using the MASW method (Olafsdottir et al. 2018b). A new algorithm for combining dispersion curves obtained based on multiple surface wave registrations has been added to the original version of MASWaves. Results of field tests carried out at two locations in Iceland are presented to demonstrate the performance of the software. At one site, results of existing Spectral Analysis of Surface Waves (SASW) and Cone Penetration Test (CPT) measurements are compared with the results obtained by MASWaves. The software can be downloaded at masw.hi.is, along with user guide and sample data.

[1]Ph.D. Cand., Faculty of Civil and Environmental Eng., University of Iceland, Reykjavik, Iceland, eao4@hi.is
[2]Prof., Faculty of Civil and Environmental Eng., University of Iceland, Reykjavik, Iceland; Pavement Technology, The National Road and Transport Research Institute, Linköping, Sweden, sigger@hi.is
[3]Prof., Faculty of Civil and Environmental Eng., University of Iceland, Reykjavik, Iceland, bb@hi.is

2. MULTICHANNEL ANALYSIS OF SURFACE WAVES

An application of the MASW method is divided into three main steps:

1) In-situ measurements to acquire multichannel surface wave records.
2) Evaluation of the experimental Rayleigh wave dispersion curve based on the recorded surface waves (dispersion analysis).
3) Assessment of the shear wave velocity profile by inversion of the experimental dispersion curve (inversion analysis) by assuming a layered, semi-infinite soil model.

The resolution of MASW diminishes with increasing depth (Foti et al. 2015); while the analysis can resolve relatively thin layers and modest V_S variations close to the surface, only major variations can be detected at greater depths. Furthermore, the prospective investigation depth range is constrained by the acquired fundamental mode dispersion curve wavelengths (Garofalo et al. 2016). The longer the maximum wavelength (λ_{max}), the greater the maximum investigated depth (z_{max}), and the shorter the minimum wavelength (λ_{min}), the better the resolution at shallow depth. A simple, widely accepted, rule-of-thumb for interpretation of fundamental mode dispersion curves (Park et al. 1999; Garofalo et al. 2016; Cox and Teague 2016) is to limit the maximum depth of the V_S profile as

$$z_{max} \leq \gamma \lambda_{max}, \quad \frac{1}{3} \leq \gamma \leq \frac{1}{2} \tag{1}$$

and, similarly, to limit the thickness of the top-most layer (h_1) as

$$h_1 \geq \zeta \lambda_{min}, \quad \frac{1}{3} \leq \zeta \leq \frac{1}{2} \tag{2}$$

When MASW surveys are carried out, the focus is commonly on achieving a particular investigation depth, and, therefore, on obtaining a certain value of λ_{max}. However, as the top-most soil layers have an influence on the entire dispersion curve, information about the short wavelength wave components is also of importance to constrain the inversion analysis, and, hence, increase the accuracy of the resulting V_S profile (Foti et al. 2015).

It is commonly recognized that the set-up of the measurement profile, e.g., the length of the receiver spread and the source offset, affects the acquired dispersion data (e.g., Dikmen et al. 2010; Ivanov et al. 2008; Olafsdottir et al. 2016; Park and Carnevale 2010). The observed effects suggest that a wider range of fundamental mode dispersion curve wavelengths, and, consequently, an increased investigation depth range, can be obtained by combination of data acquired by measurement profiles of different lengths (Ivanov et al. 2008; Olafsdottir et al. 2018a). Furthermore, the acquired multichannel surface wave records are affected by various, correlated and uncorrelated, noise sources. Hence, when numerous records are gathered at a single station, some variability among the resulting dispersion curve estimates will be observed. Multiple records thus result in multiple curves, which combined may improve the estimation of the actual dispersion characteristic of the test site.

2.1 Computational procedure

The revised version of MASWaves consists of three parts. First, a dispersion analysis tool (MASWaves Dispersion) to extract an experimental dispersion curve based on a single multichannel record. Second, a tool to add up dispersion curves obtained based on multiple surface wave registrations (MASWaves Combination). Third, an inversion analysis tool (MASWaves Inversion) to evaluate the shear wave velocity profile of the test site by backcalculation of the combined dispersion curve. An overview of the MASW method, as it is applied in this work, is provided in Figure 1. In this paper, only the fundamental mode of Rayleigh wave propagation is considered. Olafsdottir et al. (2018a, 2018b) provide a more detailed description of the computational procedures behind MASWaves Dispersion and MASWaves Inversion, and the method used in MASWaves Combination for evaluation of composite dispersion curves.

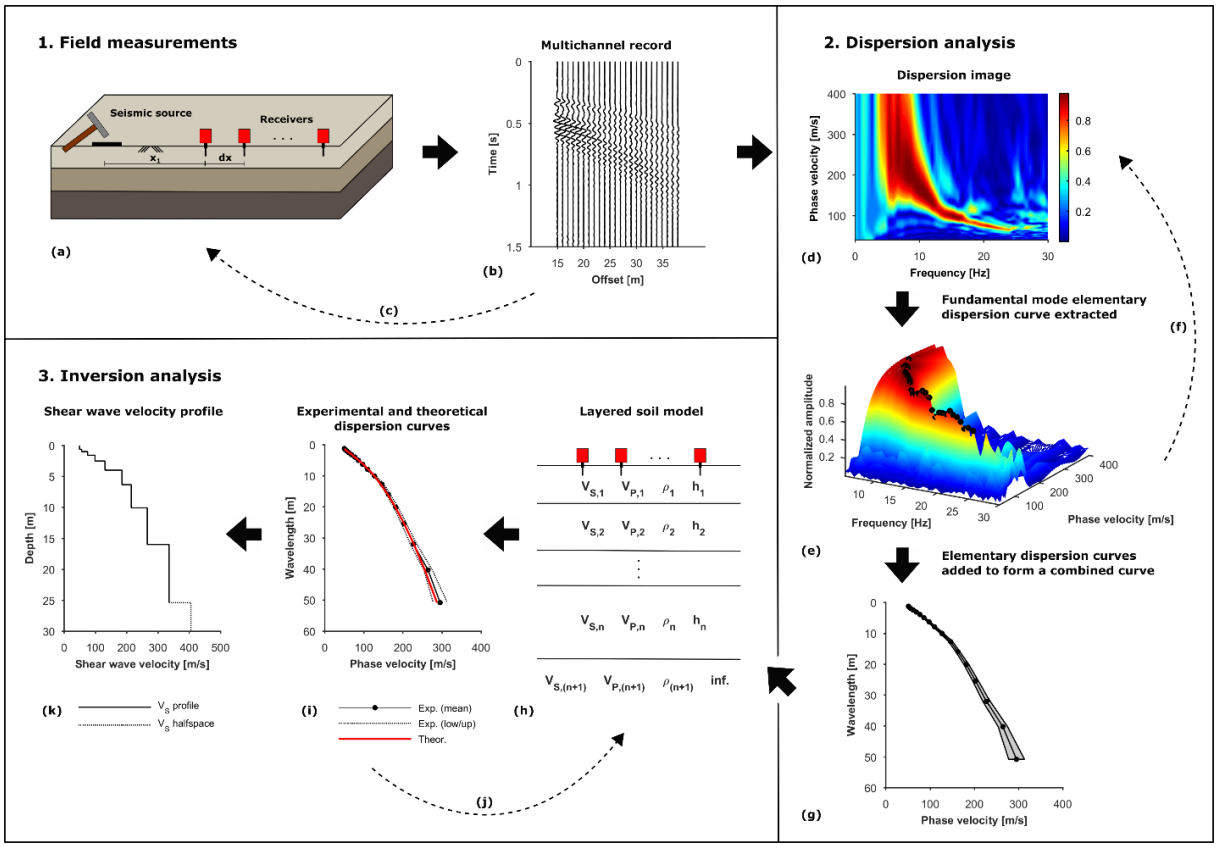

Figure 1. Application of the MASW method.

For field measurements, N low frequency geophones are lined up on the surface of the test site with equal spacing dx (Figure 1a). Hence, the length of the receiver spread is $L = (N-1)dx$. A wave is generated using an impulsive source that is applied at a distance x_1 from one end of the receiver spread and the wave propagation is recorded (Figure 1b). The data acquisition procedure is repeated several times using different measurement profile set-ups (i.e. with different values of dx and/or x_1) while keeping the midpoint of the receiver spread fixed (Figure 1c).

The analysis of the multichannel time series is carried out by using MASWaves Dispersion. A dispersion image is obtained based on each acquired record (Figure 1d) by the phase shift method (Park et al. 1998). The spectral high-amplitude bands display the dispersion characteristics of all types of waves contained in the recorded data, and are used to identify the fundamental mode of the Rayleigh wave propagation (Figure 1e). A dispersion curve obtained based on a single multichannel record is here referred to as an elementary dispersion curve. Each acquired record is processed separately (Figure 1f) and the resulting elementary curves combined within 1/3 octave wavelength intervals (Figure 1g) using MASWaves Combination. Within each interval, the identified dispersion curve phase velocity values are added up and their arithmetic mean used as a point estimate of the phase velocity of the Rayleigh wave components belonging to the given wavelength range. Alternatively, the elementary curves can be added up within intervals of different widths (e.g., 1/4 or 1/5 octave wavelength) as discussed by Olafsdottir et al. (2018a). The spread of the dispersion curve data points is represented by the standard deviation of the phase velocity values within each interval.

For inversion of the combined mean dispersion curve using MASWaves Inversion, a semi-infinite layered soil model for the test site is suggested. The thickness of the top-most soil layer and the top of the half-space are recommended to coincide with the approximate investigation depth ranges described by Equations 1 and 2, as well as any previous knowledge of the test site. The parameters needed to describe the properties of each layer are shear wave (S-wave) velocity, compressional wave (P-wave) velocity (or Poisson's ratio), mass density, and layer thickness (Figure 1h). A theoretical dispersion

curve is computed by the stiffness matrix method (Kausel and Roësset 1981) based on the assumed soil model and compared to the experimental curve (Figure 1i). Subsequently, the model parameters are updated manually and the computations repeated until the theoretical curve is sufficiently close to the experimental curve (Figure 1j). The V_S profile and the layer structure that result in an acceptable fit, and are believed to realistically represent the characteristics of the test site, are taken as the results of the survey (Figure 1k). Upper and lower boundary V_S profiles can be obtained by inverting the upper and lower boundary (mean ± standard deviation) combined experimental dispersion curves in a similar way.

2.1.1 Validation of the dispersion analysis procedure

For verification of the dispersion analysis procedure implemented in MASWaves, results obtained by MASWaves Dispersion were compared with results obtained by the Linear F-K for active experiments toolbox of the Geopsy software package [geopsy.org]. The comparison is provided in the form of dispersion images and extracted fundamental and higher mode dispersion curves. In this section, surface wave data acquired at a test site in north-western Slovakia, near the city of Žilina, is used for comparison purposes (Figure 2). Olafsdottir et al. (2018b) provide further examples, using data from other locations.

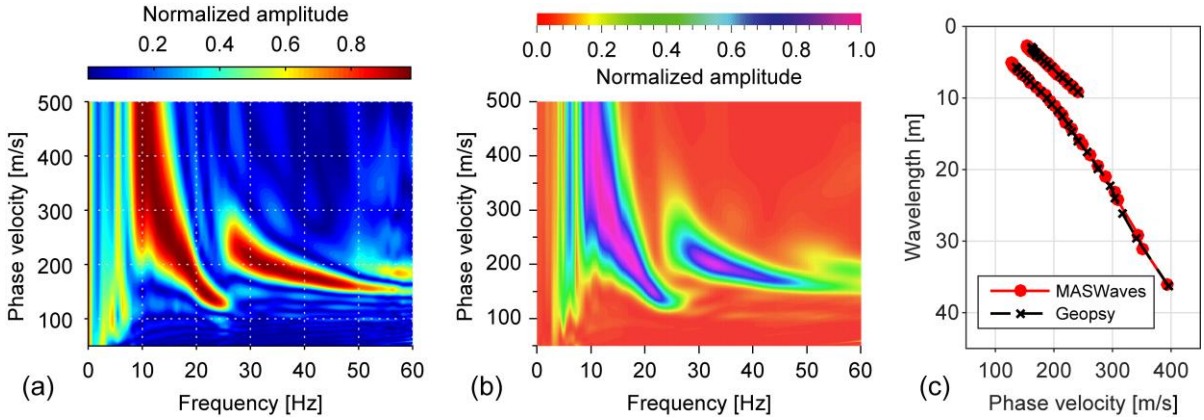

Figure 2. Dispersion images obtained by (a) MASWaves and (b) Geopsy. (c) Comparison of fundamental and higher mode dispersion curves extracted based on the spectra shown in figures (a) and (b).

The dispersion images obtained by the two software packages (Figures 2a and 2b) present nearly identical dispersion characteristics. The fundamental mode dominated the surface wave signal at frequencies in the approximate range of 10−25 Hz. At higher frequencies, however, an overtone was dominant. Likewise, the fundamental and higher mode dispersion curves, that were identified based on the two dispersion images, agreed very well (Figure 2c). Comparable results have been obtained based on records acquired at other test sites, thus, further confirming the precision of MASWaves Dispersion and its ability to identify fundamental and higher mode experimental dispersion curves.

2.1.2 Validation of the theoretical dispersion curve computations

For confirmation of the ability of MASWaves Inversion to compute theoretical fundamental and higher mode dispersion curves, as well as to comply with complex layering, the program was tested on three four-layer modes (Table 1), previously used by Tokimatsu (1997) for generation of synthetic surface wave data. The test models are referred to as profiles 1, 2, and 3, respectively. In profile 1, the shear wave velocity (stiffness) increases with increasing depth. The stiffness of the soil layers varies more irregularly in profiles 2 and 3. A stiff surface layer characterizes profile 2, whereas a stiff layer is located between two softer layers in profile 3. Hence, for profiles 2 and 3, the higher modes play a more significant role in the Rayleigh wave propagation.

Using MASWaves Inversion, the theoretical fundamental and first mode dispersion curves were computed for frequencies in the range of 3−70 Hz. The comparison of the dispersion curves obtained

by MASWaves and those presented by Tokimatsu (1997) is illustrated in Figure 3. The dispersion curves obtained by MASWaves are indicated by circles, whereas the curves obtained by Tokimatsu (1997) are shown with black lines. In all three cases, the agreement between the two sets dispersion curves was good. Olafsdottir et al. (2018b) further verify the theoretical dispersion curve computations with comparison with results obtained by the software WinSASW.

Table 1. Test profiles used for validation of the theoretical dispersion curve computations.

Layer	S-wave velocity [m/s]			P-wave velocity [m/s]	Density [kg/m^3]	Thickness [m]
	Profile 1	Profile 2	Profile 3			
1	80	180	80	360	1800	2.0
2	120	120	180	1000	1800	4.0
3	180	180	120	1400	1800	8.0
4	360	360	360	1400	1800	(Half-space)

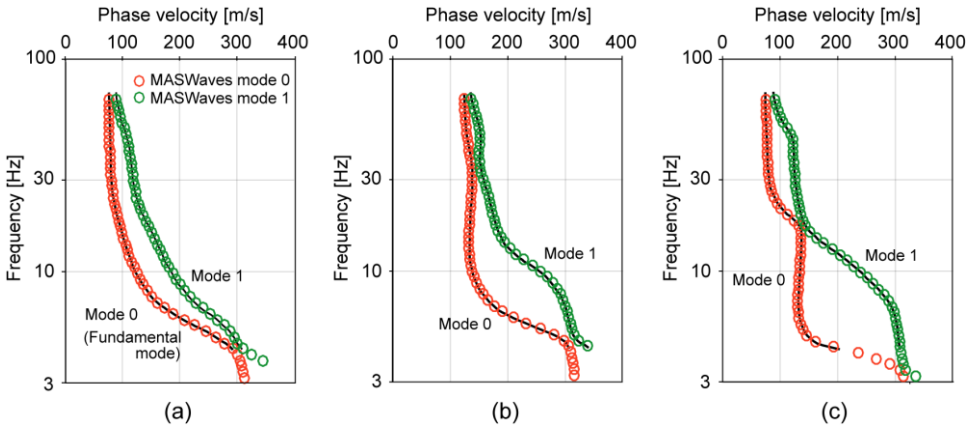

Figure 3. Comparison of theoretical fundamental and first mode dispersion curves obtained by MASWaves and presented by Tokimatsu (1997). (a) Profile 1. (b) Profile 2. (c) Profile 3.

3. FIELD MEASUREMENTS

MASW field measurements were conducted at two locations in Iceland in 2014 and 2015; at the Akureyri airport in north Iceland and close to the Landey harbour in south Iceland (see Figure 4). The Landey area mainly consists of uniformly graded dark basalt sand, whereas the soil at the Akureyri airport test site is siltier (Table 2).

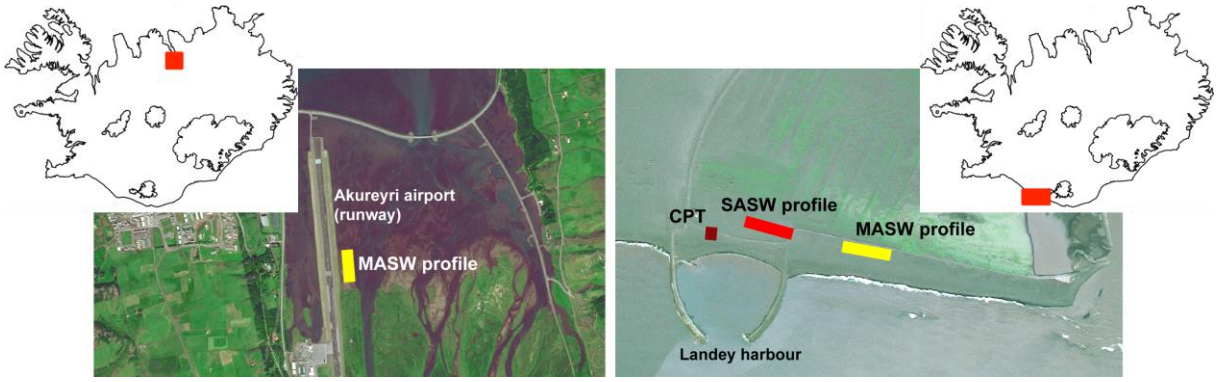

Figure 4. MASW test sites (left) at the Akureyri airport and (right) close to the Landey harbour.

At both test sites, surface wave records were collected using a linear array of 24 vertical geophones with a natural frequency of 4.5 Hz and a 6.3 kg sledgehammer as an impact source. Two measurement profiles with the same midpoint but varying receiver spacing (dx) were tested, i.e. dx = 0.5 m and dx = 2.0 m, and for each profile, the distance from the impact point load to the first receiver (x_1) was changed three or four times. For each combination of dx and x_1, six surface wave records (where each record consisted of 24 time series) were acquired. A summary of the main parameters related to the field measurements is provided in Table 2.

Table 2. Overview of site characteristics and test configuration at the Akureyri and Landey test sites.

Site characteristics			**Akureyri airport**	**Landey harbour**
Soil type			Holocene fluvial sand	Modern littoral sand
USCS classification			SM	SW
Groundwater table			At surface	At 4.0 m depth
Poisson's ratio	ν	[-]	-	0.35
Mass density	ρ	[kg/m^3]	-	2000
Saturated mass density	ρ_{sat}	[kg/m^3]	1800	1850
Field measurements				
Receiver spacing (source offsets)	dx (x_1)	[m]	0.5 (3.0/5.0/7.5) 2.0 (5.0/10.0/20.0/25.0)	0.5 (3.0/5.0/10.0) 2.0 (5.0/10.0/15.0/20.0)
No. measurements per combination of dx and x_1			6	6
Sampling rate	f_s	[Hz]	1000	1000
Recording time	T	[s]	2.4	1.2

3.1 Results of MASW measurements

Figure 5 shows dispersion images obtained at the Landey site with receiver spreads of length 11.5 m (with 0.5 m receiver spacing, Figure 5a) and 46.0 m (with 2.0 m receiver spacing, Figure 5b). The source offset was 5.0 m in both cases. Cross sections through the dispersion images at 20 Hz and 40 Hz are further shown in Figures 5c-f. The highest peaks correspond to the identified fundamental mode.

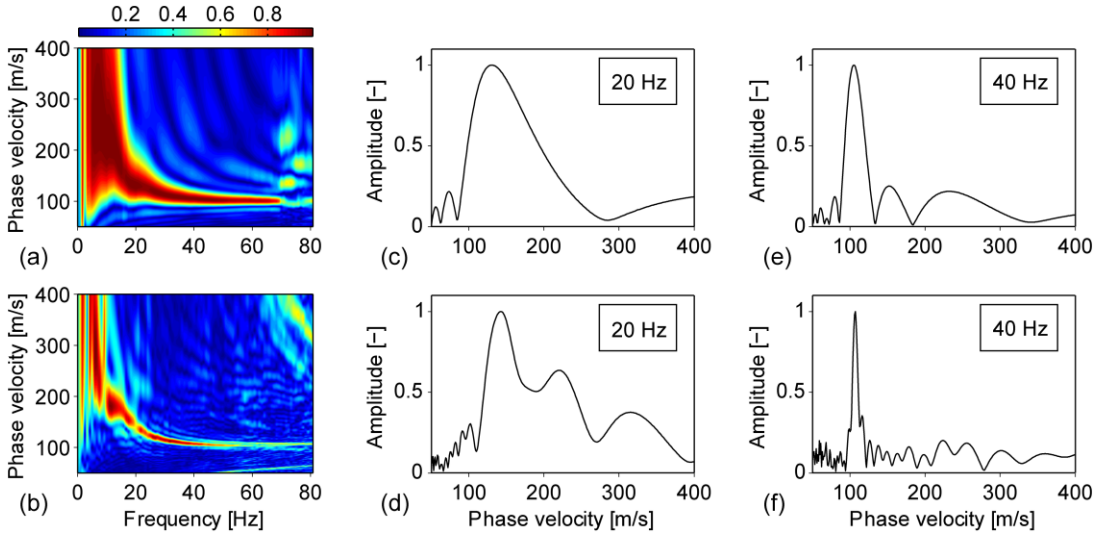

Figure 5. Dispersion images obtained with (a) 11.5 m and (b) 46.0 m receiver spreads and a source offset of 5.0 m. Cross sections through the dispersion images at (c,d) 20 Hz and (e,f) 40 Hz.

As shown in Figure 5, the length of the receiver spread had a considerable effect on the dispersion images that were obtained for the Landey site. In general, by lengthening the receiver spread, the fundamental mode high-amplitude peaks appeared sharper and better separation of overtones was observed. In general, the records acquired by the L = 46.0 m profile allowed extraction of the fundamental mode dispersion curve at lower frequencies than the records acquired by the L = 11.5 m profile. However, dispersion images obtained based on data acquired by the shorter receiver spread provided more information about the dispersion properties of the shorter wavelength (higher frequency) wave components that propagated through the top-most soil layers. The same observations were made based on the data acquired at the Akureyri site. This is further illustrated in Figure 6. These observations are in accordance with existing recommendations where the maximum investigation depth is suggested as directly related to the length of the receiver spread (Park and Carnevale 2010).

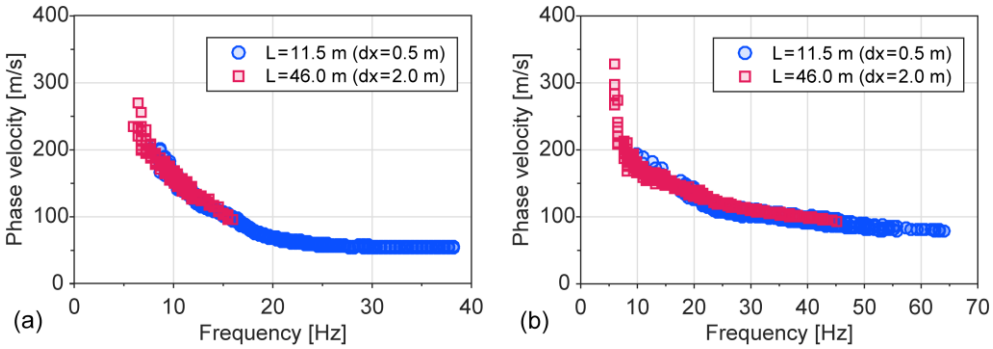

Figure 6. Fundamental mode dispersion curve estimates obtained by using receiver spreads of different lengths at (a) the Akureyri site and (b) the Landey site.

Figures 7a-c illustrate the computation of the combined dispersion curves for the two profiles (same midpoint) tested at the Akureyri site. The combined curves shown in Figures 7a and 7b were obtained by grouping data points from each set of elementary curves (i.e. 18 curves for the L = 11.5 m profile and 24 curves for the L = 46.0 m profile) together within 1/3 octave wavelength intervals. The mean phase velocity value for each interval was used as an estimate of the phase velocity of the Rayleigh wave components belonging to the given wavelength range. The upper and lower bound curves correspond to plus−minus one standard deviation (SD) of the mean curve, and, hence, provide a measure of the spread of the elementary curve data points within each interval. In general, the spread of the data points increased with increased wavelength. Furthermore, the number of points within a given interval decreased with increasing wavelength. The combined dispersion curves obtained by adding up the elementary dispersion data acquired by both profiles are shown in Figure 7c.

As indicated by Figure 6a, there was a considerable difference in the achieved combined dispersion curve wavelength ranges. The shorter profile provided combined curve wavelengths in the range of 1.3−25.4 m (Figure 7a) whereas the longer profile provided wavelengths in the range of 6.4−40.3 m (Figure 7b). Hence, by combining the 42 elementary dispersion curves acquired by both profiles, a wavelength range of 1.3−40.3 m was obtained (Figure 7c). Based on the ranges of wavelengths covered by the curves, the maximum depth of the shear wave velocity profile was estimated by Equation 1 (with $\gamma = 1/2$) as 12.7 m for the L = 11.5 m profile, and 20.2 m for the L = 46.0 m and L = 11.5 m/L = 46.0 m profiles. The minimum investigation depth, as obtained by Equation 2 (with $\zeta = 1/2$), was 0.6 m for the L = 11.5 m and L = 11.5 m/L = 46.0 m profiles, and 3.2 m for the L = 46.0 m profile.

For inversion of each combined mean curve, a layered soil model was suggested where the thickness of the top-most soil layer and the depth of the half-space top coincided with the approximate investigation depth range. To aid the comparison of the V_S profiles obtained based on the different experimental curves, the same layering was used in the three inversions, though with a reduced investigation depth for the L = 11.5 m profile and an increased first-layer thickness for the L = 46.0 m profile. The initial shear wave velocity value for each layer was obtained by mapping the points of the combined mean dispersion curves into approximate values of shear wave velocity (Park et al. 1999) and subsequently

discretizing the resulting pseudo-V_S profiles to match the previously assumed layering. The shear wave velocity values were updated during the inversion process, while the other parameters were kept unchanged. The half-space shear wave velocity was set equal to the shear wave velocity of the bottom-most finite thickness layer throughout the inversion. The misfit (ϵ) between the theoretical and experimental dispersion curves was evaluated as

$$\epsilon = \frac{1}{Q}\sum_{i=1}^{Q}\frac{\left(c_{e,i} - c_{t,i}\right)^{1/2}}{c_{e,i}} \cdot 100\% \quad (3)$$

where Q is the number of data points included in each curve, $c_{t,i}$ is the phase velocity of the i-th data point in the theoretical dispersion curve, and $c_{e,i}$ is the phase velocity of the i-th data point in the experimental curve. A convergence of the manual search procedure was defined as achieving a misfit value (Equation 3) of 2.5% or less. Furthermore, as both the Akureyri and Landey test sites are considered normally dispersive, profiles characterized by shear wave velocity reversals were not considered during the inversion process. The resulting V_S profiles for the Akureyri site are shown in Figures 7d-f (solid lines). In general, similar shear wave velocity profile estimates were obtained based on the three combined mean dispersion curves, though characterized by the different investigation depth ranges. The same was observed during inversion of the data acquired at the Landey site. The V_S profile obtained by inverting the combined experimental dispersion curve (with L = 11.5 m/L = 46.0 m) for the Landey site is shown in Figure 10b.

For inversion of the upper and lower bound combined dispersion curves, the V_S profile evaluated based on the corresponding mean curve was used as a starting profile for the trial-and-error search procedure. The V_S profiles obtained by inverting the upper and lower bound dispersion curves, respectively, are shown using dashed lines in Figures 7d-f. At wavelengths shorter than 20−25 m, the standard deviations of the combined mean dispersion curves are small (Figures 7a-c). Hence, the shear wave velocity estimates obtained based on the mean curves and the corresponding upper/lower bound curves were very consistent at shallow depth (Figures 7d-f). For deeper layers (longer wavelengths), the larger standard deviations lead to more differences among the shear wave velocity estimates.

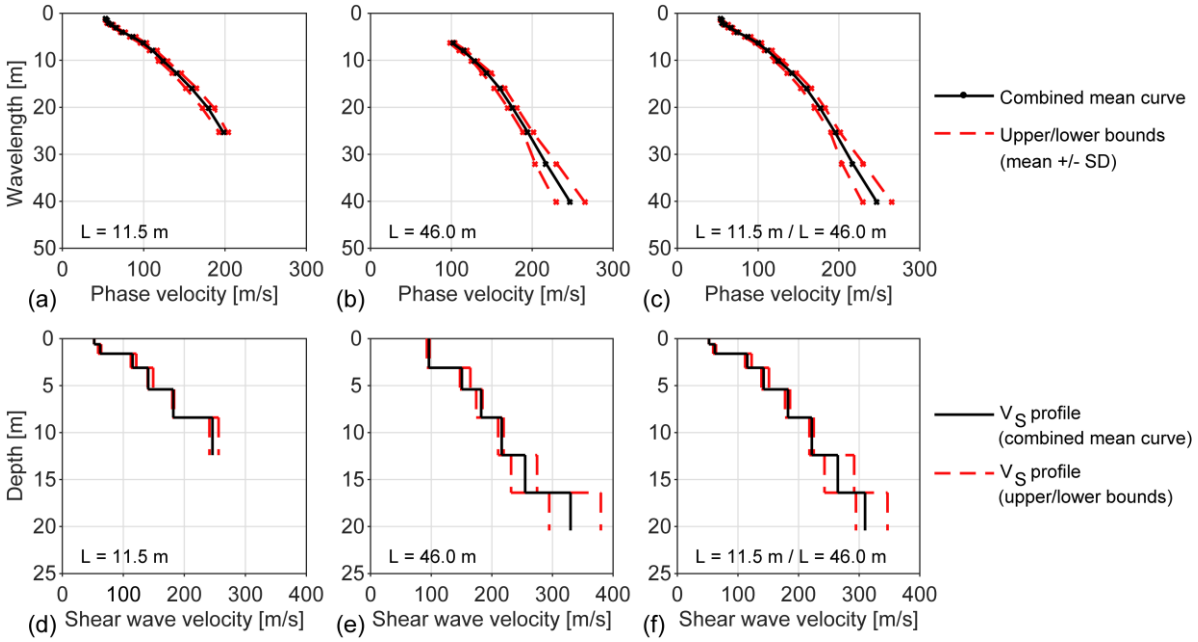

Figure 7. Combined dispersion curves for the (a) L = 11.5 m, (b) L = 46.0 m and (c) L = 11.5 m/L = 46.0 m profiles. Shear wave velocity profiles obtained based on the combined mean, upper bound and lower bound dispersion curves for the (d) L = 11.5 m, (e) L = 46.0 m and (f) L = 11.5 m/L = 46.0 m profiles.

4. COMPARISON TO OTHER MEASUREMENT TECHNIQUES

4.1 Comparison of MASW and SASW measurement results

SASW measurements were carried out in 2009 in the Landey harbour area (Bessason and Erlingsson 2011) approximately 0.5 km west of the site where the MASW field data were acquired (Figure 4). The Landey area is a long sandy beach that is considered to be quite uniform, hence, the material properties of the soil beneath the MASW receiver spread are expected to be approximately the same as the properties of the soil where the SASW data were gathered.

Figure 8 presents a comparison of the experimental dispersion curves estimated based on the 2009 SASW measurements and the 2014 MASW measurements. The SASW mean dispersion curve was obtained by adding up multiple elementary dispersion curves (computed for different receiver pairs) in a comparable way as was done for the MASW data. Both the upper and lower bound SASW and MASW dispersion curves show plus−minus one standard deviation of the corresponding mean curve. The results presented in Figure 8 show that the MASW dispersion curve agrees well with the SASW curve. Furthermore, the standard deviations of the mean MASW curve are, in general, smaller than the standard deviations of the mean SASW curve.

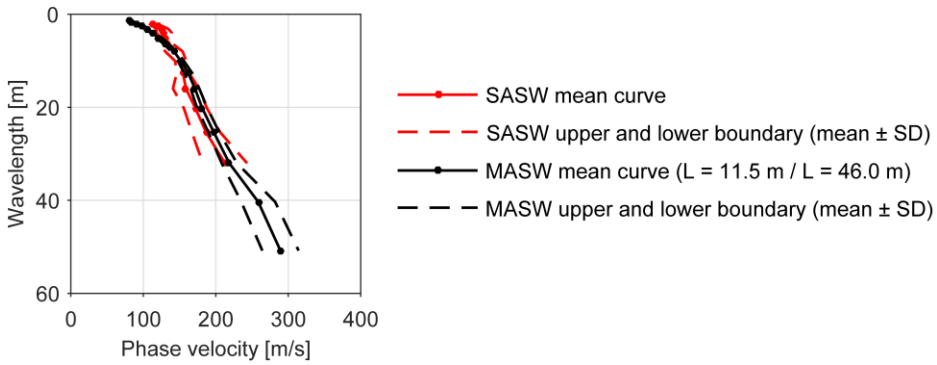

Figure 8. Experimental dispersion curves obtained at the Landey site by the SASW and MASW methods.

4.2 Comparison of MASW and CPT measurement results

Cone Penetration Testing was further carried out in 2009 close to the Landey harbour MASW test site (Figure 4). The results of the CPT measurements, presented in terms of the cone resistance (q_c), the sleeve friction (f_s), the pore-water pressure (u_2) and the friction ratio ($R_f = f_s/q_c$), are shown in Figure 9. The investigation depth of the CPT survey was 7.20 m.

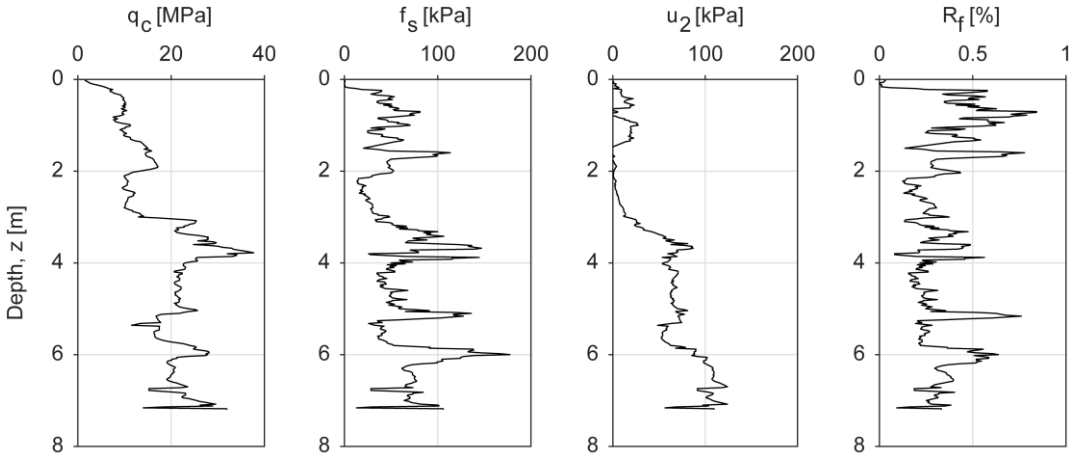

Figure 9. Results of CPT measurements in the Landey harbour area.

Various correlation equations exist between shear wave velocity and different CPT-related parameters, such as cone resistance, corrected cone resistance (q_t), sleeve friction, overburden stress (σ_{v0}), effective stress (σ'_{v0}) and depth (z). Several examples of CPT-V_S correlations, either intended for sands or for all soil types, are provided in Table 3.

Table 3. Examples of CPT-V_S correlation equations.

$V_S \approx 13.18 q_c^{0.192} (\sigma'_{v0})^{0.179}$	Hegazy and Mayne (1995)
$V_S \approx 18.4 q_c^{0.144} f_s^{0.0832} z^{0.278}$	McGann et al. (2015a)
$V_S \approx 32.3 q_c^{0.089} f_s^{0.121} z^{0.215}$	Piratheepan (2002)
$V_S \approx \left[(10^{0.55 I_c + 1.68}) \frac{q_t - \sigma_{v0}}{p_a}\right]^{0.5}$	Robertson (2009)
$I_c = [(3.47 - \log(Q_{tl}))^2 + (\log(F_r) + 1.22)^2]^{0.5}$ $\quad Q_{tl} = (q_t - \sigma_{v0})/\sigma_{v0}'$ $\quad F_r = f_s/(q_t - \sigma_{v0}) \cdot 100\%$	

q_c, q_t, f_s, σ_{v0} and σ'_{v0} in kPa and z in meters. $p_a = 100$ kPa.

Figure 10a provides comparison of the V_S profiles predicted based on the CPT-V_S correlations in Table 3 and the top-most 10 m of the V_S profile that was obtained by the MASW method (using data acquired by both the 11.5 m and 46.0 m receiver spreads). The full MASW V_S profile is shown in Figure 10b. The difference between the V_S estimates is further illustrated in Figure 11. The shear wave velocity bias ($V_{S,bias}$) (McGann et al. 2015b), used to indicate the difference between the estimated and measured V_S values, is defined as the ratio between the shear wave velocity values estimated by each of the four correlation equations (estimated V_S) and the values obtained by MASW (measured V_S) (see Equation 4). Hence, a value of $V_{S,bias}$ lower than one indicates that the shear wave velocity estimates obtained based on the CPT measurements at a given depth are lower than those obtained by MASW.

$$V_{S,bias} = \frac{\text{estimated } V_S}{\text{measured } V_S} \tag{4}$$

The results presented in Figures 10a and 11 indicate that the MASW shear wave velocity profile can be fitted adequately well with empirical correlations based on results of CPT measurements. In the depth range of 0.5–7.2 m, the mean bias for the correlations of Hegazy and Mayne (1995) and Piratheepan (2002) is very close to 1.0, indicating, on average, very comparable results to those obtained by MASW. The correlation equation of Robertson (2009) tends to provide higher V_S estimates than the results obtained by the MASW method indicate, whereas the correlation of McGann et al. (2015a) provides, on average, somewhat lower V_S estimates than were obtained by the MASW measurements.

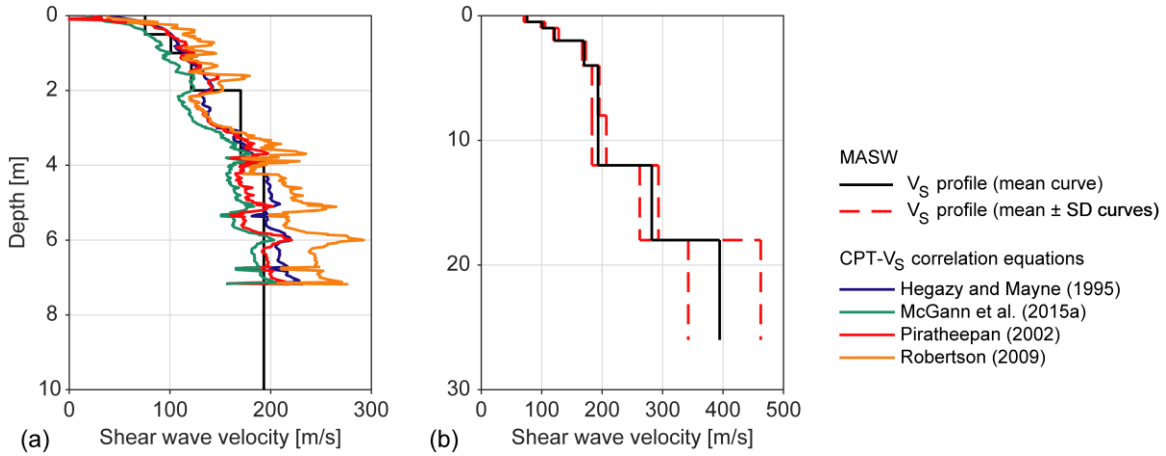

Figure 10. (a) Near-surface V_S profiles for the Landey site predicted based on selected CPT-V_S correlations and obtained by the MASW method. (b) Full MASW V_S profiles inverted based on the combined mean, upper bound and lower bound dispersion curves for the L=11.5 m/L=46.0 m profiles at the Landey site.

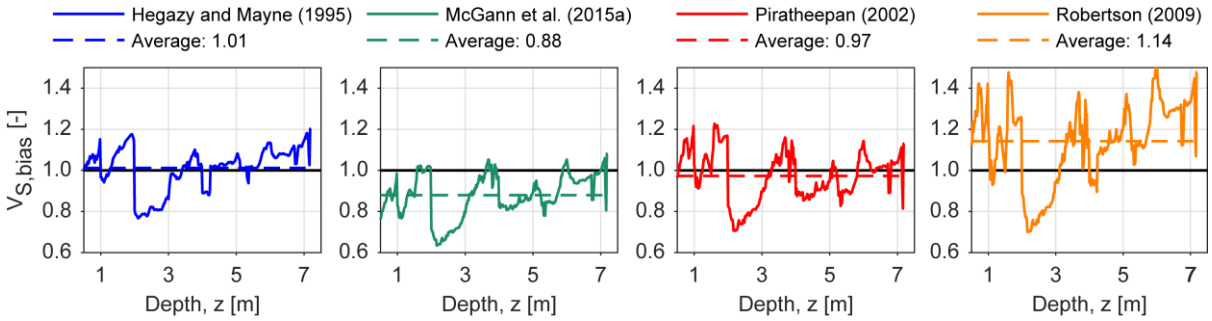

Figure 11. Comparison of near-surface V_S profiles obtained based on CPT and MASW measurements.

5. CONCLUSIONS

This paper presents a revised version of MASWaves, an open-source software for processing multichannel surface wave records using the MASW method. The software consists of three parts: a tool for dispersion analysis (MASWaves Dispersion), a tool to add up multiple dispersion curves (MASWaves Combination), and a tool for estimation of V_S profiles by inversion of the experimental dispersion data (MASWaves Inversion). The new software is further used for analysis of field data gathered at two test sites in Iceland. The software can be downloaded free of charge, along with a user guide and sample data, at masw.hi.is.

The aim of the dispersion analysis is to extract Rayleigh wave dispersion curves from the acquired data. Fundamental and higher mode dispersion curves identified by MASWaves Dispersion were compared to curves obtained by the software Geopsy. The agreement of the estimated curves was good, confirming the precision of MASWaves Dispersion and its ability to separate fundamental and higher modes. Moreover, experimental dispersion curves obtained for one test site were compared to results of SASW measurements previously carried out at the site. Good agreement between the SASW and MASW curves was observed, hence, further validating the performance of the dispersion analysis tool.

The purpose of MASWaves Combination is to combine experimental dispersion curves, which have been obtained based on different surface wave registrations, into a single curve. The set-up of the MASW measurement profile is widely acknowledged to affect the resolution and the frequency range of the dispersion data. The results of the field tests indicate that combining multiple dispersion curves that have been gathered by receiver spreads of different lengths (but with the same midpoint) can increase the maximum depth of the resulting V_S profile, improve its resolution at shallow depth, and overall improve the reliability of the results as compared to the use of a single record. Similar trends have been observed based on data gathered at other locations. However, comparable sand materials characterize the majority of these test sites. Therefore, further measurements will be required in order to conclude about sites characterized by other types of soil materials.

The inversion analysis tool consists of a mathematical model to compute theoretical dispersion curves, and, an algorithm to evaluate the misfit between the experimental and theoretical curves and to allow the user to manually update the set of model parameters. Future development of MASWaves Inversion includes replacing the latter part by a more automated search algorithm. The theoretical dispersion curve computations were validated by comparison to results presented by Tokimatsu (1997). Furthermore, the V_S profile obtained for a sandy test site was compared to empirical profiles estimated on the bases of CPT measurements carried out at the site.

6. ACKNOWLEDGEMENTS

The project is supported by grants from the University of Iceland Research Fund, the Icelandic Road and Coastal Administration and the Energy Research Fund of the National Power Company of Iceland.

7. REFERENCES

Bessason B, Erlingsson S (2011). Shear wave velocity in surface sediments. *Jökull*, 61: 51-64.

CEN (2004). EN1998-1:2004. Eurocode 8: design of structures for earthquake resistance. Part 1: general rules, seismic actions and rules for buildings, European Committee for Standardization, Brussels, Belgium.

Cox BR, Teague DP (2016). Layering ratios: a systematic approach to the inversion of surface wave data in the absence of a priori information. *Geophysical Journal International*, 207(1): 422-438. doi:10.1093/gji/ggw282.

Dikmen Ü, Arısoy MÖ, Akkaya İ (2010). Offset and linear spread geometry in the MASW method. *Journal of Geophysics and Engineering*, 7(2): 211-222. doi:10.1088/1742-2132/7/2/S07.

Foti S, Lai CG, Rix GJ, Strobbia C (2015). Surface wave methods for near-surface site characterization, CRC Press Taylor & Francis Group, Boca Raton FL.

Garofalo F, Foti S, Hollender F, Bard PY, Cornou C, Cox BR, et al. (2016). InterPACIFIC project: Comparison of invasive and non-invasive methods for seismic site characterization. Part I: Intra-comparison of surface wave methods. *Soil Dynamics and Earthquake Engineering*, 82: 222-240. doi:10.1016/j.soildyn.2015.12.010.

Hegazy YA, Mayne PW (1995). Statistical correlations between V_S and cone penetration data for different soil types. *Proceedings of the International Symposium on Cone Penetration Testing*, 4-5 October, Linköping, Sweden, Vol. 2, pp. 173-178.

Ivanov J, Miller RD, Tsoflias G (2008). Some practical aspects of MASW analysis and processing, *Proceedings of the symposium on the application of geophysics to engineering and environmental problems 2008*, 6-10 April, Philadelphia, PA, pp. 1186-1198. doi:10.4133/1.2963228.

Kausel E, Roësset JM (1981). Stiffness matrices for layered soils. *Bulletin of the Seismological Society of America*, 71(6): 1743-1761.

McGann CR, Bradley BA, Taylor ML, Wotherspoon LM, Cubrinovski M (2015a). Development of an empirical correlation for predicting shear wave velocity of Christchurch soils from cone penetration test data. *Soil Dynamics and Earthquake Engineering*, 75, 66-75. doi:10.1016/j.soildyn.2015.03.023.

McGann CR, Bradley BA, Taylor ML, Wotherspoon LM, Cubrinovski M (2015b). Applicability of existing empirical shear wave velocity correlations to seismic cone penetration test data in Christchurch New Zealand. *Soil Dynamics and Earthquake Engineering, 75*, 76-86. doi:10.1016/j.soildyn.2015.03.021.

Olafsdottir EA, Erlingsson S, Bessason B (2016). Effects of measurement profile configuration on estimation of stiffness profiles of loose post glacial sites using MASW, *Proceedings of the 17th Nordic geotechnical meeting*, 25-28 May, Reykjavik, Iceland, pp. 327-336.

Olafsdottir EA, Bessason B, Erlingsson S (2018a). Combination of dispersion curves from MASW measurements. Resubmitted to *Soil Dynamics and Earthquake Engineering*.

Olafsdottir EA, Erlingsson S, Bessason B (2018b). Tool for analysis of multichannel analysis of surface waves (MASW) field data and evaluation of shear wave velocity profiles of soils. *Canadian Geotechnical Journal*, 55(2): 217-233. doi:10.1139/cgj-2016-0302.

Park CB, Miller RD, Xia J (1998). Imaging dispersion curves of surface waves on multi-channel record, *SEG Technical Program Expanded Abstracts of the Society of Exploration Geophysicists International Exposition and 68th Annual Meeting*, 13-18 September, New Orleans, LA, pp. 1377-1380. doi:10.1190/1.1820161.

Park CB, Miller RD, Xia J (1999). Multichannel analysis of surface waves. *Geophysics*, 64(3): 800-808. doi:10.1190/1.1444590.

Park CB, Carnevale M (2010). Optimum MASW survey–revisit after a decade of use, *Proceedings of GeoFlorida 2010*, 20-24 February, West Palm Beach, FL, pp. 1303-1312. doi:10.1061/41095(365)130.

Piratheepan P (2002). Estimating Shear-Wave Velocity from SPT and CPT Data, *M.Sc. Thesis*. Clemson University, Clemson SC.

Robertson PK (2009). Interpretation of cone penetration tests-a unified approach. *Canadian Geotechnical Journal*, 46(11): 1337-1355.

Tokimatsu K (1997). Geotechnical site characterization using surface waves. *Proceedings of the 1st International Conference on Earthquake Geotechnical Engineering*, 14-16 November, Tokyo, Japan, Vol. 3, pp. 1333-1368.

Paper VI

Application of MASW in the South Iceland Seismic Zone

Elín Ásta Ólafsdóttir, Bjarni Bessason & Sigurður Erlingsson

Ólafsdóttir, E.Á., Bessason, B. & Erlingsson, S. (2019). Application of MASW in the South Iceland Seismic Zone. In *Proceedings of the International Conference on Earthquake Engineering and Structural Dynamics, Geotechnical, Geological and Earthquake Engineering, Vol. 47*, 12–14 June 2017, Reykjavik, Iceland (pp. 53–66). Cham, Switzerland: Springer. doi:10.1007/978-3-319-78187-7_5.

Chapter 5
Application of MASW in the South Iceland Seismic Zone

Elín Ásta Ólafsdóttir, Bjarni Bessason, and Sigurður Erlingsson

Abstract Multichannel Analysis of Surface Waves (MASW) is a seismic exploration method to evaluate shear wave velocity profiles of near-surface materials. MASW was applied at seven locations in or close to the South Iceland Seismic Zone, providing shear wave velocity profiles for the top-most 15–25 m. The profiles were utilized for seismic soil classification according to Eurocode 8. The results indicated that the sites that are characterized by sandy glaciofluvial, littoral or alluvial sediments fall into category C and the sites where the deposits are cemented to some degree belong to category B. Furthermore, the MASW measurements were used to evaluate the liquefaction potential at a site where liquefaction sand boils were observed during an M_w6.3 earthquake occurring in May 2008. The simplified procedure of assessing cyclic stress ratio to normalized shear wave velocity revealed that liquefaction had occurred down to 3–4 m depth, which is consistent with observations on site.

Keywords MASW · Shear wave velocity · Seismic site classification · Liquefaction potential

E. Á. Ólafsdóttir (✉) · B. Bessason
Faculty of Civil and Environmental Engineering, University of Iceland, Reykjavik, Iceland
e-mail: eao4@hi.is; bb@hi.is

S. Erlingsson
Faculty of Civil and Environmental Engineering, University of Iceland, Reykjavik, Iceland

Pavement Technology, The National Road and Transport Research Institute, Linköping, Sweden
e-mail: sigger@hi.is

R. Rupakhety et al. (eds.), *Proceedings of the International Conference on Earthquake Engineering and Structural Dynamics*, Geotechnical, Geological and Earthquake Engineering 47, https://doi.org/10.1007/978-3-319-78187-7_5

5.1 Introduction

The shear wave velocity (V_S) of near-surface materials is an important parameter in civil engineering work for characterization of natural soil sites and man-made fillings. The small-strain shear modulus (G_0) of individual soil layers is directly proportional to the square of their shear wave velocity. Furthermore, in areas where earthquakes are of concern, the shear wave velocity is fundamental in assessing both liquefaction potential and soil amplification and when defining site-specific earthquake design loading (Kramer 1996). For planning and design of structures, information about the shear wave velocity of the top few tens of meters of the soil stratum is, in general, of most importance.

Several in-situ methods can be used for determination of shear wave velocity profiles of subsoil sites (Kramer 1996). This includes methods that require a drilled borehole such as down-hole and cross-hole seismic surveys, methods where the resistance of soil to penetration is measured like the Standard Penetration Test (SPT) and the Cone Penetration Test (CPT), and surface wave analysis methods. The two-receiver seismic analysis method, Spectral Analysis of Surface Waves (SASW), has been applied at a number of sites in Iceland in the last two decades (Bessason et al. 1998; Bessason and Erlingsson 2011). Multichannel Analysis of Surface Waves (MASW) is a newer and more advanced method, based on simultaneous analysis of multiple surface wave traces acquired by an equally spaced line of receivers (Gabriels et al. 1987; Park et al. 1999). The MASW method has attracted increasingly more attention in recent years and has become one of the main surface wave analysis methods for evaluation of near-surface shear wave velocity profiles for applications in civil engineering (Xia 2014). The MASW method was first applied in Iceland in 2013 (Olafsdottir et al. 2014).

The main objective of the study presented in this paper was to map the shear wave velocity profiles of several test sites in South Iceland, in or close to the South Iceland Seismic Zone, by the MASW method and compare profiles obtained at different sites. The results of the MASW measurements were exploited to classify the soil at the test sites into ground types according to Eurocode 8. Furthermore, the results were used to evaluate the liquefaction hazard at one of the sites.

5.2 Seismic Activity in South Iceland

The seismicity in Iceland is related to the Mid-Atlantic plate boundary that crosses the island. Within the country, the boundary is shifted towards the east through two complex fracture zones (Einarsson 1991). One is located in the South Iceland Lowland, where it crosses the biggest agricultural region in the country, while the other is mostly located off the northern coast. The first is usually termed the South Iceland Seismic Zone (SISZ) and the second the Tjörnes Fracture Zone (TFZ). The

largest earthquakes in Iceland have occurred within these zones, mostly associated with a strike-slip motion at shallow depth (5–10 km).

Earthquakes in the SISZ tend to occur in sequences, typically every 100 years. One such started in 1896, when five quakes of magnitude greater than six struck the area within two weeks. Another event occurred in 1912 and is by some scientists considered to have finished the sequence. A new sequence started in 2000 when two earthquakes of magnitude M_w6.5 struck on the 17th and 21st of June. They were followed by the third one, an M_w6.3 earthquake on the 29th of May, 2008, referred to as the Ölfus earthquake. The epicentral distances between these three strike-slip quakes were less than 35 km, and they were all shallow with a hypocentral depth of less than 7 km. A great deal of structural damage occurred in these earthquakes, but no residential buildings collapsed and there was no loss of life (Bessason and Bjarnason 2016). In all these events rock fall and landslides occurred, as well as lateral spreading and liquefaction.

5.3 Multichannel Analysis of Surface Waves

Multichannel Analysis of Surface Waves is a relatively new technique for determining shear wave velocity profiles of near-surface soil materials based on analysis of Rayleigh waves. Rayleigh waves are surface waves that have the strongest wave motion closest to the surface and decay rapidly with depth (Fig. 5.1). Short wavelength (high frequency) Rayleigh wave components mainly propagate through the top-most soil layers, while longer wavelength (lower frequency) components travel deeper.

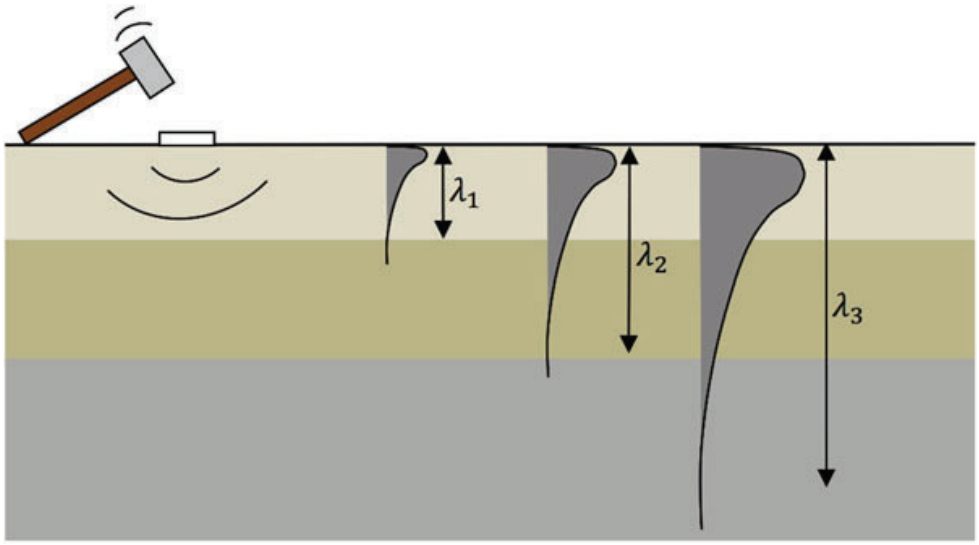

Fig. 5.1 Rayleigh wave components with different wavelengths propagating through a layered medium. Wave components with different frequencies reflect soil properties at different depths

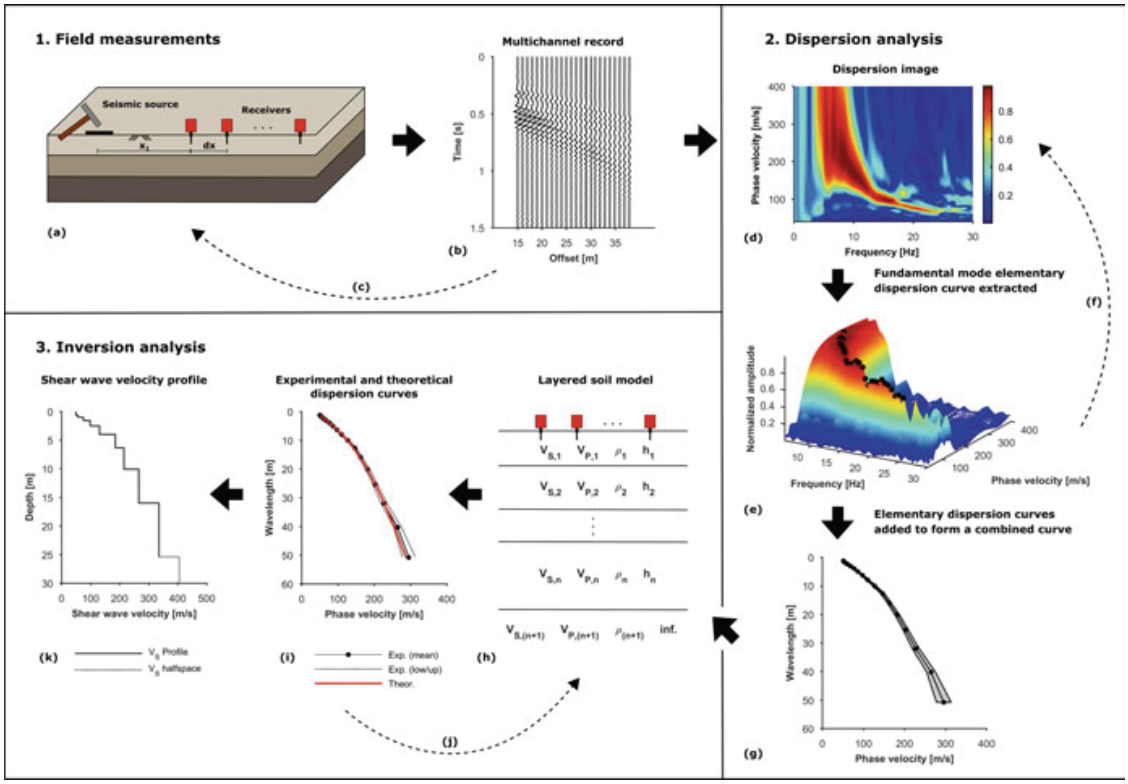

Fig. 5.2 Application of the MASW method

The phase velocity of a Rayleigh wave component propagating through a layered medium is determined by the average properties of the soil layers that it travels through. Hence, wave components with different frequencies propagate at different velocities and reflect material properties of soil layers at different depths. Waves that have a propagation velocity that depends on frequency are called dispersive waves. A dispersion curve describes the relation between frequency (wavelength) and phase velocity.

The investigation depth of a MASW survey is determined by the longest Rayleigh wave wavelength that is retrieved. A commonly used rule-of-thumb for interpretation of fundamental mode Rayleigh wave dispersion curves is that the maximum depth of the shear wave velocity profile is approximately one third to half the longest wavelength (Garofalo et al. 2016). The investigation depth that can be achieved by MASW is, in general, few tens of meters, assuming that the surface waves are generated by a reasonably heavy impact load, e.g. a sledgehammer. The observed difference between results obtained by MASW and direct borehole measurements has been evaluated as approximately 15% or less and random (Xia et al. 2002).

In its basic form, the MASW method consists of three steps as illustrated in Fig. 5.2 (Park et al. 1999).

1. Data acquisition in the field.
2. Data processing to extract an experimental Rayleigh wave dispersion curve from the acquired data (dispersion analysis).

3. Evaluation of the shear wave velocity profile by inversion of the experimental dispersion curve (inversion analysis).

For data acquisition, multiple (12 or more) low frequency geophones are lined up on the surface of the test site with equal receiver spacing dx (Fig. 5.2a). A wave is generated by an impact load that is applied at a distance x_1 from one end of the geophone line and the wave propagation is recorded (Fig. 5.2b).

It is commonly recognized that the length of the receiver spread and the source offset can have a substantial effect on the acquired records (e.g. Dikmen et al. 2010; Ivanov et al. 2008; Olafsdottir et al. 2016; Park and Carnevale 2010; Zhang et al. 2004). Applications of the MASW method at Icelandic sites have indicated that an increased range in investigation depth can be obtained by combining data recorded by measurement profiles of different lengths (Olafsdottir et al. 2016). Furthermore, combined or repeated analysis of surface wave records acquired by using several different measurement profile configurations can help confidently identifying the fundamental mode dispersion curve in the subsequent dispersion analysis. Hence, in this work, the field measurements are repeated several times using measurement profiles with different dx and/or x_1 while keeping the midpoint of the receiver spread fixed (Fig. 5.2c). Computations were carried out by using the open source Matlab software MASWaves (Olafsdottir et al. 2018) [see also masw.hi.is].

A dispersion image (Fig. 5.2d) is obtained based on each multichannel surface wave record by using the phase shift method (Park et al. 1998). The dispersion image visualizes the dispersion properties of all types of waves contained in the recorded data. Subsequently, the fundamental mode of the Rayleigh wave propagation is identified based on the spectral high-amplitude (peak energy) bands observed in the dispersion image and the fundamental mode Rayleigh wave dispersion curve is extracted (Fig. 5.2e).

The previous analysis steps (Fig. 5.2d, e) are repeated for each surface wave record (Fig. 5.2f) resulting in multiple elementary dispersion curves that are subsequently combined into a single experimental curve (Fig. 5.2g). Here, the combined (average) curve is obtained by grouping the data points included in the elementary dispersion curves together within 1/3 octave wavelength intervals. The phase velocity values within each interval are added up and their mean used as a point estimate of the phase velocity of the Rayleigh wave components belonging to the given wavelength range. The accuracy of the estimated mean phase velocity is evaluated in terms of the $p\%$ classical confidence interval for the sample mean within each wavelength interval.

Inversion problems involving the dispersion of Rayleigh waves in a layered elastic medium are by nature both non-linear and non-unique, and must be solved by iterative methods (Foti et al. 2015). Computations are based on Rayleigh wave propagation theory assuming a plane-layered earth model. The parameters required to describe the properties of each layer are shear wave velocity (V_S), compressional wave velocity (V_P) (or Poisson's ratio (ν)), mass density (ρ) and layer thickness (h). The last layer is assumed to be a half-space.

Fig. 5.3 Location of MASW test sites in South Iceland. The map is based on data from the National Land Survey of Iceland

The first step of the inversion analysis is to make an initial estimate of the layered soil model for the test site (Fig. 5.2h). A theoretical dispersion curve is obtained based on the assumed model and compared to the experimental (combined) curve (Fig. 5.2i). Here, the stiffness matrix method (Kausel and Roësset 1981) is used for computations of theoretical dispersion curves. Subsequently, the soil model is updated and the theoretical dispersion curve recomputed until the misfit between the theoretical and experimental curves has reached an acceptably small value (Fig. 5.2j). The shear wave velocity profile and the layer structure that result in an acceptable fit, and are believed to realistically represent the characteristics of the test site, are finally taken as the results of the survey (Fig. 5.2k).

5.4 MASW Measurements

MASW measurements have been conducted at several locations in Iceland from 2013 to 2016. The seven test sites reported in this paper are all located in South Iceland (Fig. 5.3). Some of the sites were in the near-fault area of the South Iceland earthquakes of June 2000 and May 2008. They are all at sites which were created by some mixture of ordinary fluvial and Aeolian processes, glacial outwash, sub-glacial outburst floods, coastal sediment transport and ash fall from volcanic eruptions. The exact origin is not well known. At some of the sites, the deposits are cemented to some degree whilst at others they are looser. The main characteristics of the seven test sites are summarized in Table 5.1.

At the seven MASW test sites, multichannel surface wave records were collected using 24 vertical geophones with a natural frequency of 4.5 Hz and a critical

Table 5.1 Overview of site characteristics and test configuration at the MASW test sites in South Iceland

Site			Arnarbæli	Bakkafjara	Hella – Gaddstaðaflatir	Hella – sandnáma	Hvolsvöllur	Múlakvísl	Þorlákshöfn
Site characteristics									
Soil type			Holocene glaciofluvial sand	Modern littoral sand	Late-glacial cemented Aeolian silty sand	Late-glacial (slightly) cemented Aeolian silty sand	[Unknown]	Modern littoral sand	Alluvial sand
USCS classification			SW-SM[a]	SW[c]			[Unknown]	SW[c]	SP[c]
Estimated location of groundwater table			At surface	At 4 m depth	At great depth	At great depth	At great depth	At 3 m depth	At surface
Mass density	ρ	[kg/m^3]		1850	2200	2200	2000	1850	
Saturated mass density	ρ_{sat}	[kg/m^3]	1800	2000				2000	1880
Poisson's ratio[b]	ν	[−]		0.35	0.35	0.35	0.35	0.35	
Field measurements									
No. geophones	N		24	24	24	24	24	24	24
No. profiles			3	3	3	2	2	3	1
Receiver spacing (source offsets)	dx (x_1)	[m]	0.5 (3.0–10.0)	0.5 (3.0–10.0)	0.5 (3.0–10.0)	0.5 (3.0–10.0)	0.5 (3.0–5.0)	0.5 (5.0–7.5)	2.0 (10.0–40.0)
			1.0 (5.0–30.0)	1.0 (5.0–30.0)	1.0 (5.0–30.0)	1.0 (5.0–30.0)	1.0 (5.0–30.0)	1.0 (5.0–30.0)	
			2.0 (5.0–30.0)	2.0 (5.0–50.0)	2.0 (5.0–30.0)			2.0 (5.0–30.0)	
No. elementary dispersion curves			95	71	113	58	43	85	26
Recording time	T	[s]	2.4	1.2	2.4	2.4	2.4	2.4	1.2

[a]Green et al. (2012)
[b]The compressional wave velocity of the saturated soil layers is specified as $V_P = 1440$ m/s
[c]Assumed

damping ratio of 0.5. Up to three measurement profiles with the same midpoint but different receiver spacing (receiver spread length) were used at each site. For each receiver spacing, several different source offsets (x_1) were used. A summary of the main parameters related to the field measurements at each site is provided in Table 5.1. The impact load was in all cases created by a 6.3 kg sledgehammer, except at the Bakkafjara site where a single jump at the end of the measurement profile was also used. No systematic difference was observed between surface wave records where the impact load was created by a sledgehammer blow and where it was the result of a jump.

5.4.1 Results of MASW Measurements

Figure 5.4a shows the combined (average) experimental dispersion curves for the seven MASW test sites in South Iceland. The shaded areas in Fig. 5.4a correspond to the 95% confidence intervals for the mean phase velocity within each wavelength interval. In general, the longer wavelength (lower frequency) parts of the dispersion curves are characterized by higher uncertainty than the shorter wavelength (higher frequency) regions.

The results of the inversion analysis are illustrated in Fig. 5.4b. The half-space shear wave velocity in each case is indicated by a broken line. The misfit between the experimental dispersion curves and the optimum theoretical curves was in all cases less than 2.5%, except at the Hvolsvöllur site where it was approximately 4.5%.

The average shear wave velocity $V_{S,d}$ of the uppermost d = [5, 10, 20, 30] m at each test site is further provided in Table 5.2. The $V_{S,d}$ velocity was obtained as (CEN 2004)

$$V_{S,d} = \frac{d}{\sum_{j=1}^{N} \frac{h_j}{V_{S,j}}} \tag{5.1}$$

where $V_{S,j}$ and h_j denote the shear wave velocity and thickness of the j-th layer, respectively, for a total of N layers down to depth d. When an estimated shear wave velocity profile went down to a depth less than d, the profile was extrapolated using the half-space velocity (Fig. 5.4b) down to depth d.

The shear wave velocity profiles and the average values presented in Fig. 5.4b and Table 5.2 indicate that the test sites can be divided into three main groups. First, the loose sand sites at Arnarbæli, Bakkafjara, Múlakvísl and Þorlákshöfn showed similar characteristics with V_S increasing from around 60–150 m/s close to ground level to 300–400 m/s at 20–25 m depth. Second, the two test sites close to Hella,

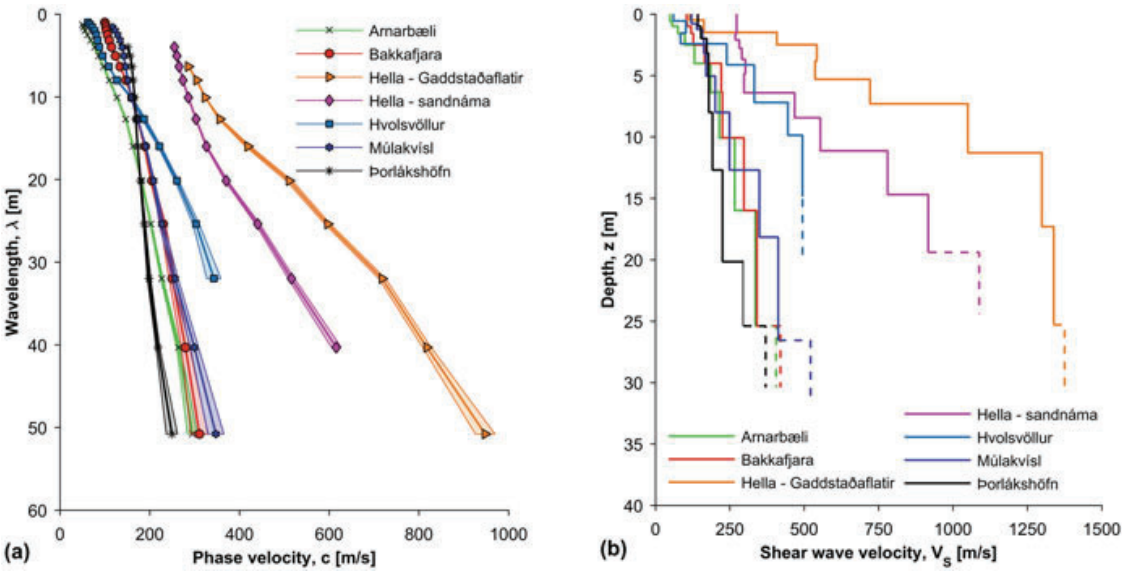

Fig. 5.4 (**a**) Combined (average) dispersion curves with 95% confidence intervals and (**b**) estimated shear wave velocity profiles for the MASW test sites in South Iceland

Table 5.2 Average shear wave velocity of the uppermost 5m, 10m, 20m and 30m at the MASW test sites

Site	$V_{S,5}$ [m/s]	$V_{S,10}$ [m/s]	$V_{S,20}$ [m/s]	$V_{S,30}$ [m/s]
Arnarbæli	93.9	129.0	178.4	215.0
Bakkafjara	142.1	174.0	223.5	258.0
Hella – Gaddstaðaflatir	284.2	425.5	637.5	774.2
Hella – sandnáma	283.6	338.8	478.3	588.2
Hvolsvöllur	127.9	192.4	277.0	(324.5)
Múlakvísl	153.5	180.0	231.2	275.3
Þorlákshöfn	163.5	173.3	192.0	222.2

characterized by cemented silty sand, showed much higher velocities, reaching values above 750 m/s and 1000 m/s, respectively, at around 10 m depth. Third, the Hvolsvöllur site was characterized by low values of V_S at shallow depths which increased rapidly with increasing depth. At the Hvolsvöllur site, however, the maximum retrievable Rayleigh wavelength was close to 30 m (Fig. 5.4a), limiting the maximum depth of the shear wave velocity profile to approximately 15 m. The increase in shear wave velocity with depth might therefore be substantially more than indicated by the estimated half-space velocity (Fig. 5.4b), leading to a higher estimate of $V_{S,30}$. Hence, for characterization of the properties of the soil at the Hvolsvöllur site based on $V_{S,30}$, further measurements are considered necessary (see also Sect. 5.5.1).

5.5 Seismic Hazard Application

5.5.1 Seismic Site Classification

In Eurocode 8, the European standard for design of structures in seismic zones, (CEN 2004) construction sites are classified into five categories, referred to as ground types A, B, C, D and E, based on the average shear wave velocity of the uppermost 30 m at the site (Eq. 5.1 with $d = 30$ m). The ground type is further used to account for the effects of the local ground conditions on the seismic action and, hence, fundamental for determination of site-specific design spectrums. The definition of ground types A, B, C, D and E, as presented in Eurocode 8, is provided in Table 5.3. The soil classification groups of the seven MASW test sites in South Iceland (Fig. 5.3) are provided in Table 5.4.

5.5.2 Liquefaction Hazard Analysis at the Arnarbæli Site

Liquefaction is attributed to the tendency of soils to compact during shaking. Furthermore, the resistance to shearing strains is highly linked to the material shear modulus. During the May 2008 M_w6.3 Ölfus earthquake, liquefaction was observed at a few places in South Iceland, among them at Arnarbæli where sand boils were found on the riverbank of the Ölfus River (Fig. 5.5a).

The Arnarbæli site is located less than 1 km from the active fault that ruptured in the Ölfus earthquake and the estimated PGA for the site (a_{max}) was in the range 0.6–0.7 g. The soil at the Arnarbæli site consists of glaciofluvial volcanic sand deposited on the western bank of the estuary of the Ölfus River. Based on a soil sieve analysis it has been concluded that the material has a 6–7% fine content (FC) and lies within the boundaries identified as potentially liquefiable soils (Green et al. 2012; Tsuchida 1970).

The simplified procedure to assess liquefaction resistance of soils based on measurements of shear wave velocity (Andrus and Stokoe 2000) was used to evaluate the liquefaction hazard at the Arnarbæli site. The method involves assessment of three parameters: (1) The cyclic stress ratio (*CSR*), describing the cyclic loading imposed on the soil by the earthquake

$$CSR = 0.65\left(\frac{a_{max}}{g}\right)\left(\frac{\sigma_{v0}}{\sigma'_{v0}}\right)r_d \tag{5.2}$$

where σ_{v0} is total overburden stress, σ'_{v0} is effective overburden stress and r_d is a shear stress reduction coefficient, here estimated based on the work of Idriss (1999). (2) The overburden stress corrected shear wave velocity (V_{s1})

Table 5.3 Identification of ground types based on $V_{S,30}$, after CEN (2004)

Ground type	Description of stratigraphic profile	$V_{S,30}$ [m/s]
A	Rock or other rock-like geological formation, including at most 5 m of weaker material at the surface.	> 800
B	Deposits of very dense sand, gravel, or very stiff clay, at least several tens of metres in thickness, characterized by a gradual increase in mechanical properties with depth.	360–800
C	Deep deposits of dense or medium-dense sand, gravel or stiff clay with thickness from several tens to many hundreds of metres.	180–360
D	Deposits of loose-to-medium cohesionless soil (with or without some soft cohesive layers), or of predominantly soft-to-firm cohesive soil.	<180
E	A soil profile consisting of a surface alluvium layer with V_S values of type C or D and thickness varying between about 5 and 20 m, underlain by stiffer material with $V_S > 800$ m/s.	

Table 5.4 Soil classification groups for the MASW test sites in South Iceland

Site	Ground type
Arnarbæli	C
Bakkafjara	C
Hella – Gaddstaðaflatir	B
Hella – sandnáma	B
Hvolsvöllur	C/B/E[a]
Múlakvísl	C
Þorlákshöfn	C

[a]Further measurements are needed

$$V_{S1} = \min\left(V_S\left(\frac{p_a}{\sigma'_{v0}}\right)^{0.25}; 1.4V_S\right) \tag{5.3}$$

where $p_a = 100$ kPa and (3) the cyclic resistance ratio (*CRR*), which for a given V_{s1} is the value of *CSR* separating liquefaction and non-liquefaction occurrences

$$CRR = \left\{a\left(\frac{V_{S1}}{100}\right)^2 + b\left(\frac{1}{V^*_{S1} - V_{S1}} - \frac{1}{V^*_{S1}}\right)\right\}\left(\frac{M_w}{7.5}\right)^n \tag{5.4}$$

with $a = 0.022$, $b = 2.8$ and $n = -2.56$ (Andrus and Stokoe 2000). V^*_{S1} is the limiting upper value of V_{S1} for cyclic liquefaction occurrence estimated as $V^*_{S1} = 215 - 0.5(FC - 5)$ m/s for sands with a fine content between 5% and 35%.

A liquefaction resistance curve (V_{S1}–*CRR* curve) scaled to account for the effects of an M_w6.3 earthquake is presented in Fig. 5.5b. The cyclic stress ratio and the normalized shear wave velocity were calculated for reference points at depth $z = [0.3, 0.8, 1.3, 2.1, 3.3, 5.2, 8.2, 13.0, 20.7]$ m, i.e. at the centre of each of the finite thickness layers indicated for the Arnarbæli site in Fig. 5.4b, and compared to the liquefaction resistance curve. The PGA of the site was estimated as 0.65 g. The

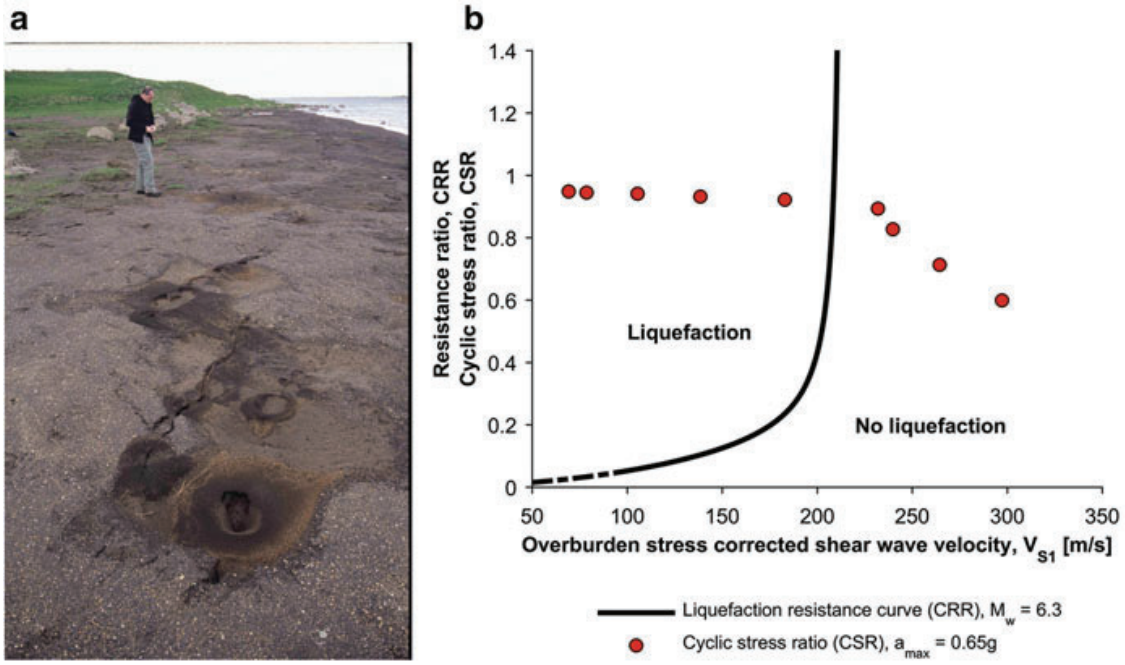

Fig. 5.5 (**a**) Liquefaction on the riverbank of the Ölfus River close to the epicentre of the M_w6.3 2008 Ölfus earthquake (photo: Oddur Sigurðsson). (**b**) Liquefaction evaluation chart for the Arnarbæli site

results, presented in Fig. 5.5b, indicate that liquefaction had occurred at the site down to around 3–4 m depth.

5.6 Concluding Remarks

MASW is a relatively new seismic exploration method to evaluate shear wave velocity profiles of near-surface materials. In this paper, the results of MASW measurements carried out at seven test sites in South Iceland are presented. Twenty-four 4.5 Hz geophones were used for recording and a 6.3 kg sledgehammer or a single jump at the end of the geophone line was used as an impact source. Several different source offset and/or receiver spacing configurations were used at each site in order to maximize the investigation depth range of the survey. This resulted in 26–113 multichannel surface wave records for each of the seven sites. Dispersion analysis and inversion were then applied to evaluate the combined (average) dispersion curve, along with upper and lower boundaries, and the shear wave velocity profile for each site. Using this set-up, shear wave velocity profiles down to 15–25 m could be obtained.

The results of the MASW measurements were utilized for seismic classification of the seven test sites according to Eurocode 8. The results indicated that the loose sand sites at Arnarbæli, Bakkafjara, Múlakvísl and Þorlákshöfn fall into category C and that the two sites close to Hella, where the deposits are cemented to some degree,

belong to category B. At the Hvolsvöllur site, further measurements are considered necessary in order to carry out seismic classification. Furthermore, the results obtained by MASW were used to evaluate the liquefaction potential of the soils at the Arnarbæli site where liquefaction sand boils were observed during the M_w6.3 Ölfus earthquake in 2008. The simplified procedure of assessing cyclic stress ratio (CSR) to normalized shear wave velocity reveals that liquefaction has occurred at the site down to 3–4 m depth, which is consistent with observations on site.

Future work includes continuing development of the MASW method, e.g. further analysis of the effects of the measurement profile configuration and a more detailed study of the uncertainty associated with the combined dispersion curves and the subsequent shear wave velocity profiles. The ongoing build-up of a database of MASW shear wave velocity profiles for the South Iceland Seismic Zone is also of importance, along with seismic soil classification and evaluation of liquefaction potentials.

Acknowledgements The project is financially supported by grants from the University of Iceland Research Fund, the Icelandic Road and Coastal Administration and the Energy Research Fund of the National Power Company of Iceland.

References

Andrus RD, Stokoe KH II (2000) Liquefaction resistance of soils from shear-wave velocity. J Geotech Geoenviron Eng 126(11):1015–1025. https://doi.org/10.1061/(ASCE)1090-0241(2000)126:11(1015)

Bessason B, Bjarnason JÖ (2016) Seismic vulnerability of low-rise residential buildings based on damage data from three earthquakes (M_w6.5, 6.5 and 6.3). Eng Struct 111:64–79. https://doi.org/10.1016/j.engstruct.2015.12.008

Bessason B, Erlingsson S (2011) Shear wave velocity in surface sediments. Jökull 61:51–64

Bessason B, Baldvinsson GI, Thórarinsson Ó (1998) SASW for evaluation of site-specific earthquake excitation. In: Proceedings of the 11th European conference on earthquake engineering, Paris, CD-ROM

CEN (2004) EN 1998–1 Eurocode 8: design of structures for earthquake resistance, part 1: general rules, seismic actions and rules for buildings. European Committee for Standardization

Dikmen Ü, Arisoy MÖ, Akkaya I (2010) Offset and linear spread geometry in the MASW method. J Geophys Eng 7(2):211–222. https://doi.org/10.1088/1742-2132/7/2/S07

Einarsson P (1991) Earthquakes and present-day tectonics in Iceland. Tectonophysics 189 (1–4):261–279. https://doi.org/10.1016/0040-1951(91)90501-I

Foti S, Lai CG, Rix GJ, Strobbia C (2015) Surface wave methods for near-surface site characterization. CRC Press, Taylor & Francis Group, Boca Raton, FL

Gabriels P, Snieder R, Nolet G (1987) In situ measurements of shear-wave velocity in sediments with higher-mode Rayleigh waves. Geophys Prospect 35(2):187–196. https://doi.org/10.1111/j.1365-2478.1987.tb00812.x

Garofalo F, Foti S, Hollender F, Bard PY, Cornou C, Cox BR et al (2016) InterPACIFIC project: comparison of invasive and non-invasive methods for seismic site characterization. Part I: intra-comparison of surface wave methods. Soil Dyn Earthq Eng 82:222–240. https://doi.org/10.1016/j.soildyn.2015.12.010

Green RA, Halldorsson B, Kurtulus A, Steinarsson H, Erlendsson OA (2012) Unique liquefaction case study from the 29 May 2008, M_w6.3 Olfus earthquake, Southwest Iceland. In: 15th World conference on earthquake engineering, Lisbon, Portugal

Idriss IM (1999) An update of the Seed-Idriss simplified procedure for evaluating liquefaction potential. In: Transportation Research Board '99 workshop on new approaches to liquefaction analysis, Publ. No. FHWARD-99-165. Federal Highway Administration, Washington, DC

Ivanov J, Miller RD, Tsoflias G (2008) Some practical aspects of MASW analysis and processing. In: Proceedings of the 21st EEGC symposium on the application of geophysics to engineering and environmental problems, Philadelphia, PA, pp 1186–1198. https://doi.org/10.4133/1.2963228

Kausel E, Roësset JM (1981) Stiffness matrices for layered soils. Bull Seismol Soc Am 71 (6):1743–1761

Kramer SL (1996) Geotechnical earthquake engineering. Prentice-Hall, Upper Saddle River

Olafsdottir EA, Bessason B, Erlingsson S (2014) Multichannel analysis of surface waves for estimation of soils stiffness profiles. In: Proceedings of the 23rd European young geotechnical engineers conference, Barcelona, Spain, pp 45–48

Olafsdottir EA, Erlingsson S, Bessason B (2016) Effects of measurement profile configuration on estimation of stiffness profiles of loose post glacial sites using MASW. In: Proceedings of the 17th Nordic geotechnical meeting, Reykjavik, Iceland, pp 327–336

Olafsdottir EA, Erlingsson S, Bessason B (2018) Tool for analysis of multichannel analysis of surface waves (MASW) field data and evaluation of shear wave velocity profiles of soils. Can Geotech J 55(2):217–233. https://doi.org/10.1139/cgj-2016-0302

Park CB, Carnevale M (2010) Optimum MASW survey–revisit after a decade of use. In: Proceedings of GeoFlorida 2010, West Palm Beach, FL, pp 1303–1312. https://doi.org/10.1061/41095(365)130

Park CB, Miller RD, Xia J (1998) Imaging dispersion curves of surface waves on multi-channel record. In: 68th Annual International meeting, SEG, Expanded abstracts 17, pp 1377–1380. doi: https://doi.org/10.1190/1.1820161

Park CB, Miller RD, Xia J (1999) Multichannel analysis of surface waves. Geophysics 64 (3):800–808. https://doi.org/10.1190/1.1444590

Tsuchida H (1970) Prediction and Countermeans against the liquefaction in sand deposits. In: Abstract of the seminar in the Port and Harbour Research Institute, Yokohama, Japan, pp 3.1–3.33

Xia J (2014) Estimation of near-surface shear-wave velocities and quality factors using multichannel analysis of surface-wave methods. J Appl Geophys 103:140–151. https://doi.org/10.1016/j.jappgeo.2014.01.016

Xia J, Miller RD, Park CB, Hunter JA, Harris JB, Ivanov J (2002) Comparing shear-wave velocity profiles inverted from multichannel surface wave with borehole measurements. Soil Dyn Earthq Eng 22(3):181–190. https://doi.org/10.1016/S0267-7261(02)00008-8

Zhang SX, Chan LS, Xia J (2004) The selection of field acquisition parameters for dispersion images from multichannel surface wave data. Pure Appl Geophys 161(1):185–201. https://doi.org/10.1007/s00024-003-2428-7

Paper VII

Open source MASW software and results from Icelandic soil sites

Elín Ásta Ólafsdóttir, Sigurður Erlingsson & Bjarni Bessason

Ólafsdóttir, E.Á., Erlingsson, S. & Bessason, B. (2019). Open source MASW software and results from Icelandic soil sites. In *Proceedings of the 17th European Conference on Soil Mechanics and Geotechnical Engineering*, 1–6 September 2019, Reykjavik, Iceland. doi:10.32075/17ECSMGE-2019-0771.

Proceedings of the XVII ECSMGE-2019
Geotechnical Engineering foundation of the future
ISBN 978-9935-9436-1-3

doi: 10.32075/17ECSMGE-2019-0771

XVII European Conference
ECSMGE 2019
Reykjavík
on Soil Mechanics
and Geotechnical Engineering

Open source MASW software and results from Icelandic soil sites

Logiciel libre pour mesures MASW et résultats des sites de sol islandais

E.Á. Ólafsdóttir
Faculty of Civil and Environmental Engineering, University of Iceland, Reykjavík, Iceland

S. Erlingsson, B. Bessason
Faculty of Civil and Environmental Engineering, University of Iceland, Reykjavík, Iceland

ABSTRACT: Multichannel Analysis of Surface Waves (MASW) is a non-invasive, fast and low-cost seismic exploration method for evaluation of near-surface shear wave velocity (V_S) profiles. MASWaves is an open source software for acquiring and analyzing MASW field data that has been under development for the past few years. To date, MASW measurements have been carried out at over twenty different locations in Iceland, ranging from sites characterized by peat and loosely compacted sand to cemented soil materials and soft rock. The methodology used for acquiring and analyzing the surface wave records is described, with emphasis on recent advances in both in-situ procedures and data analysis. A newly developed open database is further introduced where results of MASW measurements carried out at Icelandic sites can be viewed and shear wave velocity/stiffness profiles for different sites compared. The aim is to give engineers and researchers access to the data and allow utilization of the results for, e.g., evaluation of seismic hazard and liquefaction potential, and for defining site-specific earthquake loading according to EC8.

RÉSUMÉ: L'analyse des ondes de surface (MASW) est une méthode d'exploration sismique non invasive, rapide et peu coûteuse qui permet d'évaluer les profils de vitesse d'onde de cisaillement (V_S) proche de la surface. MASWaves est un logiciel libre d'acquisition, de traitement et d'analyse des données de terrain MASW en cours de développement ces dernières années. À ce jour, des mesures MASW ont été effectuées à différents endroits en Islande, allant de sites caractérisés par de la tourbe et du sable faiblement compacté aux sols cimentés et aux roches tendres. La méthodologie utilisée pour acquérir et analyser les enregistrements d'ondes de surface est décrite, en mettant l'accent sur les progrès récents en matière de procédures in situ et d'analyse de données. Une nouvelle base de données ouverte récemment développée est également introduite. Elle permet de visualiser les résultats de toutes les mesures MASW effectuées en Islande et de comparer les profils de vitesse/rigidité des ondes de cisaillement pour différents sites. L'objectif est de donner aux ingénieurs et aux scientifiques l'accès aux données et de permettre l'utilisation des résultats, par exemple. évaluation du risque sismique et du potentiel de liquéfaction, et lors de la définition de la charge sismique spécifique au site conformément à EC8. conformément à EC8.

Keywords: Multichannel Analysis of Surface Waves (MASW); shear wave velocity; stiffness; open source software; open database

1 INTRODUCTION

Surface sediments of different origins are common in Iceland and compacted soils are widely used in civil engineering structures, e.g., as foundation pads, for road construction and in various kinds of dams, dykes and other embankments. Iceland is a seismically active area, characterized by moderate to high seismic hazard, where earthquakes of magnitude up to seven can be expected in inhabited areas. Hence, in addition to obtaining general geotechnical parameters for design, it is important to, e.g., carry out seismic soil classification, map site amplifications and evaluate liquefaction hazard as a part of civil engineering work.

The shear wave velocity (V_S) is an important parameter for design of geotechnical structures subjected to dynamic loads. Various in-situ techniques can be applied to evaluate the V_S-profile of near-surface materials (Kramer 1996). These include borehole measurements, such as cross-hole and down-hole seismic surveys, methods where the resistance of soil to penetration is measured, like the seismic cone penetration test, and surface wave analysis techniques. The two-receiver Spectral Analysis of Surface Waves (SASW) method has been applied at a number of sites in Iceland (Silver et al. 1986; Bessason and Erlingsson 2011). Multichannel Analysis of Surface Waves (MASW) is a newer and more advanced technique, based on simultaneous analysis of surface wave traces acquired by an equally spaced array of receivers, (Gabriels et al. 1987; Park et al. 1999). The technique has gained momentum in recent years for applications within geotechnical and earthquake engineering. MASW can be applied at a wide variety of sites, ranging from clay and silt sites to coarse-grained gravelly sites and soft rock, hence, including locations where, e.g., penetration tests are difficult to carry out.

To date, MASW measurements have been conducted at over twenty locations in Iceland. These sites are characterized by a wide variety of soil materials. In this paper, the methodology used for acquiring and analyzing the surface wave records is described, with emphasis on recent advances in both in-situ procedures and data analysis. The first version of an open database is introduced, where results of MASW measurements, carried out at different locations in Iceland, can be viewed and shear wave velocity/stiffness profiles for different sites compared. The main aim is to give engineers and researchers access to the data and allow utilization of the results for, e.g., evaluation of seismic hazard and liquefaction potential, and for defining site-specific earthquake loading according to Eurocode 8 (EC8).

2 MASW

An application of the MASW method is, in general, divided into three steps:

1. *Field measurements:* In-situ measurements to acquire multichannel surface wave records.
2. *Dispersion analysis:* Evaluation of the experimental Rayleigh wave dispersion curve based on the recorded surface waves.
3. *Inversion analysis:* Assessment of the V_S-profile by inversion of the experimental dispersion curve.

The resolution of MASW diminishes with increasing depth (Foti et al. 2015). The prospective investigation depth range is restricted by the observed dispersion curve wavelengths. A simple, widely accepted, rule-of-thumb for interpretation of fundamental mode dispersion curves (e.g., Garofalo et al. 2016) is to limit z_{max} (m), the maximum depth of the V_S-profile, as

$$z_{max} \leq \gamma \lambda_{max} \text{ with } \frac{1}{3} \leq \gamma \leq \frac{1}{2} \quad (1)$$

where λ_{max} (m) is the longest wavelength and, similarly, to limit h_1, the thickness of the top-most layer (m), as

$$h_1 \geq \xi \lambda_{min} \text{ with } \frac{1}{3} \leq \xi \leq \frac{1}{2} \quad (2)$$

where λ_{min} (m) is the shortest retrieved wavelength.

It is commonly recognized that the set-up of the measurement profile, i.e., the length of the receiver spread and the source offset, affects the acquired dispersion data (Dikmen et al. 2010; Ivanov et al. 2008; Ólafsdóttir et al. 2016; Park and Carnevale 2010). The observed effects suggest that a wider range of dispersion curve wavelengths, and, consequently, an increased investigation depth range, can be obtained by combination of data acquired by measurement profiles of different lengths (Ivanov et al. 2008; Ólafsdóttir et al. 2018c). Furthermore, the acquired surface wave records are affected by various, correlated and uncorrelated, noise sources. Hence, when several records are gathered at a single station, some variability among the resulting dispersion curve estimates will be observed. An assessment of the uncertainty associated with the experimental dispersion curve both allows the analyst to more rationally evaluate the overall quality of the data, and to present the V_S-profile with upper and lower boundaries. Alternatively, the inversion results can be presented as a set of V_S-profiles those theoretical dispersion curves lie between the upper and lower boundary experimental curves.

2.1 MASWaves

MASWaves is an open source Matlab-based software for acquiring and processing MASW field data that has been under development at the University of Iceland for the past few years (Ólafsdóttir et al. 2018a; 2018b). The processing part of MASWaves consists of three separate tools. First, a basic dispersion analysis tool (MASWaves Dispersion) to identify an experimental dispersion curve from a single multichannel surface wave record. Second, a tool to add up dispersion curves obtained from multiple surface wave registrations (MASWaves Combination). Third, an inversion analysis tool (MASWaves Inversion) to evaluate the shear wave velocity profile of the test site by backcalculation of the combined dispersion curve. Ólafsdóttir et al. (2018a; 2018c) provide a more detailed description of the computational procedures behind MASWaves Dispersion and MASWaves Inversion, and the method used in MASWaves Combination for evaluation of composite dispersion curves. The software can be downloaded at masw.hi.is, along with a user guide and sample data.

Recently, a specialized data acquisition tool (MASWaves DAQ) was added to the software collection of MASWaves. The new tool provides a direct connection between the data acquisition hardware (for current applications, a pair of NI USB-6218 multifunction I/O devices from National Instruments) and the processing tools. That is, the data acquisition software provides the analyst the opportunity of carrying out preliminary real-time analysis of the recorded data, e.g., for quick assessments of data quality in-situ. Hence, if required, the configuration of the survey profile or values of different measurement control parameters (such as the recording time) can be adapted to better suit the characteristics of the test site, as judged based on the results of the preliminary analysis.

The performance of the dispersion and inversion analysis tools of MASWaves has previously been validated by comparison with results obtained by other software packages and theoretical results presented in the literature (Ólafsdóttir et al. 2018a; 2018b). Furthermore, for verification of results obtained by a combined use of the data acquisition, dispersion and inversion analysis tools, MASW measurements were carried out at four well-characterized geotechnical research sites in Norway (Ólafsdóttir et al. 2019a). The results indicate that the V_S-profiles obtained by using MASWaves match those measured by invasive techniques (seismic cone penetration tests and seismic dilatometer tests), thus verifying the performance of the data acquisition, dispersion and inversion analysis tools. The MASWaves V_S-profiles

further compare well with results of MASW measurements conducted in independent field testing campaigns, as well as results of laboratory tests carried out on samples collected at the Norwegian research sites.

A graphical overview of the data acquisition process and the subsequent data processing and inversion, as it is conducted in this work, is provided in Figure 1. A brief description of each step is provided in the following subsections.

2.1.1 Field measurements

For data acquisition, twenty-four low-frequency geophones are lined up on the surface of the test site with equal spacing *dx* (Figure 1a). The geophones used in this work are of type GS-11D from Geospace Technologies and have a natural frequency of 4.5 Hz and a critical damping ratio of 0.5. A wave is generated by an impact load (in most cases a sledgehammer blow) that is applied at a distance x_1 from one end of the receiver spread and the wave propagation is recorded (Figure 1b). A preliminary analysis of the recorded data can be carried out within the environment of MASWaves DAQ. The data acquisition process is repeated a few times by using different measurement profile configurations, i.e. profiles with different values of x_1 and/or *dx*, while keeping the midpoint of the receiver spread fixed (Figure 1c). For the majority of the Icelandic test sites, survey profiles with a receiver spacing of 0.5 m, 1.0 m and/or 2.0 m and a source offset in the range of 3-30 m were used. On average, four to six multichannel records were acquired with each survey profile configuration.

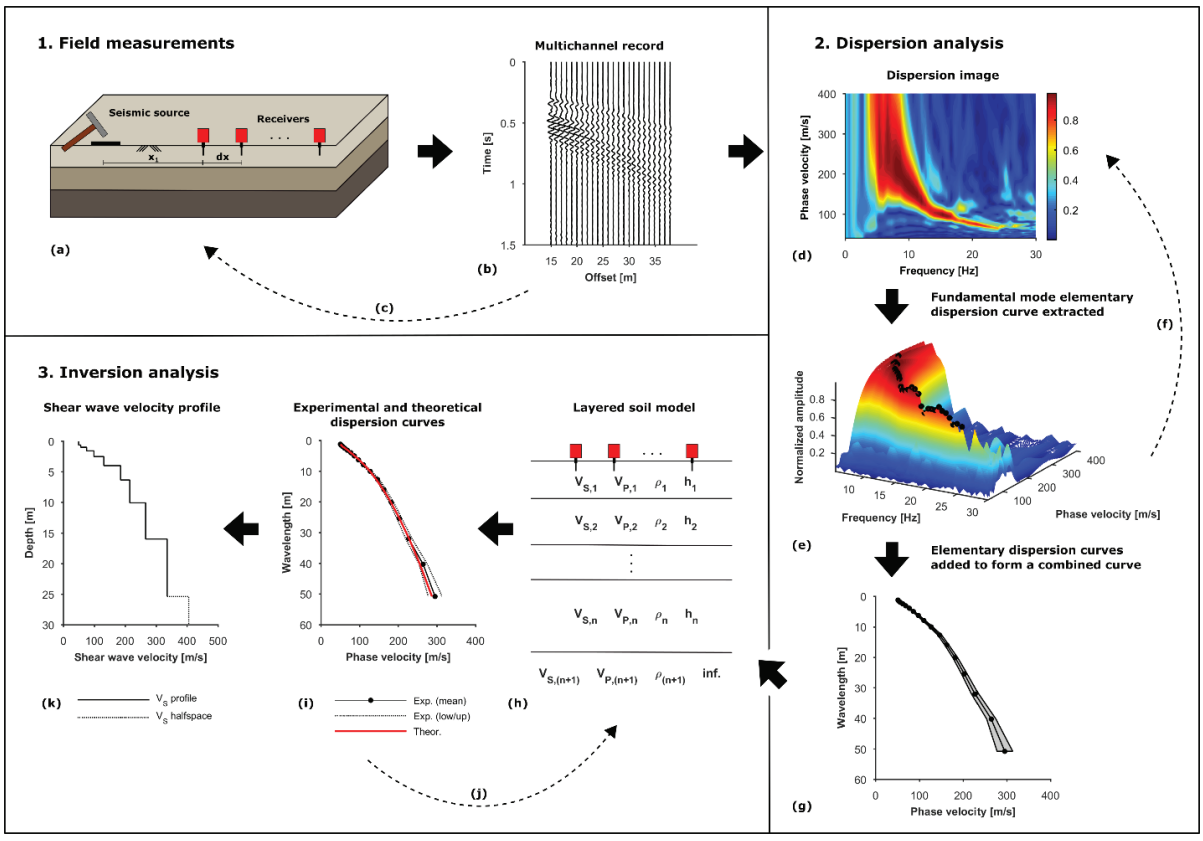

Figure 1. Application of the MASW method.

2.1.2 Dispersion analysis

The processing of the multichannel time series is carried out by using MASWaves Dispersion. A dispersion image (phase velocity spectrum) is obtained for each acquired record (Figure 1d) by the phase shift method (Park et al. 1998). The spectral high-amplitude bands display the dispersion characteristics of all types of waves contained in the recorded data and are used to identify the fundamental mode of the Rayleigh wave propagation (Figure 1e). In cases where the data quality is insufficient, stacking of several velocity spectra, prior to identification of experimental dispersion curves, can be of value.

A dispersion curve identified based on a single (stacked or unstacked) velocity spectrum is here referred to as an elementary dispersion curve. Each spectrum is processed separately (Figure 1f) and the resulting elementary curves combined within logarithmically spaced wavelength intervals (Figure 1g) using MASWaves Combination. Within each interval, the identified dispersion curve phase velocity values are added up and their arithmetic mean used as a point estimate of the phase velocity of the Rayleigh wave components belonging to the given wavelength range. The spread of the dispersion curve data points is represented by the standard deviation of the phase velocity values within each interval.

2.1.3 Inversion analysis

The inversion of the composite dispersion curve is conducted with MASWaves Inversion. The inversion is carried out based on the assumption that the underlying structure of the test site can be adequately described by a semi-infinite stratified soil model, where each layer is assumed to be flat and have homogeneous and isotropic properties. The thickness of the top-most soil layer and the depth to the top of the half-space are recommended to coincide with the approximate investigation depth range described by Eqs. (1) and (2), as well as any previous knowledge of the characteristics of the test site. The parameters used to describe the properties of each layer are shear wave velocity, compressional wave velocity (V_P) (or Poisson's ratio (ν)), mass density (ρ), and layer thickness (h) (see Figure 1h). A theoretical dispersion curve is computed with the stiffness matrix method (Kausel and Roësset 1981), based on a preliminary estimate of the soil model parameters, and compared to the experimental curve (Figure 1i). Subsequently, a Monte Carlo-based process is used to search for the V_S-profile (i.e. V_S and h for each layer) that provides 'the best fit' to the experimental data (Figure 1j). The profile that results in an acceptable fit, and is believed to realistically represent the characteristics of the test site, is taken as the result of the survey (Figure 1k). Upper and lower boundary V_S-profiles can be obtained by inverting the upper and lower boundary (mean ± standard deviation) experimental dispersion curves in a similar way. Alternatively, the inversion results can be presented as a set of V_S-profiles, those theoretical dispersion curves lie between the upper and lower boundary experimental curves.

3 MASW MEASUREMENTS IN ICELAND

Application of the MASW method in Iceland began in 2013. During the autumn of 2013, the first MASW surveys were carried out close to Arnarbæli on the bank of the river Ölfusá in South Iceland. Between 2014 and 2018 the MASW method was further applied at sixteen natural soil sites in South and North Iceland (Figure 2). The survey locations range from soft soil sites to sites characterized by cemented soil materials and soft rock. In addition, repeated field measurements have been conducted at the Arnarbæli site in order to confirm the repeatability of the analysis and the consistency of the results obtained by using the data acquisition, dispersion and inversion analysis tools of MASWaves.

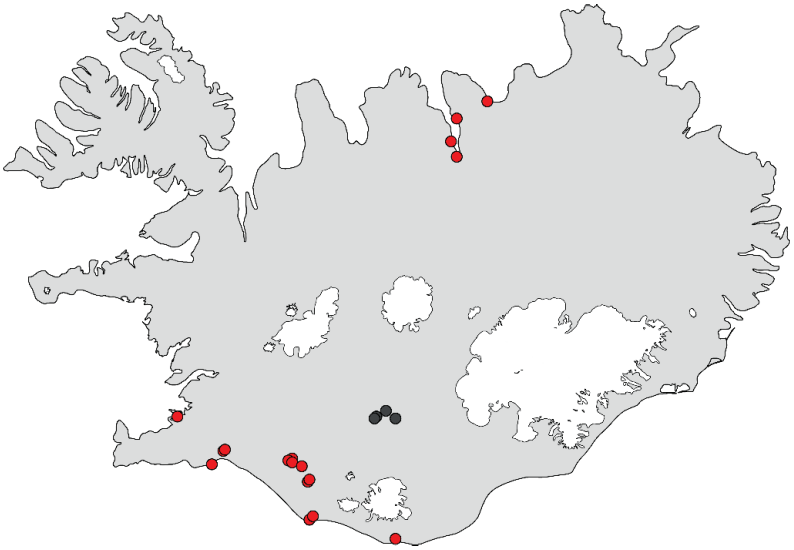

Figure 2. Sites in Iceland where MASW field data have been acquired. Natural soil sites are shown by red dots whereas man-made fillings (i.e., earth dam sites) are shown by black dots.

MASW surveys have also been conducted on the crests of three dams in Iceland's south central highlands; Sultartangi dam, Sporðalda dam and Sigalda dam. The Sultartangi and Sporðalda dams have a central core of moraine and/or loess, whereas the Sigalda dam is without a central core and has a frontal cladding of asphalt. The use of MASW for evaluation of the stiffness properties of the three dams is discussed by Ólafsdóttir et al. (2019b).

The V_S-profiles obtained for four of the natural soil sites and one of the earth dam sites are compared in Figure 3. The half-space V_S in each case is indicated by a dashed line. A brief description of the characteristic soil type at each site, along with its USCS (Unified Soil Classification System) classification, is provided in Table 1. The V_S-profiles shown in Figure 3 were selected such that they represented sites characterized by different soil types. That is, silty sand at the Akureyri airport site, well graded sand at Bakkafjara harbour, poorly graded sand at Miðalda few kilometers east of Þorlákshöfn, and cemented silty sand at the site located in the vicinity of the town Hella. The compacted rock-fill material used in the Sigalda dam is classified as well graded gravel. The investigation depth of the MASW surveys was in most cases in the range of 20-25 m, as estimated with Eq. (1). For further comparison of the estimated V_S-profiles, the average shear wave velocity ($\bar{V}_{S,d}$) of the upper-most d = [5,10,20,30] m at each site is provided in Table 1. The $\bar{V}_{S,d}$ velocity (m/s) was obtained as (CEN 2004)

$$\bar{V}_{S,d} = \frac{d}{\Sigma_{j=1}^{N}\left(\frac{h_j}{V_{S,j}}\right)} \tag{3}$$

where $V_{S,j}$ (m/s) and h_j (m) denote the shear wave velocity and thickness of the j-th layer, respectively, for a total of N layers down to depth d (m). In cases where the estimated V_S-profile goes down to a depth less than d, the profile is extrapolated using the half-space velocity down to d meters.

As shown in Figure 3, the well-compacted earth dam site has much more stiffness than the three natural sandy sites at Akureyri, Bakkafjara and Þorlákshöfn. Furthermore, the site close to Hella, which is characterized by cemented soil materials, shows even higher velocities, reaching

values above 760 m/s (i.e., engineering bedrock) at a depth of around 10 m.

In Eurocode 8, the European standard for design of structures in seismic zones (CEN 2004), construction sites are classified into five categories (ground types) based on the average V_S of the upper-most 30 m at the sites (Eq. (3) with d = 30 m). The ground type is further used to account for the effects of the local ground conditions on the seismic action and, hence, fundamental for determination of site-specific design spectra. The soil classification group of the natural test sites at Akureyri, Bakkafjara, Þorlákshöfn and Hella is provided in Table 1.

Table 1. Overview of site characteristics of four natural soil sites and one earth dam site where MASW measurements have been carried out. The soil classification is based on the Unified Soil Classification System (USCS). The values of the average shear wave velocity of the upper-most 5 m, 10 m, 20 m and 30 m at the sites are estimated by use of MASW. The Eurocode 8 ground type for the natural soil sites is further provided.

Site	**Year of MASW**	**Type**	**Soil**	**USCS group**	$\bar{V}_{S,5}$	$\bar{V}_{S,10}$	$\bar{V}_{S,20}$	$\bar{V}_{S,30}$	**EC8 ground type**
Akureyri airport	2015	Natural site	Holocene fluvial sand	SM	91	123	167	196	C
Bakkafjara harbour	2014	Natural site	Modern littoral sand	SW	142	174	224	258	C
Sand mine close to *Hella*	2015	Natural site	Late-glacial cemented Aeolian silty sand	-	284	339	478	588	B
Sigalda dam (*Sigöldustífla*)	2018	Earth dam	Well graded gravel	GW	224	278	346	387	-
Miðalda east of *Þorlákshöfn*	2015	Natural site	Alluvial sand	SP	166	174	197	221	C

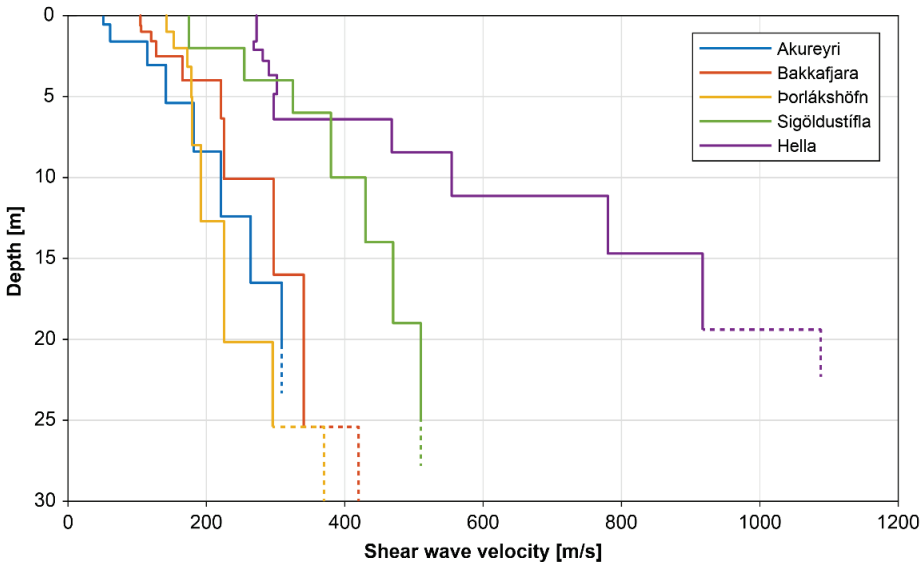

Figure 3. Comparison of shear wave velocity profiles obtained for four natural soil sites (Akureyri, Bakkafjara, Þorlákshöfn and Hella) and one earth dam site (Sigöldustífla).

3.1 Open database for MASW measurement results

The first version of an open database for storing processed MASW data has been made available on the project's webpage (masw.hi.is). As the database is under development, adjustments of the data structure and modifications of the user interface will be carried out as needed. Currently, the information stored for each test site consists of the following:

- *Site location*, including maps and GPS coordinates of MASW profile midpoints.
- *Brief site description*, including USCS classification (where available), estimated location of the groundwater table, estimated material mass density and other appropriate soil material parameters.
- *MASW profile configuration*, such as number and type of geophones and geophone layout.
- *Test results*, including experimental dispersion curves, estimated shear wave velocity profiles (as figures and tabulated values) and estimated values of the average shear wave velocity as a function of depth (as figures and tabulated values for selected depths).

4 SUMMARY

The shear wave velocity profile is a fundamental parameter in soil dynamics and geotechnical earthquake engineering. MASW is a non-invasive, fast, and low-cost seismic exploration method for evaluation of near-surface V_S-profiles. The use of MASW for characterization of Icelandic soil sites began in 2013 and MASWaves, an open source software for acquiring and analyzing MASW field data, has been under development for the past few years.

In this paper, the methodology used for acquiring and analyzing the multichannel surface wave records is reviewed, with emphasis on recent advances in both in-situ procedures and data analysis, and results of MASW measurements conducted at five natural and man-made sites are presented. The first version of an open database is further presented, where results of MASW measurements carried out at Icelandic sites can be viewed and shear wave velocity/stiffness profiles for different sites compared. The aim is to give engineers and researchers access to the data and allow utilization of the results for, e.g., evaluation of seismic hazard and liquefaction potential, and for defining site-specific earthquake loading according to EC8.

5 ACKNOWLEDGEMENTS

The project is supported by grants from the University of Iceland Research Fund, the Icelandic Road and Coastal Administration and the Energy Research Fund of the National Power Company of Iceland.

6 REFERENCES

Bessason, B., Erlingsson, S. 2011. Shear wave velocity in surface sediments. *Jökull* **61**, 51-64.

CEN. 2004. *EN1998-1:2004. Eurocode 8: Design of structures for earthquake resistance. Part 1: General rules, seismic actions and rules for buildings*, European Committee for Standardization, Brussels, Belgium.

Dikmen, Ü., Arısoy, M.Ö., Akkaya, İ. 2010. Offset and linear spread geometry in the MASW method. *Journal of Geophysics and Engineering* **7**(2), 211-222.

Foti, S., Lai, C.G., Rix, G.J., Strobbia, C. 2015. *Surface wave methods for near-surface site characterization*, CRC Press, Taylor & Francis Group, Boca Raton, FL.

Gabriels, P., Snieder, R., Nolet, G. 1987. In situ measurements of shear-wave velocity in sediments with higher-mode Rayleigh waves. *Geophysical Prospecting* **35**(2), 187-196.

Garofalo, F., Foti, S., Hollender, F., Bard, P.-Y., Cornou, C., Cox, B.R., et al. 2016.

InterPACIFIC project: Comparison of invasive and non-invasive methods for seismic site characterization. Part I: Intra-comparison of surface wave methods. *Soil Dynamics and Earthquake Engineering* **82**, 222-240.

Ivanov, J., Miller, R.D., Tsoflias, G. 2008. Some practical aspects of MASW analysis and processing. *Proceedings of the 21st Symposium on the Application of Geophysics to Engineering and Environmental Problems* (Ed. Kaufmann, R.), 1186-1198. Environmental and Engineering Geophysical Society, Philadelphia, PA.

Kausel, E., Roësset, J.M. 1981. Stiffness matrices for layered soils. *Bulletin of the Seismological Society of America* **71**(6), 1743-1761.

Kramer, S.L. 1996. *Geotechnical earthquake engineering*, Prentice-Hall, Inc., Upper Saddle River, NJ.

Ólafsdóttir, E.Á., Erlingsson, S., Bessason, B. 2016. Effects of measurement profile configuration on estimation of stiffness profiles of loose post glacial sites using MASW. *Proceedings of the 17th Nordic Geotechnical Meeting*, 327-336. Icelandic Geotechnical Society, Reykjavík, Iceland.

Ólafsdóttir, E.Á., Erlingsson, S., Bessason, B. 2018a. Tool for analysis of multichannel analysis of surface waves (MASW) field data and evaluation of shear wave velocity profiles of soils. *Canadian Geotechnical Journal* **55**(2), 217-233.

Ólafsdóttir, E.Á., Erlingsson, S., Bessason, B. 2018b. Open software for analysis of MASW data. *Proceedings of the 16th European Conference on Earthquake Engineering*.

Ólafsdóttir, E.Á., Bessason, B., Erlingsson, S. 2018c. Combination of dispersion curves from MASW measurements. *Soil Dynamics and Earthquake Engineering* **113**, 473-487.

Ólafsdóttir, E.Á., Erlingsson, S. Bessason, B. 2019a. Benchmarking of an open source MASW software using data from four GeoTest sites in Norway. *Proceedings of the XVII European Conference on Soil Mechanics and Geotechnical Engineering*.

Ólafsdóttir, E.Á., Bessason, B., Erlingsson, S. 2019b. Stiffness profiles of earth dams based on the MASW technique. *Proceedings of the XVII European Conference on Soil Mechanics and Geotechnical Engineering*.

Park, C.B., Carnevale, M. 2010. Optimum MASW survey–revisit after a decade of use. *Proceedings of GeoFlorida 2010: Advances in Analysis, Modeling & Design* (Eds. Fratta, D.O., Puppala, A.J., Muhunthan, B.), 1303-1312. American Society of Civil Engineers, Reston, VA.

Park, C.B., Miller, R.D., Xia, J. 1998. Imaging dispersion curves of surface waves on multi-channel record. *SEG Technical Program. Expanded Abstracts of the Society of Exploration Geophysicists International Exposition and 68th Annual Meeting*, 1377-1380. Society of Exploration Geophysicists, Tulsa, OK.

Park, C.B., Miller, R.D., Xia, J. 1999. Multichannel analysis of surface waves. *Geophysics* **64**(3), 800-808.

Silver, M.L., Björnsson, B.J., Kiefer, T., Sharma, M., Kotsopoulou, E., Thomas, P. 1986. *Evaluation of the seismic safety of embankment structures of the Thjorsa river basin development in Iceland, final report, Vol. 1-3*. Marshall Silver and Associates Ltd., Chicago, IL.

Paper VIII

Stiffness profiles of earth dams based on the MASW technique

Elín Ásta Ólafsdóttir, Bjarni Bessason & Sigurður Erlingsson

Ólafsdóttir, E.Á., Bessason, B., & Erlingsson, S. (2019). Stiffness profiles of earth dams based on the MASW technique. In *Proceedings of the 17th European Conference on Soil Mechanics and Geotechnical Engineering*, 1–6 September 2019, Reykjavik, Iceland. doi:10.32075/17ECSMGE-2019-0788.

Proceedings of the XVII ECSMGE-2019
Geotechnical Engineering foundation of the future
ISBN 978-9935-9436-1-3

doi: 10.32075/17ECSMGE-2019-0788

XVII European Conference
ECSMGE 2019
Reykjavík
on Soil Mechanics
and Geotechnical Engineering

Stiffness profiles of earth dams based on the MASW technique

Profils de rigidité des barrages en terre basés sur la technique MASW

E.Á. Ólafsdóttir
Faculty of Civil and Environmental Engineering, University of Iceland, Reykjavík, Iceland

B. Bessason, S. Erlingsson
Faculty of Civil and Environmental Engineering, University of Iceland, Reykjavík, Iceland

ABSTRACT: Multichannel Analysis of Surface Waves (MASW) is a non-invasive seismic exploration method for evaluation of near-surface stiffness profiles. In recent years, MASW has been applied at a number of natural soil sites in Iceland. This study aims at extending its use to the analysis of earth dams. This paper discusses the application of MASW for characterization of the stiffness properties of three dams in the catchment area of the rivers Þjórsá and Tungnaá in Iceland's south central highlands; Sigalda dam, Sporðalda dam and Sultartangi dam. The experimentally evaluated stiffness profiles are compared with profiles obtained by empirical methods and, at the Sultartangi site, results of existing in-situ measurements of shear wave velocity. Overall, the stiffness profiles obtained by MASW are consistent with the empirically evaluated profiles and compare well with the available experimental results. In practical terms, the results of the study indicate that, if appropriately conducted, the MASW method can serve as a valuable tool to evaluate the stiffness properties of earth dams in Iceland.

RÉSUMÉ: L'analyse des ondes de surface (MASW) est une méthode d'exploration sismique permettant d'évaluer les profils de rigidité proche de la surface. Ces dernières années, la technique MASW a été appliqué sur plusieurs sites de sols naturels en Islande. Cette étude vise à étendre son utilisation aux barrages en terre. L'application de MASW pour la caractérisation des propriétés de rigidité de trois barrages situés dans les hauts plateaux du centre-sud de l'Islande, les barrages Sigalda, Sporðalda et Sultartangi, est examinée. Les profils de rigidité évalués expérimentalement sont comparés aux profils obtenus par des méthodes empiriques et, sur le site de Sultartangi, aux résultats de mesures in situ existantes de la vitesse des ondes de cisaillement. Les profils de rigidité obtenus par MASW sont cohérents avec les profils de rigidité évalués de manière empirique et se comparent bien aux résultats expérimentaux disponibles. En termes pratiques, les résultats de l'étude indiquent que, si elle est correctement menée, la méthode MASW peut constituer un outil précieux pour évaluer les propriétés de rigidité des barrages en terre en Islande.

Keywords: Earth dams; surface wave analysis; Multichannel Analysis of Surface Waves (MASW); small-strain shear stiffness; shear wave velocity

1 INTRODUCTION

Hydropower is the primary source of electricity in Iceland with more than 70% of the total production in 2017 being hydroelectricity (Orkustofnun 2018). Earth- and/or rock-filled dams form an indispensable part of the Icelandic hydropower system. Due to the volcanic activity in Iceland and a long history of frequent glacial outburst floods with fast build-up of sediments,

the fill materials used in these dams are quite different from the materials used in other countries. Seismic hazard is moderate to high in Iceland due to the Mid-Atlantic plate boundary that crosses the island. Hence, the dams in the Icelandic hydropower system can be exposed to high earthquake loads and must be designed to withstand large earthquakes without developing excessive deformations.

The small-strain shear stiffness is a key parameter for dynamic analysis of earth dams. It is further directly proportional to the shear wave velocity of the soil material (Kramer 1996)

$$G_{max} = \rho \cdot (V_S)^2 \quad (1)$$

where G_{max} (Pa) is small-strain shear stiffness, V_S (m/s) is shear wave velocity and ρ (kg/m^3) is material density.

Utilization of experimentally measured values of shear wave velocity is generally considered the most reliable way of assessing the in-situ value of G_{max} (Kramer 1996). Due to potential seepage hazard associated with borehole drilling, as well as excessive cost, the use of invasive methods for evaluating the V_S-profiles of earth dams is limited (Park and Kishida 2018). Non-invasive geophysical techniques can be an appealing choice as they are low-cost and neither require heavy machinery nor risk damaging the dam structure. In cases where measurements of shear wave velocity are not available, empirical formulas, e.g. in the form of Eq. (2), relating the small-strain shear stiffness to other material properties can be used

$$G_{max} = K \cdot (\sigma'_m)^n \quad (2)$$

where σ'_m (kPa) is the effective confining pressure and K, n are material dependent correlation parameters (Kramer 1996).

Multichannel Analysis of Surface Waves (MASW) is a non-invasive seismic exploration method for evaluation of near-surface shear wave velocity profiles. The use of MASW to study the dynamic properties of earthen dams and levees has been reported by several researchers (e.g. Karl et al. 2011, Cardarelli et al. 2014, Ha 2017, Rahimi et al. 2018, Park and Kishida 2018). In recent years, MASW has been applied at a number of natural soil sites in Iceland (Ólafsdóttir et al. 2019a, 2019b). This study aims at extending its use to the analysis of Icelandic earth dam structures. In order to gain practical experience in applying the MASW method to study the stiffness properties of earth- and rock-filled dams, in-situ measurements were conducted on the crests of three dams in Iceland; Sigalda dam, Sporðalda dam and Sultartangi dam. The Sporðalda and Sultartangi dams are rock-filled dams with a central core of moraine and/or loess (Silver et al. 1986), whereas the Sigalda dam has an impervious frontal facing of asphalt (Thorlaksson et al. 1978). The experimentally evaluated stiffness profiles were compared to profiles obtained by use of empirical methods in order to find appropriate formulas and parameter sets for empirical assessments of the stiffness properties of typical Icelandic earth dams. At the Sultartangi site, it was further possible to compare the results of the MASW measurements to the results of a SASW survey previously conducted at the site.

2 TEST SITES AND SURVEY PROCEDURE

The three dams studied in this work are located in the catchment area of the rivers Þjórsá and Tungnaá in Iceland's south central highlands (Figure 1) and are all part of the hydropower system operated the National Power Company of Iceland (Landsvirkjun). At each of the sites, an array of 24 vertical geophones with a natural frequency of 4.5 Hz was used for field measurements. The data acquisition and analysis were carried out by use of the open-source software MASWaves (Ólafsdóttir et al. 2018a, see also masw.hi.is).

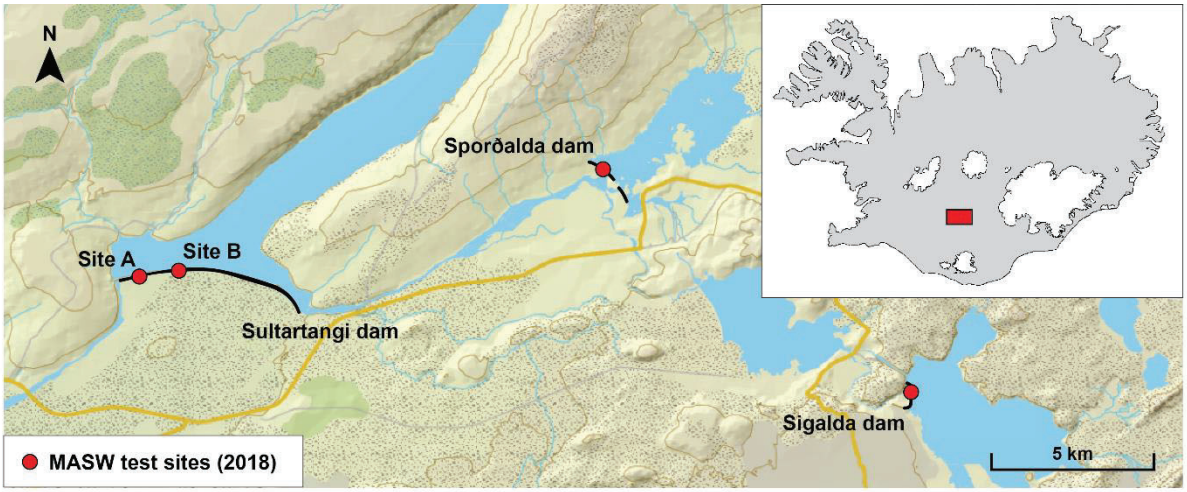

Figure 1. Location of MASW test sites at Sigalda dam, Sporðalda dam and Sultartangi dam. [The map is based on data from the National Land Survey of Iceland.]

At each of the four test locations (Figure 1), the seismic data were acquired along the dam crest with the survey profile aligned approximately along its middle line. For the Sporðalda and Sultartangi sites, the retrieved V_S-profiles are expected to be primarily representative of the core zone of the dams. However, the presence of the fill material may affect the results of the MASW survey, resulting in some kind of a composite V_S-profile for the two materials. As pointed out by Park and Kishida (2018), determination of the stiffness of the core material in an earth-core rock-filled dam can be difficult by means of a conventional MASW survey conducted on the dam crest. Due to the geometry of the dam, the acquired surface wave data might contain a combination of the response of the core and shell materials. A comparison of V_S-profiles obtained by MASW and downhole surveys for earth-core rock-filled dams in Korea, revealed that the V_S values obtained by MASW exceeded those from the borehole measurements at depths greater than 15–25 m, likely due to this effect (Park and Kishida 2018). Another recent survey on a Korean earth-core rock-filled dam, however, did not report such difference between results of MASW and borehole measurements (Ha 2017).

2.1 Sigalda dam

The Sigalda dam is a 0.93 km long asphalt face rock-fill dam, founded on moberg and postglacial lava flows (Thorlaksson et al. 1978). The dam was built in the 1970s as a part of the Sigalda hydropower scheme and forms the 14 km^2 Krókslón reservoir (Gunnarsdóttir 2016). The maximum height of the embankment is 40 m (Thorlaksson et al. 1978). The fill material of the dam consists of reworked moberg, breccia, tuff and sand, and is classified as well-graded gravel (GW) according to the Unified Soil Classification System (USCS). The unit weight of the fill material has been evaluated as 20.6 kN/m^3 and its friction angle as 38° (Thorlaksson et al. 1978, Silver et al. 1986). Due to the presence of the impervious upstream asphalt cladding, the fill material is assumed to be unsaturated.

2.2 Sporðalda dam

The Sporðalda dam was built between 2011 and 2013 as a part of the Búðarháls power station project and forms the 7 km^2 Sporðalda reservoir (Gunnarsdóttir 2016). The Sporðalda dam is an earth- and rock-fill dam with a central core of moraine with a unit weight of around 23 kN/m^3. The dam consists of two separate parts. The

north-western part is 1105 m long and 28.0 m high at its highest cross section, whereas the dam's south-eastern part is 315 m long and with a maximum height of 27.6 m. The MASW survey was conducted on the crest of the north-western part of the dam (Figure 1). The height of the embankment within the investigated section is around 25 m.

2.3 Sultartangi dam

The Sultartangi dam is the longest dam in Iceland with a total length of 6.1 km. It was built between 1982 and 1984 (Gunnarsdóttir 2016). In the late 1990s, the crest of the dam was raised by a meter in conjunction with the construction of the Sultartangi power station. After completion of the second construction phase, the maximum height of the dam is 23 m (Landsvirkjun 2011).

The Sultartangi dam is an earth- and rock-fill dam with a central core of moraine and loess. MASW field measurements were conducted at two locations on the crest of the western part of the dam, where the height of the dam is the most and its central core is primarily made of loess. The unit weight of the core material has been evaluated as 16.9 kN/m^3 and the saturated unit weight as 18.1 kN/m^3 (Silver et al. 1986). The location of the two test sites on the crest of the Sultartangi dam is shown in Figure 1. The distance between the survey locations (measured midpoint-to-midpoint) is around 1.1 km.

3 MASW MEASUREMENTS

The data acquisition was conducted using two to three survey profiles with the same midpoint but different lengths, 11.5 m, 23 m and/or 46 m. A 6.3 kg sledgehammer, struck on a 15 cm-diameter metallic base plate, was used as an impact source with shots taken at offsets in the range of 3 m to 10 m from one end of the receiver spread. Furthermore, for each measurement profile configuration, four to five multichannel records were acquired. The records were later stacked for enhanced data quality, prior to identification of experimental dispersion curves and commencement of the inversion analysis (Ólafsdóttir et al. 2018a, 2018b).

3.1 Measurements at Sigalda dam

The results of the MASW measurements conducted on the crest of the Sigalda dam are presented in Figure 2. Figures 2a-c show stacked dispersion images obtained from data acquired by using receiver spreads of different lengths; i.e. 11.5 m, 23 m and 46 m. By lengthening the receiver spread, the high-amplitude peaks appeared sharper and better separation of overtones was observed. This is in agreement with trends observed in data gathered at various natural test sites in Iceland (Ólafsdóttir et al. 2018b). Below a frequency of approximately 30 Hz, the high-amplitude band is believed to correspond to the fundamental mode of the Rayleigh wave propagation. However, between 30 Hz and 40 Hz, where the spectral images in Figures 2a, b show an abrupt upward bend, the peak energy may be jumping to a higher mode or propagating at an effective mode. This suspicion is strengthened by the dispersion image in Figure 2c, where the high-amplitude band splits into two separate parts at a frequency of around 35 Hz.

The estimated V_S-profile for the Sigalda dam site is presented in Figure 2d. The corresponding theoretical dispersion curve is compared to the observed dispersion characteristics in Figures 2a-c. For inversion of the experimental data, a constant Poisson's ratio of 0.3 was assumed for the fill material. Due to the presence of the asphalt cladding on the upstream side of the dam, the inversion was conducted based on the assumption that the fill material was unsaturated.

Overall, the results presented in Figure 2 indicate a relatively gradual increase in V_S (stiffness) down to the maximum investigated depth of 25 m. The results of the survey are further presented in the form of $\bar{V}_{S,z}$ in Figure 2e,

$$\bar{V}_{S,z} = \frac{z}{\sum_{j=1}^{N}\left(\frac{h_j}{V_{S,j}}\right)} \quad (3)$$

where $\bar{V}_{S,z}$ (m/s) is the average shear wave velocity of the uppermost z meters, and $V_{S,j}$ (m/s) and h_j (m) denote the shear wave velocity and thickness of the j-th layer for a total of N layers down to depth z (CEN 2004).

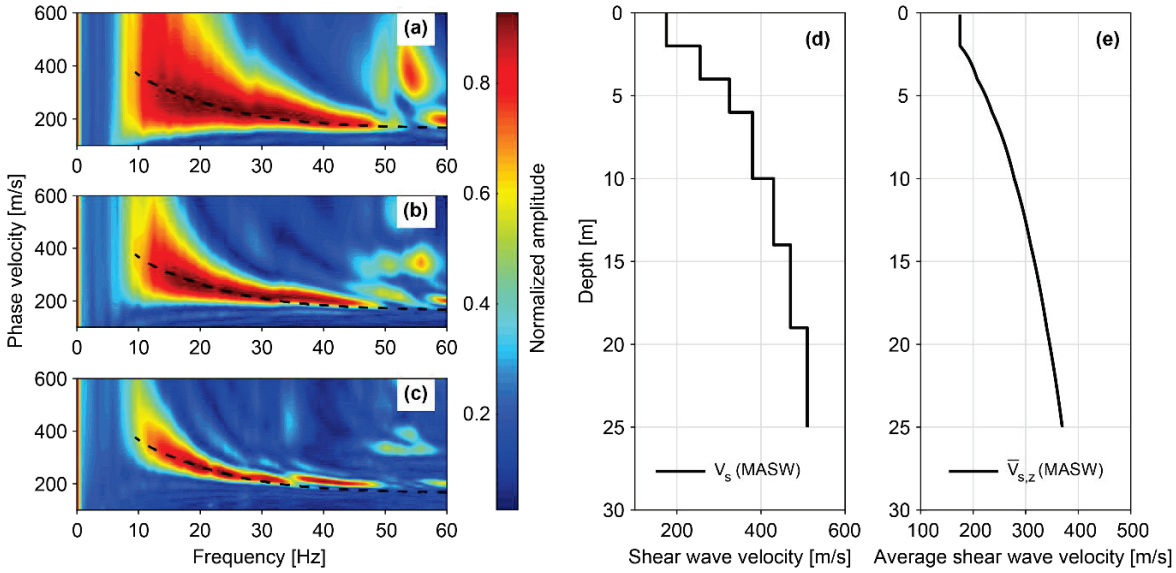

Figure 2. Results of MASW surveys at the crest of Sigalda dam. Dispersion images obtained by profiles of length (a) 11.5 m, (b) 23 m and (c) 46 m. Estimated (d) shear wave velocity (V_S) and (e) average V_S ($\bar{V}_{S,z}$) profiles for the Sigalda site. The dispersion curve corresponding to the V_S-profile in (d) is shown by a dashed line in (a)-(c).

3.2 Measurements at Sporðalda dam

The results of the MASW measurements conducted on the crest of the Sporðalda dam are illustrated in Figure 3. Figures 3a, b show stacked dispersion spectra of records acquired using receiver spreads of length 11.5 m and 23 m, respectively. As compared to the dispersion images obtained for the Sigalda dam site (Figures 2a-c), the spectra presented in Figure 3 do not display an equally continuous peak energy band. The fact that the Sporðalda dam has a central core, whereas the Sigalda dam is comprised of a relatively uniform soil material, is considered likely to contribute to this observed difference.

The shear wave velocity profile estimated for the Sporðalda dam site is shown in Figure 3c. The corresponding theoretical dispersion curve is compared to the experimental data in Figures 3a, b. The $\bar{V}_{S,z}$-profile for the site [Eq. (3)], is further visualized in Figure 3d.

For inversion of experimental Rayleigh wave dispersion curves, an estimated location of the groundwater table at the survey site is required. The depth to groundwater varies greatly within an earth dam structure. Furthermore, the level of groundwater is correlated to, e.g., the water level in the reservoir that the dam forms. Hence, considering a survey carried out on the crest of an earth dam, obtaining a clear-cut estimate of the location of the groundwater table is impossible. For inversion of the dispersion data acquired at the crest of the Sporðalda dam, the groundwater table within its central core was set at an average depth of approximately 10 m, i.e. at around 2/5 of the height of the dam as measured from the top of the structure. Furthermore, a Poisson's ratio of 0.3 was estimated for the soil layers above the

assumed groundwater table. For comparison purposes, the inversion process was repeated, assuming the same layer structure as shown in Figure 3c, based on the following two assumptions; (i) the average groundwater table is located at a depth of approximately 2 m, and (ii) the dam is unsaturated. Raising the groundwater table lead to a decrease in estimated shear wave velocities, below the depth of 2 m, in the order of 5-10%. Increasing the depth to groundwater did not have a significant effect on the estimated shear wave velocity values.

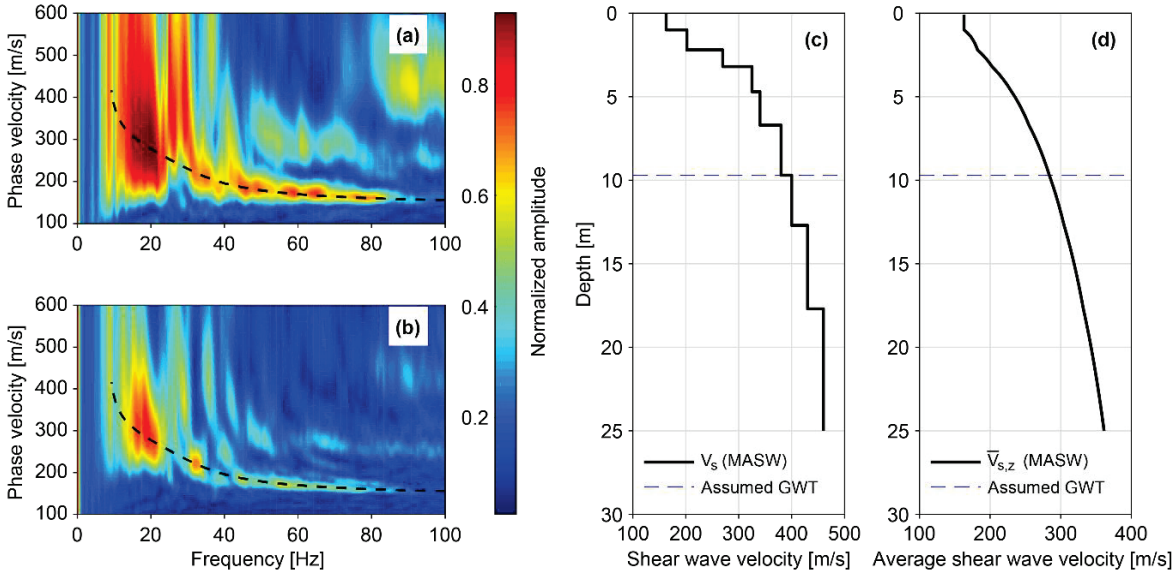

Figure 3. Results of MASW measurements conducted at the crest of the Sporðalda dam. Dispersion images obtained by using survey profiles of length (a) 11.5 m and (b) 23 m. Estimated (c) shear wave velocity (V_S) and (d) average shear wave velocity ($\bar{V}_{S,z}$) profiles for the Sporðalda dam site. The theoretical dispersion curve corresponding to the V_S-profile in (c) is shown by a black dashed line in (a) and (b). The assumed location of the groundwater table (GWT) within the central core of the dam is shown using a blue dashed line in (c) and (d).

3.3 Measurements at Sultartangi dam

MASW surveys were carried out at two locations on the crest of the Sultartangi dam, here referred to as 'site A' and 'site B' (Figure 1). The results of the MASW measurements at the two sites are presented in Figure 4. Figures 4a, b show stacked dispersion images obtained from data acquired at site A using receiver spreads of length 11.5 m and 23 m, respectively. Furthermore, the theoretical dispersion curve, corresponding to the estimated V_S-profile for site A (Figure 4c), is compared to the experimental spectra in Figures 4a, b. The dispersion images obtained for Sultartangi site B indicated comparable dispersion characteristics. The V_S-profile for site B is shown in Figure 4c using a red solid line. The $\bar{V}_{S,z}$-profiles for the two Sultartangi test sites, obtained by Eq. (3), are further compared in Figure 4d.

For analysis of the surface wave records acquired on the crest of the Sultartangi dam, the average depth to groundwater was estimated as 9 m (around 2/5 of the height of the structure as measured from its top). As observed for the Sporðalda dam test site, raising the assumed groundwater table to 2 m below the crest of the dam resulted in a decrease in estimated shear wave velocity values, below 2 m depth, of the order of 5-10%. The effects of lowering the groundwater table (i.e. below 9 m) were insignificant.

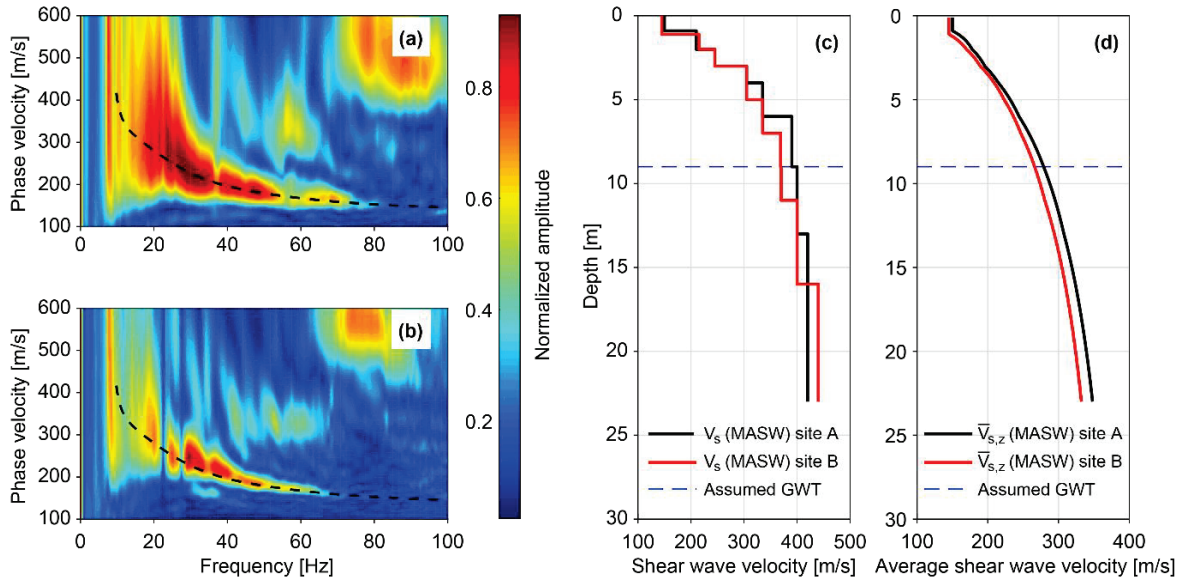

Figure 4. Results of MASW measurements conducted at two locations on the crest of the Sultartangi dam (site A and site B). Dispersion images obtained at Sultartangi site A by using survey profiles of length (a) 11.5 m and (b) 23 m. Estimated (c) shear wave velocity (V_S) and (d) average shear wave velocity ($\bar{V}_{S,z}$) profiles for the two Sultartangi dam test sites. The theoretical dispersion curve corresponding to the V_S-profile for site A is shown using a black dashed line in (a) and (b). The assumed location of the groundwater table (GWT) within the central core of the dam is shown using a blue dashed line in (c) and (d).

4 COMPARISON

Substantial research has been carried out to develop and evaluate empirical correlations between the small-strain shear stiffness (G_{max}) of soil and other material parameters, most importantly the effective confining pressure (σ'_m) and the void ratio (e). A common feature of such correlations is that G_{max} is assumed to be proportional to the square root of σ'_m (Kramer 1996), i.e. that the stress exponent in Eq. (2) is taken as $n = 0.5$.

The model of Seed and Idriss [Eq. (4)] is a well-known correlation for predicting the small-strain shear modulus of granular soils,

$$G_{max} = 1000 \cdot K_{2,max}\sqrt{\sigma'_m} \qquad (4)$$

where $K_{2,max}$ (kPa$^{0.5}$) is an empirical coefficient (Gazetas 1991, Kramer 1996). For evaluation of σ'_m, the unit weight (γ and/or γ_{sat}) and the friction angle (ϕ') of the material are required. The effects of the void ratio are taken into account by the parameter $K_{2,max}$. Suggested values of $K_{2,max}$ for several groups of granular soils (Gazetas 1991) are provided in Table 1.

Table 1. Suggested values of the coefficient $K_{2,max}$ in Eq. (4) for granular soil materials.

Soil type	$K_{2,max}$ [(kPa)$^{0.5}$]
Loose sand	8
Dense sand	12
Very dense sand	16
Very dense sand and gravel	25-40

Figure 5 shows the small-strain shear stiffness profiles for the Sigalda dam, Sporðalda dam and Sultartangi dam test sites, respectively, as obtained from the results of the MASW surveys. Figure 5 further compares empirically estimated stiffness profiles for the three sites to the

measured (MASW) profiles. The empirical profiles are obtained from the correlation of Seed and Idriss [Eq. (4)] using several values of the parameter $K_{2,max}$ within the range recommended for very dense sand and gravel (Table 1). For computation of the empirical profiles, a friction angle of 40° was assumed for the Sporðalda and Sultartangi sites. For simplification of the modelling, the material parameters were assumed to be independent of depth.

The results presented in Figure 5 indicate that the experimentally evaluated small-strain shear stiffness profiles can in general be fitted adequately well with empirical curves that assume the small-strain stiffness to be directly proportional to the square-root of the effective confining pressure ($\sqrt{\sigma'_m}$). A value of $K_{2,max}$ in the range of 30-35 seems to provide the best fit between the experimental and empirical stiffness profiles for the Sigalda and Sporðalda dams. However, for the two test sites on the crest of the Sultartangi dam (where the central core was primarily made of loess), a slightly lower value of $K_{2,max}$, or between 25-30, appears to provide the closest match between the experimental and empirical results.

4.1 Comparison of MASW and SASW measurement results

Spectral Analysis of Surface Waves (SASW) measurements were conducted on the crest of the Sultartangi dam in 1984 (Silver et al. 1986). Figure 6a presents a comparison of the shear wave velocity profiles obtained as a result of the 1984 SASW measurements and the 2018 MASW measurements. As the layer thicknesses of the three soil layer models shown in Figure 6a (i.e. MASW Sultartangi dam - site A, MASW Sultartangi dam - site B and SASW Sultartangi) differ, the estimated shear wave velocity values are further compared in terms of the $\bar{V}_{S,z}$-profiles [Eq. (3)] for the sites in Figure 6b.

In general, the SASW shear wave velocity profile agrees well with the profiles estimated for the Sultartangi dam test sites by using the MASW method. The results of the SASW survey predict somewhat higher values of V_S for the upper-most soil layers. However, below a depth of 2-3 m, the results of the SASW measurements indicate a slightly less stiff soil profile than the MASW survey, particularly at site A.

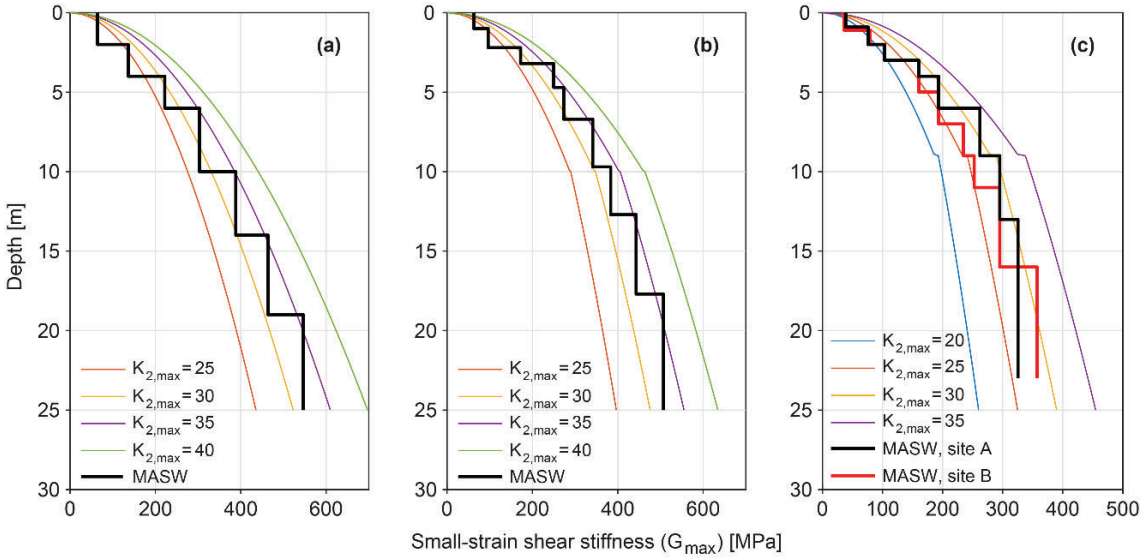

Figure 5. Comparison of empirical and experimental stiffness profiles for the (a) Sigalda dam site, (b) Sporðalda dam site and (c) Sultartangi dam sites. The empirical profiles are obtained by to the model of Seed and Idriss.

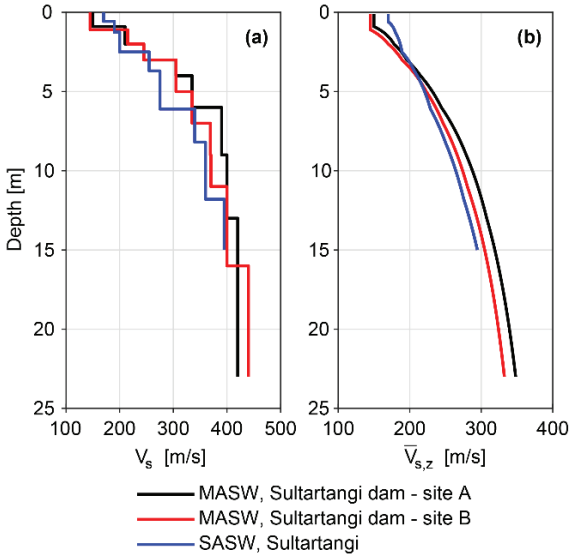

Figure 6. Comparison of (a) shear wave velocity (V_S) profiles and (b) average shear wave velocity ($\bar{V}_{S,z}$) profiles obtained at the crest of the Sultartangi dam by use of the SASW and MASW methods.

5 CONCLUSIONS

In this study, the surface wave analysis method MASW was successfully applied to evaluate the near-surface shear wave velocity/stiffness profiles of three dams in Iceland's south central highlands; Sigalda dam, Sporðalda dam and Sultartangi dam, with measurements conducted at one or two locations on the crest of each dam. The experimentally evaluated stiffness profiles were compared with profiles obtained by empirical methods and, at the Sultartangi dam site, results of existing in-situ measurements of shear wave velocity. Overall, the stiffness profiles obtained by MASW were consistent with the empirically evaluated profiles and compared well with the available experimental results. Particularly, the correlation of Seed and Idriss [Eq. (4)] with $K_{2,max}$ in the range of 25-35, depending on the type of soil material used for construction of the dam, seems to provide a good fit between the experimental and empirical profiles.

The small-strain shear stiffness is a fundamental parameter required for dynamic analysis of earth dams. Direct measurements of shear wave velocity are usually considered the most reliable way of assessing the in-situ value of G_{max}. However, at sites where measurements of V_S are not available, the use of empirical correlations, relating G_{max} to other material properties, can provide valuable estimations. Many such correlations have been developed in the past, utilizing field data collected in different parts of the world. Nonetheless, due to the unique characteristics of Icelandic soils, existing models should be evaluated against results of in-situ measurements prior to their use.

In practical terms, the results of the study indicate that, if appropriately conducted, the MASW method can serve as a valuable tool to evaluate the stiffness properties of earth dams in Iceland. At sites where in-situ values of V_S have not been obtained, the correlation of Seed and Idriss can be considered as a possible alternative to field measurements. However, comparison of experimentally and empirically estimated stiffness profiles from other dam sites is considered necessary for further verifying its applicability, and for making specific recommendations regarding appropriate values of the parameter $K_{2,max}$.

6 ACKNOWLEDGEMENTS

The project is supported by grants from the University of Iceland Research Fund, the Icelandic Road and Coastal Administration and the Energy Research Fund of the National Power Company of Iceland.

7 REFERENCES

Cardarelli, E., Cercato, M., De Donno, G. 2014. Characterization of an earth-filled dam through the combined use of electrical resistivity tomography, P- and SH-wave

seismic tomography and surface wave data. *Journal of Applied Geophysics* **106**, 87–95.

CEN. 2004. *EN1998-1:2004. Eurocode 8: Design of structures for earthquake resistance. Part 1: General rules, seismic actions and rules for buildings*, European Committee for Standardization, Brussels, Belgium.

Foti, S., Lai, C.G., Rix, G.J., Strobbia, C. 2015. *Surface wave methods for near-surface site characterization*, CRC Press, Taylor & Francis Group, Boca Raton, FL.

Gazetas, G. 1991. Foundation Vibrations. *Foundation engineering handbook, 2nd edition* (Ed. Fang, H.-Y.), 553–593. Van Nostrand Reinhold, New York, NY.

Gunnarsdóttir, H. 2016. *LV-2016-003*: *Virkjanir og veitur á Þjórsár- og Tungnaársvæði. Framkvæmdasaga 1965 til 2015* [in Icelandic], Landsvirkjun, Iceland. Retrieved from: http://gogn.lv.is/files/2016/2016-003.pdf.

Ha, I.-S. 2017. Comparison of shear wave velocities evaluated in the core zone of an existing fill dam by field and laboratory tests. *Soil Dynamics and Earthquake Engineering* **100**, 276–285.

Karl, L., Fechner, T., Schevenels, M., François, S., Degrande, G. 2011. Geotechnical characterization of a river dyke by surface waves. *Near Surface Geophysics* **9**(6), 515–527.

Kramer, S.L. 1996. *Geotechnical Earthquake Engineering*, Prentice-Hall, Inc., Upper Saddle River, NJ.

Landsvirkjun. 2011. *Aflstöðvar og orkuvinnsla* [in Icelandic]. Landsvirkjun, Iceland. Retrieved from: http://gogn.lv.is/files/2011/Aflstodvar_og_orkuvinnsla.pdf.

Ólafsdóttir, E.Á., Erlingsson, S. Bessason, B. 2018a. Tool for analysis of multichannel analysis of surface waves (MASW) field data and evaluation of shear wave velocity profiles of soils. *Canadian Geotechnical Journal* **55**(2), 217–233.

Ólafsdóttir, E.Á., Bessason, B., Erlingsson, S. 2018b. Combination of dispersion curves from MASW measurements. *Soil Dynamics and Earthquake Engineering* **113**, 473–487.

Ólafsdóttir, E.Á., Bessason, B., Erlingsson, S. 2019a. Application of MASW in the South Iceland Seismic Zone. In *Proceedings of the International Conference on Earthquake Engineering and Structural Dynamics, Geotechnical, Geological and Earthquake Engineering 47* (Eds. Rupakhety, R., Ólafsson, S., Bessason, B.), 53–66. Springer, Cham, Switzerland.

Ólafsdóttir, E.Á., Erlingsson, S., Bessason, B. 2019b. Open source MASW software and results from Icelandic soil sites. *Proceedings of the XVII European Conference on Soil Mechanics and Geotechnical Engineering.*

Orkustofnun. 2018. *OS-2018-T006-01: Installed capacity and electricity production in Icelandic power stations in 2017*. Retrieved from: https://orkustofnun.is/gogn/Talnaefni/OS-2018-T006-01.pdf.

Park, C.B., Miller, R.D., Xia, J. 1999. Multichannel analysis of surface waves. *Geophysics* **64**(3), 800–808.

Park, D., Kishida, T. 2018. Shear wave velocity profiles of fill dams. *Soil Dynamics and Earthquake Engineering* **104**, 250–258.

Rahimi, S., Wood, C.M., Coker, F., Moody, T., Bernhardt-Barry, M., Mofarraj Kouchaki, B. 2018. The combined use of MASW and resistivity surveys for levee assessment: A case study of the Melvin Price Reach of the Wood River Levee. *Engineering Geology* **241**, 11–24.

Silver, M.L., Björnsson, B.J., Kiefer, T., Sharma, M., Kotsopoulou, E., Thomas, P. 1986. *Evaluation of the seismic safety of embankment structures of the Thjorsa and Tungnaa river basin development in Iceland, final report, Vol. 1-3*, Marshall Silver and Associates Ltd., Chicago, IL.

Thorlaksson, R., Olafsson, P., Jóhannesson, P. Asphalt facing for Icelandic dam. *International Water Power & Dam Construction*, **30**(8), 33–38.